The University Of Sheffield.

Department Of Mechanical Engineering

Modelling the Effects of Blast Loads in Rail Vehicles

Thomas James **ANTHISTLE**

August 2014

Supervisor: Dr D.I. Fletcher

Thesis submitted to the University of Sheffield for the requirements of the degree of Doctor of Philosophy

Summary

This thesis describes the development of modelling techniques to understand the effects of an Improvised Explosive Device on the passengers and structure of a rail vehicle. The work aims to establish if rail vehicle design could influence the distribution of passenger injuries within a rail vehicle. Finite element models were used to predict the detonation and propagation of the blast pressures, and the structural response of a rail vehicle.

Models were developed to allow the prediction of human injury, using validated work from the open literature and from basic principles. After a detailed review of existing work on injury, chest injury from blast pressures and penetrating injuries from high speed projectiles were chosen as the injury modes to be included in the model.

To provide data to validate numerical models, experimental blast testing in confined geometry was undertaken. Four configurations of a test cell were used to gain an understanding of the effect of vertical baffles on pressures and cumulative impulse. Excellent correlation was seen between test shots in each arrangement. Baffles were seen to increase the cumulative impulse seen at the wall opposite where they were fixed, although the number and spacing of them was seen to have no significant effect.

Numerical modelling of the experimental test arrangements showed good correlation between the experimental pressure time history data and the numerical predictions. Secondary combustion was considered using an energy release function, after which cumulative impulse calculated from experimental data were was predicted by the numerical models.

Risk prediction and finite element models were combined to model the effects of an IED blast in a representative rail vehicle. A number of key variables were studied, and it was identified that although rail vehicle design can affect the injury severity, passenger spatial density was the driver for determining the distribution of injuries.

Acknowledgements

Firstly, I would like to thank my supervisor David Fletcher. His support and guidance over the last 4 years has been invaluable, and our discussions over the past 5 years have no doubt made a hugely positive impact on me as an Engineer.

I would also like to thank the Departments of Mechanical Engineering for providing the primary funding for this work, as well as the Department of Civil and Structural Engineering for their part in organising and funding the experimental testing. In that respect, particular thanks go to Jonny Reay and Steve Fay, without whom the experimental testing would not have been the success it was, and to Andy Tyas for helping me gain a greater understanding of the experimental results. I also owe my gratitude to the technical staff in Mechanical Engineering (Dave and Gary), Civil and Structural Engineering and Blastech (Mark, Roy and Mik) for their support during preparation for experimental testing.

Finally, a thank you to the family, friends and loved ones, who have offered so much support and encouragement throughout.

Contents

Nomenclature[1]

Symbol	Description	Units
α_i	Angle of incidence	radians
α_r	Angle of reflection	radians
γ	ratio of specific heats	–
δ	displacement	m
θ_x, θ_y	angle from x or y axis	degrees
ν	Specific volume	m^3/kg
ρ	Density	kg/m^3
σ	Stress	Pa
σ^2	Variance	–
A	Area	m^2
C	Damping	Ns/m
c	Speed of sound	m/s
E	Elastic modulus	Pa
E, e	Internal energy	J
F	Force	N
i_{so}	Side on / incident impulse	kPa-ms
i_r	Reflected impulse	kPa-ms
K	Stiffness	N/m
L	Length	m
M, m	Mass	kg
p_a	Atmospheric pressure	kPa
p_r	Peak reflected overpressure	kPa
p_{so}	Peak side on / incident overpressure	kPa
$P(t)$, $p(t)$	Time dependent pressure	kPa
R, r	Distance from detonation centre	m
t_a	shock wave arrival time	ms
t_d	Positive overpressure phase duration	ms
U, u	Velocity	m/s
V, v		m/s
V_d	Detonation velocity	m/s

[1]Some symbols are used for multiple definitions in this work. The most commonly referred to meanings are included in this nomenclature.

W	Mass of explosive charge	kilogram (kg)
Z_{ij}	Acoustic impedance	Pa/m/s
Z	Scaled distance	$m/kg^{\frac{1}{3}}$

Abbreviations

Symbol	**Description**
AA	Aluminium Alloy
AIS	Abbreviated Injury Score
ALE	Arbitrary Lagrangian Eulerian
AMMG	ALE Multi Material Group
ASII	Adjusted Severity of Injury Index
BREL	British Rail Engineering Limited
C4	a common plastic explosive containing 91% RDX
CCTV	Closed Circuit Television
CPU	Central Processing Unit
CT	Counter Terrorism
DIC	Digital Image Correlation
DMU	Diesel Multiple Unit
DOP	Depth Of Penetration
DVM	Digital Volt Meter
EMU	Electric Multiple Unit
EOS	Equation Of State
FSI	Fluid-Structure Interaction
FSP	Fragment Simulating Projectile
GNU	a free and open source software project
HIC	Head Injury Criterion
IED	Improvised Explosive Device
IRA	Irish Republican Army
JWL	Jones-Wilkins-Lee
LDG	Laser Distance Guage
M10, M12, M20	Metric thread designations
MMG	Multi-Material Group

MPP	Massively Parallel Processing
(N)ISS	(New) Injury Severity Score
PBIED	Person Borne IED
PE4	Plastic Explosive, UK designation for explosive similar to C4
PVB	Polyvinyl Butyral
QSP	Quasi Static Overpressure
RDX	Research Department Explosive
SDOF	Single Degree Of Freedom
SMP	Shared Memory Parallel
TBI	Traumatic Brain Injury
TNT	Trinitrotoluene, a high explosive used as a reference
UNF	Unified thread standard, fine pitch
VBIED	Vehicle Borne IED
VF	Velocity Factor

1

Introduction

1.1 A threat to infrastructure and passengers

In recent years the perceived threat of terrorist attacks across the world has increased following several deadly mass casualty attacks throughout the world, including the UK and Europe. Terrorism is not a new threat in the UK, but increased public awareness in recent years is due to a handful of high profile attacks which caused many deaths and injuries, and a resulting international military response.

The UK was the target of an IRA terrorist campaign between 1969 and 1997, which caused widespread disruption but led to relatively few fatalities, as well the Lockerbie bombing in 1988 and London nail bombings in 1999. Attacks on the world trade centres in New York in September 2001 though, brought the threat of global terrorism and mass casualties into the public eye. The response to this, the global war on terror, has been played out extensively in the media and continues to provide a reminder of these attacks. The threat posed to the UK and Europe was confirmed in 2004 and 2005, with mass casualty attacks in both London and Madrid. Since 2001, there have been a number of terrorist attacks around the world, many of which have received considerable media attention.

Transport has historically been a target for terrorists, including aircraft hijackings (particularly between Cuba and the USA in the late 1960's and 1970's) and later bombings, demonstrated by the downing of Pan AM flight 103 in December 1988 (the Lockerbie bombing). Aircraft were still hijacked in the September 2001 attacks in the USA, after which physical security on aircraft was improved further [1]. In the wake of a plot to detonate liquid explosive on aircraft in 2006 [2], restrictions were placed on liquids, prompting a further change in tactics, evidenced by a plot to detonate printer bombs [3], which were intercepted in the UK. It can be seen that bombing has become the major threat, with aircraft security constantly adapting to the threat.

For aircraft, the tactics of the terrorists have changed as security procedures have altered in reaction to previous attacks, but aircraft style security is not easily applicable to the rail system, especially in the UK. The perimeter security used at airports is not feasible on the rail system, which is much more open, and for each train there is a much higher turnaround of passengers, much shorter journeys, and the system as a whole, and each journey, has many more entry and exit points. There have been a number of attacks on the rail system in recent years, most of which follow the same bombing tactic,

facilitated by the open nature of the rail system. The most notable, from a European perspective, occurring in Madrid in 2004 and London in 2005, were responsible for the deaths of 191 and 52 members of the public, respectively. Since then, other deadly attacks have occurred on the rail system in Mumbai (July 2006), the Moscow Metro (March 2010), Minsk Metro (April 2011) and Volgograd railway station (Dec 2013). If potential attackers are not identified during the planning stage of an attack, it is difficult to prevent a potential attacker entering the system and carrying out an attack. If they do enter the system, the only way to reduce the overall impact of an attack may be to limit physical effects and improve resilience of the system itself by ensuring stations and rail vehicles have been designed with these risks in mind.

When a terrorist attack occurs, its effects are not limited to human injury and material damage. The ability of a system to recover quickly and return to the state it was in prior to an attack is also vital in determining the overall impact of an attack. The ability of a system, such as a rail network or metro system, to resist physical effects and return to normal operation in the wake of a terrorist attack can be termed its resilience. Improving the resilience in the wake of an attack requires knowledge, or an accurate prediction, of the effects that terrorist device is likely to have. In most historical cases of attacks on the UK's rail system, this is an explosive device of a size that a person can carry in luggage such as a rucksack, or attached to the body. Knowing this, the physical effect of an explosive device on the structures and people in the area surrounding the point of detonation can be predicted, and this information can then be used to help improve resilience and reduce harm to people. To investigate this, the following hypothesis is posed, with the description of the process by which it is tested shown in Section 1.2.

> "Rail vehicle design can influence the pattern of injury seen in passengers when an improvised explosive device is detonated within a rail vehicle."

1.2 Structure of this work

A test of the hypothesis above is undertaken in this thesis by breaking the problem down into 6 stages, described over Chapters 2 to 7 along with concluding remarks and recommendations of further work in Chapter 8, each building upon the last to develop techniques to investigate blast loading in rail vehicles.

Chapter 2 reviews existing work on terrorism and terrorist attacks worldwide, as well as covering pertinent theory on high explosives and shock waves, the finite element method and the design and construction of rail vehicles.

The risk to humans from blast and projectile loading has been widely studied, which is described in greater detail in Chapter 3. Risk models exist for injuries due to blast and high speed fragments and projectiles, which range from simple pressure thresholds or projectile velocities, to more complex models that use pressures and impulse to predict the velocity of the chest wall, or those that predict the depth of penetration of projectile into the body. A comparison of these risk models using experimental or numerical data has not been previously undertaken and is important to identify which models are most appropriate to be used to identify the risk that explosions, fragments, debris and projectiles pose to passengers of a rail vehicle. Chapter 3 covers specific literature on the prediction of injury patterns from IEDs. Existing techniques are reviewed and their appropriateness to the current work is discussed, as well as the applicability and

maturity of the techniques. A strategy for predicting injuries from IEDs in rail vehicles is developed using a combination of GNU Octave and LS-Dyna.

Chapter 4 introduces the finite element modelling techniques to be applied using LS-Dyna, and undertakes verification of the modelling method using empirical data from ConWep [4], and identifies the important parameters that guide the future modelling activities.

Chapter 5 presents experimental methods and findings of high explosive detonations in a confined test cell using quarter symmetry. Tests were conducted in a rigid test cell using baffles inside to alter the reflections of pressures within the cell, and these pressures were recorded for use in model validation. Tests were also conducted using a flexible structure in the centre of the test cell, where displacement data was gathered from a central point on the panel. A total of 4 different test arrangements were investigated as part of this work, with sensors moved in each test to build up a clear picture of the propagation of shock waves within the structure. The experimental technique was on the whole successful, and suggestions are given for improvements to the experimental technique for future researchers.

A fundamental test of the accuracy of any numerical model is comparison with data gathered from experiments or from first principles. Previous work has either not provided any model validation at all, or the validation of numerical models has been limited. Validation does not need to be done with full scale models or a physical version of the structure to be modelled but should seek to test the fundamental principles of the numerical modelling methods. This can be done with simple experimental tests that use scaling and symmetry to reduce the size and cost of the experiment and importantly, are easier to control and produce repeatable data from than complex full scale experiments. Chapter 6 presents numerical models using LS-Dyna of 4 different experimental test arrangements. The effect of afterburn was considered during the modelling using a simplified method.

Chapter 7 uses the techniques from Chapters 3 and 6 to investigate the effect of structure, confinement, design, internal features, and passenger density using 9 cases of a rail vehicle subjected to an IED attack. Existing finite element models based on the geometry and construction of representative vehicles which are currently in service on the network have been produced by the vehicle manufacturer and were adapted for use in modelling the effects of blast loading from explosive devices. An in depth analysis on the critical variables is produced, discussing both the effects on individuals within a vehicle and to the whole population of passengers within a rail vehicle.

Finally, Chapter 8 presents the findings of this work, together with potential areas of improvement to experimental testing methods, numerical modelling and risk prediction tools. Areas of interest for future research are also suggested, along with the implications of this research.

2

Literature Review and Theory

2.1 Terrorism and the rail system

The term 'terrorism' has very much become part of everyday vocabulary, particularly since the world trade centre attacks in 2001, but terrorism has existed for hundreds of years and has been used as a political tool throughout the last century. The recent awareness of terrorism has come about in part due to the US led global "war on terror", as well as several high profile attacks around the world that have enabled people to picture a stereotypical terrorist. Importantly for those researching terrorism and measures to counter it, they must have a clear idea about what it is, what it is trying to achieve and by what methods. Terrorism can be difficult to define, and Record [5] explains how terrorism is often defined *by* states as non-state violence and threats of violence towards states and society, and how this can potentially legitimise state terrorism against it's members if they are referred to as terrorists. It is outside the scope of this work to embark upon a thorough definition of terrorism, but some key features of a definition are required. The Oxford English Dictionary defines terrorism [6] as:

> "The unofficial or unauthorized use of violence and intimidation in the pursuit of political aims; (originally) such practices used by a government or ruling group (freq. through paramilitary or informal armed groups) in order to maintain its control over a population; (now usually) such practices used by a clandestine or expatriate organization as a means of furthering its aims."

For a terrorist or terrorist attack to achieve maximum effect, violence or threats of violence need to create maximum disruption or casualties, which often means public areas with a high density of people and important pieces of national infrastructure. This means that hotels (Mumbai, 2008 [7]), bars and tourist locations (Bali, 2002 [8]), restaurants, transportation systems (London 2005 [9], Moscow 2010 [10]) and areas of economic importance (World Trade Centre, 2001 [11]) are potential targets, as described in reports detailing trends in terrorism [12, 13]. Rail vehicles and rail infrastructure have been targets in the past, as they are often of vital economic and social importance to the cities which they serve.

Terrorist attacks have historically occurred infrequently in the UK (although historically, up the year 2000, the UK was frequently targeted by the IRA and allies), but

despite their low frequency, the level of disruption, climate of fear [14] they create in society and the economic harm they cause can be very high. The biggest threat to the rail system, both to infrastructure and passengers comes from targeted bombing of the vehicles themselves, as identified by Powell and Fletcher [14] based on data from terrorist attacks between 1998 and 2004. Notable examples of terrorist attacks on rail networks that have been widely reported in the news, in Moscow [10], Mumbai [15], Madrid [16] and London [9], have all been caused by bombs on vehicles.

Rail systems have unique features which often make application of security systems and methods developed for use in other types of transit and public spaces unsuitable. The perimeter security model of airports involves a large number of checks and requires scanning of all luggage and presentation of photo identification before an individual can access an aircraft, but this would be impractical on the rail network (described by TfL officials in [17]). The rail network has a very high number of entry and exit points (particularly metro systems such as the London Underground), and such a variable flow of passengers over short periods of time that airport style perimeter security would severely impair the smooth running of the system. It would be unlikely to be viable in terms of both installing and operating the system, and the delays it would cause given the limited frequency of such attacks.

Rail systems are very interconnected, so termini are often used for intercity, suburban and metro systems and as a result the number of passengers that use such stations is very great. In busy cities, where urban light rail such as the London Underground are the backbone of public transport, passenger numbers are similarly high. By their nature, termini are crowded places where there are predictable peaks in density of the crowds, which can potentially aid somebody who looks to create a large amount of disruption. As such rail systems can present an attractive target and pose unique problems for those who look to prevent attacks from happening, or how to best recover from one.

2.1.1 Combating terrorism

Terrorism by its nature is unconventional and unpredictable, which means that combating it requires unique and wide ranging measures. In the UK, the Home Office has developed the CONTEST [18] strategy for countering terrorism, which comprises 4 key objectives; to pursue, prevent, protect and prepare. The pursue and prevent objectives deal with identifying, investigating, disrupting and prosecuting those who may look to carry out a terrorist attack and preventing individuals being drawn into terrorism. The protect and prepare objectives involve reducing the vulnerability, strengthening protection, reducing risk, mitigating the effects of a terrorist attack that has been carried out as well as improving resilience.

Much research has been done to improve the design and technology of buildings and public spaces to reduce the likelihood of a terrorist attack. Initial attempts at designing against terrorism in the UK, such as the ‘ring of steel’ in the City of London, had a fortress like approach involving extensive use of concrete barriers, CCTV and significant access restrictions, that were not the most elegant or holistic solutions; in the wake of the September 11th terrorist attacks in the USA, this fortressing of London, with hardened areas and visible security was markedly increased [19]. Recently, there has been efforts to improve urban design by incorporating counter terrorism (CT) features into the initial design, which can both reduce the cost of implementing CT features

and improve the aesthetics, compared to retrofitted CT measures [20] such as concrete fortifications. Systems for designing against crime and terrorism have been championed by the government and police, such as the Home Office Crowded Places documents [21] and the Secured by Design [22] initiative.

Much of the recent work described above is designed with attacks from vehicle borne improvised explosive devices (VBIEDs) in mind, which are a threat where vehicles can gain access or get close to a building or space; by preventing vehicles getting close to a potential target site the threat can be reduced. Countering the terrorist threat from person borne IEDs (PBIEDs) is inherently more difficult, as humans are not restricted by roads, are more mobile and can access open public spaces freely. The focus to date has been on reducing locations to hide devices (such as removing bins from stations), improving lighting and sight lines for CCTV and intelligent CCTV technology, as well as using strengthened and improved materials [17, 14]. Importantly, these developments and any proposed future developments should be cost effective, or provide improved performance in various circumstances such as crime or passenger congestion, as the financial and risk reduction case for exclusively designing for a low frequency terrorist event are difficult to make.

The *prepare* objective of CONTEST concerns mitigation of the effects of terrorist attacks, as well as planning the response to terrorist attacks. It is economically vital to get any systems subject to a terrorist attack up and running under a normal service as soon as possible [23], which can be achieved through thorough planning. Perry [24] suggests one of the first guiding principles of emergency planning is accurate knowledge of the threat and likely predictions of human response [24], which can be achieved through studies of the interaction of certain threats with persons and their surroundings. Designs to mitigate the effect of explosions should be proportionate to the threat, as well as not adversely affecting the usability of a service or space, whether it be a public building or a moving vehicle. In the context of a rail vehicle, this prevents bomb proofing that would add unnecessary weight and features that would reduce passenger comfort or safety.

Combating terrorism on the rail network and in rail vehicles is by no means simple, and there are many challenges to be overcome if features are to be added to rail vehicles in the name of security and counter terrorism. One part of this can be predicting the likely effects of a blast, both to aid future design and assist planning and readiness in case terrorists strike. In the current project, the focus is on rail vehicles.

2.2 Explosions, explosives and shock waves

2.2.1 Shock waves

Shock waves are propagating disturbances in a medium that travel at supersonic speeds. They are typically characterised by very sharp rises in pressure and density between the unshocked regions and the region immediately behind the shock wave. The rises are so sharp they are often considered as discontinuities and across a very small region either side of the shock wave, the thermodynamic parameters are seen to jump [25]. Equations describing these jump conditions in 1D are based on conservation laws of mass, momentum and energy and derivations are found widely in the literature [26, 25]. The jump conditions describing the relationship between properties on either side of a shock wave (Figure 2.1) are shown in equations (2.1) (2.2) [26]. The property v_i is the

relative velocity, where $v_i = (u_i - U)$, the internal energy per unit mass is e_i and ν_i is the specific volume.

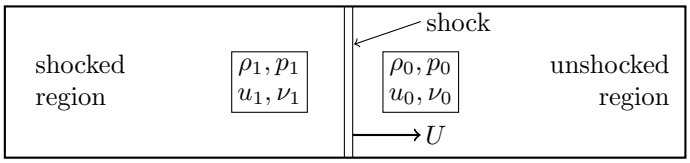

Figure 2.1: One dimensional shock in a tube

Shocks can be termed as weak or strong depending on the size of ratio's such as the shock strength p_1/p_0 and the excess pressure ratio $(p_1 - p_0)/p_0$. The lower limit of a weak shock can be seen to be a sound wave, which travels at sonic velocities [26], but weak shocks are generally considered to have a shock strength slightly over 1 and excess pressure ratio that is small, although a precise definition of the level at which shock waves are no longer 'weak' is generally not specified. Strong and weak shocks also behave radically differently when reflected, which is discussed in more detail in Section 2.2.1.1.

A combination of equations (2.1), (2.2) and (2.3) (derivations can be found widely in the literature in the same form [26, 27]) leads to the Hugoniot relation (2.5). The Hugoniot equation describes all the points p, ν that satisfy the conservation equations shown above, that is, when values of p_1, ν_1 for a given p_0, ν_0. The Hugoniot relation can be used to determine the conditions for detonations, and also to determine possible thermodynamic states a material can exist in behind a shock.

$$\rho_0 v_0 = \rho_1 v_1 \tag{2.1}$$

$$p_0 - p_1 = \rho_1 u_1 v_1 - \rho_0 u_0 v_0 \tag{2.2}$$

$$\tfrac{1}{2} v_0^2 + e_0 + p_0 \nu_0 = \tfrac{1}{2} v_1^2 + e_1 + p_1 \nu_1 \tag{2.3}$$

For the case that $u_0 = 0$ (shock moving into stationary medium) and using Equation (2.1), (2.2) becomes:

$$p_1 - p_0 = \rho_0 u_1 U \tag{2.4}$$

$$e_1 - e_0 = \tfrac{1}{2} (p_1 + p_0) (\nu_0 - \nu_1) \tag{2.5}$$

2.2.1.1 Reflection

Shock waves, as with other waves, can be reflected (as well as refracted and diffracted) when they meet discontinuities and changes in the medium they travel through. This could be a solid object, or changes in mediums properties such as density, which may be due to a boundary between two materials (such as a liquid and a gas) or meeting a shock wave travelling towards it.

Normal reflection is the simplest type of reflection and occurs when a shock wave, moving perpendicular to a flat and rigid surface, is reflected and changes direction by

180°. At their lower limit, when weak shock waves are reflected, the ratio of excess pressures (2.7) between atmospheric (p_0), incident (p_1) and reflected pressures (p_2, covered in more detail in section 2.2.1.1) is roughly equal to 2 (i.e. the shock strength is doubled), in agreement with sonic reflection [26]. Strong shock waves, which have a very large shock strength, see significant increases in the strength of the shock when it is reflected, with excess pressure ratios of 8 for gases where $\gamma = 1.4$ (such as air [28]). From Equations (2.6) and (2.7) it is clear that for normal reflection, the value of the reflected pressure p_2 is a factor of incident and atmospheric pressure, and the ratio of specific heats, γ .

$$\frac{p_2}{p_1} = \frac{\left(2\mu^2 + 1\right)\frac{p_1}{p_0} - \mu^2}{\mu^2 \frac{p_1}{p_0} + 1} \tag{2.6}$$

$$\frac{p_2 - p_0}{p_1 - p_0} = 1 + \frac{1 + \mu^2}{\frac{p_0}{p_1} + \mu^2} \approx 2 + \frac{1}{\mu^2} \tag{2.7}$$

$$\text{where} \quad \mu^2 = \frac{\gamma - 1}{\gamma + 1}$$

Regular reflection is reflection of a shockwave at an oblique angle, which results in separate incident and reflected waves propagating from the surface. Consider an incident oblique wave, as shown in 2.2, moving at angle α_i impinges on a solid surface. A reflected shock wave is set up at an angle α_r and moves independently of the incident shock, and the two waves only meet at a point on the reflecting surface. For weak shocks at their lower limit, the angle of reflection α_r is equal to the angle of incidence α_i, but as the strength of the shock increases, the relationship between α_i and α_r changes, as shown in 2.3 and deviates increasingly from the linear relation seen for weak shocks. Combinations of angles where regular reflection occurs for a given shock strength are shown as solid lines; it is clear that as shock strength increases, the range of incident angles that result in regular reflection decreases. Regular reflection happens readily for weak shocks, but for strong shocks, regular reflection can only occur when angles are small and approach normal reflection. When angles are higher and tending towards movement parallel with the reflecting surface, a phenomenon known as mach reflection occurs.

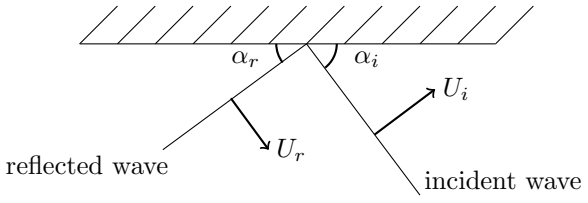

Figure 2.2: Incident and reflected plane shock wave

For each value of incident pressure, there is an angle α_{ext} which determines the limit for regular reflection. When the angle is greater than α_{ext}, i.e. the shock travelling *more* parallel to the wall, mach reflection occurs. Mach reflection occurs when reflected wave skims off reflecting surface and immediately begins to merge with incident wave. The reflected wave can have a higher speed and different angle of travel, so begins to catch up with incident wave; the meeting begins at wall but moves away into space as more of the reflected wave catches up with incident wave, known as the triple point. Between the triple point (Figure 2.4) and the reflecting surface, a mach stem occurs

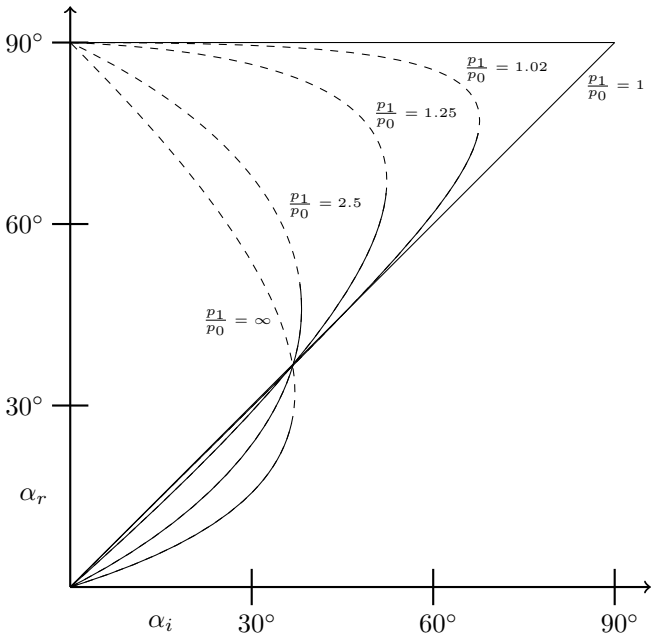

Figure 2.3: Relationship between angle of incidence, α_i, and angle of reflection, α_r for regular reflection of shocks at $\gamma = 1.4$ [29]. Combinations of angles with dashed lines not achieved in reality

and on the other side of the triple point, regular and incident waves exist separately. A contact discontinuity, shown by the dashed line labelled CD in Figure 2.4, separates the air undergoing shock from the mach stem from that shocked by the incident and reflected wave. Mach reflection is an example of interaction between shock waves, a process that has important consequences for confined environments, where there can be a number of shock reflections from various surfaces that interact with each other, as well as interaction between shock waves and discontinuities in the medium through which they travel.

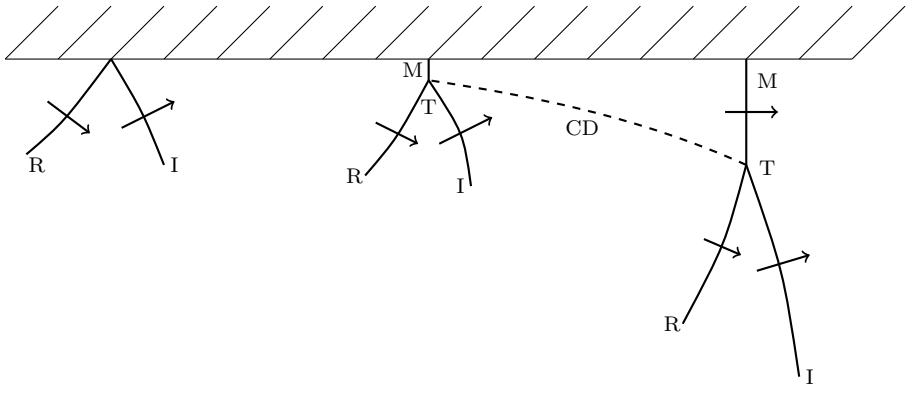

Figure 2.4: Development of a Mach stem

For shock waves meeting boundaries between media, two waves are set up when the shock meets the interface, a transmitted and reflected wave, shown schematically in Figure 2.5. A shock wave is transmitted, but the reflected wave can be either a shock wave or a rarefaction (expansion) wave, depending on the ratio of shock impedances (2.8) [30, 31]. If the ratio of shock impedances of the transmitted and incident shocks

(Z_{01}/Z_{45}, see Figure 2.5) is greater than 1 a shock is reflected, but if this ratio is less than 1 a rarefaction wave is transmitted. For the simplest case of interaction between two shocks, when two symmetrical waves meet moving towards each other normally, two shock waves result moving away from the contact point as if they were normally reflected by a rigid surface at this point, and the relations (2.1) – (2.3) stand. For analysis of interactions between shocks and interfaces, problems are typically solved numerically [32].

$$Z_{ij} = \rho_j c_j \sqrt{1 + \frac{\gamma - 1}{2\gamma}\left(\frac{p_j}{p_i} - 1\right)} \tag{2.8}$$

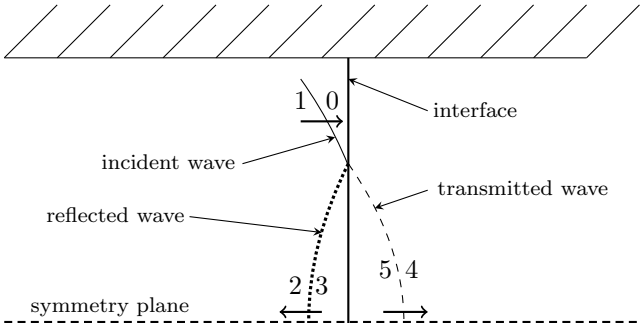

Figure 2.5: Transmission and reflection at interfaces

2.2.1.2 Spherical waves

Many relationships above make assumptions about processes, such as being 1D, isentropic and the fluid in question being an ideal gas etc, to simplify the problem and arrive at analytical solutions. In the reality, processes do not always adhere to these mathematical assumptions; blast waves are three dimensional, and assumptions of ideal gas and constant entropy not always correct. Despite this, the relationships above are useful to get an appreciation of the complexities of dealing with shock waves.

In 1D, a shock wave maintains a finite size and energy is dissipated through frictional and viscous means. In 3D, the size of the shock wave is ever increasing with distance from the point of detonation, r, and would require a constant and increasing input of energy to maintain the same strength. In reality a finite amount of energy is produced during the detonation, so as the size of shock increases the energy available in the shock to do work and compress the fluid decreases, and the peak pressure in the shock wave decreases rapidly with increasing r. This rapid decay decrease in shock strength leads to a corresponding decrease in change of entropy, such that flow behind the shock is no longer isentropic [26]. General analytical solutions for spherical waves do not exist and therefore problems are typically solved numerically, such as by Brode [33].

Explosions are rapid releases of energy, and in most cases on earth are caused by rapid and extreme heating, vapourisation or production of gas from a chemical reaction. Explosive materials cause explosions by the latter, releasing energy by a rapid chemical reaction that produces large volumes of high temperature gas. Explosives can be further categorised as high or low explosives; low explosives release their energy by deflagration,

where the chemical energy is released by a flame front that propagates through the explosives at subsonic speeds. Energy is released from high explosives by a shock wave that propagates through the material at supersonic speeds (referred to as the detonation velocity V_d, 6-8.5 km/s for high explosives), releasing the stored energy much more quickly than low explosives.

To get useful energy from low explosives they need to be confined throughout the whole chemical reaction, but they burn for long times in comparison to high explosives so are useful as propellants, in artillery shells for example. High explosives develop much higher pressures and lead to strong shock waves propagating though air, or when in contact with solid materials set up intense stress waves that can lead to rapid failure of even very thick and strong materials. The pressures generated at the surface of the explosive, which are typically in the region of several GPa, are usually far in excess of the pressure required to cause failure; when materials are subject to such loads, where the forces on them far exceed their strength, material density becomes the dominant material parameter and its behaviour is referred to as hydrodynamic.

$$P(t) = P_o \left(1 - \frac{t}{t_d}\right) exp\left(\frac{-bt}{t_d}\right) \tag{2.9}$$

Second shocks are a feature of spherical and cylindrical shocks, their approximate form shown in Fig 2.6, with S_1 showing the main shock front and S_2 showing the second shock. Their existence has been known since the first theoretical and experimental studies, but either for simplicity of lack of awareness are not commonly included when the Friedlander curve (from Equation (2.9)) is plotted. They are of small magnitude compared to the initial shock wave, and consequently are more commonly found at small scaled distances (see Section 2.2.2 for a description of scaled distance). They are formed by interactions between the negative pressure gradient rarefaction waves following the main shock and the positive gradient of the gases closer to the centre of detonation. The formation of second shocks is described in detail by Brode [33], experimental work Boyer [34] and theoretical work Friedman [35] and is a necessary feature of the 3D expansion waves. The second shock begin initially as a weak outwards travelling discontinuity that increases in magnitude, before collapsing back towards the centre of detonation and reflecting as an outwards travelling shockwave.

2.2.2 Explosions and explosive materials

If the pressure at a single point in a free field is measured when a high explosive is detonated, a characteristic curve is produced, shown in Figure 2.7. There is a sharp, almost instantaneous rise to peak overpressure, p_s, which is caused by the arrival of the front of the shock wave. A rarefaction wave follows the shock wave and leads to an exponentially decaying pressure, and this rarefaction wave typically over expands the gases, which causes the pressure to fall below atmospheric pressure before it returns to its pre shocked value.

The parameters that define each shock, such as peak overpressure p_s, cumulative impulse i_{pos}, arrival time t_a, and positive phase duration t_d, can be related for charges of different masses and stand off by a value known as the scaled distance, Z, defined in equation (2.10). The quantity R is the distance from the point of detonation, and W

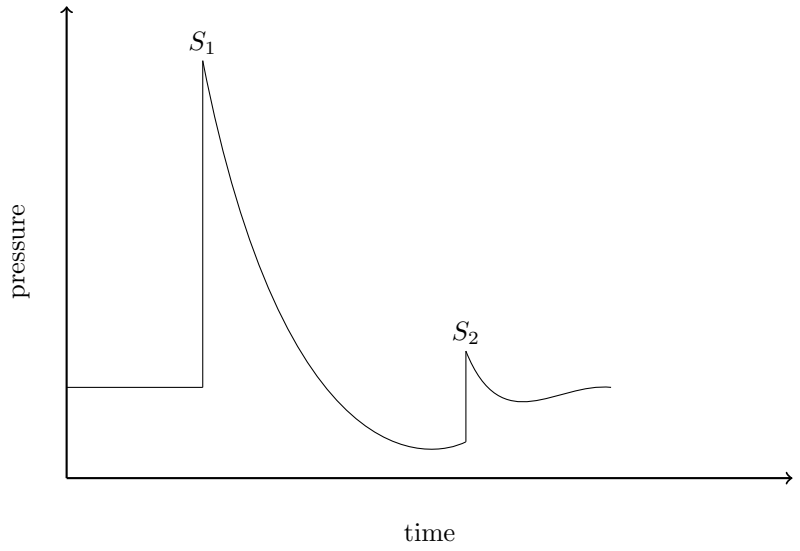

Figure 2.6: Appearance of second shock in pressure history

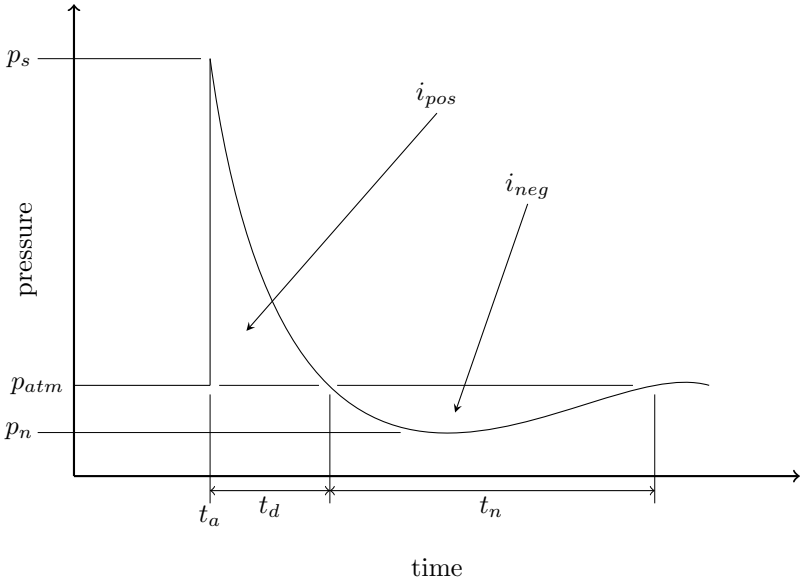

Figure 2.7: Typical pressure profile for a blast in free air

is the explosive mass. Values for shock wave parameters for a given scaled distance are given in Figure 2.8 for a free air blast using TNT, which shows that all charges of the same scaled distance have the same absolute peak pressures, and the same scaled impulse and time quantities. It is also possible to see from the scaled distance chart in Figure 2.8, that arrival time and positive phase duration are only functions of scaled distance and do not change between free field and reflected pressures at infinite rigid surface. Scaled distance charts such as Figure 2.8 are useful as they can provide a huge amount of data on a single chart, which can describe most charge and standoff combinations that are likely in reality. Scaled distance curves are based on data from a large number of experiments carried out with TNT charges, and along with the widespread use of TNT in research into explosive effects in the mid to late 20th Century which forms much of

the body of knowledge still referred to today, TNT is the reference explosive to which others are often compared. This is most commonly done by the use of mass equivalence; that is, the multiplication factor required for a given mass of non TNT explosive that gives a mass of TNT which produces identical blast wave parameters. For most plastic explosives such as PE4 and C4, a TNT equivalence of 1.2 has been found to be correct [36].

$$Z = \frac{R}{W^{1/3}} \tag{2.10}$$

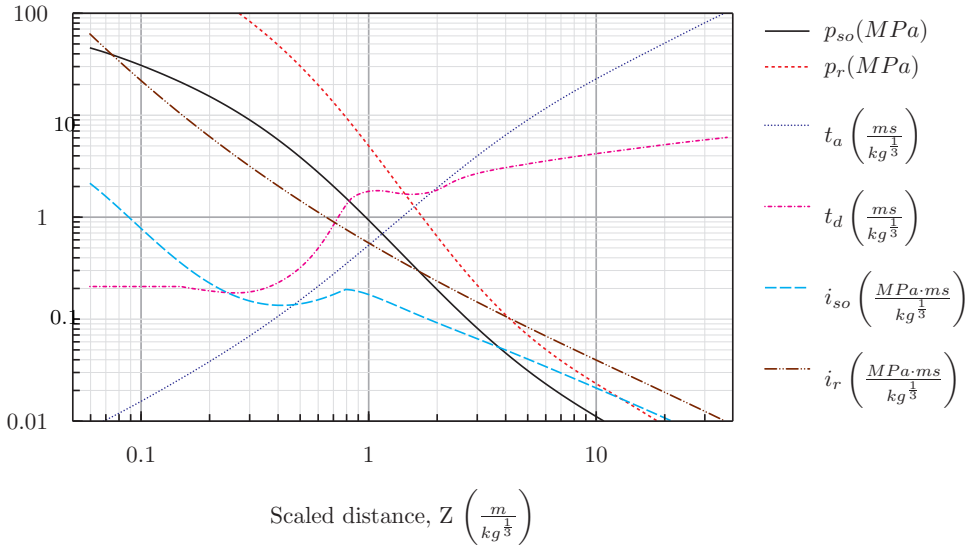

Figure 2.8: Shock wave parameters versus scaled distance for a free air blast of TNT

For the simple case of free air and surface bursts, the side on and reflected pressures on large rigid targets, as well as impulses and time have been well documented and parameters for most conceivable situations exist, in curves such as Figure 2.8 [37] and programs like ConWep [4]. When targets are finite in size, it is possible that edge effects can alter the pressure experienced over the structure and cause the pressure history to deviate significantly from that seen for simple or ideal circumstances. The interaction between pressures experienced on the face of a target and the edges is known as clearing and leads to an early and sharp drop away from the Friedlander curve during the positive phase, as shown in Figure 2.9. When a shock wave is incident on a finite target, it is reflected from the face of the target, but at the edges of the target, the shock continues undisturbed past the target. The interaction between these different movements of shock waves leads to a rarefaction wave that travels from the edges towards the centre of the target and relieves the pressure, leading to a sudden drop.

Although methods have been produced to determine clearing effects analytically, they are often only applicable under certain criteria. Tyas *et al.* [36] have applied a method developed by Hudson [38] that assumes that shocks are plane and weak (which limits the method to larger scaled distances), as well as long targets where effects from the back face can be ignored. Rigby *et al.* [39] used SDOF models to investigate the effects of clearing, and found that when the period of loading is significantly different to the natural period of the target, much lower values of peak displacement are seen compared

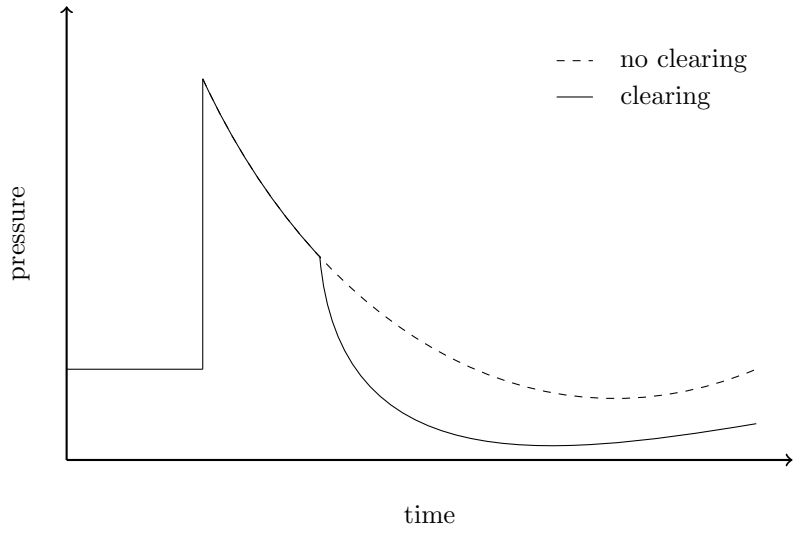

Figure 2.9: Influence of clearing on pressure history

with not considering clearing. For the situation where natural period and loading period are comparable, greater peak displacements were observed. Smith *et al.* [40] conducted experimental tests to determine the effects of clearing. They found clearing effects more noticeable at the edges of targets, and also that at large scaled distances the effects of clearing are smaller than at small scaled distances. It is important to note the authors struggled to achieve good repeatability, and that their conclusion that ConWep produces conservative estimates and is therefore satisfactory for design purposes, is in contradiction to the findings of Rigby *et al.* [39].

2.2.2.1 Secondary combustion: Afterburn

Common high explosives such as TNT and RDX contain large amount of nitrogen, which is liberated on decomposition when much of the solid explosive is turned almost instantly to high temperature gas, and examples of typical decompositions are given in (2.11), (2.12) [27] and (2.13). When the gas is produced during the detonation, it is under extreme pressure and expands very rapidly, compressing the surrounding air and producing a shock wave in the air, which propagates away from the point of detonation.

$$\text{Nitroglycerine: } C_3H_5N_3O_9 \longrightarrow 3\,CO_2 + 2{\cdot}5\,H_2O + 1{\cdot}5\,N_2 + 0{\cdot}25\,O_2 \tag{2.11}$$

$$\text{TNT: } C_7H_5N_3O_6 \longrightarrow 3{\cdot}5\,CO + 3{\cdot}5\,C + 2{\cdot}5\,H_2O + 1{\cdot}5\,N_2 \tag{2.12}$$

$$\text{RDX: } C_3H_6N_6O_6 \longrightarrow 3\,CO + 3\,H_2O + 3\,N_2 \tag{2.13}$$

Many explosives have an oxygen deficiency, the common high explosives RDX and TNT are examples, and the decomposition equation for RDX (2.13) shows CO is produced due to this incomplete reaction. This oxygen deficit indicates that additional energy is available to the reaction if there is sufficient available oxygen from other sources, such as surrounding air. The afterburn reaction happens once the decomposition of the explosive is complete and the shock wave has begun to propagate away, and relies on oxygen being drawn in and mixing with the hot products of detonation in the resulting fireball behind the shockwave. As a result, the extra energy that can be liberated does

not contribute to the magnitude of the air shock, but can increase the total impulse compared with an equivalent mass of explosive with a positive oxygen balance such as nitroglycerine (2.11) [41, 42]. Edri *et al.* [43, 44] found that there was significant under prediction of long term cumulative impulse when afterburn was not considered, compared to numerical predictions which included afterburn and experimental results, but quantitative discussion on the effects of afterburn are not given.

When a chemical reaction happens, such as combustion of a hydrocarbon, there is a difference between the enthalpy of formation for the reacted and unreacted products known as the heat of reaction, which determines the energy released or consumed during the reaction. For a reactant subject to a complete combustion, where all products are completely combined with oxygen until they reach their most oxidised state, the energy released is a special case of the heat of reaction, known as the heat of combustion. When an explosive detonates, the energy released during the decomposition (such as that shown in 2.13), not including any secondary reactions of the explosive or its products, is known as the heat of detonation. When explosives do not contain sufficient molecular oxygen to oxidise all products completely, they are known as underoxidised, and they can have a heat of detonation that is significantly lower than the heat of combustion. The difference between the energy released during detonation, the heat of detonation, and the heat of combustion of an explosive is known as the heat of afterburn [45]. This can be calculated from the differences in the heat of formation of the reactants (the underoxidised products of detonation) and their products once oxidation has taken place. The relations in Equations (2.14) and (2.15) are the afterburn reactions for TNT and RDX which show how the products of detonation are oxidised. The heat of afterburn can be calculated from these equations using Equation 2.16. Using equations (2.15) and (2.16), the heat of afterburn can be calculated using heats of formation from [28] as shown in (2.17) for a molar mass of 222.117 for RDX.

$$\text{TNT: } 3 \cdot 5\,\mathrm{CO} + 3 \cdot 5\,\mathrm{C} + 5 \cdot 25\,\mathrm{O_2} \longrightarrow 7\,\mathrm{CO_2} \tag{2.14}$$

$$\text{RDX: } 3\,\mathrm{CO} + 1 \cdot 5\,\mathrm{O_2} \longrightarrow 3\,\mathrm{CO_2} \tag{2.15}$$

$$\Delta H_r^0 = \Sigma \Delta H_f^0(\text{products}) - \Sigma \Delta H_f^0(\text{reactants}) \tag{2.16}$$

$$\begin{aligned} \Delta H_{AB}^0 &= \Sigma \Delta H_f^0(\mathrm{CO_2}) - \Sigma \Delta H_f^0(\mathrm{CO}) \\ &= 3(-393.520) - 3(-110.530) \\ &= -848.97 \text{ kJ/mol of RDX} \\ &= -3.82203 \times 10^3 \text{ kJ/kg} \end{aligned} \tag{2.17}$$

$$\text{for TNT with } M = 222.1169 \text{ g/mol} = 4.502 \text{ mol/kg}$$

Daily [46], Togashi *et al.* [47], Alves *et al.* [48] and Pope [49] have all described numerical models which include the effects of afterburn, all using a standard equation of state, the Jones-Wilkins-Lee or JWL (described later), to describe the pressure of the detonated products, with a time dependent energy addition term used to account for the afterburn. This time dependant energy addition is calculated for each explosive

case, with highly oxygen deficient explosives such as TNT (see Equations (2.12) and (2.14)) providing more afterburn energy than less oxygen deficient explosives such as RDX (Equations (2.13) and (2.15)).

Alves *et al.* [48] describe a new Jones-Wilkins-Lee (JWL) equation of state (EOS) incorporating afterburn using the form shown in Equation (2.18). The JWL equation in its normal form (see Equation (2.36) in Section 2.3.4) will give the pressure purely as a result of the energy release from detonation, but the modified form in Equation (2.18) gives the pressures from both detonation and afterburn, P_{d+ab}. This is done by simply adding an additional energy term, E_{ab}, divided by the relative volume, v, and incorporating a time dependency function, $Y_p(t)$ to give a time dependent pressure term due to afterburn. This can be implemented in software codes by either adding this extra energy to the afterburning material as a separate function to the detonation process, or modifying the numerical routine for the JWL EOS to include this extra term, and including it as a subroutine within the code.

$$P_{JWLa} = P_{JWL} + \frac{E_{ab}}{v} Y_p(t) \tag{2.18}$$

2.2.2.2 Gas pressures and venting

When explosions occur within confined structures, the confinement of the products of the explosion and any subsequent combustion can lead to the development of significant quasi static gas pressures (known as QSPs), which can in some circumstances be the dominant loads on these structures [50]. Pressure profiles in confined spaces are more complex than simple free air overpressure curve in Figure 2.7, as demonstrated in Figure 2.10. Two separate phenomena are seen on a pressure time history when explosions occur in confined environments; there are a number of reflections of the shock, characterised by a number of sharp pressures rises followed by a decay, and a QSP, where the rate of decay is slow compared to the positive phase duration of the reflected shock waves. This maintained pressure, shown in Figure 2.10, occurs when the products of the explosions can't escape quickly from the structure, and a higher volume of gases exist and create a high pressure. The magnitude and rate of decay of the QSP can be affected by the volume of the confining geometry and the presence and size of any orifices which can 'vent' the pressures to atmosphere. The behaviour of QSPs can also be affected by afterburn, which can continue to release heat energy slowly and increase the QSP compared to an equivalent charge with no afterburn [51].

It is common in process industries and in offshore installations to use blast relief panels to mitigate the effect of explosions [52], by failing rapidly and preventing significant build up of QSPs, which could lead to structural damage. In gas explosions, venting with blast relief panels can significantly reduce the peak gas pressure [50, 53, 54], but when high explosives detonate, the peak QSP is seen to be a function of the charge mass and enclosure volume, and is independent of vent area [4, 55]. Explosions in process industries and offshore applications are often caused by the deflagration of gas, vapour and dust, which have significantly lower flame speeds than high explosives. The flame in gas and dust explosions also has to propagate through the fuel mixture [56] domain for all the energy to be released, whereas with a high explosive the initial energy release is almost concentrated at a point. With high explosives there is a need for the

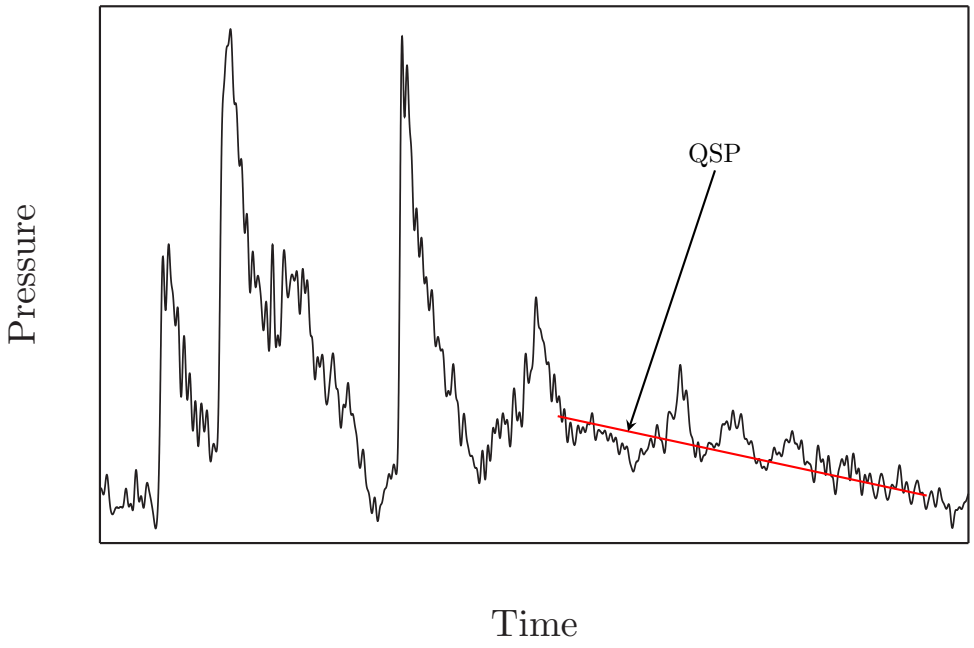

Figure 2.10: Example of reflections and development of a QSP

explosive products to expand into the confining volume, and with the effects of afterburn considered, high explosives can produce gas pressures with similar pressure time features to slower burning deflagration explosions.

2.3 Finite element method

The numerical models described throughout this work rely upon one of the most commonly used and widely applied analysis tools in engineering, the finite element method. The finite element method can be applied to a huge variety of problems, such as magnetic and electric field problems and heat transfer, but the focus in this work will be on determining structural response and the use of the Arbitrary Lagrangian Eulerian (ALE) method for treating materials that undergo significant deformation.

2.3.1 Elementary theory

One of the features of the finite element method that have led to such widespread use is the generality of the method, which means there are many ways in which the finite element method can be formulated and subsequently solved. There are though, a number of steps in development and solution of a finite element problem, which are completed in a specific sequence that is common across finite element procedures [57, 58]:

1. Discretise the structure into a number of connected elements and nodes
2. Choose functions to determine field variables in each element
3. Generate matrices to express the properties of the elements
4. Assemble matrices to generate system equations and apply boundary conditions
5. Solve the system equations for the required field variables

A simple example of these steps can be demonstrated using the direct stiffness method to develop the system equations. Figure 2.11 shows a systems of bars in 1D, with 3 ele-

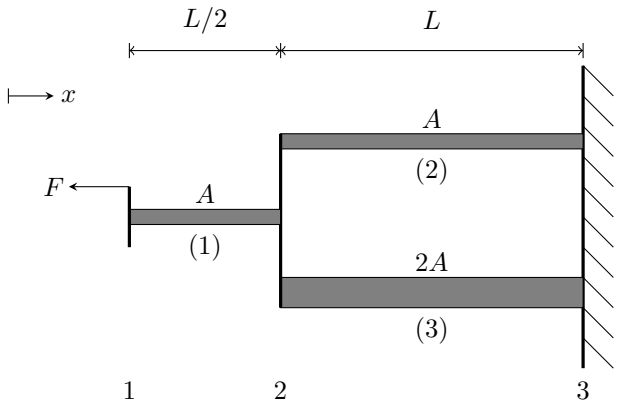

Figure 2.11: A system of bars in tension

ments (in brackets) and 3 nodes, at which interactions can take place between elements, and forces can be applied - this is step 1 in the above approach. Secondly, a function is chosen to define how a field variable (in this case, displacement) is altered by the application of a force, F, which for simplicity can take the form shown in Equation 2.19, where F, E, A, L and δ assume their usual meaning from basic solid mechanics. Considering each bar separately allows step 3 to be completed, with equilibrium equations written for each in matrix notation, shown in Equations (2.20), (2.21) and (2.22).

$$F = \frac{EA}{L}\delta \tag{2.19}$$

Element (1), cross sectional area A, elastic modulus E and length $L/2$:

$$\begin{Bmatrix} F_1 \\ F_2 \end{Bmatrix} = 2\frac{AE}{L}\begin{bmatrix} 1 & -1 \\ -1 & 1 \end{bmatrix}\begin{Bmatrix} \delta_1 \\ \delta_2 \end{Bmatrix} \tag{2.20}$$

Element (2), cross sectional area A, elastic modulus E and length L:

$$\begin{Bmatrix} F_2 \\ F_3 \end{Bmatrix} = \frac{AE}{L}\begin{bmatrix} 1 & -1 \\ -1 & 1 \end{bmatrix}\begin{Bmatrix} \delta_2 \\ \delta_3 \end{Bmatrix} \tag{2.21}$$

Element (3), cross sectional area $2A$, elastic modulus E and length L:

$$\begin{Bmatrix} F_2 \\ F_3 \end{Bmatrix} = 2\frac{AE}{L}\begin{bmatrix} 1 & -1 \\ -1 & 1 \end{bmatrix}\begin{Bmatrix} \delta_2 \\ \delta_3 \end{Bmatrix} \tag{2.22}$$

The fourth step is to construct the global structural matrix by summing the forces at each node, known as assembly. At node 1, two forces exist, which can be found from equations (2.20) and (2.21):

$$\Sigma F_1 = 2\frac{AE}{L}\cdot\delta_1 - 2\frac{AE}{L}\cdot\delta_2 + (0)\cdot\delta_3 \tag{2.23}$$

$$\Sigma F_2 = \left(-2\frac{AE}{L}\cdot\delta_1 + 2\frac{AE}{L}\cdot\delta_2 + (0)\cdot\delta_3\right) + \left(\frac{AE}{L}\cdot\delta_2 - \frac{AE}{L}\cdot\delta_3\right) + \left(2\frac{AE}{L}\cdot\delta_2 - 2\frac{AE}{L}\cdot\delta_3\right) \tag{2.24}$$

Repeating for F_3 and summing allows the global stiffness matrix $[K]$ to be constructed for Equation (2.25):

$$\{F_i\} = [K]\{\delta_i\} \tag{2.25}$$

$$[K] = \frac{AE}{L}\begin{bmatrix} 2 & -2 & 0 \\ -2 & 2+1+2 & -1-2 \\ 0 & -1-2 & 1+2 \end{bmatrix} = \frac{AE}{L}\begin{bmatrix} 2 & -2 & 0 \\ -2 & 5 & -3 \\ 0 & -3 & 3 \end{bmatrix} \tag{2.26}$$

The final assembled matrix is shown in Equation (2.27).

$$\begin{Bmatrix} F_1 \\ F_2 \\ F_3 \end{Bmatrix} = \frac{AE}{L}\begin{bmatrix} 2 & -2 & 0 \\ -2 & 5 & -3 \\ 0 & -3 & 3 \end{bmatrix}\begin{Bmatrix} \delta_1 \\ \delta_2 \\ \delta_3 \end{Bmatrix} \tag{2.27}$$

In this form, the system of equations is not solvable as there are currently 3 equations and 6 unknowns. Adding the boundary conditions $\delta_3 = 0$, $F_1 = -F$ and $F_2 = 0$ reduces the number of unknowns and yields a solvable system of equations, shown in Equation (2.28).

For the rail vehicle that will be modelled in later Chapters, shell elements will be used to discretise the rail vehicle structure, and using the appropriate material parameters, appropriate stiffness matrices can be generated. The forces applied to the nodes of the structure will be calculated from the prediction of the blast pressures, and appropriate boundary conditions for any known fixed positions on the rail vehicle will also be applied.

$$\begin{Bmatrix} -F \\ 0 \\ F_3 \end{Bmatrix} = \frac{AE}{L}\begin{bmatrix} 2 & -2 & 0 \\ -2 & 5 & -3 \\ 0 & -3 & 3 \end{bmatrix}\begin{Bmatrix} \delta_1 \\ \delta_2 \\ 0 \end{Bmatrix} \tag{2.28}$$

The assembled system matrix typically has several important features, which have important implications for storing and processing them. The size of the system matrix is governed by the number of degrees of freedom of the system under investigation. For the 3 degree of freedom system shown in Figure 2.11, the stiffness matrix is 3×3, and adding a extra spatial dimension to the same analysis would add an extra 3 degrees of freedom, leading to 6×6 matrix. The system matrices (the stiffness matrix in static analyses) are $n \times n$ in size, where n is the number of degrees of freedom, equal to the number of nodes multiplied by the number of spatial dimensions used in the analysis. From this, it is clear that 3 dimensional analyses using large numbers of nodes can

lead to very large system matrices. System matrices often have 3 important properties that can be advantageous; they can be banded, sparse and symmetric. Banding refers to the non-zero terms of the matrix being clustered around the main diagonal, and the size of the band is directly related to the maximum difference between two global node numbers within an element definition [57]. An efficient node numbering procedure will lead to a small band, but poorly numbered nodes will lead to non-zero terms a large distance from the main diagonal. The fact that non-zero terms are clustered in a band around the main diagonal, with a large number of zero terms, makes the matrix sparse. Matrices are sparse, because each element has only a small number of nodes compared to the global total, and only a limited number of elements share each node. If matrices are also symmetric, the storage space required can be almost halved, but stiffness matrices are only guaranteed to be symmetric when the structures are linear, and referred to in orthogonal coordinates [57] (which is the norm in most codes). Sparse and banded matrices are useful because they reduce the amount of memory required and improve the speed at which matrices can be processed. It is important to understand this relationship between the mesh and formation of the fundamental equations, as user generated meshes that are poorly numbered can lead to poor performance and errors.

2.3.2 Time domain dynamics

In many real engineering problems, it is not satisfactory to assume that the problem under investigation is independent of time. It may be important to identify the velocities and accelerations of certain areas of a structure, or predict how the stress field develops with a time varying load. As a result, it is important to include an inertial force term into the general form for the finite element equation from Equation (2.25), as well as a velocity dependent damping force to give the general equation of motion for the dynamic response (2.29).

$$\{F(t)\} = [M]\{\ddot{u}\} + [C]\{\dot{u}\} + [K]\{u\} \tag{2.29}$$

The finite element method requires that mass of the studied system be discretised into a mass matrix, $[M]$. The discrete representation of continuous mass of the real structure can be achieved in two ways, using either a consistent mass matrix, or by a lumped mass matrix. Consistent mass matrices are generated by using the same functions to represent the distribution of mass as used to generate stiffness matrices. Lumped mass matrices are formulated by putting a particle mass, m_i, at each nodal point of the mesh, such that the sum of nodal masses is equal to the mass of the system. Lumped mass matrices are typically used in older numerical codes (such as LS-Dyna), and those where fast transient phenomena are to be studied, as it results in a diagonal mass matrix. This is advantageous, as it is easier to form, requires less storage space, and also allows more efficient element by element processing [57, 59].

2.3.2.1 Explicit time integration

There are two methods that can be used to progress the time of a numerical solution; implicit and explicit time integration. Schemes are referred to implicit when they consider dynamic equilibrium (2.29) at $t + \Delta t$, whereas explicit integration considers dynamic

equilibrium at time t. The fact that implicit schemes require a prediction of some parameters at some point at the future time step in order to calculate all parameters at the next time step from the current time, makes them more complex than explicit integration, where all calculations are made using information from the current time step. Explicit integration uses much shorter time steps than implicit integration, with explicit solvers typically requiring 100 to 10000 extra time steps to solve a problem of the same duration. One of the disadvantages of implicit solutions though, is that calculations at each time step are significantly more complex and the computational cost at each step is unknown and variable due to the requirement for equilibrium convergence [60]. When considering highly dynamic phenomena, it is important that time steps for each calculation are short enough to capture all the required behaviour such as strain rate behaviour, wave propagation and very high accelerations, thus it is much more appropriate to use explicit schemes to model these kind of problems than using implicit schemes as full advantage cannot be taken of the significantly longer time steps. Conversely, implicit schemes are much more appropriate for studying behaviour of systems over hundreds of milliseconds or seconds, where the number of time steps required by an explicit scheme may prove unnecessarily expensive if information is not required at very short time intervals. Explicit time integration is conditionally stable and requires that the time interval between calculations be equal to or less than a critical timestep, which is equal to the time taken for a wave to cross an element. For beam, truss and shell elements, the critical timestep, Δt_c is given by (2.30), where L is the shortest distance between two nodes in any element, and c is the wave speed in the given material. A stability fraction or scale factor in the region of 0.6-0.9 is usually used to multiply critical time step computed internally within the code, to ensure that the solution is stable. As the elements deform or are removed, the internally computed time step is updated to ensure that stability remains when nodes become closer together and shorter time steps are required.

$$\Delta t_c = \frac{L}{c} \tag{2.30}$$

Time integration in explicit numerical codes is most commonly achieved using the central difference method, where known quantities from the current timestep are used to calculate nodal accelerations, velocities and displacements at the next time step, which can then be used to update element properties such as strains, stresses and pressures as well as nodal forces. An overview of the principal workings of the central difference method from Bathe [59] is given below. Implementation of the central difference method for each code is often given [60] to ensure the user is aware of exact steps.

Nodal accelerations and velocities at t can be written in terms of displacement at $t + \Delta t$ and $t - \Delta t$, where Δt is the time step.

$$\{\ddot{u}\}_t = \frac{1}{t^2}\left(\{u\}_{t-\Delta t} - 2\{u\}_t + \{u\}_{t+\Delta t}\right) \tag{2.31}$$

$$\{\dot{u}\}_t = \frac{1}{2\Delta t}\left(-\{u\}_{t-\Delta t} + \{u\}_{t+\Delta t}\right) \tag{2.32}$$

Substituting these relations into the dynamic equilibrium equation (2.29), and collecting terms for displacement at $t + \Delta t$ on the left side gives:

$$\left(\frac{1}{\Delta t^2}[M] + \frac{1}{2\Delta t}[C]\right)\{u\}_{t+\Delta t} = \{F(t)\}_t - \left([K] - \frac{2}{\Delta t^2}[M]\right)\{u\}_t - \left(\frac{1}{\Delta t^2}[M] + \frac{1}{2\Delta t}[C]\right)\{u\}_{t-\Delta t} \quad (2.33)$$

For all cycles other than the first, the entity $\{u\}_{t-\Delta t}$ can be read from the previous cycle, but in order to calculate this value for the first cycle, a combination of the initial conditions for acceleration and velocity and relations (2.31) and (2.32) is used. For the first cycle, $\{u\}_{t-\Delta t}$ is given by:

$$\{u\}_{t-\Delta t} = \{u\}_{t=0} - \Delta t\{\dot{u}\}_{t=0} + \frac{\Delta t^2}{2}\{\ddot{u}\}_{t=0} \quad (2.34)$$

2.3.3 Arbitrary Lagrangian Eulerian method

Most finite element problems use a Lagrangian formulation (as discussed so far), where the elements and nodes represent the physical structure and change shape and position as the structure deforms. This is beneficial, as there is no mass flow (or material transport) between elements, which means terms for such can be ignored and the fact the mesh distorts with the material means that although volume and density can change, the mass of an element stays the same so mass conservation is always satisfied. This means that material and structural boundaries are automatically represented, meaning that boundary conditions and contact between parts of the mesh can be handled in a straightforward manner. In contrast, Eulerian codes utilise a fixed mesh, through which material is transported at each step. This can be advantageous in some situations, where material undergoes large and complicated patterns of distortion, such as in fluid flow, where elements in a Lagrangian mesh would become highly distorted, leading to very short time steps and possibly solution instability. An illustration of the differences between Eulerian and Lagrangian solutions is shown in 2.12

It is clear that both Lagrangian and Eulerian methods have advantages over each other in given circumstances, which means that choosing one or the other could mean making a sacrifice in computational cost or accuracy, if the features of both are required in calculation (e.g. contact between highly deforming bodies). The Arbitrary Lagrangian Eulerian (ALE) method seeks to take advantage of features of both for use when neither Lagrangian or Eulerian methods are satisfactory. The ALE method for each time step is given by Zukas [58] and the LS-Dyna theory manual [60]:

1. Perform Lagrangian step (mesh and material moves together)
2. Perform an 'advection' step:
   (a) Identify nodes to move
   (b) Move nodes on boundary
   (c) Move interior nodes
   (d) Calculate transport of element variables

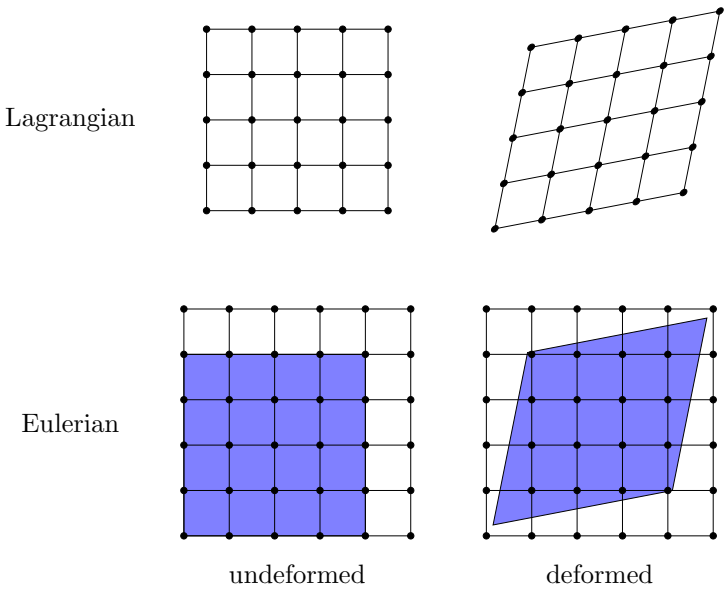

Figure 2.12: Deformed and undeformed structures using Lagrangian and Eulerian methods

(e) Calculate momentum transport and update velocities

The 'advection' step involves two distinct phases, one where changes to the mesh are made and one where transport of material is performed by calculating new values for element properties such as stress, strain and pressure and the new nodal velocities. As well as the whole process from (a) to (e) being referred to as advection, the material transport calculations methods performed at (d) and (e) are also referred to as advection algorithms. When the steps taken at a) b) and c) are required the nodes are moved according to features of the material behaviour and smoothing algorithms are required to calculate the new positions of nodes. Under some conditions, such as when explosions in air are modelled with ALE methods, it is appropriate to set the mesh velocity to zero and ignore any smoothing and nodal points are reset to their original position at every advection step.

The mesh rezoning and transport calculations are typically significantly more time consuming (2-5 times, [60]) than a Lagrangian step, but the computational cost of ALE methods can be reduced by only performing advection steps after a certain number of Lagrangian cycles.

2.3.3.1 Advection methods in LS-Dyna

The advection process in LS-Dyna consists of two separate steps, one which calculates the transport of element centred variables (ALE elements have a single central integration point) such as density and internal energy, and one which updates nodal velocities and element velocities, or the *momentum transport*.

Transport of element variables is done using either a first order or second order accurate algorithm. The first order donor cell algorithm assumes constant interpolation function, Φ, over the element, whereas the second order van Leer algorithm uses a higher order piecewise linear interpolation function to improve accuracy. The value of the interpolation function at the centre of the element (required to compute element centred variables) is considered as an average of Φ over the whole element, not specifically the

value of the function at the spatial point in the centre of the element. Both the first order and second order algorithms are one dimensional, so their use in 3D is achieved by simultaneous calculations of fluxes from element faces in each direction. This is known as isotropic advection [60], and because transport is calculated at element faces, there is no transport between elements that do not share faces. It is important to remember this when constructing meshes, as isotropic advection introduces a second order error which can be significant when the majority of transport occurs across mesh diagonals [60].

Momentum transport in LS-Dyna is calculated by the half index shift algorithm. It is an element centred momentum transport algorithm, which has advantages over other schemes by reducing dispersion and smearing of shocks.

2.3.4 Equations of state

In highly dynamic problems where wave propagation is important, it is often important to determine the pressure within solid or fluid elements. Equations of state are used to provide a relationship between the volume V, and / or density, ρ. Many equations of state (EOS) that are implemented in numerical codes are *phenomenological* and have their origins in empirical data, with the form taken to best describe the observed experimental behaviour, and input parameters determined experimentally. The empirical approach to deriving these equations of state means that most are limited to treating specific materials, specific materials phases or specific stages in a materials dynamic response. The Mie-Gruneisen EOS, for example, is one of the most commonly used equations of state used in hydrocodes to represent solids, but cannot be used for liquids or gases and cannot be used when any transitions occur between states [58].

Two important equations of state for modelling the behaviour of gases are shown below, the simple linear polynomial equation (2.35) which can be used to represent ideal gases with C_4 and C_5 set to $\gamma - 1$, and the Jones Wilkins Lee equation of state for high explosives (2.36), which is used to describe the pressure of the detonation products of high explosives. Numerical calculation of equations of state within codes also requires the calculation of the bulk modulus to identify any changes to the speed of sound caused by volumetric changes of elements, which is calculated by (2.37).

$$p = C_0 + C_1\mu + C_2\mu^2 + C_3\mu^3 + (C_4 + C_5\mu + C_6\mu^2)E_0 \tag{2.35}$$

$$\text{where} \quad \mu = \frac{1}{V} - 1$$

$$p = A\left(1 - \frac{\omega}{R_1 V}\right)e^{-R_1 V} + B\left(1 - \frac{\omega}{R_2 V}\right)e^{-R_2 V} + \frac{\omega E_0}{V} \tag{2.36}$$

$$\begin{aligned} K &= -V\frac{\mathrm{d}P}{\mathrm{d}V} \\ &= \rho\frac{\mathrm{d}P}{\mathrm{d}\rho} \end{aligned} \tag{2.37}$$

2.4 Structures under extreme loading

2.4.1 Impulsive loads on simple structures

A large body of theoretical and experimental work has been carried out on simple structures subject to impulsive loads, particularly clamped circular and square plates. Early theoretical studies of plastic deformation in uniformly impulsively loaded plates were undertaken by Wang and Hopkins [61], to begin to understand the effects of shock waves with structures. Simplifications were made by assuming the plate is sufficiently thick that bending and not membrane action dominates and that the structure is under sufficient load that it behaves plastically, as the solution assumes no elastic deformation. The plate is loaded by assuming a uniform velocity across the areas within the clamped region at $t = 0$, and use of rotational symmetry around a circular plate, allowing dependence of the problem on the radius, r, also helps to simplify the problem. Hopkins [62] presented a generalized theory on the deformation of thin plates, which is used by Cox and Morland [63] to investigate the dynamic deformation of simply supported square plates, but with simplifications to the yield criteria. Wierzbicki [64] added increased levels of complexity and realism to theoretical models by including the effect of strain rate, which was shown to bring theoretical results much closer to experimental observations. At this point, Wierzbicki notes that there are two major sources of discrepancy caused by effects that are currently not included in current theoretical results; the effect of membrane forces and the assumption of ideal impulse, where the structure under investigation is assumed to take up velocity immediately. Jones [65] undertook one of the first analyses of the combined effect of membrane action and bending for a simply supported dynamically loaded plate, and identified that membrane action is important to consider once the distance of plastic hinges from the centre of the plate has reduced to zero. Li and Jones [66] have also provided an analysis to predict the final deformation of short cylindrical shells under blast loading. Batra and Dubney [67] looked to extend the work of Jones by identifying not just the final central deformation of a panel, but also the deformed shape. The loading is applied as an instantaneous velocity to the whole panel, and strain rates and rotary inertia are ignored, as with many previous solutions. Still, the derived equations for the plate are solved numerically for incremental deformations.

To prove the validity of theoretical and numerical results, a large number of experimental tests have been undertaken and reported in the literature. Jones *et al.* [68] investigated the plastic deformation of square plates loaded by high explosive detonation, finding that strain rate effects in steel and geometry changes in the plate played an important role, and that theory at the time predicted results well for small deflections and strain rate insensitive materials. Nurick [69] investigated failure modes, and identified that failure mode was strongly dependant on the impulse delivered to the plate and the boundary conditions. Recently, Spranghers *et al.* [70] and Tiwari *et al.* [71] have both used high speed 3D DIC to improve the data yielded from experimental tests, allowing full field measurement of deformations, strains and stresses in a flat plate exposed to a blast load, making comparison with numerical results easier, as well as providing significantly more information on the behaviour of a structure that can be achieved solely with more traditional means.

Much of the above work considers shock or impulsive loading of structures, where the pressure rise time or the load application can be considered instantaneous. Highly

dynamic loading can also occur from loads where the load is not applied instantly, such as those that occur from deflagrations of hydrocarbons and dust, as described in Section 2.2.2.2. Extensive work has been undertaken at the University of Liverpool to understand the effects of structures under pulse pressure loading, where the relative rise and decay time of the pressure load can be controlled. Schleyer [72] conducted studies on clamped stiffened and unstiffened mild steel plates with a loading area of 1m × 1m with different boundary conditions. The effect of boundary conditions were seen to be important in line with prior work by Jones [73]. Where specimens were subject to in plane restraint as well as rotational restraints, peak and permanent deformation was seen to be lower, and the effect of stiffening ribs was also significant. When only rotational restraint was applied (in plane restraint purely frictional), the effect of stiffening ribs was negligible, and both peak dynamic and permanent plastic deformation were significantly higher. Investigations of aluminium panel failure using similar loading methods were conducted by Langdon and Schleyer [74]. Where failure occurred, it was seen that tensile tearing around the clamped boundaries was primarily responsible for failure, and considerable deformation and necking around the boundaries was seen when failure did not occur. It was concluded that deformation and failure modes in pulse loaded panels were in line with existing theory on impulsively loaded structures. These failure modes were defined by Menkes and Opat [75] as:

- Mode I – large ductile deformations;
- Mode II – tensile tearing at or over the supports
- Mode III – transverse shear failure at the support

Investigation of these failures has been conducted both experimentally and theoretically. Teeling-Smith and Nurick [76] conducted testing on fully clamped circular plates subject to increasing impulses, and found limiting values for each of the failure modes. Highest central deformations occurred at the limit of mode I, and subsequently central deformation decreased as applied impulse increased, with plates failing rapidly in tension or shear at the points of clamping before significant plastic deformation of the remainder of the panel was possible. Similar results for square plates were reported by Nurick and Shave [69].

As well as failure in one of the three modes described above, it is also possible for structures such as plates to fail by petalling. This can occur when a plate is struck by a projectile, but can also occur when the impulsive load provided by an explosion is applied centrally over only a portion of the plate [77].

As well as theoretical and experimental work investigating plates under blast loading, there has been much work undertaken using numerical methods, particularly the explicit finite element method. Rudrapatna *et al.* [78] investigated blast loaded square plates using a bespoke finite element code, applying a short duration rectangular pressure pulse to all elements on the plate surface. Balden and Nurick [79] combined a hydrocode (AUTODYN) and explicit dynamics code (ABAQUS) to investigate the deformation, failure and post motion failure of a panel subjected to uniform and concentrated impulsive loads. The finite element lends itself particularly well to the parametric study of complex structures, such as sandwich panels [80], which cannot be investigated analytically and are expensive to test experimentally. Although an individual modelling run is quicker than an equivalent testing program, they often take a number of hours to run,

so work continues to derive fast running models and analytical results that can be used for engineering analysis, such as work by Micallef [81] and Jones [82].

2.4.2 Complex structures under blast loading

When structures become more complex, it is significantly more difficult to provide analytical solutions for dynamic response as the structural behaviour is governed not only by material response, but geometric effects as well. As a result, numerical and experimental means are often the only way to thoroughly investigate structures beyond simple shells, such as plates, cylinders and spheres. A variety of experimental and numerical techniques have been applied to understand complex structures, whose response is difficult to compute analytically.

Security concerns in civil aviation mean that various pieces of research have been done to identify how explosions interact with aircraft structures. Simmons and Schleyer [83] investigated the performance of aircraft structural panels constructed using rivets and laser welding techniques using a pressure pulse loading rig, finding that welded panels failed more readily than traditional riveted panels. Numerical models applied pressures measured from experimental tests, as the measured pressures in the test rig did not always display the anticipated ideal triangular shape. Numerical results predicted behaviour well until failure began to occur, at which point experimental results and numerical predictions began to agree less well.

Kotzakolios [84] investigated composite aircraft fuselage sections using numerical means, using a coupled ALE and Lagrangian method in LS-Dyna, with a structural mesh composed of fibre metal laminates. The authors concede that the method is limited, in that the model is not sufficiently refined to identify important features such as crack propagation, which poses problems for coupled models where ALE and structural meshes should have similar elements sizes. Where knowledge of such phenomena is required, a decoupled approach is likely to more appropriate, where a model is run to identify the likely loads experienced, and these loads are then applied to a sufficiently refined model, where small scale effects such as crack propagation can be predicted with a greater degree of confidence.

As well as aircraft structural panels, work has been done to understand how luggage containers behave when subject to explosions. Fleisher [85, 86] and Weinstein [87] investigated the design of blast resistant luggage containers by experimental and numerical means in response by the United Stated Federal Aviation Authority's desire to reduce the vulnerability of commercial aircraft. Fleisher [86] conducted prototype testing and numerical models of luggage containers using the GLARE composite. Further work and model development was undertaken [85], identifying the effect of luggage present in the container and implementing it in models. Experiments identified that the presence of increasing volumes of luggage increased both the QSP developed and the strength of a number of shocks in the container. Work is ongoing as part of the FLY-BAG2 project, to develop a lightweight blast resistant textile luggage container. Initial testing [88] and numerical modelling identified a need to withstand both the initial propagation of the shock and the subsequent QSP that develops.

Børvik *et al.* investigated protection systems for ISO containers using experimental [89] and numerical [90, 91] means. Experimental tests were carried out on a novel protective system, to withstand the effects of explosive devices being detonated outside

of a container, which was found to effectively reduce the damage caused by the blast load and flying projectiles. Numerical models were developed, and both coupled Lagrangian-ALE and purely Lagrangian simulations were used. Comparison between experiments and models proved that no modelling method alone provided predictions that fully captured the behaviour of the container and pressures measured, and concluded that the ConWep package was not sufficient for design of flexible structures, and that experiments are always required to validate finite element based blast models. Corrugated steel structures were also investigated by Langdon and Schleyer [92] and Schleyer [93]. It was shown that consideration of supports was very important for prediction of the final deformation and that membrane action also needs to be considered to fully capture deformation behaviour, and both of these had contributed to previously conservative predictions. It was also shown that such corrugated panels are able to support large plastic deformations.

Pope [49] has described the design of an experimental test facility representing tunnels, in which various numerical models were generated to inform the design of a test facility to investigate the effects of explosions in tunnel systems, modelling both the pressure propagation and the material response of the test facility structures under blast loading. The Autodyn hydrocode was used to compute blast pressures within the tunnel using successive remapping procedures between increasingly large but coarse meshes. A 2D method was applied to model some aspects of explosive afterburning, which allowed an additional pressure time history due to secondary combustion to be calculated, which was later applied to structural models. The same 2D method was used to make a comparison with 3D models, and it was found that 3D models tended to under predict pressures and impulses by up to 25%, compared with high resolution 2D models. Computed loads were applied to structural models in LS-Dyna to identify the required properties of the structures in the test facility, such as the wall strength and supporting structures required.

2.4.3 Structural methods of blast mitigation

Smith *et al.* [94] investigated wall 'roughness elements' and their effect on blast transmission along tunnels, by means of scaled experiments. Roughness elements, in the form symmetric and asymmetric vertical plates placed along the edges of a square test section, were altered in terms of spacing and size. This could be considered analogous to a blast in a rail vehicle, with wall roughness elements in the tunnels comparable to draught screens in a rail vehicle, but in this case the blast wave was effectively planar, with the normal to the plane along the axis of the test 'tunnel' under investigation, whereas in a rail vehicle the blast wave is more likely to be spherical, and rarely plane to the axis of a carriage. It was identified that blast wave attenuation along a tunnel increased as the height of the roughness elements (protrusion into the tunnel cross section) was increased, and that best attenuation was found when spacing between these roughness elements was approximately equal to twice the height.

Berger *et al.* [95] used a number of experimental tests to identify how different orientations and geometry of wall elements alter shock propagation and mitigation in a shock tube. A combination of pressure transducers and Schlieren photography was used to understand the interaction of plane shock waves with the attenuating elements, as well as the end wall of the shock tube. No definite conclusions were made as to the best

solution for mitigating shock waves, as it was found that different sizes and angles of incidence could either attenuate or increase the strength of the shock, depending on the specific combination of size of obstacle in the tube and the angle that the shock wave makes with it.

Langdon *et al.* [96] performed an experimental and numerical investigation of the use of perforated steel plates to mitigate blast waves. A perforated plate with a number of holes in it was placed in front of a target plate within a cylindrical section, and high explosive charges of C4 were detonated to identify the effect of the different blockage ratios, which is the ratio of the total area of the plate to the area through which the blast wave cannot pass. Only with very high blockage ratios of 96%, where there is only 4% of the area of the mitigation device available for the blast wave to pass through, showed significant blast attenuation effects. Numerical models showed difficulty in picking up the behaviour of blast wave interaction with very small holes, with numerical prediction diverging from experimental results as the blocking ratio increased and the size of holes decreased.

Numerical simulations were carried out by Chaudhuri *et al.* [97] using a computational fluid dynamics code on the effect of rigid obstacles of different shapes placed within a channel subject to the flow of a shockwave, but not considering any effects of interaction of the shock wave with end boundaries of the section. Triangular (both tip and base facing the incoming shock), rectangular and semi circular objects are investigated, with transmitted shocks downstream of a matrix of these objects computed. It was found that staggered arrays of obstacles produced better pressure attenuation than non staggered arrays, and that triangular prisms with the base facing towards the incoming shock was the most effective shape for reducing the magnitude and speed of the transmitted shock.

2.5 Rail vehicle design and construction

The passenger vehicles currently in operation across the UK railway network are very diverse, comprising a variety of sizes, construction and traction methods. The rolling stock, which carries passengers and does not include power cars[1] is made up of passenger hauled locomotives, diesel multiple units (DMUs) and electric multiple units (EMUs) and is comprised of approximately 80 different classes of vehicles [98], not including those on the London Underground, which has 10 different types of rolling stock [99], including trains first built in 1972 (1972 Stock on the Bakerloo line) and the state of the art 2009 and S Stock. The large variety and age of vehicles means a number of construction techniques exist on the UK rail network, but this number is ever decreasing as older vehicles are retired.

Most modern rail vehicles are constructed using extruded aluminium sections[2], which are held together by a combination of welds and mechanical fasteners. Previous methods of construction, which are still in use across the UK network include welded monocoque steel constructions (Mark 3 and Mark 4 coaches, Sprinter Diesel Multiple Units (DMUs)) and body on frame constructions, such as the Class 14X Pacer units, which used a bus body onto a rail vehicle frame (See Figure 2.13, chassis frame clearly visible directly underneath passenger compartment shell). A thin skin is attached to the welded frame,

[1] Power cars exist to haul passengers vehicles that have no traction themselves, an examples include the Class 43 Intercity 125, and the Class 91 Intercity 225.

[2] This method of construction was developed in the UK in the 1980's, with BREL class 165 being early examples of this construction method.

with heat and sound insulation inserted in the cavity between the outer shell and the inner walls, as shown in Figure 2.14.

Figure 2.13: Class 144 'Pacer' using body on frame design, currently in service on rural and suburban routes in the UK

Figure 2.14: Exposed internal wall of a Class 14X vehicle, showing the welded construction

Aluminium extruded designs, the process for manufacturing which was developed in the late 1970's [100], have found favour as they save a significant amount construction time as they can largely be automatically welded together, as well as saving weight. One of the downsides of this construction method is that welding 5000 and 6000 series leads to heat treatment of the area surrounding the weld, leading to reduced mechanical properties at the interface between the weld metal and the heat affected zone [101]. This was a point raised after investigation of the Ladbroke Grove rail accident [102], where 'weld unzipping' was seen in an aluminium Class 165 rail vehicle, but not in the rail vehicle constructed using a full steel monocoque design. A similar failure mode was

seen in the Eschede rail disaster in June 1998. It is conceivable that under the transient loading caused by an explosion, this could also be a mode of failure that a rail vehicle could undergo following a blast load.

Figure 2.15: Rail vehicle undergoing maintenance work, with opened 'hopper' windows

Figure 2.16: Toughened glass is often used in the windows of trains

Windows on rail vehicles are often made from toughened glass, as shown in Figure 2.16, but the performance limitations of toughened glass mean that new vehicles are generally fitted with laminated glass, and recent research indicates there is a justification for replacing existing toughened glass with laminated glass [103]. Older style vehicles without air conditioning, including the Class 144 shown in Figure 2.13 and the BREL MkIII, often have windows which can be opened, such as the 'hopper' windows shown open in Figure 2.15. Modern or refurbished vehicles often have dispensed with this design, with fully sealed designs used in conjunction with air conditioning for improved passenger comfort.

Through carriage designs are increasingly popular in urban vehicles, such as the London Underground and Madrid Metro (pictured in Figure 2.17). Traditional designs

Figure 2.17: Through carriages

for such urban transport systems do not allow passenger movement between individual carriages of a train, or the gangway that connects individual carriages is very narrow, limiting any passenger flow between each carriage. Open carriage or gangway designs, such as that shown in Figure 2.17, increase the available space and allow passengers to move easily between carriage, ensuring a more even passenger density.

2.5.1 Rail vehicle structural loads

Railway Group Standard GM/RT2100 [104] sets out the requirements for design and integrity for rail vehicle structures, and as such prescribes design loads that vehicle structures should withstand. Of particular interest are the internal loading requirements for 'secondary' vehicle structures such as doors and windows, and vehicle elements interfacing with passengers such as seats, tables, draught screens and other internal glazing, which are reproduced from [104] in Table 2.1.

2.6 Fragments and ballistic loads

The study of ballistics is a very large field and a large body of work exists throughout the literature on the behaviour of materials undergoing impacts at very high speeds. Fragment impacts are not the focus of the current study, but a brief review of relevant literature is included here.

Table 2.1: Structural requirements for secondary and internal structures when subject to internal loads [104]

structure	requirements	
windows	fully serviceable over the entire area after application of a sustained pressure of 6 kPa	withstand an impact of a 50 kg pendulum from a height of 1200 mm, followed by a concentrated load of 0.8 kN over an area of 100 mm × 100 mm
doors, draught screens and internal glazing	resist a pressure load of 2.5 kPa over the surface of the door, plus a concentrated load of 0.8 kN over an area of 100 mm × 100 mm applied at any position on the surface, without significant deformation or loss of function	A perpendicular load of 2.5 kN applied over an area of 100 mm × 100 mm at any position on the surface, without significant deformation or loss of function
seats	resist significant permanent deformation when subject to a vertical load of 2 kN applied downwards over an area 380mm wide × 200mm deep	resist significant permanent deformation when subject to longitudinal loads of ± 1.5 kN applied over an area of 250 mm wide × 50 mm deep located in the centre of the uppermost part of the rear of the seat
tables	withstand without significant permanent deformation a vertical load of 1 kN in either direction	withstand without significant permanent deformation a load of 1.5 kN applied horizontally to the table in any direction and at any position

Børvik [105] used experimental and numerical means to investigate the perforation of 6005-T6 extruded aluminium panels by projectiles. Although different in scale, aluminium panels of similar extruded shape with several triangular cells are used in the construction modern railway vehicles, some of which are constructed using 6006-T6 series aluminium [101]. Johnson-Cook material parameters were determined experimentally for 6005-T6 and validated with numerical models. This data provides useful input into rail vehicle models developed in this work, which use a very similar material construction and aluminium alloy. Ogival nose projectiles with a mass of 196g were fired at extruded aluminium panels at velocities of between 300 and 170 m/s, and good correlation was found between experimental results for both 2D and 3D simulations, although it was noted that 3D simulations were very computationally intensive.

Wen *et al.* [106] have studied the impact of steel spheres on ballistic gelatin, using both a numerical and experimental approach. Good agreement was seen between experimental results and experimental studies of steel spheres incident on ballistic gelatin[3] (10% gelatin by weight, at 4 °C) at velocities of 947 and 728 m/s, both in terms of penetration data and the size of the cavity formed. Numerical models used a rigid material to model the steel spheres and an elastic plastic material with an equation of state for the gelatin, with the two interacting by a contact algorithm. As with other such problems where highly transient behaviour occurs, the difference between numerical predictions and experimental results become increasingly small as the mesh is refined.

Nyström and Gylltoft [107] have investigated reinforced concrete subject to combined fragment and blast loading. Validation and calibration tests were undertaken by conducting stand alone fragment and blast tests on concrete beams, which were used to calibrate each individual method of loading and confirm the accuracy of the prediction of separate responses due to fragments and blasts. Single degree of freedom (SDOF)

[3]Ballistic Gelatin (BG) is a tissue simulant made from powdered gelatin and water and is primarily used to replicate the response of muscle tissue to ballistic impacts.

models were used to determine how the relative arrival of blast and fragment loads affected the global response. A synergy between the loading mechanisms was identified, with the combined fragment and blast loading giving a greater mid point deflection than the sum of mid point deflection from separate blast and fragment loads. It was also identified from the SDOF models that simultaneous loading from fragments and blast loading causes the highest deflection, compared with other sequences of loading.

2.7 Conclusions

This Chapter has presented appropriate theory on the techniques to be applied throughout the course of this work, as well as findings from the open literature, which can inform the process of developing models to predict the effect of IEDs in rail vehicles. For completeness, a brief review of whist terrorism is, and the current strategies for countering were discussed, and it was seen that this can often be difficult.

There is one aspect that has not been covered in this Chapter, which is necessary to build a complete model of the effects of IEDs, is an understanding of the mechanisms by which people are injured following explosions, and the methods that can be used to predict them. A comprehensive survey of literature relating to many aspects of human injury resulting from the functioning of explosive devices can be found in the following Chapter.

3

Predicting injury and risk to passengers

When a high explosive detonates it releases large amounts of energy which is transferred to the surroundings by a shock wave and a following mass of air. This can cause severe injury to air containing organs such as the lungs and ears, brain injuries due to high accelerations of the head, as well as injuries due to high velocity projectiles accelerated by the detonation and impact injuries caused by the body being thrown against hard surfaces.

Significant efforts have been made to develop injury criteria for humans who are subjected to the effects of detonation of weapons and high explosives, some of which are detailed in this chapter. Much of the work in this field was driven by the military who have a need to understand the effect of explosions and reduce the risk of injury to their own personnel, but in recent times criteria have also been adopted for use in the civilian world due to increased risk of terrorist attacks involving explosives.

To allow an accurate risk to be calculated it is important to select or devise appropriate injury criteria which are specific to the likely modes of injury that are expected. This has been the subject of much previous work, but no definitive set of criteria for such injuries currently exist in the public domain. This chapter reviews the major works in this area and sets out criteria that will be used as a basis for prediction of likely injuries resulting from blast events in a rail vehicle. Section 3.7 brings the important criteria together with the development of numerical occupant injury predictors, including a multi-projectile risk tool.

3.1 Injuries due to explosions

Injuries resulting from the detonation of explosive devices fall into four categories; primary, secondary, tertiary and quaternary blast injuries. These classifications are almost universally agreed, and are described widely in the literature [108, 109, 110, 111, 112, 113].

Primary blast injuries are caused entirely by changes in air pressure surrounding the body, which means that primary blast injuries affect air filled or containing organs such as the lungs and ears. When the human body is subject to the significant pressure differentials caused by a blast wave, injury can be caused by both the passage of a

shock wave through biological tissue [108] and by physical compression of the body, specifically the chest wall [113, 112]. The passage of the shock wave through low density, air containing organs leads to a rapid compression of the tissue followed by a rapid expansion of the tissue, leading to the destruction of small structures such as alveoli in the lungs.

Secondary blast injuries are those caused by the effect of projectiles interacting with the human body. These are mostly fragments or projectiles specifically contained within a device to cause penetrating injuries; in the case of improvised explosive devices used in the civil and urban environment, these are often nails, ball bearings and other metallic debris. When these projectiles enter the body, they dissipate large amounts of energy through physical deceleration of the projectile and via stress waves through the tissue. This causes major disruption and can lead to severe bleeding, fractures and disruption of organ function.

Tertiary blast injuries are concerned with injuries sustained as a result of body dynamics due to the blast wind that follows the shock wave. The number and type of injury that can occur by tertiary means is almost limitless, as it depends entirely on the surroundings of the individual concerned, but typical injuries can be caused by the body being thrown against blunt or sharp objects, and also as a result of flying objects and collapsing structures caused by the blast wind.

Quaternary injuries encompass most of the rest of the potential injury types from blast events, such as flash burning and radiation effects. These are not typically a major cause of severe injury from conventional explosions; those close enough to receive significant flash burns from an explosive event are likely to be significantly more injured by primary or secondary mechanisms. Nuclear or incendiary bombs are the most likely to cause death or severe injury by quaternary means.

3.1.1 Injury Modes

Terrorist attacks often yield unique patterns of injury, with many modes of injury seen. To provide a simple but thorough risk analysis, the modes of injury that are most frequent should be included, without including unnecessary detail about injury modes that are rarely seen or difficult to predict. Terrorist attacks have been subject to much post event analysis, and extensive data exists on casualties and injury modes from the medical establishments responsible for treatment.

Waterworth [114] presents post mortem findings from an attack on 2 pubs in Birmingham in 1974. Data shows that most casualties suffered from multiple injuries, with injuries from blast alone (85% blast lung, 53% of abdominal injuries) and foreign body penetration of chest and abdomen primarily responsible for death. A review of British Army casualties in Northern Ireland between 1970-84 that were caused by explosions is presented by Mellor [115]. Their findings are consistent with Waterworth [114], with chest injuries being the most widely seen in fatal casualties (75%), with head injuries being the next most common cause of death. Ng [116] and Hart [117] present data from the London nail bombings in April 1999, from two separate hospitals that treated victims. Anecdotal evidence suggests a small charge enclosed within glass and surrounded with nails, which would explain a high prevalence of open fractures and penetrating injuries reported in both accounts.

Israel has been subject to numerous terrorist attacks, and these have been well doc-

umented. Kluger *et al.* [118], Kosashvili *et al.* [119] and Aharonson-Daniel *et al.* [120] present retrospective studies of terrorist attacks in Israel in the early 2000's. Multiple site injuries are seen to be more prevalent (44%) in the victims of terrorism compared to other trauma casualties (18%), with penetrating injuries of head and chest very common. Kosashvili *et al.* have compared patterns of injuries depending on where they happen, and identify a higher incidence of mortality in bus explosions when compared with either closed environment (bars, nightclubs etc.) or open environments, but show a lower incidence of chest and abdominal injuries in bus explosions than in other closed environment explosions. This is thought to be due to the shielding effect of seats in buses, although this is cannot be proved without further investigation.

De Ceballos *et al.* [121] describes the injuries seen in one hospital from the Madrid train bombings in 2004. Findings are in general agreement with other casualty reports above with chest injuries being seen in a large number of critically ill patients (89%), as well as a high proportion (85%) of critically ill patients with shrapnel injuries. Head injuries (52%) and fractures (55%) were also common amongst the most critically ill. The paper notes that patients admitted with critical injuries to the chest and abdomen, as well as traumatic amputations, occur very infrequently as these injuries are often the sign of the most severe injury and often lead to immediate death. This is consistent with casualty data (hospital admissions, which does not include post mortem information or deaths, as in [114] and [115]) and findings from the terrorist attacks in Northern Ireland [122]. Bellamy [123] noted that injuries to the extremities were rarely fatal, and injuries to the trunk, neck and head were the most likely to cause death.

Turégano-Fuentes [124] also review injuries for the Madrid bombings, with one important point of note; the highest levels of mortality were seen in the vehicles where doors were closed at the time of device detonation. This suggests that primary blast injuries and the effect of pressure build up within a vehicle could be very important when predicting the likelihood of fatalities in such events.

Ultimately, each event has slightly different patterns of injury, depending on the location, make up of the device and the way it is delivered. The most serious injuries - head injuries, chest and abdominal injuries and severe fractures are rarely seen exclusively and one or more is most often responsible for deaths. The number of reviews and case studies of this type is extensive (London case study, [125], review and Bali case study [126]) and each presents data slightly differently, making direct comparison between scenarios difficult.

3.2 Primary blast injury prediction

Many experiments have been undertaken on animals to improve understanding of the risk that blast waves pose to humans and develop injury criteria. As a result of the differences in methods and aims, several different models exist which vary in complexity and applicability to this work.

Primary blast injuries are caused by energy transfer to the body from pressure and shock waves in air and risks are commonly specified by the predicting the percentage of a population likely to experience a certain injury when exposed to a given pressure, impulse, positive phase duration, or a combination thereof. The peak pressure experienced (which will strongly influence the impulse experienced, but is not connected to the positive phase duration) will change depending on where and how it is measured and

different models will use a different measure of pressure depending on the experimental set up and mathematical model developed. Some models use a pressure measured near the test subject, others use idealised side on or reflected overpressures and models exist that require multiple pressure inputs from the surface of a test device. All three of these measurements will differ slightly from the pressure experienced at the surface of either a surrogate or live animal and this must be taken into account when applying these models to data from experiments or modelling.

Primary blast injuries can affect many areas of the body, including the brain, eyes, ears, gastrointestinal tract, heart and lungs [112]. The ear is extremely susceptible to primary blast injury, with thresholds for damage low and widely variable; P_{50}, the pressure level at which 50% of tympanic membranes will perforate is given as 57 – 345 kPa by Mayorga [112], and Aylwin [125] reports that 100% of seriously injured patients admitted to the Royal London Hospital after the 7/7 London bombings suffered tympanic perforations. Data from the Madrid bombings from de Ceballos *et al.* [121] showed a lower incidence, but still showed 41% of all patients, and 67% of critically ill patients suffered tympanic perforations. The ease with which damage can be caused to the ears means mechanisms and risk reduction has been well studied, particularly by the armed forces, looking to reduce hearing loss in soldiers exposed to blast. The lung is also of very high risk of injury from primary blast injury, and injuries to the lungs can potentially lead to air emboli that can damage other areas of the body [112]. Data from the Madrid bombings [121] showed blast lung injuries were found in 63% of critically ill patients. Cooper *et al.* [127] found high frequency mechanisms (wave propagation as opposed to physical deformation) as the likely cause of lung injury, with propagation of stress waves and impedance mismatches at various contacting surfaces within the thorax the cause of much of the damage.

Although ear injury is extremely prevalent in blast events, and hearing loss can be life changing for those that suffer from it, it is unlikely to be the cause of fatalities and the ease by which it is caused makes it difficult to propose ways to limit it. Ear protection is a viable and common solution on the battlefield, but this is not viable in civilian mass transit systems. Blast injuries to the lungs are more serious and realistic threat to life, so only these will be considered when identifying primary injury risks within this work.

3.2.1 Injury curves from experimental data

One of the most widely used current criteria for primary blast injury assessment in humans is presented in work by Bowen *et al.* [128], which is based on experiments conducted on a variety of animals in the 1950's and 60's, using shock tubes and high explosives, with peak pressures and positive phase durations scaled to allow data from animals of a variety of sizes to be compared. This in turn allows estimations to be made about the tolerance of human beings to blasts. Peak pressures were measured close to the animal and positive phase durations for high explosive tests were calculated from published data.

The work provides survival data for 3 scenarios; long axis (axis from head to feet) parallel and perpendicular to the direction of travel of the blast wave, and thorax next to a reflecting surface. The figures provided in Bowen *et al.*, (an example of which is shown in Figure 3.1) show peak overpressure against positive phase duration.

In the original paper, Bowen *et al.* point to a possible source of error caused by diffi-

culty in measuring the positive phase duration from experiments. Figure 3.2 shows how inaccuracies in this can lead to large differences in the calculated risk for a given peak overpressure. Bowen states that for technical reasons, the positive phase durations from high explosive tests were taken from published curves for Pentolite, and an assumption was made that this explosive 'releases 10% more energy than TNT, Comp. B or RDX,' and thus a calculation was made to get the positive phase durations for the tests where high explosives were used. It should be noted at this point that a reference is made in the work to the expected errors in the results - up to 30% for positive phase duration less than 2.8ms, and up to 15% percent for positive phase durations between 2.8 and 100ms.

The measurement of pressures during the experiments is also a possible source of error. The work states that pressures were measured as close to the target subject as possible. The location of the measuring device relative to the target can make a large difference to the measured values, and pressures measured away from the target, even by a small amount could be very different to the pressure experienced *at* the target.

Gruss [129] has provided corrections to the curves of Bowen by recalculating the positive phase duration using more accurate data on high explosive blasts. The corrected curves show a more complicated relationship between the peak overpressure and positive phase duration, that was not known when the original work was undertaken by Bowen. No new tests were undertaken by Gruss, the curves were simply redrawn to make the data that was originally plotted closer to what was actually experienced by the animals during testing, rather than what they were calculated to have experienced. This work shows that by correcting the data using modern (and widely cited) data, that the corrected 1% lethality curve crosses the original 99% lethality curve, shown in Figure 3.2.

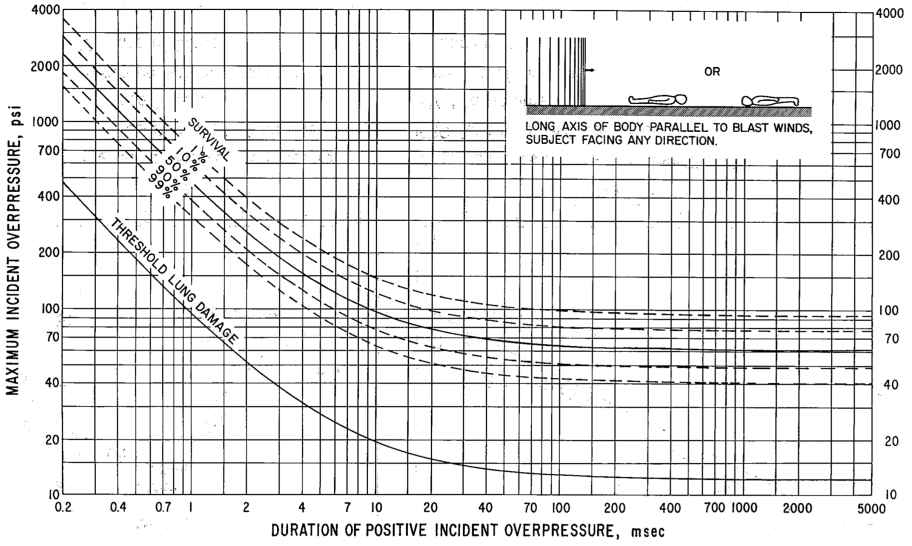

Figure 3.1: An example of the injury curves from Bowen *et al.* [128]

Despite their widespread use, there are some features of both of the above models which do not lend themselves to use in the current research. The models do not provide a generic method of calculating risk as they are limited to the 3 body positions included

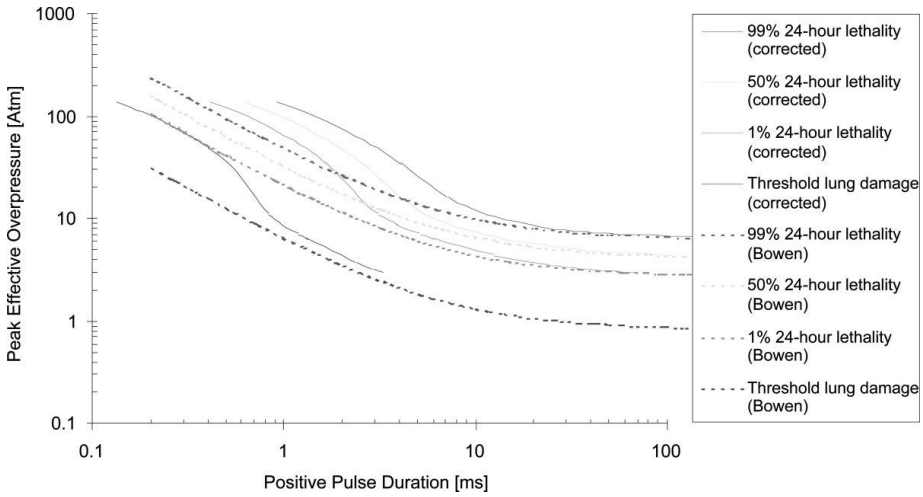

Figure 3.2: Corrected injury curves, shown in Gruss [129]

in the original work. As they use only peak pressure and time duration as the inputs and assume a smooth decay of the pressure towards atmospheric pressure, they cannot account for pressure histories where the pressure time history is complex as the result of many reflections. In some cases, especially when explosions happen inside structures without many openings for pressure to escape, the pressure may decay towards but not reach atmospheric pressure, making the measurement of positive phase duration difficult. The simplified input also makes the models difficult to apply to numerical models, as although peak pressures can be read from data series, positive phase durations are more difficult to identify from complex pressure histories and a number of data processing steps would be required to automate the use of curves within an injury prediction tool.

3.2.2 Logit models

Panzer *et al.* [130] have reviewed the experimental work in this field and devised improved blast survival and injury curves based on a much larger data set than [128], much of which is more recent, with positive phase durations taken from measurements where possible. An analysis provided in previous works by Bass [131] and Rafaels [132] (of which the work presented in [130] is a review / unification) has also suggested that the orientation of the subjects, as mentioned in Bowen, did not have a statically significant effect on risk. As a result, the survivability curves seen in this work should be considered the most up to date as they supersede the work of Bowen.

As well as providing a model for risk due to exposure to single blast waves, Panzer *et al.* also provide a model for risk due to repeated exposures to blast waves. Many experimental studies have been conducted involving exposing animals to multiple blast waves. The research has found that this exposure to repeated blasts can lead to increased injury severity compared with exposure to a single blast wave of similar magnitude [133], and also reduced overpressure threshold for injury [134]. Complex blast waves, seen when blasts occur in confined spaces, have multiple peaks. It is hypothesised by Panzer *et al.* that the risk of injury and fatality due to explosions within structures could be calculated using the developed model, by selecting a suitable number of repeated exposures in the model to artificially mimic the several peaks that would be seen in a complex blast wave. While no model currently exists for the risk of injury when the

body is exposed to these complex waves, it likely that this method should provide an improved risk analysis compared to models for exposure to more simple blast waves that do not show multiple peaks.

The model for single exposures is presented in (3.1), with the repeated exposure risk calculated by the use of an additional term to (3.1) which is a function of the number of repeated blasts which is adjusted with the use of empirically derived coefficients. The model initially defines a piecewise linear relationship (3.1) to establish a correlation between the risk of fatality, and the peak overpressure and positive phase duration. In reality, this linear model cannot properly represent this data, as in reality the outcomes can only be survival or fatality. To fit a model to the data, a transformation was applied to the linear model to ensure that probable outcomes range between 0 and 1, i.e. survival and fatality. The Panzer model uses a logistic regression to transform the probabilities, and the logistic distribution function can be seen in (3.2).

$$f(P_i^*, T_i^*) = \beta_0 + \beta_1 P_i^* + \beta_2 T_i^* + \sum_{j=1} \theta_j (T_i^* - K_j) H(T_i^* - K_j) \tag{3.1}$$

where β_i, K_j and θ_j are model coefficients, $P_i^* = \log_{10}(P)$ and $T_i^* = \log_{10}(T)$ and $H(x)$ is the Heaviside step function.

The logistic distribution function, $\Lambda(z)$, is applied to linear model, for which $(\alpha+\beta X_i)$ is used for clarity. Substituting (3.2) into (3.3) gives (3.4):

$$\Lambda(z) = \frac{1}{1+e^{-z}} \tag{3.2}$$

$$\pi_i = \Lambda(\alpha + \beta X_i) \tag{3.3}$$

$$= \frac{1}{1+e^{-(\alpha+\beta X_i)}} \tag{3.4}$$

Rearranging (3.4) generates an equation for the log odds:

$$\frac{\pi_i}{1-\pi_i} = e^{(\alpha+\beta X_i)} \tag{3.5}$$

Taking natural logarithms of both sides gives:

$$\ln \frac{\pi_i}{1-\pi_i} = \alpha + \beta X_i \tag{3.6}$$

Replacing the simplified linear model, $(\alpha + \beta X_i)$, with the linear model developed by Panzer, (3.1), an equation (3.7) is arrived at which can be used to plot risk curves and predict risks. The relation between the logit or log odds and the percentage of population affected can be seen in Figure 3.3.

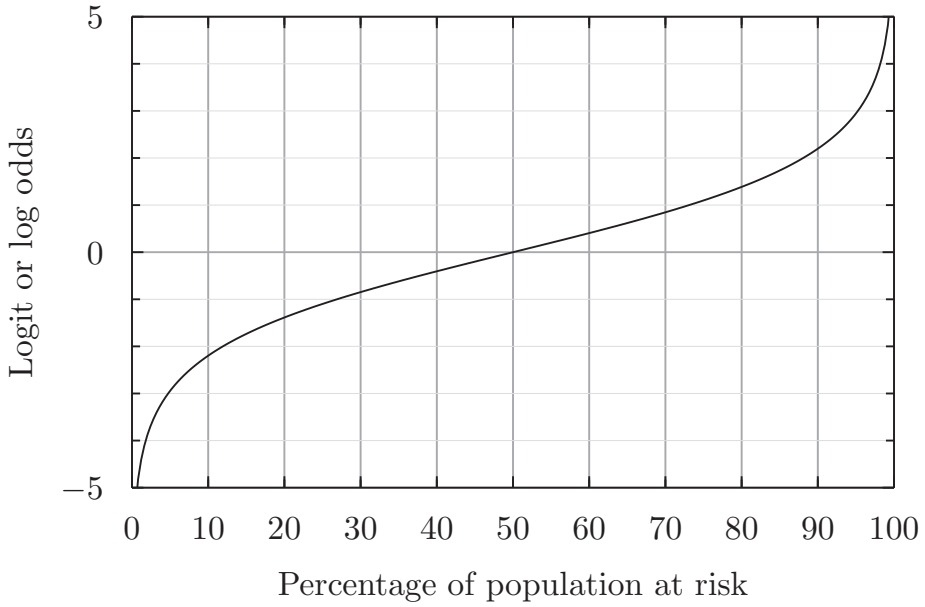

Figure 3.3: Plot of logit function

$$\ln \frac{\pi_i}{1-\pi_i} = \beta_0 + \beta_1 P_i^* + \beta_2 T_i^* + \sum_{j=1}^{k} \theta_j (T_i^* - K_j) H(T_i^* - K_j) \tag{3.7}$$

This model now allows a survival probability to be calculated based on the passing of one blast wave, with a single known peak and positive phase duration. In order to scale the risk value for multiple exposures, Panzer *et al.* propose a repeated exposure risk function, which is included as an extra term not shown in equation (3.7).

3.2.3 Probit models

Larcher *et al.* [135, 136, 137] have used a risk analysis method from Ferradas *et al.* [138]. The work by Larcher is of particular interest as it is currently the only significant recent piece of literature published regarding blast loads in rail vehicles. Larcher *et al.* also give risk analysis formulations for tertiary injuries, which are looked at in more detail later.

A probit model is a regression method similar to the logit model used by Panzer, but uses a different function to transform the probability. The probit model uses the cumulative distribution function (3.8) of the normal distribution to give the linear probit model (3.10), which gives a range of probabilities from 0 to 1, representing survival / fatality or injury / no injury. Instead of leading to log odds of an event happening, as occurs with the logit model, the probit model yields a probit value, which can then be translated into the likelihood of an event happening by the use equations or tables such as 3.1.

The cumulative distribution function (CDF) of the unit normal distribution is shown in (3.8).

$$\Phi(z) = \frac{1}{\sqrt{2\pi}} \int_{-\infty}^{z} e^{-\frac{1}{2}u^2} \, \mathrm{d}u \tag{3.8}$$

As with the logit model, substituting a linear model into the distribution functions gives the probability, π_i:

$$\pi_i = \Phi(\alpha + \beta X_i) \tag{3.9}$$

$$= \frac{1}{\sqrt{2\pi}} \int_{-\infty}^{(\alpha+\beta X_i)} e^{-\frac{1}{2}u^2} \, \mathrm{d}u \tag{3.10}$$

Typically, most of these equations are unnecessary for analysis purposes, as equations for the probit value, typically in the form $Y_i = \alpha + \beta X_i$, are given which yield the probit value, which can be used to calculate the probability from pre calculated tables or equations. An example of the probit – percentage table can be seen in Table 3.1, and when probit values are plotted against probability (or percentage of a population who will not survive), a curve is formed as shown in Figure 3.4.

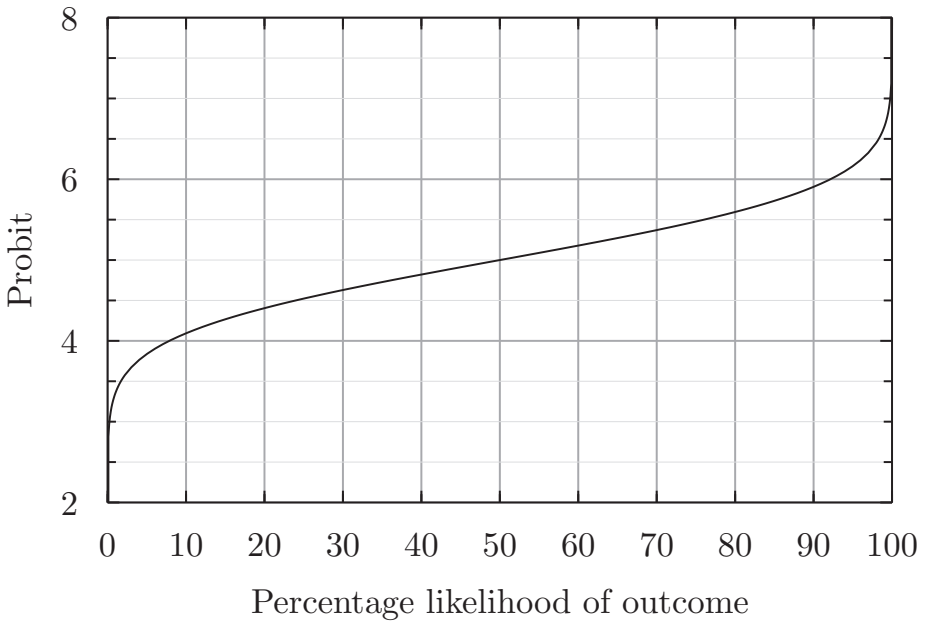

Figure 3.4: The probit function, showing probit against percentage of the population at risk

The probit equations used by Larcher *et al.* for survival due to lung haemorrhage (3.11) and risk of eardrum rupture (3.12), which return a probit value, Y_i, are shown below, where P_{max} is the maximum pressure at point within the volume under investigation. These equations are taken from [138], which in turn are taken from reference works by Lees [54] and TNO [139].

$$Y_1 = -77.1 + 6.91 \ln P_{max} \tag{3.11}$$

$$Y_2 = -12.6 + 1.524 \ln P_{max} \tag{3.12}$$

Table 3.1: Percentage – probit transformation

%	0	1	2	3	4	5	6	7	8	9
0	0	2.67	2.95	3.12	3.25	3.36	3.45	3.52	3.59	3.66
20	4.16	4.19	4.23	4.26	4.29	4.33	4.36	4.39	4.42	4.45
50	5.00	5.03	5.05	5.08	5.10	5.13	5.15	5.18	5.20	5.23
90	6.28	6.34	6.41	6.48	6.55	6.64	6.75	6.88	7.05	7.33

It is important to note the differences between the work presented in Bowen and Panzer [128, 130] and the models utilised above which do not show injuries as a function of both pressure and impulse or positive phase duration. Equations (3.11) and (3.12) give probit values purely as a function of peak overpressure. This is potentially an assumption that is incorrect, and is explained in more detail in section 3.2.5

The probit method is a popular method for survivability analysis, as it is very simple to apply to experimental data. Lees' [54] quotes a more comprehensive probit equation from TNO [139] for the risk of death from lung haemorrhage, which is given in terms of both pressure and impulse. These are given in a scaled form [140], depending on atmospheric pressure and the mass of the body that is subject to a blast load. These scaling laws, and the probit equation that uses them (3.13), were used by Baker [140] to create alternative pressure impulse diagrams based on the work of Bowen *et al.*, so the Baker model should yield risk scores that are broadly similar to those of Bowen.

$$Y = 5 - 5.74 \ln \left(\frac{4.2}{\bar{p}_a^o} + \frac{1.3}{\bar{i}} \right) \tag{3.13}$$

where $\bar{p}_a^o = \dfrac{p_r}{p_a}$ and $\bar{i} = \dfrac{i}{p_a^{\frac{1}{2}} m^{\frac{1}{3}}}$, where p_r and p_a are reflected and atmospheric pressure and m and i are mass and impulse.

This can be simplified to (3.14) by substituting a mass of 70kg and atmospheric pressure of 100kPa into scaling equations in [54]:

$$Y = 5 - 5.74 \ln \left(\frac{4.2 \times 10^5}{p_r} + \frac{1694}{i} \right) \tag{3.14}$$

3.2.4 Chest compression models

The models described above make a direct relation between pressure and impulse levels from simple waveforms, and various risks of injury in humans. These do not make a relation between the pressure, impulse and physical response of the body which causes an injury, so cannot be used when complex pressure time histories resulting from shock wave reflections are seen.

Models by Axelsson [141] and Stuhmiller [142] use mass spring damper models of the chest, where a pressure time history at the chest wall surface is an input. Axelsson *et al.* calculated the chest wall velocity of animals that were subjected to physical blast testing, allowing them to plot the risk of injury against chest wall velocity. Importantly, they provide an equation to allow the chest wall velocity to be calculated from a measured or simulated pressure time history. The mathematical model for the thorax from Axelsson is shown in equation (3.15). In the method, 4 pressure histories are taken from

Table 3.2: Injury levels and corresponding ASII and chest wall velocities

Injury Level	ASII	v_{max}
No injury	0.0 – 0.2	0.0 – 3.6
Trace to slight	0.0 – 1.0	3.6 – 7.5
Slight to moderate	0.3 – 1.9	4.3 - 9.8
Moderate to extensive	1.0 – 7.1	7.5 – 19.9
> 50 % lethality	>3.6	>12.8

sensors spaced at 90^o intervals around a cylinder in a numerical model or physical test. Velocities are calculated at each pressure sensor location from Equation (3.15) and then a mean is taken to give the chest wall velocity.

The experimental method used by Axelsson to achieve the four necessary pressure requires a cylindrical Blast Test Device, with a diameter of 305mm and a height of 762mm, which is designed to be representative of the subject under investigation. The sensor data is taken from the half height of the cylinder at 90^o intervals around the circumference.

$$M\frac{\mathrm{d}^2x}{\mathrm{d}t^2} + J\frac{\mathrm{d}x}{\mathrm{d}t} + Kx = A\left[p(t) + P_0 - P_0\left(\frac{V}{V - Ax}\right)^g\right] \tag{3.15}$$

A mass spring damper model of the chest is used to generate a differential equation linking the pressure history on the surface of the chest with the displacement of the chest wall. Solving the differential equation gives the chest wall velocity which can then be used to calculate the Adjusted Severity of Injury Index (ASII) using equation (3.16). One of the major aspects of Axelsson's work was to correlate the chest velocity with injury scores that were found from autopsies on animals used in the testing. Injury levels, ASII values peak inward chest velocities, v_{max} from Axelsson [141] can be found in table 3.2.

$$ASII = (0.124 + 0.117V)^{2.63} \tag{3.16}$$

The Axelsson method is designed to provide an effective method to predict injuries in complex blast wave environments from pressure time histories, and as such is particularly suited to closed environments, such as rail vehicles. Data can be taken directly from models and input into numerical methods to solve Equation (3.15) for the chest velocity v. This does not suggest by any means that this method provides a definitive and absolutely correct method of predicting injury - the method averages 4 calculated velocities to give an overall chest wall velocity, which could certainly be regarded as a simplification of the real world scenario. Work is ongoing in various research groups throughout the world to identify methods of predicting injury with debate still active as to what the most crucial factors are in determining primary blast injury.

3.2.5 Pressure threshold criteria

The models and curves in sections 3.2.1, 3.2.2, and to some extent 3.2.3, are alike in that the risk is considered to be both a function of peak overpressure and positive phase

Table 3.3: Injury Groups from [110]

Group	p_{so} (kPa)	Injury
1	<150	Minor – Maximum overpressure sustained sufficient to cause ruptured tympanic membrane
2	150 – 350	Moderate – Higher overpressure than Group 1, but probably insufficient to cause primary lung damage in a significant number of casualties
3	350 – 550	Severe – Sufficient overpressure to cause primary lung damage in a significant proportion of casualties
4	>550	Very severe – Sufficient overpressure to cause severe primary lung damage with a significant incidence of death

duration. This is important, as a given peak overpressure can be produced by a range of different charges, depending on distance. Mellor [110] has conducted a study of blast related deaths and injuries in Northern Ireland between 1970 and 1984, and groups the severity of injuries according to peak overpressure alone. Casualties are divided into 4 groups, each with increasing levels of injury, with 1 being the least severe, and 4 relating to a 'significant incidence of death', shown in Table 3.3. It is shown that 50% of personnel exposed to blasts with a peak overpressure of greater than 550kPa (80 psi) were killed. According to curves and models described above [128, 129, 130], this peak overpressure could be responsible for greater than 99% chance of survival, or approximately 10% chance of survival (seen in Figure 3.1), depending on the duration of the positive phase, which is a function of charge size and distance.

3.2.6 Single point models

Single point methods, such as the logit, probit and Bowen models take a single value of either incident or reflected pressure and use them to calculate the risk of primary blast injury. They have the advantage of being very simple and quick to implement in numerical environment, and although Bowen methods require digitisation and interpolation of curves to be implemented within a piece of software, they can be very quickly implemented by hand, if only a few risks need to be calculated. One of their major disadvantages though, which can have large implication for accuracies, is the neglect of shock wave interaction with both surrounding objects and the body for which injury risk is being calculated.

It is only possible to predict the actual pressure (and pressure history) at a *point* in a very limited range of scenarios:

- in a free field, with no surfaces or interacting objects close enough to alter the pressure over the time duration of interest[1]
- at a point on the surface of a rigid reflecting body normal to the direction of shock propagation which is large enough that no edge effects are experienced
- at a point on rigid finite surface where the size of the finite surface and the scaled distance (Z, see Chapter 2) is known, and the surface is normal to the direction of propagation of the shock

[1]limited exceptions to this exist - a thin wall perpendicular to direction of shock propagation will not cause significant changes in the shock wave behaviour

The Bowen method used animals in similar positions to those above, so predictions could be made when a person was in a similar scenario. When other structures, of arbitrary shape or number are within an influential distance of the body, the pressure history that would be recorded at their surface will not be the same as in these idealised situations. It will be different for every combination of number, shape and position of interacting structure, which in the case of a rail vehicle will include the number and distribution of passengers, the proximity of the explosive device and persons under investigation to structures such as the vehicle boundary, seat and draught screens.

Teland [143] suggests single point approximations to the Axelsson method, by assuming the pressures likely to exist at the 4 sensors required in the Axelsson method from the pressure at a single point. These methods were developed so that if an estimate of injury was required at a new location, not originally included in a model, an estimate can be provided from a pressure history without having to add a blast test device to the model. It makes sense to implement such a method to avoid unnecessary computational expense, but the resulting calculation does not include the contribution of the extra body to the pressures experienced at other sensor locations. Thus, these single point methods are appropriate only in certain situations, where the body under investigation does not contribute significantly to the propagation and interaction of the shock, with either itself or other bodies and structures.

3.3 Secondary injuries

Secondary injuries result from the impact of fragments and bomb debris with the body (which will be referred to as 'projectiles' from here), causing injury by penetrating trauma which can cause fatalities depending on severity. Devices designed to inflict damage either contain ready made projectiles such as nails or ball bearings, or the charge material is surrounded with a material designed to break up and be ejected at high speed. Predicting the injury from these projectiles requires knowledge of their number, direction and velocity, as well as their subsequent trajectory and contact with any structures that will alter their flight. The likelihood and location of impact with the body can then be predicted, injury criteria applied and a risk of injury calculated. For an individual projectile item this is relatively straightforward, but when hundreds and potentially thousands of projectiles are involved this becomes a much larger task. Additionally, there are many unknown factors that must be assumed, including the shape of the charge, size, configuration, shape and packing of projectiles in the device, as well as the location of the device and passengers within the at risk area.

The prediction of secondary injuries is made very difficult by a large number of unknowns and a number of variables that are difficult to quantify. This section presents methods from the literature that can be utilised to predict the risk of secondary injuries, which can be utilised in a holistic method of predicting injuries from explosive devices.

3.3.1 Analytical models

Several models have been proposed to describe the ejection, flight and injury potential of projectiles. Much research exists [144, 145, 146, 147] about the separate stages of a projectile's movement from rest to target impact and penetration, but fewer articles can be found describing a complete method for predicting injury. Those which could be

found are described below and show significant variation between methods, indicating that care must be taken where potentially outdated, inapplicable and unvalidated criteria and models are used.

Gilbert and Lees [148, 54] provide a method for predicting injury based on historical data and a collection of equations from a variety of sources, specifying mass distribution, initial velocity and angle, retardation and flight through air and finally the probability of a hit and criteria for injury. They state that data is taken partly from experimental work and partly from data from World Wars 1 and 2, and importantly is designed to model injury from projectiles produced by fragmenting munitions. Munitions are constructed differently to improvised explosive devices, and are directed against different targets, so care should be taken when applying models such as these. The model is included for completeness and as a comparison with other methods.

Radtke *et al.* [149] and Chrostowski and Gan [150] have developed similar programs for simulation of explosive hazards. Both models use a 79 Joule kinetic energy lethality criteria that have not been validated and are generally considered too simplistic [151] with Henderson [152] suggesting that the 79 Joule energy criteria corresponds to a conditional lethality probability (the probability of death given that an individual is hit) of 1%. The HAZX code developed by Chrostowski and Gan [150] is designed to be used for large explosions and the risk to both buildings and humans and as such is generally not appropriate for modelling the effects of IEDs. Radtke *et al.* provide methods for predicting the hazard from both conventional munitions and IEDs, based on experimental testing with pipe bombs. Their experimental method prevented full capture of projectile velocity and angle, so angles are assumed to follow a normal (also referred to as *Gaussian*) distribution across angle intervals, with velocity determined from experimental measurements, as a function of launch angle or average velocity. The use of validated models to describe initial conditions is promising, but insufficient detail is given for this model to be implemented here.

Pope [153] has incorporated projectile prediction into a fast running tool called the Human Injury Predictor (HIP) code by specifying the initial conditions (velocity, angles and mass distributions) and subsequently the trajectory, velocity history and the depth of penetration into a surrogate human made from ballistic gelatin. The models are designed to predict the effects from PBIEDS and have been validated by controlled tests, which is a key feature of the work, but not all parameters to calibrate equations are given, so not all features can be implemented.

3.3.1.1 Initial conditions

The accuracy of an overall prediction is dependant on the prediction at each stage. Arguably, this makes the initial conditions the most critical to predict properly, as the effect of altering them makes and impact at all stages of the calculation. For IEDs the initial conditions of primary concern are the angle and velocity at which projectiles are ejected, as well as the total mass of projectiles. The mass distribution of projectiles is stated by some models as an important initial condition, but is not of concern where devices contain predetermined projectiles of almost equal mass.

Radtke *et al.* [149] and Pope [153] suggest a probability density function for the angle of throwout in two dimensions with a multivariate normal distribution (3.17). The parameters σ_x and σ_y are not given, but it is stated that in line with numerical and

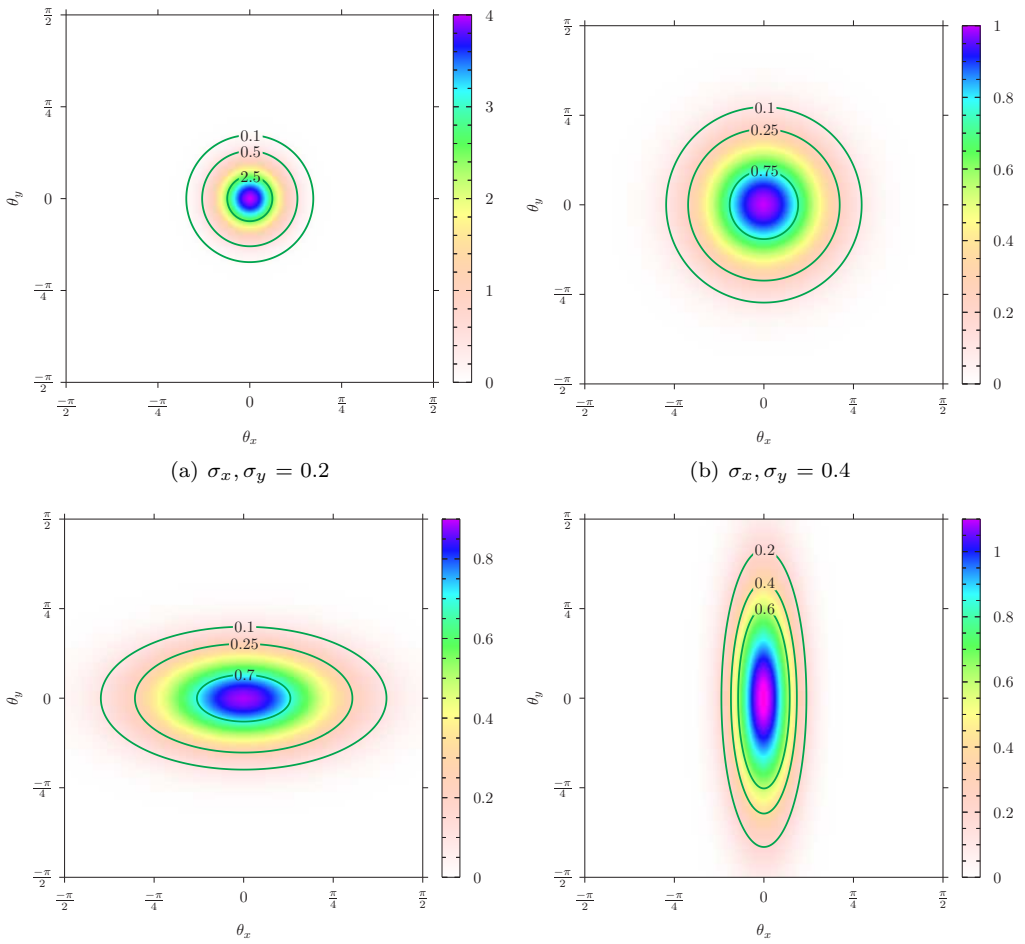

(a) $\sigma_x, \sigma_y = 0.2$ (b) $\sigma_x, \sigma_y = 0.4$

(c) $\sigma_x = 0.6, \sigma_y = 0.3$ (d) $\sigma_x = 0.2, \sigma_y = 0.7$

Figure 3.5: Effects of altering $\sigma_{x,y}$ on multivariate normal distribution for probability density

experimental finding they are strongly biased to give low values for the angles θ_x and θ_y, while maintaining an element of randomness in line with a realistic IED. As the value of the standard deviation, σ, increases in a given axis, the range of the likely distribution of angles increases, as shown in Figure 3.5. Pope assumes projectiles are ejected from a flat surface and as such the majority of projectiles make small angles with the axis normal to this surface, but for spherical or cylindrical devices, a more even distribution of across a full angular range would be expected.

$$P(\theta_x, \theta_y) = \frac{1}{2\pi\sigma_x\sigma_y} \mathrm{e}^{\frac{-1}{2}\left(\left(\frac{\theta_x^2}{\sigma_x^2}\right)+\left(\frac{\theta_y^2}{\sigma_y^2}\right)\right)} \tag{3.17}$$

Velocity is predicted in the HIP code [153] in two ways, both as a function of the trajectory angle as predicted in (3.17) and pre selected minimum and maximum velocities v_{max} and v_{min}, shown in Equation (3.18), and by use of the Gurney equations (3.19), eq:gurney-cylinder and eq:gurney-sphere [154, 155]. One of the main problems with the use of Equation (3.18), is that it is only applicable to a limited number of configurations and cannot easily be applied to a wide variety of devices with different combination of

projectiles and charge masses. As a result, the Gurney equations are also implemented in line with many other models and theories for predicting projectile effects. The Gurney equations were originally developed for predicting the initial velocities for fragmenting munitions and were validated by experimental data. There are several forms of the Gurney equations, depending on the shape and configuration of the device, shown in Equations (3.19) – (3.22). Pope makes the assumption of an asymmetric 3 layer device using Equation (3.19), consisting of a backing material with mass N, explosive charge of mass C and a total projectiles mass of M. The quantity $\sqrt{2E}$ [2] is termed the Gurney characteristic velocity for a given explosive, and v_M the velocity at which the projectiles are ejected. The Gurney velocity, which has units of speed, is determined for a variety of explosive materials and values for it can be found throughout the literature [154, 155]. Gilbert [148] makes the assumption that the device is a cylinder, Equation (3.21), with an explosive mass M and charge mass C. Similar equations for spherical devices also exist (3.22).

$$v(\theta_x, \theta_y) = v_{max} - (v_{max} - v_{min})\sqrt{\frac{\left(\theta_x/\theta_{xmax}\right)^2 + \left(\theta_y/\theta_{ymax}\right)^2}{2}} \tag{3.18}$$

$$\frac{v_M}{\sqrt{2E}} = \left(\frac{1+A^3}{3(1+A)} + A^2\frac{N}{C} + \frac{M}{C}\right)^{-1/2} \tag{3.19}$$

where

$$A = \frac{1+2M/C}{1+2N/C} \tag{3.20}$$

$$\frac{v_M}{\sqrt{2E}} = \left(\frac{M}{C} + \frac{1}{2}\right)^{-1/2} \tag{3.21}$$

$$\frac{v_M}{\sqrt{2E}} = \left(\frac{M}{C} + \frac{3}{5}\right)^{-1/2} \tag{3.22}$$

For the 3 available shapes of charge described above, the variation of velocity and angle will de different due the different way in which explosives of certain shapes expand, which is also affected by the position of detonation (which for the purposes of simplicity will be assumed to be central).

For a sphere, there will not be any particular bias for projectiles moving in a particular direction to have particularly high or low velocities, as the explosive will be expanding as a sphere and pushing all projectiles normally to their position on the surface of the sphere at that time. The initial arrangement of projectiles will determine the dominant direction, and how spread velocities will be, but for evenly distributed projectiles, an even spread of velocities and directions for all projectiles would be anticipated.

[2] Instead of using the quantity E, which is in terms of energy per unit mass, the term $\sqrt{2E}$ is normally stated, for simplicity of statement and calculation.

For a vertical cylinder, the angular spread in the radial direction should, as with a sphere, be consistent over the range of angles over which projectiles are placed, assuming no concentrations over a particular range of angles. Variation in vertical spread angle will be different, and the expansion of a cylinder would mean there will be smaller spread, with angles close to the horizontal dominating, with projectiles travelling on a vector close to the axis of cylinder less likely, and with a lower velocity. For evenly distributed projectiles, an even spread of velocities and angle would be expected in the radial direction, with vertical angular spread being limited and highest number and velocity being clustered around horizontal direction.

For projectiles placed on a flat charge, directions close to the face normal will dominate, with highest velocities for a projectile when they are ejected at low angles from the normal, and lower velocities when they make larger angles with the normal.

3.3.1.2 Trajectory and velocity change

Projectiles and debris from explosions will begin with very high velocities, many of which will initially be supersonic, that decay very rapidly due to high drag forces. As the projectiles slow down from supersonic, they will enter transonic and subsonic regimes, which will alter the retarding drag on a flying projectile. It is outside of the scope of this work to develop equations for, or model with numerical methods, the velocity characteristics of arbitrary shaped projectiles flying through air, but a number of equations exist that seek to approximate this behaviour.

In the HIP code [153], a differential equation is used for velocity calculation, Equation (3.23). Modifications of the A, B and C (coefficients for projectile drag, friction and material strength respectively) allows the equation to deal with both the flight of the projectiles through air, and the velocity behaviour of projectiles moving through solid media, which in the HIP code was crowd members formed of ballistic gelatin.

$$-m\frac{\mathrm{d}v}{\mathrm{d}t} = A(v^2) + B(v) + C \tag{3.23}$$

The United Facilities Criteria document, UFC 3-340-02 [37] gives equations for the velocity of primary projectiles (Equation (3.24)). It is stated in [37] that retardation can often be neglected, in cases where the source and target are less than 20 ft ($\approx$ 6m). Units for (3.24) and (3.25) are not given in [37], but examples given indicate they are imperial units, and comparative calculations of velocities in metric and imperial do not agree.

$$v(x) = v_0 \mathrm{e}^{-12k_v x} \tag{3.24}$$

where

$$k_v = \frac{A\rho_a C_D}{W_p} \tag{3.25}$$

Equations of a similar form are found in Gilbert [148] and Lees [54] with equations from Christopherson [156] and Zuckerman [157], (3.26), (3.27) and (3.28) used to treat the retardation of projectiles, depending on whether they are flying at super or subsonic

velocities ($M \geq 1, M < 1$). Both equations (3.26) and (3.27) are used to treat supersonic projectiles; both are similar, but (3.27) includes the additional term a.

$$\text{Where } M \geq 1,\ v(x) = v_0 \mathrm{e}^{-x/284m^{1/3}} \tag{3.26}$$

$$\text{Where } M \geq 1,\ v(x) = v_0 \mathrm{e}^{-0.00204xa/m^{1/3}} \tag{3.27}$$

$$\text{Where } M < 1,\ v(x) = v_0 \mathrm{e}^{-0.00137xa/m^{1/3}} \tag{3.28}$$

$$a = \frac{A_m}{Q^{2/3}} \tag{3.29}$$

Where v_0 is the initial velocity (ft/s), x the distance travelled (ft), m the mass of the projectile (oz), A_m the mean presented area of the projectile in ft^2 and Q the projectile volume in ft^3. In order to utilise these equations, input data in SI units will need to be converted to the correct units.

3.3.1.3 Probability of hit and injury

The path of a projectile through air is described adequately by many existing relationships, but correlation between conditions at the point of impact with tissue and the likelihood of an injury is more difficult. There is much interest in developing appropriate criteria and much work has been done with firearm projectiles to understand their behaviour under controlled conditions to assist with the design of protective armour and improve medical treatment.

Depth of penetration (DOP) is a widely used criteria for predicting the injury level from penetrating projectiles. Pope [153] has conducted experiments with 20% Ballistic Gelatin (BG) using representative projectiles, and developed criteria for depth of penetration as shown in Equation (3.30). Breeze *et al.* [146] propose DOP equations derived from tests with Fragment Simulating Projectile's (FSPs) on porcine tissue depending on weight of FSP and the body part the projectile penetrates. BG tests correlate well with penetration into muscle, but penetration into abdomen and chest cavities were not predicted well by BG tests.

Gilbert [148] uses a probability based method - probability of being hit, $P(H)$, is given as a function of the number of incapacitating projectiles at a given distance, $N(x)$, and the number of projectiles that hit a body, r, shown in Equation 3.32. Probit equations are then given for likelihood of penetration of certain areas of the body based on projectile mass, velocity and area, and further probability relations used to predict the likelihood of injury. TNO Greenbook [139] uses probit equations for projectiles up to 0.1kg (An example of which is given in equation (3.31)) depending on projectile mass and initial velocity, as does [27]. Smith [27] provides a curve from Ahlers [158] that correlates projectile mass and velocity to injury for head and body, also presented in

[159].

$$d = C1\left(\frac{(v - C2)}{C3}\right)^{C4} = \frac{0.011 \times 2 \times m^{0.95}}{\rho A C_d}\left(\frac{V - \left({}^{(80 \times A)}/_{m^{1.3}}\right)}{400}\right)^{0.55} \tag{3.30}$$

$$Y = -29.15 + 2.10\ln S \tag{3.31}$$
$$S = m v_0^{5.115}$$

$$P(H) = \frac{N(x)}{r!}\mathrm{e}^{-N(x)} \tag{3.32}$$

3.4 Other Injury risks

Much research has been done which aims to identify threshold pressure and impulse levels to determine the risk particular blast events pose to human beings. Criteria have been in place for some years and, in the absence of significant data on human response, they have been refined and revised based on the response of animals. So far, the models described can provide risk functions for survival, pulmonary and non-auditory injuries and injury risk due to impacts, but none of the models described so far take into account the risk of brain injuries due to pressure waves, or the risk posed to humans by flying debris, such as shattered glass or materials specifically used to create a projectile hazard. Clearly, if an effective threshold injury risk is to be identified, it should account for as many injury mechanisms as possible.

In Sections 3.2 and 3.3 models are presented for predicting injury from blast waves and flying projectiles and debris which are responsible for the majority of injuries when bombs or improvised explosive devices are detonated. Here, further models and risk analysis methods are presented for other injury modes not covered in Sections 3.2 and 3.3.

3.4.1 Tertiary injuries

Tertiary injuries are those which occur due to body dynamics, primarily by impact of various parts of the body with hard surfaces. Much work has been done in automotive industry to define impact injury risks for various parts of the body for both pedestrians hit by moving vehicles and occupants who make impacts with the inside of vehicle. Criteria for each injury is commonly defined by the acceleration experienced by certain body areas; crash impact dummies, both physical and numerical are fitted with accelerometers, and data from these can be input into models, such as the Head Injury Criterion (HIC) (3.33). The need to know the acceleration value (3.33) means that an understanding is needed of the interaction between a body part and the surface it impacts. There is some debate [160] as to how accurately injuries are predicted by HIC, but it remains in widespread use as one of the most dominant criteria, being used in assessment protocols by major car safety programmes [161]. Many of the widely used impact injury

criteria, such as HIC are easily implemented by using finite element models of crash tests dummies, and numerical codes such as LS-Dyna produce crash test dummy models with correctly positioned accelerometers and post processing tools to calculate injury criteria for the head, thorax and extremities. Implementation of these models would be the most accurate way to identify tertiary injuries, as minimal assumptions are required about impact conditions or loading, as the blast load and impact mechanisms could be coupled in a single solution, or the solution broken down into steps.

$$\mathrm{HIC} = (t_2 - t_1)\left[\frac{1}{t_2 - t_1}\int_{t_1}^{t_2} a(t)\,\mathrm{d}t\right]_{max}^{2.5} \tag{3.33}$$

A number of probit equations for the risk of fatal or substantial injury on hard surfaces are also in existence. Equations (3.34) and (3.35) in terms of pressure and impulse are used by Giannopoulos [135] to assess the risk of lethal injury from head and body impact due to explosions in rail vehicles. The equations are originally found in the TNO Greenbook [139], and are quoted by Lees [54] in the section for outdoor explosion injuries.

$$Y_3 = 5 - 8.49\ln\left(\frac{2430}{P_{max}} + \frac{4\times10^8}{P_{max}I}\right) \tag{3.34}$$

$$Y_4 = 5 - 2.44\ln\left(\frac{7380}{P_{max}} + \frac{1.3\times10^9}{P_{max}I}\right) \tag{3.35}$$

Lees [54] also provides probits for the probability of lethal skull impact (3.36) and lethal injury due to body translation (3.37) in terms of the impact velocity, V.

$$Y_5 = -6.04 + 7.11\ln V \tag{3.36}$$

$$Y_6 = -2.14 + 2.54\ln V \tag{3.37}$$

The dynamics of an impact scenario within a complex environment such as rail vehicle mean it is very difficult to gain a realistic insight into injury with simple probit equations. Each different surface within a rail vehicle (floor, walls seat, tables, draught screens an so on) has different force deformation characteristics, altering the acceleration. For just the head, the strength of the skull is widely variable in different orientations, and impact and different locations will lead to different injuries, depending on which direction the brain is accelerated, and how much rotation is experienced. The probit equations above are also for lethality, so provide a risk of lethality, which is difficult to translate into the severity of injury. Data from real attacks (section 3.1.1) indicates lethality is rarely from one injury alone, normally a compound of several severe injuries, so a more appropriate method would provide a scale that could rank the injury severity. Equations (3.34) and (3.35) have inputs that are relatively straightforward to generate from models, but the

velocity used as an input in (3.36) and (3.37) is much more difficult to obtain from models.

Ultimately, the dynamics of the body are generally too complex to simplify to the point where a simple pressure history at a point in space can predict the likelihood of tertiary injury; a good prediction is required for how the body accelerates from stationary (a function of body position, orientation, mass, shape and applied load), as well as what part of the body hits what kind of structure, and in what orientation. Without taking account for any of this, and without the known assumptions used in making the models described it is very difficult to understand if the equations above are in any way applicable to a rail vehicle, so their application is difficult to justify.

Injury criteria (such HIC etc.) require real accelerometer data, either from experimental data or from numerical models, and these criteria are generally accepted and widely used for use in impact trauma injuries. Unfortunately, trial models implementing numerical crash test dummies for blast events have proven unsuccessful at the current time, with poor coupling between the ALE fluid domain and the dummy shell. The numerical dummy models have a wide variety of element sizes, which will prevent good coupling between the elements of the numerical dummy that are most different in size from the ALE mesh.

Tertiary injuries are very rarely the sole cause of injuries, with accumulations of severe injuries often being responsible for mortality. Without an accurate and computationally efficient model available, it is possible that injury estimates from tertiary means from the models discussed could be largely inaccurate. In light of this, it was decided that it is better to make no prediction of this, than make an incorrect prediction for the sake of completeness. Along with development of improved criteria for primary and secondary injuries, further investigation of tertiary injuries from blasts is required.

3.4.1.1 Traumatic amputation

Traumatic amputations occur when limbs or parts of limbs are removed as a result of an accident or injury. Hull's article from 1992 [162] reports the prevalence of traumatic amputations in service personnel over an 11 year period between 1979 and 1990. It was shown that traumatic amputations were not commonly seen in survivors, with most persons close enough to suffer a traumatic amputation being killed by the associated injury. Projectile wounds and fractures were the most common associated injury. Levels of traumatic amputation in those hospitalised as a result of the Madrid and London bombings are reported by de Ceballos *et al.* [121] and Aylwin *et al.* [125], and show traumatic amputations (as with other most injuries) are higher in the critically ill patients, but are not a highly prevalent injury in survivors. This could indicate, as suggested by Hull, that those who suffer traumatic injuries often are the most seriously injured and are killed before they can receive treatment.

The method of traumatic amputation is not well understood, and no models exist in the open literature to provide validated predictions of the likelihood of traumatic amputations. As a result, the effect of traumatic amputations is not considered here when assessing risk.

3.4.2 Traumatic Brain Injury

A large body of work exists on Traumatic Brain Injury (TBI), with much of it looking to identify, how TBI can be identified and the mechanisms within that cause injury. Almost no work exists to suggest thresholds of pressure, impulse or acceleration at which TBI occurs.

Courtney [163] has provided a review of current work in the field of blast induced TBI, and a similar review of primary blast induced TBI mechanisms has been provided by Nakagawa *et al.* [164]. Although mechanisms by which TBI occurs are not exactly clear, suggested mechanisms are from [163, 164] are as follows:

- Direct transmission of blast waves through the skull to brain. This mechanism is generally not well understood despite being considered one of the most common.
- Head acceleration mechanism - where the head is accelerated purely due to the primary effects of the blast wave.
- Penetrating injuries - projectiles penetrate the skull and enter the brain tissue.
- Thoracic mechanism - pressure waves enter the thorax, in the form of a blunt trauma or penetrating injury from a projectile, and leads to a brain injury.

Elsayed [165] and Nakagawa [164] both suggest that the direct transmission of blast waves through the skull are the most common, but that the most severe injuries are caused by a combination of mechanisms, such as acceleration/deceleration and penetrating injuries. This interaction between these 3 mechanisms makes a generalised risk analysis for TBI difficult at this point in time, but threshold levels for brain injury for each mechanism are slightly easier to develop. Courtney [163] has produced threshold levels for injury via the thoracic mechanism and due to head accelerations, based on work from various experiments in the form of curve fits to limited experimental data, and as yet have not produced a mathematical model for these methods of injury. Although application of criteria for TBI would add to the completeness of any injury model, the fact that most models are only in the early stages of development and significant bodies of data on the subject do not exist, models for traumatic brain injury will not be included in the prediction of human risk considered here.

3.5 IED makeup and configuration

Many of the features described above are heavily dependent of the design of the device used. Improvised explosive devices or IEDs, particularly person borne IEDs (PBIEDs) for the case of rail vehicles, by definition have no standard construction. The important variables in device design will vary considerably across designs from different groups, which makes characterising many of the important initial parameters described above (velocity and trajectory of projectiles, blast overpressures) difficult, with a high level of variation expected between real parameters in different devices. For the purpose of analysis and prediction, it is important to define a representative device that isn't too complex to implement in models, parameters for which can then be estimated.

- main charge
  - mass

  - shape
  - type

- primary fragmentation
  - total mass
  - number
  - shape
  - positioning within device

3.6 Developing a comprehensive risk analysis formulation

3.6.1 Multiple injury accumulation

When a number of injuries occur, it is necessary to combine those injuries and identify a compound measure of how severely a person has been harmed. The Injury Severity Score (ISS) is the most commonly used anatomical trauma scoring system and is computed by taking the Abbreviated Injury Scale (AIS) values for the 3 most injured different areas of the body, squaring them and adding them together.

Table 3.4: AIS scores for injury categories

Injury	AIS
Minor	1
Moderate	2
Serious	3
Severe	4
Critical	5
Unsurvivable	6

The abbreviated injury scale (AIS) is an anatomical system used to classify injury by body region by severity on a scale of 1–6 [166]. The AIS itself includes a coding system to classify different individual injuries in each area of the body, each of which is assigned an injury score. It was originally conceived in the United States to grade injuries from automotive collisions, and it's development is led by the Association for the Advancement of Automotive Medicine, with revisions made to update the scale with advancements in medicine. It is widely used in trauma research, and forms the basis for the Injury Severity Score.

The ISS can range from 0 to 75. The New Injury Severity Score (NISS) follows the ISS, but takes the AIS for the 3 most severe injuries, regardless of which body part they occur in [167]. For comparison between the two if 3 severe injuries to the abdomen occurred, and two trivial injuries to other areas, only the most severe abdominal injury would count towards the score, plus those for the two other trivial injuries with ISS. With NISS, all three severe abdominal injuries would be counted, and the NISS score would be higher than the ISS score, which does not take account of multiple severe injuries in the same body region. NISS is more accurate and provides a better indication of mortality in the short term [168] and overall [169], and should be seen to supersede the

ISS [167]. Scope *et al.* [170] showed that ISS scored in the low 40's were associated with a high risk of death within 30 minutes of wounding.

3.6.2 Chosen methods and models

The following methods and models are identified as being the most appropriate, offering a balance of accuracy and simplicity of implementation. By no means have all possible injury models been reviewed, and it is a subject of ongoing research, particularly within civil service and defence organisations across the world, but an attempt has been made to include the most pertinent features. Additions to the AIS scale could help to address shortcomings in the work, with injuries added to the scale that are commonly seen in blast injuries, as well as further research into the mechanisms of injuries seen as a result of IED attacks.

- Primary injuries using Axelsson method
- Secondary injuries using:
  - Gurney velocity prediction with distributions
  - multivariate normal distributions for directions
  - exponential equations
  - depth of penetration for injury

In order to implement a scoring system to the injuries predicted in sections 3.2, 3.3 and 3.4, it will be necessary to assign an AIS score to the outcomes of each stage of the model. The outcomes of the models described in Sections 3.2 and 3.3 are translated into AIS scores, as shown in Tables 3.5 and 3.6, which will be used to develop a NISS score and assess the level of injury of an occupant. Data in Tables 3.5 and 3.6 is based on assumed levels of injury, as existing data could not be found in the literature.

Table 3.5: Translation of ASII to AIS

ASII	AIS
0.0 – 0.2	N/A
0.2 – 1.0	1 – 2
1.0 – 1.9	2 – 3
1.9 – 3.6	3 – 4
>3.6	5

Table 3.6: AIS values for penetration injuries

DOP	chest	head	extremities
full	5	5	4
half	4	4	3
quarter	3	3	2
< 10mm	2	2	1
none	1	1	1

3.7 Implementing risk models

3.7.1 Axelsson model

The Axelsson model can be implemented in a straightforward manner, but requires a numerical model to predict the pressure at 4 points. Model data is written out in a text file and can be read into GNU Octave (see Appendix B.2 for full code) and a numerical 4^{th} order Runge-Kutta scheme used to solve the differential equation for the velocity.

$$\frac{\mathrm{d}^2x}{\mathrm{d}t^2} + \frac{\mathrm{d}x}{\mathrm{d}t} + x = f(t) \tag{3.38}$$

To solve a second order differential equation of the form seen in (3.38), it is necessary to transform the second order problem into a pair of coupled first order equations, by introducing a variable for the first derivative, demonstrated in (3.39).

$$\begin{aligned} y &= \frac{\mathrm{d}x}{\mathrm{d}t} \\ \frac{\mathrm{d}y}{\mathrm{d}t} &= \frac{\mathrm{d}^2x}{\mathrm{d}t^2} \\ \frac{\mathrm{d}y}{\mathrm{d}t} + y + x &= f(t) \\ \frac{\mathrm{d}x}{\mathrm{d}t} &= y \\ \frac{\mathrm{d}y}{\mathrm{d}t} &= f(t) - y - x \end{aligned} \tag{3.39}$$

The 4^{th} order Runge-Kutta method for a first order differential equation is expressed by (3.40) [171], where X is the numerical approximation of x, and h is the size of the step in the t direction.

$$\begin{aligned} c_1 &= hf(t_n, X_n) \\ c_2 &= hf\left(t_n + \frac{h}{2}, X_n + \frac{c_1}{2}\right) \\ c_3 &= hf\left(t_n + \frac{h}{2}, X_n + \frac{c_2}{2}\right) \\ c_4 &= hf(t_n + h, X_n + c_3) \\ X_{n+1} &= X_n + \frac{1}{6}(c_1 + 2c_2 + 2c_3 + c_4) \end{aligned} \tag{3.40}$$

For a second order differential equation (or higher), these coefficients are solved simultaneously for each of the coupled first order equations (c_1 solved for all functions first, followed by c_2 etc.,) which gives approximations for the variables (X and Y in the case of (3.39)) at each step. In the case of the Axelsson differential equation (3.15), the step will be largely determined by the time interval from numerical data, which is input via $p(t)$.

3.7.2 Projectiles

Most of the calculations required to model the risk of injury due to projectiles are straightforward, but the large number of projectiles and persons involved, and the three dimensional nature of the problem dictate that numerical procedures are the most appropriate method. Unlike the method used in Section 3.7.1, where 4 pressures histories are known and are applied to a calculation, the initial behaviour of multi projectile devices such as IEDs is more random, and requires a different approach. This section discusses a statistical approach to identifying the initial conditions, and the subsequent methods of determining injury, as well as a description of the numerical procedure used.

3.7.2.1 Initial behaviour

The number of projectiles involved, and their inherent randomness means that statistical methods are best suited for describing their initial conditions. In line with other work described above, normal distributions are assumed for angular spreads in two dimensions, and the velocities of the projectiles. A number assumptions are made about the behaviour of the projectiles, which makes it possible to define the statistical parameters for a trivariate normal distribution, from which a random sample can be taken using the `mvnrnd` function in Matlab or GNU Octave for a given number of projectiles. For the purposes of this work, it is assumed that:

- all parameters will be normally distributed
- the mean angular projection for both direction will be 0^o
- 99.7% of all projectiles will fall within the following angular spreads from 0^o:
  - $\theta_{3\sigma} = 70^o$
  - $\phi_{3\sigma} = 45^o$
- the mean velocity will be the Gurney velocity
- fragments travelling at a zero velocity are very unlikely, so $v_{6\sigma} = \mu_v$
- there is no correlation between the two angles of projection, so $(\sigma_{\theta,\phi}) = (\sigma_{\phi,\theta}) = 0$
- the correlation between angle and velocity is the same for both the θ and ϕ directions, so $\sigma_{v,\theta} = \sigma_{v,\phi}$ (see Appendix B for a definition of θ and ϕ)
- angle and velocity are negatively correlated and will have negative covariances, calculated using (B.3) with a correlation value of -0.5

A more detailed description of this statistical model can be found in Appendix B.2. Once the initial conditions of the projectiles are specified, it is then possible to define their movement and any subsequent interaction.

3.7.2.2 Propagation and hit

A numerical process can take care of the subsequent positions of each projectile, and logical statements used to identify if and when a projectile comes into contact with an occupant, which involves checking positions of projectiles against positions of occupants. This is accomplished by defining the angular range taken up by various parts of an

occupants body, which means interactions can be checked for by checking the projectile angles against the body part angles. The 'angles' occupied by each body part of a person are computed using a function `person.m` (see Appendix B.3.3), which for a given x and y position, defines a range of angles θ_r and ϕ_r for each body part of a person[3]. With both the angles for the projectiles defined in the θ and ϕ direction, and a range of angles θ_r and ϕ_r, it is simply a case of searching for projectiles whose angles lie within both ranges for each limb, which defines a projectile hit, and is accomplished with `iswithin.m` (see Appendix B.3.3).

It is only necessary to calculate the velocity of a projectile if it will interact with an occupant, so velocities are calculated for a given projectile using Equations (3.27) and (3.28) after the hit or no hit statement has been identified. Once the velocity has been calculated it is then possible to determine the DOP and the AIS, given that the body part is already known.

3.7.2.3 Numerical implementation

Combining the initial conditions, propagation and hit stages results in a multi projectile injury risk tool, the code for which can be found in Appendix sections B.3.2 and B.3.3. The code can be visualised by the flow diagram in Figure 3.6. Data on the occupants of a vehicle and the device are input into the model at the start, with the occupants input as a series of x, y points in the vector `D`. The angles of the person are defined for each body part, and then it is possible to loop over occupants, projectiles and body parts to determine hits. If hits are identified, injury calculations can be made, and once all occupants have been checked for interactions and data compiled in the hit matrix `HM`, it is possible to compile hit statistics for each person, in terms of the total number of hits, hits on each limb and the New Injury Severity Score purely for projectiles, which can be written out to file.

The modular nature of the code means that it is simple to extend and improve the code, particularly for projectile velocity, depth of penetration and AIS, by editing the functions that calculate these values.

3.7.3 Calculating the risk for occupants

Methods for determining two types of injury are presented, which can be solved to give an Abbreviated Injury Scale (AIS) value. They do not lend themselves to being solved within the same code (one is in steps of distance, and one in steps of time), so separate solutions can be computed. The individual AIS values calculated for each injury for a defined occupant are output from each model, ranked and combined to give an Injury Severity Score (ISS or NISS). Full details of the code used can be found in Appendix B.2 and application for a rail vehicle found in Chapter 7.

3.8 The next steps

A summary of the open literature on mechanisms and prediction methods for injuries as a result of detonations of explosives and explosives devices is presented here, with a focus on the types of injuries expected from the detonation of an improvised explosive device.

[3]Currently, this function only considers standing persons, with shoulders aligned with the axis of the vehicle.

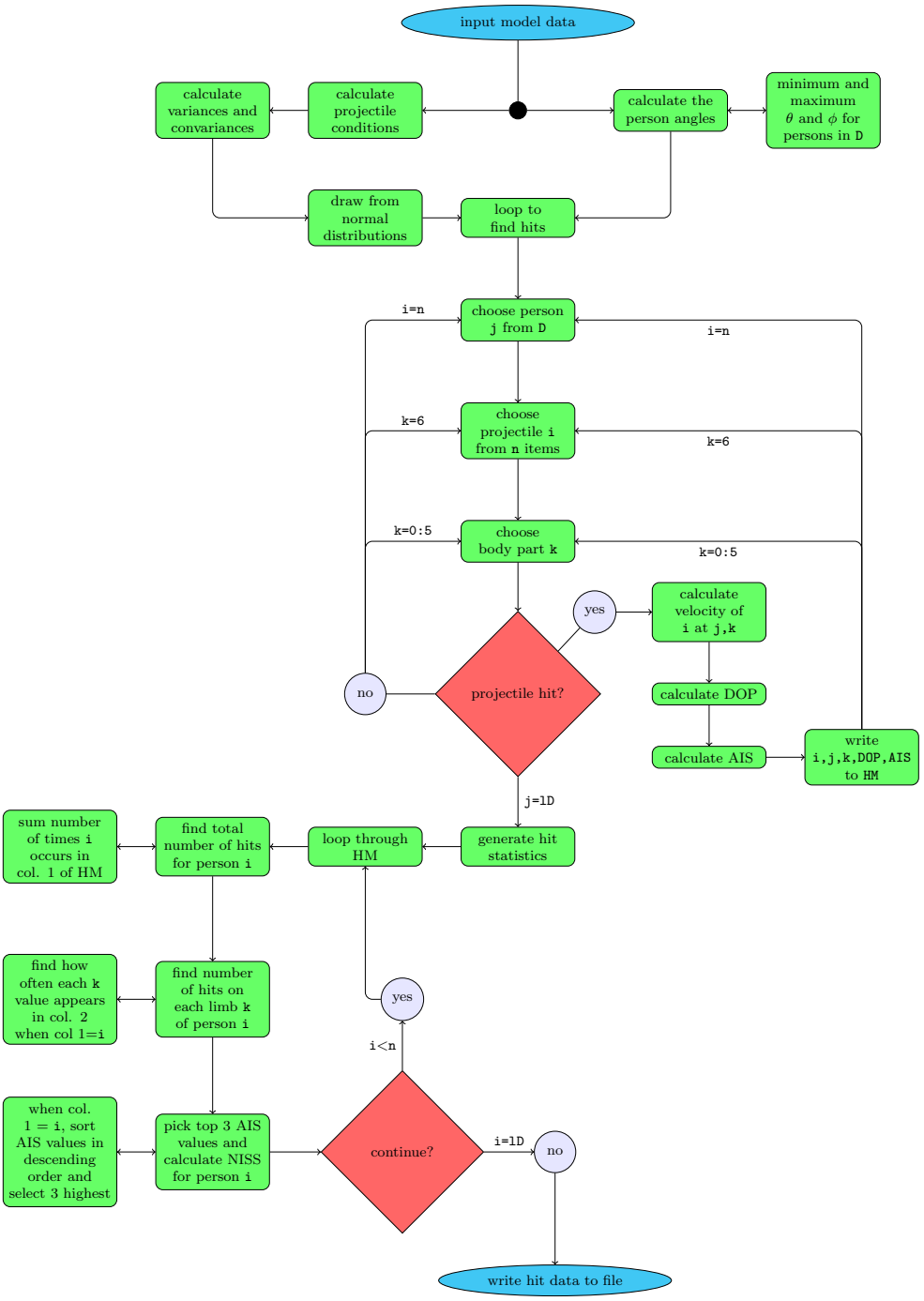

Figure 3.6: Visual description of multi projectile injury model

The literature shows that there are a large number of injury mechanisms at work, but that predicting them can often by difficult and that existing techniques are immature, particularly in the case of impact injuries to the head and traumatic amputation of limbs. As a result it was decided that the focus of the injury predictions in this work would be those caused by blast pressures and flying projectiles.

A projectile injury prediction method has been fully described, as has a method for predicting the injuries to the chest using a complex blast pressure time history, such as that generated by an explosion in a confined space like a rail vehicle. The following chapters present a method for predicting this blast pressure history using explicit finite

element analysis, as well as providing verification and validation that the results are accurate and comparable with empirical predictions and experimental measurements of blast parameters.

4

Modelling Methods and Verification

4.1 Blast Characterisation in LS-Dyna

LS-Dyna is a general purpose explicit finite element code which is widely used for simulations of highly transient and non linear behaviour, such as ballistics, impact and crashworthiness. LS-Dyna is also used widely to model the effects of shock loads on structures and components and loading can be applied to a structural (typically Lagrangian) finite element model in a variety of ways. This chapter presents an overview of the methods available within LS-Dyna, and provides a verification of the coupled ALE method which will be applied in later work.

4.1.1 Empirical methods for applying blast loads

For many engineering applications, blast loads can be applied to the structural model using idealised pressure time histories that are taken from data on explosions under controlled situations. Pressure time histories from real explosions in free air (no reflecting surfaces) take the form of the Friedlander curve (see Section 2.2.1.2 and Equation (2.9)) during the positive phase, with negative phase parameters calculated separately where deemed necessary (see Section 2.4 for more details).

In LS-Dyna, empirical methods can be implemented using one of two built in functions, LOAD_BLAST and LOAD_BLAST_ENHANCED, which are implementations of a program called ConWep [172]. ConWep uses equations derived from an experimental testing (the same experimental testing used to produce the curves in [37]) to calculate the peak pressure, positive phase duration and impulse experienced at a particular distance from a charge of TNT. This allows the pressure time history at the surface of a structure to be calculated very quickly when the user specifies the distance from the point of detonation and the size of the charge. The method is very accurate when used appropriately, but cannot take account of some important real world effects that can make large differences to the pressure experienced on a structure, which can lead to inaccuracies if the method is applied without consideration to the assumptions and limitations. Empirical methods such as these do not take account of the effects of clearing around small finite structures, confinement and reflection, negative phase effects (although these are treated to some

Table 4.1: Equation of state parameters for high explosives

Explosive	A (GPa)	B (GPa)	$R1$	$R2$	ω	E_0 (GPa)
TNT [173]	371.20	3.23	4.15	0.95	0.30	7.00
C4 [173]	598.20	13.75	4.50	1.50	0.32	8.70

Table 4.2: Material model parameters for high explosives

Explosive	ρ (kg/mm^3)	V_{det} m/s	P_{CJ} (GPa)
TNT	1.59E-06	6930.00	23.70
C4	1.61E-06	8040.00	28.10

extent by LOAD_BLAST_ENHANCED) and the effects of curved blast fronts that exist at small scaled distances, when the shock wave cannot be considered plane.

4.1.2 Arbitrary Lagrangian Eulerian methods

The Arbitrary Lagrangian Eulerian (ALE) method with Fluid Structure Interaction (FSI) models the detonation of a high explosive, the subsequent propagation of the shock and pressures waves through the air and couples this to a structural finite element problem. The solution combines both a Lagrangian mesh for the structure and an ALE mesh through which the fluids move.

It is possible to use the ALE method with both 2D shell elements and 3D solid elements, both of which are used here. The 2D method has the advantage of being significantly faster and requiring fewer elements to model a given problem, but is limited to axisymmetric problems, and 3D ALE domains are required for FSI calculations under most circumstances.

4.1.2.1 ALE Material Model parameters

For air and high explosives that are characterised with the ALE method, a material model and an equation of state are required. A high explosive is modelled with a combination of MAT_008 (HIGH_EXPLOSIVE_BURN) and the Jones–Wilkins–Lee equation of state (EOS_JWL) (Equation (2.36)), and the air is modelled using MAT_009 (MAT_NULL) and a simple linear polynomial equation of state (EOS_LINEAR_POLYNOMIAL) (Equation (2.35). Equation of state parameters for 3 high explosives can be seen in table 4.1 and parameters for high explosive material models and air in tables 4.2 and 4.3.

Table 4.3: Material model and EOS parameters for air

ρ (kg/mm^3)	γ	E_0 (GPa)
1.01E-09	1.4	2.6E-04

4.1.2.2 Use of 2D and 3D models

The 2D ALE method uses axisymmetric multi material 4 node shell elements. The detonation and initial propagation of blast waves from spherical charges is particularly suitable for application of symmetry, but all charge shapes with axisymmetrical properties can be effectively simulated using this 2D method. The 2D method is used for modelling the high explosive charge and the air that is close to it and it is possible to save the data from either the whole simulation or the last cycle and map this on to either a different 2D or a full 3D model. The advantage of this method over a single modelling stage with a full 3D model are 2 fold; the detonation process can be modelled with shell elements with a much smaller element size to give high resolution data at much better computational efficiency than using solid elements of the same size. Secondly, the detonation process typically requires finer mesh elements than subsequent propagation and interaction, this use of mapping means that subsequent meshes onto which the initial 2D data is mapped can avoid transitions between small elements in the charge and larger elements elsewhere, which reduces the time taken to generate meshes and prevents unnecessarily small time steps involved with small elements. The 2D simulation of detonation and initial propagation can also make use of a radial type mesh when spherical charges are being modelled, which avoids problems with transport across element diagonals, as mentioned in Chapter 2.

The mapping process is accomplished by using the command `'map=map_filename'` on the command line when running the model, and the use of the keywords INITIAL_ALE_MAPPING or BOUNDARY_ALE_MAPPING in the input files of the models that will receive mapping data, to map either the last cycle or the solution history on to the new solution. Mapping the last data from the first 2D model onto the second model means that the second model effectively 'begins' at the time the first model ends which has both advantages and disadvantages. The primary disadvantage is that no data can be recorded from the second model before the termination time of the first model, so the initial behaviour is effectively missing. This can be an advantage if this data is not required though, less computation time is required if the second simulation can skip a large number of cycles at the start.

The 2D ALE method can be used to model blast wave interaction with rigid objects due to the significant reduction in computational cost involved. Structures are modelled by fully constraining the nodes that form the boundary of a structure at that point. This can be very useful if a structure is very big and too expensive to model in 3D, assuming the structure is rigid, but can only be used when there are no anticipated out of plane effects, or out of plane effects can be shown to be insignificant.

It is not always possible to simplify models to an extent that allows a 2D method to be used. The full 3D method applied here uses 8 node solid multi material ALE elements with a single integration point. Where possible, symmetry is used and a regular hexahedral mesh[1] for air can be initialised with explosion data from 2D runs. If symmetry cannot be used, the charge must be meshed into the air domain, which brings with it problems of severe element size transition within the mesh, as well as longer problem set up time and increased computational effort associated with a higher number of elements used in models that cannot utilise symmetry.

[1] The mesh is made up of identical size cuboidal elements.

Table 4.4: Constraints for symmetry boundary

Plane	TC_x	TC_y	TC_z	RC_x	RC_y	RC_z
y-z	1	0	0	0	1	1
x-z	0	1	0	1	0	1
x-y	0	0	1	1	1	0

4.1.2.3 ALE Boundary Conditions

There are 3 boundaries to consider when modelling the fluids in the ALE domain: the boundary to infinity / free space, symmetry boundaries and rigid boundaries. Rigid boundaries are enforced by applying single point constraints to boundary nodes on one or several faces of the ALE domain in all degrees of freedom, which simulates the presence of a rigid and perfectly reflecting surface. Symmetry boundaries are also specified by applying translational and rotational single point constraints to the faces of the ALE domain in the symmetry plane, as shown in Table 4.4.

At the edge of an ALE domain where there is neither symmetry nor a rigid boundary, the ideal boundary conditions would allow pressures to dissipate and prevent any reflections. This boundary does not physically exist in the real world as the air surrounding a structure (above and to the sides) is effectively infinite. In a model, free boundaries will cause reflections to some degree which leads to contamination of results with unrealistic phenomena. Current boundary treatment options for ALE elements in LS-Dyna are limited - the BOUNDARY_NON_REFLECTING keyword works by computing an impedance function based on the assumption of linear material behaviour [174] which is not appropriate for highly non linear air shock waves. Perfectly matched layers are extra layers of a material that mathematically simulates an unbounded medium, absorbing and attenuating waves, and are currently implemented in LS-Dyna for the boundaries of some Lagrangian materials, but as yet are not implemented for ALE elements. In the absence of appropriate boundary conditions or implementations of effective absorption and attenuation materials, the best practice is to use an ALE mesh that is large enough that no boundary phenomena will reach the area of the model under study during the time period that is of interest.

4.2 Verification study

4.2.1 2D simulation of blast in free air

Two dimensional quarter symmetry ALE models were conducted to ensure the method accurately simulated the detonation and initial propagation of the blast wave as well as identifying appropriate element size and density to achieve mesh independence. An example of the input files for these models can be found in Appendix A.1.1.

Models of a 320 gram equivalent explosive charge are used in this verification study as it accurately represents the charge configuration used in the experimental tests. The experimental study utilises quarter symmetry and an 80 gram charge moulded into a quarter sphere of radius 36mm, which is equivalent to a 320 gram charge (radius 36mm) when the symmetry planes are removed. The charge mass of 80 grams is the maximum that can be used in the experimental test cell.

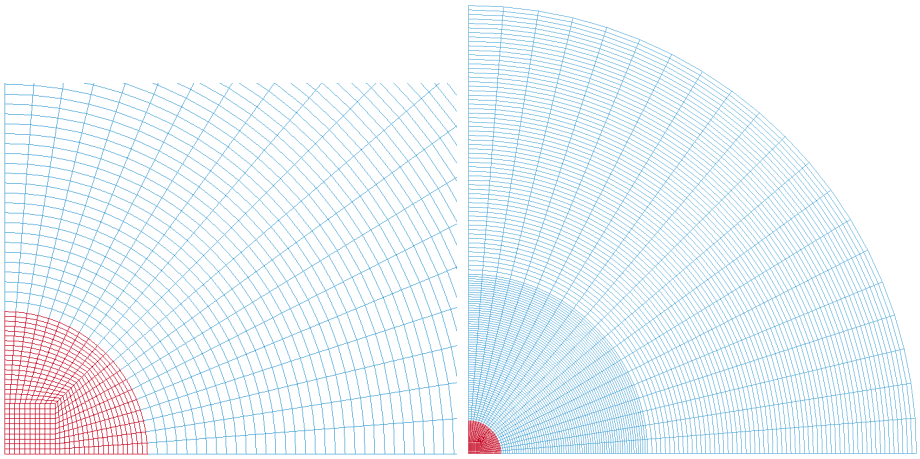

(a) Charge mesh (b) Charge and air mesh

Figure 4.1: Mesh configurations for 2D ALE model

4.2.1.1 Mesh effects

A explosive charge is modelled in 2D using symmetry as a quarter of a circle with a 36mm radius using a butterfly type mesh, and air is modelled to a distance of 500mm from the point of detonation with a radial type mesh. The configuration and shape of the mesh is shown in Figure 4.1. Four different mesh densities are chosen as shown in Table 4.5 that are dictated by the number of elements around the circumference of the charge with the smallest element at the centre of the charge, which are referred to in figures as 20, 40, 80 and 160.

The resolution of the mesh has 2 main effects on the accuracy of the predictions that 2D models produce; peak values in the time history are lower, and the time taken to reach this peak is longer in models with coarse meshes compared to more refined meshes. Figures 4.2 and 4.4 show that coarse meshes tend to produce a similar shape and the key features are similar, but as the mesh is refined the changes experienced within the fluid occur more rapidly. The cumulative impulse (Figure 4.3) shows that slower rise time and lower peak pressure seen in Figure 4.2 lead to a corresponding slower rise in the cumulative impulse, but also shows that the impulse continues to rise after the impulse has become constant in other models. This leads to a peak impulse cumulative for a coarse mesh which is closer to that of finer meshes when compared with plots for pressure or shock wave velocity.

The finest mesh produces only small changes in the prediction of pressure, impulse and shock wave velocity compared with one that has half the number of elements around the circumference, but Figure 4.5 shows that there a significant increase in computational effort required for this. The trend shows an exponential increase in the computational time as the mesh is refined that lead to increasingly small changes in the predictions from the model, so for this particular problem a mesh with 160 elements around the circumference is suitably accurate.

Table 4.5: 2D mesh details

Elements around charge	Smallest element (μm)	Total number
20	1230	2980
40	603	12200
80	290	35680
160	150	87360

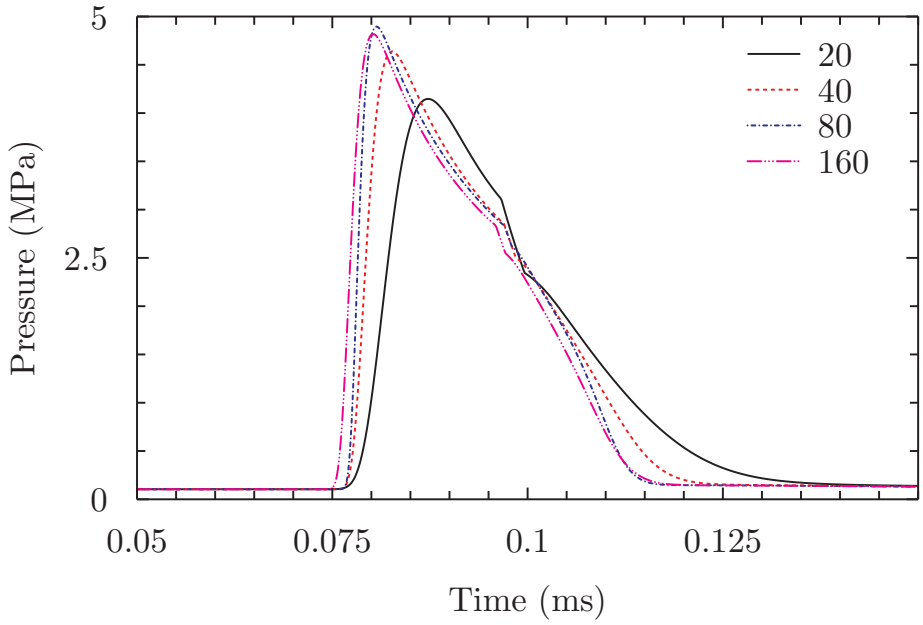

Figure 4.2: Pressure history 300mm from charge centre

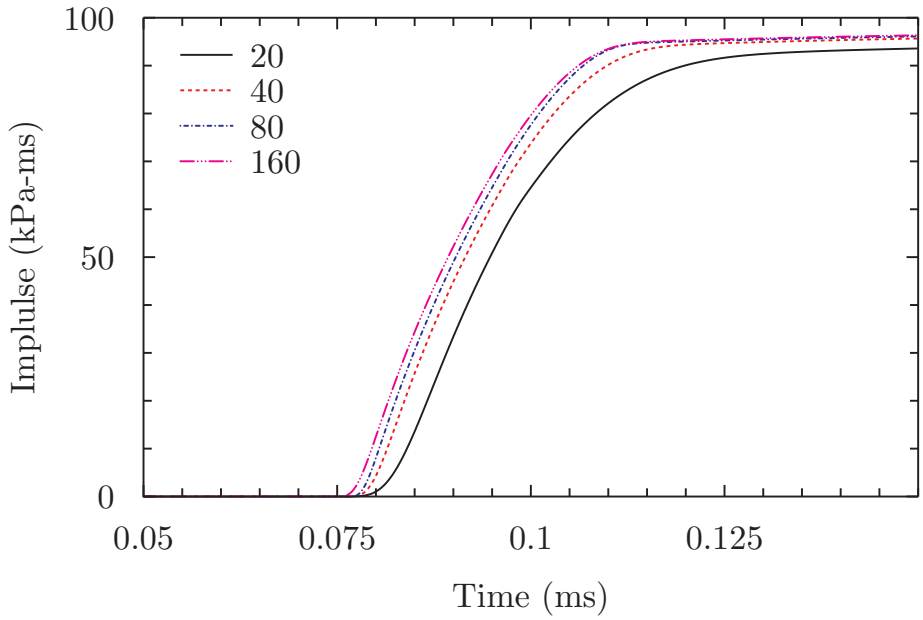

Figure 4.3: Cumulative impulse 300mm from charge centre

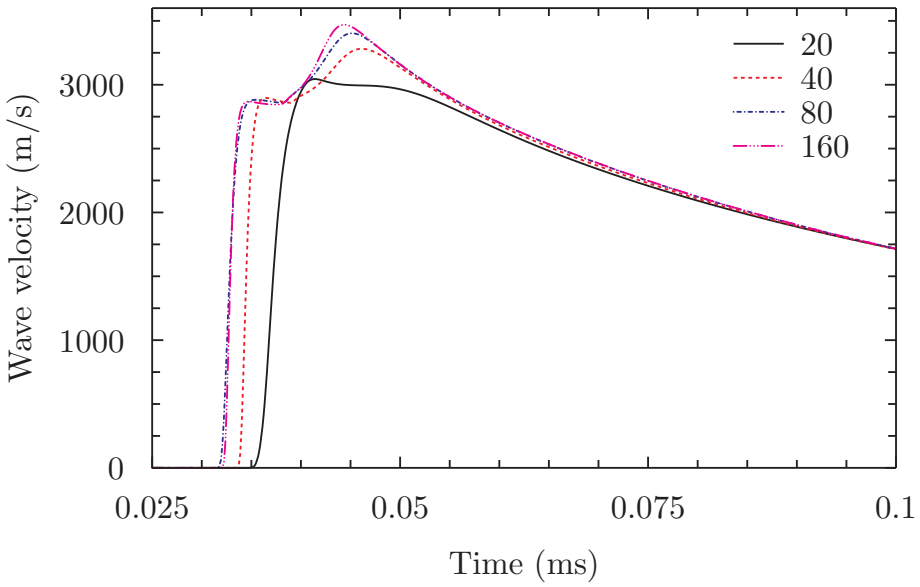

Figure 4.4: Sock wave velocity 180mm from charge centre

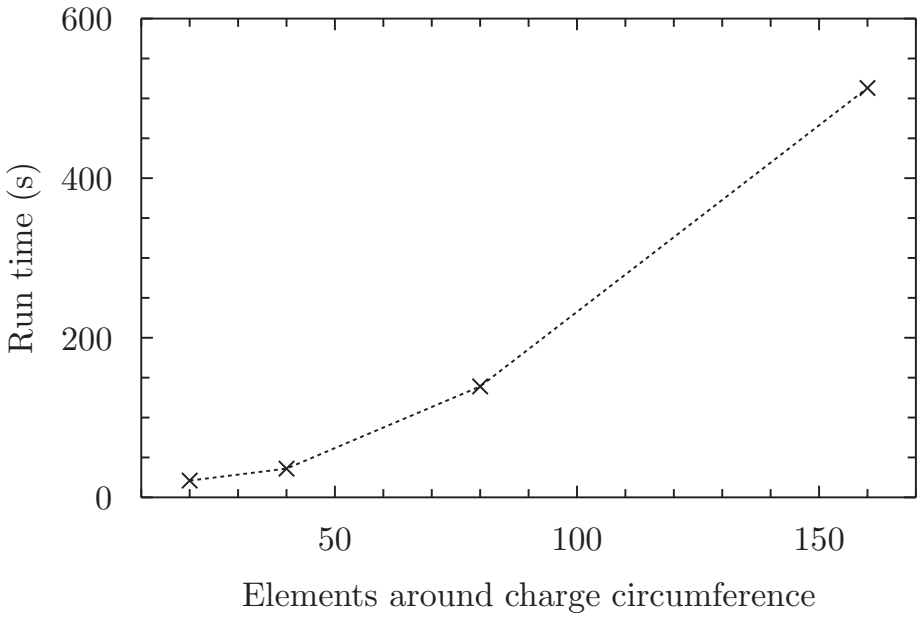

Figure 4.5: Effect of mesh density on model run time

4.2.1.2 Comparison of Models with ConWep

Blast parameters from a model can be verified by comparing them with data from the ConWep program [175]. The numerical model utilises the same 320g charge with quarter symmetry that is used in Section 4.2.1.1, and an equivalence value of 1.2 [36] is used to calculate an equivalent TNT charge mass of 384g for use in ConWep.

Data from numerical models used for the mesh study in Section 4.2.1.1 is mapped onto a new, larger 2D domain of square shell elements with overall mesh dimensions of 2500 × 2500 mm in the x-y plane.

As the ConWep program utilises empirically derived equations, the output data is only valid within the range of scaled distances at which measurements were taken during the original experiments. The ConWep program should therefore be used to calculate blast

Table 4.6: Numerical and empirical impulses

R (m)	Z ($kg/m^{\frac{1}{3}}$)	Positive phase incident impulse (kPa-ms) ConWep	LS-Dyna	% difference
0.852	1.17	110.8	111.1	0.3
1.100	1.50	86.8	88.7	2.2
1.274	1.75	75.5	80.3	6.4

parameters at scaled distances of greater than $Z = 1$, which for a charge of 384g gives a minimum distance of 727mm from the point detonation, shown in Equation (4.1). ConWep is an empirical tool, and gives parameters to allow the Friedlander curve to be plotted for the positive phase of a blast. ConWep does not consider the negative or underpressure phase of a blast, which cannot be plotted by assuming the extension Friedlander curve into the negative phase.

$$\begin{aligned} Z &= \frac{R}{W^{\frac{1}{3}}} \\ W &= 0.384\,kg \\ \text{for } Z &> 1\ kg/m^{\frac{1}{3}} \\ R &> 1 \times 0.384^{\frac{1}{3}} \\ R &> 0.727m \end{aligned} \tag{4.1}$$

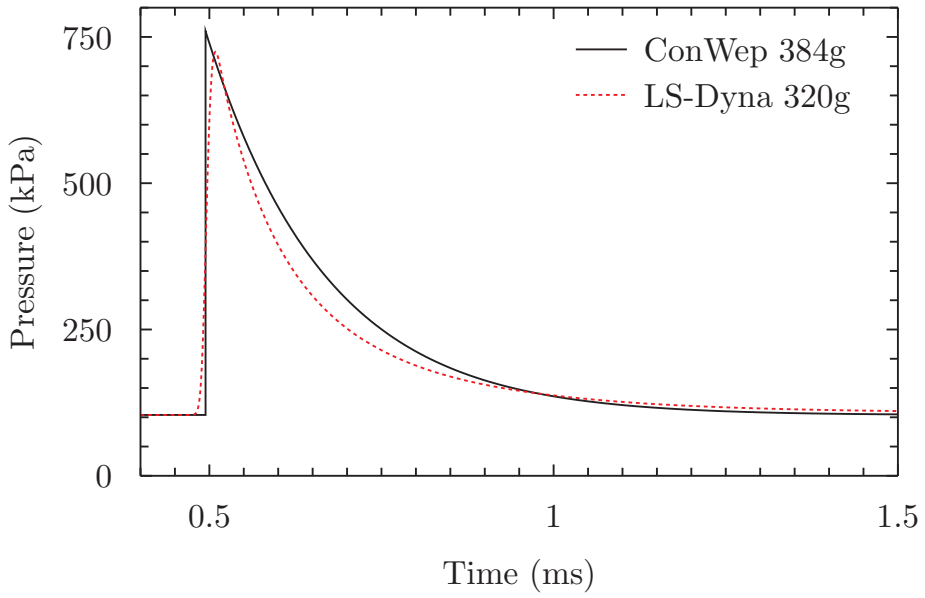

Figure 4.6: Numerical and empirical results at Z=1.2

Predictions of free air blast parameters from numerical models generally show excellent

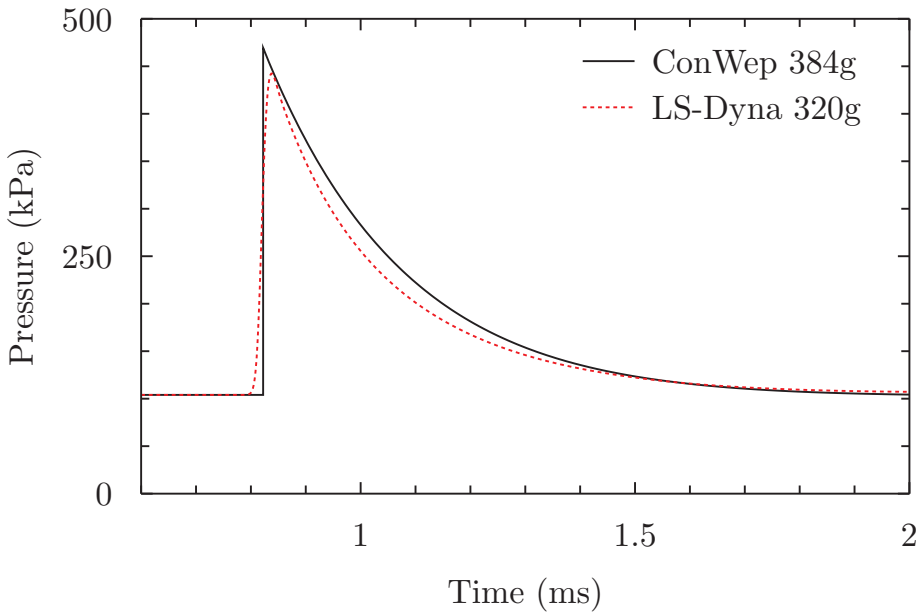

Figure 4.7: Numerical and empirical results at Z=1.5

agreement with curves generated from empirical data provided by ConWep and confirm the assumption of a TNT equivalence of 1.2 is valid. Figures 4.6 and 4.7 show good agreement between the peak pressure, arrival time and decay history at two different scaled distances, with pressures decays in both figures shown to be slightly more pronounced in numerical models than in Friedlander curves fitted via the decay parameter, b, according to impulses given by ConWep.

It should be noted that numerical and empirical results do not match perfectly, which is in large part due to the limitations of numerical methods caused by finite mesh sizes. The numerical method is not capable of modelling a discontinuity such as a shock, so the discontinuity, which is an almost infinite gradient in real life, is modelled as a sharp gradient across a number of elements. If elements are large, the shock is smeared[2] across a large physical space and there is a corresponding large time between arrival of the shock front and the peak overpressure. As the elements get smaller the number of elements the shock is smeared across remains constant, but the physical space across which the shock is smeared is reduced and the time taken for the pressure to rise to the peak value is reduced, leading to sharper pressure rises as the elements reduce in size. This means that the almost infinite gradient seen in reality would require almost infinitely small elements, which is not feasible. As a result, numerical models with coarse meshes will 'miss' the peak overpressure due to shock smearing, which is seen in both Figures 4.6 and 4.7. Instead of continuing to rise to the peak pressure, the pressure in the numerical model decays in line empirical data. Effectively the sharp changes in pressure experienced at a point, are smoothed out by the numerical model, and the extent of this smoothing and resolution of sharp changes is a function of element size.

[2]Shock smearing [174] is introduced by bulk viscosity, which adds a viscosity term to pressures to turn shocks into rapid but continuous transitions, which is necessary for solution stability.

4.2.2 Boundary effects in ALE domains

Understanding the effect of mesh area and proximity of measurement to free boundaries is important to ensure that boundary effects are not misinterpreted as real physical phenomena. Figure 4.9 shows pressure histories taken at 3 different locations in a mesh with a small area, with and without a non-reflection (NR) boundary conditions applied, and at the same spatial points within an enlarged mesh. The location of the pressure measurements with the mesh and the relative mesh area is shown in Figure 4.8.

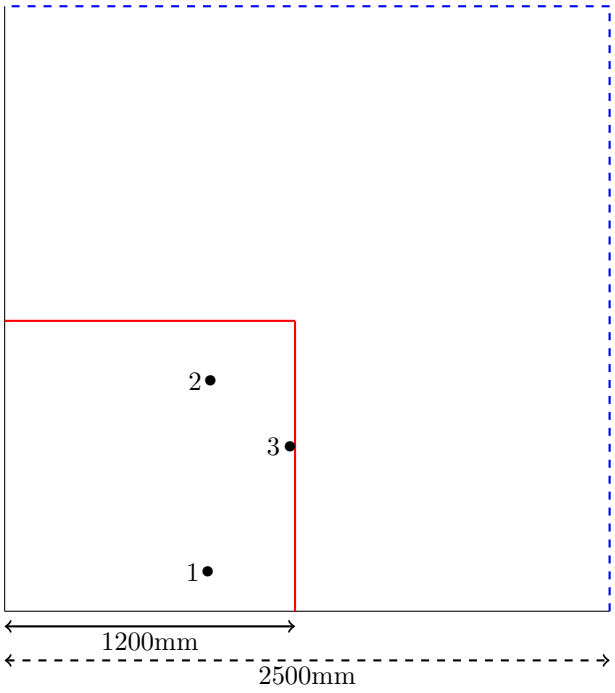

Figure 4.8: Locations of measurements in relation to boundary of two different meshes. The enlarged mesh free boundaries are shown with a dashed blue line and the smaller mesh with a solid red line.

The pressure at location 1 is shown in Figure 4.9(a) which shows very similar pressure histories for both models with a small mesh and the enlarged mesh, including the small second shock at 2.9ms. This point is sufficiently far from the free boundary to avoid any noticeable edge effects in this particular model, but if the solution was run over a longer time expansions waves from the boundary are likely to have been visible. Figures 4.9(b) and (c) show pressure histories closer to the boundary which both show deviations from the expected pressure history due expansion waves from the boundary. At point 2, Figure 4.9(b), pressures in the small mesh follow the pressure in the enlarged mesh up until 2.1 ms, when expansion causes a pressure drop away from the pressure seen at the same point in the enlarged mesh. Boundary effects also lead to the rise back to atmospheric pressure, and the pressure jump at 3.5ms is a result of interaction between the second shock (also seen in the enlarged mesh) and boundary effects. At position 3, shown in Figure 4.9(c), the boundary effect is not immediately obvious unless compared with the result from a larger mesh. At the point the shock wave reaches position 3, an expansion wave is immediately emitted from the boundary. The expansion wave does not effect the peak pressure experienced, but leads to a more rapid decay in the pressure predicted at this location than for an enlarged mesh in which no boundary effects are

observed. The smaller mesh also does not pick up the second shock seen at 3.75ms in the enlarged mesh.

Positive phase impulses before the second shock is observed are compared in Table 4.7 and show large differences between models where boundary effects are observed. At position one, the cumulative impulse before the second shock for both the small mesh and enlarged mesh is similar, with the smaller mesh predicting a 2% lower impulse than the enlarged mesh. At both positions 2 and 3, the cumulative impulse difference between the 2 models is much larger. At position 2 the cumulative impulse is identical for the two models until the expansion waves cause a dip below atmospheric pressure at 2.1ms, at which point the cumulative impulse begins to decrease. This dip below atmospheric leads to a difference in cumulative impulse of 26% at 3.7ms. At point 3 the small mesh predicts an impulse 48% lower than that predicted with an enlarged mesh at 3.7ms due to expansion waves from the boundary. It should be noted that for impulse, as well as pressure histories, no measurable difference between unconstrained nodes and a non-reflecting boundary condition (NR BC) is observed.

Table 4.7: Boundary effects on positive phase impulse

	Positive phase impulse (kPa-ms)		
Point	Small mesh	Enlarged mesh	% difference
1	186	190	2
2	116	156	26
3	79	153	48

4.2.3 3D simulation of blast wave pressure and fluid structure interaction

As well as testing if a model can predict free field pressures, it is important to ensure that they can predict pressures when blast waves interact with structures in 3D, as this will be important for future work in this thesis. The nature of the 3D effects seen in blast waves mean that empirical or analytical solutions only exist for the simplest cases, such as normally or obliquely reflected pressures, but if models are to make predictions in complex environments they should be proven to work for these simple cases.

4.2.3.1 Model description

The 3D model of an air domain measuring 1000 × 1000 × 1000mm was constructed using a regular cuboidal hexahedral mesh and 8 node solid elements in LS-PrePost. The model was run with several mesh densities to identify how the resolution of the mesh alters the results, which can be seen in table 4.8. To improve computational efficiency, the mesh was built utilising quarter symmetry, so three faces of the model have appropriate symmetry boundary conditions applied and the remaining three faces are left without boundary conditions (boundary conditions for each plane can be found in Table 4.4). Symmetry boundaries are found on the innermost faces of the domain as shown in Figure 4.10, with the 3 symmetry planes meeting at the point **O**.

Solid elements are specified as 1 point ALE multi-material elements, which allows between 1 and 3 different ALE Multi-Material Groups (AMMG) to exist within an ALE element at any time. Each AMMG represents an individual material, either in physical

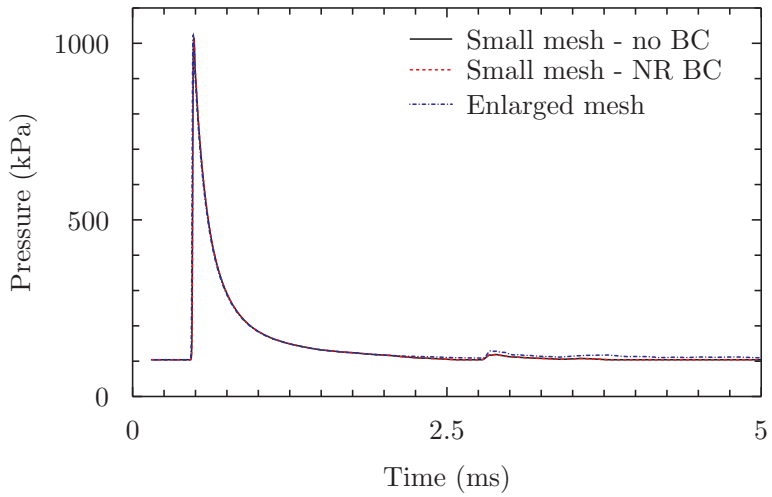

(a) Position 1

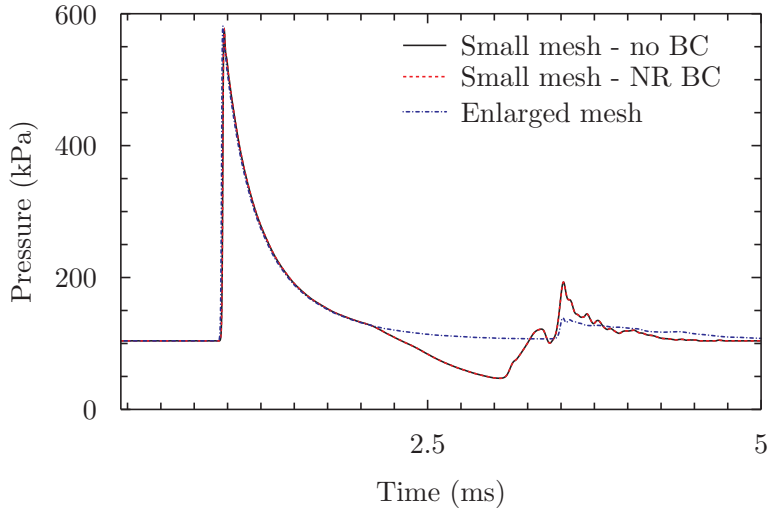

(b) Position 2

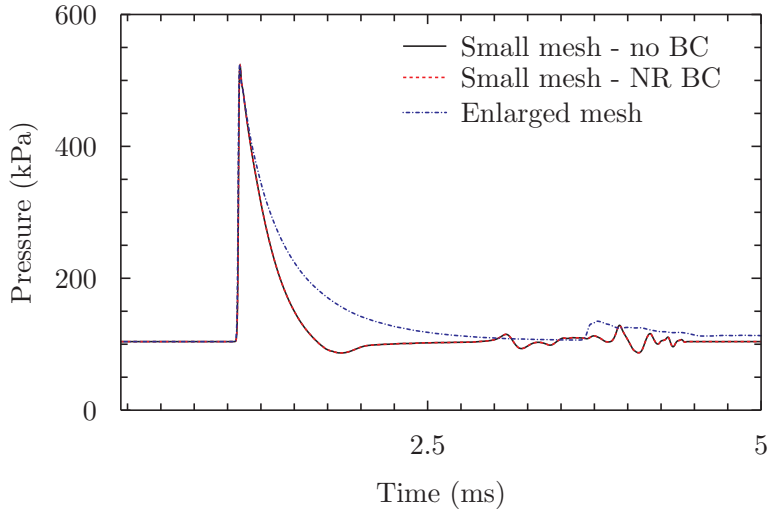

(c) Position 3

Figure 4.9: Effect of measurement location proximity to free boundary on pressure time history. In b) and c), pressure histories with and without boundary conditions are identical and overlapping.

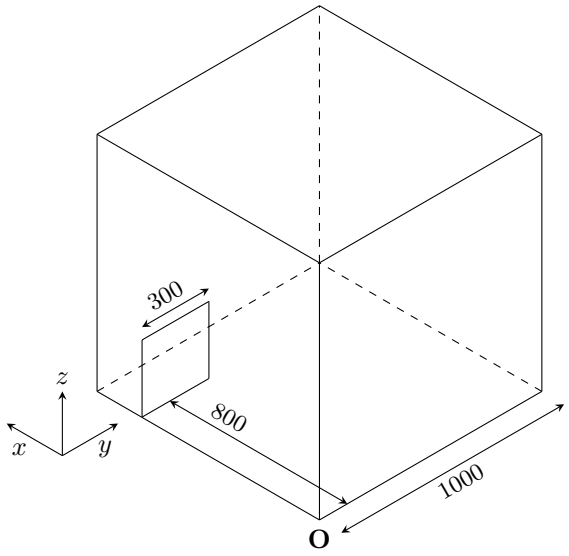

Figure 4.10: Setup of 3D model

space or its properties, which can interact with other AMMG and Lagrangian structures. The multi-material groups are specified with the ALE_MULTI-MATERIAL_GROUP keyword and the physical properties of the materials are specified on the PART card, which is as an input for AMMG. Data on AMMGs is mapped between 2D and 3D models, so it is important that there is consistency in part numbering between models to ensure the correct initialisation of the 3D models. Although no physical explosive is present in the 3D model (the mesh is constructed for the air domain), products of the explosion will exist, so both physical data for explosive and air (Tables 4.2 and 4.3) are included in the 3D model.

As with 2D models above, initial conditions are provided by mapping data from a 2D model onto the 3D domain, utilising symmetry conditions. The 2D model uses a charge with a radius of 36.4mm, which for a full sphere of PE4 would have a mass of 320g, equivalent to 384g of TNT, which is run until 0.15ms, at which point it is terminated and final cycle data written to a mapping file which becomes the initial data for the first cycle of the 3D run.

A reflecting structure at 800mm from the point of detonation measuring 300 × 300mm (See Figure 4.10) was modelled using both single point nodal constraints, and using a Lagrangian structure coupled to the ALE domain. The Lagrangian structure was constructed of shell elements of equal size (between nodes on an edge) to the ALE elements and is positioned within the ALE, but offset by a small amount so nodes of the ALE and Lagrangian mesh are not exactly coincident. The coupling between the ALE fluid and the Lagrangian structure is achieved by the CONSTRAINED_LAGRANGE_IN_SOLID keyword, which allows specification of the Lagrangian structure and distinct AMMG that will interact with it, as well as the method used to couple the two and many other control parameters. For this model, penalty coupling was chosen between the Lagrangian structure and all AMMGs in the model - full details of the parameters for this keyword can be found in Appendix A.1.2. Global parameters to govern ALE behaviour are set using the *CONTROL_ALE, with only two parameters changed from their defaults. The DCT parameter was set to -1, which is specifically recommended in the users manual [174] for use with high explosives, and METH, which controls the advection method,

Table 4.8: Mesh sizes for 3D models

ALE element size	number of elements
20	125,225
10	1,000,900
6	4,574,296

was set to -2 as recommended for simulation of high explosives.

4.2.3.2 Results - free air

A comparison between the 3D ALE models at different mesh resolutions and a curve plotted from ConWep data is shown in Figure 4.11. Pressure history data (4.11(a)) shows a shock arrival time for the models between 0.16ms and 0.18ms (the coarser model arrives slightly earlier than the other models), but a later arrival time of 0.195ms from the ConWep prediction. After the shock arrival, the gradient of the slope similar is for all models, but the time to reach the peak pressure value decreases with mesh refinement, at 0.18 for the fine model and 0.195 for the coarse model. The values of the peak pressure show that this is particularly sensitive to the resolution of the mesh, with the pressure in the fine model more than 500 kPa higher than that seen in the coarse model. The peak pressure in the coarse model is 270 kPa below that predicted by both ConWep and the mesh with medium resolution (10mm), which in both show lower peak pressures than those predicted by the model with a fine mesh, which shows a peak pressure of 2300 kPa. Once the peak pressures are reached, the pressure in the three models begins to decay, and very similar rates of decay are seen between 0.195 and 0.25ms, over which period the decay rate is also similar to that seen in the ConWep curve. At 0.26ms, the decay rate in the medium and fine models begins to reduce compared with both the coarse model and ConWep, which subsequently lead to a longer positive phase in the medium and fine models. The effect of this can be seen in the cumulative impulse curve (Figure 4.11(b)), where the impulse continues to rise for both these models, while the coarse model and the ConWep prediction show plateaus. The similarity in decay rates up until 0.26ms means that impulse histories are very similar for all models and the ConWep prediction until 0.3ms, at which point some divergence occurs. As a result, the peak cumulative impulse in the coarse mesh is lower than the peak predicted by ConWep, which is again lower than that predicted by the fine and medium mesh models. The fine mesh, although it over predicts the peak pressure relative to ConWep, shows the closest peak cumulative impulse, whereas the coarse model underpredicts both the peak cumulative impulse and peak pressure, and the medium model predicts the peak pressure, but over predicts the cumulative impulse.

4.2.3.3 Results - normal reflection

Pressure and impulse history at a reflecting surface was modelled using two different methods, a nodal constraint (NC) approach, and with a Lagrangian surface and the CONSTRAINED_LAGRANGE_IN_SOLID (CL) coupling algorithm, shown in Figures 4.12 and 4.13 respectively.

The pressure histories for both models show similar trends to those seen in the free

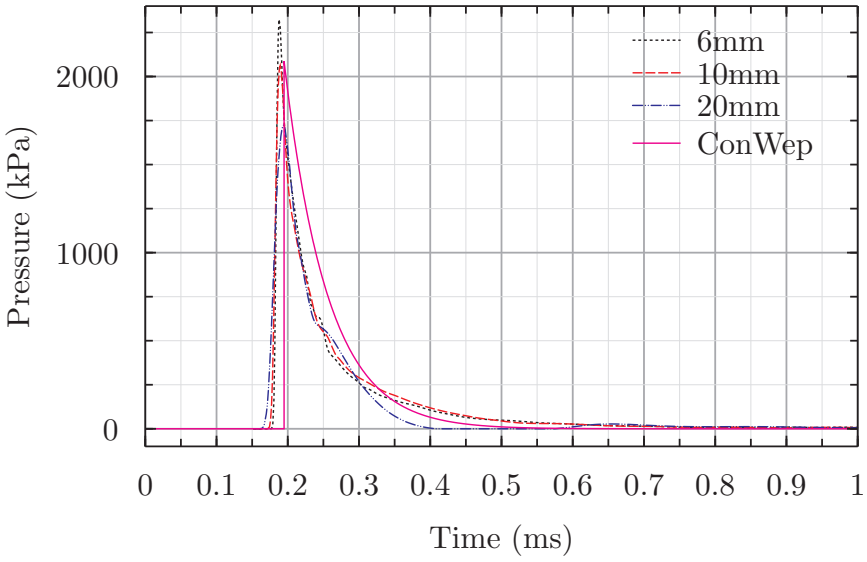

(a) Pressure

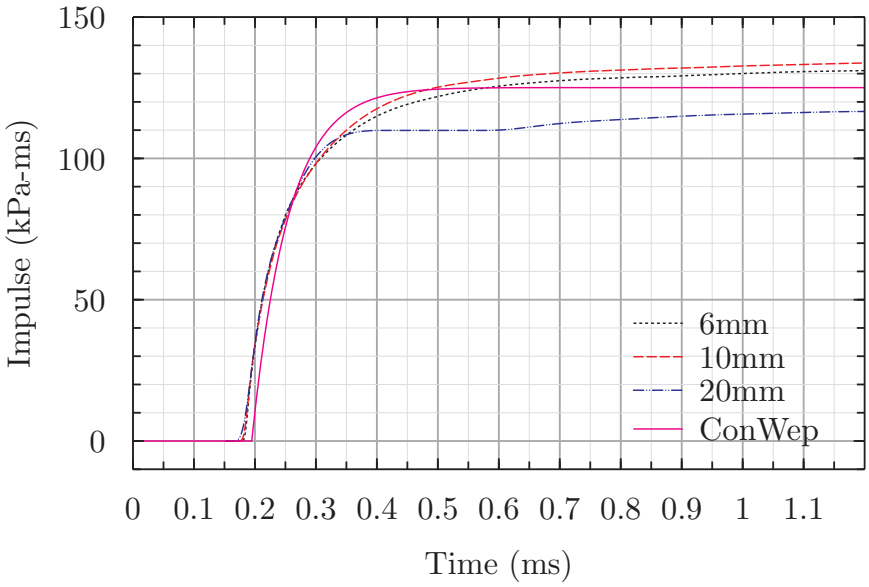

(b) Impulse

Figure 4.11: Effect of mesh refinement on free air pressure and impulse in 3D ALE models

air models above, but with the issues seen in Section 4.2.3.2 more pronounced in the models here for reflected pressure, with big variations in peak pressure, gradient and rise time. For the NC model, there is a 1250 kPa difference between the peak pressure in the coarse and fine models and for both the NC and CL models. Whereas there was a less than 0.01ms difference in the times of the peak pressures in the free air model, there is a difference of 0.05ms between peaks of the coarse and fine models in the NC and CL models. The arrival time for reflected models is slightly altered compared with the free air models, with the coarse model arriving 0.05ms before the ConWep predicted arrival time, but the medium and fine mesh arriving 0.15ms before, compared with 0.3ms and 0.25ms for the free air model. In contrast to the free air models, the models for reflected pressure show that the peak pressure is under predicted by all models, and by more in the CL models than the models using the NC method. The peak numerical model

pressure in Figure 4.12 is 3250 kPa, compared with 3050 kPa in the fine model in Figure 4.13. The peak pressure values on these curves tend to fall on the decay line of the ConWep and the subsequent decay is typically consistent with that seen in ConWep. The decay is slightly masked by oscillations in the finest two meshes in both models, but the decay seen in the NC models is closer to that seen in ConWep than that from the CL models, which decays more strongly.

Across all mesh resolutions for both methods, the cumulative impulse is under predicted relative to ConWep. For the NC method, the peak cumulative impulse is the same for all mesh resolutions at 330 kPa-ms, and despite the clear change in behaviour made by mesh resolution changes such as peak pressure and rise time, the impulse stays the same and is unlikely to change at further mesh refinement. For CL method, less consistency in the under prediction is found, with the medium mesh being further away from the ConWep prediction than the coarse mesh, and the fine mesh closer than both with a peak cumulative impulse of 300kPa-ms, compared to the ConWep prediction of 360kPa-ms. The fine mesh in the CL method is the closest to the prediction given by ConWep, but it is not possible to identify a trend, or if a finer mesh resolution would lead to a different impulse. Comparison with the behaviour of the NC model would suggest that this model will always under predict compared to ConWep, and the combination of a sharper decay and lower peak pressure would indicate the CL model will under predict by more than the NC model.

In both Figure 4.12(a) and 4.13(a), a number of oscillations are seen in the decay phase that are not seen in the decay phase in Figure 4.11(a). It is difficult to identify a real physical phenomena that could cause this oscillation in the pressure, which would indicate it is caused by some features specific to the numerical model, and is especially prominent in Figure 4.13(a). The way the ALE mesh, Lagrangian mesh and tracer particle (for pressure history) are positioned using the CL method means that the Lagrangian mesh is half way across an ALE element, but the pressure history must be taken from an adjacent ALE element, due to the thickness offset of the Lagrangian structure. Figure 4.14 shows that changing the relative positions of these can yield a pressure history that is much smoother and shows no oscillations in either the rise or the decay of the pressure. Despite this though, as it is necessary to move the Lagrangian structure to make it close to the boundary of an ALE element, a corresponding peak pressure drop will be seen if the structure is moved further from the centre of the detonation, as is seen in 4.14(a). Although the peak pressure drop is quite noticeable, the improved rise and decay behaviour leads to a small increase in impulse (*towards* the ConWep prediction), shown in Figure 4.14(b).

4.2.3.4 Discussion

Data has shown it is possible to achieve reasonable predictions of the ConWep values from numerical models, but also that these solutions are strongly dependent on how the problem is specified. The most critical parameter is the mesh resolution, which strongly affects the peak pressure and rise time. This is caused by shock smearing, necessary in numerical codes to prevent instability, and means that if the shock is smeared over a number of elements, as the size of those elements decreases, the closer the model can come to simulating a true discontinuity. Larger elements mean the shock is smeared over a larger physical space, and consequently the gradient of the pressure-time slope

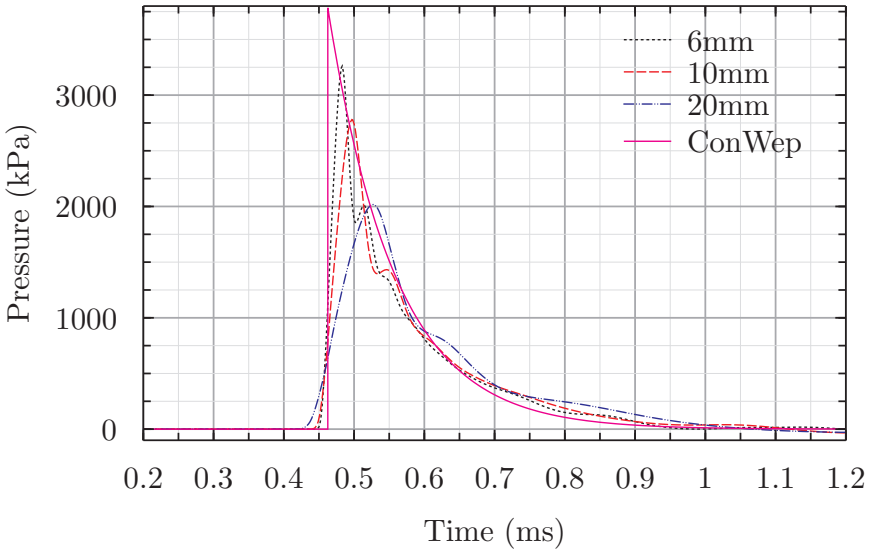

(a) Pressure

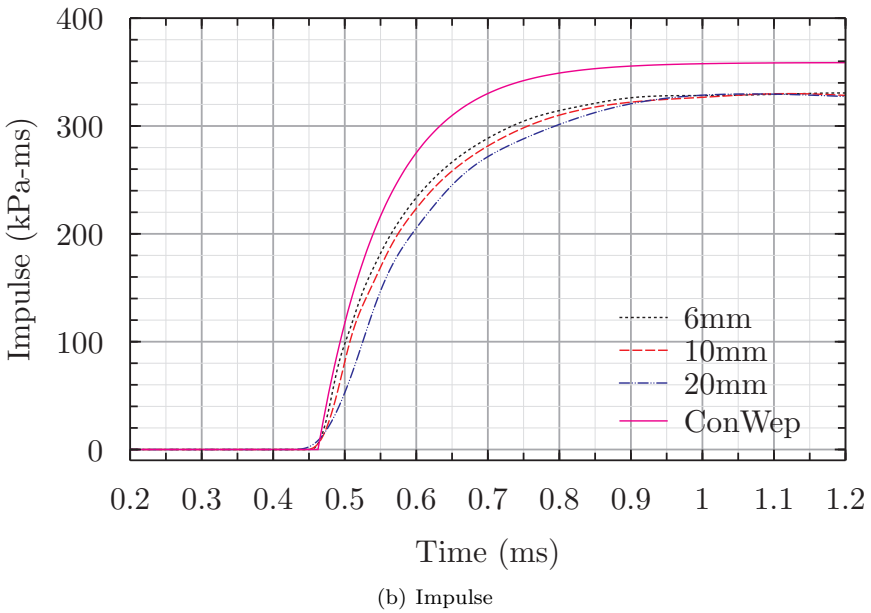

(b) Impulse

Figure 4.12: Effect of mesh refinement on the reflected pressure and cumulative impulse in 3D ALE models using nodal constraints to model a reflecting surface

is reduced and the full peak pressure cannot be reached before the shock wave has passed and pressure begins to decay. Clearly, infinitely small elements are not possible, and the mesh resolutions must be chosen to satisfy both the need for accuracy, and the computational resources available, considering that under some circumstances (see Figure 4.12) mesh refinement does not lead to more accurate solutions.

There is also a mesh effect caused by relative positioning of Lagrangian and ALE elements, and relative pressure sensor positions. The pressure is typically constant throughout an ALE element, except in cases where a coupled structure is present, and under certain combinations of positions of these elements and sensors it is possible to get some oscillation about the true pressure history, as shown in Figure 4.14. Better results were found when Lagrangian structures were positioned such that when the coupling thickness is considered, the edge of the Lagrangian element lies close to the boundary

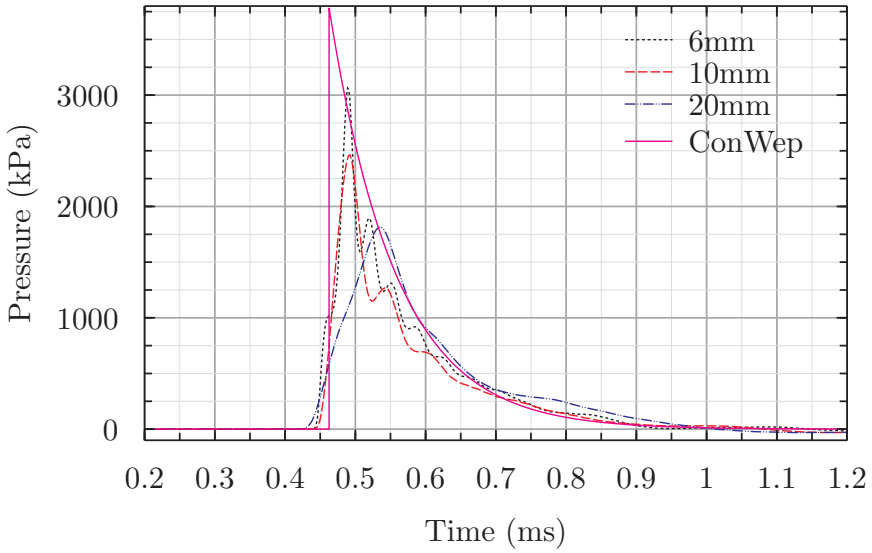

(a) Pressure

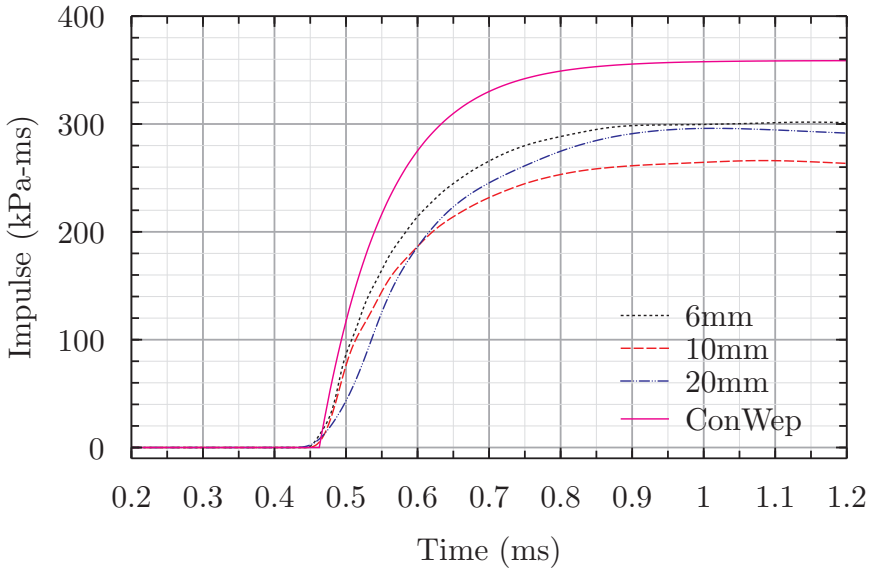

(b) Impulse

Figure 4.13: Effect of mesh refinement on the reflected pressure and cumulative impulse in 3D ALE models using a physical structure to model a reflecting surface

of an ALE element, with the sensor positioned within the adjacent ALE element on the 'shocked' side of the Lagrangian structure. This does not require any prior knowledge of the solution, but indicates that it is important that the thickness of the shell, the size of the ALE element and the position of the sensor need to be considered together at each mesh density.

Other model features also alter the solution, one being the choice of method for modelling a perfectly reflecting surface. It is clear from Figures 4.12(a) and 4.13(a) that the peak pressure in models using the nodal constraint method was higher than when the coupling method is used. The reflection at nodal constraints if effectively perfect, as nodal constraints ensure the velocities at the nodes is zero, whereas the coupling method must apply a force to the ALE material to prevent it passing the Lagrangian surface, which is inherently more complex and does not yield the same perfect reflection.

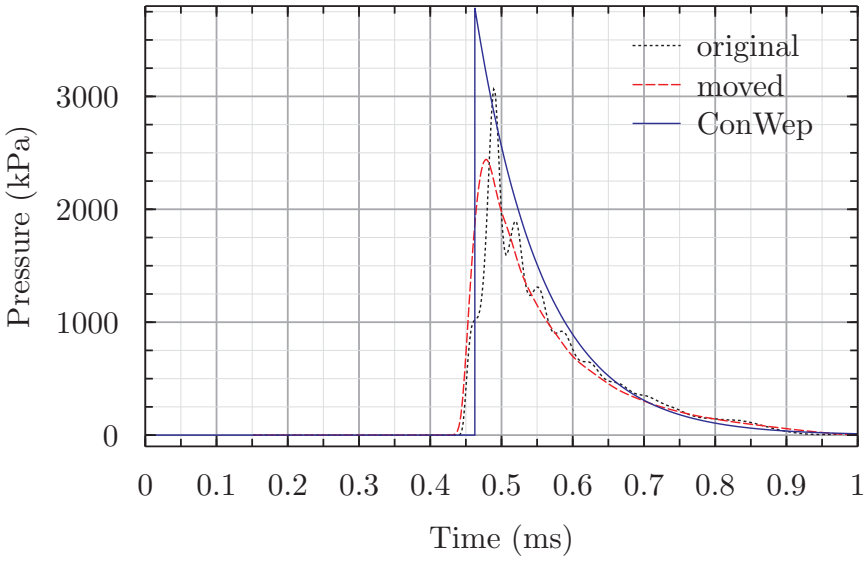

(a) Pressure

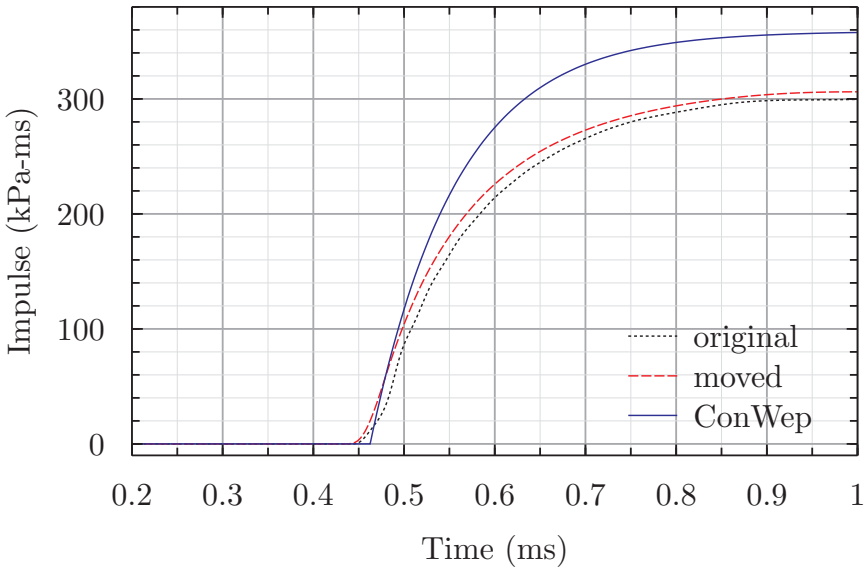

(b) Impulse

Figure 4.14: Effect of changing the relative positions of Lagrangian surface, ALE element and tracer particle history

Although this coupling stiffness can be artificially modified, the available contribution to the pressure increase is negligible.

The predictions made here using ConWep have assumed a TNT mass equivalence of 1.2, and the data presented shows that this is appropriate. Arrival times, positive phase duration and decay all match well, but this case is only for simple reflections, and in real testing there will be no need for equivalence as the model and tests use the same explosive.

4.2.4 Conclusions and implications for further work

Across both 2D and 3D ALE methods, the resolution of the mesh is very important and is the primary variable responsible for accurate peak pressure prediction from models. Coarse meshes were seen to cause slower rises to the peak pressure, resulting in under

prediction of the value of the peak pressure and the peak cumulative impulse. It is plausible that this could cause many issues with further models, and if an excessively coarse mesh is used when short duration shocks are expected, it is possible these shocks will be missed, or their contribution greatly underestimated. It is clear that the positioning of a Lagrangian structure within an ALE mesh is also important, and relative position between the two meshes and pressure sensors can cause some non physical effects to be seen in models. It was also obvious from 2D ALE models that boundary effects can adversely influence models, and care should be taken to plan the size of the ALE mesh to ensure that boundary effects will be minimized within the area of interest.

Although peak pressures and peak cumulative impulses were under predicted for a fully reflected shock in 3D, the ALE method was shown to be capable of predicting the dominant behaviour in the circumstances investigated. Experimental investigation of blast pressures in a more confined environment will allow further validation of the ability of numerical model to predict the pressure history. Given the results presented here, it is likely that some compromise between model accuracy and available numerical resources will need to be made.

Chapter 5 presents experimental data on pressures in confined environments, which can be used to further validate numerical modelling techniques presented in this chapter.

5

Experimental measurement of pressures and structural deformation in confined environments

5.1 Introduction

Numerical models can be used to predict blast parameters and structural deformation, but the accuracy of these predictions can only be confirmed by validating models with reliable experimental data. This chapter describes a series of bespoke experimental tests designed to identify blast parameters and structural deformation in confined environments, which can be used to validate numerical models. The tests were originally planned primarily with validation in mind, and less with comparison between arrangements, but despite this an effort has been made to make comparisons between arrangements and make deductions from this.

The test program aimed to:

- provide pressure, cumulative impulse and displacement data to validate numerical models
- generate standalone data to confirm similarity between repeated tests of identical arrangements
- identify what effect rigid and deformable structures have on the pressures in a confined environment

5.2 Test design

The tests described here are experimental and the method, including design, fabrication, instrumentation, preparation and running of each test cycle were all generated within and specifically for this work. As a result much was learned along the way and provides useful guidance for future similar tests which is covered by the discussion of the method

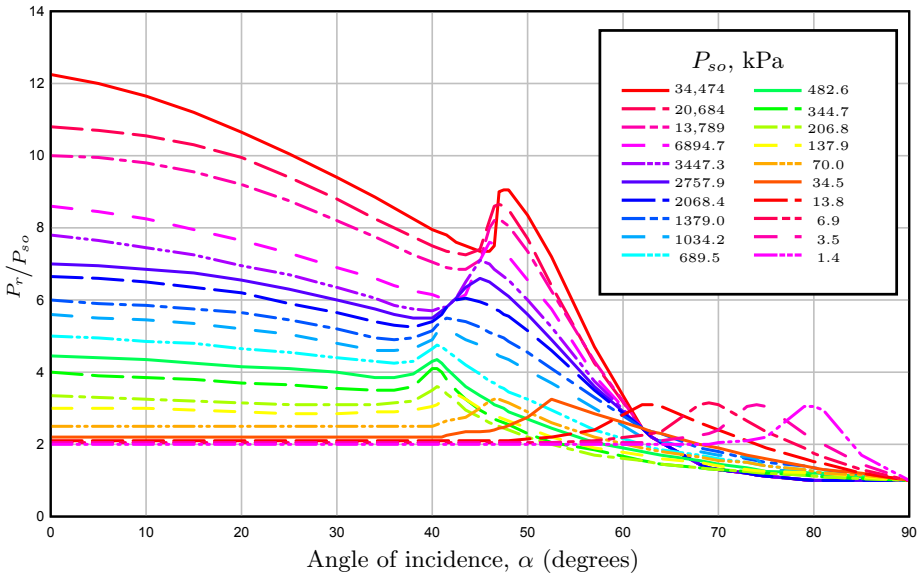

Figure 5.1: Reflection coefficient versus angle of incidence, reproduced from UFC 3-340-02, Fig 2-193 [37]

and results presented here. By their nature, new and experimental test set ups will have some features that did not work out as expected, and this work is no exception.

5.2.1 Test Design Criteria

Efforts to validate models and confirm modelling techniques that will be used when modelling different or more complex situation would be wasted if no similarities existed between these new models and the experimental tests and the models they validate. The primary reason for undertaking these experimental tests is to provide validation data for numerical models. These modelling techniques will then be applied in more complex and realistic models, with the assumption of validity based on the idea that similarities exist between the underlying physical phenomena that dictate the behaviour in the experimental test, the validation models and numerical models of rail vehicles. It is therefore important that the experimental tests are designed to replicate some of the features and behaviour that would be expected in a rail vehicle under blast loading.

The test design is limited by the space, materials and construction effort required. The University of Sheffield Blast and Impact Laboratory at Harpur Hill provides facilities and space for testing, and discussion with the staff identified an existing test cell which could be modified to satisfy the desired criteria. The test cell was a steel box with 19mm thick walls that was known to be quasi rigid for charges up 100 grams and had been used previously to investigate the behaviour of blasts in confined environments [153]. The box has internal dimensions of 1456 × 1456 × 2980 mm and is constructed of 19mm mild steel plate, giving an approximate mass of 2.9 tonnes. The mass and size made moving the box difficult and few workshops can accommodate a workpiece of such a size, so any modifications or additions had to be made with the box in situ. The test programme should be designed to fulfil the following criteria:

- simulate features particularly applicable to blast loads in rail vehicles

- be designed with subsequent modelling effort in mind
- avoid unnecessary complexities that would:
  - lead to a large spread in experimental data
  - prove excessively time consuming or complex to model with the required level of accuracy
- provide reliable, repeatable experimental data
- modifications to box feasibly completed with portable or hand held tools
- be cost effective

5.2.2 Fulfilling test criteria

There are many features of a rail vehicle which were thought might alter the behaviour of shock waves, some of which are listed below. They could protect some passengers by shielding them from blast waves and flying fragments, but may also confine and reflect the shock waves and lead to a higher chance of injury. Deformation and failure of the vehicle structure is also possible, and how this affects passengers, infrastructure and passengers surrounding the vehicle has not been thoroughly investigated and quantified. Not all features can be studied or easily simulated in experimental tests, so the most dominant, common or least understood features should be investigated. Notable features of a rail vehicle that could be investigated experimentally are:

- seats
  - size and shape
  - materials and construction
  - positioning
- draught screens and partitions
  - material
  - density / spacing
  - size
- through train design versus closed carriage design
- structural deformation / vehicle body construction
- effect of passenger presence

There are a number of scenarios that could also be investigated by experimental means that were not considered as they were deemed to be difficult to achieve or outside of the scope of the current project.

- complete destruction of vehicles due to very high charge masses (PBIED)
- effects on a moving train (derailment etc.)
- damage to infrastructure (tunnel, railhead, platform damage)

- weapon / IED characterisation and performance
- effect of combined fragment and blast loading[1]
- characterisation and performance of materials and structure common to rail vehicles under blast loading
  - extruded wall panels[1]
  - glass (laminated and toughened)
  - wood
  - polymers
  - composites

5.2.2.1 Applicability and feasibility

Seats are common to every passenger rail vehicle but their size, shape, construction and positioning varies hugely depending on the application the vehicle is used for. Intercity commuter trains typically have larger, heavier and more cushioned seats with more space between them than suburban or local services, as passengers typically sit for much longer periods of time on these services. Urban trains and light rail, such as the Underground and trams have unique seating patterns, often with bench seats mounted along the walls of the carriage, or large spaces between seating areas to accommodate the maximum number of standing passengers. A parametric study of how construction, size and positioning alter the behaviour of blast loads in rail vehicles could provide interesting information that could inform future design and validation data would be vital to ensure the complex models that would be required are reliable. In reality, seats prove difficult to implement in experimental tests due to time, size and cost limitations. The existing test cell was too small to accept full size rail vehicle seats, and only a limited number of old and obsolete designs were available. Fabrication of accurate and representative scaled models is prohibited by limited budget and project time scales.

Draught screens and partitions are a feature common to many rail vehicles and have the potential to dissipate the energy from a shock wave and mitigate its effect on passengers. These structures are typically made from toughened glass and are designed to be tough to deal with being held and leant on by passengers, as well as impacted by luggage and other items that may be moved through a carriage. These could be simulated within the given test cell with either toughened glass similar to that used in a rail vehicle, or with a rigid structure such as a steel plate which would provide a similar effect to the glass partitions by disrupting the shock wave. As these structures typically run from floor to ceiling in a rail vehicle, they can be recreated inside the existing test cell with minimal cost and fabrication time.

Through train designs (see Chapter 2) with gangways between vehicles are becoming more common in urban rail vehicles in the UK, to help ease overcrowding and make the most efficient use of floorspace. Their effect on the propagation of blast waves and on

[1]Earlier in the course of this work, experimental testing was planned using some material salvaged from a rail vehicle to undertake combined blast and impact assessment. A high explosive charge was to be surrounded with a specified number of ball bearings and detonated a short distance from a series of sections cut from the wall of a rail vehicle. Unfortunately, the sections of rail vehicle were not forthcoming so alternative plans were made for experimental testing. This initial testing plan would have likely yielded interesting data, but could have proved difficult to validate and of limited applicability to the research aims and objectives as a whole.

passenger injury has been investigated in part using numerical models as part of the RAILPROTECT project [176], where work concluded that open carriage designs could increase the risk to passengers. Experimental testing or validated modelling is required to determine the accuracy of this claim - open carriages could either expose a larger number of people to dangerous overpressures and flying projectiles, or could reduce the build up of pressures that would be seen in traditional closed carriage designs, resulting in a lower risk to passengers in the carriage where a device is detonated. To investigate this experimentally, structures would be required within the test cell that give a good spatial representation of the cross sectional and inter-carriage separation differences between the two different designs. Spatial limitations, particularly the relatively short length of the box, prevent entirely representative experiments from being designed. Experimental investigation of through train designs would be best studied in a test cell that has a length much longer than was available for this work.

The role of structural deformation in the build up of pressures and reflection of shock waves from explosions inside a complex and confined environment has not been extensively studied, and the lack of data means studies in this area are of much interest and good quality data could provide important work in its own right. Furthermore, a key feature of rail vehicle numerical models and a measure of their accuracy is how well they can predict vehicle wall deformations under highly transient loading. Experimentally, structural components can be mounted in many orientations in the given test cell, but the closest similarity to a rail vehicle would be achieved by mounting a wall structure of interest vertically along the long axis of the box to simulate the side wall of a rail vehicle.

Some previous work on the effect of blast loads in rail vehicles has ignored the presence of passengers when undertaking modelling, which could have a noticeable effect on both structural deformation and the risk to passengers themselves. Although precise representations of the human body are not possible, surrogates will be used that can mimic the passage of shock waves over the body and allow pressures to be measured at the surface of a surrogate, which could give interesting stand alone data, as well as validating the use of any surrogates in further numerical models. The presence of surrogates (or any significant structure) within the experimental test cell will alter pressures experienced by sensors at the wall, and it will be important to ensure that numerical models can take account of this. Two surrogates were placed within the test cell, one with instrumentation for measuring pressure and one without.

5.2.2.2 Reliability

Test repeatability and reliability depends greatly on preparing each test in an identical manner to the previous one, but some features of the test design can affect the reliability of the results. Sensor positioning and behaviour of proposed structures of test arrangements should be chosen to reduce any possible variation between tests, so the following guidelines will be adhered to where possible:

- sensor positioning
  - avoid possible fragment or fireball damage
  - away from features such as holes and bolt heads, which cannot easily be accounted for in models

- structures should
  - avoid any deformation if being retained between repeat tests
  - be replaced between repeat tests if deformation is expected

5.3 Test layouts

With the above criteria in mind, four test arrangements were designed. The test arrangements looked to identify the effect of passenger surrogates, draught screens and baffles and structural deformation on pressures and cumulative impulses within a confined environment.

All experimental test arrangements made use an existing test cell structure, a steel box with internal dimensions of 1456mm square in cross section and 2980mm in length, with a wall thickness of 19mm, effectively making these walls rigid for a charge size of 80 grams. One end of the test cell is completely open. The existing test cell was configured to have a quarter spherical charge placed at half height in the test cell in the corner between long and short walls of the test cell, and as such the two walls which the charge lies on the corner of, can be seen as symmetry planes, and the whole test cell is representative of a charge of 320 grams, in a structure measuring 5690mm long, 2915mm wide and 1456mm high

Rigid, fixed steel cylinders were used as passenger surrogates, as they allow pressure sensors to be mounted within them more easily than with a surrogate made from a deformable tissue simulant material such as ballistic gelatine.

5.3.1 Arrangement 1

Arrangement 1 (A1), which is shown approximately to scale in Figure 5.2 (dimensions are given in Appendix D), had only rigid cylinders (surrogates) in place. The cylinders are 814mm high and 114mm in diameter with a wall thickness of 8mm and are attached to the box with an M20 threaded bar, which was fastened to the base of the box and was in the same location for each subsequent test in each arrangement. Scaling these dimensions is possible to make these surrogates 'representative' of the human form, but in this work no such scaling was undertaken, and the cylinders are present purely to identify the effect they have on the pressures at this particular scale, and to provide test data for validation. The test allowed pressures in an empty box to be compared with those when increased complexity and confinement are present, as two pressure sensors are kept in a constant location for all 4 tests. The tests also confirm repeatability between tests in a relatively simple environment, and have minimal set up time so focus can be directed towards instrumentation and data acquisition reliability.

Pressure sensors were mounted at five locations, four within the walls of the box and one inside cylinder 1, all being flush to the inside surface of the test cell or the outer radius of the cylinder. Other than the pressure sensor mounted inside the cylinder, the sensors were mounted on the same plane at half height in the box. The pressure sensor in the cylinder is mounted lower than half height for two reasons; firstly because clearing effects[2] are likely from the circumference of the cylinder, as well as to a lesser

[2]Clearing is discussed in detail in Chapter 2. Clearing is an effect caused by shock wave interaction at the edges of finite targets, where rarefaction waves travel inwards from the edges of a target and reduce the pressure on it.

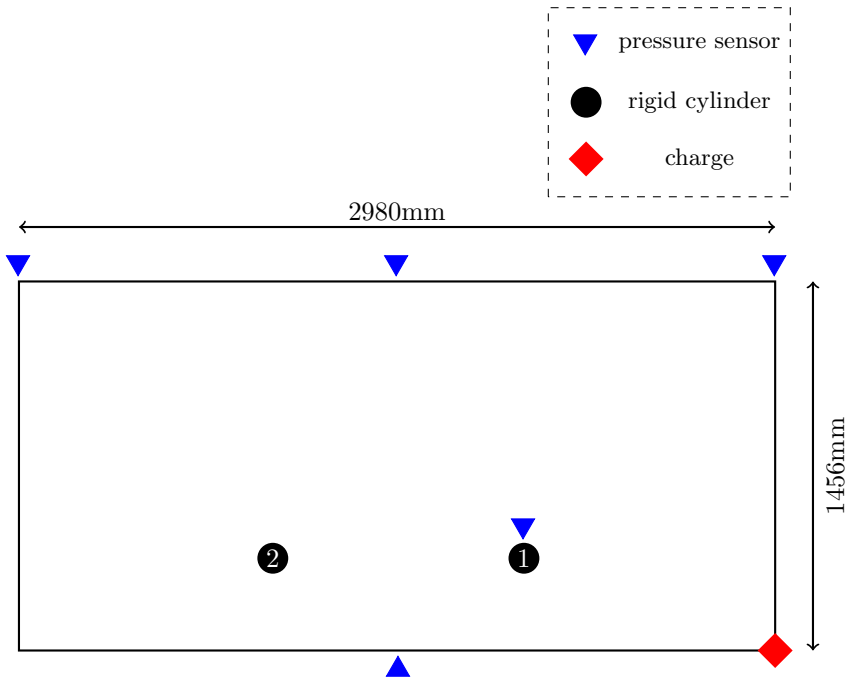

Figure 5.2: Plan view of test A1

extent from the top of the cylinder. By distancing the sensor away from the top of the cylinder, it was thought it would be easier to differentiate these effects in the results. Secondly, the half height on the box is very near the top of the cylinder, so mounting a pressure sensor at half height would be mounting at 'head height' in the surrogate (by proportion of the total height of the cylinder, not by any scaling). Instead, the pressure sensor is mounted at a height (600mm) that is proportional to the chest height of human standing in the box, which has the potential to provide more useful data to input into other models. The sensor was mounted pointing towards the long wall furthest from the cylinder as opposed to pointing towards the charge, firstly to make repeatability of sensor position easier, but importantly for later experiments, to reduce the risk of damaging the sensor, which would be exposed to more shock and heat if directed at the point of detonation. As the sensor was mounted on a cylinder, consistent results were considered likely to be more difficult to achieve than with sensors mounted on a flat wall, as only small changes in angle and pressure of the incident wave can lead to large differences in pressure (see UFC 3-340-2, Fig 2.193 [37]), and with the sensor mounted almost side on to the incident wave (as opposed to normally to it), clearing effects are also likely to be present.

5.3.2 Arrangement 2

The second test arrangement (A2, shown in Fig 5.3) was designed to identify the effect of structures like draught screens on measured pressures. Two 10mm thick steel plates were mounted, equally spaced on the long side of the box, opposite to where the charge was be mounted and detonated, which will be referred to as 'baffles' from herein. These were be mounted on sections of angle iron and fixed in the box with threaded fasteners.

The sensors in the cylinder and on the long side nearest the rigid cylinders were kept in the same position as A1, with other sensors moved to measure how the baffles alter

the pressure reflections around the box. One sensor was mounted inside the baffle, with the sensor facing towards the end wall on which the charge is located. The other sensors are mounted halfway between the corner of the box and the first baffle, and at the point the second baffle meets the wall of the box.

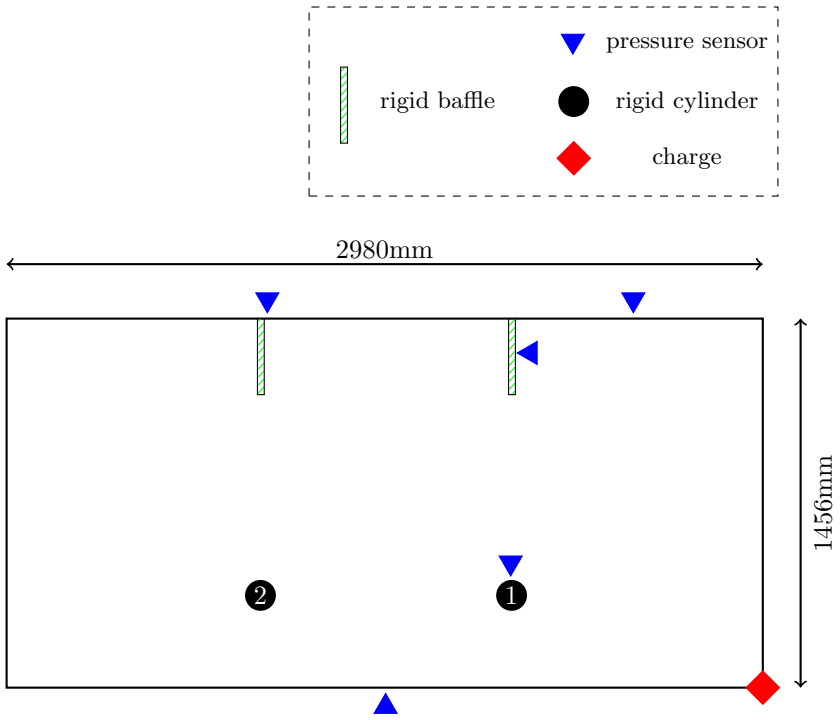

Figure 5.3: Plan view of test A2

5.3.3 Arrangement 3

Arrangement 3 (A3) was used to compare how altering the spacing of baffles alters the pressure experienced within the box. Three baffles will be equally spaced along one wall, as shown in Figure 5.4 and fixed in place in the same way as baffles in the previous arrangement.

Pressure sensors were mounted at broadly similar areas to A2, at the central face of the baffle, at the point where the baffle meets the wall halfway between the first baffle and the end wall.

5.3.4 Arrangement 4

For the fourth test arrangement (A4), a flexible aluminium panel was mounted vertically along the centre of the box to identify the effect of deformation and fluid structure interaction on pressures in the box. The aluminium sheets were 3.2 mm thick and were clamped in place between two pieces of right angle steel section on the roof, floor and end wall of the box. Sections of right angle steel were fixed with bolts to the floor, ceiling and end wall of the box. Further sections of angle were then used to sandwich the aluminium sheet and threaded fasteners used to provide a clamping force between the two sections of angle iron. Clearance holes of 20mm were drilled in the aluminium sheet to ensure that the clamping force between the angle holds the sheet in place,

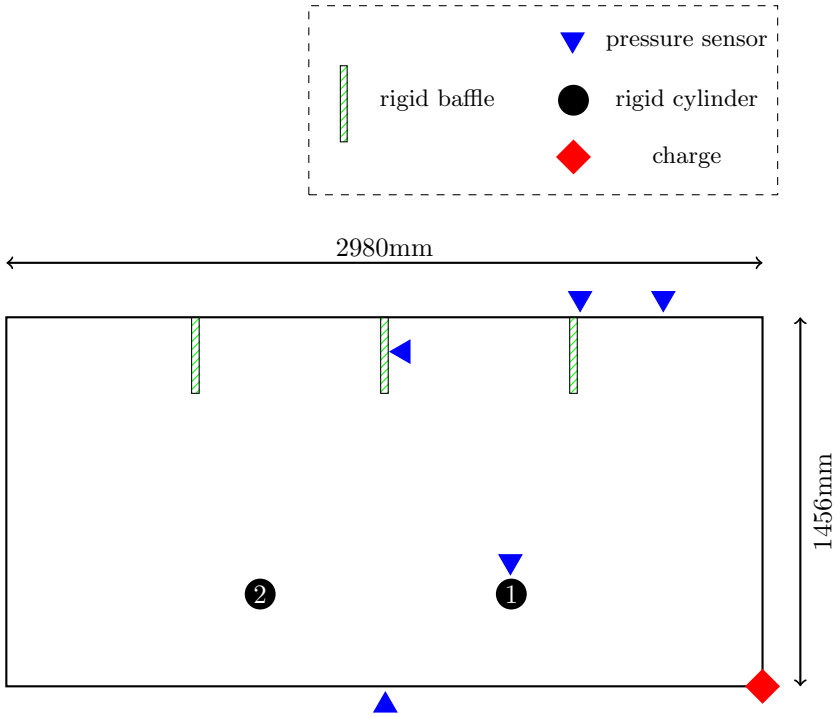

Figure 5.4: Plan view of test A3

and that bolt shanks (M12) do not make contact with aluminium sheet to ensure that experimental boundary conditions can easily be replicated in numerical models.

A laser distance gauge was used for this test, which was mounted so that the deformation of the centre of the aluminium panel is measured. The laser displacement gauge is mounted on a rigid bracket behind (the charge was in front) the aluminium panel on the long wall, as shown in Figure 5.5.

5.4 Test method

5.4.1 Pre test work

Before any test cycles could take place, structures to be placed inside required fabrication, and the existing test cell required disassembly and modification.

5.4.1.1 Fabrication

A list of the fabricated structures is below, full dimensions can be found in drawings in Appendix E.

- steel baffles
- aluminium panels
- angle sections to mount baffles and panels
- laser gauge bracket

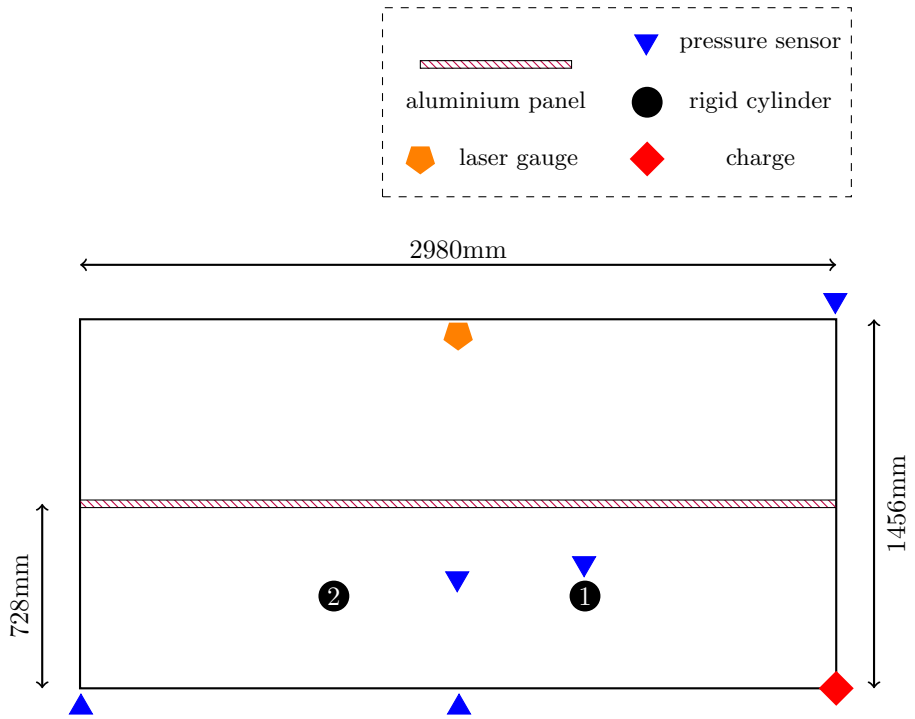

Figure 5.5: Plan view of test A4

5.4.1.2 Modifications to existing test cell

Tests on the existing test cell had used a hinged door (can be seen in Figure 5.6(b)) in one corner so the firing officer could prepare, secure and place the charge with two hands before closing and securing the door. A hole in the door had previously been used to run the detonator cable out to the firing officer, but the hole previously used was not at half height, as required by the current tests. The door hinge was removed and a hole drilled at half height, i.e. 728 mm, from the inside floor of the box.

Previous test cell users had mounted structures using several large holes around the box, some of which were very close to locations in which sensors were to be positioned. To minimise any effect that the holes had on the results, those near sensors or sitting on the same plane as sensors (the half height plane in the box) were plugged with an adhesive filler and backed with short sections of wood to reduce the possibility of the plug being blown out by the blast, shown in Figure 5.6.

5.4.1.3 Mounting of structures

All structures within the test cell were mounted with mild steel angle sections of 80 × 80 × 8mm which were fixed to the walls with M12×50 bolts. The baffles were fixed to the angle sections using M10 bolts, and the aluminium panel was fixed by clamping between pairs of angle section with M12 bolts.

5.4.2 Data acquisition

A schematic of the data acquisition system used throughout the testing is shown in Figure 5.8, with the laser displacement gauge used only for test A4.

Kulite HEM and HKM piezoresistive pressure sensors were mounted into position in the test cell with screw threads (3/8 UNF or M10x1), and were powered by and returned

(a) Long wall opposite charge (b) Long wall adjacent to charge

Figure 5.6: Filled and backed holes on the line of pressure sensors

(a) Panel in position along centre of box (b) Laser distance gauge aiming at rear of panel

Figure 5.7: Laser gauge and panel in place

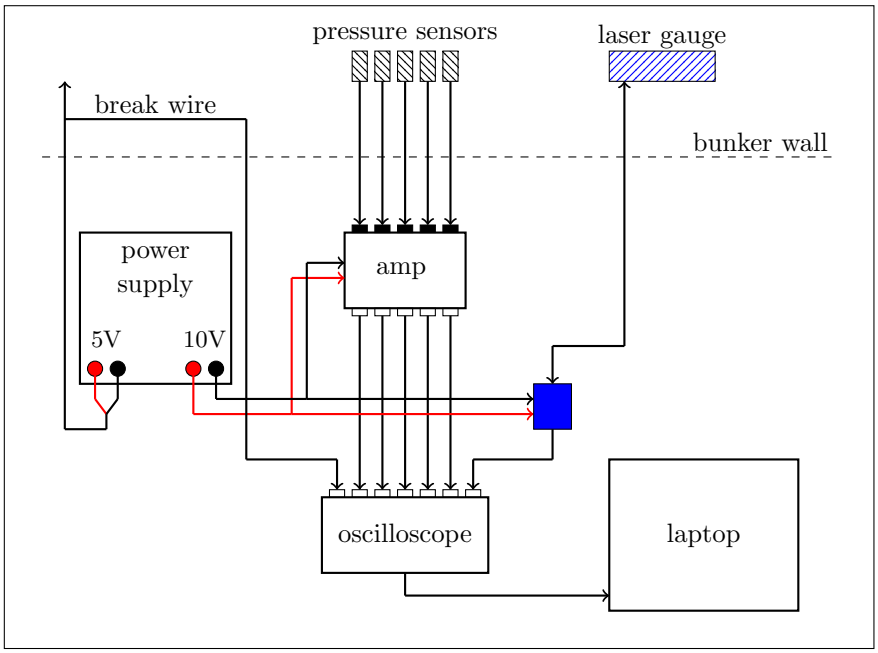

Figure 5.8: Data acquisition schematic

voltages to an amplifier box via 5 pin DIN connectors (see Figure 5.9). Extension cables between pressure sensors and the amplifier were used which were tested for continuity, and an effort was made to ensure that extension cables were of a similar length. Ultimately cables were chosen based on those with the best performance that were available. To demonstrate the significance of cable length at this scale, Equation (5.1) shows the time taken for a signal in coaxial cable with a velocity factor (speed of transmission relative to the speed of light, c), VF, of 0.66 (lowest velocity factor in common coaxial cables, from [177]), to travel 1 metre. For two cables, one of 5m and one of 50m (actual difference between cable lengths was smaller than this), the difference in travel time in the cable will be 202 ns. The anticipated timescale of interest was between 10 and 100 μs, so the difference in cable length makes negligible difference. The performance of the cables was of primary importance, and several cables showed considerable voltage oscillation on the laptop display when there was no load on the pressure sensors, so these cables were removed and replaced with cables that didn't display such oscillations under zero load.

$$\begin{aligned} t &= \frac{1}{0.66c} = \frac{1}{0.66 \times 299792458} \\ &= 5.05ns \end{aligned} \tag{5.1}$$

An MEL M7L400 laser distance gauge (LDG) was used to capture the displacement time history of the aluminium panel at its centre. The LDG was mounted behind the aluminium panel and attached to the wall of the box with a rigid bracket, which can be seen in Figure 5.7(b), with a 5mm layer of PVC between the sensor head and the mounting bracket to isolate it from shock transmitted through the box wall. The LDG performs best when the laser is reflected from a matt white surface, so the aluminium panel was roughened with sand paper and coating with a matt white spray paint over

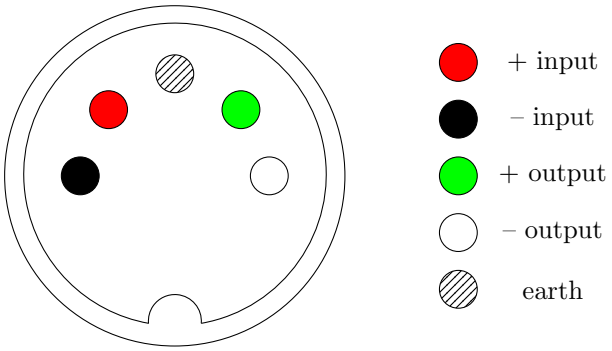

Figure 5.9: 5 Pin DIN connector

the area of interest on the surface facing the LDG. The LDG was powered by a bench supply at 20V and connected directly to a USB oscilloscope (see Figure 5.8).

For the pressure sensors, an amplifier box was connected to a power supply at 10V DC, which was measured with a digital voltmeter (DVM) and recorded each time the power supply was switched on, as the input voltage supplied to the sensors is directly proportional to the output voltage readings. The amplifier has the option of amplifying signals at 1× or 100× gain, but to avoid clipped or topped out signals caused by the amplifier trying to deliver voltage outputs beyond its operating range, the gain was set to 1×. Similarly, the scope has a range over which it can record, F_a, and clearly it is best to try and get this ratio as close to unity as possible, to make the most of the resolution of the oscilloscope. With only a limited gain range in the amplifier, it was therefore not possible to adjust this (it is a multiplier for the signal voltage, F_s) to achieve a perfect match. If the signal is amplified by 100×, two undesirable situations can occur; the amplifier can 'top out', where any signal causes the amplifier to try and deliver a signal above it's output voltage is simply limited to the maximum output of the amplifier, or the oscilloscope will not have sufficient range (or counts, C) and some data will be missed, and a higher bit (n) resolution will be required. If a higher bit resolution is chosen, the total time over which data can be recorded and the frequency of recording is reduced. The count number, C, oscilloscope and signal voltage range, F_a and F_s and oscilloscope resolution in bits, n, are related by equation (5.2).

The amplifier box was in turn connected to two, 4 channel TiePie Handyscope HS4 USB oscilloscopes with coaxial cables 1-2m in length. A break wire around the detonator was used to trigger the recording, which consists of a powered length of coaxial cable, plugged into the oscilloscope, where the outer shield and inner cables are connected by a loop of thin wire which is wrapped around the detonator. The voltage in the break wire drops when the break wire cable is cut by the expansion of the detonator, and a voltage window is specified in the data acquisition software, which begins recording when the voltage recorded is no longer within this range.

The oscilloscope was connected to a laptop computer with a single USB lead, and data recorded for 100,000 samples at a sampling rate of 1.562MHz with 14 bit resolution using the TiePie Multi Channel software provided with the oscilloscopes. The data capture software continually records and overwrites data until the data recording is 'triggered' by the break wire (this is the zero time), and a certain value of pre trigger can be specified, which determines the amount of data that is saved *before* the zero time. A pre trigger of 6.4ms was specified, so with a total recording time of 64 ms, data is recorded for the first

57.6 ms of the event with maximum of a 16384 counts in the voltage (y axis) direction. Data from each test cycle was recorded in a single semicolon delimited file with a single column of time data in (s) and subsequent columns of raw sensor output voltage (V).

$$C = \frac{F_s}{F_a} \times 2^{(n-1)} \tag{5.2}$$

5.4.3 Shot preparation

Each test cycle involves one 'shot' of an 80g charge of PE4, moulded into a quarter sphere as shown in Figure 5.10 using a bespoke laser sintered nylon mould.

Figure 5.10: 80 gram PE4 charge inside hemispherical mould with central hole prepared for detonator

The charge was mounted on a hinge at one corner of the box with the centre of the charge and point of detonation 728mm above the floor of the box. To protect the hinge material and ensure the flat faces of the charge are level with the inside faces of the test cell, the charge was mounted on 18mm standoff packing, as shown in Figure 5.11(b). The standoff packing from shot 3 in A1 and all subsequent shots was fabricated from layers of corrugated cardboard bonded together with PVA adhesive to the correct thickness (18mm) and cut with a bevelled edge to fit tightly in the recess between the hinge and inside faces of the test cell and was held in place with adhesive fabric tape. Packing for shots 1 and 2 in A1 was broadly the same, but cardboard was not bonded together and edges were not bevelled, leaving a slight air gap between the vertex of the charge and the wall of the hinge behind it.

Prior to the detonator and charge being attached in place, the break wire was threaded through a hole in the hinge below the charge and away from the hole through which the detonator is mounted (Figure 5.11(a)). The charge was then mounted in place (Figure 5.11(b)) and a non-electric shock tube detonator pushed firmly into the back of the charge through a hole in the hinge, using the charge mould to maintain the shape. The charge was then secured in place with adhesive fabric tape (Figure 5.11(c)) and the hinge closed and secured with a tapered bar, shown in Figure 5.11(d), and the shock

(a) Detonator with breakwire wrapped around and secured with tape

(b) Charge positioned over detonator, directly onto standoff packing

(c) Charge secured in position with tape

(d) Hinge secured, detonator shock tube (top) and breakwire seen protruding from hinge vertex

Figure 5.11: Procedure for preparing each shot

tube run back to the firing location. The shock tube, which consists of a flexible plastic tube whose inner surface is coated with RDX and Aluminium powder, was manually triggered by an electric initiator once it was determined the test area was clear and it was safe to make the shot.

Table 5.1: Pressure sensor details

Sensor	S312	S402	S358	S311	S101
Model	HEM375	HEM375	HKM375M	HKM375	HKM375
Rating	500PSI	250PSI	7BAR	500 PSI	100 PSI
Rating (kPa)	3447	1724	700	3447	689
S (mV/PSI)	0.201	0.382	–	0.200	0.903
S (mV/BAR)	–	–	14.396	–	–
CF (kPa/V)	34302.2	18049.07	6946.37	34473.73	7635.38

5.5 Results

5.5.1 Data processing

Data from sensors, referred to by their serial number (details in Table 5.1) was read into GNU Octave for processing (scripts can be found in Appendix C.1). Several operations are performed on the data to get legible pressure, cumulative impulse and displacement histories:

- remove zero shift
- convert raw voltage data to appropriate units
- calculate impulse from pressure history
- filter data to remove noise

5.5.1.1 Pressure histories

When zero (atmospheric) pressure is applied to sensors, the sensors give a non-zero voltage reading due to the electrical resistance in the circuit and is not representative on any physical effects. This zero shift is removed first to ensure that on average, voltage readings are zero when sensors are exposed only to atmospheric pressure. This is achieved by averaging the 2000 data points immediately preceding the arrival of the shock wave and subtracting this value from all voltage data. This prevents any drift in the zeroing, which could occur if values at the start of the data series are used. Although the effect of small drift is unlikely to be noticeable on pressure curves, cumulative impulse curves are very sensitive to such drifts as they are the integral of pressure over time, which can lead to spurious cumulative increases or decreases in the calculated values.

Voltage values are then converted to pressure values using calibration factors (CF) derived from the sensitivity (S) (Table 5.1) which is given by the manufacturer in calibration certificates for each sensor. An example of how the calibration factor is calculated for S312 is shown in Equation (5.3). In (5.3), the sensitivity, S is inverted and multiplied by 1000 to give PSI/V as the oscilloscope output is in V, then multiplied by a conversion factor from PSI to kPa, F, to give a calibration factor in kPa/V.

$$CF = \frac{1000}{S} \times F \tag{5.3}$$
$$= \frac{1000}{0.201} \times 6.894745$$
$$= 34302.2$$

Data from sensors is noisy; the noise can be introduced from sources such as cables, connectors and amplifiers. Noise reduction is typically implemented using a low pass filter, but can also be achieved using wavelet transform de-noising. Full details of filtering methods applied, including comparisons between parameters and methods can be found in Appendix F. The wavelet method with hard thresholding was found to be the most effective at removing noise and retaining experimental features, but introduces additional features to the data which could be misinterpreted. Data from pressure sensors is therefore filtered using a Butterworth filter and a normalised cut off frequency of $\omega_n = 0.02$, where ω_n (in π radians per sample) is the cutoff ω_c frequency normalised by half the sampling frequency ω_s.

$$\omega_n = \frac{2\omega_c}{\omega_s} \tag{5.4}$$

5.5.1.2 Displacement histories

The LDG provides voltage outputs between -10 and +10 V D.C and these output voltages are proportional (by the laser doppler factor, LDF, provided by manufacturer) to the distance reading in mm between the sensor head and the structure under investigation. Voltages 0 -10V correspond to a distance of 480mm from the gauge head, and voltages of +10V are produced for the maximum measurable displacement of 880mm. The raw voltages were divided by LDF for this gauge, -0.05, to give absolute distance from the gauge head and a displacement time history of the panel relative to it's original position was computed by subtracting the displacement at $t = 0$ from all displacement values. A Butterworth filter was applied to reduce the noise on the data, but the noise from the gauge on raw experimental data was significantly less noticeable that on the pressure gauges.

5.5.2 Arrangement 1

Pressure history data and the calculated cumulative impulse from sensor 312 are shown in Figure 5.13, which is located as shown in Figure 5.12. The pressure history is plotted over the first 20ms, which represents the most interesting and dynamic region recorded by this sensor, and also allows a clearer view of the transient data making comparison between the traces easier. Cumulative impulse data is calculated and plotted over the entire measured time as it gives a very sensitive comparison of similarity between the shots.

Over the pressure history shown in Figure 5.13(a), shots 1, 2 and 3 show very good consistency between shots in terms of number, time of arrival and decay of primary and reflected shocks. The only discrepancy in the data is between peak pressure values for the first two shocks experienced by the sensor. The first shock, at 1.7ms, shows peak

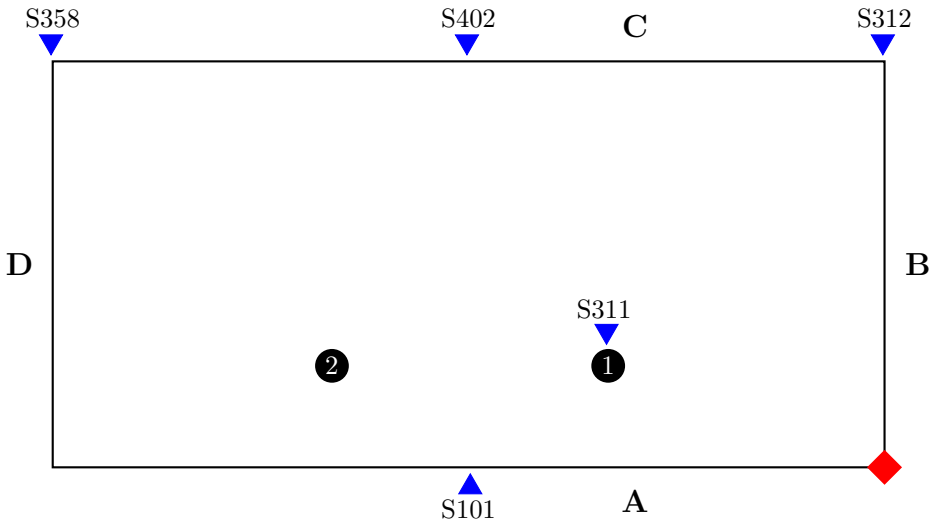

Figure 5.12: Sensors and positions for test A1, shots 1 – 3

values of 550kPa and 520kPa for shots 2 and 3 respectively, but only 420kPa for shot 1. Shock 2, at 2.85ms, shows a peak pressure of 600kPa for shock 1, but only 380kPa for shot 2 and 775kPa for shot 3. This could be caused by sensor overshoot and ringing at peaks [36], leading to overly high readings, where the arrival of the shock front can cause an over read on the sensor, and can be seen more clearly on comparisons between analytical and experimental data presented by Tyas *et al.* [36]. Although the peaks are very sharp, there are a number of data points either side of each peak, so the peaks are not caused by single erroneous data values. Sampling at 1.562MHz means there are 1562 data points per ms.

Cumulative impulse curves for the three shots (Figure 5.13(b)) over the full recorded duration show that the high pressure experienced for shot 3 does not lead to a visible deviation from the general trend shown by other shots until after 15ms. Data is shown over the entire period of measurement to identify and explain features that are not apparent on the pressure data curve where differences between shots after 20ms are difficult to distinguish. The low pressure experienced at the second peak for shot 2 does slightly reduce the impulse seen at 3.7ms, shifting the whole cumulative impulse curve down. The differences in the peak pressure in the first shock between shots makes no noticeable difference to the cumulative impulse, as they are visibly identical until the arrival of the second shock at 2.8ms.

In general, the cumulative impulse curves shown in 5.13(b) show very good similarity between shots 1 and 2 given that integrals lead to additive errors over the time history. All three shots show the same features and follow each other closely (with a slight shift in the case of shot 2, as mentioned above) to 15ms, where shot 3 begins to deviate from shots 1 and 2. Figure 5.13(a) shows that at this point the pressure has returned to and is oscillating around zero, so small average shifts above or below zero can lead to dramatic differences in impulse. Between 15ms and 60ms, the impulse seen in shot 3 increases to 1150kPa-ms, as opposed to 100 – 200 kPa-ms seen in shots 1 and 2, approximately 1000kPa-ms, which over 45ms equates to an average difference of only 22kPa between 15 and 60ms. The difference is made more striking as the pressures oscillate around zero, as a shift below zero cause a decrease in cumulative impulse and vice versa. Importantly,

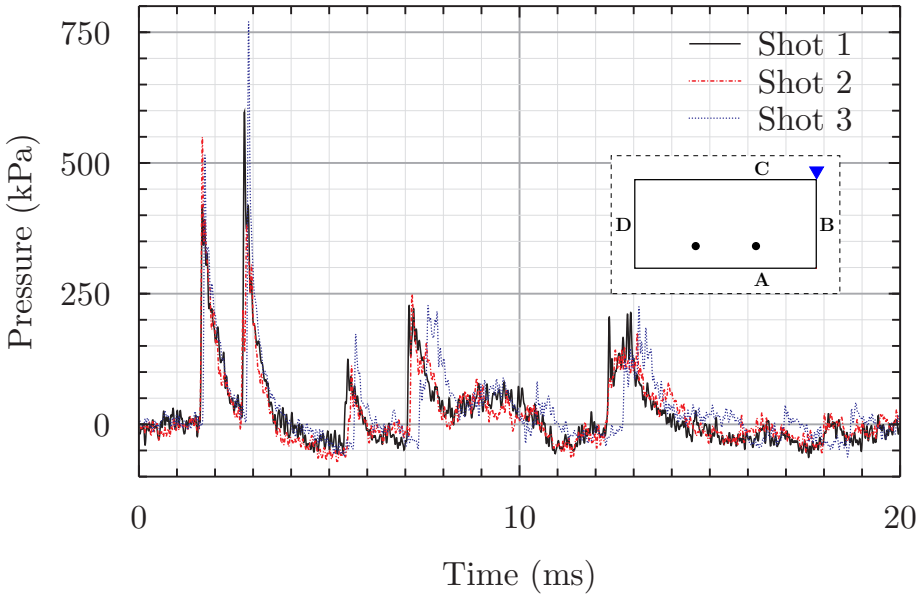

(a) Overpressure time history over first 20ms

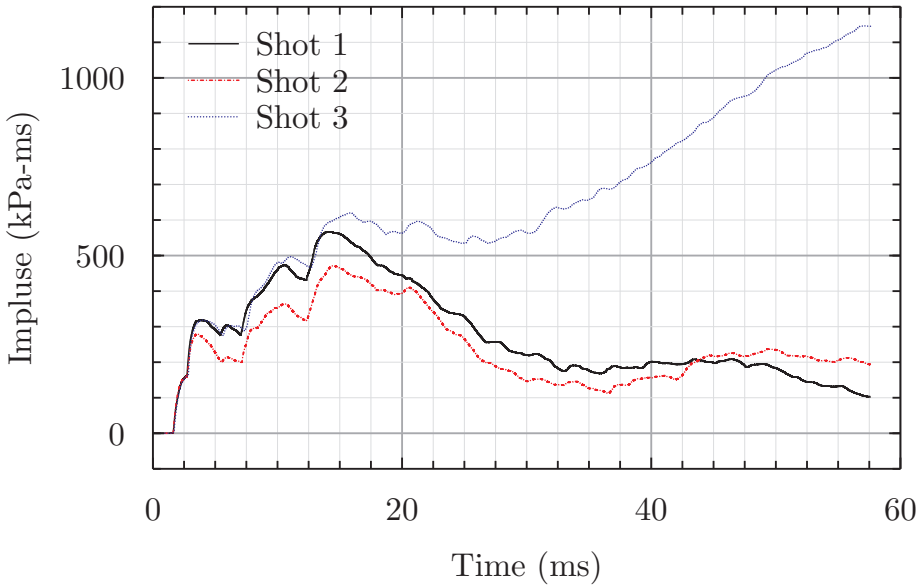

(b) Cumulative impulse over entire recorded time

Figure 5.13: Sensor 312, pressure history and calculated cumulative impulse

despite the deviation from shots 1 and 2, the cumulative impulse for shot 3 shows a similar shape to the other shots, being distinctly bi-linear after 15ms. For shots 1 and 2 the pressure dips below atmospheric until approximately 30ms, during which a gradual decay in impulse is seen, followed by a return to atmospheric pressure leading to a constant non increasing impulse for the remainder. For shot 3, instead of becoming negative, the pressure remains around atmospheric until 30ms, so when a positive shift is experienced at this time, cumulative impulse increases instead of becoming constant as seen in shots 1 and 2.

Sensor 358 shows good consistency in pressure time history (Figure 5.14(a)) over the recorded range, with only small differences between the two highest peak pressures at 5.5 and 10ms. For both of these, shot 1 shows a slightly higher pressure than both shot and shot 3 respectively. At this location, more significant and longer periods of negative

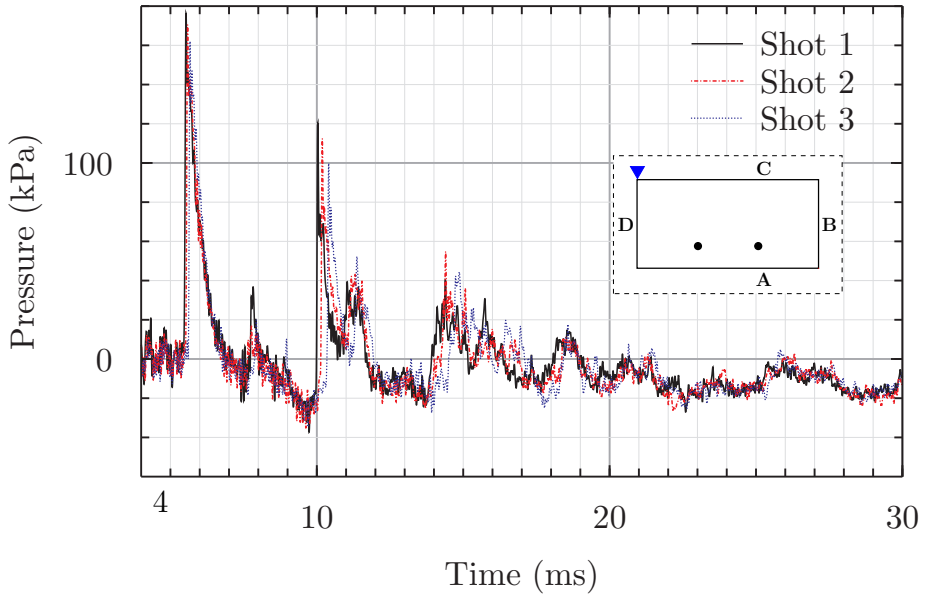

(a) Pressure

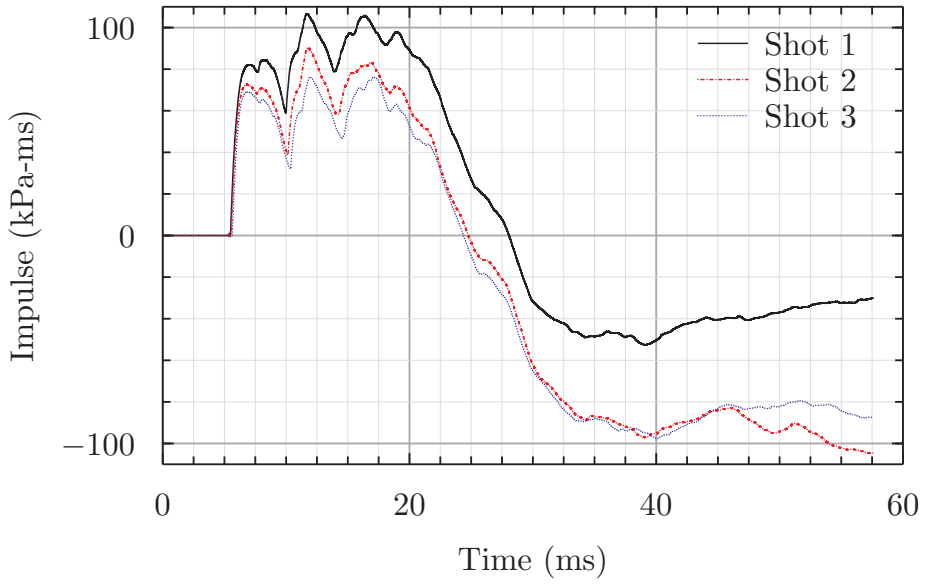

(b) Impulse

Figure 5.14: Sensor 358, comparison between shots

pressure are seen, compared with the sensors 402 (see Appendix G) and 312 (5.13). All three shots show similarity in both magnitude and duration of these negative phase areas, particularly between 12 and 14ms and 20 to 30ms.

Cumulative impulse plots (Figure 5.14(b)) for all 3 shots at sensor 358 show similar behaviour, but as with other cumulative impulse curves show a small shift, although by a smaller amount than seen at other locations. Cumulative impulse for shot 1 rises higher at 7ms, but from the pressure curve in (a) it is difficult to see a significant difference in the pressure curves. A higher peak at 8ms on (a) again causes a small positive shift for shot 1 in the impulse curves. Shot 2 and 3 show almost identical impulse until 15ms, when shot 3 rises away from shot 2. From the pressure curve in (a) it can be seen that between 15 and 17.5 ms the peaks are of a smaller magnitude, leading to a lower cumulative impulse.

5.5.3 Arrangement 2

For A2, sensors 312, 402 and 358 are moved to different location and sensors 311 and 101 remain in the same location as before as shown in Figure 5.15.

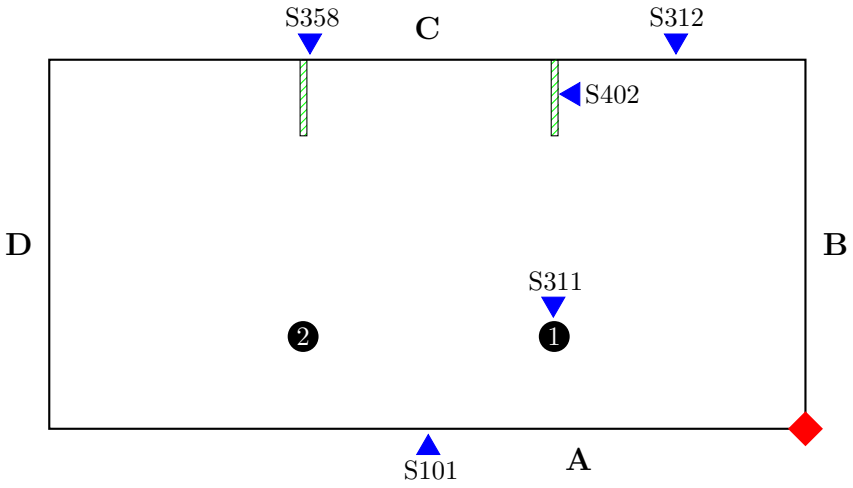

Figure 5.15: Sensor locations for test arrangement 2

Sensor 402 is mounted at half height and half width in the first baffle, as shown in Figure 5.15. Pressure history data in Figure 5.16(a) shows 4 individual shocks and reflected shocks in first 4 ms, which are effectively invisible on the cumulative impulse plot. The positioning of the sensor perpendicular to wall C leads to this concentration of reflections which are not seen in sensor 312 despite their relative proximity. The incident shock is reflected obliquely on the baffle, which itself is reflected from wall C and returns shortly after, followed by reflection of shock wave that was normally incident on wall C. By considering the major reflecting surfaces and the time taken for wave propagation, it is possible to identify there is also a reflection from the ceiling, although it is more difficult to identify at exactly what time this arrives without further data. Good similarity for arrival time, magnitude and decay rate is seen between all 3 shots across the 4 shocks between 1.9 and 3.5ms, although there was a big spread seen for the shock at 3ms (350kPa to 500kPa). A strong negative phase begins at 4.2ms, similar to that seen at a similar time at sensor 312, which then a series of small reflections, followed by a strong negative phase and return to atmospheric pressure which can be seen in Figure 5.16(b).

Data from sensor 101 again shows excellent agreement between all 3 shots. Cumulative impulses histories are very close over most of the range of recorded data, but are particularly close up to 13ms. Pressure history data over the dynamic region is also very consistent, with good agreement between peak pressures at 1.8ms and 5.3ms and to a slightly lesser extent at 2.8ms and 7.4ms. The two initial shocks up at 1.7 and 2.8ms (Figure 5.17(a)) add a small amount to the cumulative impulse (Figure 5.17(b)) relative to other curves with shocks at similar time at other locations in this arrangement, and as a proportion of the peak delivered impulse at 15ms, as seen in 5.17(b). The peak in cumulative impulse occurs at approximately 15ms as with other sensors, and a similar increase in impulse is recorded over the interval 5-15ms (≈300kPa-ms), but only 100kPa-ms of impulse is added in the period to 4ms, whereas at other location, increases of roughly 300kPa-ms are seen over a similar interval. The arrival time, positive phase

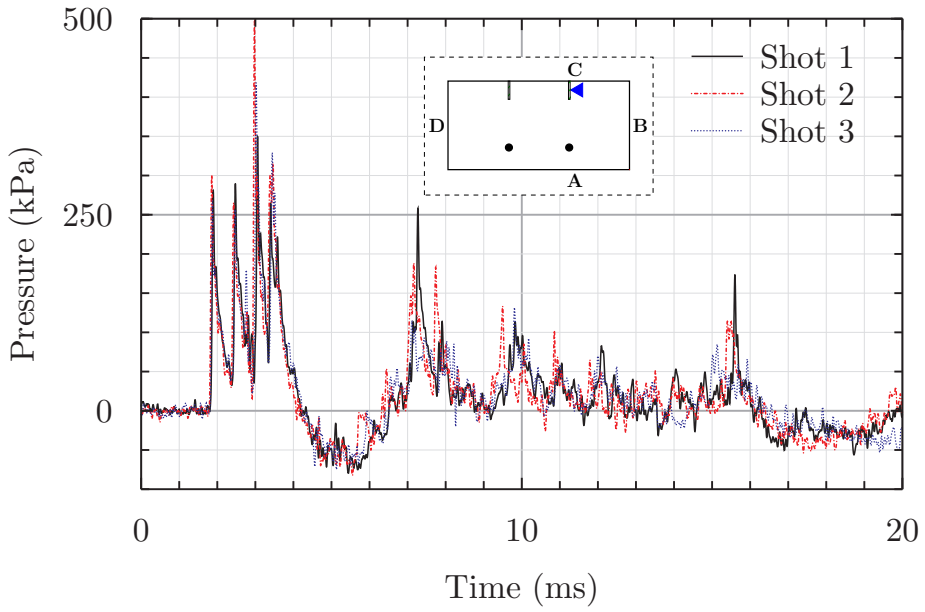

(a) Overpressure

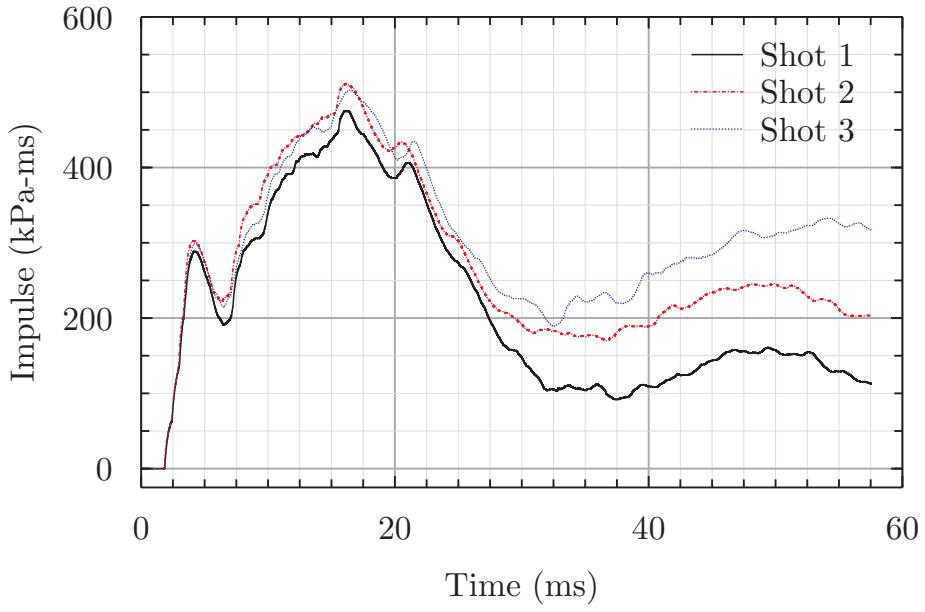

(b) Cumulative impulse

Figure 5.16: Pressure and cumulative impulse data for sensor 402, A2

duration and decay rate of the shocks at 1.7ms and 2.8ms are comparable with sensor 312 for this arrangement, but the peaks are significantly lower at sensor 101, as this sensor is mounted with the measuring surface perpendicular to the direction of travel of the shock wave. As a result sensor 101 measured the side on overpressure, whereas 312 was mounted facing the direction of the incoming shock so measured the reflected overpressure and the corresponding higher reflected impulse. The pressure measured at sensor 101 will not be the ideal side on overpressure as a real structure cannot act as a perfect plane of symmetry - there will be some element of interaction between the shock wave travelling perpendicular to wall A, and wall A.

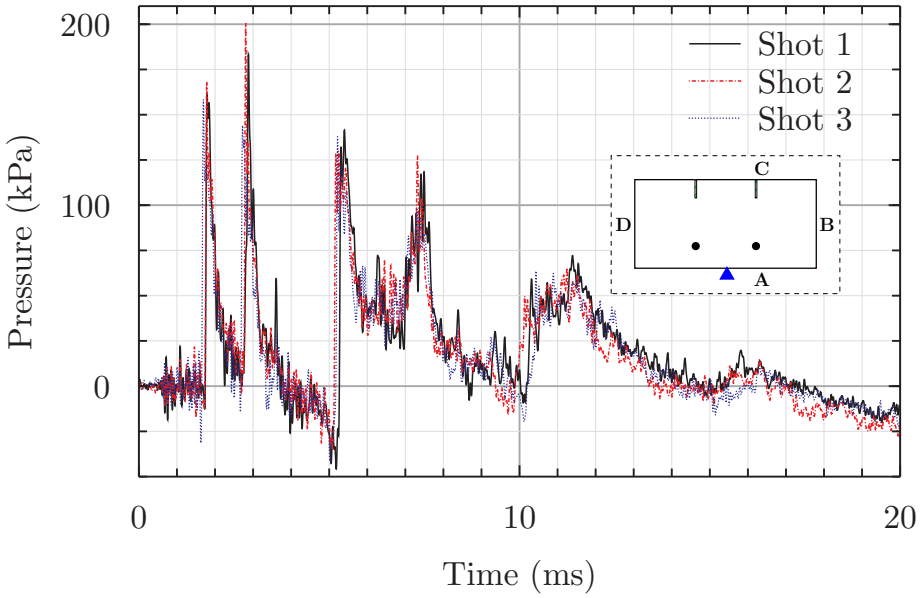

(a) Overpressure

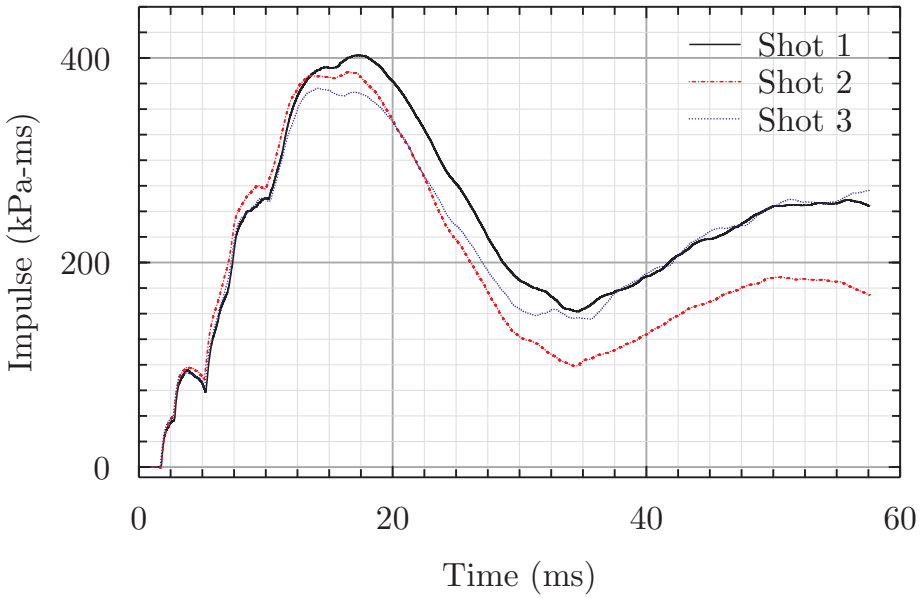

(b) Cumulative impulse

Figure 5.17: Pressure and cumulative impulse data for sensor 101, A2

5.5.4 Arrangement 3

The sensor and baffle locations are changed for A3, details for which are shown in Figure 5.18.

Sensor 402 is mounted on wall C at the intersection between baffle and wall C, as shown in Figures 5.18 and 5.19. Pressure traces in 5.19(a) show similar double peak behaviour seen in other arrangements (Figures 5.13(a) and 5.17(a)), apart from on baffles or located at the box end. This location shows the highest measured pressures in any arrangement, as well as highest total and peak cumulative impulse. Peak reflected overpressures at 2ms and 3ms are higher at sensor 402 than seen at similar positions in other arrangements, which occurs because the corner sees a meeting of reflected shocks from waves incident on both baffle and wall C, as opposed to the reflection of a single incident shock as

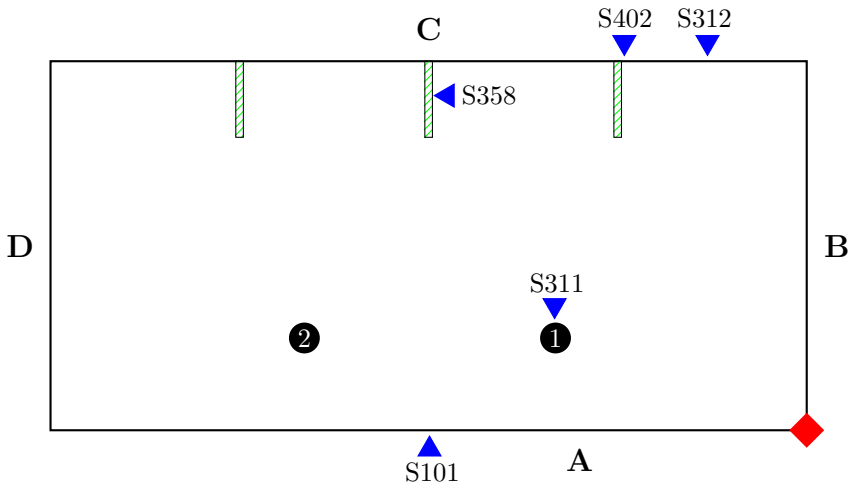

Figure 5.18: Sensor locations for A3

seen in other locations. The peak values are higher for both first and second shock as reflected shocks from the floor and ceiling are focussed towards the corner, but it should be noted that shock arrival times are consistent with an incident wave from the charge then a reflected wave from the floor and ceiling.

Cumulative impulse data (Fig 5.19(b)) shows good agreement for shots 1 and 3, but peak and final cumulative impulse data for shot 2 is lower. If data from shot 2 is assumed to have a slight negative shift[3] (features and timings across all 3 shots still show excellent agreement), peak and final cumulative impulses at this location are higher than other locations, even those that are closer to the detonation such as sensor 312 in A1. The higher peak overpressures seen at 2ms and 3ms, compared to A1 S312, Fig. 5.13(a) (which are consistent for shots 1 and 3, but reduced for shot 2) lead to a proportionately larger cumulative impulse up to 4ms, and a higher number of reflected shocks between 4 and 17ms contribute to the high peak cumulative impulse. Behaviour between 17ms and 60ms is largely the same as most other locations, with a negative phase between 17ms and 30ms leading to a impulse drop of approximately 300kPa-ms, followed by an increase to 650 kPa-ms until 50ms and then a plateau. As a result, the final cumulative impulse at this location is a greater proportion of the peak impulse than seen at other similar locations.

Pressure data from sensor 358 (Figure 5.20(a)) shows 4 reflections over first 4ms, and shows close qualitative agreement with similarly positioned sensor (402) in A2 (Figure 5.16). Agreement between all 3 shots for sensor 358 in A3 is excellent, which can be seen in both Figures 5.20(a) and (b). At both sensor 402 in A2 and 358 here, the 3rd peak is the highest, but despite the baffle and sensor being further away in A3, the 3rd peak at 3.5ms in Figure 5.20(a) is higher than that shown in Figure 5.16) at 3ms. Sensor 402 in A2 shows peak values at shock 3 of 350, 420 and 500kPa, whereas sensor 358 and A3 shows peak values of 470, 560 and 590kPa at shock 3 for shots 1, 2 and 3 respectively. More in line with anticipated behaviour (peak pressures reduced at further distances from charge, see Chapter 2), peaks 1, 2 and 4 are lower at the sensor 358 in

[3]All data is has the zero shift removed in the same way and is not artificially corrected on a sensor by sensor basis. Because the method used is not perfect, and the data from some sensors can be noisy immediately before a shock arrives (see Fig 5.17), it is perfectly plausible that zero shift removal could lead to a slight positive or negative bias

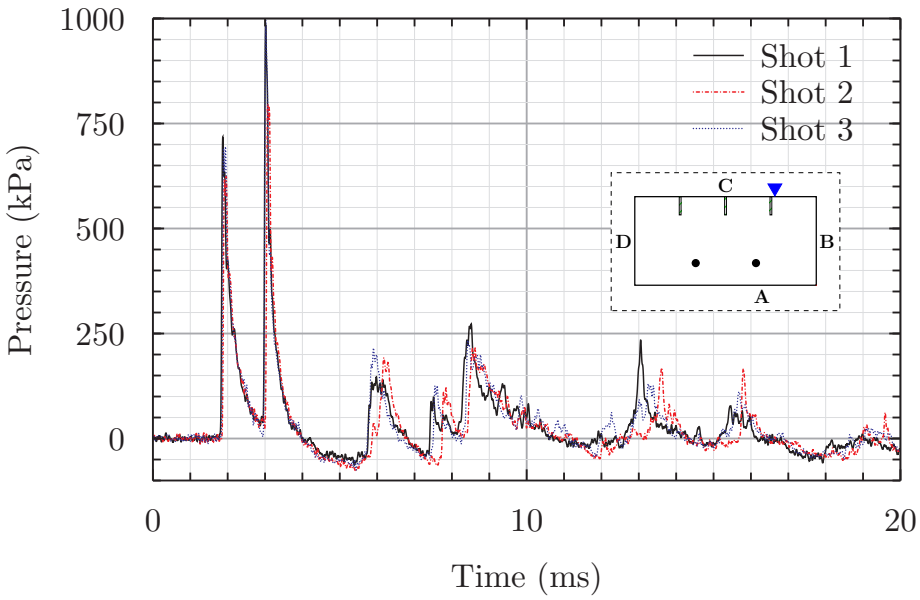

(a) Overpressure

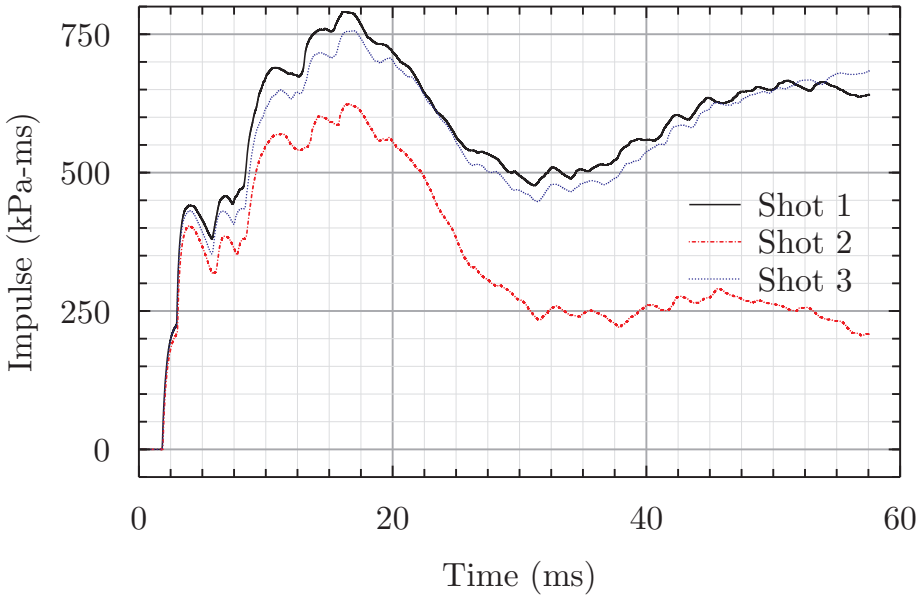

(b) Cumulative impulse

Figure 5.19: Pressure and cumulative impulse data for sensor 402, A3

A3 compared with sensor 402 in A2. Cumulative impulse in Figure 5.20(b)) shows a slightly higher peak and final cumulative impulse for sensor 358 in A3 than for sensor 402 in arrangement 2 (Figure 5.16(b)). Despite the higher peak seen in A3, the impulse delivered over the first 4ms is 50kPa-ms lower for A3 than A2, which would be expected due to the difference in distance from the charge.

Comparisons between sensor 101 across different arrangements is useful because it is in an identical position for each test, and is away from direct influence of the baffles and so gives a clearer idea of how the baffles (or lack of) alter the pressures in the box as a whole, not just along the walls in which the baffles are mounted. Impulse histories for sensor 101 in A3, Figure 5.21(b), show peak and final across all 3 shots are very similar to those seen for A2 at the same sensor in Figure 5.17(b). Peak impulse across all 3

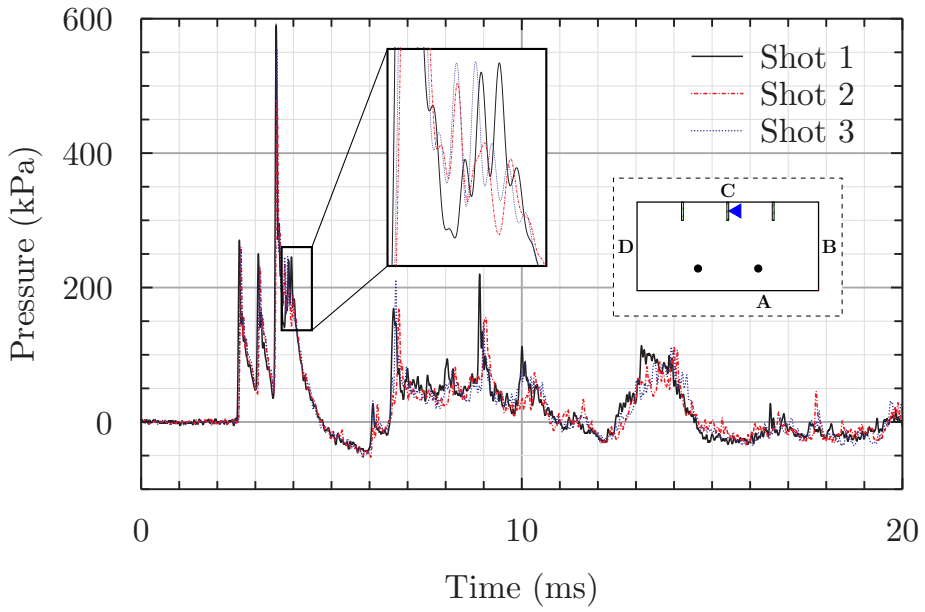

(a) Overpressure

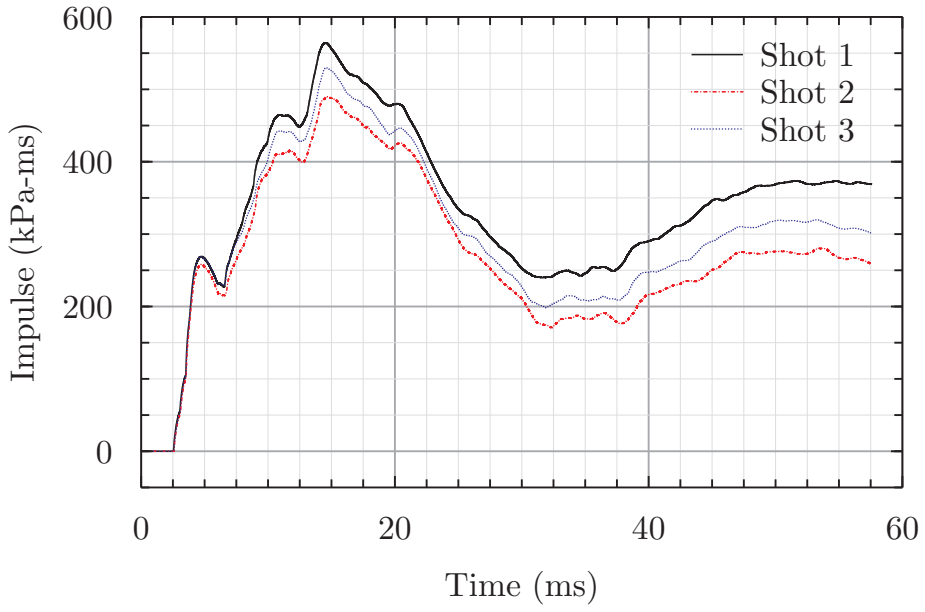

(b) cumulative impulse

Figure 5.20: Pressure and cumulative impulse data for sensor 358, A3

shots in both arrangements vary between 360 and 400kPa-ms, and if the impulses of the most similar shots are considered both arrangements, cumulative impulses at 55ms are approximately 260kPa-ms for both arrangements. As anticipated, pressure histories over the initial 4ms are very similar (reflected waves from wall C have not arrived), with similar peak pressures for shocks at 1.7 and 2.8ms (Figures 5.21(a) and 5.21(a)), and initial positive phase duration of 4ms and almost identical cumulative impulse of 100kPa-ms at this time (Figures 5.21(b) and 5.21(b)). Although the impulse history is very similar for both, there are some differences in pressure histories at this location for arrangements 2 and 3. Figures 5.21(a) and 5.17(a) shows 3 clear peaks between 5 and 12ms, but the magnitude and timing of them are different between the two arrangements. Between 5 and 10ms, peaks occur at different times and have different magnitudes and

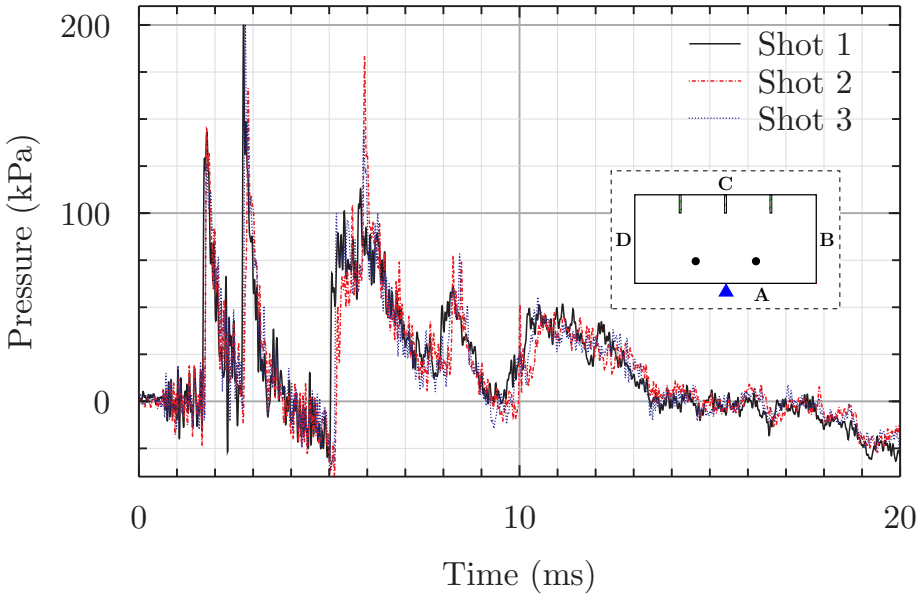

(a) Overpressure

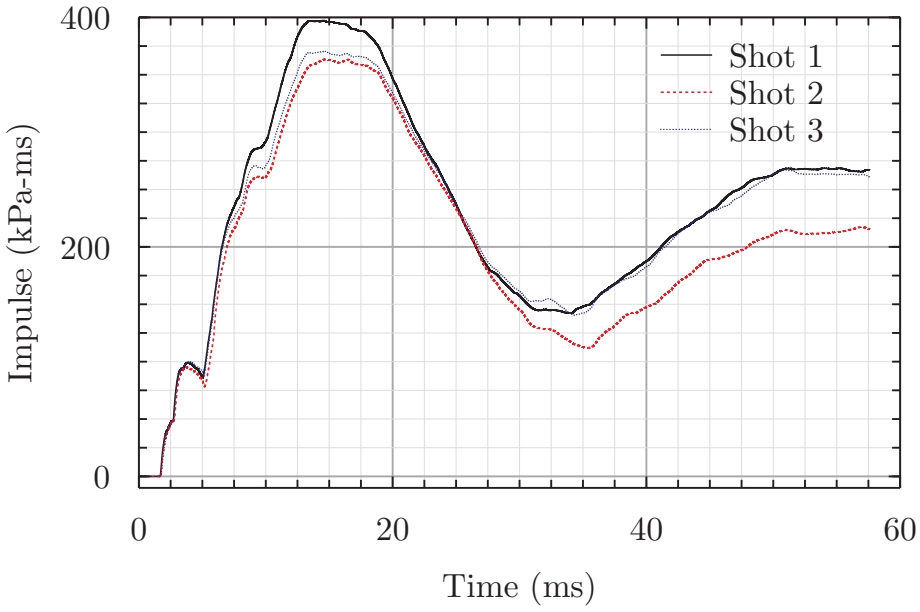

(b) Cumulative impulse

Figure 5.21: Pressure and cumulative impulse data for sensor 101, A3

decay rates, which suggests that this behaviour is a result of the different configuration of baffles on wall C between the two arrangements.

5.5.5 Arrangement 4

The positioning of sensors for A4 is shown in Figure 5.22 and is similar to other arrangements, with the exception of a centre panel and sensor 312 which is located in the roof and the addition of a laser distance gauge. Sensor 402 was located behind the panel to identify any pressures transmitted through or causes by the central aluminium panel.

After a visual inspection of the first test in this arrangement it was found that the fixations holding the angle to the box had failed and that the panel had not remained fixed at the boundary for the duration of the test. The mechanical fastenings display

a wide variety of failure mechanisms, detailed in Figure 5.23(a), with some showing ductile failure characteristics (see ①), others a more brittle fracture (see ②) and some through shearing of threads (see ③). From some of the post failure shapes of the bolts, it was clear that they had failed through combined bending and tension loads, such as the bolt shown by ①. Despite the failure on the bolts, the post failure position visible in Figure 5.23(b) shows the panel has remained in an upright vertical position and is similar to the central pre shot position shown in Figure 5.7. The aluminium panel remained fixed within the angle sections at all points, but there are indications that the experimental boundary conditions experienced were not perfect. There was only small amounts of failure observed in the aluminium panel near to the corner where vertical and horizontal angle section are closest, caused by relative movement between the angles which compressed and bent aluminium and led to crack formation. The out of plane deformation of the panel was enough to overcome the clamp friction and pull the panel through the clamping between angle sections, which caused contact between the bolt shank and the clearance hole, leading to elongation and stretching of the hole (see Figure 5.23(c)). This also generated a bulge on the lower edge of the panel, which is clearly visible against the angle section in Figure 5.23(c). From the position of this bulge and shape of the marks above the bolt holes it can be deduced that the panel has moved horizontally as well as vertically in the clamp, as the marks curve and the bulge is not directly in line with the bolt.

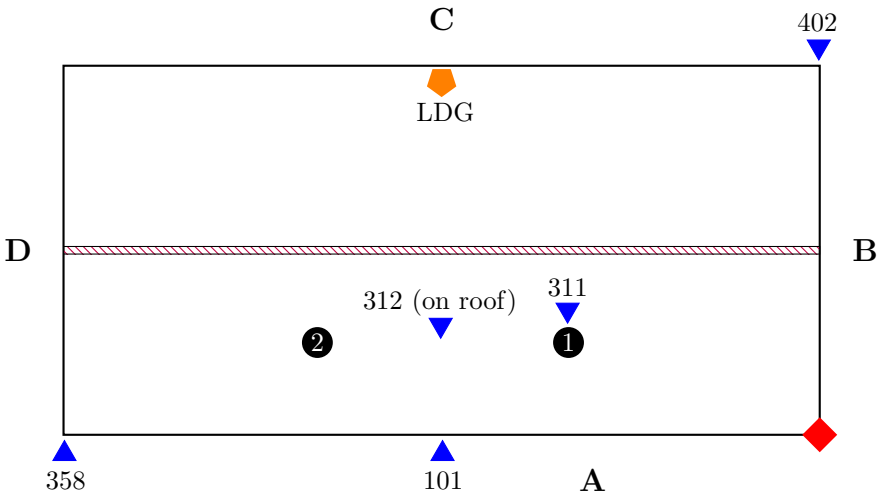

Figure 5.22: Plan view of test A4

Cumulative impulse and pressure history data for sensor 312 is shown in Figure 5.24. Pressure history data in (a) shows only one distinct large and two smaller shocks, which is overlaid on a quasi static pressure (QSP) of small magnitude that begins at 5ms continues until 11ms before becoming negative. Other than the shocks at 2, 3.1 and 4ms, no other clear shock peaks exist, although some behaviour may be obscured by the high amount of noise seen on the trace. The cumulative impulse increases to 12ms, peaking at 420 kPa-ms before continually decreasing for the remainder of the recorded data. Unlike cumulative impulse histories seen in previous arrangements, and data from sensor 101 in this arrangement (Fig. 5.26(b)), the cumulative impulse continues to decrease continuously over the measurement period without a sustained second rise.

Sensor 402 is located behind the panel in the corner between walls B and C at half

(a) Failed bolts

(b) Panel showing final shape and failure of fixings along top section of angle

(c) Clamping bolt shank stretching panel hole

Figure 5.23: Failure of structural components

height in the box. This sensor was located here to confirm that pressures behind the panel were minimal and insignificant, but Figure 5.25 shows clearly that pressures not to dissimilar to those on the charge side of the panel were developed, and the cumulative impulse developed is considerable. It is worth noting at this point that 2 of the 3 baffles present in A3 were retained for this test, with the central one being removed to allow the LDG to be fixed to wall C. Figure 5.25(a) shows the arrival of a shock at 2.3ms with a peak reflected (the shock wave will have been travelling normal wall C before it is incident, thus is reflected at the point of measurement) pressure of 50kPa which begins to decay immediately as expected, but the decay is interrupted the arrival of a small shock. High speed video data at this point, shown in Figures 5.28(d) and (e) indicates that although there is an intense fireball and indications of lens flare, no flash appears on the opposite side of the panel to the detonation, suggesting that at this point (≈3ms) no failure of the panel at wall B has occurred. There are 3 further distinct shocks at 5.7, 6.7 and 10ms, and a steadily increasing QSP exists between approximately 7 and 14ms. This is followed by an expansion to an underpressure of a similar magnitude to peak overpressure with a slightly shorter duration, which leads the cumulative impulse at 30ms to decrease to 60 kPa-ms from a peak of over 600 kPa-ms at 18ms, as shown

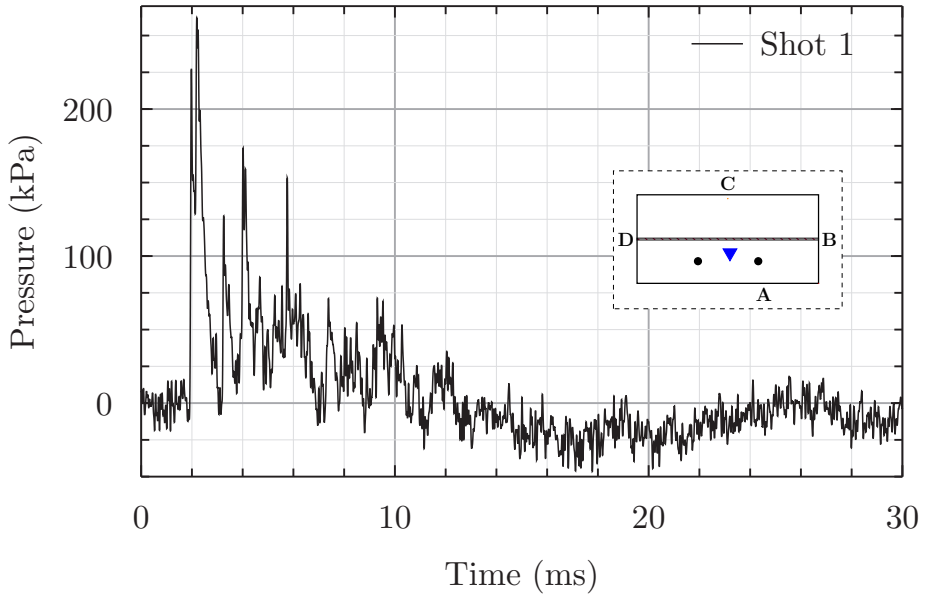

(a) Overpressure

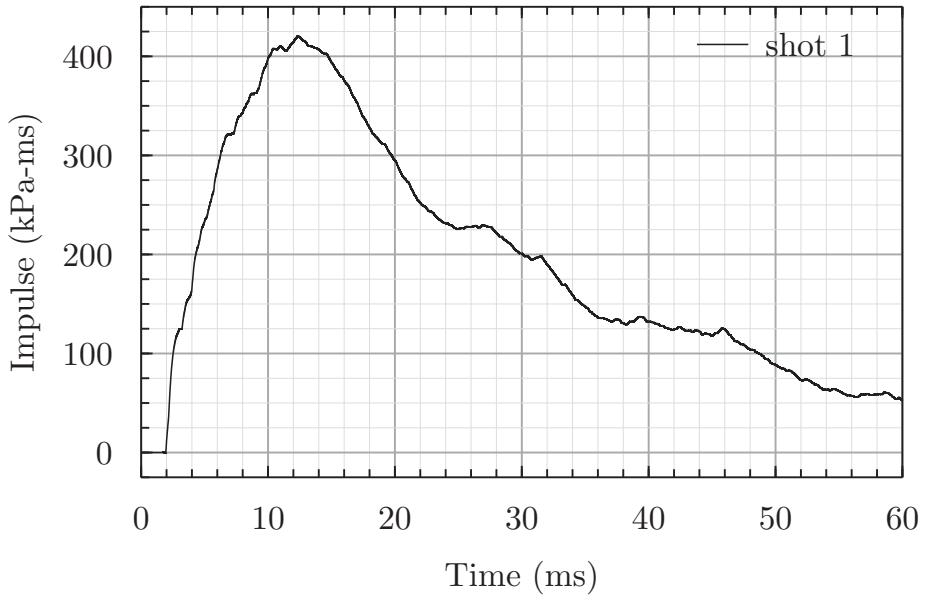

(b) Cumulative impulse

Figure 5.24: Pressure and cumulative impulse data for sensor 312, A4

in Figure 5.25(b). Pressure and cumulative impulse both show slow increases, with the cumulative impulse rising again to 260 kPa-ms at 50ms. Although there are noticeable shocks present in 5.25(a), the overriding and defining process that characterises the behaviour at this point is the slower almost sinusoidal rise and fall of the pressure and impulse, as individual shocks have neither the magnitude nor the duration to contribute significantly to the impulse.

The pressure history from sensor 101 is shown in Figure 5.26(a) and displays more significant distinct shocks than sensor 312 (Fig 5.24(a)). Between 1.8 and 8.2ms there 5 distinct shocks incident on wall A at sensor 101, with the shocks at 2.7 and 4.9ms

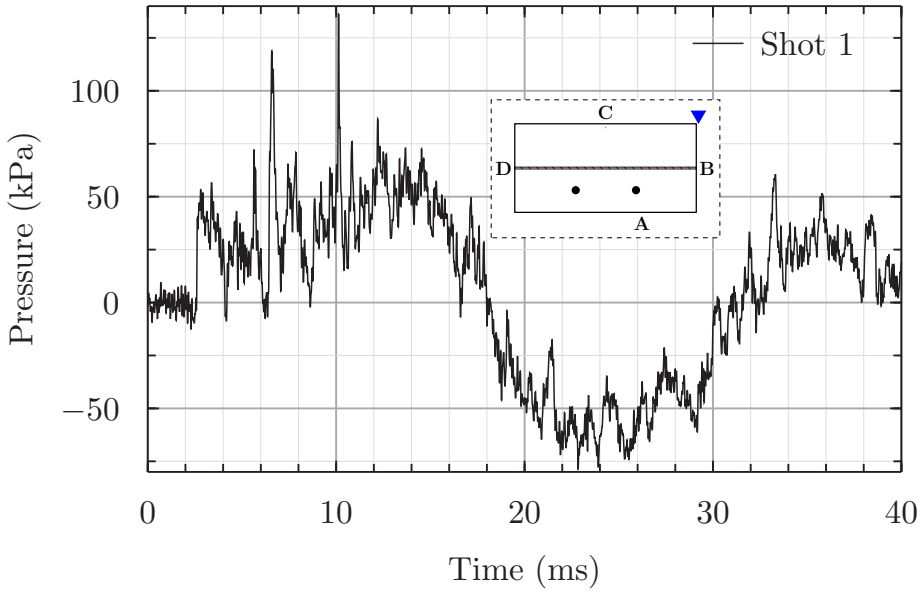

(a) Overpressure

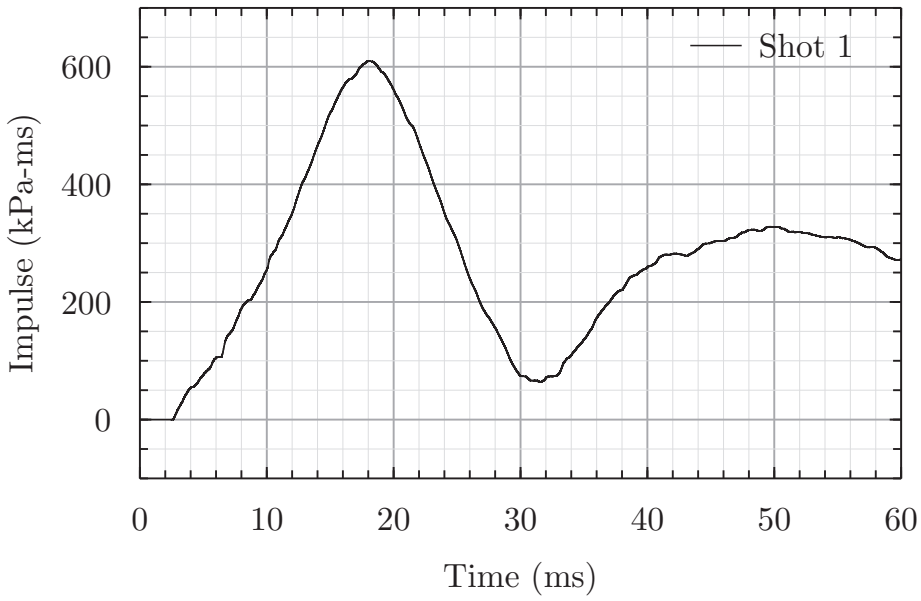

(b) Cumulative impulse

Figure 5.25: Pressure and cumulative impulse data for sensor 402, A4

being significantly stronger than the others, almost twice the strength of the first one that arrives at 1.9ms. As with a sensor 312 for the same arrangement, a QSP develops at approximately 7ms and lasts until 12ms, but is more clearly visible for sensor 101 in Figure 5.26(a) than in sensor 312 5.24(a). The cumulative impulse (Figure 5.26(b)) rises steadily to a peak value of 475 kPa-ms at 12ms, which then drops to 275 kPa-ms at 34ms before rising to 325 kPa-ms at 46ms, which is maintained until the end of the recorded data.

Displacement data for the central point of the aluminium panel is shown in Figure 5.27. It should be noted immediately that displacement data from this gauge has several issues, which limit the extent to which this data can be used. Many portions of the data show very steep gradients and suggest velocities which do not correspond with data from

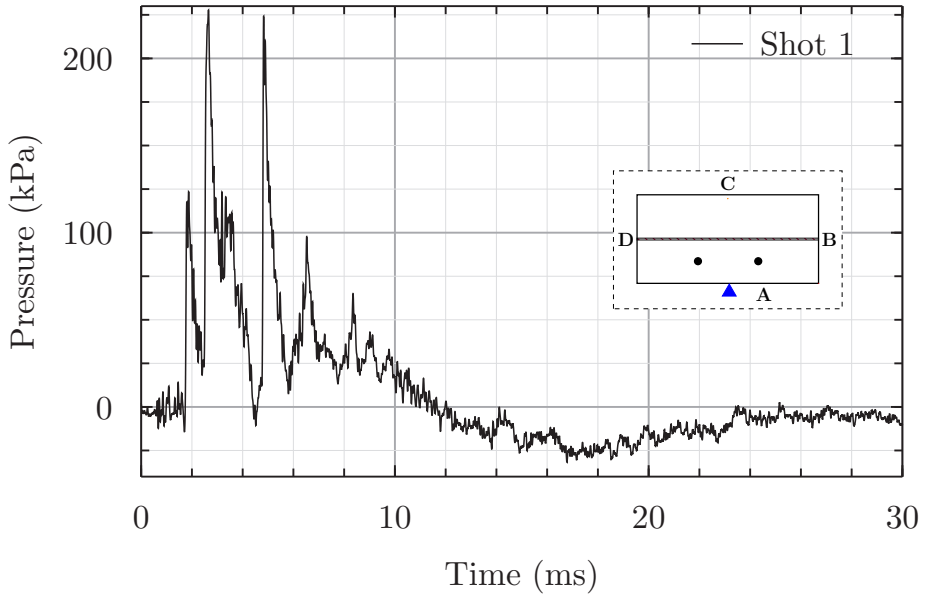

(a) Overpressure

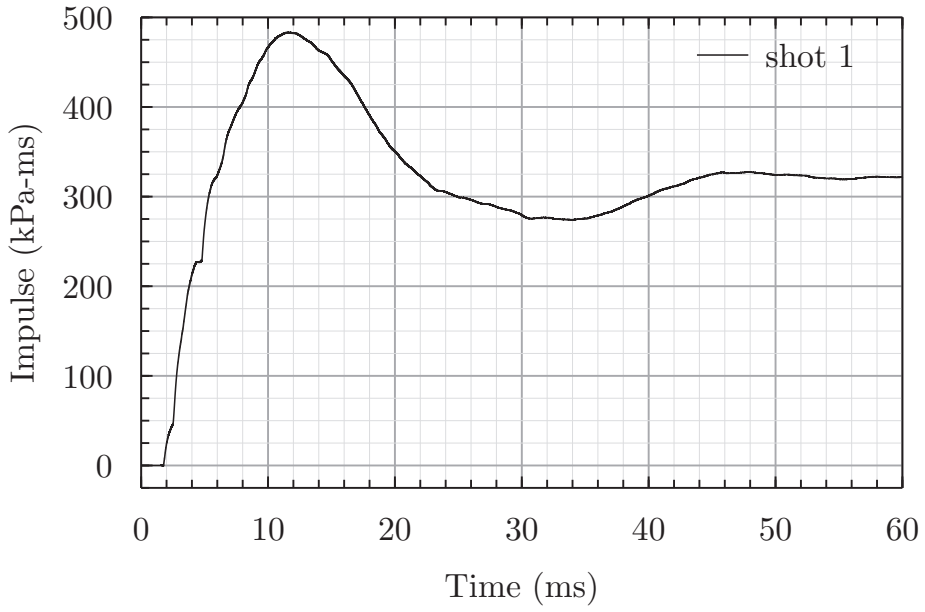

(b) Cumulative impulse

Figure 5.26: Pressure and cumulative impulse data for sensor 101, A4

pressure sensors, high speed photography and the final condition of the panel and test cell. The zoomed region shows that the panel begins to move in the positive direction (towards wall C), but at 2.9ms the panel appears to become negatively displaced, going through 4 rapid changes of direction before continuing with positive displacement at a more realistic[4] gradient from 3ms. The graph also suggests that between 8.6 and 8.8ms the panel moves 240mm, which would indicate a velocity of 1200 m/s in the negative direction (towards wall A). Pressure curves for sensors 312 and 101 do not show behaviour at this time that could generate such a high velocity. The portion of displacement data that appears to be most reliable is between 2.4 and 6.5ms, if the area

[4]It is difficult to specify a precisely why something is 'realistic', but a judgement is made based on the loading and the anticipated behaviour

between 2.9 and 3.8ms is ignored (it is unlikely that real behaviour has been measured) and the area before and after the sudden apparent change in direction are assumed to be connected. The deformation begins slowly at 2.3ms and accelerates over the next 1.5ms to reach a velocity of approximately 50 m/s, which is maintained between 4 and 6.4ms. From 6.6ms, the data appears to become increasingly unstable, with many rapid jumps between recorded position that would imply very high velocities, with little physical evidence of pressures that may cause this. If these sharp changes in velocity and direction are ignored, the trend appears to show a quasi-sinusoidal motion of roughly 50Hz.

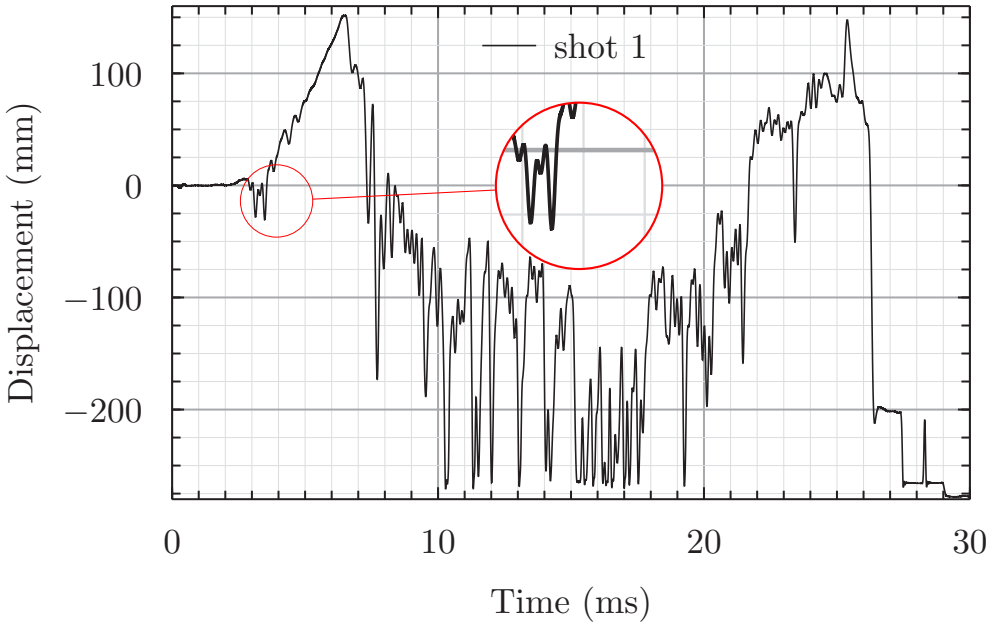

Figure 5.27: Displacement history from laser distance gauge

To compliment pressure and LDG data, high speed video was captured from a position looking directly into the end of the box, stills from which are shown in Figure 5.28. The images were taken using a Vision Research Phantom camera at a rate of 6400 frames per second with an exposure time of 90μs, at a resolution of 480 $\times$ 480. Selected still images were chosen to confirm previous findings or identify features that are not visible in other data.

Image (a) shows the setup 156 μs before detonation; the central vertical line is the end of the aluminium panel, and the processing box for the laser distance gauge and vertical steel baffles can be seen on the left hand side of the image. The detonation of the charge can be seen in (b), which has at this point in time not undergone any significant volume expansion. There is then a 1ms time gap before frame (c), as the intense flash from detonation and subsequent expansion between images (b) and (c), which shows the generation and growth of a fireball which is beginning to envelop the first cylinder. At this point the attaching angle sections on the floor and roof of the box are visible due to the flash, which at this point are still in the same position and failure has not occurred, and no deformation is noticeable at the end of the panel. In image (d), at 1.87ms a shock wave is visible on the floor of the box over halfway between the two cylinders, caused by the disturbance of debris on the floor of the box. The position of the shock wave at this point can be confirmed by data from sensor 101 (Fig. 5.26(a))

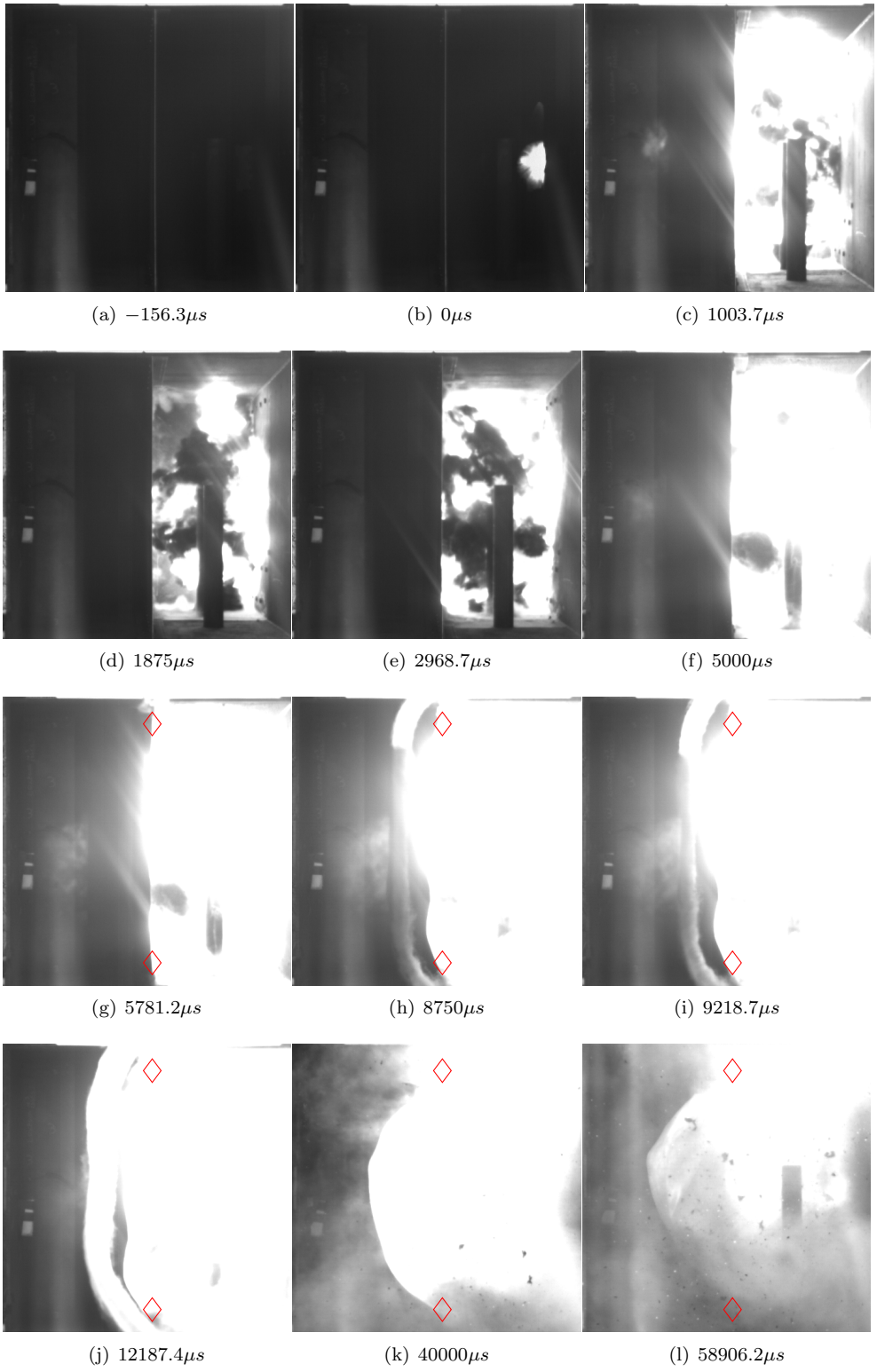

(a) $-156.3\mu s$ (b) $0\mu s$ (c) $1003.7\mu s$

(d) $1875\mu s$ (e) $2968.7\mu s$ (f) $5000\mu s$

(g) $5781.2\mu s$ (h) $8750\mu s$ (i) $9218.7\mu s$

(j) $12187.4\mu s$ (k) $40000\mu s$ (l) $58906.2\mu s$

Figure 5.28: Stills from high speed video

which indicates the arrival of the first shock at 1.8ms. At 2.97ms, shown in (e), the shock wave can be seen to be in line with cylinder 2, with the panel and attaching angle section appearing unchanged in position from (c) and (d). The fireball is still very obvious, but at this point is clearly still confined to one half the box by the aluminium panel and angle sections and no flash can be seen on the opposite side, suggesting no failure has

taken place at this point. The flash begins to obscure the frame again at 5ms (f) and the end of the aluminium panel is beginning to show deformation, although the visible angle section on the roof of the box does not appear to have moved. From 5.78ms the position of the angle sections becomes increasingly difficult to identify in the images due to the flash, so diamond shapes are added to the images from (g) onwards to show the original location of the angle section to determine whether or not the angle sections have become detached. The deformation in (g) appears asymmetrical, with points of highest deformation above and below the centre line. This behaviour is much more pronounced in (h), where a clear shape is obvious with a much higher deformation on the top half of the panel. The position of the top of the panel relative to the diamond also suggests the panel is no longer attached to the top of the box. Images (h) and (i) also show the diffraction of the shock wave on the left hand side of the panel, with a strong reflection of the flash from the top of the diffracted shockwave. At 12.2ms (j), the deformation begins to become more uniform and the points of high deformation become less distinct, and the panel seems to have moved significantly from its attachment point with the ceiling. Between 13 and 40ms, bright flash once again obscures the frame. In image (k) at 40ms, the top angle section has completely detached and the deformed shape has become much more symmetrical with the highest point of deformation in the centre of the panel. The flash is beginning to reduce by 59ms (l), but the shock wave has begun to disturb the ground in front of the camera, leading to more obstruction of the frame. Flying debris is visible and the deformation mode has begun to change as the weight of the angle section bends the aluminium panel, and reflection in the panel at this point show that the panel is most highly deformed and displaced at the open end of the box.

5.6 Discussion

5.6.1 Experimental issues

The aims of the series of experimental tests were to generate data to validate numerical models and standalone data to confirm similarity between shots in identical confined and complex geometries. The experiments also looked to identify if an effect on pressures was caused by the presence of deforming structures.

The data from tests in A1, A2 and A3 was generally very good, showing excellent similarity in pressures and cumulative impulses between each shot in each configuration. Not only does this mean that validation can be done with confidence, but it also provides good standalone data that shows the inherent variability between tests is low. A spread was seen in cumulative impulses across shots in each arrangement, and in some cases there was a single shot of the three that clearly differed from the 2 other curves. The cumulative impulse is very sensitive to shifts in the values of the data, as illustrated in Figure 5.29, which shows the effect of adding an arbitrary but small positive and negative shift to the data. The impulses quickly begin to diverge and the error accumulates, with final impulses significantly spread from one another. Given this sensitivity, experimental measurement and processing error combined with the *small* inherent variability in the charge can explain why there are few cases of large differences between final impulses (A1 s312 for example, Figure 5.13). However, in the majority of cases where impulses are very close, it can be concluded that the data is of high quality and very reliable. The small spread between results means that models that can replicate this data, as opposed

to lying within a large spread of experimental data, can be shown to be valid.

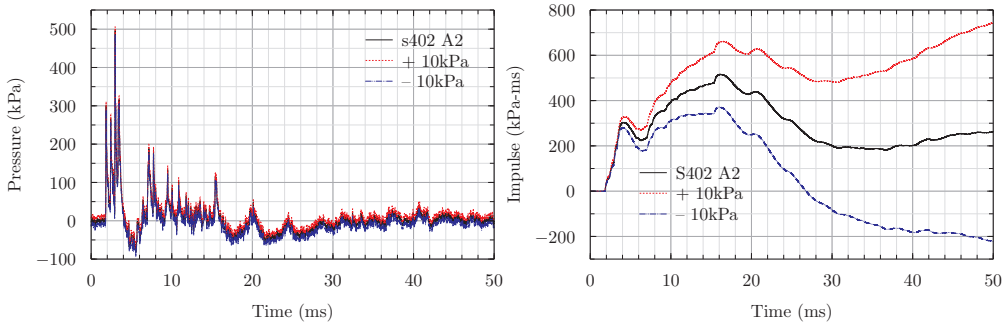

(a) Pressure difference almost invisible

(b) Large effect on cumulative impulse

Figure 5.29: Effect of a small positive or negative shift on impulse

Although good data was generated from the tests, there are some components of the data produced and physical test setup that it is important to be aware of to avoid drawing false conclusions. Peak side-on and reflected overpressures are often cited as key parameters, but in practice it is not always easy to identify these from experimental results. Voltages from the pressure sensor can 'overshoot' at the arrival of the shock wave, an effect known as sensor ringing [36], before settling and giving more accurate reading once the shock front has begun to pass. This isn't clearly visible on the curves presented in Section 5.5, but plotted over a shorter period of time (Figure 5.30) the initial overshoot is more clear, as is the normal decay that follows. If the shape of the normal decay was tracked backwards it will intersect with the rising pressure at the arrival of shock wave, which would give the side on or reflected pressure that is reported by ConWep or UFC 3-340-02. Experimental results therefore should be compared to each other and numerical results by looking at how the peak pressure and decay relate to one another, as clearly the ringing phenomenon seen experimentally will not be present in numerical results.

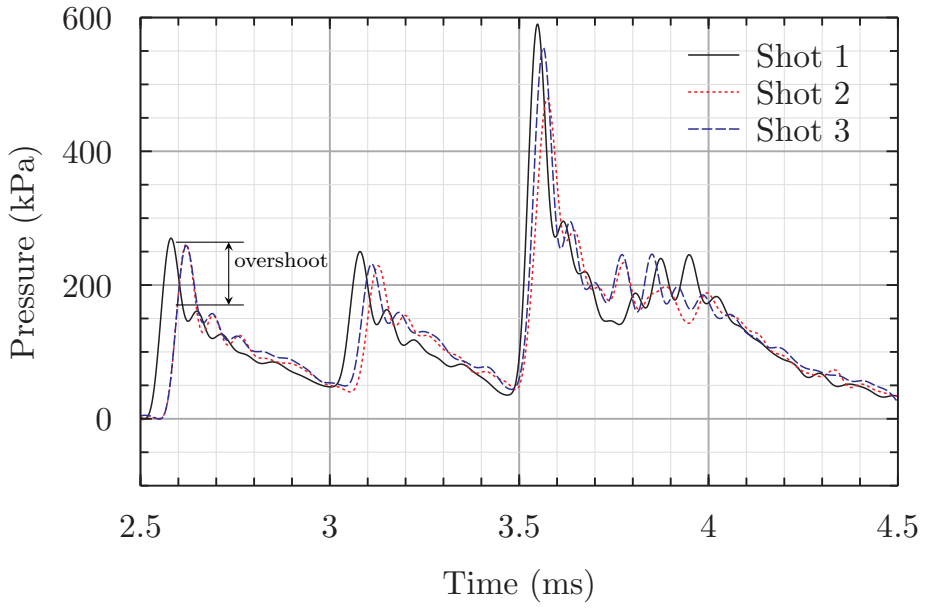

Figure 5.30: Ringing and overshoot for peak pressure values

Figure 5.31 shows how the sensitivity of the gauges affected background noise, as well as the presence of shock though walls and how it affects sensors. The raw voltage recorded at each channel shows similar levels of noise, introduced not only by the sensor, but by the cables and amplifier unit. The difference in noise level between the gauges is introduced when the raw voltages are converted to pressures as the less sensitive, higher capacity gauges require multiplication by a larger number for conversion, which in effect amplifies the noise. For sensor 312 (Figures 5.31(a) – (d)), it's high capacity leads to much higher levels of noise than in sensor 101 (Figures 5.31(m) – (p)), which can lead to greater uncertainty in the measured values. Although it is important to make sure the gauges selected will cope with the pressures experienced, it is of greater importance to match them closely with the expected pressures to avoid unnecessary background noise. Figure 5.31 also shows the presence of shocks travelling through the walls of the test cell, which is shown in (i) – (l) and (p) as an increase in signal towards the end of the displayed time. This occurs only when sensors are located in wall A, and wall shock is not seen when sensors are located on wall C, the baffles, or the roof. The charge itself is not in contact with the walls on which sensors are located, but mounted on a hinge that is attached to walls A and B, but the shock can be transferred to these walls through the hinge. The box is constructed of several plates held together with angle sections with a weld joining the two touching surfaces, meaning that shock waves cannot pass easily between walls of the box, limiting the wall shock experienced to walls A and B. In the current tests no sensors were mounted on wall B, but it is likely a wall shock would have been experienced with a magnitude proportional to the distance of the sensor from the hinge.

Data from the cylinders was not presented in Section 5.5 as it did not provide useful information and was difficult to interpret and compare with other data. The data, which can be found in Appendix G, is much noisier than other data and does not show the expected clear shocks and reflections over the expected time durations as shown by images in Figure 5.28. To attempt to identify if any expected phenomenon were recorded, pressures were plotted over just a few milliseconds though (see Figure 5.32), results are easier to interpret, with some shocks visible. A shock wave arrives at 1ms in (a), (b) and (c) but decays rapidly, becoming negative within 0.2ms (ConWep predicts a positive phase duration of 1.2ms) across arrangements, seen in Figure 5.32, with some other shocks seen in various arrangements. The very short initial positive phase durations of 0.2ms could be caused by clearing effects (see Chapter 2 Section 2.2.2) around the cylinder, but the typical wave form caused by relief waves is not seen in any of the pressure curves. The shocks are difficult to identify precisely as there is a continuous high amplitude noise signal running through all traces which obscures features, but it is possible to identify at least 2 further shock arrivals in the first 4 ms on many traces. Figures G.3 G.8 G.11 show that impulses generally were not consistent among shots, limiting the confidence of accuracy in the results.

With hindsight, there were several issues with the setup of the sensor and conditions that it experiences that make reliable data more difficult to achieve. The sensor was difficult to fully tighten within the cylinder, which could have led to movement and vibration of the sensor and increased the noise in the signal. It is also possible to see from HSV data in Figure 5.28 that the cylinder was within the fireball, which would have caused heating and could have taken the sensor outside of it's calibrated range.

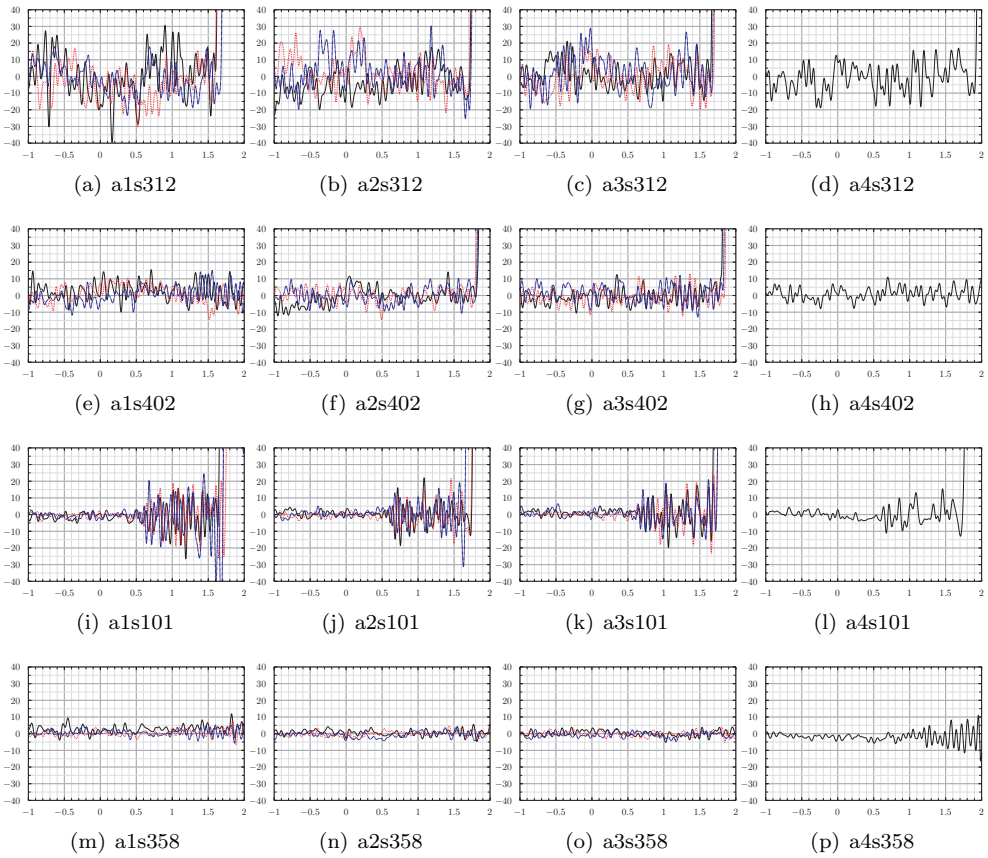

(a) a1s312 (b) a2s312 (c) a3s312 (d) a4s312

(e) a1s402 (f) a2s402 (g) a3s402 (h) a4s402

(i) a1s101 (j) a2s101 (k) a3s101 (l) a4s101

(m) a1s358 (n) a2s358 (o) a3s358 (p) a4s358

Figure 5.31: background noise and wall shock with all curves on the same scale to allow visual comparison

Only some of the available sensors were high temperature gauges, but the sensors chosen for use within the cylinders were chosen for pressure capacity and not heat resistance. Along with issues with noise as explained above, it is clearly important to select sensors with care based on good assumptions of behaviour, although for these tests limitations were imposed by the lack of availability of a wide variety of sensors.

There were several issues with the test conducted using arrangement 4 which affected the usefulness of the data, some of which with hindsight could have been planned for and prevented. The primary problem was the failure of the supports for the central aluminium panel, shown in Figure 5.23. This creates problems for validation of the data, as the boundary conditions for the panel become unknowns, as well as causing displacement outside the expected range of the LDG which could not be recorded. Preliminary calculations identified that the aluminium panel itself would not fail, but loads expected on individual bolts were not calculated. As a result the load the bolts experienced in various modes was too high for the size chosen and widespread failure occurred; had the expected load on the bolts been considered more substantial bolts with a higher failure load would have been used, reducing the likelihood of failure. A major learning point here is that is can be all to easy to overlook the strength of supporting structures when designing experiments. Had this been undertaken with some conservative hand calculations, it is likely that such a failure could have been prevented. One potential issue that could have exacerbated the failure that occurred was an unzipping mode; if some bolts fail prematurely, their load is transferred to the next bolt, which then sees

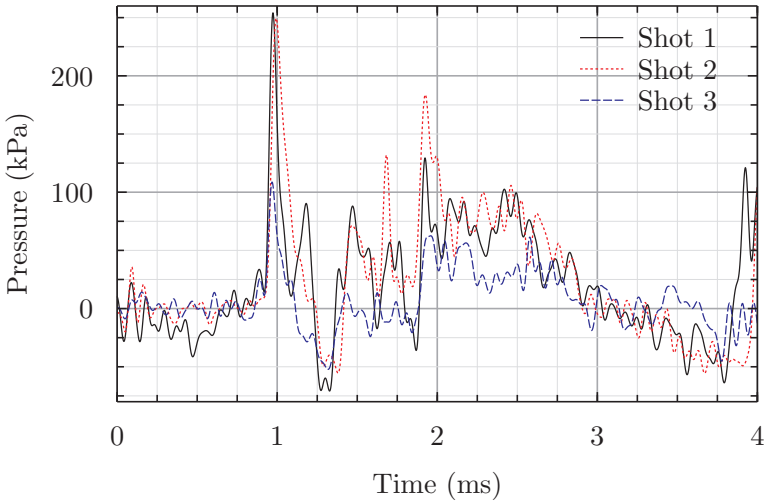

(a) Sensor in cylinder, A1

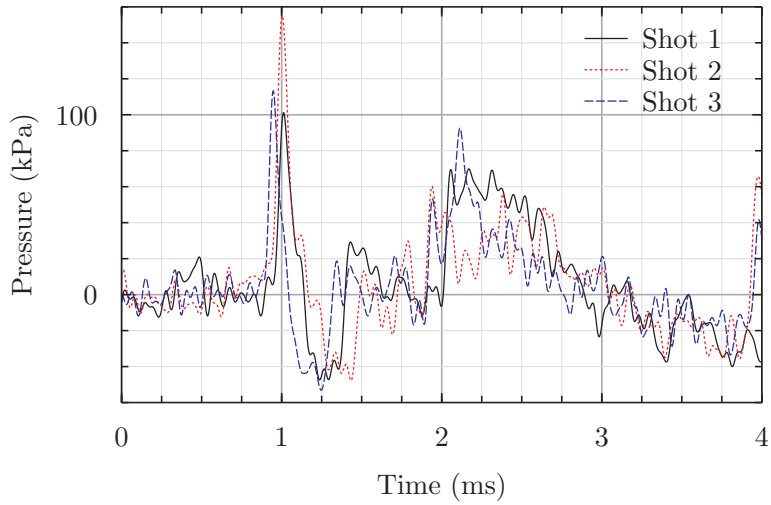

(b) Sensor in cylinder, A2

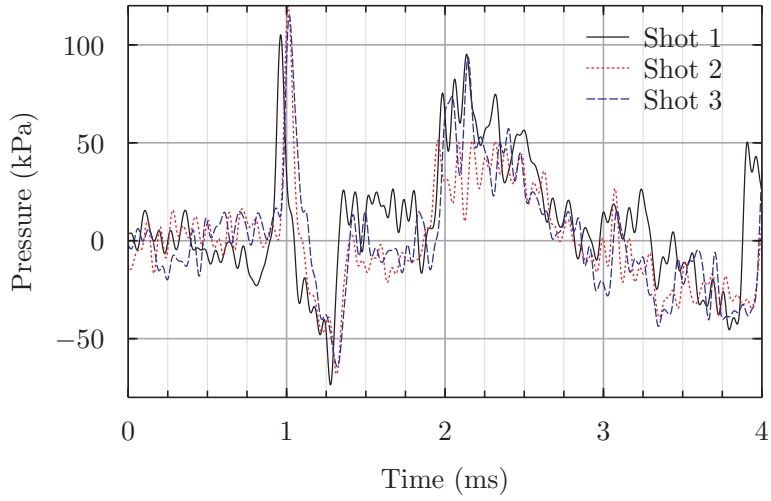

(c) Sensor in cylinder, A3

Figure 5.32: Pressure sensor data from cylinders plotted over short duration where very short duration shocks can be seen

a sudden jump in the applied load that could lead to failure. This could have been a particular issue for some bolts which were left in place for a number of weeks prior to the test, which were subsequently exposed to the elements and developed surface corrosion. As mentioned in Sections 2.4.1 and 2.4.2, the effect of boundary conditions can have a strong influence on the predicted deformation, and the uncertainty in the experimental boundary condition could lead to issue in predicting the deformation using numerical methods.

The data from the LDG data was largely unusable, due to instabilities. These are likely to have been caused by the bright flash of detonation and fireball interfering with the optical sensor used to receive the laser, and changes in angle of the plate. According to the user manual for the sensor [178], angular changes and direct radiation such as sunlight can considerably reduce the accuracy. Although it is difficult from the results to determine the conditions such as the angle and amount of stray light received by the sensor, these are thought to be the most likely causes of error given the very bright flash seen on the high speed video data and high deformation of the panel. The failure of the bolts along the top section of angle not only caused the panel to exceed the range of the gauge, but opened a gap allowing strong light from the fireball to interfere with the LDG. High speed image data shown in Figure 5.28 shows that at 8.7ms, although the top section of angle has not moved significantly, the bright light is reflected from the diffraction wave, which will also cause interference with the optical sensor on the LDG. Data from the LDG shows that interference and instability occurs from 6.7ms. It is recommended that in similar testing in the future efforts be made to limit the light corruption by shielding the LDG, which will help to prevent stray light being incident on the optical sensor.

5.6.2 Pressures and impulses on wall A - a comparison between arrangements

Only 1 sensor remained in the same place throughout tests, which was sensor 101 on wall A. Figure 5.33 compares data from a single shot for each arrangement, which were chosen from the repeated shots conducted for each arrangement. A comparison of individual shots was chosen for visual clarity and they were not selected to illustrate any specific similarities or dissimilarities between arrangements. Comparisons between data sets from sensor 101 shows that despite significant physical differences between the set up each arrangement, many features of the data are consistent throughout all tests. Both the arrival time and magnitude of the first shock at 1.8ms is the same for each of the four arrangements, with impulses matching at 2.8ms. At this point, behaviour in A4 begins to deviate from that in A1, A2 and A3 as the aluminium panel is much closer to wall A than wall C is, leading to earlier reflections, which interact differently with each other. Differences in A1 - A3 do not appear until after the reflected wave from wall C reaches sensor 101 at 5ms, at which point the impulse in A2 and A3 increase compared to A1. Although A2 and A3 offer some small but noticeable differences between 6 and 12ms, the similarity of the impulse in Figure 5.33(b) between the different arrangements is very good and much closer agreement is found between these two shots, even in different arrangements, than is seen between impulse data from different shots in the same arrangement.

The number of baffles has limited effect on peak cumulative impulse, with almost no

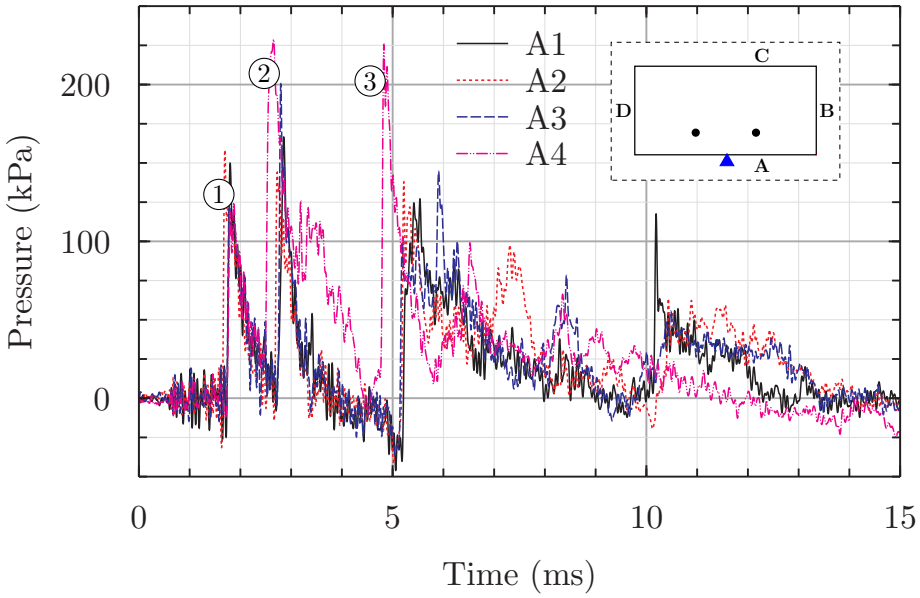

(a) Overpressure

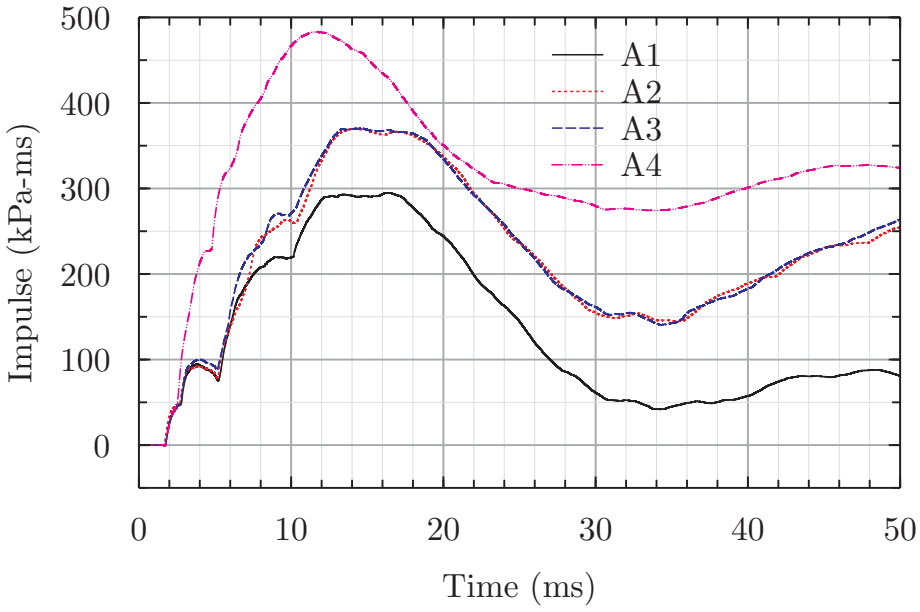

(b) Cumulative impulse

Figure 5.33: Comparison between pressures and impulses on wall C for all arrangements, with circled numbers used to identify 3 peaks to aid comparison between arrangements

difference between A2 and A3 in Figure 5.33(b) - the main differences in A2 and A3 occur between 5 and 11ms, after the arrival of the most significant shocks, but during a period where there are many reflections and the behaviour is very transient. The shock that arrives at 5ms is less strong in A3 compared to A2, but a shock is present in A3 at 6.9ms that is not seen A2. Unique shocks in A2 and A3 are then seen at 7 and 8.2ms respectively, but the similarity in magnitude cancels out any differences by 11ms.

Although the impulse is almost identical between A2 and A3, it is clear the impulse is higher in both of these arrangements than seen in A1. The divergence between the impulse curves for A1 and A2/3 in Figure 5.33(b) occurs between 6 and 14ms, after which the impulse curves between the three arrangements show close similarity (ignoring the

y axis shift) with the same duration plateau between and same gradient between 18 and 34ms. The reflections described above that occur between 5 and 10ms are not seen in A1, and between 11 and 12ms, pressures in A1 return to atmospheric before those in A2 and A3, which leads to a slightly prolonged rise in impulse in A2 and A3. As the major differences occur between 5 and 10ms, it is plausible that pressure and impulse behaviour over this time period is dominated by effects of shock reflection from wall C. Although the baffles make a distinct difference to both pressure and impulse history at sensor 101, their effect is only noticeable over a short period of the measured data. The likely effect of this on passengers in a rail vehicle is difficult to quantify from a single measurement, but this shows there is a noticeable difference and that is worth further investigation.

It is clear that the increased confinement created by the addition of the aluminium panel in arrangement 4 leads to higher reflected pressures and cumulative impulse, as well as altering the time at which particular features are seen. Shock 1 (shown by ① in Figure 5.33) arrives at the same time and of the same magnitude across arrangements. As with A1, A2 and A3, this is effectively the side-on overpressure of the initial spherical expanding shock front that is created by the detonation. At this time, reflection will be occurring from the floor and ceiling, as well as the aluminium panel in the centre of the box. The shallow angle that the incident waves make with reflecting surfaces, as well as the strength of the shocks mean that Mach reflection at the walls is likely to occur at this point (see Figure 5.34), but the similarity between all arrangements suggests the triple point has not moved far enough from the reflecting surface to reach wall A and influence the pressure. If this was not the case, the presence of some extra feature such as an increase in pressure or difference in time would be visible in A4, where an extra mach stem would be present from the aluminium panel, which would yield the same reflection as the floor or ceiling, as it the same distance from the point of detonation, merely in a different plane.

Shock 2 arrives 0.2ms earlier in A4 than in other arrangements, due to the simultaneous meeting of reflected shock waves from the floor, ceiling and the aluminium panel at a point before sensor 101 on wall A, as they all share the same distance and angle between point of detonation, first reflecting surface and sensor 101. This increases the strength of the shock compared to that seen in other arrangements, which results in a faster propagation of the shock wave and reduces the time taken to arrive. According to Figure 5.34, Mach reflection becomes possible at the panel in A4 (or the floor or ceiling, recall they are the same point from the detonating charge) when the incident wave makes an angle of 33°, which is approximately 500mm along the reflecting surface, and should be the only reflection possible for angles above 40°, 645mm along the reflecting surface. Although it is clear that directly above, below and normal to sensor 101 that Mach reflection will be occurring, outside the Mach stem and above the triple point, there will still be two clear distinct incident and reflected shocks, although the following reflected shock will be rapidly approaching the incident front. It is these reflected waves from floor, ceiling and panel, as well as secondary reflections from floor and ceiling (which rapidly catch up with the first reflection travelling through shocked air) which lead to the behaviour seen at point ②. The interaction between several waves and interaction with wall A around sensor 101 also leads to a maintained higher pressure and delayed decay at ②.

Shock 3, (shown by ③) arrives in other arrangements as a reflection from wall C, which is twice the distance from wall A as the aluminium panel that runs along the centre of the box in A4. A description of the mechanism for shock 2 in Figure 5.33(a) indicates that the initial reflection from the panel that is incident on wall A arrives there at 2.4ms. For the shock wave to arrive at the same time at sensor 101, it would suggest that it would need to travel a similar distance, indicating that the wave seen at ③ in A4 is likely to be the second reflected from the central aluminium panel, having previously been initially reflected from the panel and wall A. The shock strength gained during these reflections causes an increase in shock wave velocity, leading the shock to arrive more quickly in A4 than in other arrangements. It should be noted that the change of angle with each reflection due to the strength of the shock amongst other factors such as interaction with other shock waves, means that it is not possible for shocks to keep reflecting between walls and increasing strength indefinitely, as ultimately energy is dissipated and moved away from the source of detonation as smaller and smaller components of the shock reflect normally to the reflecting surface. For arrangement 4, it is the specific combination on angles of reflection in A4 which leads the strong peak at sensor 101 at this time.

The cumulative impulse is higher in A4 compared with other arrangements; an identical first shock at 1.8ms means impulses are the same at this point, but the early arrival of shock at ②, the maintained pressure between 2.9 and 3.7 and the earlier arrival of shock ③ (which itself prevents a negative phase seen between 4 and 5.1ms in A1, A2 and A3) leads to difference of 150kPa-ms between A4 and other arrangements (which are the same as one another) at 5.1ms. The difference between the peak impulses in A4 and other arrangements is 190kPa-ms for A1 and 110kPa-ms for A2/A3. This shows that less impulse is added from 5-12ms in A4 compared to A3/A4, but slightly more is added over the same period compared to A1. Clearly it is the magnitude and duration of the shocks over the first 5.1ms that differentiates the peak impulse in A4 from the other arrangements.

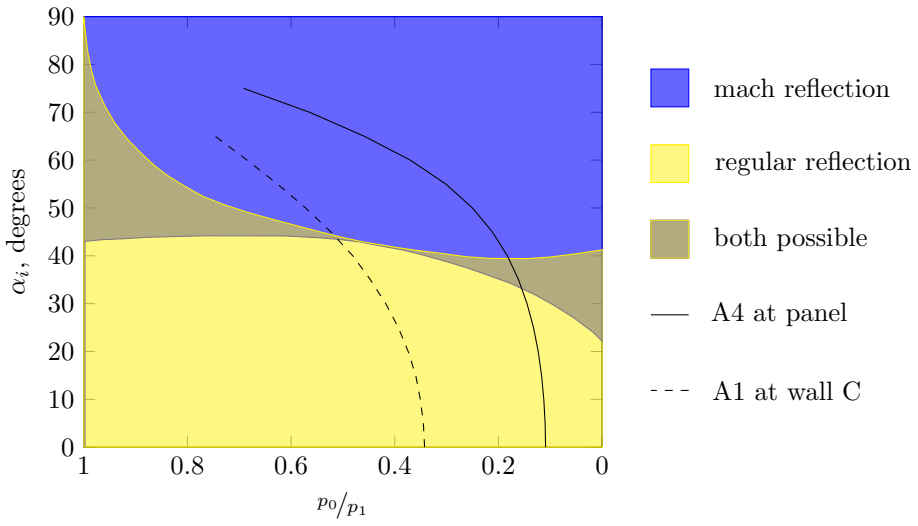

Figure 5.34: Transition between regular and mach reflection, with combinations of pressures and angles at reflecting surfaces plotted for A1 and A4. This gives much the same data as Figure 2.3 from Chapter 2, but in a way that makes the particular cases shown easier to visualise.

5.6.3 Pressures and impulses at baffles on wall C

At the point where baffles and walls meet, much higher pressures and impulses are experienced than on perfectly reflecting surfaces or between baffles. Away from the baffles, their effect on pressures and impulses in the arrangements tested is small. Comparisons from data from 3 locations, one in A1 and 2 in A3 illustrate this point; A1-312 (Figure 5.13), is the sensor at half height, at the junction between walls B and C in arrangement 1, A3-312 (Figure G.10) is on wall C, halfway between wall B and the first baffle and A3-402 (Figure 5.19) is on wall C at the junction between the wall and the baffle. It is difficult to distinguish between A1-S312 and A3-S312 over the first 5 shocks, as pressure and impulse curves, arrival times and magnitudes are all very similar. Once this initial phase is over, where the strongest shocks are present, the reflected shocks seen in A3-S312 between 5 and 15ms are less strong, because waves are not reflecting normally from surfaces as they are in A1-S312. Arrival times, magnitudes and decay rates for the first 5 shocks in these two are similar, which indicates that reflections of shock waves around the box over the first 15ms are very similar for both arrangements.

There are some visible differences in peak pressure between data in for A1-312 and A3-312 (Figures 5.13 and G.10), but comparison of impulse data between 0-4ms and 5-15ms shows little major differences and no extra shocks are seen in A3-312 as a result of reflections from the baffle. For A3-312, the peak impulse over 0-4ms ranges between 420 and 620kPa-ms, and between 450 and 550kPa-ms for A1-312. There is considerable similarity between the data, suggesting the influence of the baffle is limited - impulses over 60ms do not suggest a trend of higher impulses when the baffle is present. Although the shock wave meets the baffle at an oblique angle, the angle is not high enough to cause reflection parallel to wall C, so pressures and impulses are not very distinguishable between A1 and A3 when the sensor is placed on a wall away from the baffle. For cases with different width baffles, or differently placed charges, which result in waves being more normally incident on the baffle, waves are more likely to reflect parallel to wall C and lead to a greater number of reflections at a higher amplitude and a consequently higher impulse.

At the point where the baffle and the wall meet in A3, the recorded pressures are much higher (A3-402 Figure 5.19) than seen at A1-S312 and A3-S312, and there are an increased number of stronger reflections, which leads to both a higher impulse over the first 4 ms and a higher peak impulse at 16ms. The spherically expanding shock in incident on the baffle at approximately 60°, which even at low shock strengths will lead to Mach reflection according to theory, shown in Figure 5.34. The wave incident on wall C will have an angle of incidence of approximately 30°, which is unlikely to display Mach reflection unless the incident pressure is greater than 1200MPa, which it is not at this point. The presence of only two shocks over the first 4ms in A3-402, in line with behaviour at A1-S312 and A3-S312 where there is no visible effect from the baffle, indicates that the regular reflection from wall C and Mach reflection from the baffle are incident on A3-S402 at identical times.

Comparison of data from A2 and A3 shows that distance from detonation and position of sensor in relation to reflecting surfaces not always determining factor for peak pressure and impulse. Impulses for sensor A3-358 (central baffle in A3 Figure 5.20) are higher by 50kPa-ms across all shots than sensor A2-402 (first baffle in A2, shown in Figure 5.16. The impulse in A3 is slightly lower than in A2 at 5ms (260 kPa-ms vs 300 kPa-ms),

but the negative phase seen in both arrangements between 4 and 6.3ms is of greater magnitude and duration in A2. The primary difference between 6.3 and 15ms, where there are a number of weaker reflected shocks (all less than 250kPa for both sensors) and a period of maintained pressure above atmospheric. The complex nature of shock reflections mean that it is difficult to state exactly where they are from without a full field visualisation of the propagation and reflection of all shocks. The separation between reflecting surfaces (wall B for A2, and the baffle ahead for A3) is the most likely cause of differences in reflected shock pattern, and secondary combustion effects could lead to a maintained high pressure over several milliseconds.

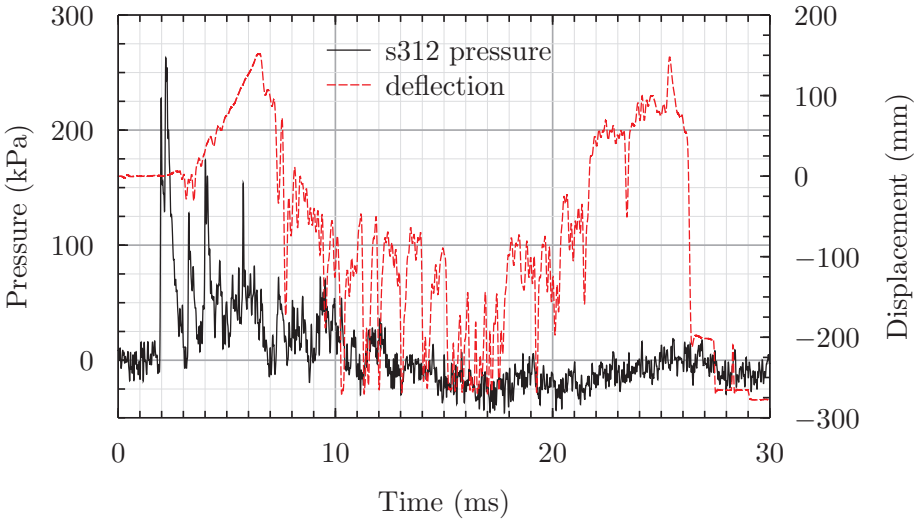

(a) Pressure at sensor 312 and deflection history of panel

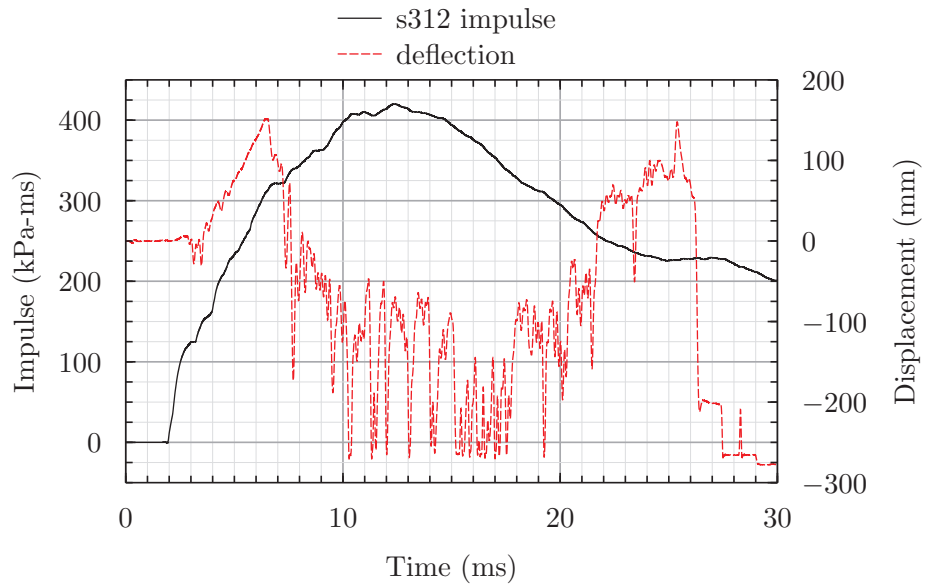

(b) Cumulative impulse from sensor 312 and deflection of panel

Figure 5.35: Comparison of displacement with pressure and impulse data for sensors 312 in A4

5.6.4 Deflection, pressure impulse and experimental issues in A4

One of the main aims of A4 was to determine if there was any relationship between pressures within the box and the deformation of a flexible structure. Although only

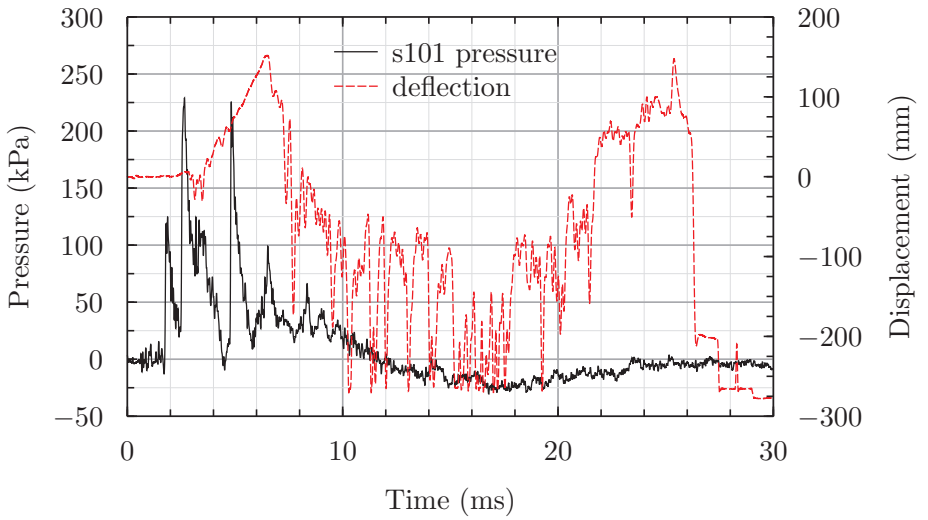

(a) Pressure at sensor 101 and deflection history of panel

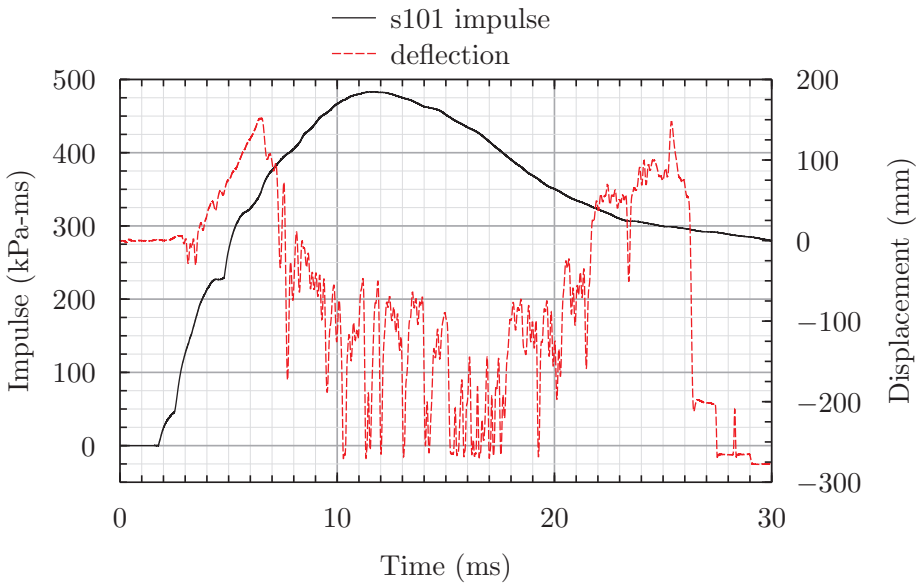

(b) Cumulative impulse from sensor 101 and deflection of panel

Figure 5.36: Comparison of displacement with pressure and impulse data for sensors 101 in A4

one test cycle was performed for arrangement 4, it is possible to identify from the data that for this arrangement that the displacement of the aluminium panel has limited effect on the pressures within the test cell over the most transient period of data, but the unreliability of the displacement data after 6.5ms prevents analysis of longer term effects, such as cumulative impulse. Figure 5.35 shows the impulse and pressure data from sensor 312 on the roof of box and the displacement data from the LDG for the centre of the aluminium panel. It should be noted that Sensor 312 is not measuring pressure at surface of panel, and is much closer to the edge of panel than the centre. In the absence of sensors on the panel surface (thickness and flexibility prevent this) data from sensors close to the panel were used. The panel begins to deform at 2.3ms, by which point the first shock has arrived and is decaying. The three most prominent shocks have arrived and decayed by 6ms, by which point the panel has only deformed by approximately 50mm. This is not sufficient deformation to make a noticeable difference

to reflections, and also most reflections have already occurred by this point. For pressure reflections at this point of measurement, the positive phase durations are a maximum of 1ms, during which the panel moves by 50mm at its maximum velocity between 2.3 and 6.5ms. Given that the time taken to rise from pre shocked to shocked pressure is only a fraction of a millisecond, the panel is essentially almost stationary while the reflection is taking place. In a rail vehicle, it would therefore suggest that by the time any window begins to deform, or is pushed clear enough of the rail vehicle to provide a noticeable venting area, the most transient behaviour will be complete.

Figure 5.36 shows pressure and cumulative impulse sensor 101 at the centre of wall A and deflection time history for the centre of the panel. The second shock, which reflects from both the panel, the floor and ceiling, is incident on wall A before any significant deflection has occurred in the panel, although it should be noted that the deflection does begin before the shock is incident on wall A. There is some correlation in time between the appearance of a discontinuity in the deflection at 2.8ms and a jump in the pressure at 3.1ms, suggesting that the two could be linked, but the magnitude of the pressure feature at this point and the apparent effect on the panel (displacement will not create spurious behaviour, but a bending or bulging effect at this point could yield odd LDG data) do not correlate. The third shock, at 4.8ms (a second reflection from the panel) arrives at wall A at a time when the panel has undergone 75mm of deflection at its centre. The panel begins to develop a visible curved shape at the open end at 5ms, but is still quite flat at 5.7ms and is not obviously very distorted at the open end until 8.7ms (shown in Figure 5.28(a – h), edges still in position at 5.8ms). It is possible to speculate that if some failure of the panel begins to occur between 5.8 and 8.7ms (over which time the LDG data becomes unreliable and inconclusive) that the shape may change significantly and alter the way any subsequent reflections happen after this time. Although the lack of fixation would not prevent the panel from reflecting a shock (Figures 5.35 and 5.36 show that this happens over a very short period of time and it would not be possible for the panel to 'move out the way'), the shape could either disperse or focus any shock fronts that interact with it' leading to a stronger or weaker shock meeting wall A than would occur with a flat, rigid wall in place of the panel.

Figures 5.35(b) and 5.36(b) show peak impulses of 420 kPa-ms and 480kPa-ms. This can be used to make a rough estimate of the magnitude of velocity this impulse would generate in the panel. Impulse, J, is change in momentum ($\Delta\mathbf{p}$) from Newtons second law (5.5). Dividing through by area (5.6) gives the specific impulse (termed impulse throughout this work, in Pa-s) as a function of the change in velocity Δv and the areal density ρ_A. Rearranging gives the velocity of a body as a function of the applied impulse and areal density (5.7).

$$J(N \cdot s) = \Delta\mathbf{p} = m(v - u) \tag{5.5}$$

$$\frac{J}{A} = I((^N/_{m^2}) \cdot s) = \frac{m}{A}\Delta v \tag{5.6}$$

$$I(Pa \cdot s) = \rho_A \Delta v$$

$$\text{or} \quad \Delta v = \frac{I}{\rho_A} \tag{5.7}$$

$$\Delta v = \frac{I}{\rho_A} = \frac{420}{8.8} = 47.7 \text{ m/s} \tag{5.8}$$

$$\Delta v = \frac{I}{\rho_A} = \frac{480}{8.8} = 54.5 \text{ m/s} \tag{5.9}$$

The aluminium panel used had a thickness 3.2mm and a volumetric density of 2750 kg/m^3, which gives an areal density, ρ_a, of 8.8 kg/m^2. If peak impulses seen at sensors 101 and 312 were experienced over the whole panel, velocities similar to the peak recorded by the LDG are predicted (equations (5.8) and 5.9). This analysis is highly simplified, and assumes no action from the supports and the application of a uniform impulse over the whole panel and does not consider that the peak impulse at the panel could be higher than that seen at sensor 101 or 312. Even though this analysis is highly simplified, and would not be a suitable method for fully characterising the behaviour of the panel, it provides rough figure that can guide further investigations.

The pressures and cumulative impulse behind the aluminium panel was measured at mid height in the corner between walls B and C (see Figure 5.22) and are shown alongside deflection data in Figure 5.37. The baffles from A3 were retained in place for this test, with only the central baffle removed to allow the mounting of the laser distance gauge. A shock can be seen arriving at sensor 402 at 2.6ms followed by a maintained pressure at a similar magnitude for 1ms, as opposed to the rapid decay seen in other locations across arrangements. Stronger and more typical, rapidly decaying shocks are seen at 5.7, 6.5 and 10.1ms, but the cumulative impulse seen in Figure 5.37(b) are primarily driven by a rising quasi-static positive pressure between the arrival of the first shock at 2.6ms and the beginning of a negative phase at 18.2ms. It is interesting that a point not directly exposed to the blast shows a cumulative impulse that is a similar magnitude to some of the highest peak cumulative impulses at 600kPa-ms. The mechanism for the arrival of the shock at 2.6ms is not immediately clear from visual information from high speed video, post inspection of structures or pressure time history, but it is possible to eliminate several potential causes and arrive a suitable explanation. The shock is too strong and arrives too late to be caused by transmission of shock waves in the wall of the test cell, as shown in Figure 5.31. Post test visual inspection of the panel shows no bursting, and high speed video shows no visible movement of the unsupported panel edge until 5ms and no flash on the other side of the panel, which prevents an air shock directly passing between sides of the panel at this time. The relative impedances of air and aluminium prevent a shock being passed between air on either side of the panel as ratio of acoustic impedances between air and aluminium mean most pressure is reflected at the boundary between the two, not transmitted (see Chapter 2 Section 2.2.1.1).

In the absence of other explanations, a process of elimination suggests that physical movement of the panel is responsible for developing the shock, in a similar way to a piston creating a shock in a cylinder (see Chapter 2). The relation between the strength of the developed shock and velocity of the piston is given in Liepman and Roshko [25] and shown in Equation (5.10), where u_p is the velocity of the cylinder and a_1 the speed of sound in the transport medium. If it is assumed that the shock incident on wall C at this point is weak, the coefficient of reflection will be 2 and therefore the magnitude of the incident shock (it is the reflected shock that is measured) will have an overpressure of approximately 20kPa. For a speed of sound of 340 m/s, this would require a piston

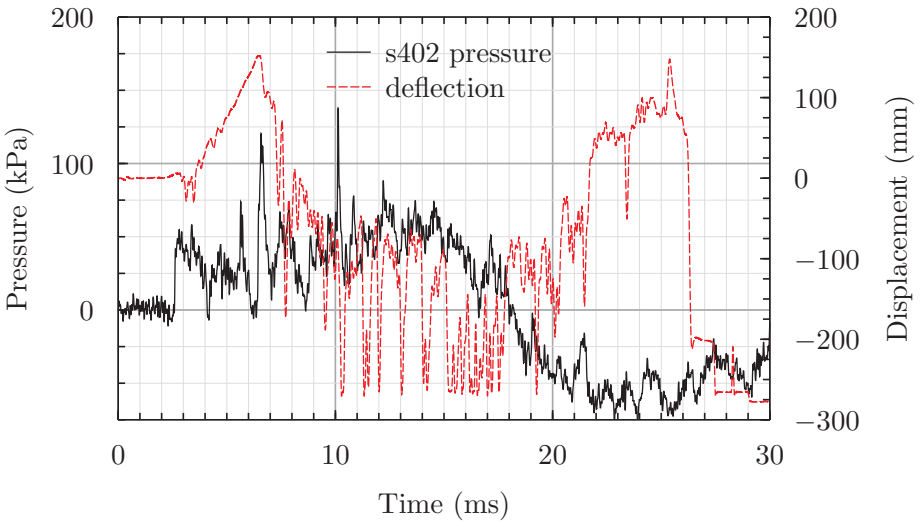

(a) Pressure measurements between walls B and C behind aluminium panel and deflection history

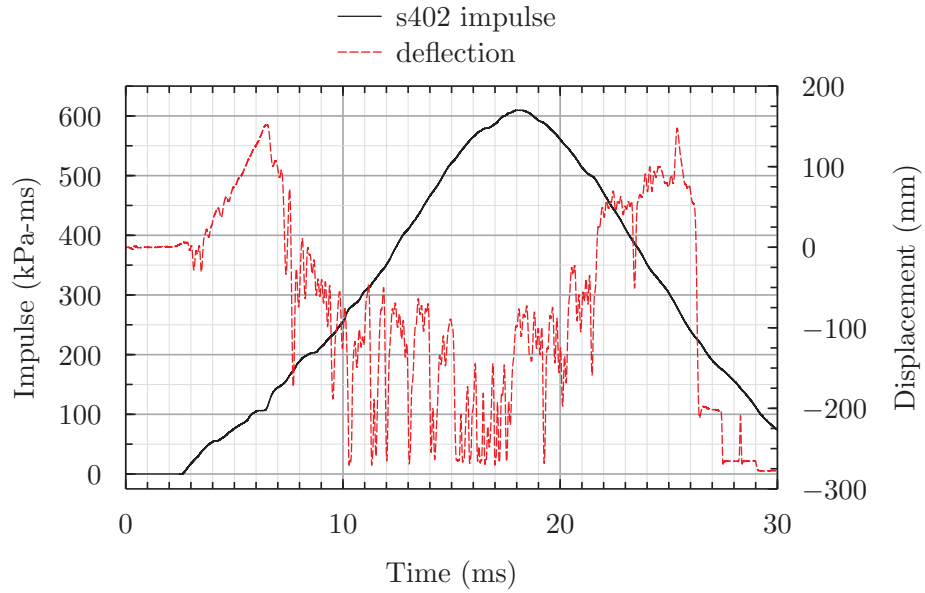

(b) Cumulative impulse from sensor 402 and deflection data for aluminium panel

Figure 5.37: Comparison of displacement with pressure and impulse data for sensors 402 in A4

speed of approximately 45 m/s (Equation (5.11)). In reality, the panel does not move like a piston in a cylinder as the air behind it is not completely enclosed, and will have a velocity profile across it with the edges on the panel having a reduced velocity compared to the less restrained central areas where the influence of the supports is witnessed by the panel more quickly. The data from LDG shows that the central portion of the panel is not moving at 50m/s until 1.5ms after the shock arrives at sensor 402, but the end of the panel opposite sensor is much closer to the charge and the angle of loading is closer to normal at the surface of the panel, so it could be assumed that the panel would begin moving earlier here. However, the increase in strength of the shock at this point may be offset by the proximity to the fixed supports. Further analysis of the panel behaviour is required to confirm the likely distribution of velocity across the panel to confirm this as the mechanism for development of this shock.

$$u_p = \frac{a_1}{\gamma}\left(\frac{p_1}{p_0} - 1\right)\left[\frac{\frac{2\gamma}{\gamma+1}}{\frac{p_1}{p_0} + \frac{\gamma-1}{\gamma+1}}\right]^{1/2} \tag{5.10}$$

$$\begin{aligned} u_p &= \frac{340}{1.4} \times \left(\frac{120}{100} - 1\right) \times \left[\frac{\frac{2 \times 1.4}{1.4+1}}{\frac{120}{100} + \frac{1.4-1}{1.4+1}}\right]^{1/2} \\ &= 44.9 \text{ m/s} \end{aligned} \tag{5.11}$$

The area directly behind the panel in A4 sees a much longer delay between arrival of shocks and peak impulse, compared with other arrangements. Although a number of shocks are seen, most of the impulse is added due to a quasi static increasing pressure between 8 and 18ms. The exact cause of this is not straightforward to pinpoint, due to uncertainties in the behaviour of the panel and effects such as after burn that are not trivial to quantify. Vertical and longitudinal waves of motion and reflections of shocks between the walls could cause some of the behaviour seen, as could the failure of the panel, although it should be noted that the panel was still in contact with wall B post testing, with a single bolt holding the angle sections in place, which would limit the passage of shock waves between the two halves of the box. Failure of the panel along the top angle section could cause some passage of shock between the roof and wall C, as well as causing some hot gases to spill over onto the other side of the panel, and these may well still be undergoing a burning process as atmospheric oxygen is drawn in to complete combustion of the detonation products. The presence of the baffle on wall C will serve to increase the confinement around sensor 402, potentially leading to a greater number of reflections and limiting the ability of pressures to 'escape', which would provide and explanation of the longer term build up of pressures, especially if secondary combustion was present. Ultimately the mechanisms are difficult to determine from the limited data, but clearly significant pressures and impulses are generated on the non-load side of the panel. In the context of a rail vehicle this could be a mechanism by which passengers outside of a rail vehicle (e.g. on the platform) are injured, which is worthy of further investigation.

5.7 Conclusions

The experiments reported here were designed to produce data to validate numerical models. This requires that the data itself be a good representation of the physical process, with good agreement between measurements. With the exception of arrangement 4, where only a single test cycle was completed, each arrangement showed excellent agreement between individual shots, especially during the most transient phase where a number of shock reflections were present. Although pressure histories are very consistent across arrangements, cumulative impulses show deviation towards the end of the measured time. This difference is caused by cumulative errors in recording and processing data and the minor differences in output of an explosive that are compounded when pressure data is integrated over time. The secondary combustion process (see Section

2.2.2) that occurs may contribute to this error too and although no data on this was gathered from this series of tests, it should be considered a potential contributing factor and certainly worthy of further investigation.

The experimental method generated good quality data, but several additions would be made to any subsequent similar test series. Although useful comparisons and analysis can be made with the data acquired here, altered sensor positioning would make comparisons more straightforward. By positioning sensors in consistent locations in the 3 similar arrangements, and as similar as possible in the fourth arrangement, it would have been possible to better compare the effects of baffles and spacing. The tests were not planned specifically with this comparison in mind initially, but with hindsight this would have been a valuable addition to the experimental tests. Optical displacement measuring, such as the laser distance gauge employed in arrangement 4, have many advantages over mechanical displacement measuring methods; the lack of moving electrical connections avoids problems with skipping connections and the non-contact nature prevents physical resistance in the measuring device which would influence the behaviour of the structure under investigation. For high explosive testing and very flexible structures the optical method employed proved that it can be unstable, yielding poor results. It is recommended that in future work, the deformation of the structure is restricted to ensure that measurement of the deflection of the panel was more reliable, as well as providing some form of shielding to reduce the influence of stray light on the optical sensor.

The presence of baffles in A2 and A3 did not lead to reduced impulse or reduced pressures within the box, with impulses on wall A, opposite wall C on which baffles were placed, higher than those seen without baffles. The angles that the incident shock waves make with the baffle means that reflection towards wall A is greater when baffles are in place, but interestingly this does not necessarily correspond to significant differences in impulses on wall C itself, other than at points where baffles and the wall meet, where coincident shock waves lead to very high pressures and impulses. Data also shows the number of baffles itself made almost no difference to the impulse at wall A in the box, with differences in the pattern and timing of reflections effectively cancelling out any differences between the two arrangements with different baffles. Only a small amount of data gathered for arrangement 4 is useful, but appears to show that over short durations the deflection of the panel makes little difference to the experienced pressures and build up of impulse. This period of time may be the most important when considering how passengers are injured, so this is a potentially important conclusion. Although the displacement data showed several issues, the measured velocity over the most stable period agrees with a simplified analysis for an impulsively loaded plate.

The deformation of the panel also led to shock waves on the side that was not directly exposed to the blast energy. A simplified analysis can explain the presence and magnitude of a single shock, but not a number of other shocks and a long term pressure build up between the aluminium panel and wall C. Although the overpressures are generally low (not more than 150 kPa) they are still significant as the impulses developed over 18ms are of a similar magnitude to the highest seen at locations directly exposed to the blast. The confinement caused by wall C and baffles in part leads to maintaining a higher pressure, and this could have important implications for explosions in other confined spaces such as tunnels, where passengers, or structures outside of a targeted rail

vehicle may be at greater risk than previously thought. It will therefore be important to investigate how this longer duration build up of pressure compares with shorter duration build ups when considering both the risk to passengers and surrounding structures.

The testing has identified various physical phenomena that must be modelled correctly, or require further investigation and may adversely affect the results from numerical models. Although it is not present in all models, any negative phase can make reductions to the impulse, so failing to capture it fully is likely to lead to inaccuracies in the peak cumulative impulse. The high number of reflections and short duration of positive and negative phases mean that a fine mesh will be required to resolve such pressure gradients. Although currently not implemented in LS-Dyna, equations of state to consider the effects of secondary combustion phenomena in high explosive detonations may be important for predicting the build up of pressures over durations longer than those of individual shock waves. This should be considered as a likely source of error in numerical models, especially over longer duration models, which without taking into account secondary combustion will under predict the cumulative impulse. The test cell was always open at one end, which prevents significant build up of quasi static pressures (QSPs) due to the large area to vent pressures, but for structures that are completely enclosed with no large vent at one end, QSPs may have a more significant effect on long term impulse, which should be subject to further investigation to identify important parameters.

The mechanism that develops pressures behind the aluminium panel and leads to the long term build up of pressures and a number of shock waves is not fully understood, and could have important implications when considering a rail vehicle under blast loading, as well and people and structures close by. Although further experimental testing to investigate this is not within the scope of this work, suitable numerical models may be able to shed light on the cause and identify any implications for passengers, rail vehicles or surrounding infrastructure.

The presence of baffles in the experimental tests reduced the impulse experienced at some locations within test cell, but also significantly increased the peak pressures in other area. Generally, baffles appear to slightly reduce the impulse experienced in the test cell (and it follows, a rail vehicle carriage), but the number and spacing along the wall was not found to play a significant role.

6

Numerical modelling of experimental test arrangements

6.1 Introduction

The numerical method used for modelling blasts loads in rail vehicles has been verified with the use of analytical and empirical solutions for blast pressure and structural deformation, but to ensure that the models make accurate predictions in more complex scenarios it is necessary to validate their output with experimental data. A series of bespoke experiments were described in Chapter 5 and building on numerical modelling work from Chapter 4, this Chapter describes the development and results of numerical models of those experimental tests using LS-Dyna.

6.2 Model development

In Chapter 4 a method and series of verification models was presented, which identified the important parameters which can affect solution accuracy. Chapter 5 presented experimental data for high explosive detonations in confined spaces, and this Chapter aims to use that experimental data, along with techniques from Chapter 4 to produce accurate and valid numerical models, that can be used to model the effect of high explosive detonations in rail vehicles.

This section presents the process of model refinement, achieved by adjusting parameters within models and comparing them with each other and data from a single experiment. The experimental test A1 is used to guide the mesh refinement and specification of boundary conditions. The steps taken are as follows:

1. identify appropriate boundary conditions
    (a) ensure free edges of mesh are an appropriate distance from points of measurement
    (b) select boundary techniques for modelling structural boundaries
2. refine mesh appropriately using experimental data

3. check and ensure no non-physical behaviour is happening
   (a) ALE material leakage
   (b) pressure oscillation, such as those described in Section 4.2.3.4

6.2.1 Accounting for secondary combustion

As discussed in Section 2.2.2.1, when some high explosives detonate the products can be further oxidised to release energy as heat. The experimental tests reported in Chapter 5 used the RDX based explosive PE4[1], which can release an additional 3.8 $\times 10^3$ kJ/kg of energy on top of the 6.3 $\times 10^3$ kJ/kg of energy released at detonation (see Section 2.2.2.1). The combustion of binding agents and plasticisers, as well as any other combustible material within the fireball of detonation can also add to energy released during combustion, although the difficulty in identifying the exact composition of the explosive makes quantifying this more difficult. The secondary combustion of detonation products and other materials makes a significant contribution to the energy of the gas within the enclosure of the test cell, therefore it is necessary to account for this additional energy in the solution.

The LS-Dyna code is not designed to cope with simulation of the complex thermochemistry involved in either the detonation or the secondary combustion of explosives, and as a result relationships between the reaction chemistry and variables computed within LS-Dyna are defined using empirical relationships. For the detonation process, the combination of a high explosive material model and an equation of state for the detonation products (see Chapter 2, Section 2.3.4) is widely used, but the solver does not account for how the detonation products subsequently flow and mix with other materials. The secondary combustion process requires a knowledge of the chemical formulation of the explosive charge, and the reactions which take place, which are governed by the products made during detonation (which become the reactants for the secondary combustion process, along with any other combustible materials), the temperature and the flow of gases. These things are not possible within LS-Dyna, so it is necessary to use a significantly simplified method to account for additional energy.

6.2.1.1 Internal energy deposition

LS-Dyna and other hydrocodes are capable of solving, to some extent, the basic flow behaviour of materials based on their momentum, but they are not designed to solve gas flow problems and do not account for significant effects such as turbulence and mixing, which would be better modelled with one of a vast of number of Computational Fluid Dynamics packages. Video footage from experimental testing shows flame front propagation and turbulence over almost the whole test cell enclosure (the brightness of the flame obscures some of the later behaviour), which hydrocodes are not designed to simulate. To account for the secondary combustion it is necessary to account for the contribution of combustion energy over the whole volume of test cell.

The secondary combustion energy is assumed to do negligible work [47, 179], so all the heat energy from combustion will manifest itself as an increase in internal energy, in accordance with the first law of thermodynamics. For explosives where the chemical

[1]PE4 formulations vary slightly between manufacturers, and the exact composition rarely available. Typically, PE4 is about 91% RDX, with plasticisers and binding agents added, such as oils and synthetic rubbers.

reactions occurring during this secondary combustion are known (or can be a assumed with a good level of confidence), the energy released can be calculated (see Equation (2.16) in Chapter 2).

A simple and robust method of achieving this increase in internal energy is by adding it directly into the energy term in the equation of state, which can be achieved in LS-Dyna with the *EOS_LINEAR_POLYNOMIAL_WITH_ENERGY_LEAK keyword, which is identical to Equation (2.35) (on page 25), but the internal energy is increased according to an energy deposition (power) versus time curve. The integral of power over time is the total energy, so the integral of the defined power time curve should be equal to the total amount of energy available for secondary combustion. It is necessary to make some assumptions about the energy release, and it seems sensible to assume a reaction that begins slowly, increasing to a maximum then slowing as the mass of reactants reduces. The total energy released in such a system is assumed by the author to take the form of a sigmoid curve, although in reality the reaction rate is governed by the mixing, relative volumes of reactants, and temperature thus is typically solved numerically [51]. If the total energy is to take a sigmoid form, the secondary combustion power curve will take the form shown in Equation (6.1), and the energy added takes the form shown in Equation (6.2), both of which are shown graphically in Figure 6.1.

$$P_{sc}(t) = \frac{e^{-t}}{(1+e^{-t})^2} \tag{6.1}$$

$$\int_0^t P_{sc}(t)\,\mathrm{d}t = \frac{1}{1+e^{-t}} = E_{sc} \tag{6.2}$$

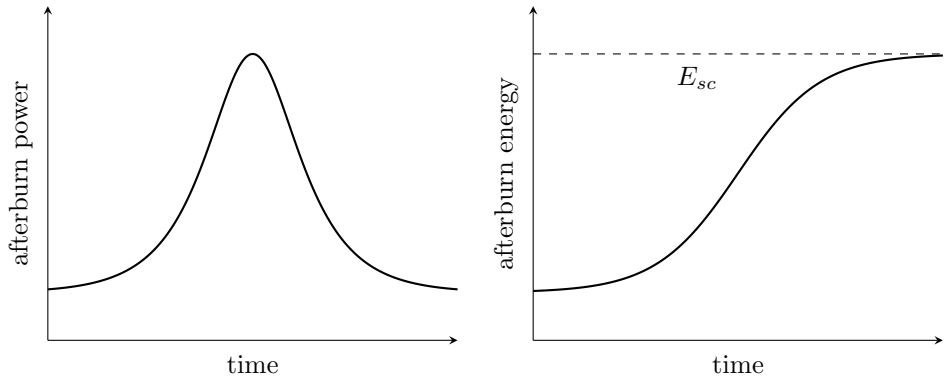

Figure 6.1: Plot of energy time curve and differential

With a function form defined it is necessary to define parameters to modify the curve to give it the correct magnitude and shape, giving a curve with the form shown in Equation (6.3). The equation of state uses energy per initial volume, so the total energy available for secondary combustion calculated in Section 6.2 is divided by the volume of the test cell. The energy release rate can be modified through the parameter b and the time of peak energy release altered via c. These parameters will need to be modified using data from experiments.

$$P_{sc}(t) = \frac{E_{sc}}{V_0} \cdot \frac{be^{-b(t-c)}}{(1+e^{-b(t-c)})^2} \tag{6.3}$$

This approach offers a simple way of accounting for secondary combustion energy, but there are a number of drawbacks to this method of modelling the additional energy release. Firstly, it requires a knowledge of the timing of peak energy and the time of peak energy release, which to a large extent can only be identified from experimental data, although many parameters for phenomenological equations of state (such as the JWL) are also derived experimentally. Secondly, to ensure that secondary combustion energy is only added inside the test cell (and not to air on the other side of the test cell wall) it is necessary to define material outside of test cell as a separate ALE multi-material group, and ensure additional energy is added only to the material that initially fills the test cell, although ideally, this extra energy would be added only behind the flame front. Finally, this method assumes a spatially uniform deposition of energy. In reality the spatial distribution of energy deposition is based on the flow of the products and the propagation of flames, which cannot be predicted by LS-Dyna.

6.2.2 Investigating variables

Numerical models were constructed of test arrangement 1 (A1), with physical geometry of the test cell as shown in Figure 6.2. The planes xz and yz that pass through the point **O** represent two walls of the physical test cell, and are modelled using nodal constraints. The outer boundaries of the test cell were modelled in two different ways, firstly using nodal constraints and specifying an air domain only as large as the physical test cell, and secondly by using the fluid structure interaction method, where a physical model of the test cell geometry is constructed using shell elements placed within an appropriate sized mesh for the air domain.

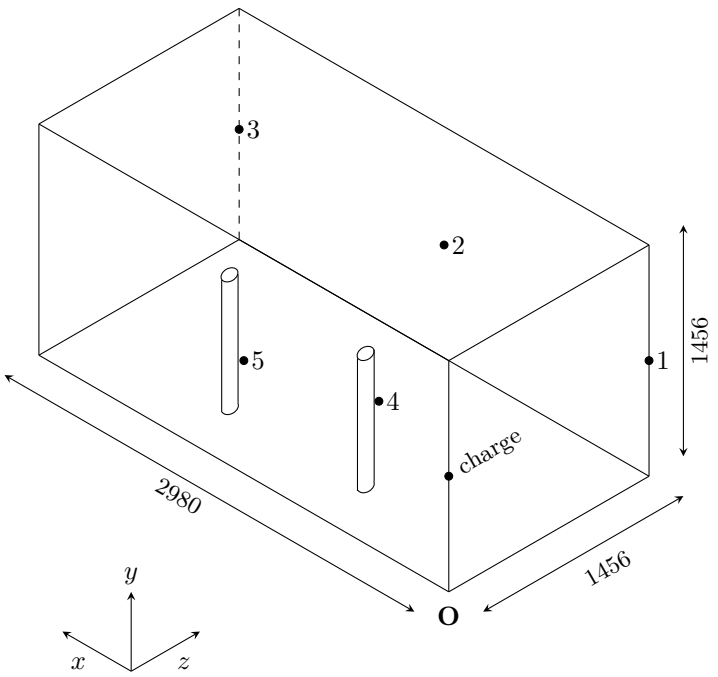

Figure 6.2: Setup of 3D model

The DATABASER_TRACER keyword is used to specify the output from numerical models, and mimics the physical data gathering system used in physical tests as closely as possible. Five measurement locations are specified, corresponding as closely as possible

Table 6.1: Physical test and numerical model measurement locations

		all in mm		
test sensor	model measurement location	x	y	z
S312	1	10	728	1450
S402	2	1490	728	1450
S358	3	2930	728	1450
S311	4	990	615	422
S101	5	1490	728	10

to the physical locations of the sensors, described in Chapter 5, Figure 5.12. Data is sampled from numerical models every 1.53μs, which is approximately the same sampling frequency used during experimental testing. In the physical tests, sensors are located at the surface, but in numerical models data base tracer points are positioned slightly away from the surface to ensure that pressure measurements are taken in the air, and not in line with nodal constraints or Lagrangian surfaces, which could lead to incorrect predictions.

An advantage of the numerical modelling methods such as finite element analysis, is the ability to get a full field visualisation of physical variables occurring in the model, such as pressure and density. This is particularly useful for identifying the propagation and reflection of shock waves which would otherwise simply just be seen as a peak in a pressure time graph, or how particular shocks interact. This is achieved in LS-Dyna using the DATABASE_BINARY_D3PLOT keyword, which produces a data file with information on every element at a chosen time interval, which can be visualised with LS-PrePost. Their usefulness for comparison with experimental data is limited as similar data cannot be replicated using the available experimental techniques, so were not used extensively for validation.

As with previous 2D and 3D models reported in Chapter 4, extensive use was made of the 'mapping' feature available in LS-Dyna. A quarter symmetry 80g charge of PE4 was modelled in 2D, using ALE shell elements, which generated a single mapping file that served as the initial conditions for all 3D models. The positioning of the initial charge and the vectors around which the 2D data is revolved to achieve a 3D map is controlled by the *INITIAL_ALE_MAPPING keyword card. The centre point of the charge is positioned as shown in Figure 6.2, at $x = 0, y = 728, z = 0$, and revolved around unit vectors from this point in the x, y and z directions to give the desired full 3D initialisation of the blast wave with symmetry in xy and yz plane. The 3D models use 1 point hexahedral ALE multi-material elements, and are run to 15ms.

A number of variables were studied to arrive at a satisfactory modelling method. The effect of structural boundary conditions, ALE domain sizes and mesh refinement were all seen to influence the results, and a description of these models, along with the results of the study of these variables can be found in Appendix H. A study of the effect of secondary combustion is shown here, which was seen to play a significant role in predicting the correct behaviour of shocks and values of cumulative impulse.

6.2.2.1 Secondary combustion

Secondary combustion is accounted for in a number of models, as discussed in Section 6.2.1.1. Table 6.2 shows the parameters used to study the effects to altering the energy release on the pressures experienced within the test cell, with a range of different peak energy release times and energy release coefficients, to identify those which best match the real scenario.

Table 6.2: Parameters used for secondary combustion study

identifier	energy release coefficient, b	time offset, o
E1	0.5	10
E2	0.5	15
E3	1	5
E4	1	10
E5	1.5	5
E6	1.5	10

6.2.2.2 A note on LS-Dyna versions

There are essentially 4 versions of LS-Dyna, which can be split into 2 groups; Shared Memory Parallel (SMP) and Massively Parallel Processing (MPP). Both of these versions have single (32 bit) and double (64 bit) precision versions, which affects the size of floating point values that can be stored in arrays and the amount of memory required to store these arrays. Single precision floating point numbers are generally limited 7 decimal points of accuracy, whereas double precision floating point numbers generally are accurate to 16 decimal places. As a result, single precision versions of LS-Dyna are more liable to roundoff errors, which can lead to a loss of accuracy when small values (such as for small deflection) are subject to mathematical operations or models which are run over a long period of time, where the roundoff error accumulates as the solution progresses. Single precision is also limited to approx 2000m words of memory [180], which corresponds to about 8GB for 32bit architecture. Double precision versions of LS-Dyna do not have this limit, but use about double the amount of memory - for a problem that requires 2000m words of memory, the double precision version would require 16GB, as opposed to 8GB for the single precision version [181].

The memory limit with single precision versions of LS-Dyna can be somewhat circumvented by using the single precision MPP version of LS-Dyna. The MPP code works by decomposing the solution so it can be solved in parallel on n processors, and then passing information about boundary data between each decomposed section of the model. The memory required is specified per processor, which means that if 2000E06 are specified, it is possible to solve models that require greater total memory than can be solved using the single precision SMP code. In terms of performance, the SMP version outperforms the MPP version when small number of processing cores are used, due to the extra computational effort required to decompose the solution and pass information between memory of each processor. The performance disadvantage of using the MPP code decreases as the number of processing cores over which the solution is decomposed increases, and the gains begin to outweigh the losses when more than 8 processors are

used.

6.2.3 Results

6.2.3.1 Secondary combustion

The effect of secondary combustion was considered by adding additional internal energy to the solution using a sigmoidal function to define the total additional energy added. To investigate the effect of changes to this function, the models were run using a coarse (20mm) mesh, to reduce the computational effort but still identify the effect of changing parameters. Each of the six models is prefixed with an 'E' to differentiate them from other parameter studies in Section H, and the differences between each are shown in Table 6.2.

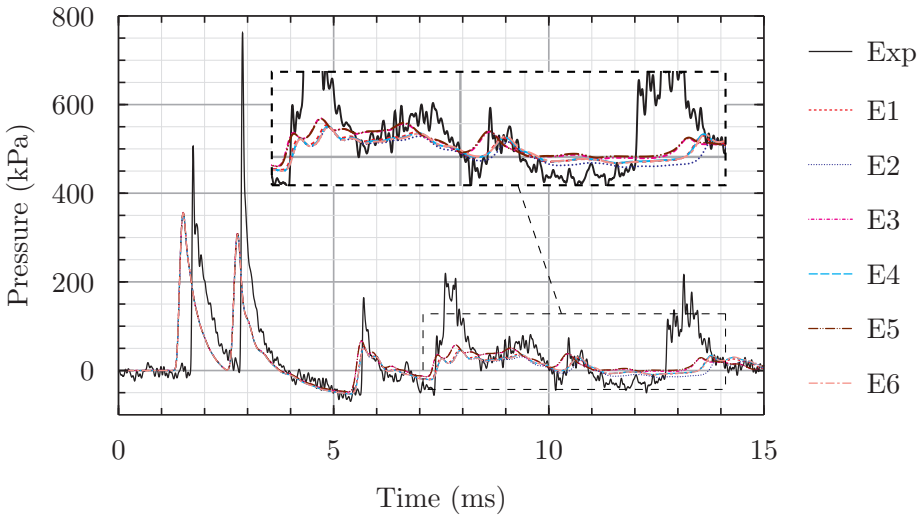

(a) Pressure time history for experimental and numerical data

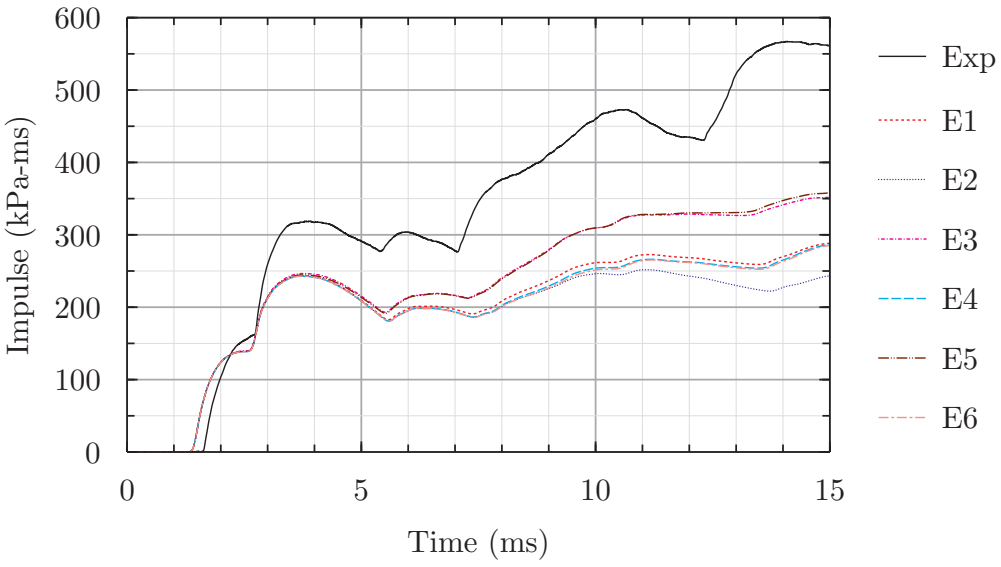

(b) Cumulative impulse

Figure 6.3: measurement location 1, showing the effect of changing secondary combustion energy release parameters

Figure 6.3 shows pressures and cumulative impulse histories for experimental and 6 numerical cases from measurement location 1, as shown in Table 6.2 in Section 6.2.2.1.

The initial two shocks in Figure 6.3(a) show no difference between the models as expected, as the additional energy from secondary combustion at this point is negligible. The third shock at 5.5ms shows a very marginally earlier arrival in models E3 and E5, with identical behaviour from the other four models. The later time behaviour is marginally more different between cases, and is shown in more detail in the close up region in Figure 6.3(a). Models E5 and E3 show a higher pressure and earlier arrival of pressures than the other models, and at later times E2 begins to show a slightly later arrival than E1, E4 and E6. As the simulation progresses, it become more obvious there is grouping of the curves, which is shown clearly in the cumulative impulse curve in Figure 6.3(b). Models E3 and E5 and models E1, E4 and E6 appear grouped together, and reference to Table 6.2 shows that these groups refer to the time offset applied to each load curve. The largest increase in the cumulative impulse occurs in models E3 and E5, where the lowest offset, representing the earliest onset of secondary combustion, of 5ms is used and the cumulative impulse at 15ms is 350kPa-ms, compared with 200kPa-ms in the same model without secondary combustion. The smallest increase is shown in model E2, where the offset is at the largest studied value of 15ms and the cumulative impulse at 15ms is only 50kPa-ms greater than without considering secondary combustion. This follows the expected behaviour, as the time shift can reduce the total value of the power integral over the simulated time, reducing the total additional energy added to the solution.

Although accounting for secondary combustion has reduced the difference between the model and experimental results, the presence of two shocks at 7.8ms and 13ms are not accounted for, which are primarily responsible for the difference between experimental and numerical results.

The effect the additional secondary combustion energy is more clear in Figure 6.4, which shows experimental and numerical data from location 3. The pressure and impulse curves display the same grouping as seen before, with the lowest time offsets yielding the largest increase in pressure, but one of the drawbacks of the method mentioned in Section 6.2.1.1 is clearly visible in the results from models E3 and E5 in Figure 6.4, where pressure begins to rise before the arrival of the first shock. Clearly this is not physically realistic and is responsible for these models over predicting the impulse by around 20kPa-ms as shown in Figure 6.4(b). Aside from this, both the models with a 10ms (E1, E4 and E6) and 5ms (E3 and E5) offset predict the shock features in Figure 6.4(a) well, although each of these groups of models has areas where it predicts less accurately. E3 and E5 predict arrival time of shock at 8 and 14.5ms and the magnitude of negative pressure between 8 and 10ms, but do not predict the arrival times or decay of significant shocks at 10.3ms and 11.3ms as accurately as E1, E4 and E6. Figure 6.4(a) also shows that none of the groups predict the magnitude of the shock at 10.3ms, although all models predict the magnitude of the shock at 11.3ms

The same groupings and behaviour are seen at measurement location 5, shown in Figure 6.5. The shock arrival at 5.2ms in Figure 6.5(a) is well predicted by all models, but the peak in pressure at 5.5ms is over predicted in all models, with E3 and E5 being the highest at 155kPa, compared to 115kPa in experimental data. From 6.5ms, the decay shape and magnitude of the pressure is predicted better by E3 and E5 than in other models, where there is a consistent under prediction. All models fail to predict the correct time for the shock 10ms, with models predicting a much stronger shock than

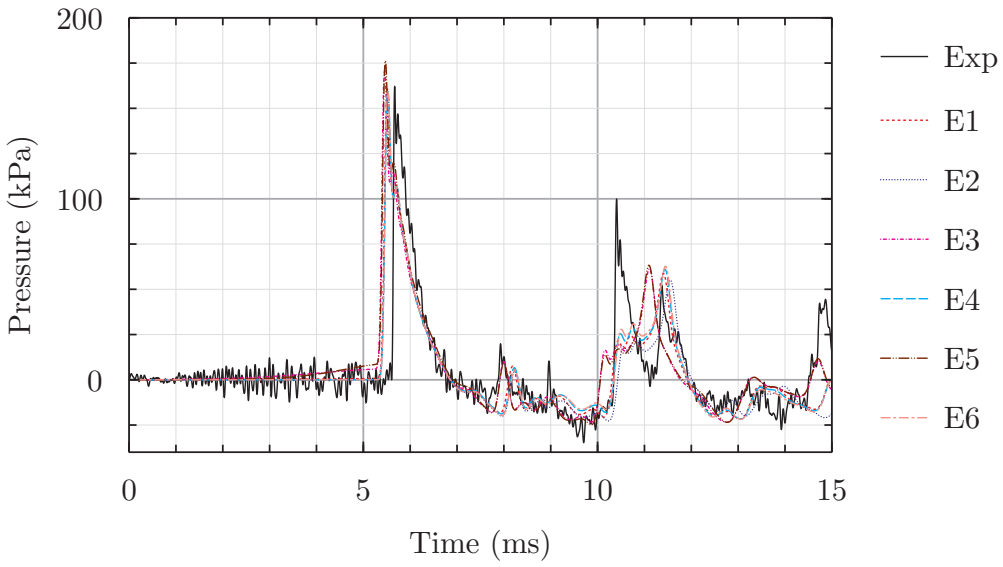

(a) Pressure time history for experimental and numerical data

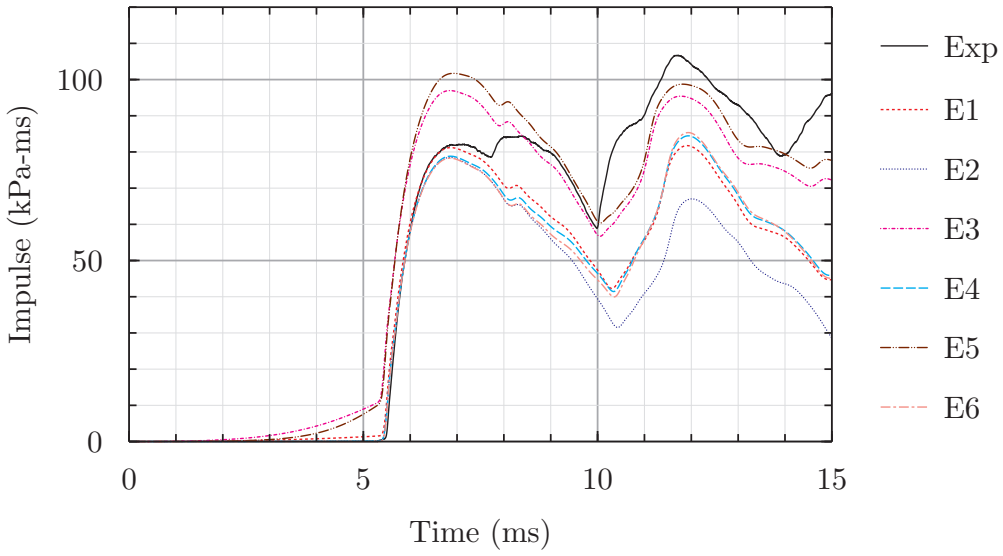

(b) Cumulative impulse

Figure 6.4: measurement location 3, showing the effect of changing secondary combustion energy release parameters

seen in experiments, but all at a later time. The models with a 5ms offset, E3 and E5 predict an earlier arrival and a lower magnitude as shown in experiments, but the arrival at 11.1ms is still 1.1ms behind that seen in the experiment. From 13ms the pressure begins to decay in 5ms model, which is not quite in line with experimental data, which between 13ms and 15ms shows a constant pressure around atmospheric, but performance of models using the 10ms offset do not show this issue to the same extent.

The higher peak and longer duration pressures in the models at 5.5ms in Figure 6.5(a) lead to a steeper rise in impulse compared with experimental data, as seen in Figure 6.5(b). At 6.5 ms the 10ms offset group, E1, E4 and E5 impulse plateaus, whereas the rise continues in the 5ms offset group, with a gradient similar to the experimental data. The impulse calculated from experimental data shows an increased gradient from 10ms, but begins to drop in the numerical data. When the shock arrives in the models at around 11ms, the rise in impulse is much stronger than seen in the experimental data,

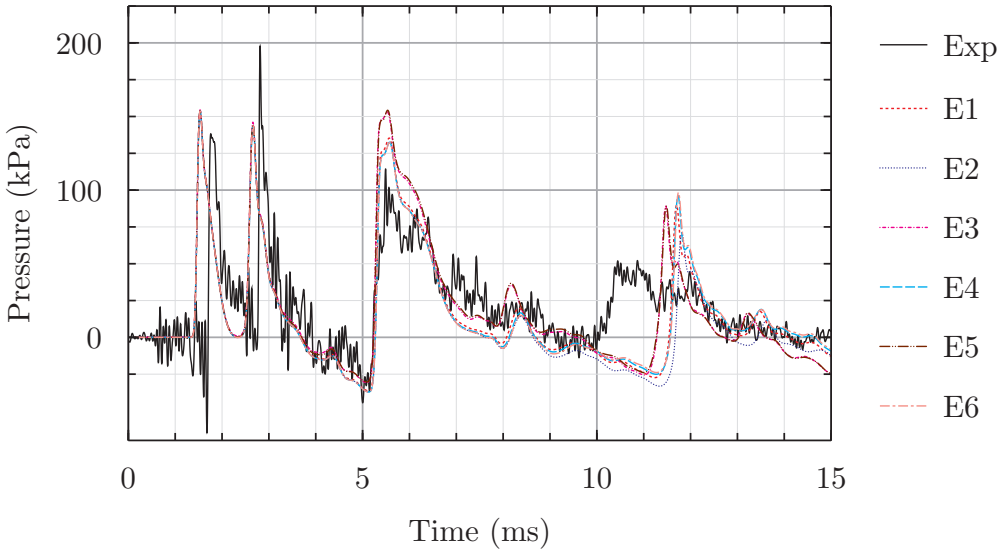

(a) Pressure time history for experimental and numerical data

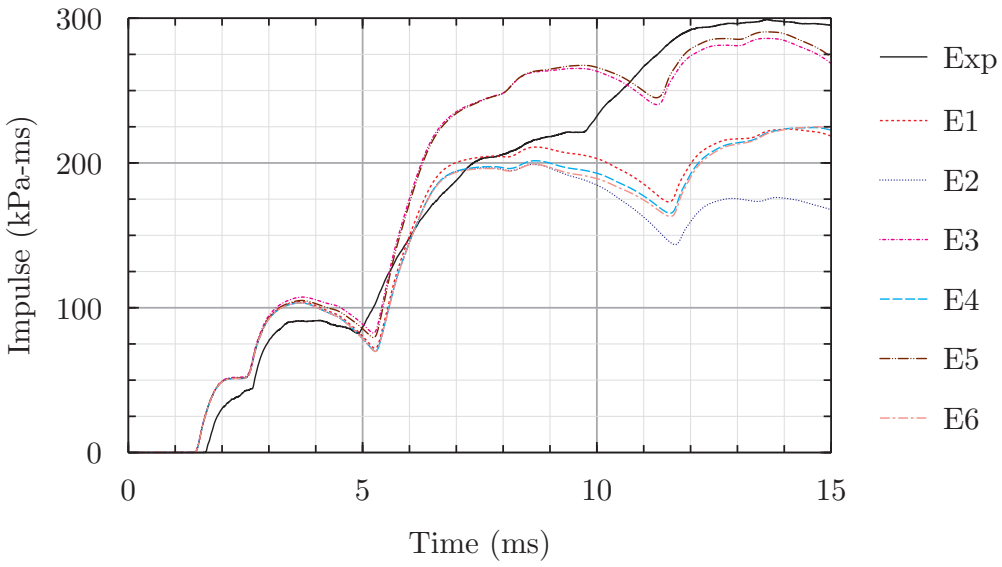

(b) Cumulative impulse

Figure 6.5: measurement location 5, showing the effect of changing secondary combustion energy release parameters

but although the rise is sharper, the amount of impulse added from this point is 50kPa-ms lower in the models than in experimental data, due to the shorter positive pressure duration in the models. The shape of all the model impulse curves are very similar, but the 5ms offset models show a final impulse that is closer to experimental results, compared to the other models.

Accounting for secondary combustion by addition of internal energy to the solution is shown here to produce models where the results provide a much closer representation of the physical behaviour than achieved when secondary combustion is not considered. The shape of the energy release function makes little difference to the behaviour of the models, but the time offset clearly makes a significant difference to model results, with earlier accounting for additional energy proving to be a more accurate depiction of reality than when energy is accounted for later in the solution. The method should be used with caution though, as adding additional energy into the solution too early can lead

to unrealistic pre shock arrival pressure rises. An offset of 7.5ms and an energy release coefficient of 1.5 were decided as the most appropriate parameters for the secondary combustion model.

6.2.3.2 Conclusions

Section 6.2.3 presents the results of the study of boundary conditions, mesh refinement and secondary combustion on the results from numerical models, and compared these with experimental results.

Correct definition of boundary constraints was identified, and symmetry boundary conditions were found to give a good representation of the experimental results. The size of the ALE air domain was also investigated, and an optimal size was determined for use when running models to 15ms. For models run for longer than 15ms, an enlarged mesh is necessary.

Mesh refinement was identified as an important parameter, but models run with a medium and fine mesh showed only limited difference, with an increase in peak pressure for some shocks, but no noticeable difference across many of the shocks and the cumulative impulse history. A refinement level of 15mm for the ALE elements within the test cell walls was shown to offer a good level of accuracy.

Secondary combustion was investigated by running a number of models with different energy release parameters, which showed that earlier addition of secondary combustion energy produced noticeably more realistic results, but the assumption of additional energy added at the same time in all locations necessitated by the method can yield some unrealistic results, with energy at the correct time for some locations, but too early for others, particularly those at the end of the test cell.

The results from Section 6.2.3 have contributed to the modelling methods described and developed in Chapter 4, and a satisfactory method has now been identified by considering the effects of secondary combustion, which can be used for modelling the experimental test arrangements.

6.3 Comparison of numerical models and experimental data

Three sets of experimental data were recorded for arrangements A1, A2 and A3, with only 1 for A4, and comparison of model data with all available experimental data is important to identify how the trends in experimental data match with numerical models. With a modelling method defined, it is necessary to compare models for each arrangement against all the sets of experimental data. The modelling methods to be applied have been discussed extensively in this Chapter and Chapter 4, so only a brief explanation of the methods applied is provided below.

6.3.1 Method

The method for modelling A1, A2, A3 and to a large extent A4 follows the modelling method described at the end of Section 6.2.3. The ALE mesh is the same for all models and uses the 15mm mesh described in Section H.1.3 with appropriate symmetry boundary conditions applied to nodes, as described in Section H.1.1. Data was mapped on to the 3D ALE domain from 2D models to initialise the blast load and an ALE Multi-Material Group was defined within the walls of the test cell using an initial volume

fraction, as required by the model for secondary combustion.

To match experiments, only the test cell structure is changed between each model (with the exception of A4, which has some further modification made as described in 6.3.1.1) which means modifying the Lagrangian structure which lies within the ALE mesh. The baffles in A2 and A3 are modelled with a single layer of shell elements at the appropriate location, with nodes merged with the mesh of the test cell geometry. The baffles were designed to remain rigid and experimental tests showed no evidence of deformation, so as with the walls of the test cell itself the baffles are modelled using a rigid material. The geometry of the Lagrangian model for A1 is shown in Figure 6.2, and plan views of the Lagrangian geometry and measurement locations for A2 and A3 are shown in Figure 6.6.

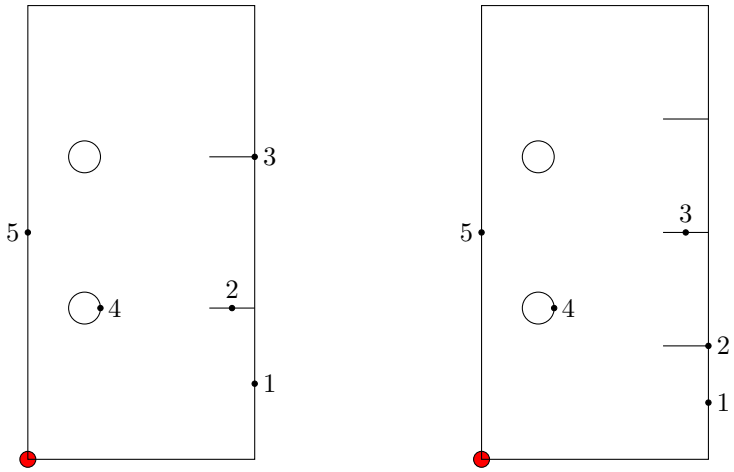

Figure 6.6: Measurement locations for A2 and A3

6.3.1.1 Additional model features for A4

The primary difference between A4 and other experimental tests was the presence of a large deformable aluminium panel, fixed vertically along the axis of the test cell. In the experiments, the panel was held in place between right angle steel sections which were held in place with bolts. Detailed modelling of the response of these bolts within the whole model for the test arrangement is unnecessary and counter productive, as the extremely small element size required for accurate modelling of the bolts would significantly reduce the critical time step for the solution, thus increasing the run time for the model significantly. The panel used was made from grade 1050 aluminium alloy, which has mechanical properties as shown in Table 6.3. Data from Higashi *et al.* [182] gives stress strain data for 1050 aluminium at 3 strain rates, and shows similar stress strain curves for $10^{-3}s^{-1}$ and $1s^{-1}$, with an increase in the yield stress and ultimate tensile stress at strains of $2 \times 10^{3}s^{-1}$, with a failure strain of around 0.45 common over strain rates.

Bolted connections are considered using beam elements, which has proven effective [183] for modelling dynamic loading of bolts under a variety of loading modes. Type 9 beam elements in LS-Dyna are specifically designed for use with *MAT_SPOTWELD and were used in conjunction with a contact definition to tie the shell elements of the panel to the wall of the test cell. The angle sections increase the stiffness around the edge of the aluminium panel, which is accounted for with a layer of shell elements with

Table 6.3: Mechanical properties for 1050 Al

ρ (kg/m^3)	E (GPa)	ν	σ_y (MPa)	ϵ_f
2710	71	0.33	100	0.45

Table 6.4: Mechanical properties for bolts using *MAT_SPOTWELD

ρ (kg/m^3)	E (GPa)	ν	σ_y (MPa)	E_{tan} (GPa)	ϵ_f
7500	210	0.30	800	0.20	0.35

the same thickness as the angle sections. The bolts used in the test were grade 8.8 with material data in Table 6.4 supplied by the manufacturer.

Secondary combustion is accounted for based on the volume of the enclosing geometry (see Section 6.2.1.1), which with the presence of the panel A4 reduces the volume by a factor of 2. This means it was necessary to define a different initial volume fraction containing only the air on the side of the panel exposed to the blast, and generate a new energy deposition curve for the altered volume.

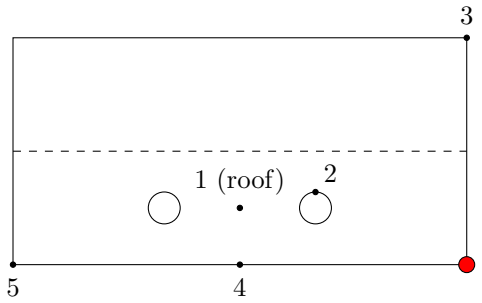

Figure 6.7: Plan view of measurement locations for A4, with small dots showing the positions of sensors and the dotted line showing the position of the aluminium panel

Sensors in the experimental testing were moved for A4 and the presence of the panel meant that sensors positions were changed to ensure their rated pressure levels matched the expected levels, and for ease of post processing this was matched in the positioning of tracer points in the ALE domain for A4. Figure 6.7 shows the positions of pressure sensors in A4 in plan view. Sensors 3, 4 and 5 lie at half height, sensor 1 is in the roof and sensor 4 is the sensor on the cylinder and is the same as previous arrangements.

6.3.2 Arrangement 1

A comparison between data from measurement location 1 in the model and three shots recorded experimentally by sensor 312 is shown in Figure 6.8. The pressure time history in Figure 6.8(a) shows that the model captures the features of the experimental results well, with some minor discrepancies in time and magnitude. Experimental data shows peak pressures for the first shock at 1.7ms of between 400 and 550 kPa, and model data shows a peak of 450kPa at 1.4ms. The rate of decay between the peak of shock 1 and the arrival of the second shock is well replicated by the model, and the arrival time of the

second shock in the experimental data between 2.6ms and 2.8ms is better predicted by the model where the shock arrives at 2.5ms. The experimentally measured peak pressure at shock 2 ranges between 390 and 760kPa for the three shots, but the model value of 410kPa is likely to be an under prediction of the true value, given that experimental pressures of 600kPa and 760kPa were measured at this location. The following decay and shock arrival at 5.5ms match well, and although the magnitude is under predicted, the arrival of the shock at 7ms is predicted by the model. Between 8ms and 10ms there is a period of sustained positive pressure in experimental data which is predicted by the models. The model does not accurately predict the arrival of the shock seen in experimental data between 12.3 and 12.8ms, but the model does show a pressure rise at 13.2ms which indicates that some aspect of this shock is present in the numerical model.

Impulse data in Figure 6.8(b) shows a close match between experimental and numerical data, with all the major changes in gradient of the impulse curve in experimental data mirrored in the curve produced from the model. The primary differences between model and experimental data occur after 7ms and the under prediction of shocks at 7ms and 12ms ultimately lead to a cumulative impulse at 15ms which is lower than that measured by experiments.

Figure 6.9 again shows good correlation between all 3 experimental data series and data from the numerical model at measurement location 5. As with data in Figure 6.8(a), the shock arrives earlier in the model than in experimental data in Figure 6.9(a), but with a much closer prediction of the value of peak pressure. The magnitude and arrival time of the second shock is also well predicted, with the model under estimating the value of the peak pressure by around 50kPa. The arrival time, magnitude and decay of the shock at 5ms is predicted very well by the model up to 10ms, and this similarity between model and experimental pressure data is confirmed by the cumulative impulse curve in Figure 6.9(b), which is almost identical for the 3 experimental data sets and the model data up to 10ms. The shock that arrives at 10ms in experimental data is predicted by the model, but is predicted later at 11.4ms, and the drop in impulse leads to a model under prediction of the experimental cumulative impulse by approximately 75kPa-ms at 15ms.

6.3.3 Arrangement 2

Pressure data from measurement location 2 in A2 presented a slightly more challenging situation for the model to capture, with a larger number of shocks seen over short space of time compared to many other models. Pressure data in Figure 6.10(a) shows that 4 shocks present between 1.8ms and 4.5ms are predicted by the model at the correct time and with the correct magnitude, with only the magnitude of the lowest pressure between shock 2 and 3 and shock 3 and 4 showing any noticeable difference. Experimental data between 6.5 and 15ms shows a very transient pressure history, with a high number of peaks over this time. This is also reproduced by the model data, with the only significant feature that is not replicated by the models being a shock that arrives at 7ms in the experimental data. The similarity over 15ms is shown by the cumulative impulse curve in Figure 6.10(b), where model data and experimental data are closely matched.

Figure 6.11 shows data from measurement location 3 and sensor 358 in A3, which is positioned at the junction of wall C and the third baffle. Figure 6.11(a) shows that it proved challenging to capture some of the features in the model, but cumulative impulse

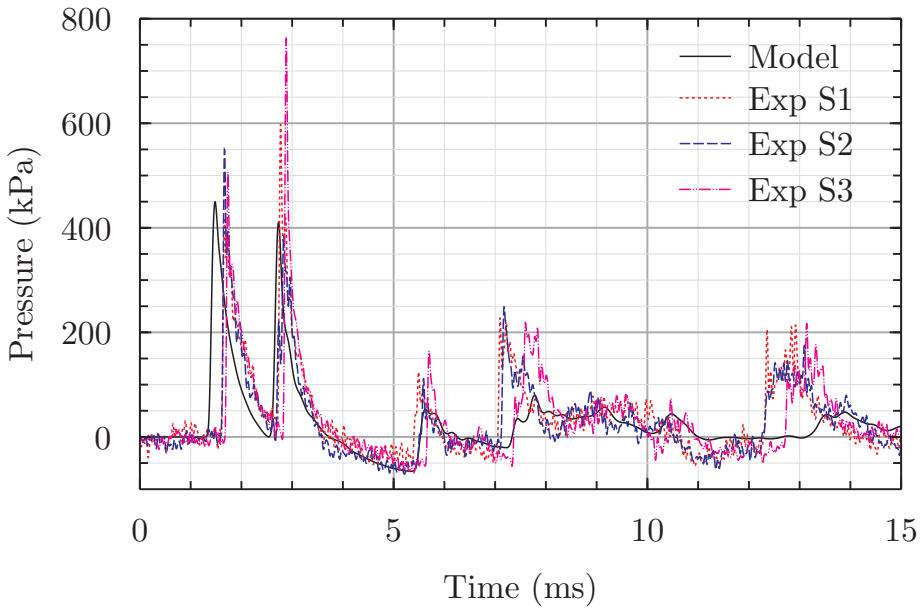

(a) Pressure history

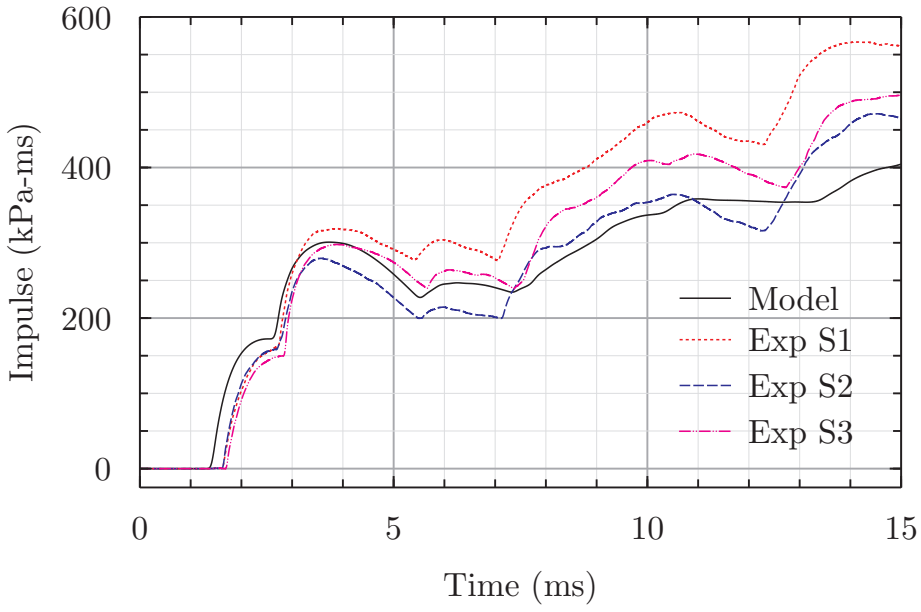

(b) Cumulative impulse

Figure 6.8: Comparison of model and experimental data from measurement location 1 in A1

data shown in Figure 6.11(b) indicates a good degree of similarity between the models. The first shock in Figure 6.11(a) is well predicted by the model in terms of arrival time and peak pressure, but the arrival of the second shock is slightly earlier in the model than seen in the experimental data. The arrival of a significant shock at 8ms is not entirely missed by the model, but only a small pressure rise to a maximum of 50kPa is seen in the model, compared to a peak shock magnitude of 250kPa seen in experimental data. Similarly, between 10ms and 15ms there is a significant pressure rise in the experimental data, and the time and magnitude of this is not captured by the model, which leads to a noticeable deviation in the cumulative impulse data in Figure 6.11(b) after 13ms.

In Section 5.6.1 issues with the experimental test data from sensors within the cylinders

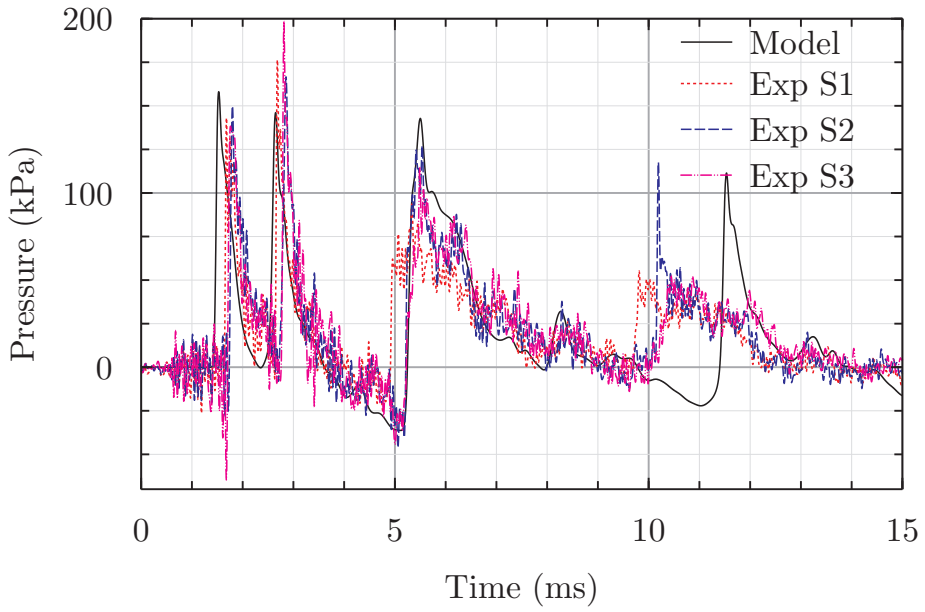

(a) Pressure history

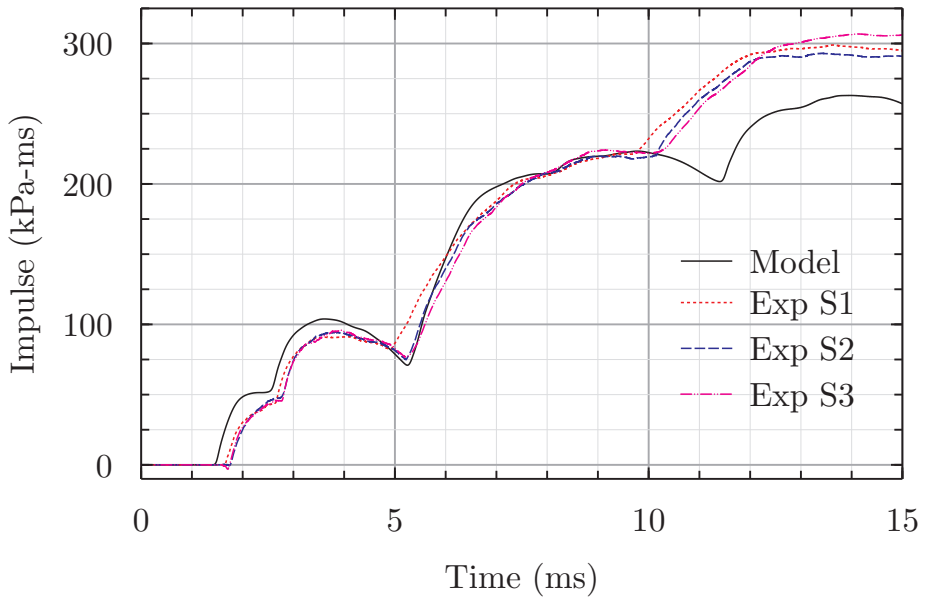

(b) Cumulative impulse

Figure 6.9: Comparison of model and experimental data from measurement location 5 in A1

was discussed, and it was mentioned that data from the cylinders was not presented due to difficulties in examining the data and lack of confidence in the results. Figure 6.12 shows model data and experimental data from the cylinder in A2, and excellent similarity is seen between the 4 data sets. The primary difference between experimental and numerical data occurs between 0.8ms and 1ms, where the model predicts a higher peak shock pressure and positive phase duration, which leads to a corresponding over prediction of the cumulative impulse at this time, which is shown in Figure 6.12(b). Over the remaining time, the model predicts both the arrival time and magnitude of shocks very well, and also predicts the value of quasi-static pressures between shocks well. This leads to a good prediction of the cumulative impulse history, with the major

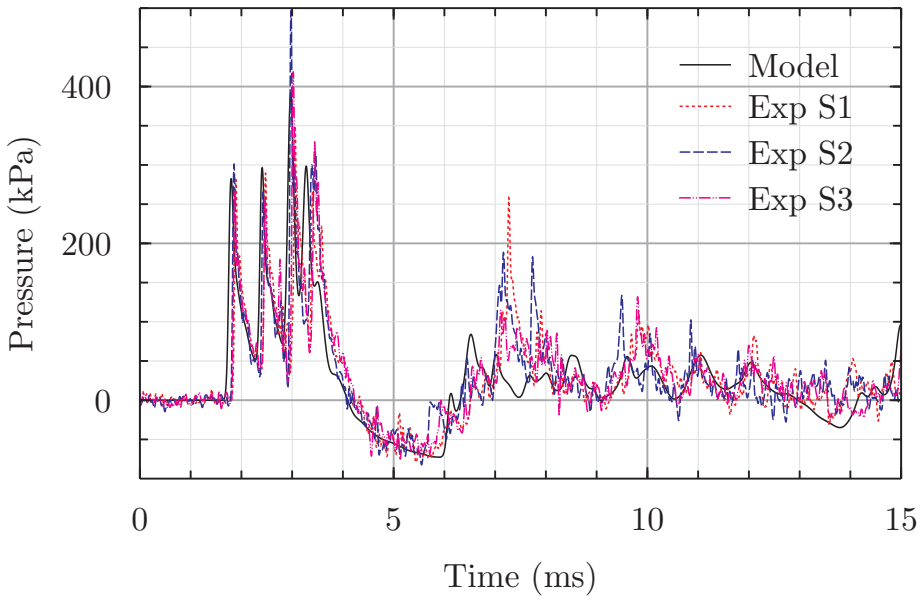

(a) Pressure history

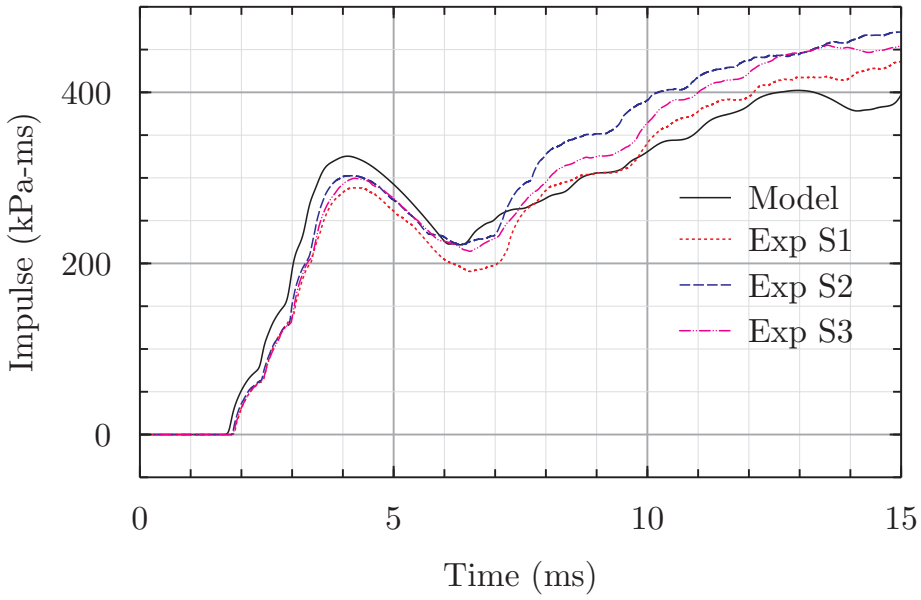

(b) Cumulative impulse

Figure 6.10: Comparison of model and experimental data from measurement location 2 in A2

difference between the final cumulative impulse between the model and experimental shots 1 and 3 being caused by the over prediction of the first shock parameters.

6.3.4 Arrangement 3

Figure 6.13(a) shows some of the closest similarity between experimental data and model, with the time, magnitude and duration all the major features of all 3 experimental test shots replicated well by the numerical model. As with other arrangements, the arrival first shock in the model is slightly early, and the peak pressure in the first 2 shocks is under predicted, and it can be seen that the shock at 13ms arrives later in models than in experiments. The effect of this can be seen in the cumulative impulse plot in Figure

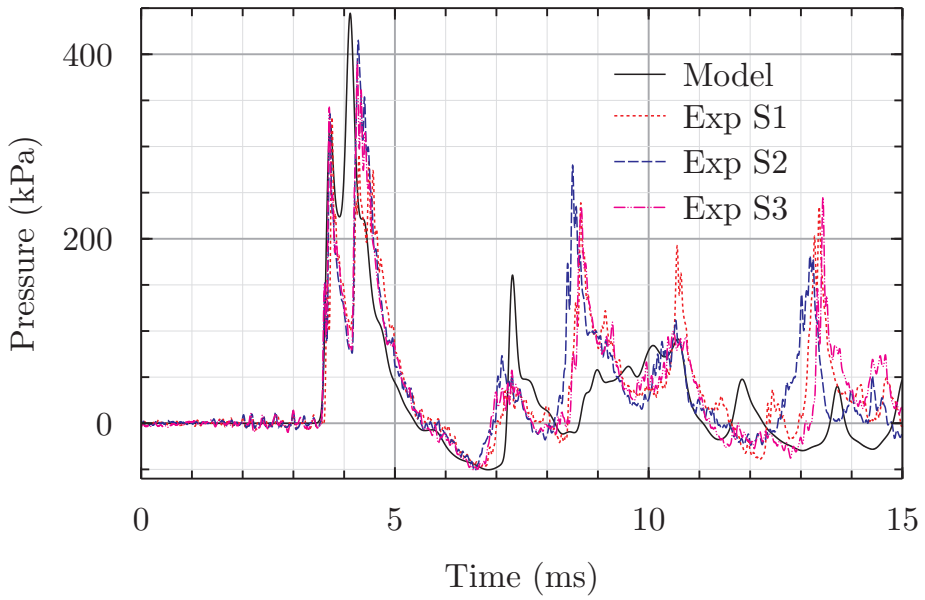

(a) Pressure history

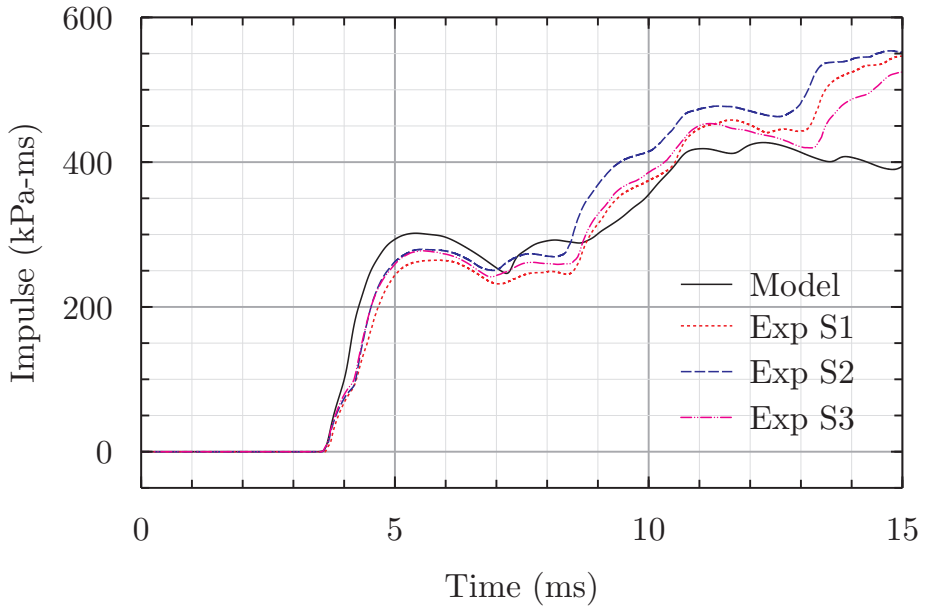

(b) Cumulative impulse

Figure 6.11: Comparison of model and experimental data from measurement location 3 in A2

6.13(b), where the magnitude of the cumulative impulse at 4ms is marginally higher for the numerical model, and the sharp rise seen in the experimental data at 13ms is later and less significant in the models.

Measurement location 3 in A3, shown in Figure 6.14, offers similar challenge for modelling to capture as seen at measurement location 2 in A2, with a number of reflected shocks over a short space of time between 2.5ms and 4ms, caused simultaneous reflections from a number of surrounding surfaces. The first two shocks seen in Figure 6.14(a) are predicted well by the model, but the third shock arrives earlier in the model and under predicts the peak pressure by around 250 kPa. It should be noted at this point that the experimental peak at 3.6ms is exceptionally sharp, with an almost indistinguishable

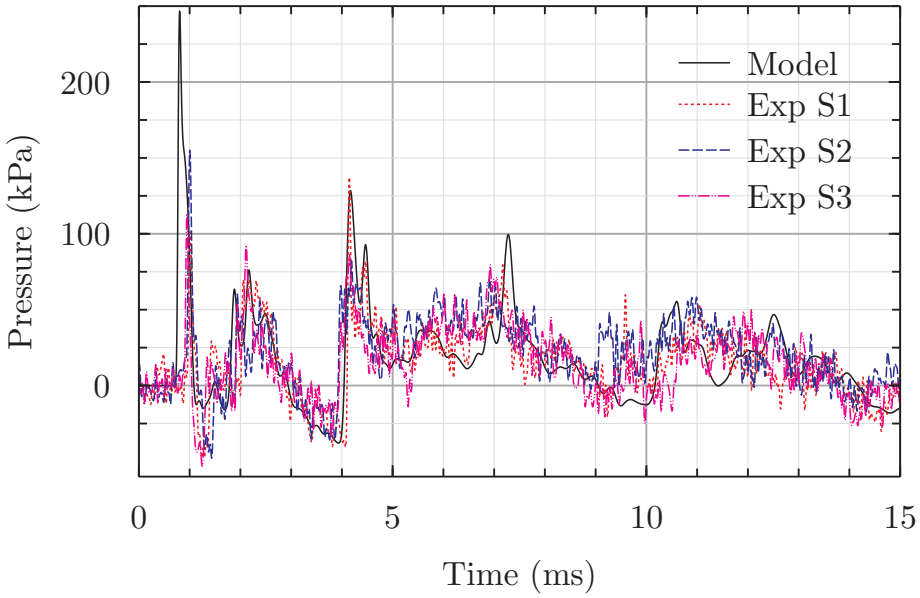

(a) Pressure history

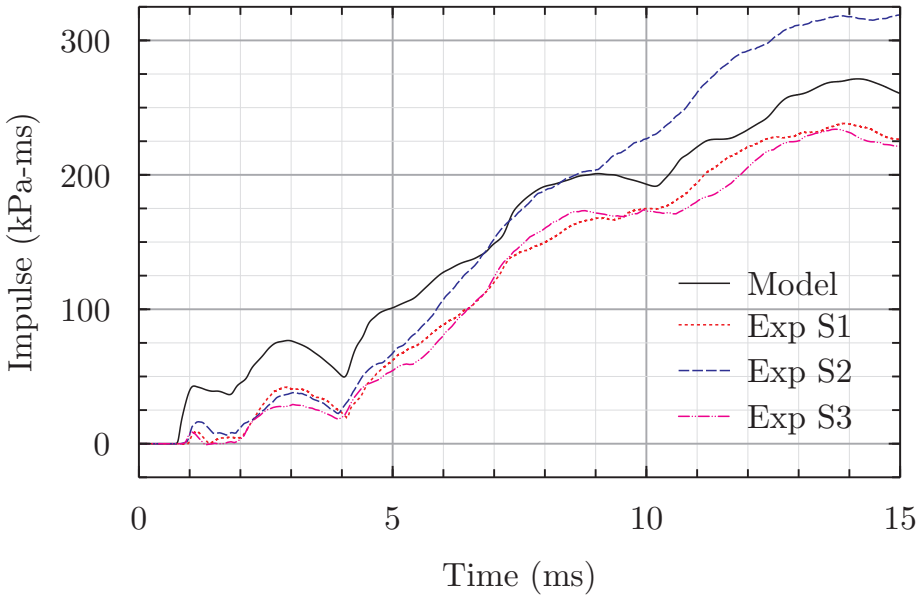

(b) Cumulative impulse

Figure 6.12: Comparison of model and experimental data from measurement location 4 in A2

width between the ascending and descending lines, which given the mesh required to resolve this is unlikely to be well revealed other than by exceptionally finely meshed models. Between 7ms and 12ms the model shows all the same features as the experimental data, but can be seen to have a positive and negative shift which prevents the data lying on top of each other. Over the period between 7ms and 9ms, the model data shows much the same shape, but is 50kPa lower than experimental data, whereas between 10.5ms and 12ms the model data is 50kPa higher. The effect of this can be seen on the cumulative impulse in Figure 6.14(b), where the model impulse deviates away at 7ms, but catches up with the experimental curve at 12.5ms. This indicates, as with other models, that over the initial time where no secondary combustion is considered, the model is very capable of predicting the impulse behaviour, although peak pressures

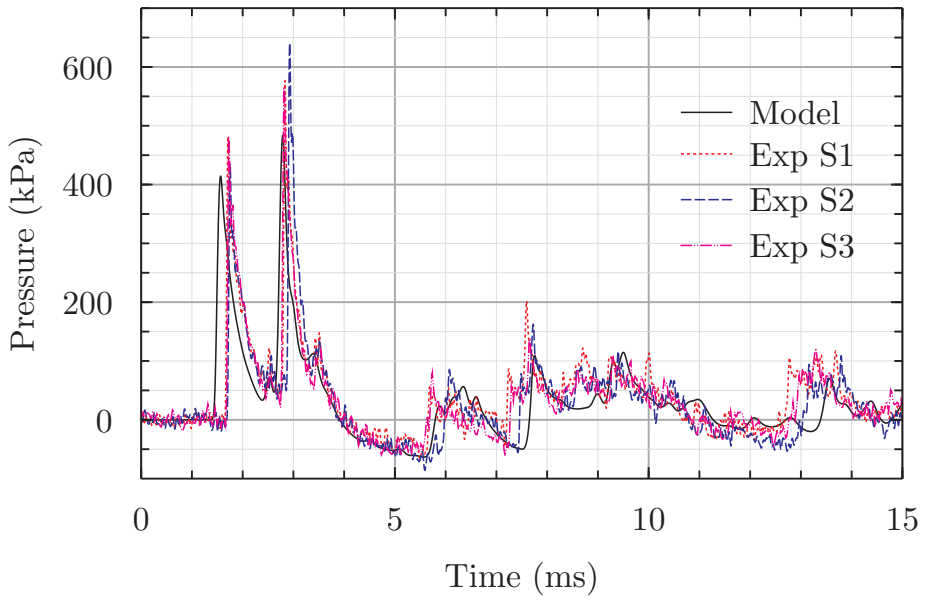

(a) Pressure history

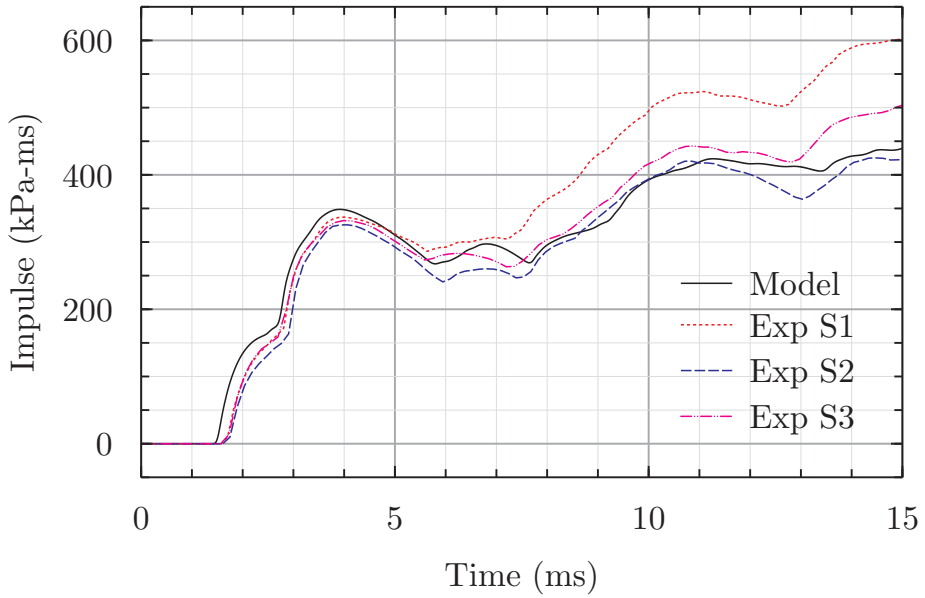

(b) Cumulative impulse

Figure 6.13: Comparison of model and experimental data from measurement location 1 in A3

are under predicted, especially where the peaks are sharp as shown in Figure 6.14(a) 3.6ms. Later time pressures between 7ms and 15ms where afterburn energy is considered by the model, a good general trend is seen between the models, but this would indicate that the simplified afterburn model performs less well in this location than in others, such as shown in Figure 6.13(a).

Figure 6.15 shows pressure and impulse at measurement location 5, and follows Figure 6.8 by showing good similarity between numerical and experimental data between 0ms and 15ms, but fails to predict the time of the shock at 10ms, which consequently results in the model failing to capture the value of the cumulative impulse at 15ms, despite the excellent prediction up to 10ms. Importantly, the model captures the stand out feature that differentiates the pressure history at location 5 in A3 compared with A1, with the

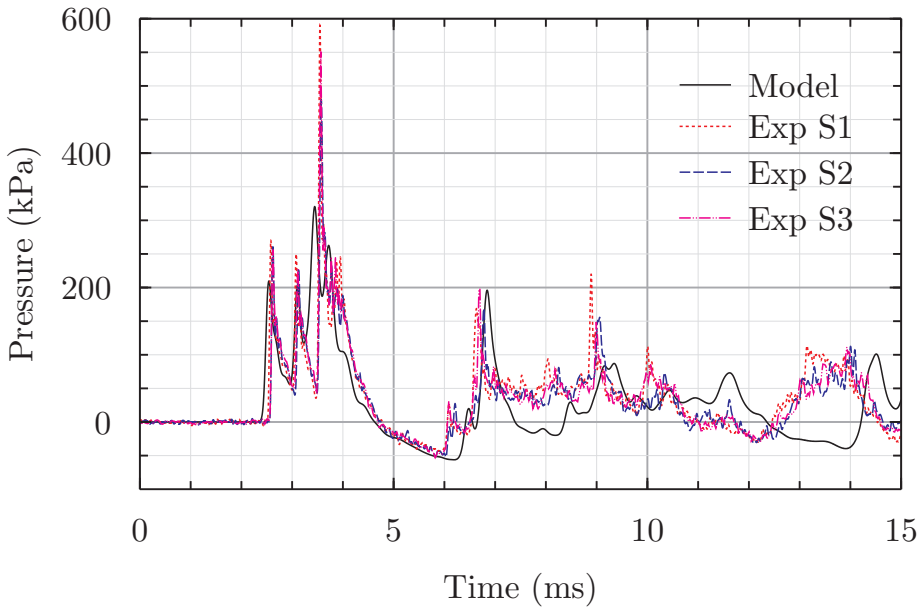

(a) Pressure history

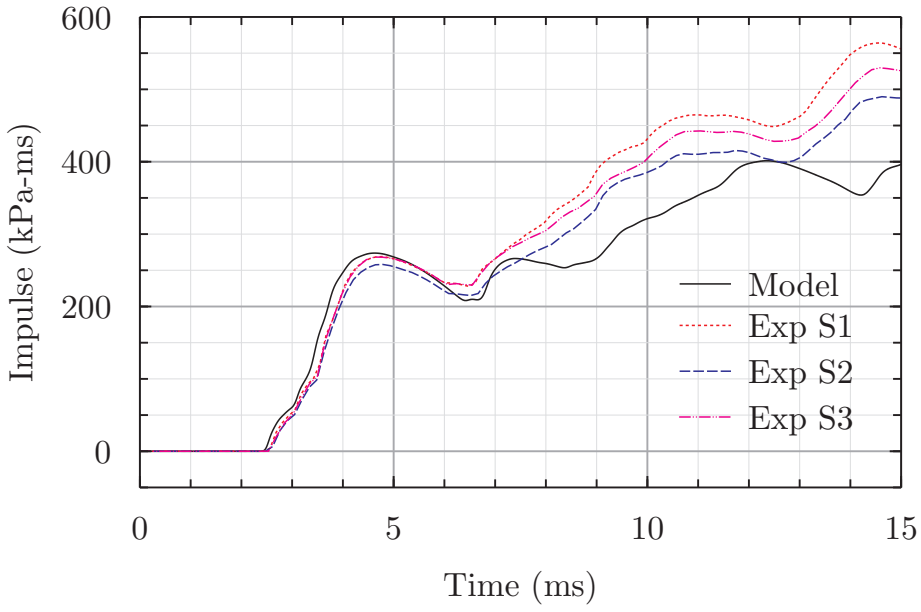

(b) Cumulative impulse

Figure 6.14: Comparison of model and experimental data from measurement location 3 in A3

magnitude, duration and timing of the shock at 8.3ms matching very closely with the experimental data.

6.3.5 Arrangement 4

This arrangement made use of a central aluminium panel to investigate deformation and it's result on pressures. The displacement of a central point on the panel begins for both the model and experimental data is shown in Figure 6.16. Displacement starts at a similar time for both the model and experiment, but correlation is difficult to identify between 3ms and 4ms as some instabilities were identified in the experimental data, as discussed in Section 5.5.5. If experimental displacement history assumed positive

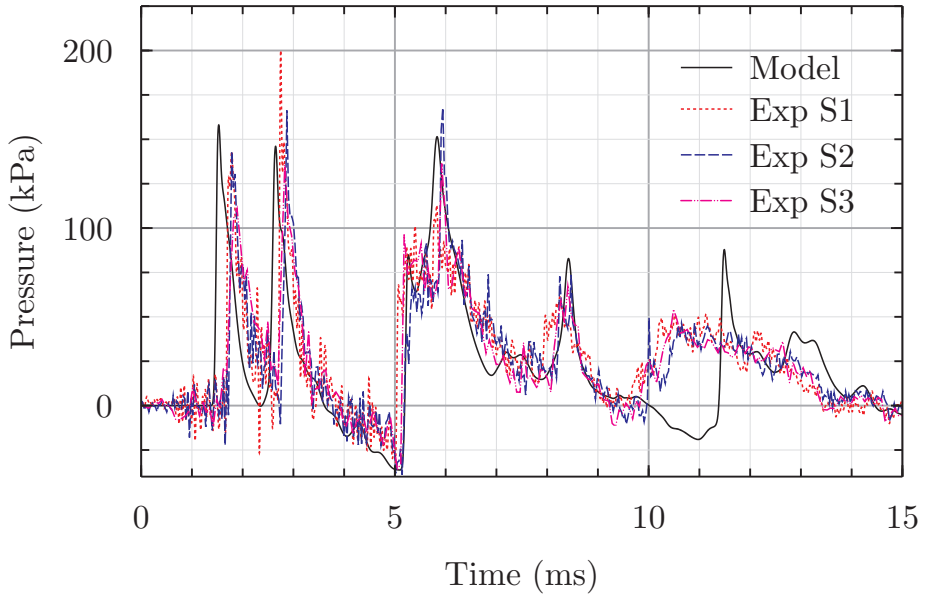

(a) Pressure history

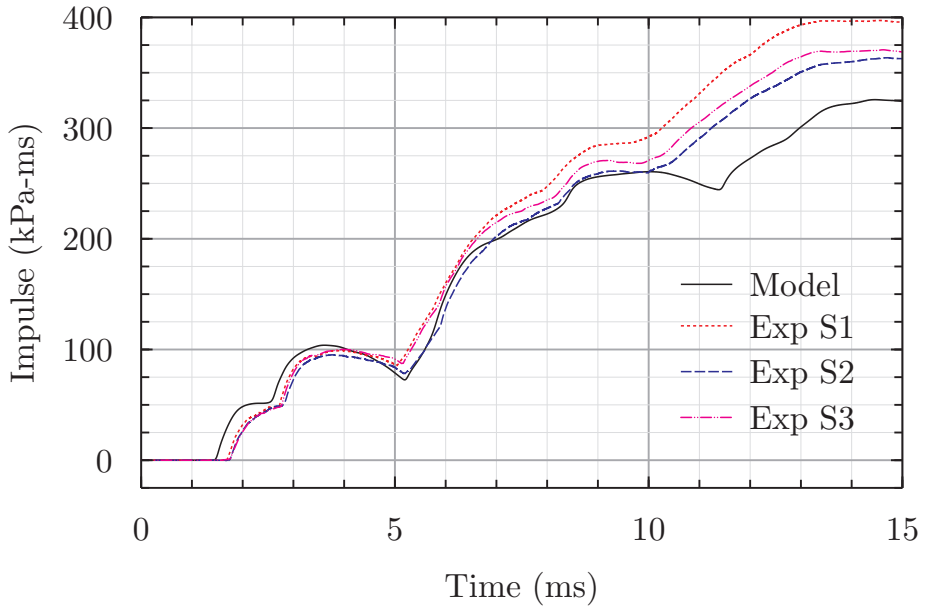

(b) Cumulative impulse

Figure 6.15: Comparison of model and experimental data from measurement location 5 in A3

through this phase (to 4ms) and a smooth curve drawn through experimental data between 2.8ms and 5ms, good agreement would be found with modelling between 0 and 4.5ms for displacement, as similar gradients are seen between the two data sets either side of the area of instability. At 5.2ms, the rate of displacement begins to decrease in the numerical model, reaching a peak displacement of 100mm at 6ms, while the experimental measurement of displacement continues at the same rate until 6.3ms, at which point a peak displacement of 150mm is reached and a much more rapid deceleration of the panel follow, compared to the model. Experimental data past this time is difficult to interpret, although instabilities suggest some failure at or around the fixings adjacent to the measurement point around this time, whereas a maintained displacement slightly

below the peak value shows the panel has remained fixed in position in the model.

A more full field visualisation of the displacement history can be seen in Figure 6.17, which shows a comparison between stills from high speed video (HSV) data and snapshots from animation of numerical models. It is difficult to make a quantitative comparison between the data, as no scale was used in the experimental testing, but it provides a graphical comparison of the deformation modes seen in the models and experimental data, and rough quantitative data can be gathered knowing the dimensions of the test cell. At 3ms, displacement at the end of the panel is negligible in both the experimental and the model data, as shown in Figure 6.17(a) and (b), and fringes of z displacement in (c) confirm deformation is confined to the half of the panel closest to the charge. High speed video data at 8.75ms in Figure 6.17(d) shows high deformation at the end of the panel, with a deformation mode such that a central portion of the panel is displaced less than areas above and below it. This deformation is seen, although to a lesser extent, in the numerical model in (e) at this time, but the level of displacement is much lower. By measuring the point between the left hand test cell wall in the panel in both Figure 6.17(a) and (d) it is possible to identify a displacement of the lower region of the panel in (d) of approximately 85mm compared to 55mm in the model, which can be seen in Figure 6.17(f). There is also deformation mode similarity at 12ms, but the deformation mode shown experimentally in (g) is less pronounced than in (d) as the centre point of the panel continues to displace outwards, whereas model data shows more displacement mode similarity between (e) and (h). Figure 6.17(i) shows that the point of peak deformation remains in largely the same place over the course of the simulation, whereas data in Section 5.5.5 shows that the most significant permanent deformation in the experiment was seen at free end of the panel.

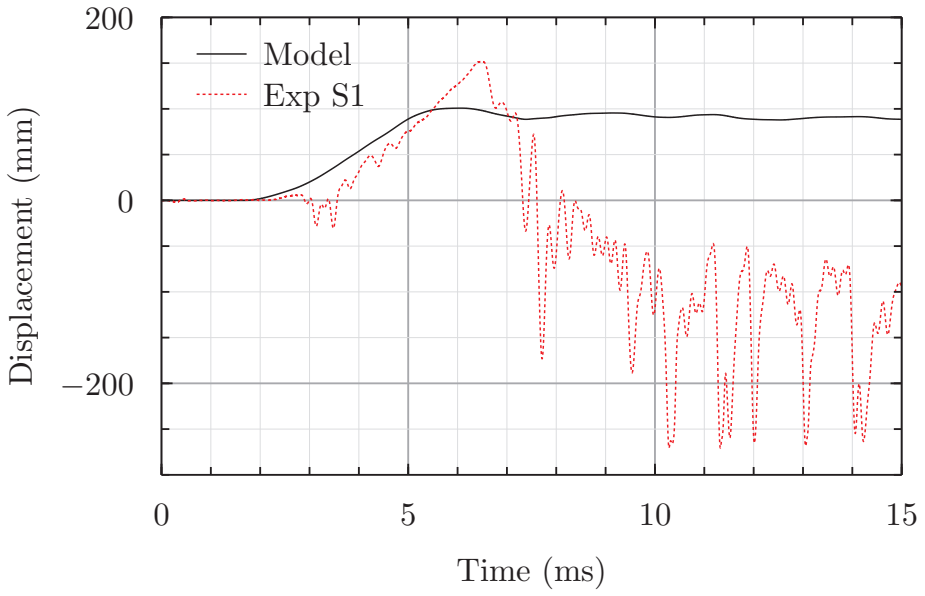

Figure 6.16: Displacement history for central point on panel for both model and experimental test A4

Pressure and cumulative impulse data from the model and experimental data at location 1 are shown in Figure 6.18. Experimental and model pressure history data in Figure 6.18(a) show the arrival of two shocks in quick succession over a period of 0.3ms, followed by a decay to reach atmospheric at 3ms. The model predicts slightly early ar-

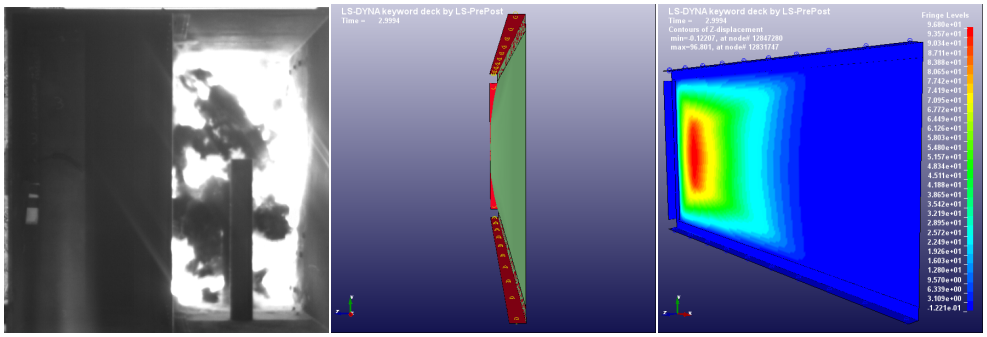

(a) HSV data at 2.97ms (b) end view of panel at 3ms (c) fringes of displacement at 3ms

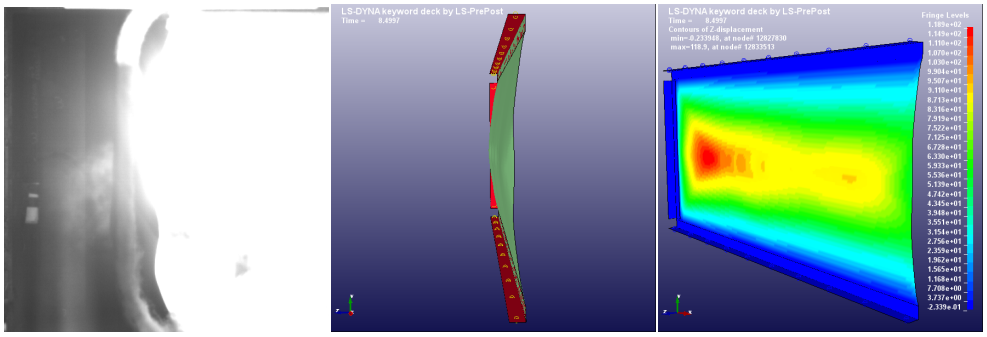

(d) HSV data at 8.75ms (e) end view of panel at 8.5ms (f) fringes of displacement at 8.5ms

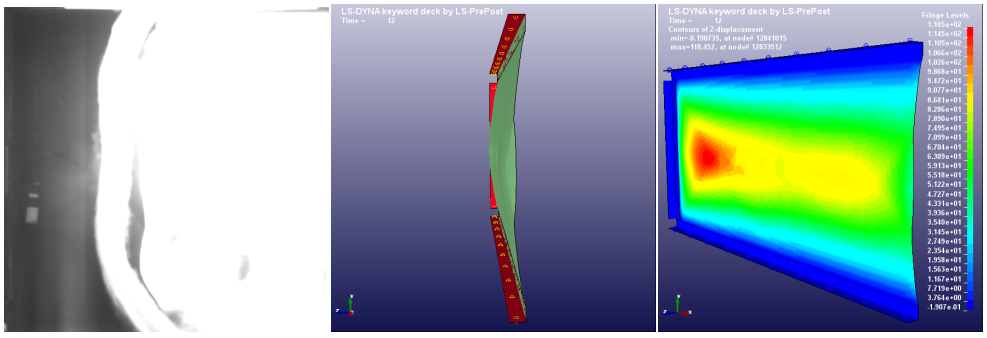

(g) HSV data at 12.19ms (h) end view of panel at 12ms (i) fringes of displacement at 12ms

Figure 6.17: Stills from high speed video alongside panel displacement data from LS-Dyna

rival of the first shock, but the timing of the second at 2.2ms is well predicted, although the peak pressure of both shocks is over predicted by the model by between 25kPa and 50kPa. The next two shocks between 3ms and 4.5ms show in reasonable agreement between experimental and model data, with the arrival of the model data lagging behind experimental data, and an under prediction of the peak pressure by 20kPa for the third shock and 70kPa for the fourth. A period of maintained high pressure follows between 5ms and 7ms which is not well predicted by the model, although a shock that exists in the experimental pressure trace at 5.7ms is present, albeit at a much lower magnitude, in the model data. It is at this point that cumulative impulse data in Figure 6.18(b) shows a significant deviation between the model data and experimental data, with impulse continuing to rise in the experimental data but plateauing in model data, leading to a cumulative impulse difference of 100kPa-ms at 6.5ms. Experimental data and model

data for pressure show similarity again after this time, meaning that this difference in cumulative impulse is maintained over the remaining duration, shown by the similarity in shape between model and experimental data between 7ms and 15ms.

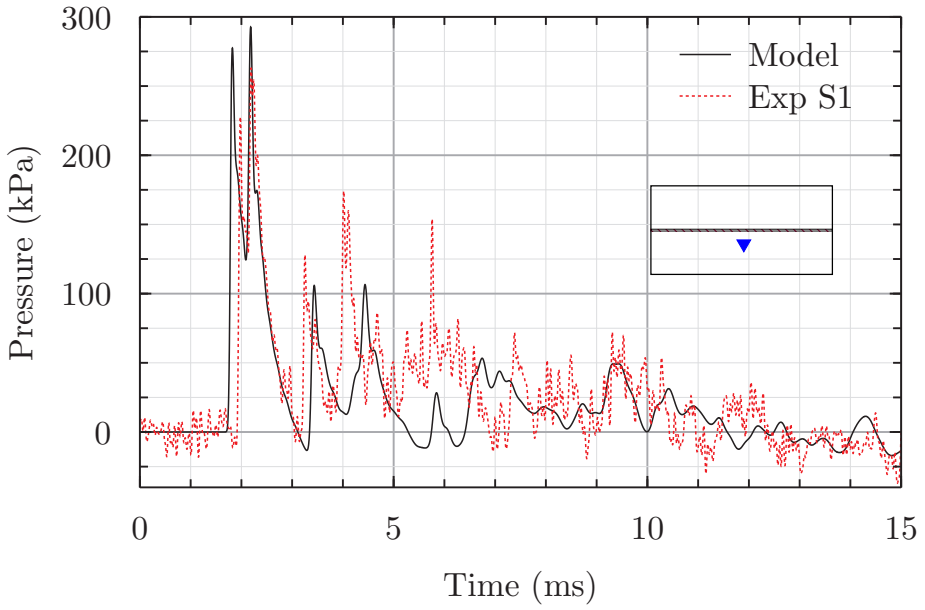

(a) Pressure history

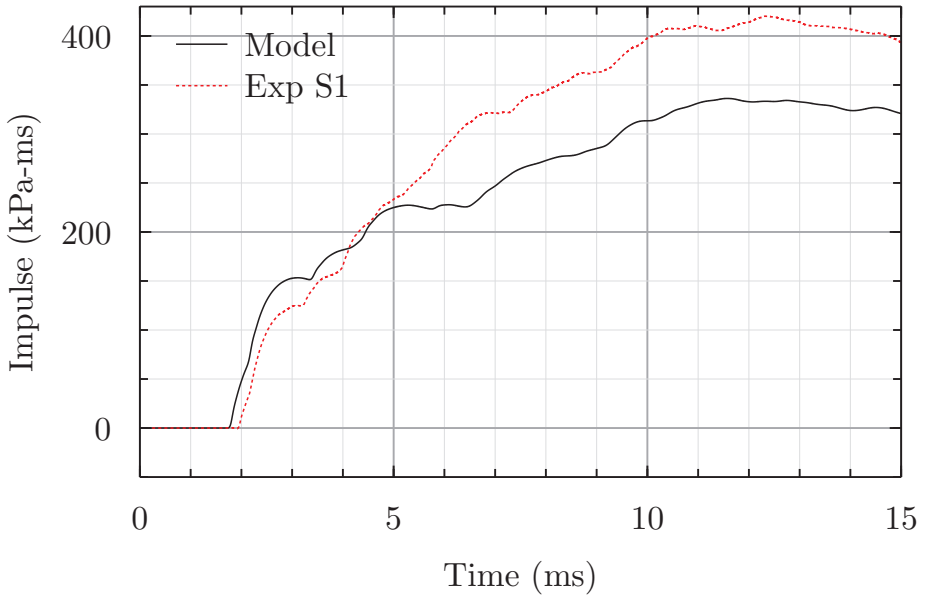

(b) Cumulative impulse

Figure 6.18: Comparison of pressure history data from location 1 on the roof of the test cell in A4

Data from pressure sensor location 4 are shown in Figure 6.19(a). Similarity is seen between the first 2 shocks, with the model predicting slightly earlier arrival of the first shock, and over prediction of both by approximately 30kPa. The experimental pressure between 4.8 and 8ms is less well predicted by the model, with the experimental data showing a strong shock at 4.8ms, but only 2 much weaker shocks are seen in the model at a similar time. There is also a decay to below atmospheric pressure seen in the model between 6ms and 7.5ms, whereas the experimental data is shows a maintained pressure

25kPa above atmospheric. The contrast between model and experimental data over this period leads a noticeable divergence in numerical and experimental impulse, shown in Figure 6.19(b). Pressure data similarity improves between 8 and 15ms, with both model and experimental data showing a almost linear decay of pressure from 25kPa to -25kPa over the period of 9ms to 15ms, leading to a close match in the shape of the impulse curve between 9ms and 15ms, with difference in impulse of 150kPa-ms maintained.

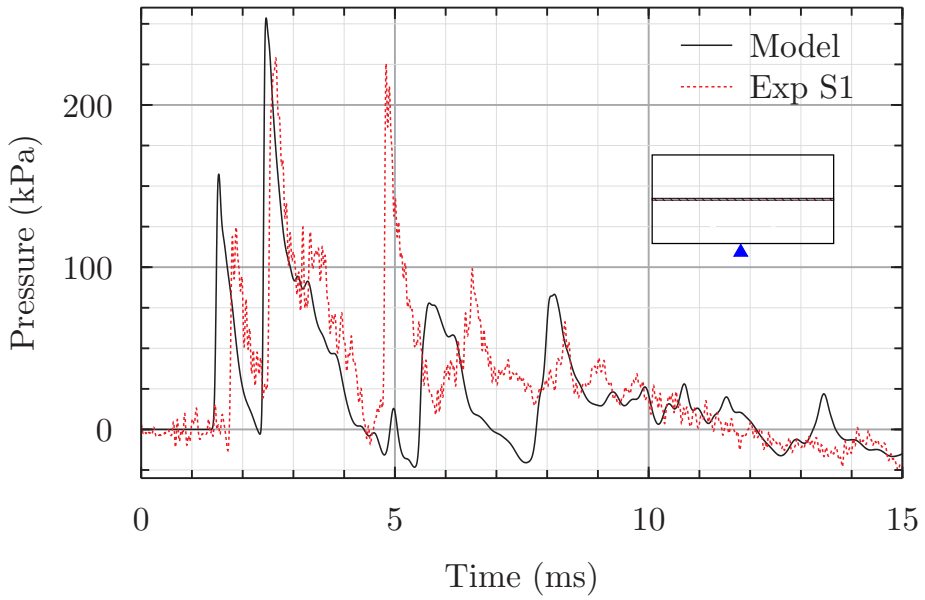

(a) Pressure history

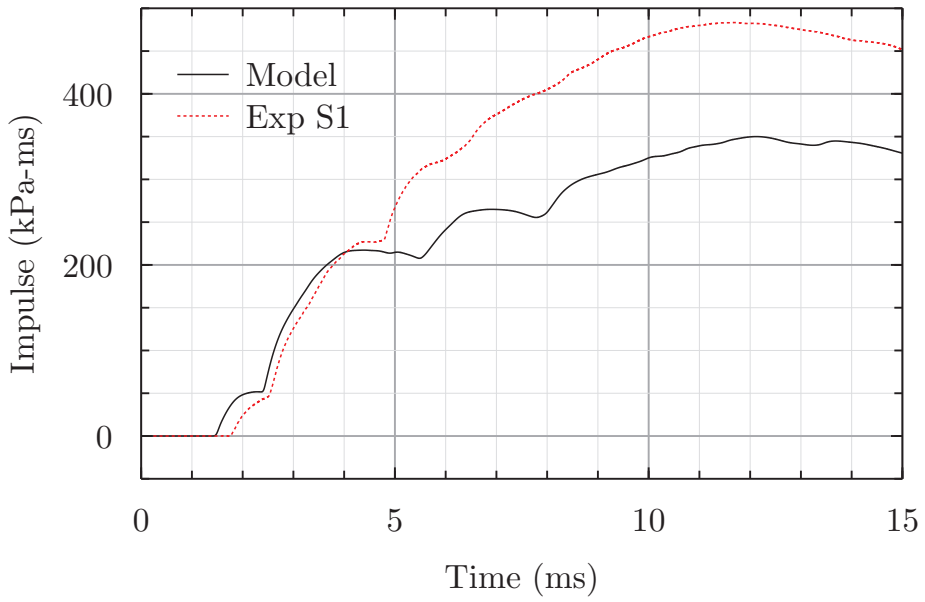

(b) Cumulative impulse

Figure 6.19: Comparison of pressure history data from location 4 in A4

Data from pressure sensor location 5 are shown in Figure 6.20(a). As with other locations, the arrival time and magnitude of the first shock is well predicted by the model, but differences between the model and experimental data begin as the pressure decays, with a slower decay predicted by the model, reaching atmospheric pressure 1.3ms after the pressure in the experimental test. Both experimental and model data show a

shock arrival around 7ms, but it is predicted later in the model, with a peak pressure value 100kPa lower than the peak of 225kPa seen in the experiment. Both sets of data then show a decay to below atmospheric, but it is occurs earlier and reaches a larger peak underpressure of -60kPa at 8.9ms in the experiment, compared to 30kPa at 9.9ms in the model. The cumulative impulse is shown in Figure 6.20(b), and shows similarity in the impulse shape until 10ms, after which there is very little agreement between either the magnitude or shape of the impulse curves.

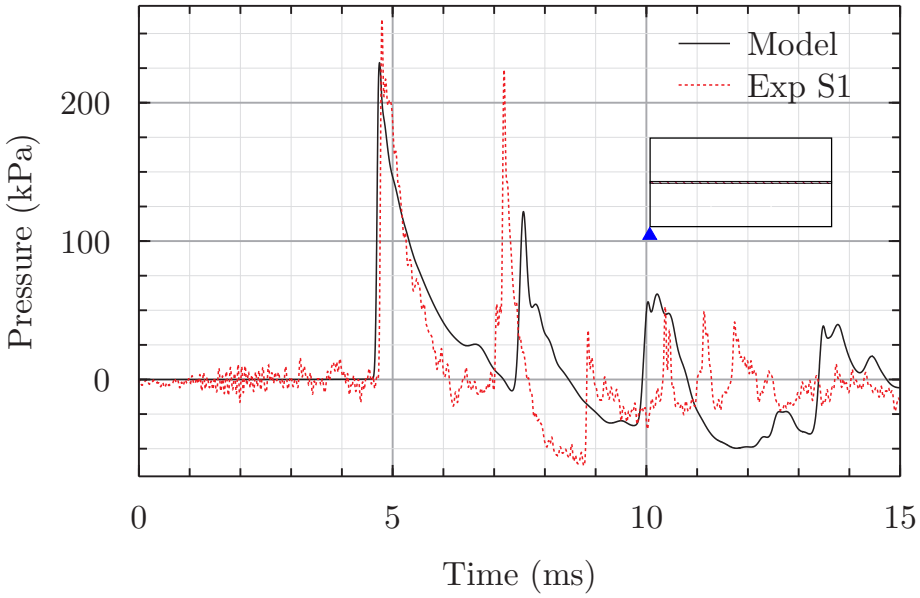

(a) Pressure history

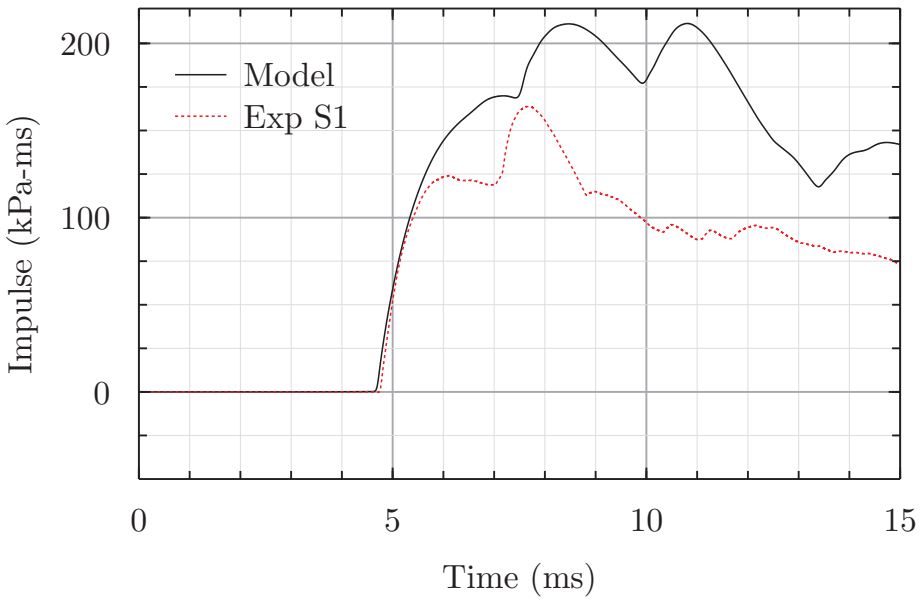

(b) Cumulative impulse

Figure 6.20: Comparison of pressure history data from location 5 in A4

6.4 Discussion

6.4.1 A1, A2 and A3

The quality of the data produced by numerical models has been shown to reproduce the data from experiments well, but there are still a number of occasions in which model data and experimental results do not exactly match.

Of the presented results, A2 location 3 (Figure 6.11 and A3 at location 3 (Figure 6.14) show most difference between models and experimental data, and of the data sets shown here these locations were the furthest from the point of detonation. As seen in Section 6.2.3.1, the presence of additional secondary combustion energy can modify not only the magnitude of shocks, but the time of their arrival too, thus the requirement in this modelling of adding all the secondary combustion energy at the same time is a likely source of error. As discussed in Section 6.2.3.2 the energy from secondary combustion does not manifest itself at all points of the air within the enclosure at the same time as assumed by the model, but follows behind the initial shockwave and occurs as the detonation products behind the shock mix with atmospheric air. The data shown in pressure plots for A2 location 3 and A3 location 3 does not entirely miss features, rather predicts them at the wrong time or magnitude, which is thought to be caused by the effects of secondary combustion. Accounting for the different arrival times of secondary combustion throughout the air domain has the potential to correct these errors. Despite this, the simplified account of secondary combustion presented here is generally effective, and ensures that results are significantly closer to the experimental results than they would be without it. Further understanding of secondary combustion is needed to accurately predicts it's effect, which would require some bespoke experiments, and could involve taking measurements not often taken as part of blast tests, such as temperature.

In most cases the experimental impulse were predicted well by the models, but where impulses are not well predicted, the differences between models and experimental data typically occur after 10ms. In many models, shocks that occurred between 10ms and 15ms had a smaller magnitude and later time of arrival than in experiments, which leads to a corresponding drop in impulse in the models compared to experimental data over this time period. This reduction and delay in the shocks in models is due to a combination of shock smearing and secondary combustion effects, both of which can alter the time and peak pressure of shocks.

Shock smearing occurs as result of the necessity to represent shock discontinuities in a rapidly changing but continuous manner, and the effects are particularly noticeable at locations where fluid structure interaction takes place. This leads to an under prediction of peak pressures which subsequently leads to a slower wave compared to a correct peak pressure prediction, and this effect compounds with each reflection. In some locations there is indication that shock smearing is not the primary cause of discrepancy between models and experimental data, particularly at sensor location 5 shown in Figures 6.9(a) and 6.15(a), where the value of the peak pressure in the shock at 10ms is higher in the models than experiments, but the shock arrives 1.5ms later.

Comparison between experimental and model data shows that the modelling method can pick up key features and is suitable for the purposes required for further modelling. Data from sensor location 5 shown in Figures 6.9 and 6.15 on pages 154 and 160 shows

that the effect of the baffles on pressure history is captured accurately by the models. The extra shock caused by the presence of the baffle occurs at 8ms in Figure 6.15(a), and the magnitude and time of this is very well reproduced well by the numerical model. Model data also confirms that pressure histories from sensors on cylinders can be predicted well. Together the experimental and numerical data give a good deal of confidence in both the validity of the experimental and numerical data. The angle of the tangent to the cylinder at the sensor location is the crucial feature determining the pressure, and the location of the sensor in both the experiment and models means that the pressure measured is neither the fully reflected nor the side on overpressure. This is complex from a modelling perspective and the angular dependence means only small differences in the position of the sensor can lead to dissimilarity between experimental and model data. Minor differences between the position of the sensor in the experimental test and the models is likely, given the difficulty in precisely positioning the cylinder in the experiments. Importantly, good predictions of the pressure time history are made, which forms the input for injury models described in Chapter 3 and used in Chapter 7.

6.4.2 A4

6.4.2.1 Boundary conditions

With hindsight the restraint of the plate used in the experimental testing was insufficient, leading to difficulties in replicating the experimental data with numerical models, and this is a learning point for future work.

Model data for arrangement 4 followed previous arrangements in showing generally good agreement with experimental data, but the single test conducted with arrangement 4 behaved in a way which caused a number of uncertainties that have proved difficult to model accurately.

The restraint of the clamped plate in the experimental testing was difficult to determine exactly, which causes a number of problems for the modelling effort. The description of the failure in Section 5.5.5 indicates a number of ways in which restraint differed from the fully clamped condition the bolted joint were supposed to achieve. In the experiment, bolts were used to hold the supporting angle section to the test cell, and were also used to provide clamping force to hold the aluminium panel in position on the support, and prevent any relative slip between the panel and support. Had both of these connections behaved as designed, this would have provided a good representation of a perfectly clamped boundary condition, and could have been implemented in a numerical model very simply, purely with nodal constraints. In reality, the experimental restraint failed in 2 ways; failure of the bolts connecting the support to the test cell, and insufficient restraint of the panel within the support causing significant slippage. This added complexity into the numerical model by attempting to account for this behaviour, by physically modelling the supporting structure and the bolted connection, although no attempt was made to account for slippage between the panel and support.

The boundary conditions in the model did not behave in the same way as the restraint in the experimental test, which can account for a significant amount of the discrepancy seen between model and experimental data for A4. The bolts were modelled in a simplified manner, and this connection method proved much more resilient than the physical bolted connections used in the test. The modelling method for these bolts would have been greatly improved by undertaking validation testing on bolted connections, but

limited time and experimental facilities prevented this.

The modelling method applied allows some unrealistic structural behaviour of the connection to occur, which is partly responsible for the lack of failure in the numerical model. A certain amount of relative motion was possible between the ends of the beam elements used to model bolts, as the element is 10mm long, and is constrained at one node (closest to the test cell structure) and fixed to the support at the other node. This is as if there is a 10mm between the surfaces being bolted, as no shear force can be generated against the sides of the hole using the current model, as this interaction is not considered. In reality, relative motion between the support and the test cell creates a shear force on the bolt at the point where a wall of the test cell meets the supporting angle section, which is not accounted for in the bolt model used. In addition to this, a certain amount of preload[2] was placed on the bolts under test, which was not accounted for in the model. A greater appreciation of the combined effects of preload and relative node motion could have improved the accuracy of the model. The modelling method also used a tied nodes to surface contact, which for most connections was appropriate, but a few of the bolted connection in the experimental test showed the bolt being pulled through the angle section. The contact method used would not allow such failure, and even a dedicated model of that joint using a full solid element 3D model would struggle to fully capture this behaviour.

As noted earlier the panel in the model was assumed to have no motion relative to the support, which was not what happened in reality. Although this was known when the model was generated, it proved difficult to find a way of modelling this connection. Failure to model this behaviour no doubt led to a reduced peak deflection, which in turn would have generated different forces on the support and subsequently the bolts.

With hindsight, the experimental restraint, or failure of, hindered the validation process and made it difficult to produce models which were an entirely accurate depiction of the physical problem. As well as improving the restraint, improvements could be made to the overall test and modelling programme to improve the validation effort. Dynamic mechanical testing of the bolted connections under the loading modes expected would have produced better models of this connection, and identified how well the applied method could represent the physical bolted connections. A wealth of data is available from numerical models, and with further measurements taken from experimental data it may have been possible to provide a more complete comparison of the mechanical behaviour of the panel, not merely deflection, which proved difficult to measure. Data from strain gauges, or providing a simple way of timing any failure, seem in retrospect simple and effective ways to expand the amount of data collected and thus improve the validation study.

6.4.2.2 Displacement and deformation

The displacement of the panel occurs by a travelling hinge, a commonly seen deformation mode when structures are subject to an impulsive load. As well as this deformation hinge travelling from the top and bottom of the panel, there is also a hinge travelling from the end of the panel end opposite the charge towards the free end, and after this elastic response leads to oscillations at the centre of the plate, as seen in Figure 6.16. This process continues for longer and reaches a higher value in the experiments, which can

[2]The torque applied to a bolt is directly related to the tension, and it is this tension, used to provide the clamping force, which is not accounted for.

in part be explained by vertical translation of the panel within the support, allowing a certain amount of movement before the force of the support led to the formation of the hinge. As this is not represented in the model, the hinge forms and begins to propagate inwards earlier, and therefore peak displacement occurs earlier, and the lack of initial slip at the boundaries leads to a lower peak deformation.

The movement of these hinges is responsible for the deformation mode seen at the free end of the model. The hinges propagated from the top and bottom supports along the length of the panel, and as they reached the free end of the panel they caused the deformation mode seen in both the experimental test images and the model in Figure 6.17. The level of deformation is clearly higher in the experimental test data, but similar behaviour shown in Figure 6.21 is seen in Figure 6.17(d) and (g), with hinges moving towards the centre of the free end of the panel. Stiffer response of the fully clamped model compared to much more free experimental test means it takes longer for hinges to reach the centre of the panel, and this increased stiffness in the model compared to the experiment also contributes to the lower deformation at the free end.

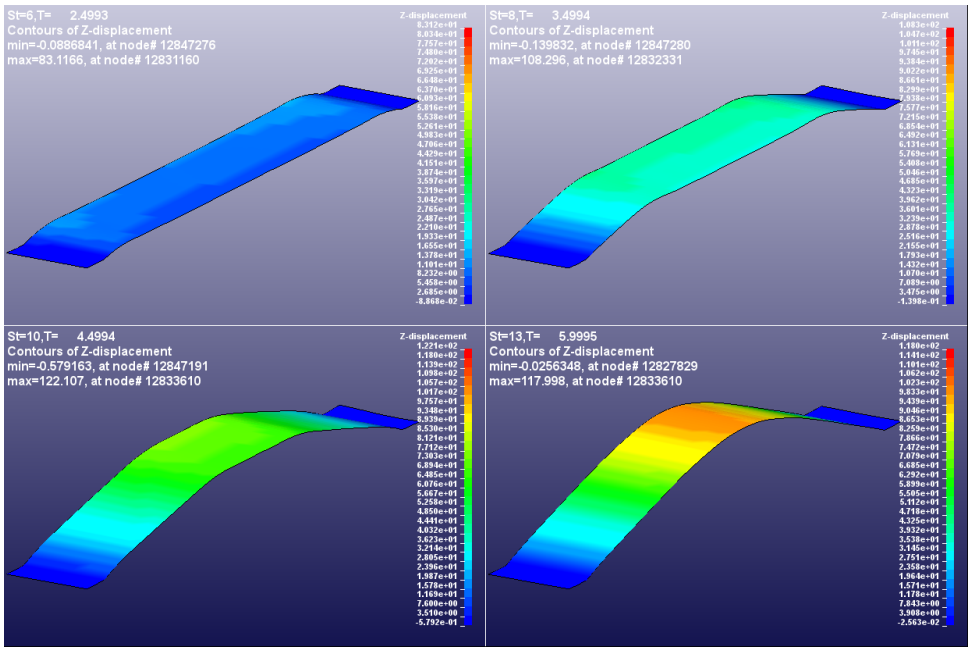

Figure 6.21: Progression of hinge travelling inwards on a strip of the panel

As well as boundary conditions, the loading applied to panel could contribute to the inconsistencies seen between the deformation of the model and that seen in the experiment. The loading is applied using a penalty method as described in Chapter 4, where a force is applied to the ALE fluid to prevent penetration though a Lagrangian surface, and it is this force which is used to provide loading for the structure. If this coupling force is not sufficient it can lead to lower predicted overpressures, and a lower force being applied to the structure, subsequently leading to a lower displacement. The mesh density can play a significant role in the determination of this coupling force, and the control card allows the user to modify a number of very specific parameters which control the way coupling is handled by the code. Rather than be able to achieve anything the user desires within this control card, it is designed to overcome instabilities and poor coupling under complex scenarios, where the defaults are insufficient. Without better controlled experimental data, it could prove a significant challenge to identify which of

the many issues discussed here was responsible for differences between experimental and numerical data.

It was evident from the model that strain rates remained of the order of magnitude $10^{-2}s^{-1}$ or below in the aluminium panel throughout, and lower still in the supporting steel angle section, which justifies the use of the simple plasticity models, where strain rate was not considered. Use of complex models such as the Johnson-Cook model would have only added significantly to the computation time, and would be expected to give little improvement in results.

6.4.2.3 Pressure histories

Figures 6.18, 6.19 and 6.20 all show periods where the reflection of shocks within the test cell in the models was not consistent with that observed in experiments. At location 1 (Figure 6.18), the period of inconsistency is very small, but it is more considerable at location 4 (Figure 6.19) and further still at location 5 (Figure 6.20). At location 1, the sensor is positioned perpendicular to the wall, and as a result sees very few reflection that have originated from a normal reflection on the aluminium panel. Both locations 4 and 5 on the other hand, are located opposite the panel, so any reflections that arrive normally at these sensors will have originated from the panel. Between 5ms and 6ms, shocks in the experiments are missed by the models at locations 1 and 4 (although there are features displayed in the experimental data that are captured well by the model at this location, which is covered later in this section). In the experiment, it has been inferred that the panel has deformed more than in the model, which should mean that the model would predict an earlier and stronger reflection, but this is not the case. Although a full field visualisation of data is available from the numerical models, identifying what leads to these differences is difficult without also knowing the particular shock reflections that occur in the experiment. It is likely though, that what is missed at both location 1 and 4 between 5ms and 7ms originates at the panel, through 2 shocks combining, or due to differences in the deformation and the subsequent shock reflection.

Pressure data at location 5 shows the highest deviation between model and experimental data of the three pressure sensor locations. This is caused primarily by the significant difference in the deformation of the panel end directly opposite this sensor location, and extension of the symmetry boundary condition along the entire face of the model, compared to the experiment in which shocks can diffract around the edge of the test cell. From Figures 5.28 and 6.17 it can be seen that the shape the reflecting surface is very different in the experiment and the model, which will make a significant difference to the shocks experienced on the wall directly opposite. The high curvature of the experimental panel may have served to slightly confine the shocks at this point, which would explain the higher number of reflections seen, especially between 10ms and 12ms. The strength of the reflected shocks is higher at this location in the model, which can be seen clearly in the cumulative impulse curve in Figure 6.20(b). The fact that shocks are reflected more normally in the model, due to the lower deformation in the model compared to the experiment, is the likely cause of this. The symmetry boundary condition is also not the same in the model and the experiment; the symmetry boundary condition is applied to the whole xy face of the ALE model, but the experimental symmetry boundary breaks down at the end of the test cell, where shocks are free to diffract into free space, which cannot be considered with the current model.

There are a number of features of the pressure curves that show good agreement between experimental data and models. Good agreement between arrival time and peak pressure of both incident and reflected shocks is seen over the first 5ms is seen in all models, before significant deformation of the panel has taken place. Importantly, at both locations 1 and 4 there are non shock quasi static pressures between 9ms and 15ms which are predicted well by the model, which validates the use of functions to add additional energy to the simulation to account for secondary combustions. This contribution leads to very good agreement between the shape of the experimental and numerical impulse curves at these location, and without this additional energy the cumulative impulse curve at both of these locations would not show a continued rise at 12ms, which is seen in both experiment and model at locations 1 and 4. Although the agreement between experimental and numerical pressure traces is not as good as seen in arrangements without a flexible wall, model data at locations 1 and 4 in A4 give a good level in the prediction capabilities of the developed modelling method.

6.5 Conclusions and implications

Numerical models of the experimental test arrangements presented in Chapter 5 have been presented, and on the whole show the modelling methods developed in both this Chapter and Chapter 4 are capable of predicting the behaviour measured in experimental tests. There are cases where there is excellent agreement, and where agreement is less good the causes can be understood.

It was seen that prediction of the arrival time for shock waves was very good early on in numerical predictions, but as the solutions progressed shock smearing caused increasingly later predictions of the arrival time. Over the times modelled here though, this was not seen to make significant impact on the ability of models to predict cumulative impulse histories. Over the relatively short durations where the pressure affects the chest wall velocity prediction, as shown in Chapter 7, the impact of reduced accuracy of pressure predictions at later times is not significant.

Large differences between the boundary conditions in the experiment and model meant that pressure and deformation histories for arrangement 4 were not entirely in agreement. Failure of the supporting structures in the experiment led to a significantly different deformation of the aluminium panel, which in turn altered the pattern of reflection within the test cell, compared to the model. Time and finance restrictions, unfortunately prevented this section of testing work being repeated. Despite this, pressure history data from at least some of the measured locations agreed well, with good prediction of shock pressures and quasi static pressures.

A simplified method was applied in numerical model to account for additional energy released as a result of secondary combustion or afterburn. The method was shown to improve the prediction of the timing of shocks, quasi static pressures and cumulative impulse histories over the modelled time, but the method used does have some disadvantages that limits its applicability to a wide range of problems. In its current form, additional energy is added to all elements of the fluid within an ALE multi-material group at the same time, which is not appropriate for all problems. Improving the method to allow energy addition to be considered as a function of both time and distance from charge, instead of purely as a function of time would allow significant improvements to the method, as would experimental studies of the effect of secondary combustion on

pressures at different distances from the point of detonation.

The capture of pressure differences due to the effect of baffles, as well as good agreement between model and experimental data for pressures measured at the cylinders are important results for modelling in the following Chapter. This gives confidence in the ability of the modelling method to capture the effect of features such as draught screens, partitions and seats on the dynamic pressure history, as well as predicting the pressures experienced around a cylinder representing a person, which forms a crucial part of the input into the injury model tool developed in Chapter 3.

The following Chapter uses the modelling methods developed and described here to predict the effect of blast loads on rail vehicles and the passengers they carry.

7

Vehicle models

7.1 Parametric study of rail vehicle design and operational variables

In Chapter 1, the hypothesis below was posed. Previous chapters have described the development of techniques for predicting injury and structural deformation that can feed into a engineering model to answer this hypothesis.

> "Rail vehicle design can influence the pattern of injury seen in passengers when an improvised explosive device is detonated within a rail vehicle."

To answer this hypothesis, this chapter describes the use of ALE models of rail vehicles in conjunction with injury models to investigate a number of different cases (referred to using the prefix C throughout this chapter) of both design and operational variables. The effect of the structural modelling technique (full or rigid), windows, doors, tunnels open carriages, presence of seats and draught screens and passenger density are all investigated, and a summary of the features investigated in each case can be found in Table 7.9.

The parametric investigation found that although some design features can alter the risk of injury, the passenger density was a greater driver of differences in injury prediction. Chest wall velocities were seen to be lower when passengers were shielded from high pressures by either structures, other passengers, or when reflecting surfaces are removed such as in the case of open doors or through carriage designs, and higher when the presence of either a passenger or structure served to reflect pressures toward one of the numerical sensor locations (prefixed with S throughout this chapter) placed on the surface of the surrogate passenger.

Computational limitations meant that mesh refinement to the levels described in Chapter 6 could not be used, and as a result the prediction of peak pressures experienced by passengers will be lower than that seen in reality. The secondary combustion model described in Chapter 5 could also not be used due to geometrical limitations of the model, which were discussed in Chapter 5 and described in relation to rail vehicles here in Section 7.3. The failure to include the secondary combustion model is unlikely to significantly alter the predicted levels of injury, but the level of mesh refinement is likely to lead to underpredictions of the peak chest wall velocity, and the effect of this on overall injury levels is discussed in Section 7.6.

7.1.1 Structure of this chapter

This chapter first looks at the development of an appropriate and representative rail vehicle finite element model, which is based on an existing model of a Class 165 rail vehicle. A verification of the performance of these features such as doors, windows and draught screens against railway group standard GM/RT2100 has been undertaken and shows that these features perform as well in the model as they would be expected to perform in a rail vehicle in service. A mesh refinement study on the rail vehicle is undertaken, which also identifies the finest mesh that could be utilised within reasonable limitations of time and computational resources.

Following this, 9 cases, C1 to C9 are defined to investigate the effect of design parameters on injury to passengers. A number of passenger positions (prefixed by P throughout this chapter) are defined, and these are used to compare different cases. A prediction of fragment injuries and chest wall at different passenger locations is made, using the techniques developed in Chapter 3.

Finally, an analysis of the results is undertaken to answer the hypothesis, draw out some of the limitation of the applied techniques and discuss where future efforts may be best directed.

7.2 Development of a rail vehicle FE model

A model for predicting the pressures resulting from an explosion has been described in Chapter 6, therefore it is now necessary to develop an accurate model of a rail vehicle to investigate the effects of blast loads in rail vehicles. Chapter 2 describes the current state of rolling stock on the UK railway network, with around 90 different classes of vehicles operating across the London underground and mainline network. To develop an appropriate finite element model, it is necessary identify a representative vehicle and it's geometry, materials and construction.

7.2.1 Class 165 rail vehicle

The Class 165 rail vehicle is part of the 'Networker' family of vehicles that was produced by British Rail Engineering Limited (BREL), which includes the Class 166 DMU, and Classes 365, 465 and 466 EMUs[1]. These vehicles were subsequently the basis for Electrostar (EMU) and Turbostar (DMU) families of vehicles currently manufactured by Bombardier, and as such is representative of a reasonable proportion of vehicles in service in the UK, as shown in Table 7.1.

An existing finite element model of the Class 165 was provided by Bombardier, where it had previously been used as part of work investigating weld unzipping in Aluminium rail vehicles [101] during railway collisions. The model provided (see Figure 7.1) consists of a whole single vehicle, but without the presence of glazing and seating. It includes the front cab of the vehicle which is necessary for correct prediction of the collision investigations for which the model was developed, as well as the bogie centre pivots (or pin) at each end[2] and distributed mass elements, which represent equipment and

[1] Although built in the early 1990's, these vehicles are expected to have a life in excess of 30 years, and thus are still relevant.

[2] The bogie of a rail vehicle hold the axles and wheels, provides primary and secondary suspension and is connected to the rail vehicle by a central pin or pivot on the rail vehicle, which locates in a vertical hole in the bogie frame [184].

Table 7.1: Volume of networker and derivative vehicles on the UK rail network, from data in Network Rail's Route Utilisation Strategy [98]

Family	Class	Number
Networker	165	48
	166	21
	365	40
	465	147
	466	43
Electrostar	357	74
	375	102
	376	36
	377	205
	379	36
Turbostar	168	19
	170	132
	171	16
	172	39
total		958
proportion of total rolling stock		21.7%

features in the vehicle where consideration of their mass was necessary but modelling of the structure itself was not required.

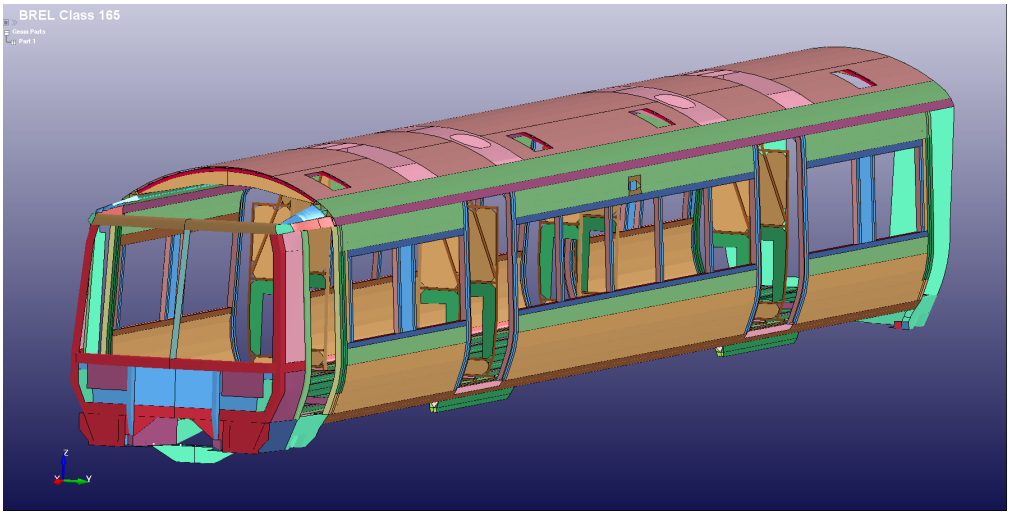

Figure 7.1: Finite element model of Class 165, as provided by Bombardier, reflected in the XZ plane to show the shape of the whole vehicle, as the model uses half symmetry along it length

The structure of the Class 165 consists of double skinned extruded aluminium panels which are bolted or welded together, with the extrusions having different wall thickness over the cross section depending on service loads expected. A view of the cross section geometry and a selection of the thickness of the various parts of the extruded shape are shown in Figure 7.2. The cross section varies along the vehicle to some extent, and the section in Figure 7.2 is taken away from the doors and between windows. Where windows exist, the section which is filled with solid colour on the right hand side of Figure 7.2 would be a window, and where doors exist much of the side wall, up to about

2000mm above the height of the floor is replaced by a moveable door. The door makes a minimal contribution to the vehicle stiffness, so the floor panel at its outer edge is strengthened with an additional structure.

The model provided by Bombardier was built for modelling vehicle crashworthiness and whole vehicle behaviour under those circumstances. For the current project, the Lagrangian rail vehicle model was rebuilt and modified to make it suitable for investigation of blast loading using ALE methods.

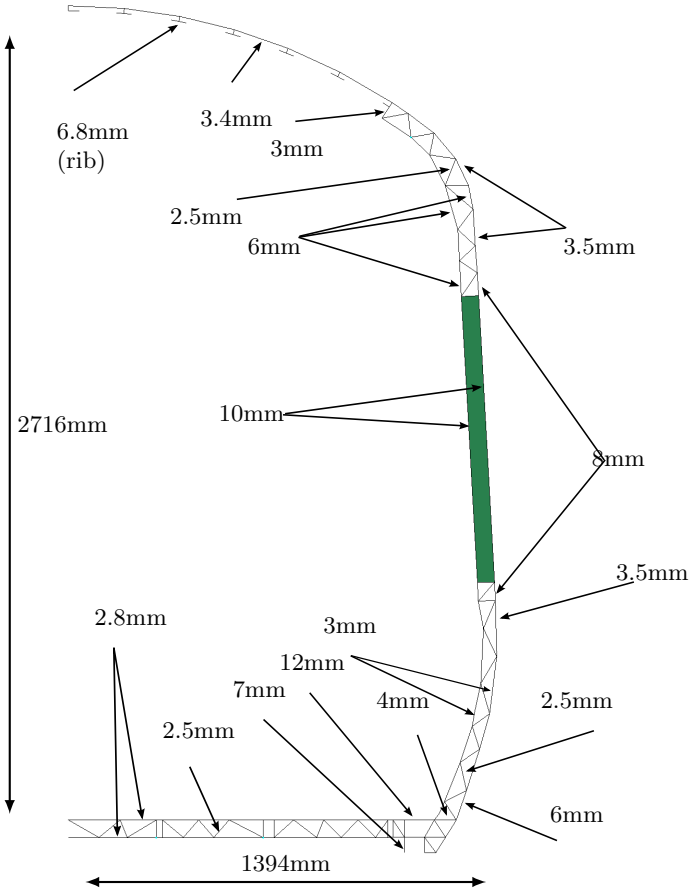

Figure 7.2: Cross section of Class 165 model

7.2.2 Reconstruction of Class 165 model shell

The existing Lagrangian rail vehicle model could have been coupled to the ALE blast model with no modification, but the wide variation in element size and the complexity of the model demanded that it be rebuilt using the geometry from the original Class 165 model, but with a more consistent element size throughout. The following steps were taken to reconstruct the model for use in this work:

- removal of front half of vehicle to utilise quarter symmetry of the internal passenger compartment
- removal of central pivot
- tracing and minor simplification of the existing geometry using LS-PrePost
- export geometry as CAD file

Table 7.2: Part numbers and wall thickness for the main vehicle model

part	18	19	20	21	22	24	26
thickness (mm)	16	3	12	15	3.4	5	8
part	27	28	29	30	31	32	33
thickness (mm)	10	4.5	7	6	4	6.5	2.5

- edit and clean up geometry, define parts, using FreeCAD
- import the geometry from FreeCAD to Hypermesh
- surface mesh the geometry with appropriate element size

Figure 7.3 shows the original and new meshes for the 165 rail vehicle. The central pivot (not visible in Figure 7.3(a)) was removed as its presence was not deemed necessary for blast modelling. Some extra stiffening elements seen at the end of the original model were also removed, as they were at the furthest point in the rail vehicle from the centre of detonation. Simplifications took place around the roof and door edges, where openings (for air conditioning, exhausts, cabling etc.) were removed from the original model and door edges were considered as homogeneous with the rest of the wall structure. It was important to remove the openings from the roof of the original model, as although there may be a reduced structural strength in the areas in the real vehicle, an opening allows pressure to escape from the vehicle with no impedance, which is not an accurate depiction of reality. The reconstructed model in Figure 7.3(b) shows consistent element sizing across the model, which results in a purely Lagrangian mesh with 63,593 40mm shell elements, as opposed to 30,724 for the original model when quarter symmetry is applied.

7.2.2.1 Description of reconstructed Class 165 model (R165)

The final reconstructed model labelled R165 was created in the CAD package FreeCAD and consists of 16 parts. As the model was to be meshed using shell elements, no thickness was included in the CAD geometry and parts were defined by grouping the areas of the model which shared the same thickness. Each part of the main vehicle model shown in Figure 7.3(b) has a different thickness, which is shown in Table 7.2.

The R165 model is 9500mm long with vertical and horizontal dimensions as shown in Figure 7.2 and only encompasses the vehicle body shell, not including doors, windows, seats, draught screens or other internal or movable features, which are discussed in Section 7.2.3, but does include holes into which windows and doors can be positioned. The end of the vehicle, shown on the extreme left in Figure 7.3, was modelled at this stage using single layer of elements and no opening, as the effect of different end arrangements is discussed in Section 7.4.4.

7.2.3 Doors, windows, seats, draught screens and occupants

The original Class 165 model included a single pair of draught screens either side of the main doorway, but doors, windows and seat structures were not included, as they were unnecessary for the crash investigation that the original model was designed for.

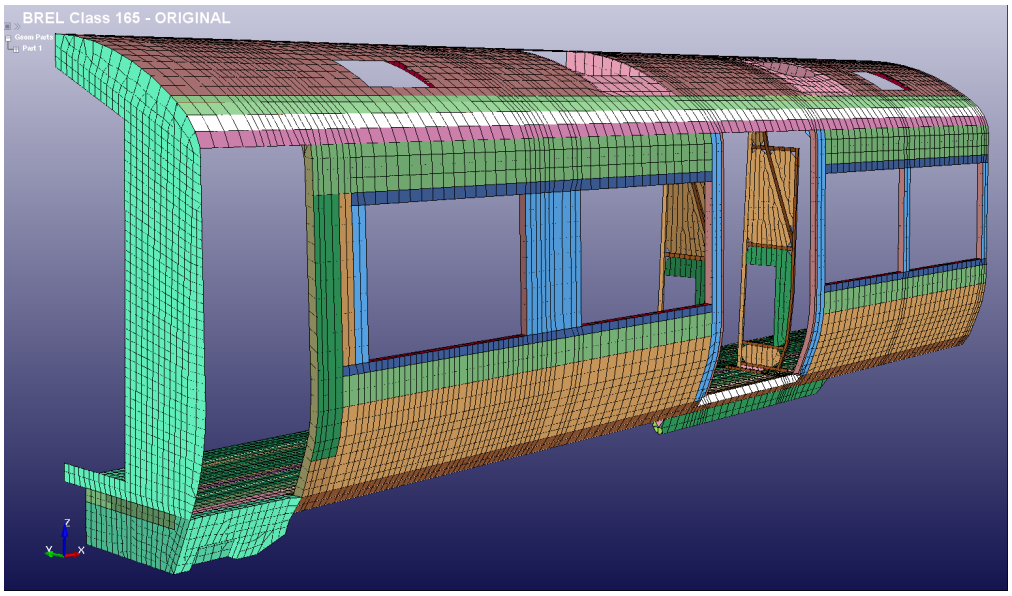

(a) Original Class 165 model

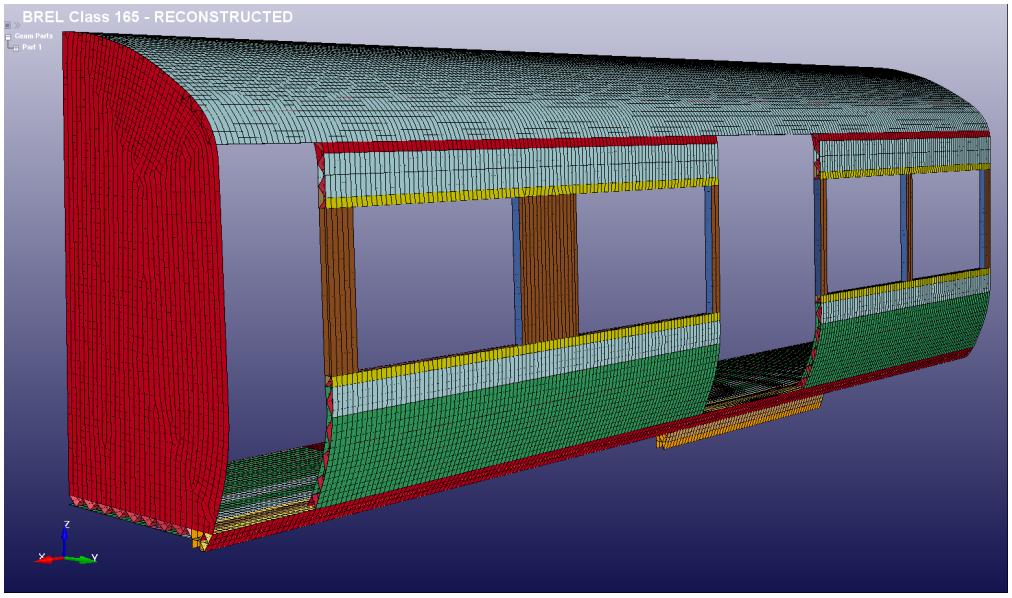

(b) Reconstructed Class 165 model

Figure 7.3: Meshes of both the original and reconstructed Class 165 models, showing the differences in element sizes

When investigating the effects of blast loads though, these features are important as they will affect the propagation of the blast wave and the subsequent pressures experienced throughout the vehicle. The exact response of doors, windows, seats and occupants is not the primary focus of this work, and as such highly geometrically accurate and finely resolved finite element models are not appropriate, but simplified representations are necessary, unlike the global vehicle structure described in Section 7.2.2.1, where fewer simplifications have taken place.

As well as the features mentioned above playing a significant role in altering the pressures experienced in a rail vehicle, occupants themselves will have a similar effect, but in a much more variable way. The positions of seats and draught screens are known and constant, but the number, size and positioning of passengers varies significantly across each rail vehicle and time of day. As with features described above, a precise finite element model to identify the physical response of occupants is outside the scope of this work, and the response in terms of injury is discussed in Chapter 3, so a simplified approach was required.

7.2.3.1 Simplified modelling of doors, windows, seats and draught screens

The design and structural requirements of these features are discussed in more detail in Section 2.5.1, so this section focuses on the modelling techniques used.

In the absence of specific data, and due to the amount of variation over rolling stock in the UK, some assumptions are made about the size and construction of vehicle features to allow the finite element model to be constructed. The draught screen geometry was extracted from the original Class 165 model to be used as the basis for draught screens in the R165 model. Doors on rail vehicles have the same shape as the body shell walls, but are typically thinner, often with windows. A single layer of shell elements was chosen to represent the door structure. Rail vehicle windows are typically rounded squares or rectangles, but for simplicity windows and the location in which they sit are considered to have right angled corners. The seats of rail vehicles come in a variety of shapes and configurations as shown in Figure 7.4, which depend strongly on the kind of service the vehicle will be used for. Metro services tend to have basic seating, where passengers are only likely to be sat for limited periods of times, whereas intercity services have more substantial seating to offer improved passenger comfort over longer journeys. A simple seat, such as shown in Figure 7.4(a) offers an adequate compromise between longitudinal bench seats in metro trains shown in Figure 7.4(c) and more complex and heavy duty intercity seats as shown in Figure 7.4(b). Seats arranged in a transverse formation, such as those in Figure 7.4(a) are more representative of the type of seating throughout rail vehicles in the UK, where longitudinal seating in (c) is typically restricted to metro services such as the Glasgow Subway and London Underground, although Class 378 Capitalstar[3] of the London Overground uses longitudinal seating throughout.

Laminated glass is used extensively throughout rail vehicles and is now mandatory for bodyside windows that form part of the interior[4] and when used in the construction of glazed partitions, doors, draught screens and luggage storage [104]. In some older rolling stock, toughened glass is still common, although it is gradually being replaced.

[3]The Capitalstar vehicle is based on the Bombardier Electrostar, which is in turn based on the Class 165.

[4]If single glazing is used, it must be made of laminated glass, and if double glazing is used the inner pane must be laminated, and the outer pane may be toughened.

(a) Train seats in outer suburban vehicle

(b) 1st class seat from a Mk3 carriage, removed from vehicle

(c) 1967 stock London Underground longitudinal bench seats

Figure 7.4: Examples of train seats in different UK rolling stock

Laminated glass can be modelled in a simplified and straightforward manner in LS-Dyna using the inbuilt laminated glass material model, *MAT_32. Through this model it is possible to define the material parameters for both the polymer and the glass, and up to 32 layers of glass and polymer. The thickness and position of each layer is defined by a user defined through thickness integration rules using the *INTEGRATION_SHELL keyword. Laminated glass in rail vehicles consists of 2 layers of glass and a layer poly vinyl butyral (PVB) of either 0.76 or 1.52 mm [103] between them. Data on the properties of laminated glass is reported widely in the literature [185, 186, 187, 188], and for this work a laminated glass panel with glass layers of 3mm and an interlayer of 1.52mm was used.

As well as laminated glass, there are a number of other materials used in the manufacture of internal features of rail vehicles, such as woven fabrics and polyurethane foams for seats, a variety of polymers used extensively for structural and aesthetic purposes, such as ABS, and wood used in flooring and as part of features such as tables. Modelling of these materials is not considered here as it was deemed to be unimportant, and in some cases are a considerable challenge to model in their own right. The unknowns and uncertainty in modelling these materials would add an extra level of uncertainty to the model, which if anything is detrimental to accuracy of the outcomes of the modelling

effort.

Rail vehicles contain a number of ways of joining parts and components, including welding, mechanical fastening and bonding. Continuous welds and mechanical fastenings are present in the body shell of the vehicle where they are used to hold the extruded panel sections together, but these are not considered in the R165 model as there is no separation between each extruded panel. Connections of interest are those that connect windows to the vehicle body and bolted connection that attach draught screens and seats. Simplified bolted connections can be considered in a number of ways, including tiebreak contacts and constraint options, but a successful simplified modelling of dynamic bolted joint behaviour has been reported [183] using a combination of beams, *MAT_SPOTWELD and a contact definition to tie the beam ends to the surfaces to be bolted. This method, explained in more detail in Chapter 6, was utilised to model bolted connections. Modelling of window fixation was handled simply using the surface to surface tiebreak contact definition in LS-Dyna, which allows a simple definition of failure stress to model the behaviour of the window bonding.

7.2.3.2 Occupants

The shape of the human body is extremely complex, but the primary effects of the presence of occupants were considered using a simplified method. As discussed in Chapter 3, the chest wall injury model relies on pressure histories taken at 90°intervals around a cylinder of a specified diameter, and this cylinder and sensor configuration must be used if pressures histories are to be applied to the chest wall injury model with confidence. As the physical deformation of the occupants is not of interest, but the effect of the body presence on pressure is, rigid but movable cylinders of appropriate diameter and mass will be used to model occupants.

7.2.4 Description of the modelling methods applied

7.2.4.1 Aluminium

In the UK, 6005 T6 aluminium alloy (AA) is typically used for rail vehicle extrusions [101]. The main alloying elements of 6000 series aluminium are magnesium and silicon, with iron, copper, manganese with other elements also present in smaller quantities [189]. The T6 temper indicates that the alloy is solution heat treated (heating to a point where constituents can enter solid solution) and artificially aged at elevated temperature [190].

Investigations of extruded 6000 series T6 aluminium panels have been conducted using experimental and numerical means under a variety of loading mechanisms. Zheng *et al.* investigated a 6000 T6 series AA[5] extrusion to identify bending strength and fracture properties and validate numerical modelling work, where the material model was input in the form of a stress strain curve from experimental tests. Tensile test specimens cut orthogonally from the extrusions indicated that this particular alloy did not demonstrate significant anisotropic behaviour. Borvik *et al.* [105] studied perforation of 6005 T6 AA panels when impacted by ogival (pointed) nose projectiles using numerical and experimental means. Testing at a variety of strain rates was carried out using servohydraulic testing machines for low strain rate testing and split Hopkinson tensions bars for testing

[5]This is referred to in the article as 6600 AA, but this specification does not exist according to the relevant international standards. No response from the author was available, so it is assumed this is 6060 AA

Table 7.3: General and Johnson Cook parameters for 6005 T6 Aluminium [105]

E (GPa)	ν	ρ (kg/mm^3)	σ_y (GPa)	A (GPa)	B (GPa)
70	0.3	2700×10^{-6}	0.275	0.270	0.134
n	$\dot{\epsilon_0}$ (1/ms)	C	m	α	–
0.514	0.1	0.0082	0.703	0.9	–
D1	D2	D3	D4	D5	–
0.06	0.497	-1.551	0.0286	6.80	–

up to strain rates of 1000s^{-1}. Moderate anisotropy was found, with the best performing specimens being cut at 45°to the extrusion direction, and worst performance perpendicular to the extrusion direction. The moderate effect of anisotropy meant that it was not considered in the numerical model and material parameters were taken parallel to the direction of extrusion. Strain rate dependency was exhibited by 6005 T6 AA, with increasing strength with increasing strain rates, but nominal stress strain behaviour between 0.87^{-1} and 270^{-1} was very similar, indicating that strain rate dependence over a range of moderate strain rates is not high. At extremely high or low strain rates, the effect of strain rate was noticeable but not considered particularly significant. Chen [191] *et al.* investigated the stress-strain behaviour of 6000 and 7000 aluminium alloys at T6 temper and confirmed that anisotropy in 6000 series T6 AA extrusions was not significant, and that there was not significant strain rate dependence in 6060 and 6082 AA.

Previous users of the Class 165 model used the Gurson model for AA [101], specifically to model fracture in welds. Borvik *et al.* [105] have validated a numerical model in LS-Dyna for 6005 T6 with penetration tests after characterising the material experimentally, producing coefficients for the modified Johnson-Cook material, implemented in LS-Dyna as *MAT_107. Coefficients for the model can be found in Table 7.3. The material model includes a function to calculate the Von Mises stress as a function of the strain rate, and a plastic strain at failure, as a function of the plastic strain, Von Mises stress, hydrostatic stress and temperature.

The models used were run using the plastic kinematic model (*MAT_003) with no rate dependency, and with the Johnson-Cook model using the strain hardening parameters A, B and n and the strain rate parameter C as shown in Table 7.3.

7.2.4.2 Laminated glass

The mechanical properties for glass and PVB are included in the *MAT_32 input, along with which properties to assign to each integration point defined in a user integration scheme, *INTEGRATION_SHELL. The input for the user defined integration specifies the normalised position of each layer and it's weight factor (the thickness related to the integration point divided by the thickness of the whole shell), and the material input defines the mechanical properties of each of these layers. A total of 6 integration points are used through the thickness, 4 for the glass (2 bottom, 2 top) and 2 for the interlayer. Input data for the material model and user defined integration rule are shown in Tables 7.4 and 7.5.

Table 7.4: Material properties for use with laminated glass model

	ρ (kg/m^3)	E (GPa)	ν	σ_y (GPa)	E_{tan} (GPa)	ϵ_f
glass	2500	74	0.20	0.070	70.00	1.2 $\times 10^{-3}$
PVB	1100	0.95	0.49	0.011	8.54×10^{-3}	2.0

Table 7.5: User defined integration rule

integration point	normalised position	weight factor ($\Delta t_{ip}/t$)
1	0.800	0.199
2	0.402	0.199
3	0.101	0.101
4	-0.101	0.101
5	-0.402	0.199
6	-0.800	0.199

7.2.4.3 Connections

All of the additional features added to the vehicle body shell require a connection to 'secure' them in place, just as occurs in a physical rail vehicle. This can be achieved in a simplistic and slightly unrealistic way by merging the nodes of the added structures with the body shell itself, which can prove to be an efficient strategy if the strength of the connection is significantly higher than the strength of body shell or connected structure. This not always the case, and the method of connection can often play an important role in the response of the structure. Connections between structures were modelled by using methods that are significantly simpler than precisely modelling the real connection, but maintain the expected modes of failure.

The connection of windows to the vehicle shell was modelled using the automatic surface to surface tiebreak contact definition. The automatic surface to surface contact definition reduces the orientation dependence of the contact, and the surface to surface approach allows sets of segments or shells to be used to define the contact. The surfaces in a tiebreak contact are initially tied together, but failure can be specified between the two contact surfaces based on the normal or shear contact stress, computed from the contact force (the force required to keep the contact surfaces tied together) and the projected area of the surface contacts. The window and body shell connection was modelled by defining a contact surface between the segments along the edge of the window and corresponding segments on the vehicle body shell, and failure stress was determined from the failure stress of rubber, which is typically used to mount windows [103].

Doors on modern rail vehicles often have a complex sliding mechanism, as do all vehicles on tube and metro systems. A detailed design of rail vehicle door opening mechanisms was not available, and the modelling effort required to generate a realistic functioning door for use in this model was not deemed appropriate. The effect of the presence of doors, door failure and deformation can be considered with simplified approaches, which do not add significant computational cost. Doors were modelled using a combination of beam elements and a tied node to surface contact definition. Beam

elements use the default Hughes-Liu formulation and are placed at the corners of each door, with nodes on the body shell side fixed in all degrees of freedom and nodes at the other end 'connected' with a nodes to surface contact. This allows each door to be constrained at each corner until a failure criteria is satisfied in the beam elements or corresponding elements on the door itself, at which point element deletion means the door is no longer fixed.

Draught screens are typically constructed from a section of laminated glass attached to a frame (which often doubles up as a handrail) by a clamped connector. This was recreated in the numerical model, and the laminated glass is held in place by contact with several lug on the surrounding metal frame. The frame is constrained at the top and bottom and along the bodyside edge, as it would be when in position in a rail vehicle.

7.2.5 Verification of features

A number of secondary features have been described above, and the requirements from the Railway Group Standard GM/RT2100 [104] provide a standard against which the modelling method can be verified. The relevant structural requirements for this work are shown in Table 2.1 and involve point loads and pressure loads. Loading the modelled structures allows confirmation that they are representative of real vehicles, by conforming to the same standards.

The standards dictate that for almost all the proof loads described in Table 2.1 on page 34 that the structure resist significant deformation and remain functional, with the exception of the window impact load, with the standards simply stating that this impact should be withstood. An explicit finite element model was generated to investigate window impact loading, and implicit finite element models were used to investigate static loading requirements.

Data on real door and window performance under the GM/RT2100 could not be found in the open literature, so this section served to ensure that the model features give a level of performance in line with the required standards, in the absence of validation data from real railway vehicle features.

7.2.5.1 Windows

The response of the window to an impact load is shown in Figure 7.5. Figure 7.5(a) shows the result deformation of a node on the window which is located at the point at which the sphere impacts the window. Peak deformation of 94mm occurs at 37.5ms, but this peak is not an entirely plastic response and includes the effects of some material elasticity which leads to some oscillation of the window about its final peak deformation. The model was not run to a time where the final deformed shape is attained, but inspection of the deformation history between 50ms and 75ms indicates final peak central window deformation of 75mm. Importantly, the window has been held in position; had the connection failed, the resultant deformation would continue to rise over the whole solution time. Although the high peak deformation suggests that failure of the glass layers would be expected, as long as the whole window is retained the test is passed, as specified in the Railway Group Standard [104], and shown in Table 2.1 in Section 2.5.1.

The plastic strain history for an element at the centre of the window is shown in Figure 7.5(b), and shows that plastic strain peaks at the point of maximum deflection,

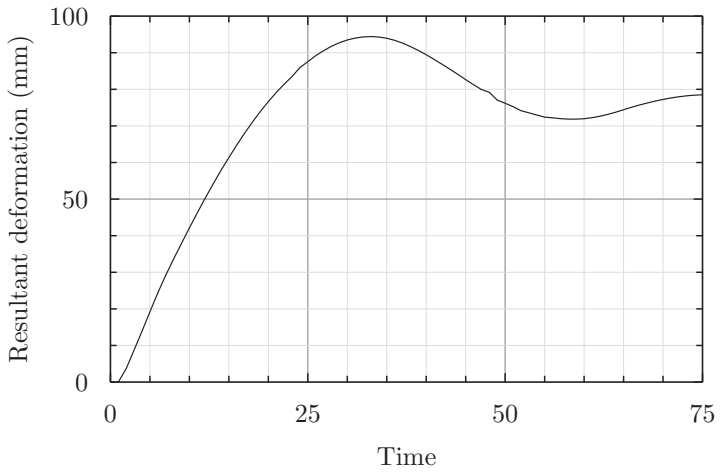

(a) Resultant deformation history from the central node in the window

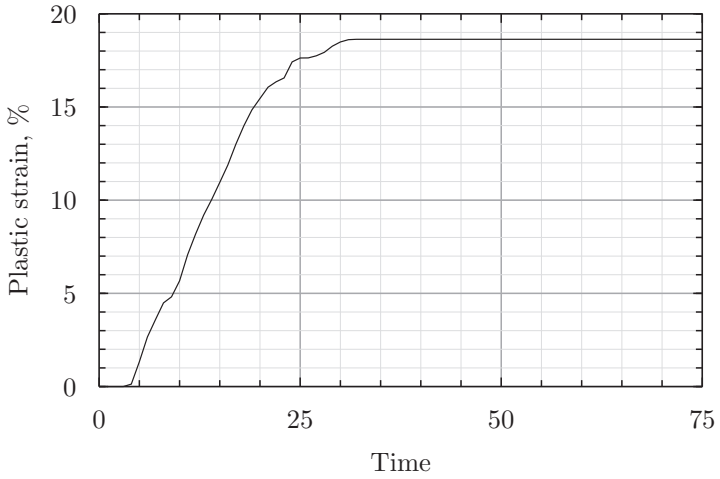

(b) Plastic strain history from an element at the centre of the window

Figure 7.5: Data from the point of highest deformation under a 50kg spherical impact load

as expected. The model cannot distinguish between the plastic strain for each material, and as a result it is necessary to assume that in any areas in which there is some plastic strain, the glass layer has failed and the plastic strain value is that of the PVB interlayer, since glass can typically sustain negligible plastic strain. The peak plastic strain value indicates that failure in the PVB interlayer will not occur, with a peak plastic strain of 18.7% or 0.187, compared to literature reported failure strains above 0.5 [192]. It should be noted here that strain rate dependency is identified as an important feature of laminated glass response, with high strain rates leading to more glassy behaviour of the PVB layer [185, 193] compared to lower strain rates, which is not considered by this model.

The deformation of the window under a sustained pressure of 6kPa is shown in Figure 7.6, which shows a peak deformation at the centre of the window of 4.95mm. Plastic strain contours are not shown, as no plastic strain was recorded at any point in the model. Conditions state that after loading the window should be 'fully serviceable', and the low deformation and lack of any material plasticity indicates that the modelled window would continue to function after this load and remain fully serviceable.

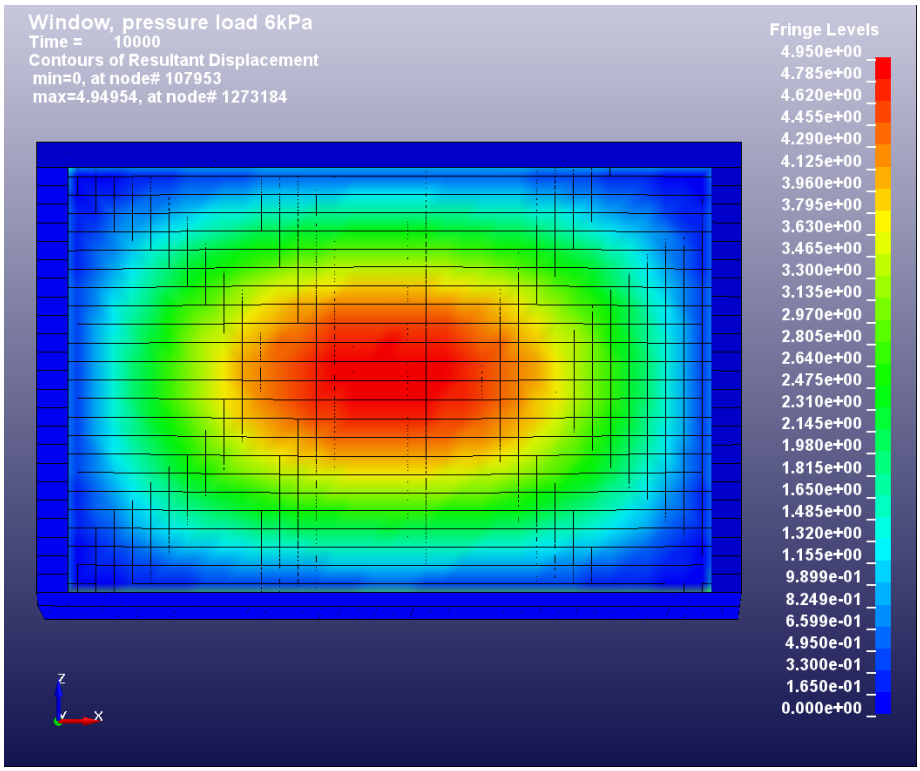

Figure 7.6: Resultant displacement for window under sustained 6kPa pressure load

7.2.5.2 Doors

The resultant deformation of two doors under different loads is shown in Figure 7.7, with the left hand door being subject to a combined pressure of 2.5kPa and distributed load of 0.8kN over 100 mm by 100mm, and the right hand door subject to a distributed load of 2.5kN over 100mm by 100mm. The highest deformation is seen with the 2.5kN distributed load with a deformation at the point of loading of 24mm. The highest deformation in the left hand door is also at the point where the distributed load is applied, but is lower at 16.8mm. Neither door experienced any plastic strain, and static equilibrium reached as part of the implicit solution indicated that the door connections did not fail. The requirements for the doors are as with the window above, and state the door must remain serviceable after application of these loads, which would appear to be fulfilled by the results presented.

7.2.5.3 Draught screens

The draught screen model is shown in Figure 7.8, under 2 different loading conditions, each of which have 2 different positions for the loading. Under both combined loading from a pressure and a distributed load (Figure 7.8a and b), and purely a distributed load (Figure 7.8c and d) the distributed load was applied at both the edge and centre of the draught screen. Peak final deformation under any loading case was found with the higher distributed load only applied to the edge of the draught screen, which caused a deformation at the point of load application of 18mm. Plastic deformation was not seen at any point, and deformation is low throughout all models, which again indicated that the numerical models satisfy the required criteria.

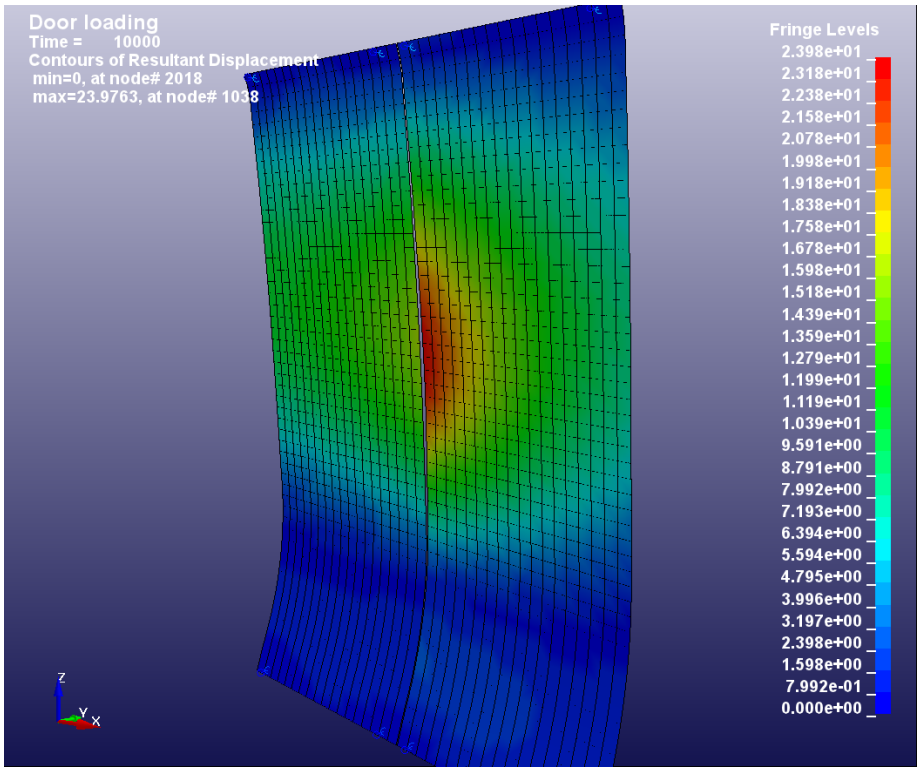

Figure 7.7: Resultant displacement for door under combined and distributed loading

7.3 Application of blast load to rail vehicle

Applying a blast load to a rail vehicle structural model and predicting not only the structural deformation but the pressures throughout the vehicle form the core interest of this work. A rail vehicle body shell and various features have been verified by comparison with the appropriate railway group standards where possible, and a method of predicting the blast load pressures and the influence of shock wave interaction with the structure itself have been described and validated in Chapter 6. As discussed in 6.4, the secondary combustion model used works well on the model tested, but difference in aspect ratio between the test cell and a rail vehicle means secondary combustion cannot be considered to take place at similar time scales over the entire length of the vehicle.

Currently, no work in the open literature is known of that addresses the secondary combustion effects from high explosives as a function of the distance along a tubular structure, such as a tunnel or rail vehicle. As discussed previously, the secondary combustion effects are dependent on the temperature of the reactants and the availability and mixing of reactants and atmospheric oxygen. It is possible to model this with a combined CFD and chemical equilibrium model, similar to the approach used by Togashi [47] *et al.* to model a similar phenomenon in a series of connected rooms, but this is beyond the scope of this research. In LS-Dyna, it is theoretically possible to use a similar method to that described in Chapter 6 to consider the effects of secondary combustion, and introduce a number of time dependent energy release functions for different spatial positions along the rail vehicle. A lack of data to ensure that such a model accurately simulates the real world problem prevents this from being applied here. To apply such a model, or develop a more elegant approach, further experimental work or CFD and thermo-chemical equilibrium calculations will be required to allow a simplified imple-

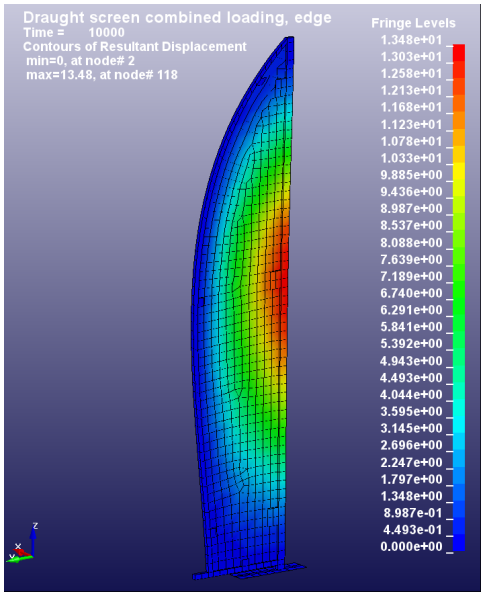

(a) Combined loading, distributed load applied at edge

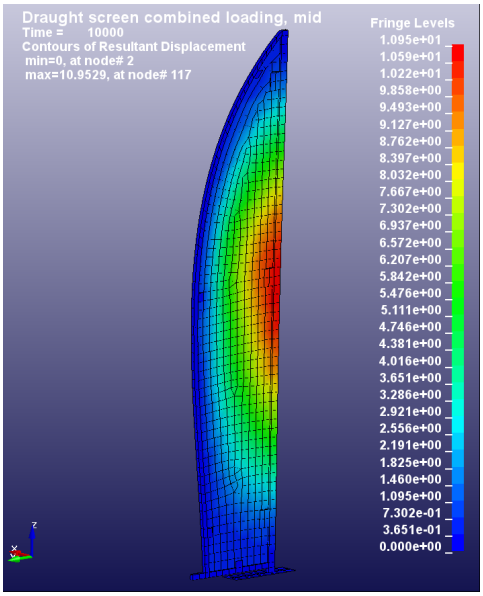

(b) Combined loading, distributed load applied in centre

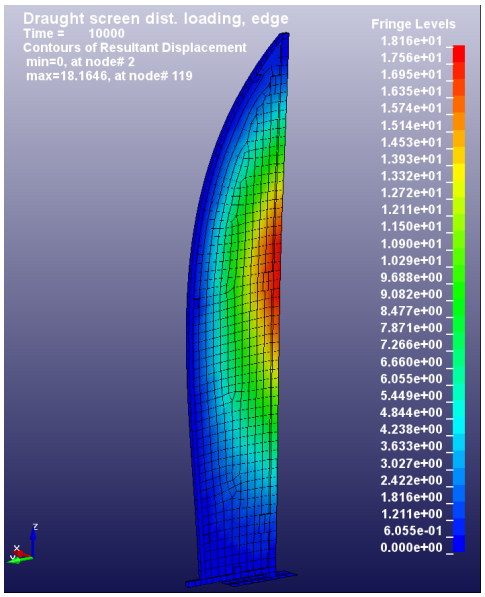

(c) Distributed load applied at edge

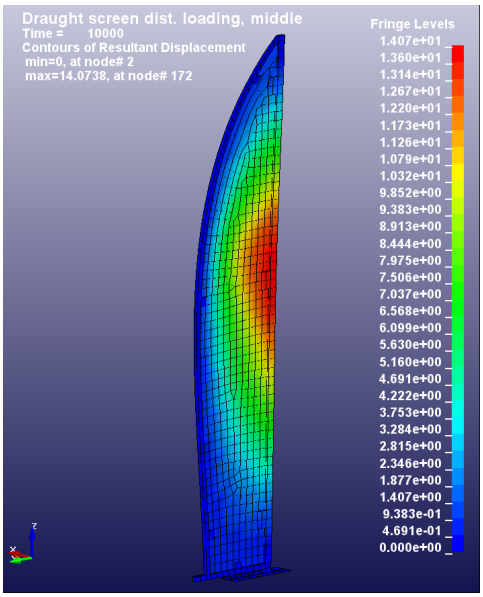

(d) Distributed load applied at centre

Figure 7.8: Resultant displacement fringe plots for different loading scenarios on a draught screen

mentation of spatially dependent secondary combustion effects. As a result, the effect of secondary combustion is not considered in the rail vehicle models, which will result in under prediction of cumulative impulses. Quantitative comparison between models can still be undertaken, due to the consistency of modelling technique between them.

There is a need to determine both the most critical technical model parameters to investigate, as well as a number of global solution parameters to ensure that the most effective modelling solution is identified. These are:

- technical parameters
  - mesh size
  - influence of material model on deformation
  - influence of deformation on pressures
- global solutions parameters
  - charge size, shape and material
  - termination time
  - influence of technical parameters on run times
  - confirmation of model stability

There is always a compromise to be reached between the level of complexity of a model, the accuracy it provides and the accuracy required, and the amount of real time that a model takes to run to the desired completion time, typically in ms. Of the parameters above, only the charge itself has no direct influence on the run time.

7.3.1 Modelling method and parameter study

This section discusses a number of parameters of interest, and describes modelling runs used to undertake a preliminary investigation of blast loading of rail vehicles using the developed ALE method. Some parameters are of interest in both this section and in terms of occupant injury, so are discussed here, with results presented later.

Although not strictly a parameter study, it is necessary to predict or calculate an appropriate amount of time to run the solution for, also known as the problem time, which is the amount of time dependent information required from the model and is specified by the user. In the context of this section it is important to differentiate this time from the clock time or computation time, which is the amount of time taken to physically process and compute the solution, which is a function of many parameters, such as the problem time, the mesh size, material model and element types, contact definitions and CPU speed.

The time at which a shock arrives at a point can be accurately estimated using ConWep, assuming it has not been reflected from other surfaces, or been influenced by other reflecting waves. This time is a function of the charge size, material, and distance between the charge and the point of interest. In a confined geometry, such as a rail vehicle, there will be a period of time after the arrival of this first shock where the pressure history is highly transient and there are a number of reflections, as shown in Chapter 5. It is this time that needs to be estimated, so all necessary data can be gathered.

In experimental tests shown in Chapter 5, highly transient effects happened over a period of 15-20ms, with distance from the point of detonation not necessarily determining

how long the most interesting transient effects occurred for, with level of confinement and complexity more responsible for prolonged transient behaviour. As a best case scenario, experimental results indicate that 3 times more data is required than the time taken to capture the first shock where the test cell was open to atmosphere, but under the more intense confinement, transient behaviour continued for 7.5 times longer than taken to record the arrival of the first shock. The peak cumulative impulse is normally reached at a similar time to the end of the most transient phase, which can be used in combination with the estimation of extra time required to identify the most appropriate problem time.

7.3.1.1 Charge details

In this work the effect of a terrorist detonating an improvised explosive device is to be studied, and accordingly such a device could be constructed from any explosive an attacker chooses. In recent attacks a variety of explosives have been used, including military grade plastic explosives and home made peroxide based explosives. On the 29th October 2010 IEDs were found within printer cartridges in aircraft cargo holds at East Midlands airport in the UK, constructed from PETN a common secondary high explosive with a similar structure to nitroglycerine, but with a similar power to RDX. Ammonium nitrate, when mixed with a suitable fuel source such as sugar or diesel fuel, is also a powerful explosive and was used in the Oklahoma bombing.

It is possible to find the equation of state coefficients for many of these explosive materials, such as peroxides, ANFO, and PETN [173, 194]. Although this presents a method for modelling realistic devices that could be used in an attack, the improvised nature of explosive devices used by terrorists means that a model using one of these explosives is unlikely to be any more representative than using another of them. Deciding on a particular material implies that it is deemed a more likely threat than an other material, but current evidence does not point towards a trend for using any particular explosive compound. Furthermore, a validated model for a known explosive has been presented in Chapter 6 and although it is not highly likely that PE4 will be used in an improvised explosive device, it represents a worst case scenario in terms of explosive output, and the use of a well defined and consistent explosive material is important.

The size of the charge is clearly an important parameter, but as with the explosive material itself, the improvised nature of terrorist explosive devices means there is significant variation in the size of charges used in attacks. Previous work in this area has used a variety of charge sizes, from 0.5kg [137] to 16.3kg [135]. Larcher *et al.* [136] state that charges of between 8 and 12kg were used in the Madrid attacks in 2004. There can be an added difficulty in estimating the size of device, given that the device is destroyed during it's function, and possibly the attacker themselves; even if an unexploded device is subsequently found and linked to an attacker, it is only speculation that they are the same size as the device used. Estimating the size can be based on forensic evidence and description of the device from attackers if it exists, as well as the physical damage caused.

It is easy to focus on the most memorable attacks of this kind as a basis for scenario development, namely the London and Madrid bombs, which have been intensely and visibly scrutinised and investigated in the media and in academic work. It is important to be aware of other similar attacks elsewhere (such as Moscow and Minsk) and avoid

suggestion that the isolated attacks in Madrid and London form a template for future attacks. A charge mass of 5kg was used in this work, and although the effects of different charge masses can be discussed qualitatively, modelling of a variety of charge masses was not considered for investigation.

The charge was modelled in the same way as described in Section 4.1.2.2 using the 2D ALE method with quarter symmetry, with material parameters as shown in Tables 4.1 and 4.2 on page 68. The 5kg charge has a radius of 91mm and was meshed with 112200 shell elements. The radius of the ALE domain including the charge and air was chosen as 1400mm using a total of 269100 shell elements, which allows the blast wave to propagate up to a point where the shock is just about to make contact with the vehicle, when mapped onto a 3D domain. The charge was mapped onto the 3D ALE domain at half height in the rail vehicle, at 1358mm.

7.3.1.2 Mesh refinement

As discussed in Chapters 4 and 6 the mesh resolution of the ALE domain can have a significant effect on the pressures predicted. No significant effect on cumulative impulses was seen when the ALE was refined below 15mm in Chapters 4 and 6, but peak pressures continue to rise as the mesh is refined, as the effect of shock smearing is reduced. Ideally, all meshes would be refined to a point when both the peak pressure and impulse values predicted by the model are totally mesh independent, but this is very much limited by the computational resources available. The ALE method requires a large number of elements, and as the elements are refined, the effect on various computational parameters is large. Halving the size of the solid hexahedral elements used for the ALE domain creates a mesh with 8 times as many elements. The solution must then be carried out with a time step half the size and process 8 times as many elements.

The rail vehicle model has a very different aspect ratio to models used previously in this work, as its length is significantly larger than the height of the vehicle. This naturally means that there is an increase in the number of elements required in the ALE domain to account for this extra size, as similar resolution is still required along the height and width of the vehicle. These extra elements do mean that within the bounds of the computational resources available, a coarser mesh than used in other models is necessary. The complexity of the vehicle structural model also means that Lagrangian elements contribute more significantly to the computational cost than with models described previously. A mesh refinement study was carried out in a similar way to seen in Chapters 4 and 6, with three mesh densities chosen. The details of the three meshes are chosen are shown in Table 7.6, showing the total number of elements in the ALE and structural meshes. The maximum and minimum dimensions of the ALE meshes used vary slightly for each model, and are shown in Table 7.7, where x is the dimension in the direction of travel of the vehicle, y the width and z the height. The ALE dimensions are varied based on the appropriateness for each model, and were typically constructed based on the minimum mesh dimensions to allow a stable solution in which the structural model and the passengers were not affected by boundary effects.

7.3.1.3 Material model and structural simplification

Chapter 6 showed that rigid materials can be used effectively when there is minimal plastic deformation, with considerable computational saving. In the models presented

Table 7.6: Mesh resolutions and number of elements for model C1

ALE element size (mm)	n
40	1,111,273
30	2,464,911
20	6,992,360

Table 7.7: ALE air domain dimensions in mm for C1-C9

	min			max		
model	x	y	z	x	y	z
C1	0	0	-1150	10,000	2600	3400
C2	0	0	-350	10,000	2000	3000
C3	0	0	-1150	10,000	2600	3400
C4	0	0	-2180	10,500	3600	4400
C5	0	0	-1150	14,000	1800	3290
C6	0	0	-1150	15,000	2600	3400
C7	0	0	-1150	10,000	2600	3400
C8	0	0	-1150	10,000	3100	3400
C9	0	0	-1150	10,000	2600	3400

here, significantly higher charge masses are applied and consequently the levels of deformation are such that a rigid material model is no longer a good representation of the structural behaviour. The material model chosen can play a significant part in the computational cost of a finite element model, with rigid material models being very quick and complex material models such as the Johnson-Cook strain rate dependent plasticity and damage model incurring a significant time penalty compared to simple models. It is often possible to use much simpler models for failure and plasticity such as *MAT_003 or *MAT_024 in LS-Dyna, where plasticity and strain rate dependence can be modelled less accurately, but at a significant cost saving compared to models such as the Johnson-Cook model.

In Chapter 6, numerical models of the experimental tests found relatively low strain rates, which demonstrated it was not necessary to use strain rate dependent models for the aluminium panels. Strain rate sensitive models are typically used in conjunction with finely resolved meshes, where local strain rate can have a significant effect on the prediction of the mechanical behaviour. It is possible that when using the higher charge masses described above, that local regions of high strain rate would be experienced within a rail vehicle, where shear or tensile forces are very high, leading to material failure, but the mesh resolution which can be used in these models (in the region of tens of millimetres) is not sufficient to capture this behaviour. For this reason, the Johnson-Cook model described above is not applied, as the increased computational expense cannot be justified, as it is difficult to be confident that it will result in any improved accuracy in the current model.

Explosive venting is used in industry to reduce the build up of pressure in critical areas, due to explosions from gas and dust. Blast walls on oil rigs and blast relief panels are often used to reduce the effects of extensive pressure build ups, and it could be

considered that windows and doors in rail vehicles can achieve a reduction in passenger injury. Work by Larcher *et al.* [195] investigated the effect of vent area and window material on the risk to passengers inside a vehicle, and concluded that windows do not offer a an opportunity to significantly reduce risk to passengers, although a quantitative comparison between the pressure in models with and without windows is not provided. There is anecdotal evidence (See Section 3.1.1 on page 38) that open doors can reduce the risk of injury, but qualitative work to identify how failure and material models for doors and windows alter the pressure history in their immediate vicinity and in the vehicle as a whole has not been investigated.

7.3.2 Effect of mesh refinement

ConWep predicts an arrival time for the first shock at 9500mm (the end of the vehicle, assuming and explosion in the centre of the vehicle) of 17.5ms, which serves as a starting point for making estimates about the most appropriate termination time to select. The actual arrival time may be smaller, due to the reflections of the shock waves along the vehicle. A termination time of 30ms was chosen for the models, which is sufficient time to identify the differences in models with different mesh resolution. Computational limitations on both desktop Linux machines and the University of Sheffield HPC 'iceberg' meant that the model meshed with 20mm elements could not be run, but the model meshed with 30mm elements ran to completion at 30ms in 45 hours and 2 minutes, compared to 17 hours and 14 minutes for the model using 40mm elements.

Contours of resultant displacement are shown for both the 30mm and 40mm models in Figures 7.9 and fig:meshref-resdisp40 respectively, and a similar pattern of displacement is seen for both, with both levels of mesh refinement predicting points of high and low deformation in the same area at 10ms, 20ms and 30ms. At 6ms (top right image in both a and b), both levels of mesh refinement predict only deformation in one half of the vehicle structure, with floor and ceiling panels showing the only significant displacements of around 250mm. The floor and ceiling panels continue to show the peak displacement in both models at 20ms with the floor panel reaching a peak displacement of 380mm directly below the charge (lower left hand image), but the end wall begins to a show high displacement of 370mm at 30ms (lower right hand image) in both models. Displacement alone suggests the effect of mesh refinement is small.

Differences in the stress distribution over the structure of the models is shown for different mesh resolutions in Figures 7.11 and 7.12. Stresses at a peak of 350MPa occur at many locations in the vehicle, which shows that plastic deformation is widespread throughout the vehicle, given the specified yield stress of 275MPa. At 10ms, the 30mm model shows the highest stress at the floor panel in location of door, which is also shown by the 40mm model, but this model shows a stress concentration at the meeting of floor and sidewall near the symmetry plane. Both models show similar stress distributions at 20ms, with points of highest stresses in the bogie mounting frame and where the end wall meets the roof section. Deformation is low at this time, so it is clear the stress peaks before deformation reaches its maximum at 30ms. By this time, there are again differences in the stress distributions between the models, with higher stress concentrations seen around the window supports in the 30mm model, whereas the 40mm model shows areas of high stress in the structure above the central door frame. Finer meshes typically result in more accurate solutions, and there is no reason to doubt this

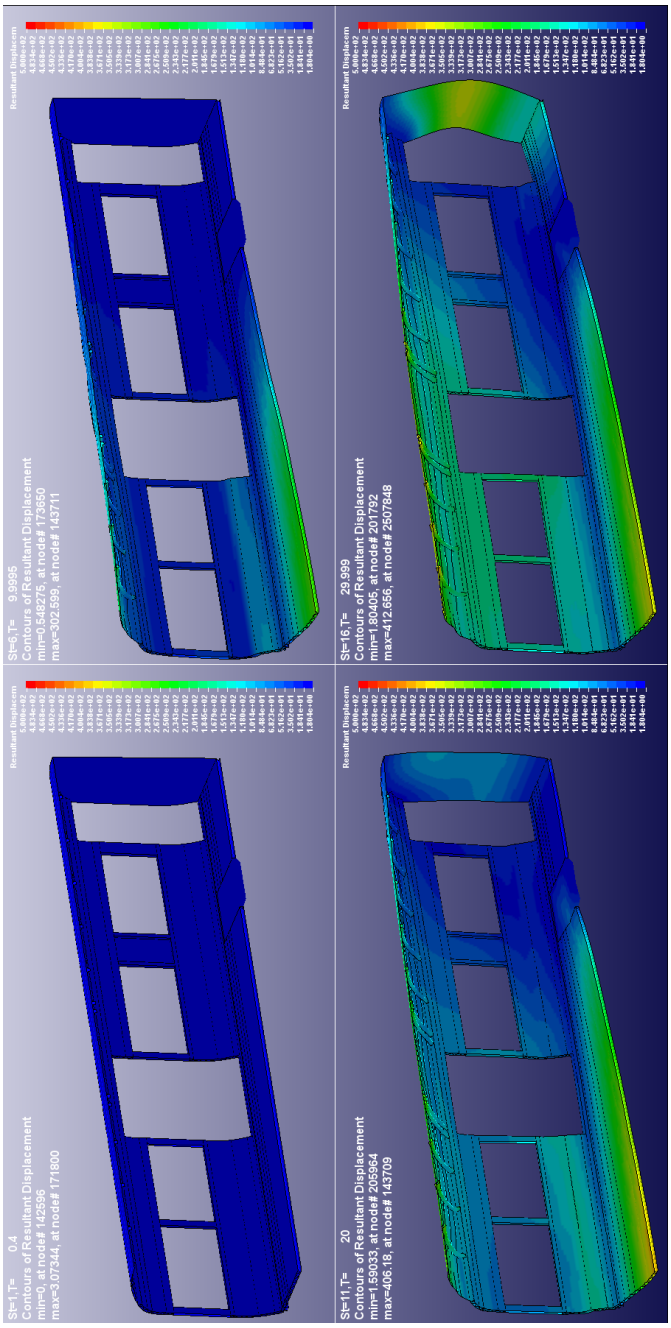

Figure 7.9: Resultant displacement fringe plot with 30mm mesh

is the case here.

Pressure histories and cumulative impulses at 2 locations are shown in Figures 7.13 and 7.14. Location 1, shown in Figure 7.13 lies 2000mm along the axis of the vehicle at 1330mm above floor level. Figure 7.13 shows minimal difference between both the pressure and cumulative impulse histories, with the arrival and magnitude of each shock predicted similarly at both mesh resolutions, and only relatively small difference of 25kPa-ms is seen between the final cumulative impulses at 30ms.

Location 2, shown in Figure 7.14, is located the same distance along the vehicle as location 1, but close to the window, as opposed to within the centre of the vehicle. Both pressure and cumulative impulse here show a larger difference between the models, with difference in final cumulative impulse of over 100kPa, giving a percentage difference of

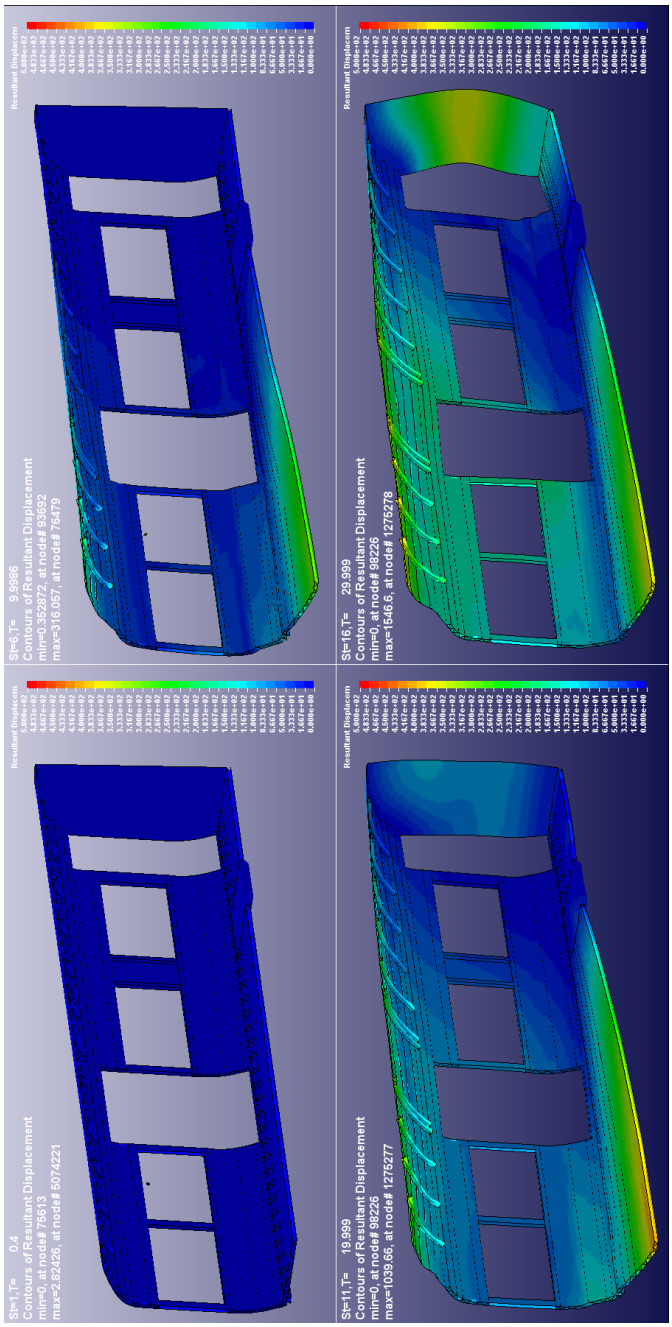

Figure 7.10: Resultant displacement fringe plot with 40mm mesh

18%, compared to only 3% difference between the final cumulative impulses at location 1.

7.3.3 Discussion of vehicle structural model

The effect of mesh resolution was discussed in Chapters 4 and 6, and is included here as the modelling effort has a focus on the analysis of both the structure and the propagation of the blast pressures. It was seen in Chapters 4 and 6 that the mesh resolution could lead to significant differences in the predicted reflected overpressure and impulse, which was also shown in the models here. Ideally, the validated results of the mesh refinement study from Chapter 6 could be applied and an element size of 15mm used, which was shown

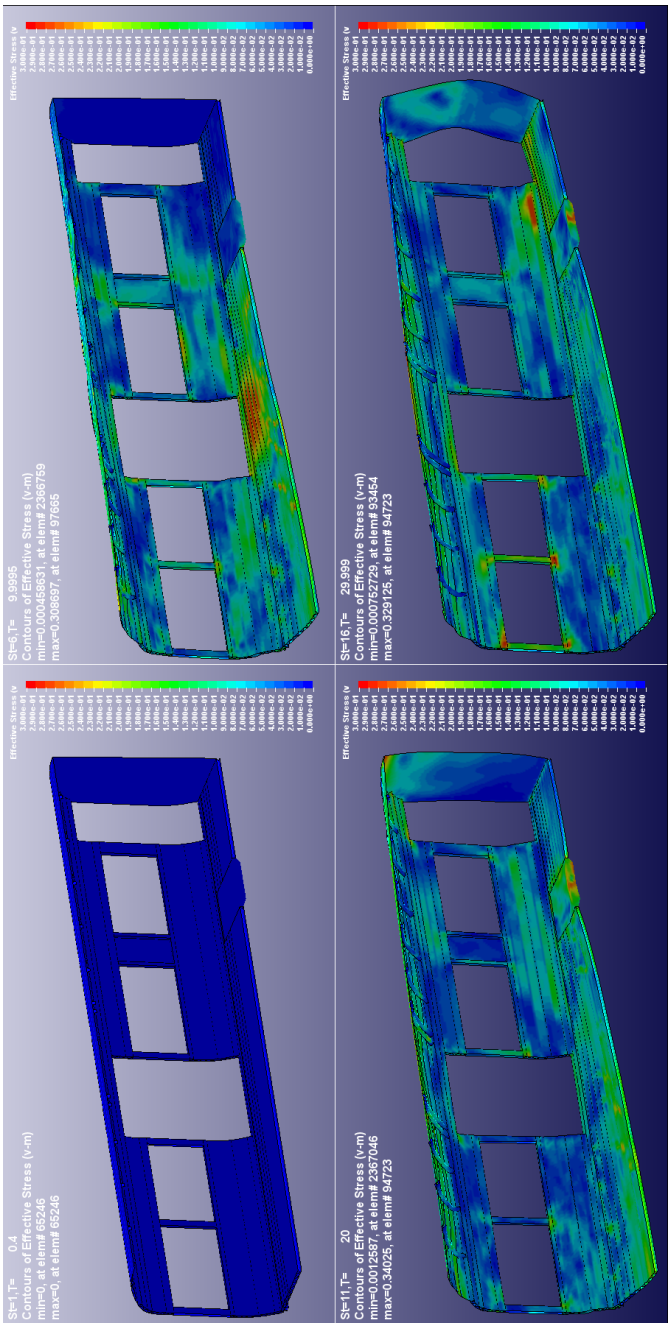

Figure 7.11: Von Mises stress fringe plot with 30mm mesh

to predict similar pressures as those measured in experiments, could be used universally over all the models, but this was not possible when applying a blast load to the rail vehicle models due to computational limitations. The number of shock reflections seen in both Figures 7.13(a) and 7.14(a) are limited, but in models from Section 7.4 onwards, the cylinders placed within the rail vehicle to simulate blast interaction with passengers will lead to many more reflections, and it is therefore necessary to reduce the element size as much as possible.

The use of coarse elements also affects how the structure performs. Failure of the vehicle body shell was not seen on either the 30mm or 40mm models, and the mesh resolution limits the ability of the model to fully examine the effects of stress concentrations that can lead to crack propagation and subsequent widespread structural failure. Stress

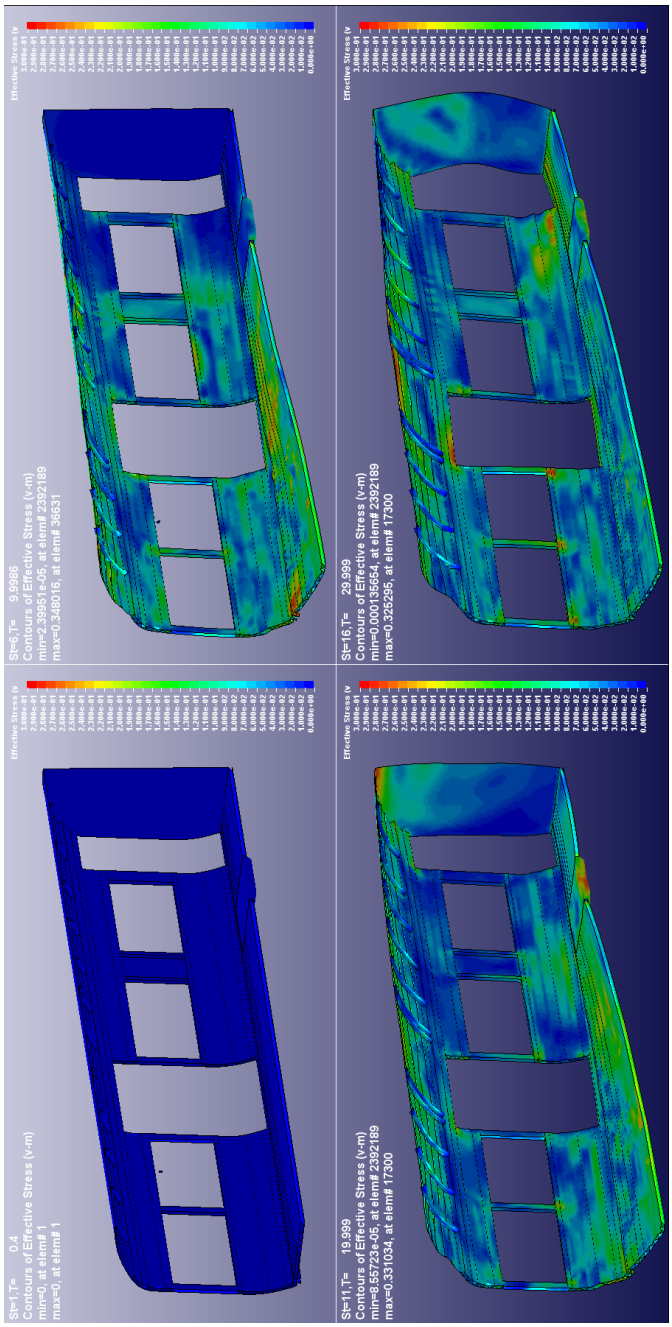

Figure 7.12: Von Mises stress fringe plot with 40mm mesh

concentrations on a macro scale (over tens of millimetres) can be seen in Figures 7.11, but there is limited scope for reducing the resolution of the structural mesh to investigate these further, as there is a requirement to maintain similar mesh resolutions between the ALE and structural mesh, thus the limit of the ALE element size is effectively the limit for the structural mesh. LS-Dyna implements ways of improving coupling to ensure each Lagrangian element contains 2 to 4 coupling points for each ALE element when the Lagrangian elements are coarser than ALE elements, but it is fundamentally not possible to achieve such coupling if Lagrangian elements are considerably smaller than ALE elements, without refining the ALE mesh.

Based on the modelling undertaken in Chapter 6, a simple strain rate independent plasticity model was implemented based on the assumption that strain rates were not

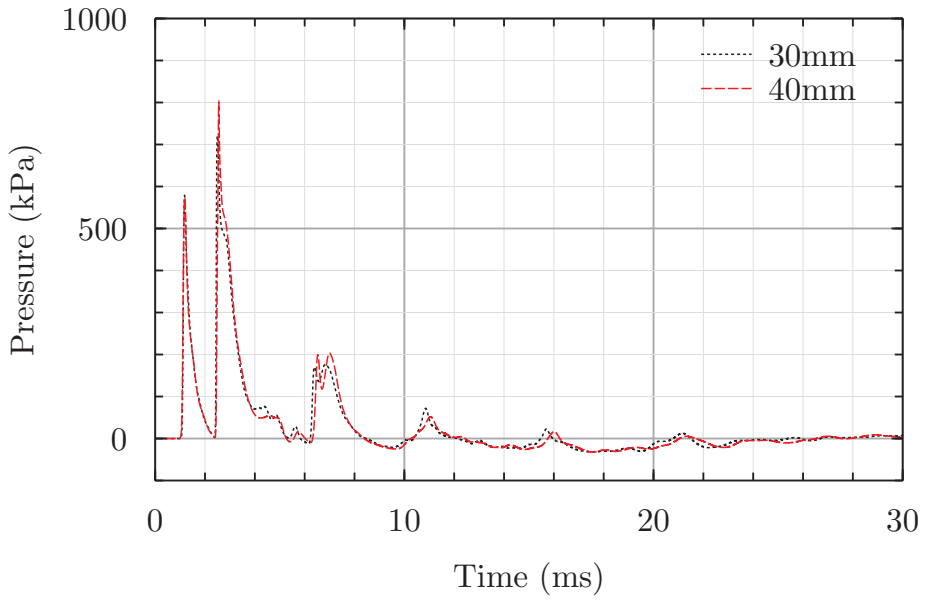

(a) Pressure time history

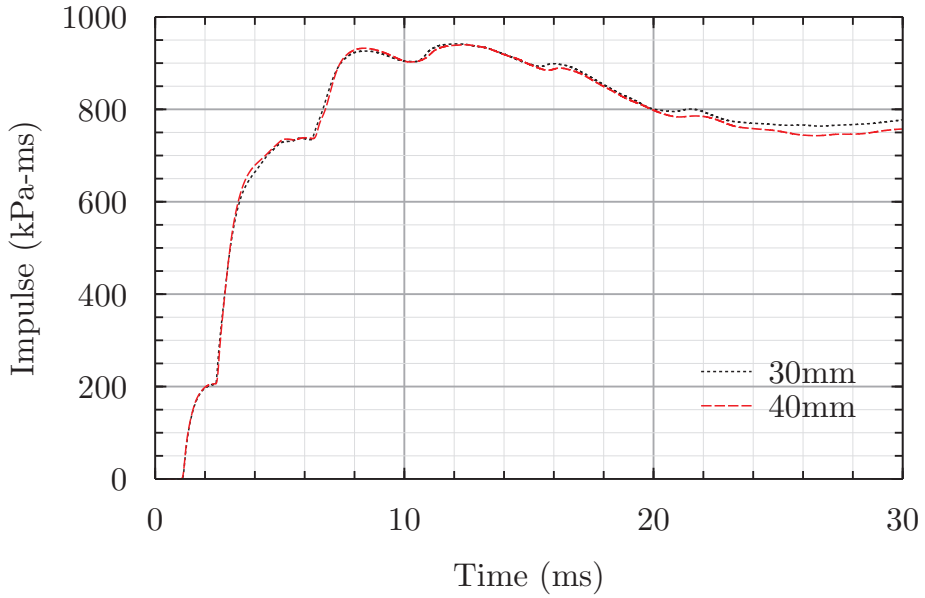

(b) Cumulative impulse history

Figure 7.13: Pressure and impulse at a point on the symmetry plane

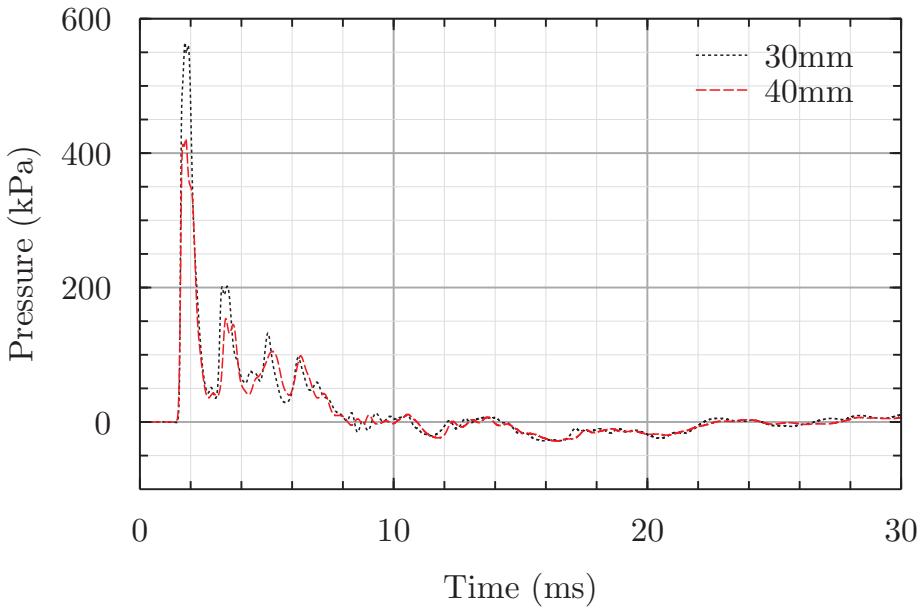

(a) Pressure time history

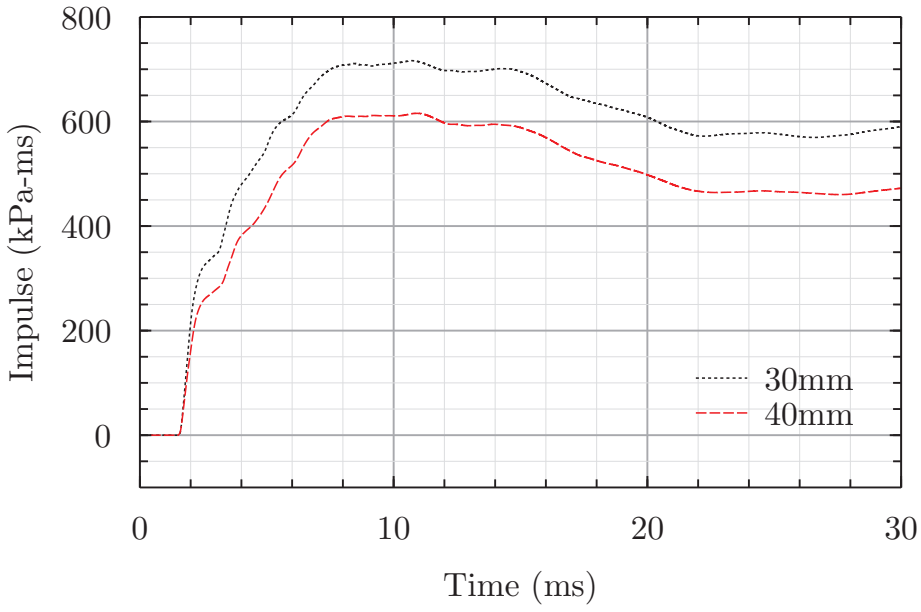

(b) Cumulative impulse history

Figure 7.14: Pressure and impulse at a point near a bodyside window

high enough to justify the extra computational effort to utilise the Johnson-Cook model was not justified. Strain rates remained low in the rail vehicle structural model, and were not above 10^1/s over the whole solution. This again justifies the use of strain rate independent models, but does not necessarily imply that strain rate effects do not occur and may not be important in some failure modes that may be seen experimentally, such as weld or bolted connection failure, or crack propagation in the structure.

An investigation of some important model parameters has been undertaken here, and some results of these presented. It is now necessary to introduce the methods used to model injury within a rail vehicle, and the variables that will be studied, before full models are presented and discussed in Section 7.5.

7.4 Modelling injury and scenario variables in rail vehicles

To answer the hypothesis posed in Chapter 1, a modelling method for predicting injury in rail vehicles, and understanding what could affect the likelihood and level of injury experienced is required. This Section describes the implementation of the risk models described in Chapter 3 using the methods described earlier in this Chapter. A number of generic 'scenario variables' of interest were chosen, to identify how certain common variables seen by vehicles across the network can affect structural deformation and / or human injury.

The effect of the windows, doors and the rigidity of the vehicle structure is of interest, to identify if any of these can make a change to the pattern of injury experienced by occupants. An investigation of the injury patterns in a full rail vehicle model can be compared with investigations of injury using models that represent the lower or upper limit, such as a fully rigid rail vehicle, or windows and doors with negligible resistance to blowout. Such investigations allow these effects to be discounted from future investigation outside of this work if they prove to yield no benefit, or to be investigated further if they show significant deviation from the injury predicted using the full model of a current vehicle.

Tunnels are a common feature across the rail network, and depending on the clearance around the train itself have the potential to confine the blast and increase the magnitude and number of reflections. Tunnels can also limit the amount of structural deformation a rail vehicle can undergo in certain dimensions, which could in turn alter the way reflection occur, as identified in Chapter 5. Likewise, the internal design of rail vehicle, including draught screens and seats has the potential to change the reflection of pressures around a vehicle, which could either increase or reduce the risk to people from pressure type injuries.

Open carriages or wide gangway vehicles have a negligible change in cross section between adjacent vehicles of each train, and are increasingly used to increase standing capacity and allow easier redistribution of passenger loads throughout the whole train. Unlike closed gangway vehicles, there is no physical barrier at the end of each vehicle, which means pressure reflections at the end of each carriage are reduced, but passengers in a connected carriage adjacent to an explosion are likely to be exposed to pressures and flying projectiles.

Passengers themselves can significantly alter the progress of flying projectiles, as well as the reflection and propagation of shocks, which means passenger density is one of the most significant variables to be studied here. A reduced passenger density means

fewer are present to be injured, but also the reduced density means shocks and flying projectiles can propagate further without being disturbed, which may increase the radius at which deadly effects are experienced.

7.4.1 Implementing risk models

In Chapter 3 injury models were developed to report the risk of chest and penetrating high velocity projectile injuries, using pressure history data from finite element models and statistical techniques. Pressure history data can be taken from the full scale rail vehicle model described in Section 7.3.3, to make predictions and estimations about the scale and distribution of injuries throughout a rail vehicle.

Pressure history data was taken from the finite element models by defining a rigid cylinder with a diameter of 305mm and a height of 1700mm at the positions at which chest injury risk is to be calculated, and pressure sensor locations are defined at 90°intervals around the circumference. The fragment injury model takes no data from the finite element model, and the input data is purely based on the position of the device and passengers, the mass of the charge, the mass and number of projectiles included within the device, and an assumed directional spread of projectiles in the vertical and horizontal directions.

7.4.1.1 Description of implementation for a rail vehicle

The implementation of these models starts by generating position data for the 'passengers' that will be studied, using a Matlab script `generate.m`, which can be found in Section B.1, which provides the position input for both the chest injury and projectile injury models. The reason for automating this is twofold; firstly to ensure that identical position data is used in both pressure and projectile injury models, and secondly to ensure that the positions are defined such that each subsequent location in the passenger matrix is further away from the device than all previous locations as shown in Figure 7.15, which is necessary for correct functioning of the projectile injury model. The input to this script is simply the x and y positions of any number of passengers. From this, the array `D` is written to file to be used in the fragment injury model, and 4 pressure sensor locations are defined and written to file in a form that can be directly interpreted by LS-Dyna using the *DATABASE_TRACER keyword. With the positions known, a finite element model can be generated, using the rail vehicle model described above and rigid cylinders to represent persons, using xy position data from `generate.m` to define the axial position of each cylinder.

Fragment injury data is generated for each position, which is output to a text file for standalone inspection and a detailed breakdown of the 'hits' generated by each fragment, and in formatted matrix data form for use in visualisation (see Sections B.3.2 and B.3.3 for code). Once the solution to the finite element model is complete, it is post processed to generate a matrix of pressure history data for all points, and peak chest wall velocity for each sensor location and subsequently each 'passenger' is generated and is output again in formatted matrix form and as a text file, as shown in Appendix B.2.

Once fragment and chest injury has been generated, it can be visualized in 2D using the new injury severity score (NISS, defined in Section 3.6) to give a prediction of those passengers who are most and least likely to be killed. A plan view of the quarter symmetry section modelled is shown, with coloured circles representing the position and

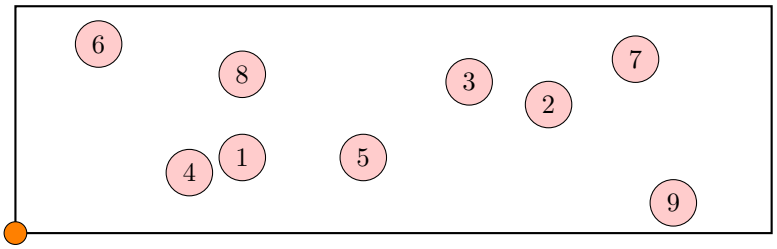

(a) Incorrect ordering of passengers in the array

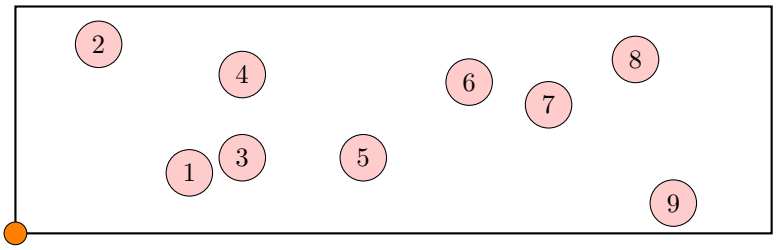

(b) Correct ordering of passengers in the array

Figure 7.15: Ordering of passengers in the array `D` must be correct, otherwise physically unrealistic behaviour may occur. The location of the device is shown with a filled orange circle in the bottom left hand corner.

injury risk for each 'passenger'. An example of this visualisation is shown in Figure 7.16, where each passenger is plotted as circle which is filled with a colour that corresponds to the NISS score, with a unique colour for each NISS value. It is possible to provide a scale of NISS values instead of simply providing a qualitative assessment of risk, but this arguably detracts from the simplicity and usability of the figure in its current form.

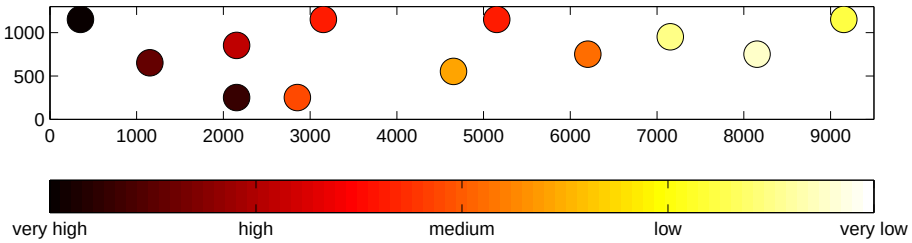

Figure 7.16: 2D visualisation of probability of serious injury or death

7.4.1.2 Defining the passenger density

The passenger positions are required as an input to the models, so it is important to have an idea of the typical number and distribution of passengers.

The number of passengers on a rail vehicle varies widely, depending on the time of day and the route of a particular service. Passenger loads are highest at rush hour periods on suburban and intercity routes, and can be particularly high around major populations centres and economic hubs. Studies on wheelset design and maintenance [196] have provided data on the percentage of unladen (tare) load at each axle, which can be used to define the high, low and medium densities of passengers. Based on an average person mass of 76kg and passenger loads at 10%, 1% and 0.01% of running time, the percentage of tare load and subsequent number of passengers was predicted, as shown in Table 7.8. The numbers shown in Table 7.8 for cases D1 to D3 represent

Table 7.8: Passenger density cases

case	% of running	passenger load (kg)	number	density (p/m^2)
D1	10	2100	28	0.61
D2	1	5400	71	1.5
D3	0.001	9000	118	2.6

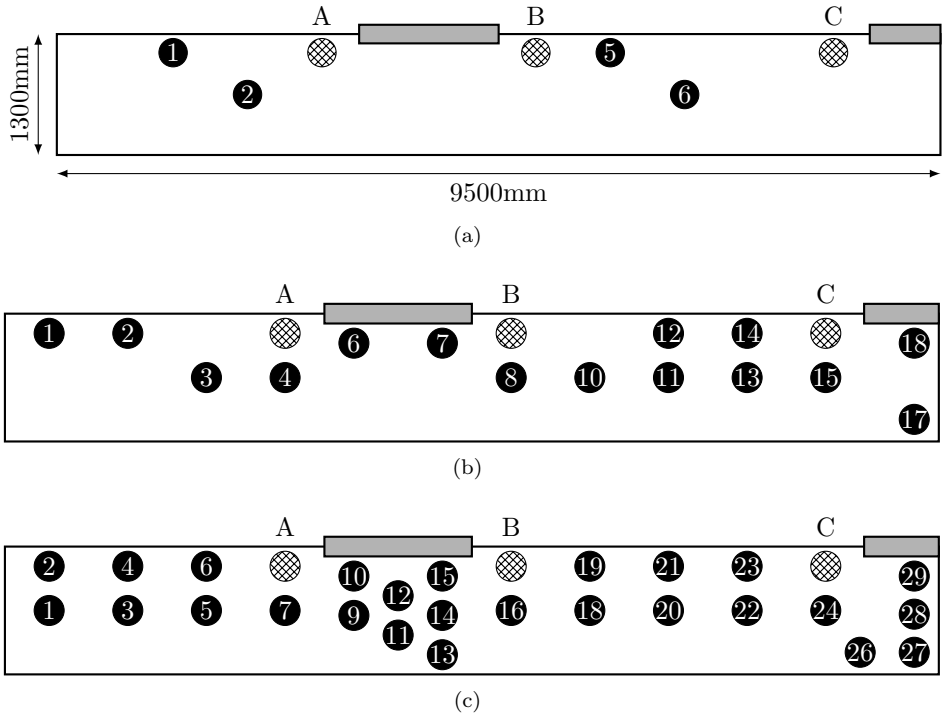

Figure 7.17: Three different passenger densities, D1 (a), D2 (b) and D3, including positions for reference passenger locations A, B and C and location of doors or opening (grey box). Reference locations A, B and C have been specified to allow comparison of 3 fixed positions across all three passenger densities. Some passengers are also referred to by numbers throughout the discussion, and these are also included here.

30%, 76% and 127% of the seated capacity of a Class 165 vehicle, as shown in [98]. The location of passengers shown for D1, D2 and D3 are shown in Figure 7.17. All variables were studied using the D2 passenger density, other than the study of passenger density itself, where comparisons are made between all 3 densities.

For each density, passenger positions are defined as if the rail vehicle is configured with transverse seating, with passengers typically seated in pairs of seats situated either side of a central aisle. Facing seats, where tables exist, or changes in the seat direction are not considered.

7.4.2 Vehicle structure

The relationship between the vehicle structure and features with the risk of human injury was studied with 4 models. A base case, case 1, is defined using the full rail vehicle model as described in Section 7.2.2.1, where the deformation of the vehicle occurs over the whole model as loads are applied, with windows and doors fixed in place until

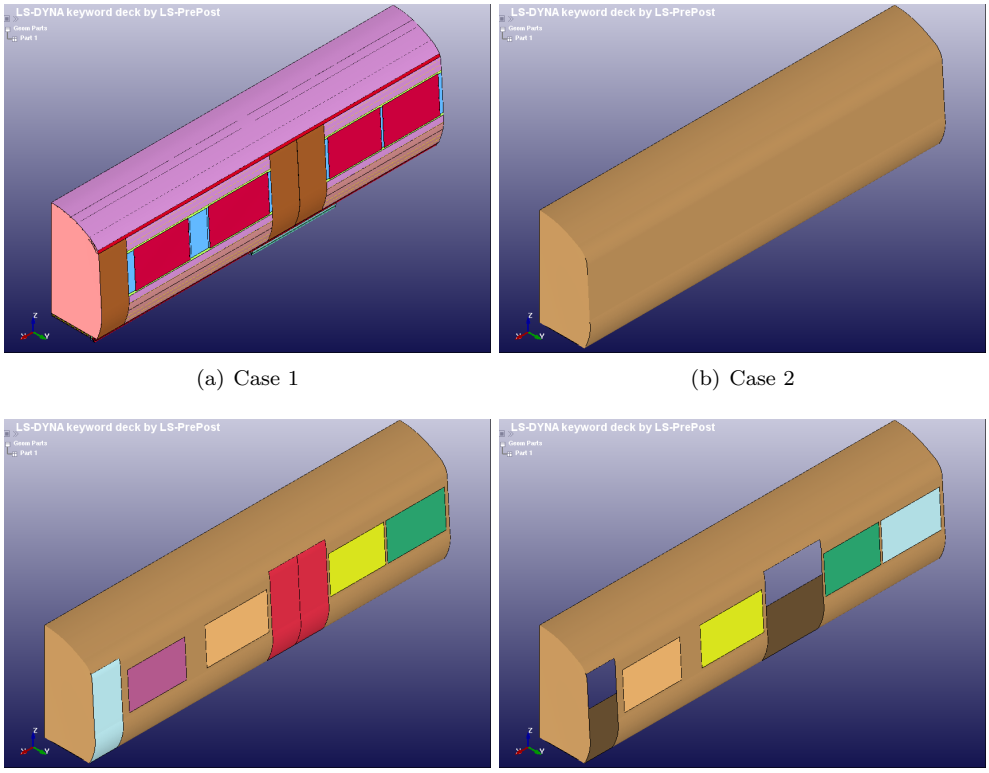

(a) Case 1 (b) Case 2

(c) Case 3 (d) Case 4

Figure 7.18: Structural models used for cases 1 to 4

failure criteria is reached. A further 3 models were constructed, using a rigid rail vehicle structure (the internal surface of the full rail vehicle model) each with a variation on the modelling of the doors and windows. Case 2 is simply the whole rail vehicle shell modelled with no openings for doors or windows, so no pressure can escape the vehicle. Case 3 models windows and doors using rigid but unattached shell elements of the correct mass, to identify the best possible reduction in injury that can occur purely as a result of venting. Finally, case 4 examines the effect of open doors by eliminating their presence, with windows modelled in the same way as case 3. This is an attempt to support of anecdotal evidence of reduced injury when train doors are open (see Section 3.1.1). The passenger density D2 is used for cases 1, 2, 3 and 4. An overview of the structure for each case is shown in Figure 7.18.

7.4.3 Tunnels

Tunnels on the UK rail network do not have a standard size and differ between individual routes, due in part to the historically separate nature of the rail infrastructure, as well as the typical requirements and vehicles used on different parts of the network. As such it is difficult to identify a 'standard' tunnel, but using clearance guidelines from Railway Group standards, it is possible to determine a minimum size for a tunnel, which can act as the lower limit for the effects to injury and structural deformation of confinement within tunnels. With the exception of some tunnels that are constructed with tunnel boring machines, and are thus necessarily circular in cross section, most tunnels have an elliptical cross section, or with vertical walls and an arch. For simplicity, a tunnel is defined as shown in Figure 7.19, with vertical walls and a circular arc for the roof, which

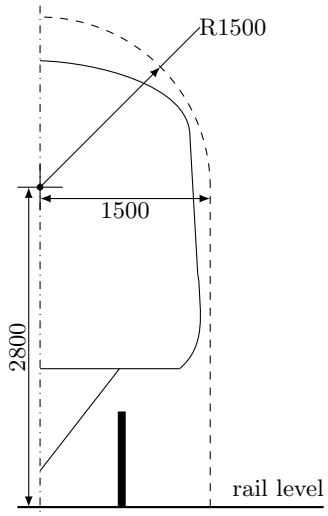

Figure 7.19: Tunnel and rail vehicle drawn to scale, all in mm

maintains a clearance of 100mm between the vehicle and the tunnel structure at the closest points, as defined in GC/RT5212 [197]. This represents the most extreme case with the smallest possible dimensions, but in most cases a rail vehicle's will be much larger than that shown in Figure 7.19.

For case 5, a tunnel is modelled and is assumed to be fully rigid, using shell elements and a rigid material model. In keeping with the symmetry applied throughout the modelling work, only 1 side of the tunnel is modelled. The vertical tunnel wall is assumed to begin at rail level and rises to 2800mm, and the roof of the tunnel is assumed to follow a arc with a radius 1500mm from the vertical section to the highest point of the tunnel at 4300mm ARL, as shown in Figure 7.19. The vehicle is modelled using the full vehicle model as used for case 1, and passenger density D2. The vertical side walls are modelled with rigid nodal constraints and using the *RIGIDWALL keyword, and the roof of the tunnel is modelled using a single layer of shell elements, as shown in Figure 7.20.

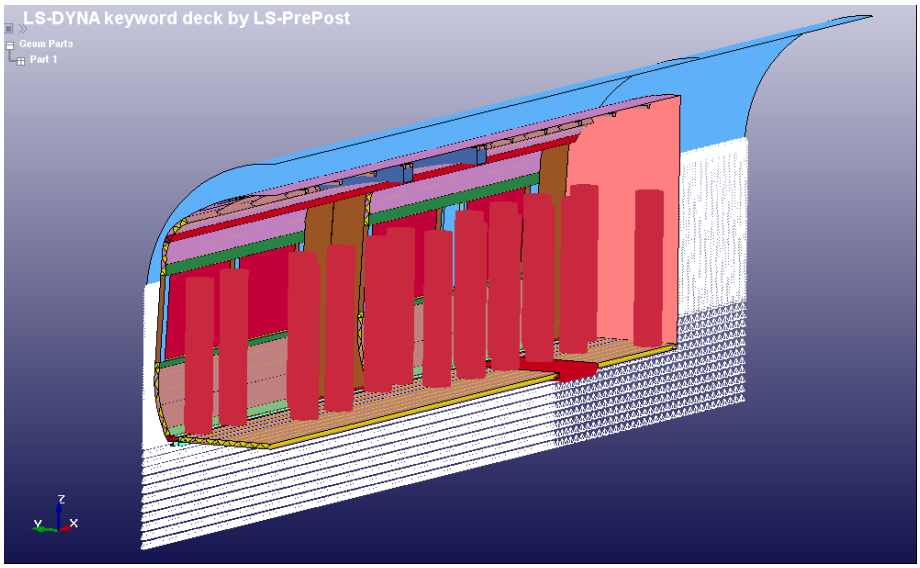

Figure 7.20: Roof and wall of tunnel shown for case 5

7.4.4 Open carriages

In case 6, Open carriages are modelled by removing a large part of the end of the carriage as a reflecting surface, and increasing the size of the ALE domain in the x direction to allow pressures to escape from the end of the vehicle with significantly reduced reflections, as shown in Figure 7.21. The risk of injury in other neighbouring carriages is not considered.

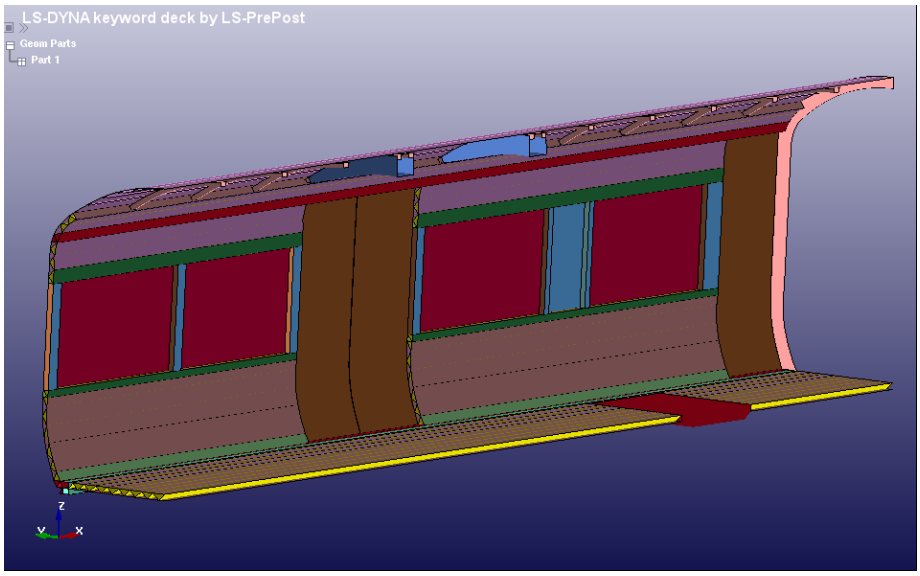

Figure 7.21: Structure of vehicle for case 6

7.4.5 Draught screens and seats

For case 7, the effect of draught screens and seats are implemented in the model by using the draught screen models described in Section 7.2.3.1, and seats are modelled using rigid shell elements for both the seat base and seat back, as shown in Figure 7.22. Seats are modelled regardless of whether a 'passenger' is located in that position, and seats are modelled facing in both directions.

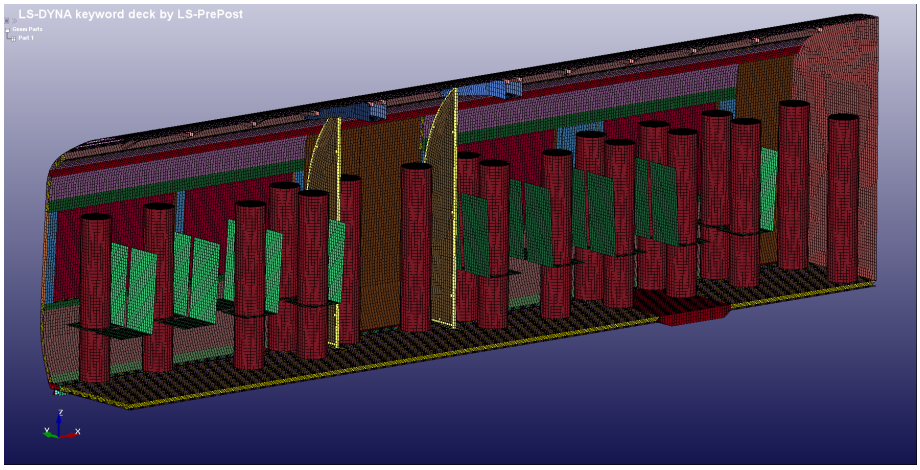

Figure 7.22: Position of seats and draught screens in C7

Table 7.9: Summary of cases C1 to C9. In the case of ✓[a], openings exist instead of doors within the doorway

case	structure	windows	doors	tunnel	open	seats	draught screen	density
C1	F	✓	✓	✗	✗	✗	✗	D2
C2	R	✗	✗	✗	✗	✗	✗	D2
C3	R	✓	✓	✗	✗	✗	✗	D2
C4	R	✓	✓[a]	✗	✗	✗	✗	D2
C5	F	✓	✓	✓	✗	✗	✗	D2
C6	F	✓	✓	✗	✓	✗	✗	D2
C7	F	✓	✓	✗	✗	✓	✓	D2
C8	F	✓	✓	✗	✗	✗	✗	D1
C9	F	✓	✓	✗	✗	✗	✗	D3

7.4.6 Passenger density

The full vehicle was modelled with a medium passenger density for case 1, and cases 8 and 9 use the same model vehicle structural model, but with a varied passenger density as shown in Figure 7.17. Case 8 uses the low passenger density D1, and case 9 uses the high passenger density D3, which are compared to the results of case 1. The models here do not consider the effect of seats, draught screens or tunnels, and studied purely the effects of passenger density.

7.5 Results and discussion

The results and discussion of cases C1 to C9 are presented here, and Table 7.9 should be used as a quick reference to identify the differences between each case. This includes the use of full (F) or rigid approximation (R), as well as passenger density, internal and external features. A copy of the input file for model C1, of which much is common across all models, is shown in Appendix A.3.

7.5.1 Global structural behaviour and injury

A comparison of adjusted severity of injury index (ASII, see Section 3.2.4) scores for C1 to C4 is shown in Figure 7.23, with the first passenger removed from the figure to aid visualisation, due to the significantly higher ASII scores found at this location, compared to over the rest of the vehicle. Chest wall and ASII values for person 1 for C1 to C4 can be found in Table 7.11.

Table 7.11 and Figure 7.23 show that passenger 1 (see Figure 7.17) has the highest risk of injury across all models and has a high likelihood of being fatally injured, according to correlated injury levels from Axelsson [141], seen in Table 7.10. Figure 7.23 shows that passenger 2 in all models is likely to suffer moderate to extensive chest injury according to Table 7.10, but models where a rigid vehicle shell is used, C2 to C4, have much higher ASII scores (3.5 to 5.1) than seen in C1 (2.5), where the vehicle shell was modelled with deformable elements.

Figure 7.23(a) shows that ASII scores for the first passenger shown in C1 are lower than for the same position in C2. As the passengers are modelled in the same way, and the same mesh resolutions and pressure mapping file are used, it is not surprising that

Table 7.10: Injury levels corresponding to ASII scores and chest wall velocity from Axelsson [141]

injury level	ASII	CWV (m/s)
no injury	0 – 0.2	0 – 3.6
trace to slight	0.2 – 1.0	3.6 – 7.5
slight to moderate	0.3 – 1.9	4.3 – 9.8
moderate to extensive	1.0 – 7.1	7.5 – 16.9
>50% lethality	>3.6	>12.8

Table 7.11: ASII and chest wall velocity for the first passenger in C1 to C4

model	ASII	CWV (m/s)
C1	6.6	16.5
C2	10.5	19.8
C3	8.8	18.5
C4	9.9	19.4

pressures from sensors facing the two symmetry planes (S1 facing towards the x axis, and S2 towards the y, see Figure 7.31 for diagram of S1 to S4) are very similar in both C1 and C2, but despite this the ASII scores are quite different. Examining the pressure times histories shows that peak pressures at S3, which faces the vehicle bodyside wall, are much lower in C1 than C2, which leads to the lower ASII scores. Comparing pressures for passenger 2 on C2 and C4 shows that as expected, peak pressures for S1 and S2 are very similar for C2 compared to C4, but at S3 in C4 there is a stronger secondary pressure reflection in passenger 2 at 1.1ms compared to the same point in C2, which lead to a slightly later higher peak in the chest wall velocity at this location in C4. The magnitude of the reflected pressures at a point closer to the detonation mean the effect of pressure reflections has a stronger influence on the chest wall velocity and thus the ASII scores here, compared with further along the vehicle, but the effect of differences in the reflection of shocks is seen along much of the vehicle.

In all models, no injury (ASII <0.2) is seen past 5500mm along the vehicle in Figure 7.23, but in C4, where no doors were present and pressures were not reflected, no injury was seen past 3000mm, which is lower than all the other models. Passengers at 3500mm and 4500mm along the vehicle in C4, in line with the positions of opening (see Figure 7.17) showed lower ASII values than C3, where doors, even though unattached, were present. Interestingly, the risk of injury of these persons at 3500mm and 4500mm is similar in both C2, where no doors or windows were present, and C3, where doors and windows with no physical restraint were placed, indicating that any 'venting' offered by these has no effect, but the lack of pressure reflecting surface in C4 due to the removal of the doors has a much more noticeable effect.

Plotting the chest wall velocity history for C1 to C4 for reference points B (near the door) in Figure 7.24 and C (near the vehicle end) in Figure 7.25 shows how more significant chest wall velocity reductions are made near to the door than at the end of the vehicle, which is also shown by the ASII scores shown in Table 7.12, where only moderate differences are seen at reference location C for all models, but differences of over 50% are seen at reference location B. At B, velocity in C2 peaks at 7.8ms at 7.5

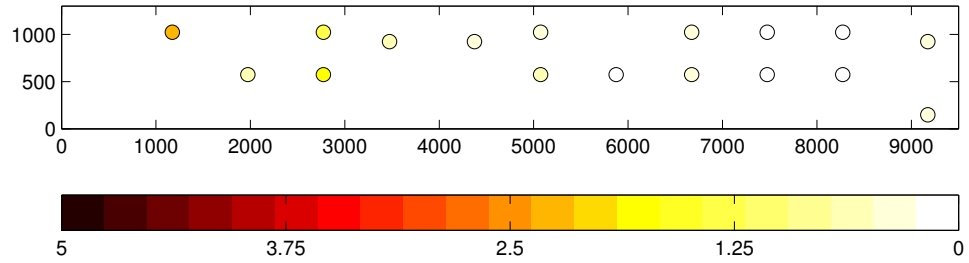

(a) C1

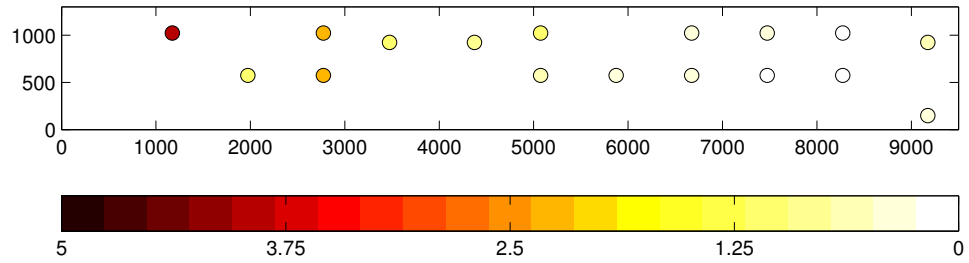

(b) C2

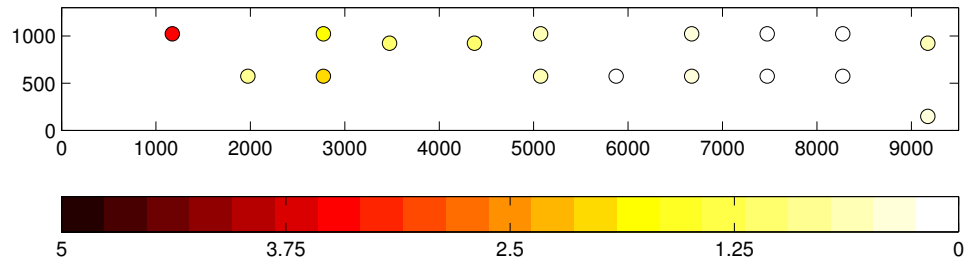

(c) C3

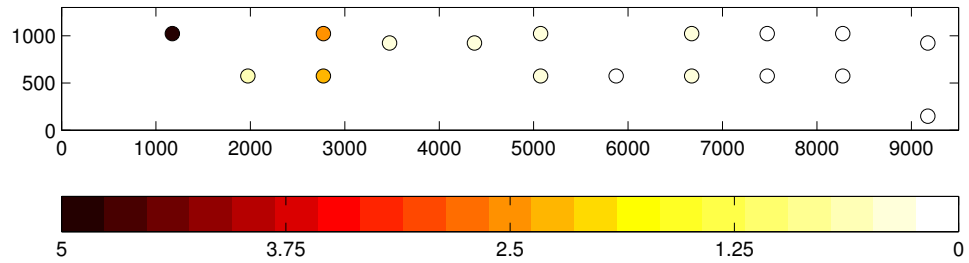

(d) C4

Figure 7.23: Comparison of ASII scores for chest wall injury for C1, C2, C3 and C4

Table 7.12: ASII values for reference locations in models C1 to C4. See Figure 7.17 for locations of A, B and C

	ASII			
Reference location	C1	C2	C3	C4
A	1.28	2.34	1.98	2.54
B	0.41	1.00	0.65	0.38
C	0.09	0.16	0.13	0.11

m/s, with the C3 peak at 6.2m/s at the same time, and the peak in C4 at 4.95 m/s at 8.1ms, which represents a difference of 45% between the peak chest wall velocity in C2 and C4 at point B. At C, shown in Figure 7.25, a smaller difference is seen between peak values for different models with a difference of 28% between maximum and minimum values in C1 and C2. In model C2, where the structure is rigid and there are a greater number and strength of reflections and the pressure is maintained above atmospheric for a much greater period of time, the chest wall velocity history is much more transient than that seen in C1, C3 or C4, with several periods of acceleration of equal magnitude to that caused by the arrival of the initial shock. Although purely speculation, it would be reasonable to think this was much damaging to the body than the chest wall velocity history seen at other locations, although in the criteria used in this work, these effects, due to later time reflections and increased quasi-static pressures are not considered, as only the peak velocity, not the acceleration or any cumulative metric, is used. Figure 7.26 shows that for a typical example, the peak chest wall velocity occurs shortly after the peak pressure, and thus the total cumulative impulse is not a driver for determining the peak velocity.

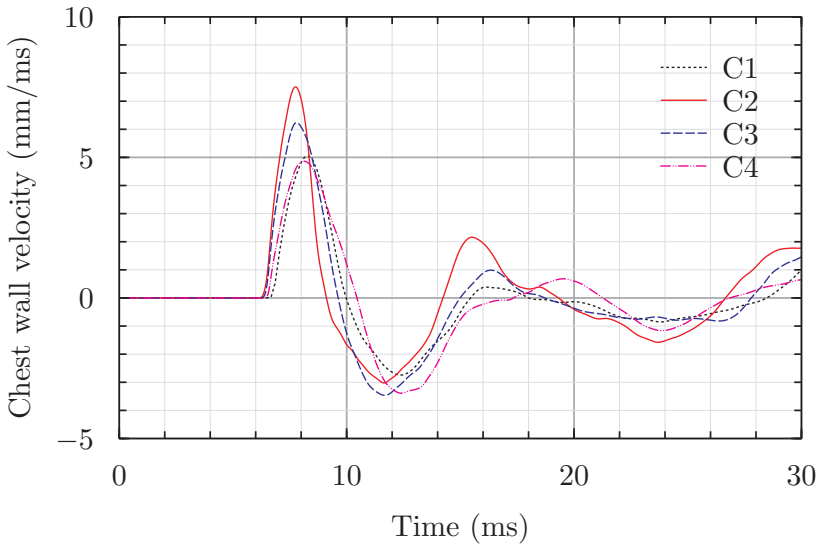

Figure 7.24: Chest velocity history for C1 to C4 at reference point B

Projectile injury predictions for passenger density D2 (used for cases C1 to C7) for 3 different draws from the normal distribution are shown in Figure 7.27. Each draw is taken using the same statistical parameters as described in Section 3.7, and the inherent variability caused by taking random draws from a multivariate normal distribution can be clearly seen. For many of the passenger positions, the predicted likelihood of a life threatening or fatal injury is the same, but in some positions there are a range of predictions. Between 3500mm and 4500mm along the vehicle, the two passengers in both cases are subject to similar risks for each random draw, but in (a) and (c) are subject to medium risk of lethal injury, whereas in (b) a high to very high risk is seen at the same location. At the passenger location at 9100mm along the vehicle, close to the centreline, the risks of lethal of life threatening injury for these three particular draws vary from very low to very high.

When injury prediction scores for both projectile and chest wall injury are combined, as shown in Figure 7.28 where the fragment output from the 3rd draw in Figure 7.27(c)

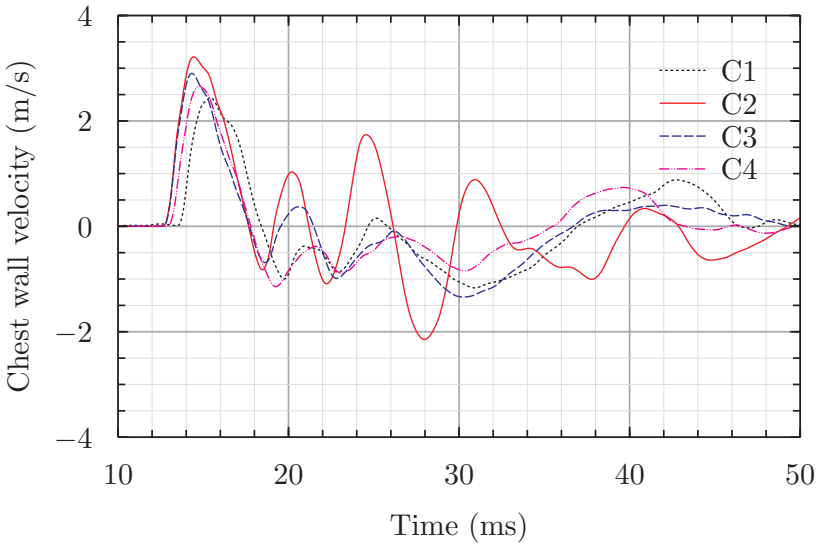

Figure 7.25: Chest velocity history for C1 to C4 at reference point C

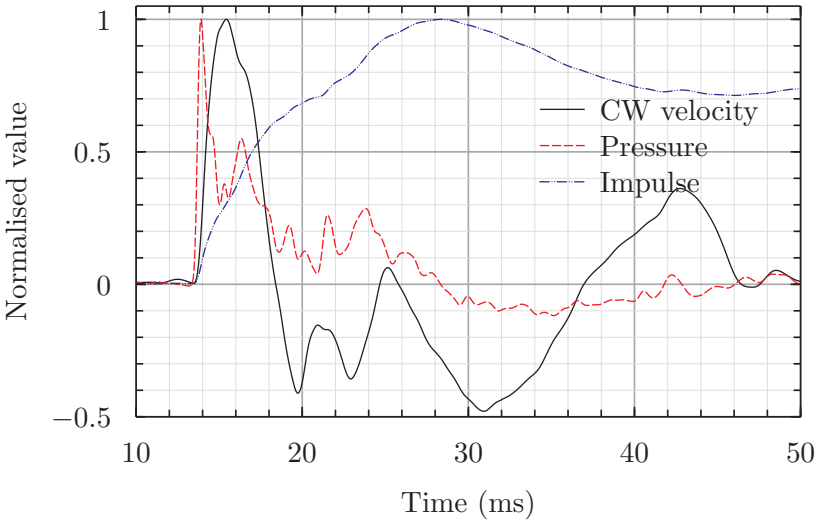

Figure 7.26: Values at location C in case 1, normalised by the peak value in each data series

is used, it is clear that the effects of projectile injury dominate in this case. In (a), (b), (c) and (d) the injury prediction is almost identical, and only the closest passenger in (a), who has a lower chest wall velocity as discussed above, is different. It is only at this first passenger location across all cases that the pressure injury dominates over the projectile injury, and under a different draw from the normal distribution this may not be the case.

It has been identified here that structural deformation itself plays an insignificant role in determining the shock wave injuries experienced by passengers as shown in Figure 7.23, and that with the device specified (5kg of explosive with 1kg of projectiles), the risk from flying projectiles is much higher than the risk posed by the shock waves themselves. It was noted that removing the doors reduced the chest wall velocity of passengers positioned near these doors due to the significant reduction in the pressure experienced on one side of the chest, but for the given charge size the pressures experienced were not high enough to cause significant injury in any case. For a higher charge with a lower

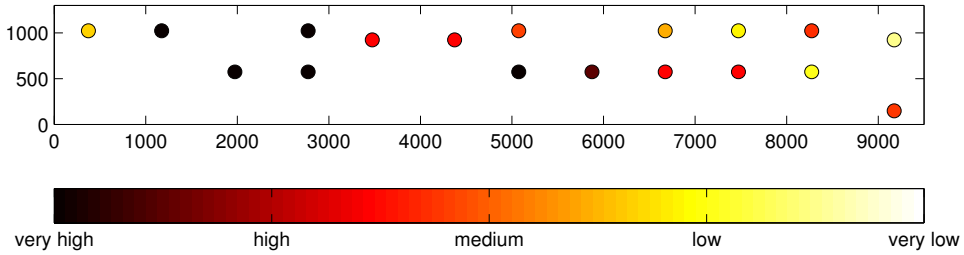

(a) 01

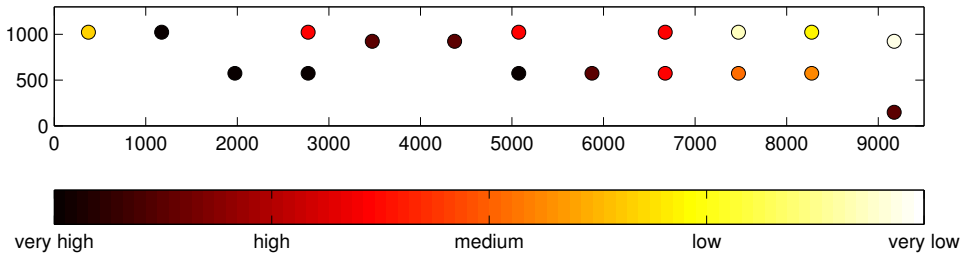

(b) 02

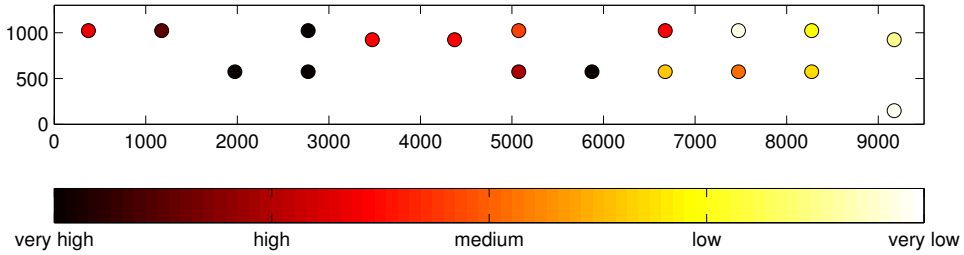

(c) 03

Figure 7.27: Results from three runs (01, 02 and 03) of projectile injury model for a passenger density of D2, showing the likelihood of a fatal or life threatening injury

volume of injury causing projectiles, injury patterns would be expected to be different where doors were not present, compared to scenarios where either rigid reflecting surfaces, or doors and windows. It is therefore pertinent to look at the effect that addition or removal of reflecting surfaces which can confine the blast wave can have on chest wall injury.

7.5.2 Confinement

Figures 7.29 shows the distribution of ASII scores and peak chest wall velocity values for rail vehicles within a tunnel (C5) and with an open carriage end (C6). Comparison of chest wall velocity in (a) and (b), and ASII distribution in (c) and (d) is largely the same throughout both vehicles, indicating that the confinement offered by tunnels does not yield a higher number or likelihood of passengers experiencing chest wall injuries, even when compared to C6, where fewer reflections from the vehicle end may be expected to reduce the expected injuries.

The effect of removing the reflecting end of the vehicle in C6 can be seen in Figure 7.30, where the chest wall velocity for passenger position 18 (see inset) is shown for cases C1 as a reference case, C5 and C6. A very similar peak chest wall velocity is seen for C1 and C5, but a much reduced chest wall of 2.5m/s was seen in C6 compared

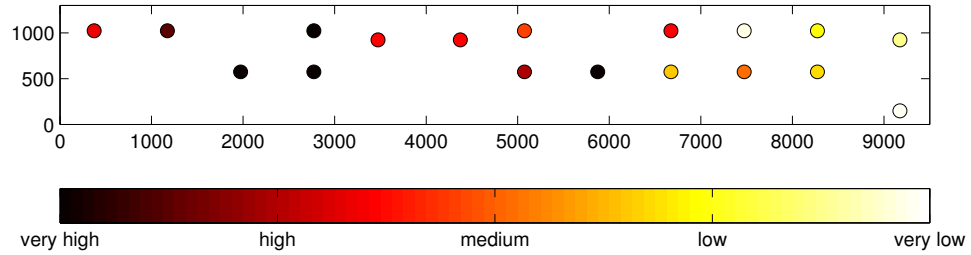

(a) C1

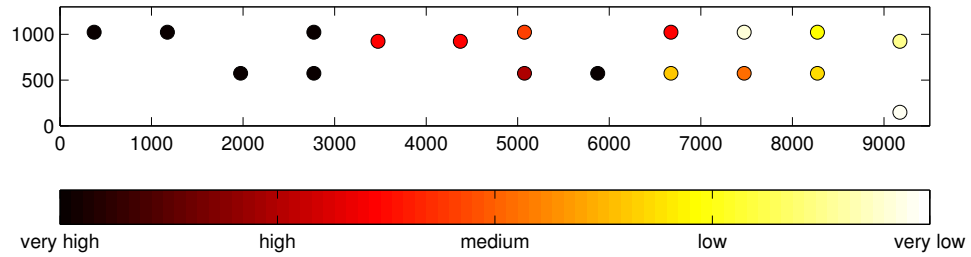

(b) C2

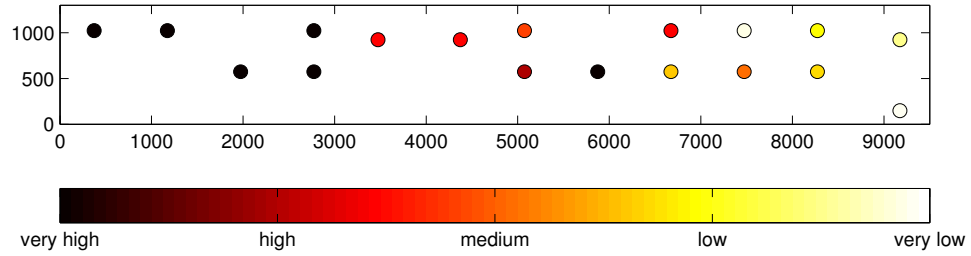

(c) C3

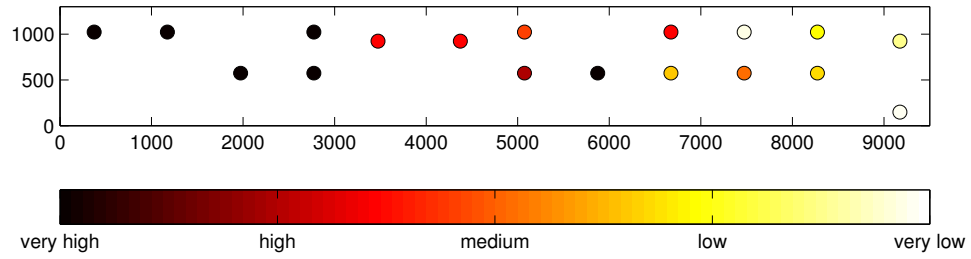

(d) C4

Figure 7.28: Comparison of total injury scores for C1, C2, C3 and C4

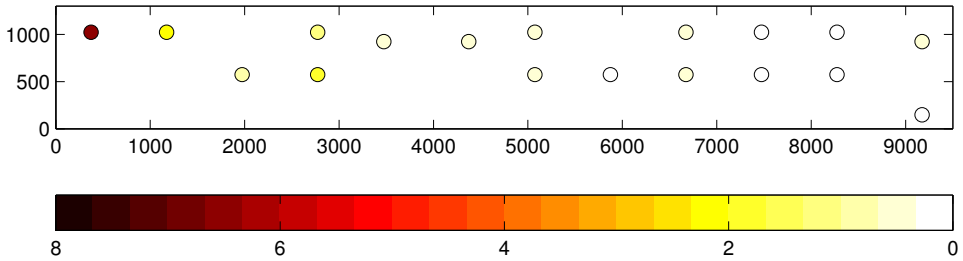

(a) C5 ASII

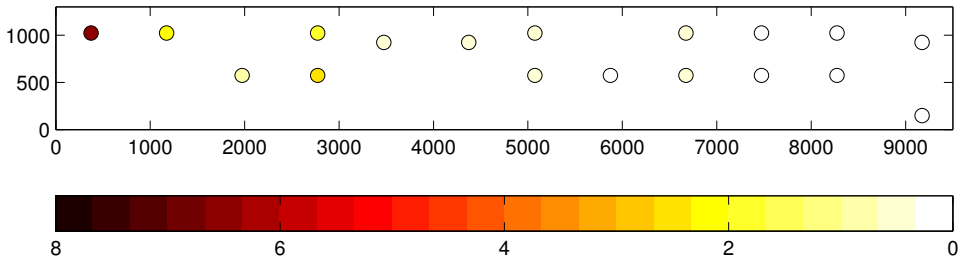

(b) C6 ASII

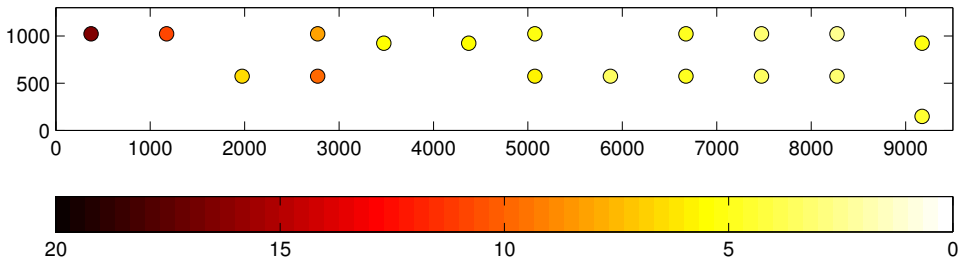

(c) C5 chest wall velocity (m/s)

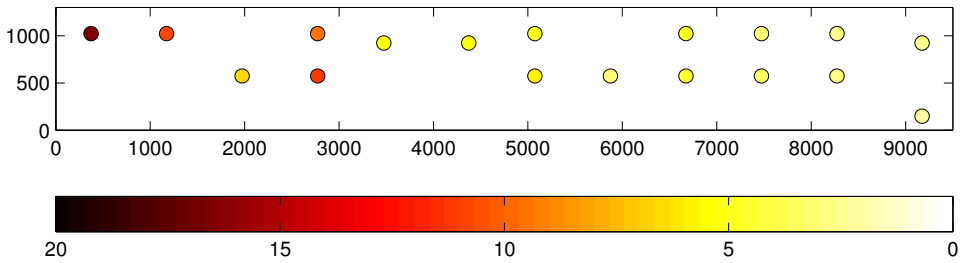

(d) C6 chest wall velocity (m/s)

Figure 7.29: Effect of confinement on pressure injury

to 5.1m/s seen in C5. The reasons for the reduction in the chest wall velocity at the end of the vehicle are shown in Figures 7.31 and 7.32, which show normalised values of the pressure time histories for each of the four sensors around the cylinder at passenger position 18, along with the velocity time history. Pressures in both Figures 7.31 and 7.32 are normalised by the peak value of the all four sensors for that particular case, which in the case of C5 is S4, and for C6 is S2. These sensor positions are shown in both Figures 7.31 and 7.32, and are a plan view of the passenger position shown in Figure 7.30, with S4 facing towards the end of the vehicle (or in the case of C6, an open end), with S3 facing towards the vehicle outer wall. The value of the peak pressure at S2 is the same in both C5 and C6, as would be expected, but the higher chest wall velocity in C5 is due to a much higher value of the reflected pressure at S4 which is 34% higher than the peak in S2. For C6 the peak pressure at S4 is 53% less than S2. In the velocity history of P18 in C5 shown in Figure 7.31, there is a noticeable change in the chest wall velocity at 17.3ms caused by the strength of the pressure at S4, as well as reflections that are visible in P2 and P3, which have a similar magnitude to the peak pressure seen in S1. Figure 7.30 shows that it is at 17.5ms where the velocity time histories diverge, with the chest wall velocity continuing to increase in C5, but shortly after this it reaches the peak value in C6. The reduction in the peak velocity in C6 is due to the reduction in reflected pressure at S4, and the absence of the extra reflections seen in Figure 7.31 at 17.1ms, which are not seen in Figure 7.32.

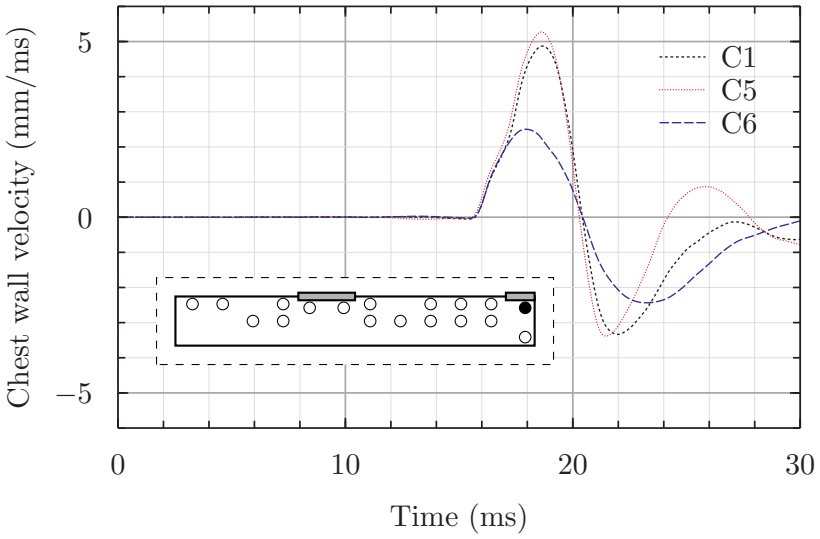

Figure 7.30: Effect of confinement on chest wall velocity of passenger 18, with position shown filled in black

Figure 7.31 also shows a period of sustained pressure above atmospheric after 20ms, which is not visible in Figure 7.32. The sustained pressure here would appear to affect the chest wall velocity after 20ms in C5, where the relative peak negative velocity (relative to the maximum positive velocity) is lower in C5 than in C6, as shown in Figures 7.31 and 7.32. In C6, there is also a slower response from the chest wall between 20ms and 30ms, with the velocity returning to zero at 30ms, whereas in C5 the velocity has returned to a positive value by 25ms. As was discussed in Section 7.5.1, this shows that although quasi static and later time pressures after the initial few reflections are unlikely to affect the value of the peak chest wall velocity, they can have a noticeable effect on the later time chest wall response.

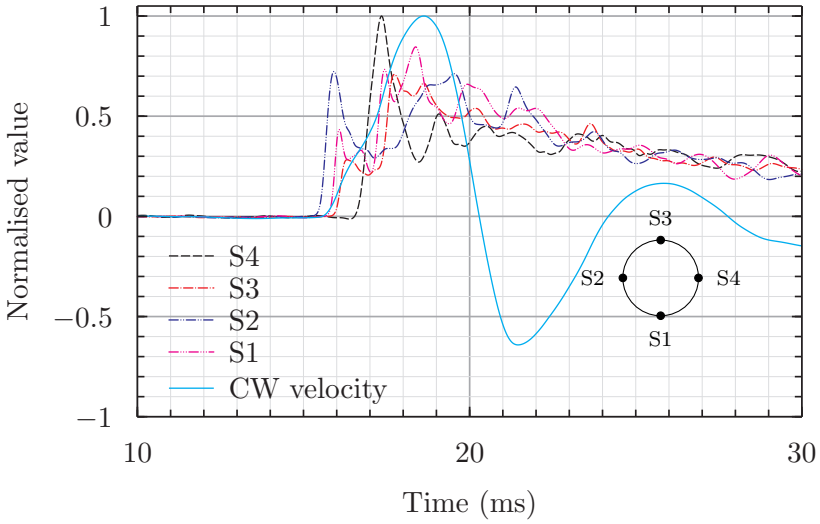

Figure 7.31: C5 passenger 18, comparison of 4 pressure histories and cwv

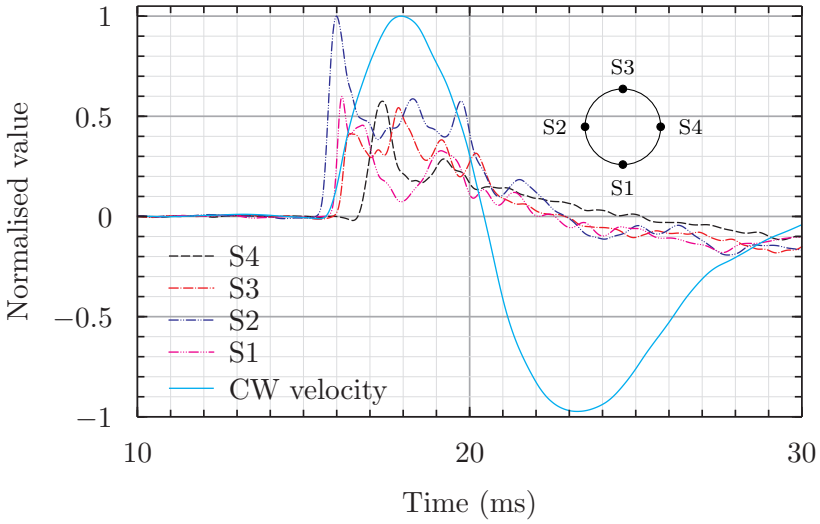

Figure 7.32: C6 passenger 18, comparison of 4 pressure histories and chest wall velocity

For the charge used in the modelling here, chest wall injury predictions indicate that the pressures experienced are not significantly magnified or reduced by changes in the levels of the vehicle confinement (higher in C5, lower in C6, compared to C1, for example) to increase or reduce the likelihood of a serious chest injury. In most cases, only persons very close to the charge are subject to chest wall velocities high enough to cause injury, and it is the incident pressures on the passengers and the immediate reflections from the walls of the rail vehicles that are the drivers of the peak chest wall velocity. Given sufficiently high pressures from a much larger explosive device, the data from C6 indicate that passengers positions very close to the end of a vehicle may be exposed to a lower risk compared to those in a normal vehicle. The data however does not support the hypothesis of increased injury risk to passengers with a vehicle located in a tunnel, although transient chest wall velocity response, which is not used as a measure of injury in the current criteria, is altered by later time pressures, seen when explosions occur in more confined spaces such as tunnels.

Table 7.13: ASII and peak chest wall velocity for P1 in C1 and C7

model	ASII	CWV (m/s)
C1	6.6	16.46
C7	18.9	25.08

7.5.3 Internal features and injury

Case 7 was used to investigate the effect of internal features such as draught screens and seats on the distributions of injuries within a rail vehicle. Figure 7.33 shows the distribution of ASII scores and peak chest wall velocity in C1 and C7, with data from passenger position 1 removed to allow improved visualisation, and shown in Table 7.13 instead. The ASII scores and chest wall velocity seen for passenger location 1 in both C1 and C7 are significantly higher than those seen at other locations throughout the rail vehicle, and removal of data from this position allows a better graphical comparison of scores between cases and over the whole rail vehicle. Projectile injury predictions are not included here, as they are identical between both cases C1 and C7 as the projectile injury model does not include the interaction of projectiles with draught screens, although in reality there will be some form of screening. Fragment injury also dominates in this scenario, but a closer investigation of pure blast injury is shown as the results are certainly relevant to situations where fragment injury risk is lower.

Data from Table 7.13 shows that the predicted level of chest wall injury for P1 (the closest passenger to the charge, shown inset in Figure 7.34(b)) is significantly higher in C7 than C1. Pressure reflection from the rigid seat is responsible for the increase in injury criteria here, with the sensor facing the seat back significantly showing a much higher peak overpressure in C7 at 3.5MPa compared to 1.16MPa at the same position without the seat present in C1.

Figure 7.33 shows peak ASII and chest wall velocity values over excluding passenger 1 over the whole quarter of the modelled rail vehicle. It is clear that the presence of seats and draught screens leads to significant changes in the predicted chest wall velocity, which in turns leads to differences in the prediction of ASII scores for many passenger locations between C1 and C7. Figure 7.33(a) and (b) show that for passenger positions up to 3000mm along the carriage, seats and draught screens can simultaneously increase the risk of a severe chest injury in some locations and reduce it in other. In C7, reductions in ASII are seen in P2 and P4 (shown in (a)), but increases are seen at P3 and P5, due to increase in reflection from the seat. Even at P3, significant reduction in peak pressure on the sensor facing the seat in front are seen in C7 compared to C1 with peak pressures down from 1.5MPa to 0.95MPa, but higher reflected pressures from the sensors facing towards the seat back are seen, leading to an increase in the predicted chest wall velocity and therefore the ASII score. A similar effect can be seen due to the draught screens, where a similar chest wall velocity is seen at locations P6 and P7 in C1, but in C7 a reduced chest wall velocity is seen at P6, with a slight increase in the chest wall velocity at P7. C1 and C7 also show differences at P8 and P9, and P11 and P12, where chest wall velocities shown in Figure 7.33(d) are higher than for the same positions in Figure 7.33(c). In these cases the blocking effect of the draught screens and the seats, and the peak pressure experienced by all sensors other than that facing the aisle see significant

reduction in peak pressure compared to the same location C1. Interestingly, in the case of P10 the chest wall velocity is similar in C1 and C7, and although the peak pressures for all 4 sensor locations at P10 are lower in C7 compared to C1, extra reflections are seen in C7, which bring peak chest wall velocities into line.

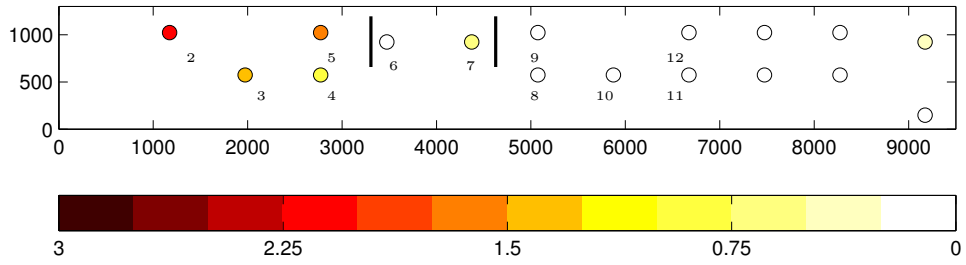

(a) C7 ASII

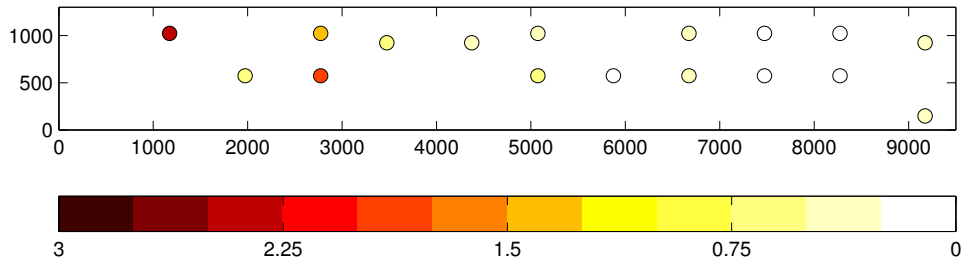

(b) C1 ASII

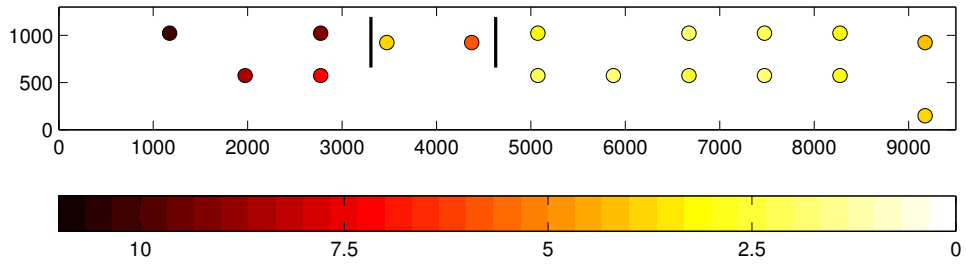

(c) C7 chest wall velocity (m/s)

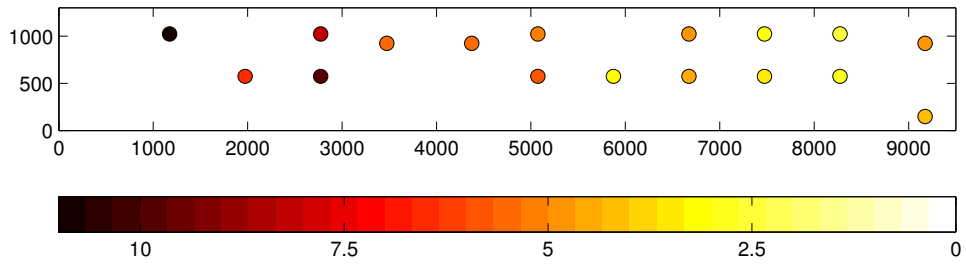

(d) C1 chest wall velocity (m/s)

Figure 7.33: Case 1 and 7 chest injury predictions, with person 1 removed to aid visualisation

Chest wall velocities at the end positions of the vehicle, furthest from the point of detonation are similar for both C1 and C7. This indicates that any disruptive effect that draught screens and seats may have on the progression of the shock wave and subsequent reflections along the vehicle are not sufficient to reduce the chest wall velocity and thus the likelihood of severity of the injury at the end of the vehicle, if the pressure was

sufficiently high to cause a chest injury. Despite being shielded from the blast by seats in front, passenger reference location C, shown in Figure 7.34(b) shows a higher peak chest wall velocity in C7 compared to C1, due to the orientation the seat, which in this case does not shield the passenger from the blast, but reflects the blast back towards the passenger. Contrasted with location B, shown in Figure 7.34(a), where both the seat and the draught screen provide a shielding effect in C7, the peak chest wall velocity of C1 is 2m/s higher than the peak value of C7.

Draught screens and seats were seen to offer protection in positions throughout the rail vehicle, and in others increase the risk of injuries. As with other cases mentioned in previous sections, in many cases the pressures experienced were not sufficient to cause lethal injuries, but patterns in increase and decrease in injury were seen, particularly in terms of the position of the passenger relative to draught screens, and the orientation of the seat relative to the passenger. Where passengers were positioned such that a seat or draught screen shielded them from exposure to incident shocks the risk of injury was reduced, but in the case were the seat orientation or passenger position relative to the draught screen was such that significant shock reflections back towards the sensor closest to the reflecting surface was seen, increases in injury risk were predicted. Clearly the effect of objects such as seats and draught screens within a rail can play a noticeable role in altering the reflection of pressure and subsequently the pattern of injuries. The seats here were modelled by using a rigid material and a single layer of shell elements. Given that seats can have a role in increasing the value of pressure experienced by passengers, a more thorough investigation of pressure reflections from such structures should take place, but the assumption of a rigid reflecting surface here serves to give a worst case scenario.

7.5.4 Passenger density and injury

Chest wall velocities for 3 passenger reference locations are shown in Figure 7.35. At reference position A (Figure 7.35(a)) chest wall velocity history is very similar for densities D1 and D2, with both reaching a peak of 8.6 m/s at 3.7 ms, and returning to a velocity of 0m/s at a similar time. The peak chest wall velocity in D3, which has the highest density of passengers, is lower than both D1 and D2, showing a maximum value of 7.1m/s at 4.3ms. The primary difference in D3 compared to other models, is that the peak pressure measured on S2 (facing the point of detonation, shown in (c)) is almost twice as high in D1 and D2 compared to D3. Past 8ms, the oscillatory response of the chest wall at position A for all three densities is seen to be similar indicating the pressures experienced after this time are not significantly different between the models, and any differences are not a significant driver in determining the chest wall velocity. In Figure 7.35(b), which shows chest wall velocity histories from reference point B, a more noticeable difference is seen between D1, D2 and D3, although a difference of 0.5 m/s is seen between peak velocity in D1 and D2, D3 shows a more significant difference in peak velocity of 1.7m/s and 1.2m/s compared to D1 and D2 respectively. The least difference in pressure is seen facing the window at S3, and once again the value of the pressure at S2 is the driver, and is twice the value in D1 compared to at the same measurement point in D3, but all peak pressures are lower and arrive 0.5ms later in D3. Figure 7.35(c) shows the velocity time history at reference location C, and shows a significant difference between the predicted chest wall velocity at this point for all three

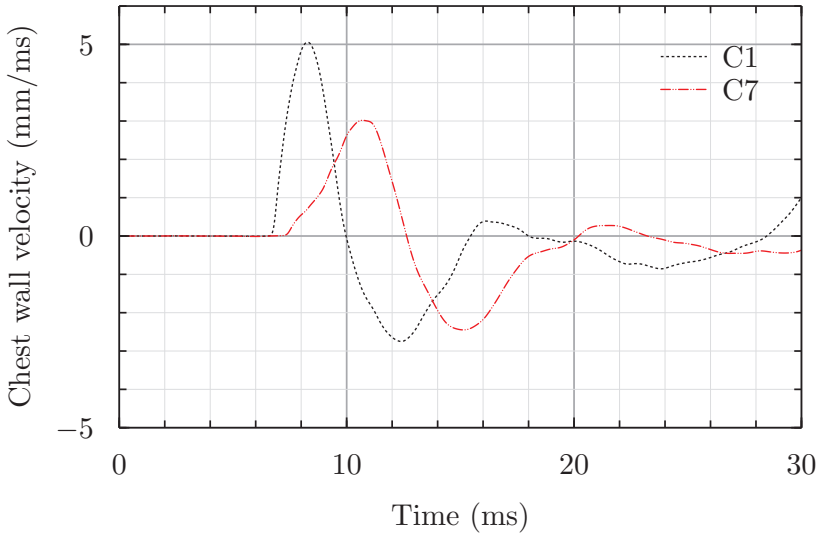

(a) Reference location B

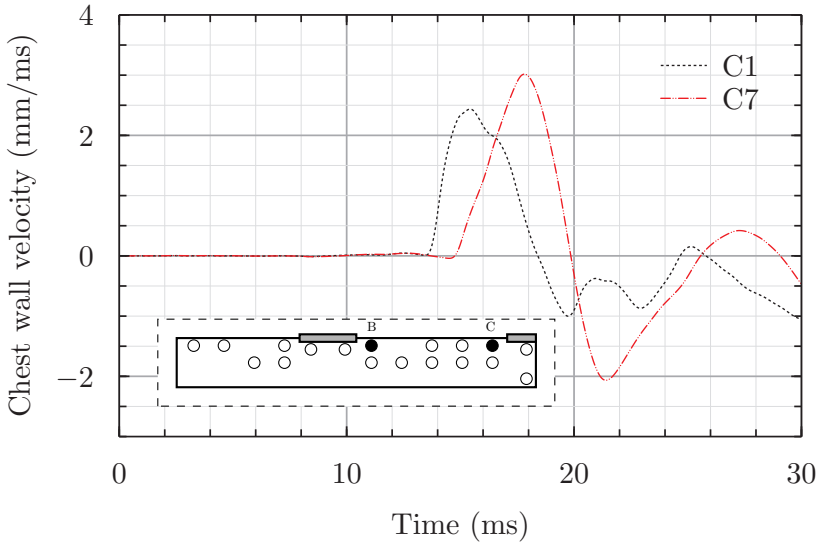

(b) Reference location C, showing positions of reference locations B and C

Figure 7.34: Chest wall velocity histories for C1 and C7 at reference locations B and C

passenger densities. Once again, the highest velocity is predicted for D1, but unlike with at other locations, where D2 and D1 were similar, D2 at location C shows a noticeably lower peak chest wall velocity. The peak velocity in D3 is again lower than both, but also has a much lower acceleration than both D2 and D1; D3 takes 3.6ms to reach peak velocity, whereas both D2 and D1 take less than 2ms. The initial acceleration is slightly lower, due to the lower pressures experienced at this position in D3 compared to D1, but reflections in pressure in D3 at 16.5 to 17ms cause an extra jump in velocity, leading the velocity to continue to increase albeit quite slowly. Without these reflections, peak velocity would have occurred around 16ms, with a value of approximately 1.4m/s, based on the assumption of similar behaviour to D1 and D2.

Where differences exist between peak chest wall velocity for different passenger densities, it is largely the pressure at S2, and to a lesser extent the pressure at S1, that is responsible for difference. This indicates that surrounding passengers have the impact of reducing the value of the shocks incident or the areas of the passengers that face the direction detonation. This effect can be seen more clearly in Figure 7.36, which shows ASII scores for chest injury on the whole vehicle with different passenger densities, again with the first passenger position omitted to aid visualisation. Figure 7.36 shows how the risk of chest wall injury drops off with distance from the point of detonation, and as the passenger density increases, the radius over which there is a risk of injury reduces. This is less noticeable between D1 and D2 as there are fewer points for which comparisons can be made (although the ASII score for the person at 5000x1100mm in D2 shows a lower ASII score than the same position in D1) but is more noticeable when D3 is compared to both D2 and D1. In D3 in Figure 7.36(c), ASII values above 0.2 are not seen past 4500mm along the vehicle, but this is seen to occur in both D1 and D2. The effect of passengers shielding each other from harmful pressures is also seen closer to the point of detonation, with ASII values of less than 1 seen from all points past 1500mm in D3, whereas values above 1.5 are seen up to almost 3000mm along the vehicle in D1 and D2. Similar patterns are seen when total injury is considered.

The total injury risk prediction (which combines the pressure and pressure and projectile injury) for 3 passenger densities is shown in Figure 7.37. It is clear that the as density increases, the extent of the lethality of the device reduces due to the shielding effect of passengers. In (a), a very high risk of life threatening injury is seen all the way too almost 7000mm along the vehicle, with all persons within that part of the vehicle potentially exposed to a similar level of risk. For density D2, shown in (b), very high risks of life threatening injury are seen all the way to almost 6000mm along the vehicle, but there are also cases nearer where only medium risks of injury are seen; these people are likely to still be 'hit' but are not in line of sight with the charge, and as a result the fragment velocity is reduced due to passing through another passenger and thus the likelihood of injury. Passenger density D3 in Figure 7.37(c) shows the region of very high risk only extends less than 4000mm along the vehicle, with those further than 4000mm along the vehicle largely spared to exposure to significant risks.

This projectile injury risk is quantified for reference positions A, B and C in Table 7.14, which shows new injury severity score (NISS) values for 3 different draws, F1, F2 and F3, from a multivariate normal distribution, as described in Chapter 3. NISS values for each draw were averaged at each position to provide an overall NISS score for the reference locations at each density. This shows how both the injury level drops

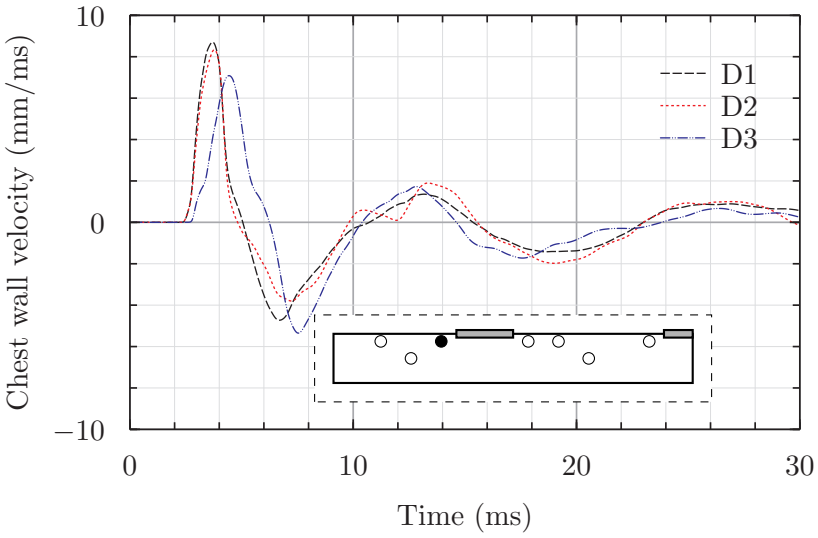

(a) CWV for reference position A, with position A shown for D1

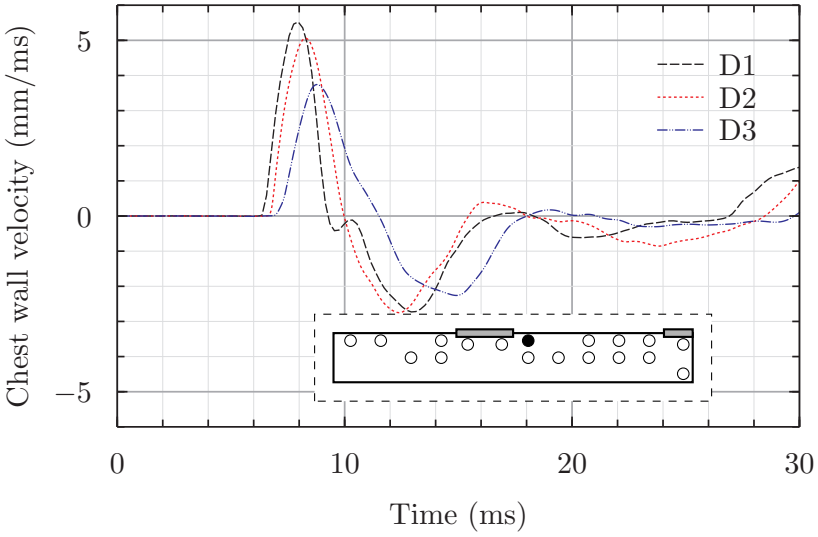

(b) CWV for reference position B, with position B shown for D2

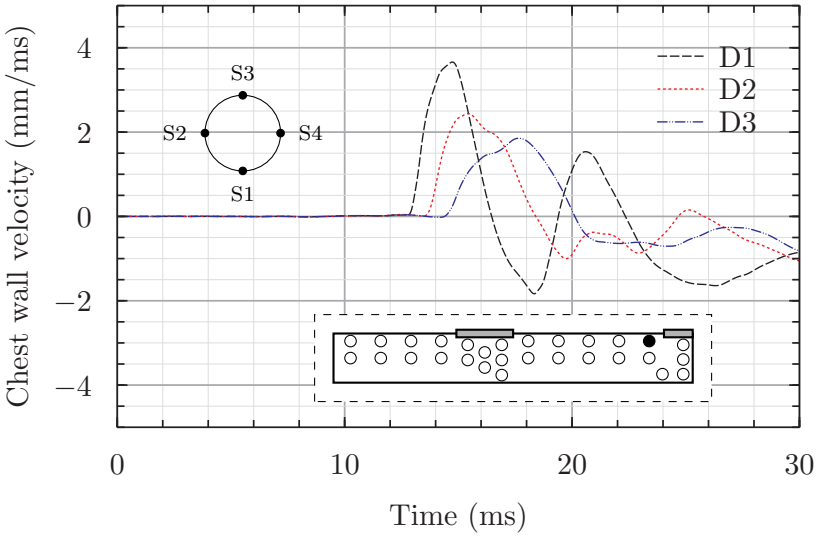

(c) CWV for reference position C, with position C shown for D3, also showing the locations of pressure sensors S1 to S4

Figure 7.35: Chest wall velocity history for 3 reference locations at 3 different passenger densities

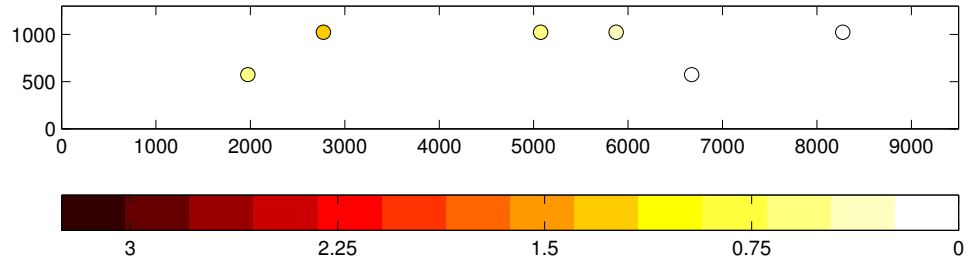

(a) D1

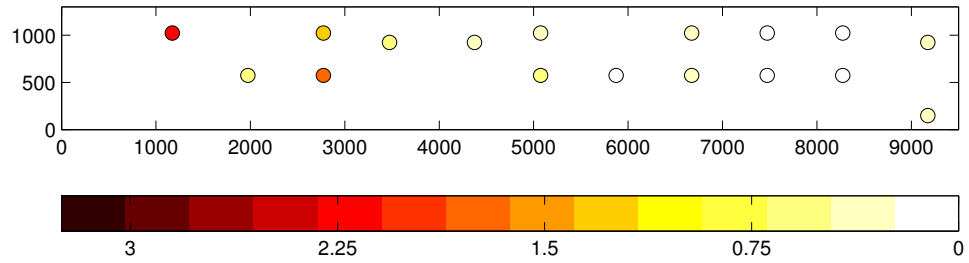

(b) D2

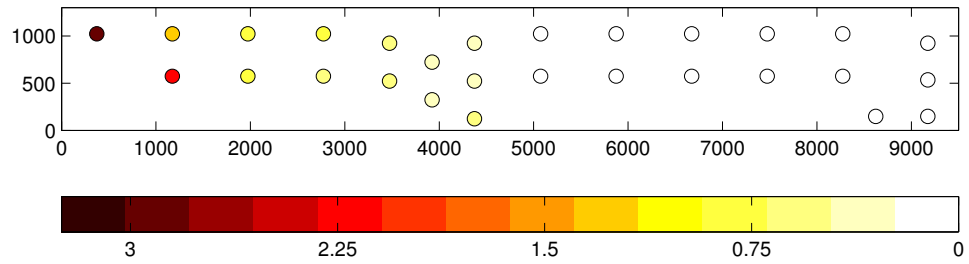

(c) D3

Figure 7.36: Effect of passenger density on ASII

off at further locations from the point of detonation, but also how increasing passenger density influences the likely radius of severe injury. The case of location C in density D2, shown in Table 7.14, does indicate a shortcoming of the current method, with an anomalous high value that is significantly higher than that seen at D1 caused by the inherent variability of taking random draws from a normal distribution. Taking a single value from the random draw from a normal distribution gives 1 possible outcome from an infinite number of possible cases, and averaging the results a few of these, as shown in Table 7.14 goes some way getting a more realistic idea of the 'probable' outcome for a generic device with the statistical parameters that are defined. Taking hundreds or thousands of repeated random draws from a distribution, commonly referred to as Monte Carlo methods, would likely see this value for C at D2 fall into line with the pattern of the other results. Further discussion of this is given in Section 8.2.

7.6 Discussion

A combination of numerical, and statistical methods for predicting injuries in rail vehicles in a number of cases has been presented, to gain an increased knowledge of the factors that drive injury when IEDs are detonated in rail vehicles. The LS-Dyna finite element code was combined with a chest wall model (described in Section 3.2.4) to predict the

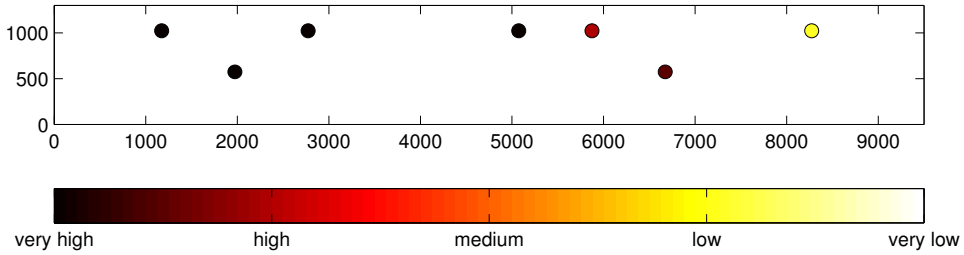

(a) D1

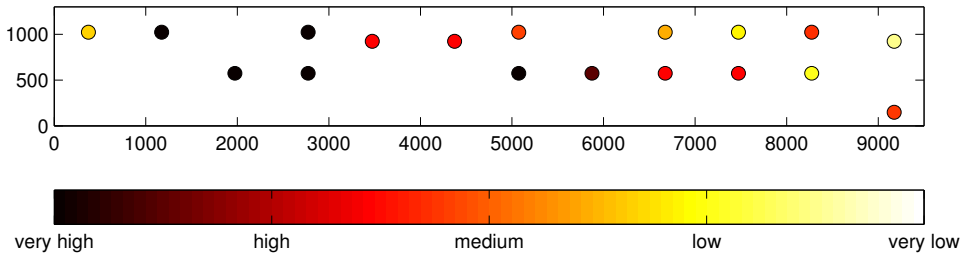

(b) D2

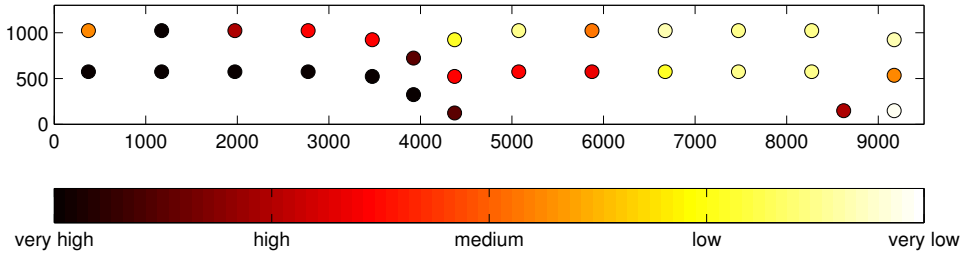

(c) D3

Figure 7.37: Effect of passenger density on combined pressure and projectile injury

Table 7.14: NISS scores for projectile injury for reference

		projectile NISS score			
location	density	F1	F2	F3	Av
A	D1	75	75	48	66
	D2	75	48	75	66
	D3	48	48	57	51
B	D1	75	32	66	58
	D2	41	48	41	43
	D3	8	11	12	10
C	D1	16	41	0	19
	D2	43	21	20	28
	D3	9	11	0	7

injuries due to shock waves and blast pressures within the confined space of a rail vehicle, and a statistical model was used to predict the injuries due to multiple flying projectiles. The model for flying projectiles extended existing work undertaken in the field, where no consideration had been made for penetrating injuries.

In Chapter 6, it was identified that a sufficiently fine mesh was required to predict the peak pressures at reflecting surfaces, and that inclusion of secondary combustion energy was required to predict the longer term pressures. In the model applied in this Chapter, it was not possible to refine the mesh to the levels used in the experimentally validated models in 6 due to computational limitations, and it was also not possible to implement secondary combustion energy due to limitations of the developed model to account for it. Failure to include secondary combustion means that later time pressures, including QSPs, are less accurately predicted in rail vehicle models than would be the case were computing resources and the maturity of the model sufficient for its inclusion. The effect of this on the injury predictions is limited, as the chest wall velocity was seen to be driven by the pressures seen within the first few reflections, and pressures happening later on were seen to have little effect on the peak chest wall velocity. The fact that the chest wall velocity is driven by the magnitude of the first few pressure reflections though, does mean that failure to predict the peak pressures early will mean an underprediction of the chest wall velocity across the cases studied. Chest injury was only seen to be a cause of severe injury in a few locations in the results shown in this Chapter, but to some extent this could be caused by insufficient mesh resolution and failure to capture the true pressures, which in turn could lead to false conclusions about the importance, or lack of importance, of chest injury in prediction of the overall injury state of a passenger. Despite this, in almost all passenger positions where the is a prediction of low levels of injury, even very significant jumps in pressure are unlikely to push the chest wall velocity from a level of minor injury to a very high level of injury. In areas where moderate risks of pressure injury are seen though, underprediction of peak pressures and thus chest wall velocity could push the risk in some passenger locations to higher levels. Although these limitations appear significant, comparisons between design features and operational parameters are still valid as the method used across all is consistent, and as such the conclusions drawn in relation to the hypothesis remain valid. Moreover, the methods developed here can be applied to new blast data in the future as this become available.

Where full field data of all the passengers is presented, the injury is visualised at each discrete passenger position, and not as a contour map. The issue with contour maps for predicted risks is that injury can only happen at the discrete passenger locations, and is not a continuously varying parameter, which is what is shown by a contour map. For a given passenger position, a contour map requires interpolation between the injury values in the surrounding locations. In reality, the presence of this extra passenger would change the risk to the surrounding passengers, which shows that plotting a contour map is often misleading. Injury happens at discrete locations, and the passengers themselves alter both the pressure and projectile behaviour, therefore plotting contour maps will most likely be largely incorrect and should not be constructed for this type of problem.

The work presented here shows that projectiles contained within an IED are the driver of injuries, and that injuries due to the shock wave alone were confined to passenger positions very close to the point of detonation. When surfaces around the passenger served

to increase the strength of the shocks reflected towards the passenger, the prediction of the peak chest wall velocity was higher, but in many cases the increase in chest wall velocity was not sufficient to significantly alter the expected level of injury. It was also seen that when surfaces were positioned such that passengers were shielded from the blast so shocks directly from the device were not incident on passengers, chest wall velocities and thus the prediction of injuries was reduced. In most cases the pressures experienced at these locations dictated that low chest wall velocities were experienced, and increase or decreases in the value were not sufficient to yield ASII scores that led to injury. However for a higher charge mass, where higher pressures are experienced, it is likely that these shielding and reflecting effects may be more of a driver of injury. The value of the peak shock pressure is much more quickly reduced in air than the value of the fragment velocity though, and it is for this reason pressure injuries were seen to be of lesser importance than projectile injuries.

Where passengers were exposed in line of sight to flying projectiles, most were seen to be at moderate to very high risk of lethal or severe injury. These projectiles retain their velocity and in many cases fully penetrate the body, yielding very high levels of injury, and also exposing those behind to injury, albeit at a lower level. In the model presented here, the velocity of fragments can only be modified by the penetration of the passengers, and there is a need to add to the model to consider fragment interaction with physical structures within a rail vehicle, which is discussed further in Section 8.2. Importantly though, the inclusion of projectile injury was seen to be vital, as without it the predicted injury pattern would have been significantly different, with only a small number of people predicted to be injured by the shock pressure alone.

For modelling the injury due to pressures, a number of factors were investigated, including the effect of the vehicle structure and how important structures such as windows and doors are to predicting injury. Where a fully rigid rail vehicle structure was used with no windows or doors present, a moderate increase in chest wall velocity was seen, but no significant change in the ASII scores (and therefore the likelihood of injury) was seen compared to models in which effect of windows, doors and structural deformation were considered. When doors were removed, as if the doors were open at the time the device detonated, reduction in the chest wall velocity of those passengers close to the opening was seen, and for a case where higher charge mass was used and subsequently the blast overpressures were higher, this could be a driver for injury. Higher charge masses may also lead to different patterns of injury with internal structures such as seats and draught screen, and this can act as a guide for those taking on similar modelling tasks in the future. As the deformation of the structure was seen to have little impact on the injury, it is reasonable to suggest that modelling it with a rigid material is a suitable simplification, as for the charge mass considered here the effects deformation of the structure are not significant enough to alter the value of the pressure experienced over the few milliseconds where it is important. The effect of doors and windows in this circumstance was not seen to make significant changes to the injury pattern seen, but changes in the value of the chest wall velocity history were seen when doors and windows were not included. In any further investigation, where a different charge type or size is used for the improvised explosive device, it would be recommended that the effects of windows and doors be included. Passengers themselves, and structures within the cross section were seen to make by far the largest difference to chest injury patterns, and for

that reason it is these which are the most pertinent to include in future models. The complex nature of shock reflection means that without including these, over or under prediction, often within the same modelling run, are highly likely.

This chapter has presented modelling methods for investigating the effects of improvised explosive devices on rail vehicle structures and the passengers within them, investigating parameters that have been investigated previously by other researchers, or deemed important or interesting by the author of this work. The methods used have not been used by previous researchers in the area of rail vehicles, and although such may have been undertaken by researchers within governments, their agencies or private companies, no comparable work in the open literature exists. As a result, many of the techniques have scope for further development. This, along with conclusions to the body of work presented here as a whole, are the subject of Chapter 8.

7.7 Conclusions

The use of numerical injury models for pressure and projectiles, as well as finite element models has identified a number of parameters involved in the injury of passengers from IED attacks in rail vehicles.

The vehicle design itself can alter the pressures within the vehicle, and it was seen that seats, draught screens and open carriages can alter the chest wall velocity of passengers throughout the vehicle. At the studied charge size this did not lead to large changes in the predicted injury levels, but for higher charges this will not necessarily be the case. It was seen that modelling the internal features of the rail vehicles was more important than modelling the vehicle body shell structure, which made no significant difference to the pattern of pressure injury experienced throughout a rail vehicle.

The key driving parameter for passenger injury was seen to be the spatial density of these occupants, which has a much larger effect on the distribution and pattern of injury than any of the other variables studied with the current model.

8

Conclusions and further work

This chapter concludes the findings of this work, and discusses some points raised in this research that could not be fully investigated in the scope of the project, but which could be the subject of further research projects at a variety of levels.

8.1 Conclusions

In Chapter 1, the following hypothesis was presented, along with a proposed method for testing it.

> "Rail vehicle design can influence the pattern of injury seen in passengers when an improvised explosive device is detonated within a rail vehicle."

In Chapter 7 it was found that rail vehicle design can influence the pattern of injury seen in the passengers, but that the spatial density of the passengers had a greater effect on passenger injury distribution.

8.1.1 Vehicle design and passenger injury

Full rail vehicle models, along with injury models for passengers within them were shown in Chapter 7. A finite element model of a rail vehicle was combined with statistical and numerical models to predict injuries in a number of cases, that were used to identify which of the investigated parameters was the most important.

The flexibility and construction of the vehicle structure was tested in cases C1 to C4, and was seen to make little difference to the overall pattern of injury. The highest chest wall velocity at any passenger location (19.8 m/s) was seen when using the rigid rail vehicle shell model, compared to the lowest value of 16.5 m/s seen with the flexible shell in C1. For passengers in the highest risk locations (closest to the point of detonation), up to a 45 % difference in the ASII scores were seen (6.6 to 10.5), but this made no difference to the category of injury of the passenger, and all passengers at this location in all models were expected to suffer lethal injuries. At some of the furthest locations from the point of detonation, peak variation in injury score was seen to be 56%, but as with other locations, despite a high variation in injury score, all passengers in the locations furthest away from the blast fell into the 'no injury' category, regardless of structural model, with injury scores from 0.09 to 0.16. Similar patterns were seen when opening were included in the rigid vehicle model, and despite clear reductions in chest

wall velocity across passenger locations, and a peak variation in ASII score of almost 90% at one location between C2 and C4, the passenger at the location still remained within the trace to slight injury category.

The effect of a device detonation when the vehicle was stationed in a tunnel was investigated, and found to have negligible influence on the pressure injuries experienced. Only the initial few shock reflection influenced the peak chest wall velocity, and the QSP increase within the tunnel was seen to have no effect on the chest wall velocity.

Open carriage designs were investigated, and in almost all cases passengers were seen to have similar patterns of chest injury to those seen in non open carriage designs. Noticeable differences were seen at the point where carriages joined (and thus reflecting surfaces were removed in open carriage designs) and in one location a 50% reduction in chest wall velocity is seen from 5 m/s to 2.5 m/s, which is sufficient to move the passenger in the open carriage into the 'no injury' category at this location.

Seats and draught screens were investigated, and seen to simultaneously reduce risk in some areas and increase it in others. In the most extreme circumstances, seats increased the reflected pressure at one passenger location from 1.16MPa to 3.5MPa, which increased the ASII score from 6.6 to 18.9, compared to the case where seats were not modelled. Conversely, peak reflected pressures in some locations are reduced by 45% when seats and draught screens are included in the model. No definite conclusion can be drawn from this work with regards the effect of seats and draught screens, other than their presence will make significant differences to the pressures experienced by passengers, and in some cases can protect passenger, and in other increase the likelihood of being injured.

The projectile injury model could not be applied in the cases above, as interaction with the rail vehicle or surrounding structures is not included. Despite this, the projectile injury predictions showed that in all cases the number and level of injury was much higher for projectile injury than chest injury. In the most severe cases of lethal chest injury were never seen further than 3m from the point of detonation, but the projectile injury model showed that most people within 6m of the device would be at a high risk of a life threatening injury.

Both the projectile and pressure injury models were used to investigate the effect of passenger density on the distribution of injuries. Increasing passenger density was seen to reduce both the predicted chest wall velocity, and the predicted level of projectile injury. Chest wall velocities were reduced by up to 20% with the highest density of passengers at a close proximity to the charge compared to lower densities of passengers, and by 50% at much larger distances from the charge. The total predicted injury score, which is dominated by the projectile injury mechanism, is 25% lower for the highest density of passengers compared to lower densities of passengers when those passengers are close to the point of detonation. Further away from the point of detonation, reductions in total injury levels were up to much greater in the highest passenger density case, compared to the lowest passenger density. Distance from the point of detonation wasn't seen to be the driver in the reduction of risk with increasing passenger density, and local density of passengers (the number immediately surrounding the passenger in question) was seen to be more important.

8.1.2 Risk and injury analysis models

The injury models described were developed in Chapter 3, where existing models were surveyed and their suitability to the current project identified, and where necessary models were developed from basic principles. From a number of possible injury modes seen to occur in IED attacks, the injury to the chest from the shock pressures, and to the whole body by penetrating projectiles were chosen to be included in the injury model.

A method developed by Axelsson was chosen to predict chest injury, which was validated against animal models [141]. The model was implemented using GNU Octave to solve the model's second order differential equations using a fourth order Runge-Kutta scheme, using a pressure time history from a finite element model as an input.

A multi projectile model was developed from scratch, using established relationships and principles to predict the initial behaviour of the projectiles. The Gurney method was used to predict the initial velocity, which was considered as the mean velocity, and the angular spread was assumed based on the likely spread of projectiles from a flat faced IED. Velocity and angular deviation from a mean of 0°were considered to be moderately correlated, and specific values for angle and velocity of each projectile were generated using a random draw from a multivariate normal distribution. Interaction, depth of penetration and perforation of the target were subsequently identified in the code, from which an injury score was generated based on the depth of penetration and number of hits.

Both the pressure injury model and multi projectile injury model output a score known as the Abbreviated Injury Scale (AIS), which can be combined to give an overall injury score known as the NISS. The calculation of this was handled automatically within the developed code.

8.1.3 Experimental investigation of confined explosions

In Chapter 5, experimental testing was undertaken to measure pressure in confined and complex environments, using a quarter symmetry experimental method. The results showed excellent consistency between experimental test shots, both in terms of the pressure history and the calculated cumulative impulse. The experimental results showed cumulative impulse increases when baffles were used along one wall of the test cell, although the number and spacing of these was not shown to have an effect on the impulse.

One test cycle was undertaken using a centrally mounted aluminium panel, with an optical displacement gauge placed behind to measure the central deflection history, but failures of the panel restraint and the bright flash from the explosive caused a number of issues, from which valuable lessons were learned. High speed video data proved useful both for understanding the progression of the shock, and for visualising the panel behaviour, both of which could be used as part of the numerical validation below.

8.1.4 Numerical validation using experimental data

Chapter 6 presents numerical models of the experimental test arrangements in LS-Dyna using the multi-material ALE method with fluid structure interaction. On the whole, numerical models captured the shock reflection behaviour within the test cell, and once the effects of secondary combustion was considered cumulative impulse predicted numer-

ically were also in line with those calculated from experimental pressure time histories. Secondary combustion was considered in a simplified way, by adding a calculated amount of extra energy to the ALE domain within the enclosure in the model according to a energy release function. Numerical modelling of the fourth test arrangement showed the importance of having well controlled experimental boundary conditions, as they were difficult to recreate in the numerical models. At the point where experimental and numerical displacements of the aluminium panel were at their greatest, the highest difference was seen between the pressure time history in the experimental and numerical data, indicating the importance of deformation when reflections in a confined environment are seen.

Although in many cases experimental and numerical peak pressures were the same, there was a tendency for numerical methods to under predict peak overpressures, primarily down to the effects of shock smearing with a coarse mesh. As always there are computational and code limitations, and this work was no exception.

8.2 Further work and improvements to the current methods

8.2.1 Secondary combustion

Consideration of secondary combustion, or afterburn, was an important aspect of achieving results from numerical models that accurately matched the physical conditions measured in experiments. The developed model is suitable for scenarios where the effect of afterburn is experienced over much of an environment simultaneously, where the time taken for the propagation of the flame front to reach all extremities is similar to or shorter than the timescales at which the secondary combustion reactions occur. Problems occur with the current model when the secondary combustion occurs in different areas of the model at different times, where the assumption of the same energy deposition rate at all points within a structure is no longer valid. This is particularly likely in very large enclosures, or when one length scale of a structure is vastly different to the other, such as with a long cylinder, where the time taken for shocks to reach the extremity of the geometry is much shorter than the time taken for the flames to propagate all the way to the extremities. As a result, further investigation of this phenomenon is required.

A thorough investigation of secondary combustion is required to fully quantify it's effects, particularly in large or long structures. It is possible that this could be done via numerical means with a combination of CFD codes and thermochemical codes, using a similar method to that employed by Donahue [51], but an experimental investigation would still be required to validate the models. An experimental investigation should look to identify the following:

- total energy released during secondary combustion of a common explosive
- time distribution of secondary combustion energy
- spatial distribution of secondary combustion energy
- difference in pressure time history when a detonation occurs in an inert atmosphere
- how fully enclosed and vented structures alter secondary combustion effects

This work can subsequently feed in to empirical models, allowing prediction of the effects of secondary combustion in enclosed environments. As well as providing parameters such as the total energy output and time taken for energy release based on the volume of enclosure and charge size and type, such a model could also predict the likely QSP occurring from secondary combustion.

There is also a need to use such a model to provide input into numerical codes such as LS-Dyna, so that secondary combustion effects can be accurately considered in situations where a simple time dependent energy release function such as that described in Chapter 6 is not appropriate. Such a model could be in the form of the one used in this work, but the author has identified there is a difficulty getting such a model to be anything other than time dependent over the entire domain, and as discussed the process of secondary combustion is unlikely to be so simplistic. Therefore, a new model is required to describe the spatial behaviour of the flame front, and the energy release of the secondary combustion.

The spatial behaviour is required so the appropriate volume over which the secondary combustion is happening can be specified, and additional energy added only to these volumes. Once this is defined, an equation of state can be defined, based on empirical relationships, which can be applied within this volume to account for secondary combustion energy. The definition of this volume, and thus the switch from a normal equation of state to one considering secondary combustion, could possible be achieved by changing part definitions throughout the simulation based on a particular growing volume or shape, but in trying to implement a similar scheme for this work, the author was unsuccessful. Another option would be to define an equation of space based on some spatial parameter, or the arrival of a shock and a parameter which defines how closely the flame front follows the shock.

From a purely scientific point of view, not related to rail vehicles, it would be interesting to identify how secondary combustion can affect structural deformation, the experimental investigation of which could be used to validate any numerical implementation of afterburn effects in Finite Element codes. Ultimately these codes are designed for predicting material and structural response, and as such validation should also include structural response.

8.2.2 Injury modelling

8.2.2.1 Multi-projectile injury model

Although closed source, proprietary and confidential multi projectile and weapon fragment injury models exist across the world, the projectile injury model in this project, despite not being unique in the techniques applied, is unique in the sense that it is open, and has allowed work that is not protected by security or commercial concerns. As many of the techniques have been taken from existing validated work in the open literature such as the HIP code [153] and Gurney Equations [154], or are based on engineering judgement by the author, further validation against existing codes or validation against experimental testing is required. Of particular need to investigate by experimental means are:

- mean and variance of velocities for a number of projectiles ejected from a device
- mean and variance of angular spreads for projectiles from a simulated IED

- relationship between angle of a projectile and its velocity
- statistical relationship between velocity, projectile form and the depth of penetration or severity of wound

On top of developing these relationships, there is also a need to develop an improved relationship between the velocity of the projectile and the likely level of wounding or injury. A very simple relationship between depth of penetration (DOP) and injury level is used in this work, following Pope [153], and as discussed in that article, more sophisticated methods exist and could be applied. The design of the code means that implementing improvements such as the relationship between DOP and injury, or the DOP itself, is very straightforward as each of these is designated as a separate function which can easily be changed as long as the same input and output stream is maintained.

From a statistical point of view, there is a need to improve the multi-projectile model. At the moment, the predictions of injury are based on a single, or small number of random draws from a normal distribution. Repeating the draw many times will generate a range of possible injuries for each passenger, and it is then possible to define a range of likely injuries, or more importantly a most likely injury for a specified location. Such repeated sampling of random numbers is known as a Monte Carlo simulation, and applying such techniques would add a much more rigorous mathematical element to the model.

The final feature which is a necessary addition to the model is the interaction of projectiles with structures within the rail vehicle. Impact of projectiles with the structures in the vehicle is likely to slow them down, or potentially stop them, but this is highly dependent on the structure itself. If the behaviour of the projectiles is significantly altered by the structures within a rail vehicle, a significant difference would be expected in the pattern of injury. Including this injury prediction within the model will require a knowledge of the penetration characteristics of the chosen projectiles into the structures, and the retardation of the projectiles through these structures. This can be done by either an experimental or numerical means. Inclusion of this information in the model can then be achieved by the same logical means as the current hit and retardation prediction.

8.2.2.2 Chest wall injury model

Fundamentally, there is a lack of understanding in the open literature about how shock waves cause injury, particularly to vulnerable and vital organs such as the heart, lungs and brain. A number of methods exist, as described in Chapter 3, and the chest wall injury model was chosen because of it's ability to deal with complex pressure time histories which made it particularly appropriate for the current work, it's already conducted experimental validation, and it's ease of implementation numerically. Until a new or improved model is created, or significant new research points to a particular mechanism of injury or a better validated and more appropriate criteria, this model remains very good, but improvements can be made to the implemented method. The model from Axelsson [141] generates an Adjusted Severity of Injury Index (ASII) score, and there are very broad bands of these scores that define each level of injury. The relationship between ASII and Abbreviated Injury Scale (AIS) is assumed to be linear throughout, but a more scientific rigorous derivation of the relationship is required, so the ASII score can be used with more confidence to feed into the New Injury Severity Score (NISS).

As described above for projectile injury, an improved relationship can again be easily implemented in the code by simply modifying the function that translates ASII to AIS.

8.2.2.3 Distribution and usability of injury model

As mentioned in Section 8.2.2.1, closed source or proprietary injury model codes exist, which in some ways may hinder their development, and certainly prevents research groups without the means to develop their own from conducting research where injury prediction, particularly from multiple flying projectiles, is necessary. Development of this model, by opening the existing code up to any user who could make beneficial use of it, both within the University and at others within the UK and overseas, it is possible the validation and improvement of this can happen more rapidly.

The injury model developed in the current work was written in a very functional manner. In it's current form, it could be rewritten to improve readability, as well as portability between GNU Octave (for which it is written), and Matlab. Currently, it is necessary to run 4 separate scripts to get injury data; one to generate the input to further models, next to get projectile injury predictions, next for chest wall injury and a final one visualise the data if required. Combining the final three, or possibly all of them, and automating processing such as input and output stream naming, as well as removing the need to transfer variables between each codes via files, could reduce the risk of user error.

A further and more detailed rewrite could involve providing a graphical front end for the code, so visualisation could occur on screen and significantly more user friendly interface could allow more widespread use. Some difficulties with this could be posed by the need to take some output from a finite element model as an input, but it is possible such a process could be automated in some way. Reliance on the proprietary Matlab code, or on having a reliable Octave build which is not always straightforward on all systems could be reduced by writing in a compiled language such as Java or C, which would facilitate the development of a graphical user interface.

References

[1] Butcher, L. "SN/BT/1246 - Aviation: Security." www.parliament.uk/briefing-papers/SN01246.pdf, 2014.

[2] Financial Times. "MI5 tracked group for a year.", 2014. URL http://www.ft.com/cms/s/0/041a9e68-28da-11db-a2c1-0000779e2340.html#axzz3AHNED3b6.

[3] BBC News. "Bomb 'meant to explode on plane'.", 2014. URL http://www.bbc.co.uk/news/world-us-canada-11657486.

[4] Hyde, D. "CONWEP, Conventional Weapons Effects Program." *US Army Engineer Waterways Experiment Station, Vicksburg, MS*, 1992;.

[5] Record, J. *Bounding the global war on terrorism*. Strategic Studies Institute, 2003.

[6] Oxford English Dictionary. "terrorism, n." http://www.oed.com/view/Entry/199608?redirectedFrom=terrorism, 2013.

[7] BBC News. "Special Reports |2008 Mumbai Attacks." http://news.bbc.co.uk/1/hi/in_depth/south_asia/2008/mumbai_attacks/default.stm.

[8] BBC News. "The 12 October 2002 Bali bombing plot."

[9] BBC News. "BBC News | Special Reports | London Explosions." http://news.bbc.co.uk/1/hi/in_depth/uk/2005/london_explosions/default.stm, 2009.

[10] BBC News. "BBC News | Moscow Metro hit by deadly suicide bombings." http://news.bbc.co.uk/1/hi/8592190.stm, 2010.

[11] BBC News. "Terrorist attacks on the us." http://news.bbc.co.uk/1/hi/world/1537652.stm, 2001.

[12] Chalk, P, Hoffman, B, Reville, R, and Kasupski, A. "Trends in terrorism." *Rand Corporation*, 2005;.

[13] Perl, R. "Trends in terrorism." *DTIC Document*, 2006;.

[14] Powell, J and Fletcher, DI. "The need for developing an effective and acceptable engineering response to terrorist attacks on railway systems." *Proceedings of the Institution of Mechanical Engineers, Part F: Journal of Rail and Rapid Transit*, 2011;225(4):359–371.

[15] BBC News. "BBC News | In Depth | 2004 | Mumbai train attacks." *http://news.bbc.co.uk/1/hi/in_depth/south_asia/2006/mumbai_train_attacks/default.stm*, 2003.

[16] BBC News. "BBC News | Special Reports | 2004 | Madrid train attacks." *http://news.bbc.co.uk/1/hi/in_depth/europe/2004/madrid_train_attacks/default.stm*, 2009.

[17] Loukaitou-Sideris, A, Taylor, BD, and Fink, CNY. "Rail Transit Security in an International Context." *Urban Affairs Review*, 2006;41(6):727.

[18] HM Government, Home Office. "CONTEST - The United Kingdom's Strategy for Countering Terrorism." https://www.gov.uk/government/policies/protecting-the-uk-against-terrorism, 2011.

[19] Coaffee, J. "Rings of steel, rings of concrete and rings of confidence: designing out terrorism in central london pre and post september 11th." *International Journal of Urban and Regional Research*, 2004;28(1):201–211.

[20] Coaffee, J, Moore, C, Fletcher, D, and Bosher, LS. "Resilient design for community safety and terror-resistant cities." *Proceedings of the Institution of Civil Engineers Municipal Engineer*, 2008;161(ME2):103 – 110.

[21] The Home Office. "Protecting Crowded Places." https://www.gov.uk/government/publications/protecting-crowded-places.

[22] ACPO. "Secured by Design." http://www.securedbydesign.com/.

[23] Litman, T. "Terrorism, transit and public safety: Evaluating the risks." *Center for Urban Transportation Research*, 2005;8(4):33.

[24] Perry, RW and Lindell, MK. "Preparedness for emergency response: guidelines for the emergency planning process." *Disasters*, 2003;27(4):336–350.

[25] Liepmann, HHW and Roshko, A. *Elements of gas dynamics*. Dover Publications, 2001.

[26] Courant, R and Friedrichs, KO. *Supersonic flow and shock waves*, volume 21. Springer, 1976.

[27] Smith, PD and Hetherington, JG. *Blast and ballistic loading of structures.* Butterworth-Heinemann, 1994.

[28] Beck, S, Brown, M, Blakey, S, Chin, S, Nicolleau, F, Qin, N, and Wilson, C. *The Little Book of Thermofluids.* The University of Sheffield Department of Mechanical Engineering, 3 edition, 2006.

[29] Wright, JK. *Shock tubes.* Methuen, 1961.

[30] Haselbacher, A. "On impedance in shock-refraction problems." *Shock Waves*, 2012;22(4):381–384.

[31] Henderson, L. "On the refraction of shock waves." *Journal of Fluid Mechanics*, 1989;198:365–386.

[32] Polachek, H and Seeger, R. "On shock-wave phenomena; refraction of shock waves at a gaseous interface." *Physical Review*, 1951;84(5):922.

[33] Brode, HL. "A calculation of the blast wave from a spherical charge of tnt." *Technical report*, DTIC Document, 1958.

[34] Boyer, D. "An experimental study of the explosion generated by a pressurized sphere." *Journal of Fluid Mechanics*, 1960;9(03):401–429.

[35] Friedman, MP. "A simplified analysis of spherical and cylindrical blast waves." *Journal of Fluid Mechanics*, 1961;11(1):1–15.

[36] Tyas, A, Warren, J, Bennett, T, and Fay, S. "Prediction of clearing effects in far-field blast loading of finite targets." *Shock Waves*, 2011;21(2):111–119.

[37] Department of Defense. "UFC 3-340-02 Structures to Resist the Effects of Accidental Explosions." `www.wbdg.org/ccb/DOD/UFC/ufc_3_340_02.pdf`, 2008.

[38] Hudson, C. "Sound pulse approximations to blast loading (with comments on transient drag)." *Technical report*, Sandia Corporation Technical Memorandum SC-TM-191-55-51, 1955.

[39] Rigby, S, Tyas, A, and Bennett, T. "Single-degree-of-freedom response of finite targets subjected to blast loading–the influence of clearing." *Engineering Structures*, 2012;45:396–404.

[40] Smith, P, Rose, T, and Saotonglang, E. "Clearing of blast waves from building facades." *Proceedings of the Institution of Civil Engineers: Structures and buildings*, 1999;134(2):193–9.

[41] Cullis, IG, Schofield, J, and Whitby, A. "Assessment of blast loading effects–types of explosion and loading effects." *International Journal of Pressure Vessels and Piping*, 2010;87(9):493–503.

[42] Salzano, E and Basco, A. "Comparison of the explosion thermodynamics of tnt and black powder using le chatelier diagrams." *Propellants, Explosives, Pyrotechnics*, 2012;37(6):724–731.

[43] Edri, I, Feldgun, V, Karinski, Y, and Yankelevsky, D. "Afterburning aspects in an internal tnt explosion." *International Journal of Protective Structures*, 2013;4(1):97–116.

[44] Edri, I, Feldgun, V, Karinski, Y, and Yankelevsky, D. "On blast pressure analysis due to a partially confined explosion: Iii. afterburning effect." *International Journal of Protective Structures*, 2012; 3(3):311–332.

[45] Cooper, PW. *Explosives engineering.* Wiley–VCH, New York, 1996.

[46] Daily, LD. "Simulating afterburn with LLNL hydrocodes.", 2004.

[47] Togashi, F, Baum, J, Mestreau, E, Löhner, R, and Sunshine, D. "Numerical simulation of long-duration blast wave evolution in confined facilities." *Shock Waves*, 2010;20(5):409–424.

[48] Alves, S, Kuhl, A, Najjar, F, Tringe, J, McMichael, L, and Glascoe, L. "Building an efficient model for afterburn energy release." *Technical report*, Lawrence Livermore National Laboratory (LLNL), Livermore, CA, 2012.

[49] Pope, D. "Design of a full-scale experimental blast tunnel." *Proceedings of the ICE - Engineering and Computational Mechanics*, 2013;166(3):149 – 159.

[50] Baker, W, Hokanson, J, Esparza, E, and Sandoval, N. "Gas pressure loads from explosions within vented and unvented structures." *Technical report*, DTIC Document, 1983.

[51] Donahue, L, Zhang, F, and Ripley, R. "Numerical models for afterburning of TNT detonation products in air." *Shock Waves*, 2013;1–15.

[52] The Steel Construction Institute. "Structural strengthening of offshore topsides structures as part of explosion risk reduction methods." *RESEARCH REPORT 489*, Health and Safety Executive, 2006.

[53] Bradley, D and Mitcheson, A. "The venting of gaseous explosions in spherical vessels. I-Theory." *Combustion and Flame*, 1978;32(0):221 – 236.

[54] Lees, F. *Loss Prevention in the Process Industries: Hazard Identification, Assessment, and Control, Volumes 1-3.* Butterworth-Heinemann, 2001.

[55] Anderson Jr, CE, Baker, W, Wauters, DK, and Morris, BL. "Quasi-static pressure, duration, and impulse for explosions (eg HE) in structures." *International Journal of Mechanical Sciences*, 1983;25(6):455–464.

[56] Cooper, M, Fairweather, M, and Tite, J. "On the mechanisms of pressure generation in vented explosions." *Combustion and flame*, 1986;65(1):1–14.

[57] Huebner, KH. *The Finite Element Method for Engineers.* John Wiley & Sons, 1975.

[58] Zukas, J. *Introduction to hydrocodes*. Elsevier, 2004.

[59] Bathe, KJ. *Finite element procedures*, volume 2. Prentice Hall, 1996.

[60] Hallquist, J. "LS-DYNA Theory Manual." *Livermore Software Technology Corporation*, 2006;.

[61] Wang, AJ and Hopkins, HG. "On the plastic deformation of built-in circular plates under impulsive load." *Journal of the Mechanics and Physics of Solids*, 1954;3(1):22–37.

[62] Hopkins, HG. "On the Plastic Theory of Plates." *Proceedings of the Royal Society of London. Series A. Mathematical and Physical Sciences*, 1957;241(1225):153–179.

[63] Cox, A and Morland, L. "Dynamic plastic deformations of simply-supported square plates." *Journal of the Mechanics and Physics of Solids*, 1959;7(4):229–241.

[64] Wierzbicki, T. "Impulsive loading of rigid viscoplastic plates." *International Journal of Solids and Structures*, 1967;3(4):635–647.

[65] Jones, N. "Impulsive loading of a simply supported circular rigid plastic plate." *Journal of Applied Mechanics*, 1968;35:59.

[66] Li, Q and Jones, N. "Blast loading of a "short" cylindrical shell with transverse shear effects." *International journal of impact engineering*, 1995;16(2):331–353.

[67] Batra, R and Dubey, R. "Impulsively loaded circular plates." *International Journal of Solids and Structures*, 1971;7(8):965–978.

[68] Jones, N, Uran, TO, and Tekin, SA. "The dynamic plastic behavior of fully clamped rectangular plates." *International Journal of Solids and Structures*, 1970;6(12):1499–1512.

[69] Nurick, G and Shave, G. "The deformation and tearing of thin square plates subjected to impulsive loads-an experimental study." *International Journal of Impact Engineering*, 1996;18(1):99–116.

[70] Spranghers, K, Vasilakos, I, Lecompte, D, Sol, H, and Vantomme, J. "Full-field deformation measurements of aluminum plates under free air blast loading." *Experimental Mechanics*, 2012; 1–14.

[71] Tiwari, V, Sutton, MA, McNeill, S, Xu, S, Deng, X, Fourney, WL, and Bretall, D. "Application of 3D image correlation for full-field transient plate deformation measurements during blast loading." *International Journal of Impact Engineering*, 2009;36(6):862–874.

[72] Schleyer, G, Hsu, S, White, M, and Birch, R. "Pulse pressure loading of clamped mild steel plates." *International journal of impact engineering*, 2003;28(2):223–247.

[73] Jones, N. "Influence of in-plane displacements at the boundaries of rigid-plastic beams and plates." *International Journal of Mechanical Sciences*, 1973;15(7):547–561.

[74] Langdon, G and Schleyer, G. "Inelastic deformation and failure of clamped aluminium plates under pulse pressure loading." *International Journal of Impact Engineering*, 2003;28(10):1107 – 1127.

[75] Menkes, S and Opat, H. "Broken beams." *Experimental Mechanics*, 1973;13(11):480–486.

[76] Teeling-Smith, R and Nurick, G. "The deformation and tearing of thin circular plates subjected to impulsive loads." *International Journal of Impact Engineering*, 1991;11(1):77 – 91.

[77] Wierzbicki, T. "Petalling of plates under explosive and impact loading." *International Journal of Impact Engineering*, 1999;22(9-10):935 – 954.

[78] Rudrapatna, N, Vaziri, R, and Olson, M. "Deformation and failure of blast-loaded square plates." *International Journal of Impact Engineering*, 1999;22(4):449–467.

[79] Balden, V and Nurick, GN. "Numerical simulation of the post-failure motion of steel plates subjected to blast loading." *International Journal of Impact Engineering*, 2005;32(1):14–34.

[80] Zhu, F, Zhao, L, Lu, G, and Gad, E. "A numerical simulation of the blast impact of square metallic sandwich panels." *International Journal of Impact Engineering*, 2009;36(5):687–699.

[81] Micallef, K, Fallah, A, Pope, D, and Louca, L. "The dynamic performance of simply-supported rigid-plastic circular steel plates subjected to localised blast loading." *International Journal of Mechanical Sciences*, 2012;65(1):177 – 191.

[82] Jones, N. "Dynamic inelastic response of strain rate sensitive ductile plates due to large impact, dynamic pressure and explosive loadings." *International Journal of Impact Engineering*, 2013;.

[83] Simmons, M and Schleyer, G. "Pulse pressure loading of aircraft structural panels." *Thin-walled structures*, 2006;44(5):496–506.

[84] Kotzakolios, T, Vlachos, DE, and Kostopoulos, V. "Blast response of metal composite laminate fuselage structures using finite element modeling." *Composite Structures*, 2010;93:665–681.

[85] Fleisher, H. "Modeling the effects of luggage on blast loadings from internal explosive detonations." In "Transactions on Modelling and Simulation," volume 22, 1999; .

[86] Fleisher, H. "Design and explosive testing of a blast resistant luggage container." In "International Conference on Structures Under Shock and Impact IV," , 1996; 51–60.

[87] Weinstein, E. "Design and test of a blast resistant luggage container." In "Structures under Shock and Impact VI," , 2000; .

[88] Dotoli, R, Bozzolo, A, Fay, S, and Bardaro, D. "Experimental testing and numerical simulation to design an innovative blast resistant textile luggage container." In "27th Congress of the International Council of the Aeronautical Sciences," , 2010; .

[89] Børvik, T, Burbach, A, Langberg, H, and Langseth, M. "On the ballistic and blast load response of a 20ft ISO container protected with aluminium panels filled with a local mass—Phase II: Validation of protective system." *Engineering Structures*, 2008;30(6):1621–1631.

[90] Børvik, T, Hanssen, A, Langseth, M, and Olovsson, L. "Response of structures to planar blast loads–A finite element engineering approach." *Computers and Structures*, 2009;.

[91] Børvik, T, Hanssen, A, Dey, S, Langberg, H, and Langseth, M. "On the ballistic and blast load response of a 20 ft ISO container protected with aluminium panels filled with a local mass—Phase I: Design of protective system." *Engineering Structures*, 2008;30(6):1605–1620.

[92] Langdon, G and Schleyer, G. "Inelastic deformation and failure of profiled stainless steel blast wall panels. part i: experimental investigations." *International Journal of Impact Engineering*, 2005;31(4):341–369.

[93] Schleyer, G, Lowak, M, Polcyn, M, and Langdon, G. "Experimental investigation of blast wall panels under shock pressure loading." *International journal of impact engineering*, 2007;34(6):1095–1118.

[94] Smith, P, Vismeg, P, Teo, L, and Tingey, L. "Blast wave transmission along rough-walled tunnels." *International journal of impact engineering*, 1998;21(6):419–432.

[95] Berger, S, Sadot, O, and Ben-Dor, G. "Experimental investigation on the shock-wave load attenuation by geometrical means." *Shock waves*, 2010;20(1):29–40.

[96] Langdon, GS, Rossiter, IB, Balden, VH, and Nurick, GN. "Performance of mild steel perforated plates as a blast wave mitigation technique: Experimental and numerical investigation." *International Journal of Impact Engineering*, 2010;37(10):1021–1036.

[97] Chaudhuri, A, Hadjadj, A, Sadot, O, and Ben-Dor, G. "Numerical study of shock-wave mitigation through matrices of solid obstacles." *Shock Waves*, 2012;1–11.

[98] Network Rail. "Network RUS: Passenger Rolling Stock.", 2011.

[99] Transport for London. "London Underground Rolling Stock." `http://www.tfl.gov.uk/corporate/modesoftransport/londonunderground/1612.aspx`, 2014.

[100] Bauser, M, Sauer, G, and Siegert, K. *Extrusion*. ASM International, 2nd edition, 2006.

[101] Kotsikos, G, Robinson, M, Zangani, D, and Roberts, J. "Investigation of the weld unzipping failure mode during collisions of welded aluminium rail vehicles." *Proceedings of the Institution of Mechanical Engineers, Part F: Journal of Rail and Rapid Transit*, 2008;222(1):59.

[102] Health and Safety Executive. "The train collision at Ladbroke Grove 5 October 1999 - Report of the HSE investigation." *Technical report*, HSE, 2000.

[103] Rail Safety and Standards Bureau. "Bodyside window containment tests for existing vehicle designs." *Research Brief T878*, RSSB, 2009.

[104] Railway Group Standard. "GM/RT2100 Issue 5 - Requirements for Rail Vehicle Structures.", 2012.

[105] Børvik, T, Clausen, A, Eriksson, M, Berstad, T, Sture Hopperstad, O, and Langseth, M. "Experimental and numerical study on the perforation of AA6005-T6 panels." *International Journal of Impact Engineering*, 2005;32(1-4):35–64.

[106] Yaoke, W, Cheng, X, Haosheng, W, Chen, A, and Batra, R. "Impact of steel spheres on ballistic gelatin at moderate velocities." *International Journal of Impact Engineering*, 2013;62:142–151.

[107] Nyström, U and Gylltoft, K. "Numerical studies of the combined effects of blast and fragment loading." *International Journal of Impact Engineering*, 2009;36(8):995 – 1005.

[108] Mayo, A and Kluger, Y. "Blast-induced injury of air-containing organs." *ADF Health*, 2006;7(1):40–44.

[109] Katz, E, Ofek, B, Adler, J, Abramowitz, H, and Krausz, M. "Primary blast injury after a bomb explosion in a civilian bus." *Annals of surgery*, 1989;209(4):484.

[110] Mellor, S. "The relationship of blast loading to death and injury from explosion." *World journal of surgery*, 1992;16(5):893–898.

[111] Moore, D, Jérusalem, A, Nyein, M, Noels, L, Jaffee, M, and Radovitzky, R. "Computational biology–Modeling of primary blast effects on the central nervous system." *Neuroimage*, 2009;47:T10–T20.

[112] Mayorga, M. "The pathology of primary blast overpressure injury." *Toxicology*, 1997;121(1):17–28.

[113] Elsayed, N. "Toxicology of blast overpressure." *Toxicology*, 1997;121(1):1–15.

[114] Waterworth, T and Carr, M. "An analysis of the post-mortem findings in the 21 victims of the birmingham pub bombings." *Injury*, 1975;7(2):89–95.

[115] Mellor, S and Cooper, G. "Analysis of 828 servicemen killed or injured by explosion in northern ireland 1970–84: the hostile action casualty system." *British journal of surgery*, 1989;76(10):1006–1010.

[116] Ng, R, James, S, Philp, B, Floyd, D, Ross, D, Butler, P, Brough, M, and McGrouther, D. "The soho nail bomb: the uch experience. university college hospital." *Annals of The Royal College of Surgeons of England*, 2001;83(5):297.

[117] Hart, A, Mannion, S, Earnshaw, P, and Ward, A. "The London nail bombings: the St. Thomas' Hospital experience." *Injury*, 2003;34(11):830–833.

[118] Kluger, Y, Peleg, K, Daniel-Aharonson, L, and Mayo, A. "The special injury pattern in terrorist bombings." *Journal of the American College of Surgeons*, 2004;199(6):875 – 879.

[119] Kosashvili, Y, Loebenberg, MI, Lin, G, Peleg, K, Zvi, F, Kluger, Y, and Blumenfeld, A. "Medical consequences of suicide bombing mass casualty incidents: The impact of explosion setting on injury patterns." *Injury*, 2009;40(7):698 – 702.

[120] Aharonson-Daniel, L, Klein, Y, Peleg, K *et al.* "Suicide bombers form a new injury profile." *Annals of surgery*, 2006;244(6):1018.

[121] de Ceballos, J, Gutierrez, P, Turégano-Fuentes, F, Perez-Diaz, D, Sanz-Sanchez, M, Martin-Llorente, C, and Guerrero-Sanz, J. "11 March 2004: The terrorist bomb explosions in Madrid, Spain – an analysis of the logistics, injuries sustained and clinical management of casualties treated at the closest hospital." *Critical Care*, 2004;9(1):104.

[122] Hadden, W, Rutherford, W, and Merrett, J. "The injuries of terroist bombing: A study of 1532 consecutive patients." *British Journal of Surgery*, 1978;65(8):525–531.

[123] Bellamy, RF. "The medical effects of conventional weapons." *World journal of surgery*, 1992; 16(5):888–892.

[124] Turégano-Fuentes, F, Caba-Doussoux, P, Jover-Navalón, J, Martin-Perez, E, Fernández-Luengas, D, Diez-Valladares, L, Perez-Diaz, D, Yuste-Garcia, P, Guadalajara Labajo, H, Rios-Blanco, R *et al.* "Injury patterns from major urban terrorist bombings in trains: the madrid experience." *World journal of surgery*, 2008;32(6):1168–1175.

[125] Aylwin, C, König, T, Brennan, N, Shirley, P, Davies, G, Walsh, M, and Brohi, K. "Reduction in critical mortality in urban mass casualty incidents: analysis of triage, surge, and resource use after the London bombings on July 7, 2005." *The Lancet*, 2007;368(9554):2219–2225.

[126] Morley, B and Leslie, GD. "Terrorist bombings: Motives, methods and patterns of injuries." *Australasian Emergency Nursing Journal*, 2007;10(1):5 – 12.

[127] Cooper, G, Townend, D, Cater, S, and Pearce, B. "The role of stress waves in thoracic visceral injury from blast loading: modification of stress transmission by foams and high-density materials." *Journal of biomechanics*, 1991;24(5):273–285.

[128] Bowen, I, Fletcher, E, and Richmond, D. "Estimate of man's tolerance to the direct effects of air blast." *Technical Report DASA-2113*, Lovelace Foundation for Medical Education and Research, 1968.

[129] Gruss, E. "A correction for primary blast injury criteria." *The Journal of Trauma*, 2006; 60(6):1284.

[130] Panzer, M, 'Dale' Bass, C, Rafaels, K, Shridharani, J, and Capehart, B. "Primary blast survival and injury risk assessment for repeated blast exposures." *The Journal of Trauma and Acute Care Surgery*, 2012;72(2):454.

[131] Bass, C, Rafaels, K, and Salzar, R. "Pulmonary injury risk assessment for short-duration blasts." *The Journal of Trauma*, 2008;65(3):604.

[132] Rafaels, K, Bass, C, Panzer, M, and Salzar, R. "Pulmonary injury risk assessment for long-duration blasts: a meta-analysis." *The Journal of Trauma*, 2010;69(2):368.

[133] Richmond, D, Yelverton, J, and Fletcher, E. "The biological effects of repeated blasts." *Technical report*, DTIC Document, 1981.

[134] Yang, Z, Wang, Z, Tang, C, and Ying, Y. "Biological effects of weak blast waves and safety limits for internal organ injury in the human body." *The Journal of trauma*, 1996;40(3S):81S–84S.

[135] Giannopoulos, G, Larcher, M, Casadei, F, and Solomos, G. "Risk assessment of the fatality due to explosion in land mass transport infrastructure by fast transient dynamic analysis." *Journal of Hazardous Materials*, 2010;173(1-3):401 – 408.

[136] Larcher, M, Casadei, F, Giannopoulos, G, Solomos, G, Planchet, J *et al.* "Determination of the risk due to explosions in railway systems." *Proceedings of the Institution of Mechanical Engineers, Part F: Journal of Rail and Rapid Transit*, 2011;225(4):373.

[137] Larcher, M, Casadei, F, and Solomos, G. "Risk analysis of explosions in trains by fluid–structure calculations." *Journal of Transportation Security*, 2010;3(1):57–71.

[138] Ferradás, E, Alonso, F, Miñarro, M, Aznar, A, Gimeno, J, and Pérez, J. "Consequence analysis by means of characteristic curves to determine the damage to humans from bursting spherical vessels." *Process safety and environmental protection*, 2008;86(2):121–129.

[139] The Netherlands Organisation for Applied Scientific Research. "Methods for the determination of possible damage to people and objects resulting from releases of hazardous materials." *Technical Report CPR-16E*, TNO, 1989.

[140] Baker, W, Cox, P, Westine, P, Kulesz, J, and Strehlow, R. *Explosion Hazards and Evaluation.* Elsevier, 1983.

[141] Axelsson, H and Yelverton, J. "Chest wall velocity as a predictor of nonauditory blast injury in a complex wave environment." *The Journal of trauma*, 1996;40(3S):31S.

[142] Stuhmiller, JH, Ho, KHH, Vander Vorst, MJ, Dodd, KT, Fitzpatrick, T, and Mayorga, M. "A model of blast overpressure injury to the lung." *Journal of biomechanics*, 1996;29(2):227–234.

[143] Teland, JA, van Doormaal, J, van der Horst, M, and Svinsås, E. "Single point methods for determining blast wave injury." *Technical report*, FFI/RAPPORT-2011/00130, 2011.

[144] van der Voort, M, van Doormaal, J, Verolme, E, and Weerheijm, J. "A universal throw model and its applications." *International Journal of Impact Engineering*, 2008;35(2):109–118.

[145] Stone, GW. "Projectile penetration into representative targets." *NASA STI/Recon Technical Report N*, 1994;95:22726.

[146] Breeze, J, Hunt, N, Gibb, I, James, G, Hepper, A, and Clasper, J. "Experimental penetration of fragment simulating projectiles into porcine tissues compared with simulants." *Journal of Forensic and Legal Medicine*, 2013;20(4):296 – 299.

[147] Gan, W and Chrostowski, JD. "3D Fragment Throw Simulation to Determine Fragment Density and Impact on Buildings." *Technical report*, DTIC Document, 2010.

[148] Gilbert, S, Lees, F, and Scilly, N. "A model for injury from fragments generated by the explosion of munitions." *Technical report*, DTIC Document, 1994.

[149] Radtke, F, Stacke, I, Rizzuti, C, Brombacher, B, Voss, M, and Haering, I. "Newest developments in the german explosive safety quantitative risk analysis software (esqra-ge)." *Technical report*, DTIC Document, 2010.

[150] Chrostowski, JD, Gan, W, Murray, D, and Pollan, W. "HAZX Part 1. An Explosives Hazard Assessment Tool." *Technical report*, DTIC Document, 2010.

[151] McCleskey, F, Neades, D, and Rudolph, R. "A comparison of two personnel injury criteria based on fragmentation." *Technical report*, DTIC Document, 1990.

[152] Henderson, J. "Lethality criteria for debris generated from accidental explosions." *Technical report*, DTIC Document, 2010.

[153] Pope, D. "The development of a quick-running prediction tool for the assessment of human injury owing to terrorist attack within crowded metropolitan environments." *Philosophical Transactions of the Royal Society B: Biological Sciences*, 2011;366(1562):127–143.

[154] Gurney, R. "The initial velocities of fragments from bombs, shell, grenades." *Technical Report BRL-405*, Ballistics Research Laboratory, Aberdeen Proving Ground, 1943.

[155] Jones, GE, Kennedy, JE, and Bertholf, LD. "Ballistics calculations of RW Gurney." *Am. J. Phys*, 1980;48(4):264–269.

[156] Christopherson, D. "Structural defence." *UK Ministry Of Home Security, Civil Defence Research Committee paper RC*, 1946;450.

[157] Zuckerman, S. "Textbook of air armaments.", 1952.

[158] Ahlers, EB. "Fragment hazard study." *Technical report*, DTIC Document, 1969.

[159] Baker, W. "A manual for the prediction of blast and fragment loadings on structures." *Technical report*, DTIC Document, 1981.

[160] Hardy, WN, Khalil, TB, and King, AI. "Literature review of head injury biomechanics." *International journal of impact engineering*, 1994;15(4):561–586.

[161] European New Car Assessment Programme (Euro NCAP). "Assessment protocol - adult occupant protection." http://www.euroncap.com/files/Euro-NCAP-Assessment-Protocol—AOP—v5.5—0-c9cbb083-b4e6-4788-8496-81394a8788a7.pdf, 2014.

[162] Hull, J. "Traumatic amputation by explosive blast: pattern of injury in survivors." *British journal of surgery*, 1992;79(12):1303–1306.

[163] Courtney, M and Courtney, A. "Working toward exposure thresholds for blast-induced traumatic brain injury: Thoracic and acceleration mechanisms." *NeuroImage*, 2010;.

[164] Nakagawa, A, Manley, G, Gean, A, Ohtani, K, Armonda, R, Tsukamoto, A, Yamamoto, H, Takayama, K, and Tominaga, T. "Mechanisms of primary blast-induced traumatic brain injury: Insights from shock-wave research." *Journal of Neurotrauma*, 2011;28(6):1101–1119.

[165] Elsayed, M and Agoston, DV. "Serum-based protein biomarkers in blast-induced traumatic brain injury spectrum disorder." *Frontiers in Neurology*, 2012;3(107).

[166] Association for the Advancement of Automotive Medicine. "What is the Abbreviated Injury Scale?" `http://www.aaam1.org/ais/`, 2014.

[167] Osler, T, Baker, SP, and Long, W. "A modification of the injury severity score that both improves accuracy and simplifies scoring." *The Journal of Trauma and Acute Care Surgery*, 1997;43(6):922–926.

[168] Brenneman, FD, Boulanger, BR, McLellan, BA, and Redelmeier, DA. "Measuring injury severity: time for a change." *The Journal of Trauma and Acute Care Surgery*, 1998;44(4):580–582.

[169] Jamulitrat, S, Sangkerd, P, Thongpiyapoom, S, and Na, N. "A comparison of mortality predictive abilities between niss and iss in trauma patients." *Journal of the Medical Association of Thailand*, 2001;84(10):1416.

[170] Scope, A, Farkash, U, Lynn, M, Abargel, A, and Eldad, A. "Mortality epidemiology in low-intensity warfare: Israel defense forces' experience." *Injury*, 2001;32(1):1–3.

[171] James, G, Burley, D, Dyke, P, Searl, J, Steele, N, and Wright, J. *Advanced modern engineering mathematics*. Prentice Hall, 2 edition, 1999.

[172] Randers-Pehrson, G and Bannister, KA. "Airblast loading model for DYNA2D and DYNA3D." *Technical Report ARL-TL-1310*, Army Research Laboratory, 1997.

[173] Dobratz, BM and Crawford, P. "LLNL Explosives Handbook. Properties of Chemical Explosives and Explosive Simulants.", 1985.

[174] Livermore Software Technology Corporation (LSTC). "LS-DYNA Keyword User's Manual Version 971 R6.0.0." *Volume 1*, 2012;1–1385.

[175] Hyde, D. "ConWep: Application of TM5-855-1." *Structural Mechanics Division, Structures Laboratory, USAE Waterways Experiment Station, Vicksburg, Mississippi*, 1992;20.

[176] Solomos, G. "RAILPROTECT Project." `http://elsa.jrc.ec.europa.eu/showproject.php?id=13`, 2009.

[177] Silver, WH. *The ARRL Handbook for Radio Communications*. ARRL, 2012.

[178] MEL Mikroelektronik GmbH. "Optical Distance Sensors M7 – Manual." `http://www.melsensor.com/subversion/mel/optische-sensoren/pdf/db-m7l-e.pdf`, 2013.

[179] Neuscamman, S, Pezzola, G, Alves, S, Glenn, L, and Glascoe, L. "Incorporating afterburn effects into a fast-running tool for modeling explosives in tunnels." *Technical Report LLNL-CONF-599056*, Lawrence Livermore National Laboratory (LLNL), Livermore, CA, 2012.

[180] Slavik, T. "Re: Possible bug in ls-dyna." Personal correspondence, 2014.

[181] Lin, YY and Kan, CD. "A performance study of ls-dyna on vehicle crash simulation." In "Proceedings of the sixth International LS-DYNA Users Conference," , 2000; 17–24.

[182] Higashi, K, Mukai, T, Kaizu, K, Tsuchida, S, Tanimura, S *et al.* "Strain rate dependence on mechanical properties in some commercial aluminum alloys." *Journal de Physique IV*, 1991; 1(C3).

[183] Sonnenschein, U. "Modelling of bolts under dynamic loads." *LS-Dyna Anwenderforum, Bamberg*, 2008;.

[184] Okamoto, I. "How bogies work." *Railway Technology Today*, 1998;5.

[185] Pyttel, T, Liebertz, H, and Cai, J. "Failure criterion for laminated glass under impact loading and its application in finite element simulation." *International Journal of Impact Engineering*, 2010;In Press, Corrected Proof:–.

[186] Vallabhan, CG, Das, Y, and Ramasamudra, M. "Properties of PVB interlayer used in laminated glass." *Journal of materials in civil engineering*, 1992;4(1):71–76.

[187] Zang, M, Lei, Z, and Wang, S. "Investigation of impact fracture behavior of automobile laminated glass by 3D discrete element method." *Computational Mechanics*, 2007;41(1):73–83.

[188] Larcher, M, Solomos, G, Casadei, F, and Gebbeken, N. "Experimental and numerical investigations of laminated glass subjected to blast loading." *International Journal of Impact Engineering*, 2012;39(1):42–50.

[189] BSOL. "BS EN 573-3:2013 - Aluminium and aluminium alloys - Chemical composition and form of wrought products - Part 3: Chemical composition and form of products." *Technical report*, BSI Standards, 2013.

[190] BSOL. "BS EN 515:1993 Aluminium and aluminium alloys - Wrought products - Temper designations." *Technical report*, BSI Standards, 1993.

[191] Chen, Y, Clausen, A, Hopperstad, O, and Langseth, M. "Stress–strain behaviour of aluminium alloys at a wide range of strain rates." *International Journal of Solids and Structures*, 2009; 46(21):3825–3835.

[192] Munsch, M, Bourdet, N, Deck, C, and Willinger, R. "Lateral glazing characterization under head impact: Experimental and numerical investigation." In "21ST Internation Technical Conference on the Enhanced Safety of Vehicles (ESV)," , 2009; .

[193] Timmel, M, Kolling, S, Osterrieder, P, and Du Bois, PA. "A finite element model for impact simulation with laminated glass." *International Journal of Impact Engineering*, 2007;34(8):1465–1478.

[194] Price, MA and Ghee, AH. "Modeling for detonation and energy release from peroxides and non-ideal improvised explosives." *Central European Journal of Energetic Materials*, 2009;6(3):239.

[195] Larcher, M, Casadei, F, and Solomos, G. "Influence of venting areas on the air blast pressure inside tubular structures like railway carriages." *Journal of Hazardous Materials*, 2010;.

[196] DeltaRail. "Optimising wheelset design & maintenance - data analysis and fatigue design." *Technical Report T356 WP3*, RSSB, 2008.

[197] Railway Group Standard. "GC/RT5212 Requirements for Defining and Maintaining Clearances.", 2003.

[198] Soong, TT. *Probabilistic modeling and analysis in science and engineering*. Wiley New York, 1981.

[199] Chatfield, C. *Statistics for technology: a course in applied statistics*, volume 3. Chapman and Hall, 1983.

[200] Dunteman, GH. *Introduction to Multivariate Analysis*. Sage, 1984.

[201] "Basic human body measurements for technological design Part 2: Statistical summaries of body measurements from national populations." *Standard CEN ISO/TR 7250-2:2010+A1:2013 (E)*, BSi, CEN, ISO, 2013.

[202] Donoho, D, Maleki, A, and Shahram, M. "Wavelab 850." *Software toolkit for time-frequency analysis*, 2006;.

Appendices

Appendix A

LS-Dyna input files

The models here are shown with reduced input, not including *NODE, *ELEMENT, *SET_NODE or any other highly repetitive input.

A.1 Method and Verification models

A.1.1 2D Models

```
$# LS-DYNA Keyword file created by LS-PrePost 3.2 (Beta) - 10Jun2011(03:22)
$# Created on Jun-22-2011 (12:05:41)
*KEYWORD
*CONTROL_ALE
$#     dct       nadv      meth      afac      bfac      cfac      dfac      efac
        -1          0        -2     0.000     0.000     0.000     0.000     0.000
$#   start       end     aafac     vfact      prit       ebc      pref   nsidebc
     0.0001.0000E+20  1.000000 1.0000E-6         0         0  1.04E-04         0
$#    ncpl      nbkt    imascl    checkr
         1        50         0     0.000
*CONTROL_TERMINATION
$#  endtim    endcyc     dtmin    endeng    endmas
      5.00         0     0.000     0.000     0.000
*CONTROL_BULK_VISCOSITY
1.5,0.06,-1,0
*INITIAL_ALE_MAPPING
$#     pid       typ    ammsid
         2         1        50
$#      x0        y0        z0       vid
     0.000     0.000     0.000         1
*DEFINE_VECTOR
         1     0.000     0.000     0.000     1.000     1.000     0.000         0
*DATABASE_BINARY_D3PLOT
$#      dt      lcdt      beam     npltc    psetid
       1.0         0         0         0         0
$#   ioopt
         0
*DATABASE_TRHIST
$#      dt    binary      lcur     ioopt
  1.500E-4         1         0         1
*DATABASE_TRACER
$#    time     track         x         y         z      ammg       nid
$# first two Z < 1
     0.000         1   420.000   350.000     0.000         0         0
     0.000         1   560.000   270.000     0.000         0         0
     0.000         1   840.000   160.000     0.000         0         0
     0.000         1  1000.000   340.000     0.000         0         0
     0.000         1   650.000   550.000     0.000         0         0 $#R=852
     0.000         1   730.000   800.500     0.000         0         0
     0.000         1   750.000   805.500     0.000         0         0 $#R=1100
     0.000         1   850.000   950.000     0.000         0         0 $#R=1274
*CONTROL_TIMESTEP
$#  dtinit    tssfac      isdo    tslimt     dt2ms      lctm     erode     ms1st
     0.000  0.600000         0     0.000     0.000         0         0         0
$#  dt2msf   dt2mslc     imscl
     0.000         0         0
*MAT_HIGH_EXPLOSIVE_BURN_TITLE
ChargeC4
$#     mid        ro         d       pcj      beta         k         g      sigy
        21 1.6050E-6 8040.0000 28.000001     0.000     0.000     0.000     0.000
*EOS_JWL_TITLE
ChargeC4
$#   eosid         a         b        r1        r2      omeg        e0        vo
         2 598.20001  13.75000  4.500000 1.5000000  0.320000  8.700000  1.000000
```

```
*PART
$# title
Charge
$#     pid     secid       mid     eosid      hgid      grav    adpopt      tmid
         1         1        21         2         0         0         0         0
*SECTION_ALE2D
$#   secid   aleform       aet    elform
         1        11                14
*MAT_HIGH_EXPLOSIVE_BURN_TITLE
Charge
$#     mid        ro         d       pcj      beta         k         g      sigy
        20 1.5900E-6 6930.0000 23.700001     0.000     0.000     0.000     0.000
*EOS_JWL_TITLE
Charge
$#   eosid         a         b        r1        r2      omeg        e0        vo
         1 372.20001   3.23100  4.150000 0.9500000  0.300000  7.000000  1.000000
*PART
$# title
Air
$#     pid     secid       mid     eosid      hgid      grav    adpopt      tmid
         2         1        22         3         0         0         0         0
*MAT_NULL_TITLE
Air
$#     mid        ro        pc        mu     terod     cerod        ym        pr
        22 1.3000E-9 -1.000E-6     0.000     0.000     0.000     0.000     0.000
*EOS_LINEAR_POLYNOMIAL_TITLE
Air
$#   eosid        c0        c1        c2        c3        c4        c5        c6
         3     0.000     0.000     0.000     0.000  0.400000  0.400000     0.000
$#      e0        v0
 2.6000E-4  1.000000
*SET_PART_LIST_TITLE
ALE
$#     sid       da1       da2       da3       da4    solver
         1     0.000     0.000     0.000     0.000MECH
$#    pid1      pid2      pid3      pid4      pid5      pid6      pid7      pid8
         1         0         0         0         0         0         0         0
*SET_PART_LIST_TITLE
ALE
$#     sid       da1       da2       da3       da4    solver
         2     0.000     0.000     0.000     0.000MECH
$#    pid1      pid2      pid3      pid4      pid5      pid6      pid7      pid8
         2         0         0         0         0         0         0         0
*ALE_MULTI-MATERIAL_GROUP
$#     sid    idtype    gpname
         1         1
         2         1
*SET_MULTI_MATERIAL_GROUP_LIST
$ This is used in the mapping
        50
         1         2         0         0         0         0         0         0
*BOUNDARY_SPC_SET
$#    nsid       cid      dofx      dofy      dofz     dofrx     dofry     dofrz
         1         0         0         1         0         1         0         1
*BOUNDARY_SPC_SET
$#    nsid       cid      dofx      dofy      dofz     dofrx     dofry     dofrz
         2         0         1         0         0         0         1         1
*BOUNDARY_SPC_SET
$#    nsid       cid      dofx      dofy      dofz     dofrx     dofry     dofrz
         3         0         1         1         1         1         1         1
*INCLUDE
mesh2.k
$*INCLUDE
$dbt.k
*END
```

A.1.2 3D Models

```
$*******************************************************************************
$ Tom Anthistle, UoS MERail Rail Research Group
$*******************************************************************************
$*******************************************************************************
$ Initial and Boundary Conditions
$*******************************************************************************
*KEYWORD
*INCLUDE
mesh6.k
*CONTROL_TERMINATION
$#  endtim    endcyc     dtmin    endeng    endmas
     2.000         0     0.000     0.000     0.000
*CONTROL_TIMESTEP
$#  dtinit    tssfac      isdo    tslimt     dt2ms      lctm     erode     ms1st
     0.000  0.600000         0     0.000     0.000         0         0         0
$#  dt2msf   dt2mslc     imscl
     0.000         0         0
*INITIAL_ALE_MAPPING
```

```
$#     pid       typ    ammsid
         2         1        50
$#      x0        y0        z0       vid
     0.000     0.000     0.000         1
*BOUNDARY_SPC_SET
$#    nsid       cid      dofx      dofy      dofz     dofrx     dofry     dofrz
         1         0         1         0         0         0         1         1
*BOUNDARY_SPC_SET
$#    nsid       cid      dofx      dofy      dofz     dofrx     dofry     dofrz
         2         0         0         1         0         1         0         1
*BOUNDARY_SPC_SET
$#    nsid       cid      dofx      dofy      dofz     dofrx     dofry     dofrz
         3         0         0         0         1         1         1         0
*BOUNDARY_SPC_SET
$#    nsid       cid      dofx      dofy      dofz     dofrx     dofry     dofrz
         7         0         1         1         1         1         1         1
$*********************************************************************************
$ Output / database details
$*********************************************************************************
*DATABASE_BINARY_D3PLOT
$#      dt      lcdt      beam     npltc    psetid
         1         0         0         0         0
$#   ioopt
         0
*DATABASE_TRHIST
$#      dt    binary      lcur     ioopt
 1.5300E-3         1         0         1
*DATABASE_TRACER
$#    time     track         x         y         z      ammg       nid
     0.000         1   500.000     0.000     0.000         0         0
     0.000         1   500.000   200.000   200.000         0         0
     0.000         1   500.000   400.000   400.000         0         0
     0.000         1   500.000   600.000   600.000         0         0
     0.000         1   803.000     5.000     5.000         0         0
     0.000         1   802.000     5.000     5.000         0         0
     0.000         1   801.000     5.000     5.000         0         0
     0.000         1   800.000     5.000     5.000         0         0
     0.000         1   799.000     5.000     5.000         0         0
     0.000         1   798.000     5.000     5.000         0         0
     0.000         1   797.000     5.000     5.000         0         0
     0.000         1   796.000     5.000     5.000         0         0
     0.000         1   795.000   300.000     5.000         0         0
$*********************************************************************************
$ Material Cards
$*********************************************************************************
*MAT_HIGH_EXPLOSIVE_BURN_TITLE
$# becomes mat null on 3d card
ChargeC4
$#     mid        ro         d       pcj      beta         k         g      sigy
         1 1.6050E-6 8040.0000 28.000001     0.000     0.000     0.000     0.000
*MAT_NULL_TITLE
Air
$#     mid        ro        pc        mu     terod     cerod        ym        pr
         2 1.3000E-9 -1.000E-6     0.000     0.000     0.000     0.000     0.000
*MAT_PLASTIC_KINEMATIC_TITLE
Steel
$0.2/FS = 0.66. where 0.2 = UTS (500MPa) - SIGY (300MPa)
$#     mid        ro         e        pr      sigy      etan      beta
        11 7.5000E-6 207.00000  0.300000  0.300000  0.660000     0.000
$#     src       srp        fs        vp
 0.0000000  0.000000  0.300000     0.000
*MAT_JOHNSON_COOK
$#     mid        ro         g         e        pr       dtf        vp    rateop
        12 2.684E-06    26.000    69.000     0.300     0.000     0.000     0.000
$#       a         b         n         c         m        tm        tr      epso
      0.27     0.134     0.514     0.008     0.703   893.000   293.000     1E-06
$#      cp        pc     spall        it        d1        d2        d3        d4
   910.000         0  2.000000     0.000     0.060     0.497    -1.551    0.0286
$#      d5      c2/p      erod     efmin
     6.800     0.000         0 1.0000E-6
$ This model is for 6005-T6 \cite{borvik2005experimental}
*MAT_LAMINATED_GLASS_TITLE
Pane
$#     mid        ro        eg       prg       syg       etg       efg        ep
        13 2.5000E-6 70.000000  0.230000  0.030000  0.060000  0.001500  0.950000
$#     prp       syp       etp
  0.490000  0.015000  0.010000
$#      f1        f2        f3        f4        f5        f6        f7        f8
     0.000     0.000  1.000000  1.000000     0.000     0.000     0.000     0.000
$*********************************************************************************
$ Equations of State
$*********************************************************************************
*EOS_JWL_TITLE
Charge
$#    eosid         a         b        r1        r2      omeg        e0        vo
         1 598.20001  13.75000  4.500000 1.5000000  0.320000  8.700000  1.000000
*EOS_LINEAR_POLYNOMIAL_TITLE
```

```
Air
$#   eosid         c0         c1         c2         c3         c4         c5         c6
         2     0.000      0.000      0.000      0.000   0.400000   0.400000      0.000
$#      e0         v0
 2.6000E-4   1.000000
*EOS_LINEAR_POLYNOMIAL_TITLE
6005-T6Al
$#   eosid         c0         c1         c2         c3         c4         c5         c6
        12     0.000     76.000      0.000      0.000   0.000000   0.000000      0.000
$#      e0         v0
     0.710   1.000000
$*******************************************************************************
$ ALE Specific Cards
$*******************************************************************************
*ALE_MULTI-MATERIAL_GROUP
$#     sid    idtype    gpname
         1         1
         2         1
*SET_MULTI_MATERIAL_GROUP_LIST
$ This is used in the mapping
        50
         1         2         0         0         0         0         0         0
*CONSTRAINED_LAGRANGE_IN_SOLID
$ Need one for each set
$#    slave    master     sstyp     mstyp     nquad     ctype     direc     mcoup
         3         1         0         0         0         4         1         0
$#    start       end      pfac      fric    frcmin      norm   normtyp      damp
     0.0001.0000E+10  0.990000     0.000  0.500000         0         1     0.000
$#       cq      hmin      hmax     ileak     pleak   lcidpor     nvent  blockage
     0.000     0.000     0.000         0   0.10000         0         0         0
$#  iboxid   ipenchk   intforc   ialesof    lagmul    pfacmm      thkf
$         0         0         0         0     0.000         0     0.000
$*******************************************************************************
$ initial volume fraction / alemmg setup
$*******************************************************************************
$*******************************************************************************
$ Control Cards
$*******************************************************************************
*CONTROL_ALE
$#     dct      nadv      meth      afac      bfac      cfac      dfac      efac
        -1         0        -2     0.000     0.000     0.000     0.000     0.000
$#   start       end     aafac     vfact      prit      ebc      pref   nsidebc
     0.0001.0000E+20  1.000000 1.0000E-6         0         0  1.04E-04         0
$#    ncpl      nbkt    imascl    checkr
         1        50         0     0.000
*CONTROL_ENERGY
2,2,1,1
$*******************************************************************************
$ Contact
$*******************************************************************************
$*******************************************************************************
$ MISC (vectors, integration definitions, etc...)
$*******************************************************************************
*DEFORMABLE_TO_RIGID
10
*DEFINE_VECTOR
         1     0.000     0.000     0.000     1.000     1.000     1.000         0
*HOURGLASS_TITLE
ALE
$#    hgid       ihq        qm       ibq        q1        q2    qb/vdc        qw
         1         1 1.0000E-6         0  1.500000  0.060000  0.100000  0.100000
*HOURGLASS_TITLE
LAG
$#    hgid       ihq        qm       ibq        q1        q2    qb/vdc        qw
        10         1  0.100000         0  1.500000  0.060000  0.100000  0.100000
$*******************************************************************************
$ Part sets
$*******************************************************************************
*SET_PART_LIST_TITLE
ALE
$#     sid       da1       da2       da3       da4    solver
         1     0.000     0.000     0.000     0.000MECH
$#    pid1      pid2      pid3      pid4      pid5      pid6      pid7      pid8
         1         2         0         0         0         0         0         0
*SET_PART_LIST_TITLE
Lagrangian
$#     sid       da1       da2       da3       da4    solver
         3     0.000     0.000     0.000     0.000MECH
$#    pid1      pid2      pid3      pid4      pid5      pid6      pid7      pid8
        10         0         0         0         0         0         0         0
$*******************************************************************************
$ Parts
$*******************************************************************************
*PART
Charge
$#     pid     secid       mid     eosid      hgid      grav    adpopt      tmid
         1         1         1         1         1         0         0         0
```

```
*PART
Air
$#     pid     secid       mid     eosid      hgid      grav    adpopt      tmid
         2         1         2         2         1         0         0         0
*PART
Air
$#     pid     secid       mid     eosid      hgid      grav    adpopt      tmid
        10         9        11         0        10         0         0         0
$*********************************************************************************
$ Sections
$*********************************************************************************
*SECTION_SOLID_TITLE
ALE
$#   secid    elform       aet
         1        11         0
*SECTION_SHELL_TITLE
Shell2mm
$#   secid    elform      shrf       nip     propt   qr/irid     icomp     setyp
         9         2  1.000000         2         1         0         0         1
$#      t1        t2        t3        t4      nloc     marea      idof    edgset
  1.000000  1.000000  1.000000  1.000000     0.000     0.000     0.000         0
*SECTION_SHELL_TITLE
Shell19mm
$#   secid    elform      shrf       nip     propt   qr/irid     icomp     setyp
        10         2  1.000000         2         1         0         0         1
$#      t1        t2        t3        t4      nloc     marea      idof    edgset
 19.000000 19.000000 19.000000 19.000000     0.000     0.000     0.000         0
*SECTION_SHELL_TITLE
Shell8mm
$#   secid    elform      shrf       nip     propt   qr/irid     icomp     setyp
        11         2  1.000000         2         1         0         0         1
$#      t1        t2        t3        t4      nloc     marea      idof    edgset
  8.000000  8.000000  8.000000  8.000000     0.000     0.000     0.000         0
*END
```

A.2 Experimental validation model

A.2.1 LS-Dyna A4 keyword file input

```
$*********************************************************************************
$ Tom Anthistle, UoS MERail Rail Research Group
$*********************************************************************************
$*********************************************************************************
$ Initial and Boundary Conditions
$*********************************************************************************
*KEYWORD
*INCLUDE
mesh2.k
*INCLUDE
lcidA4.k
*CONTROL_TERMINATION
$#  endtim    endcyc     dtmin    endeng    endmas
    15.000         0     0.000     0.000     0.000
*CONTROL_TIMESTEP
$#  dtinit    tssfac      isdo    tslimt     dt2ms      lctm     erode     ms1st
     0.000  0.600000         0     0.000     0.000         0         0         0
$#  dt2msf   dt2mslc     imscl
     0.000         0         0
*CONTROL_OUTPUT
$#   npopt    neecho    nrefup    iaccop     opifs    ipnint    ikedit    iflush
         0         0         0         0     0.000         0       100      1000
$#   iprtf    ierode     tet10    msgmax    ipcurv
         0         0         2        50         0
*INITIAL_ALE_MAPPING
$#     pid       typ    ammsid
         2         1        50
$#      x0        y0        z0       vid
     0.000   728.000     0.000         1
*BOUNDARY_SPC_SET
$#    nsid       cid      dofx      dofy      dofz     dofrx     dofry     dofrz
         1         0         1         0         0         0         1         1
*BOUNDARY_SPC_SET
$#    nsid       cid      dofx      dofy      dofz     dofrx     dofry     dofrz
         2         0         0         1         0         1         0         1
*BOUNDARY_SPC_SET
$#    nsid       cid      dofx      dofy      dofz     dofrx     dofry     dofrz
         3         0         0         0         1         1         1         0
*BOUNDARY_SPC_SET
$#    nsid       cid      dofx      dofy      dofz     dofrx     dofry     dofrz
         8         0         1         1         1         1         1         1
*BOUNDARY_SPC_SET
$#    nsid       cid      dofx      dofy      dofz     dofrx     dofry     dofrz
        18         0         1         1         1         1         1         1
$*********************************************************************************
$ Output / database details
```

```
$*******************************************************************************
*DATABASE_BINARY_D3PLOT
$#      dt      lcdt      beam     npltc    psetid
       7.5         0         0         0         0
$#   ioopt
         0
*DATABASE_BINARY_D3PART
$#      dt      lcdt      beam     npltc    psetid
  0.500000         0         0         0        11
*DATABASE_GLSTAT
$#      dt    binary      lcur     ioopt
 1.5300E-3         1         0         1
*DATABASE_MATSUM
$#      dt    binary      lcur     ioopt
 1.5300E-3         1         0         1
*DATABASE_TRHIST
$#      dt    binary      lcur     ioopt
 1.5300E-3         1         0         1
*DATABASE_TRACER
$#    time     track         x         y         z      ammg       nid
0,1,1490,1450,364,0,0
0,1,990,600,425,0,0
0,1,5,728,1452,0,0
0,1,1490,728,3,0,0
0,1,2930,728,3,0,0
*DATABASE_NODOUT
$#      dt    binary      lcur     ioopt      dthf     binhf
 1.5000E-3         1         0         1     0.000         0
*DATABASE_HISTORY_NODE
$#     id1       id2       id3       id4       id5       id6       id7       id8
12837531,12837530
*DATABASE_ELOUT
$#      dt    binary      lcur     ioopt
 1.5000E-3         1         0         1
*DATABASE_RCFORC
$#      dt    binary      lcur     ioopt
  1.500E-2         1         0         1
*DATABASE_HISTORY_BEAM_SET
$#     id1       id2       id3       id4       id5       id6       id7       id8
1
$*******************************************************************************
$ Material Cards
$*******************************************************************************
*MAT_HIGH_EXPLOSIVE_BURN_TITLE
$# becomes mat null on 3d card
ChargeC4
$#     mid        ro         d       pcj      beta         k         g      sigy
         1 1.6050E-6 8040.0000 28.000001     0.000     0.000     0.000     0.000
*MAT_NULL_TITLE
Air
$#     mid        ro        pc        mu     terod     cerod        ym        pr
         2 1.3000E-9 -1.000E-6     0.000     0.000     0.000     0.000     0.000
*MAT_PLASTIC_KINEMATIC_TITLE
Steel
$0.2/FS = 0.66. where 0.2 = UTS (500MPa) - SIGY (300MPa)
$#     mid        ro         e        pr      sigy      etan      beta
        11 7.5000E-6 207.00000  0.300000  0.300000  0.660000     0.000
$#     src       srp        fs        vp
 0.0000000  0.000000  0.300000     0.000
*MAT_PLASTIC_KINEMATIC_TITLE
1050 Aluminium
$0.2/FS = 0.66. where 0.2 = UTS (500MPa) - SIGY (300MPa)
$#     mid        ro         e        pr      sigy      etan      beta
        14 2.7100E-6  71.00000  0.330000  0.100000  0.500000     0.000
$#     src       srp        fs        vp
 0.0000000  0.000000  0.450000     0.000
*MAT_JOHNSON_COOK
$#     mid        ro         g         e        pr       dtf        vp    rateop
        12 2.684E-06    26.000    69.000     0.300     0.000     0.000     0.000
$#       a         b         n         c         m        tm        tr      epso
      0.27     0.134     0.514     0.008     0.703   893.000   293.000     1E-06
$#      cp        pc     spall        it        d1        d2        d3        d4
   910.000         0  2.000000     0.000     0.060     0.497    -1.551    0.0286
$#      d5      c2/p      erod     efmin
     6.800     0.000         0 1.0000E-6
$ This model is for 6005-T6 \cite{borvik2005experimental}
*MAT_LAMINATED_GLASS_TITLE
Pane
$#     mid        ro        eg       prg       syg       etg       efg        ep
        13 2.5000E-6 70.000000  0.230000  0.030000  0.060000  0.001500  0.950000
$#     prp       syp       etp
  0.490000  0.015000  0.010000
$#      f1        f2        f3        f4        f5        f6        f7        f8
     0.000     0.000  1.000000  1.000000     0.000     0.000     0.000     0.000
*MAT_RIGID
$#     mid        ro         e        pr         n    couple         m     alias
        20 7.5000E-6   207.000     0.300     0.000     0.000     0.000
```

```
$#      cmo      con1      con2
     0.000         0         0
$# lco or a1       a2        a3        v1        v2        v3
     0.000     0.000     0.000     0.000     0.000     0.000
*MAT_SPOTWELD
$#      mid        ro         e        pr      sigy        et        dt     tfail
       100 7.5000E-6   210.000     0.300     0.800     0.200     0.000     0.000
$#    efail       nrr       nrs       nrt       mrr       mss       mtt        nf
     0.350     0.000     0.000     0.000     0.000     0.000     0.000     0.000
$*********************************************************************************
$ Equations of State
$*********************************************************************************
*EOS_JWL_TITLE
Charge
$#    eosid         a         b        r1        r2      omeg        e0        vo
         1 598.20001  13.75000  4.500000 1.5000000  0.320000  8.700000  1.000000
*EOS_LINEAR_POLYNOMIAL_TITLE
Air
$#    eosid        c0        c1        c2        c3        c4        c5        c6
         2     0.000     0.000     0.000     0.000  0.400000  0.400000     0.000
$#      e0        v0
 2.6000E-4  1.000000
*EOS_LINEAR_POLYNOMIAL_WITH_ENERGY_LEAK
$#    eosid        c0        c1        c2        c3        c4        c5        c6
        18     0.000     0.000     0.000     0.000  0.400000  0.400000     0.000
$#      e0        v0      lcid
 2.6000E-4  1.000000        10
*EOS_LINEAR_POLYNOMIAL_TITLE
6005-T6A1
$#    eosid        c0        c1        c2        c3        c4        c5        c6
        20     0.000    76.000     0.000     0.000  0.000000  0.000000     0.000
$#      e0        v0
     0.710  1.000000
$*********************************************************************************
$ ALE Specific Cards
$*********************************************************************************
*ALE_MULTI-MATERIAL_GROUP
$#      sid    idtype    gpname
         1         1
         2         1
         3         1
         4         1
         5         1
*SET_MULTI_MATERIAL_GROUP_LIST
$ This is used in the mapping
        50
         1         2         0         0         0         0         0         0
*CONSTRAINED_LAGRANGE_IN_SOLID
$ Need one for each set
$#   slave    master     sstyp     mstyp     nquad     ctype     direc     mcoup
         3         1         0         0         0         4         1         0
$#   start       end      pfac      fric    frcmin      norm   normtyp      damp
     0.0001.0000E+10  0.100000     0.000  0.300000         0         1     0.000
$#      cq      hmin      hmax     ileak     pleak   lcidpor     nvent  blockage
     0.000     0.000     0.000         0  0.110000         0         0         0
$#  iboxid   ipenchk   intforc   ialesof    lagmul    pfacmm      thkf
$        0         0         0         0     0.000         0     0.000
$*********************************************************************************
$ initial volume fraction / alemmg setup
$*********************************************************************************
$*INITIAL_VOLUME_FRACTION_GEOMETRY
$ FMSID,FMIDTYP,BAMMG,NTRACE
$2,1,2,5
$ conttyp,fillopt (0=head, 1=tail),fammg
$1,1,3
$ sid,stype,normdir,xoffset
$9,0,,
$*********************************************************************************
$ Control Cards
$*********************************************************************************
*CONTROL_ALE
$#     dct      nadv      meth      afac      bfac      cfac      dfac      efac
        -1         0        -2     0.000     0.000     0.000     0.000     0.000
$#   start       end     aafac     vfact      prit       ebc      pref   nsidebc
     0.0001.0000E+20  1.000000 1.0000E-6         0         0  1.04E-04         0
$#    ncpl      nbkt    imascl    checkr
         1        50         0     0.000
*CONTROL_ENERGY
2,2,1,1
$*********************************************************************************
$ Contact
$*********************************************************************************
*CONTACT_TIED_NODES_TO_SURFACE_ID
$#     cid                                                                   title
        11
$#    ssid      msid     sstyp     mstyp    sboxid    mboxid       spr       mpr
        17        10         4         0         0         0         0         1
```

```
$#      fs        fd        dc        vc        vdc     penchk        bt        dt
     0.000     0.000     0.000     0.000     0.000          0     0.0001.0000E+20
$#     sfs       sfm       sst       mst      sfst      sfmt       fsf       vsf
  1.000000  1.000000     0.000     0.000  1.000000  1.000000  1.000000  1.000000
*CONTROL_CONTACT
$#  slsfac    rwpnal    islchk    shlthk    penopt    thkchg     orien    enmass
  0.100000     0.000         2         0         0         0         1         0
$#  usrstr    usrfrc     nsbcs    interm     xpene     ssthk      ecdt   tiedprj
         0         0         0         0  4.000000         0         0         0
$#   sfric     dfric       edc       vfc        th     th_sf    pen_sf
     0.000     0.000     0.000     0.000     0.000     0.000     0.000
$#  ignore    frceng   skiprwg    outseg   spotstp   spotdel   spothin
         0         0         0         0         0         0     0.000
$#    isym    nserod    rwgaps    rwgdth     rwksf      icov    swradf    ithoff
         0         0         0     0.000  1.000000         0     0.000         0
$#  shledg    pstiff    ithcnt    tdcnof     ftall    unused    shltrw
         0         0         0         0         0         0     0.000
*RIGIDWALL_PLANAR_ID
1
$# NSID NSIDEX BOXID OFFSET BIRTH DEATH RWKSF
20,0,0
$# XT YT ZT XH YH ZH FRIC WVEL
1490,1456,730,1490,1800,730
*RIGIDWALL_PLANAR_ID
2
$# NSID NSIDEX BOXID OFFSET BIRTH DEATH RWKSF
20,0,0
$# XT YT ZT XH YH ZH FRIC WVEL
1490,0,730,1490,-1800,730
*RIGIDWALL_PLANAR_ID
3
$# NSID NSIDEX BOXID OFFSET BIRTH DEATH RWKSF
20,0,0
$# XT YT ZT XH YH ZH FRIC WVEL
0,730,730,-1000,730,730
*CONSTRAINED_EXTRA_NODES_SET
$# pid, nid
10,18
$*******************************************************************************
$ MISC (vectors, integration definitions, etc...)
$*******************************************************************************
*DEFINE_VECTOR
         1     0.000     0.000     0.000     1.000     0.000     1.000         0
*HOURGLASS_TITLE
ALE
$#     hgid       ihq        qm       ibq        q1        q2    qb/vdc        qw
         1         1 1.0000E-6         0  1.500000  0.060000  0.100000  0.100000
*HOURGLASS_TITLE
LAG
$#     hgid       ihq        qm       ibq        q1        q2    qb/vdc        qw
        10         1  0.100000         0  1.500000  0.060000  0.100000  0.100000
$*******************************************************************************
$ Part sets
$*******************************************************************************
*SET_PART_LIST_TITLE
ALE
$#      sid       da1       da2       da3       da4    solver
         1     0.000     0.000     0.000     0.000MECH
$#     pid1      pid2      pid3      pid4      pid5      pid6      pid7      pid8
         1         2         5         0         0         0         0         0
*SET_PART_LIST_TITLE
Lagrangian
$#      sid       da1       da2       da3       da4    solver
         3     0.000     0.000     0.000     0.000MECH
$#     pid1      pid2      pid3      pid4      pid5      pid6      pid7      pid8
        10        11        12        20        30         0         0         0
*SET_PART_LIST_TITLE
cylinders
$#      sid       da1       da2       da3       da4    solver
         9     0.000     0.000     0.000     0.000MECH
$#     pid1      pid2      pid3      pid4      pid5      pid6      pid7      pid8
        11        12         0         0         0         0         0         0
*SET_PART_LIST_TITLE
interest
$#      sid       da1       da2       da3       da4    solver
        11     0.000     0.000     0.000     0.000MECH
$#     pid1      pid2      pid3      pid4      pid5      pid6      pid7      pid8
        20        30       120         0         0         0         0         0
$*******************************************************************************
$ Parts
$*******************************************************************************
*PART
Charge
$#      pid     secid       mid     eosid      hgid      grav    adpopt      tmid
         1         1         1         1         1         0         0         0
*PART
Air
```

```
$#     pid     secid       mid     eosid      hgid      grav    adpopt      tmid
         2         1         2        18         1         0         0         0
*PART
Air
$#     pid     secid       mid     eosid      hgid      grav    adpopt      tmid
         3         1         2         2         1         0         0         0
*PART
Air
$#     pid     secid       mid     eosid      hgid      grav    adpopt      tmid
         4         1         2         2         1         0         0         0
*PART
Air
$#     pid     secid       mid     eosid      hgid      grav    adpopt      tmid
         5         1         2         2         1         0         0         0
*PART
$# title
Box
$#     pid     secid       mid     eosid      hgid      grav    adpopt      tmid
        10         8        20         0        10         0         0         0
*PART
$# title
Cyl1
$#     pid     secid       mid     eosid      hgid      grav    adpopt      tmid
        11         8        20         0        10         0         0         0
*PART
$# title
Cyl2
$#     pid     secid       mid     eosid      hgid      grav    adpopt      tmid
        12         8        20         0        10         0         0         0
*PART
$# title
NS-end
$#     pid     secid       mid     eosid      hgid      grav    adpopt      tmid
        13         9        11         0        10         0         0         0
*PART
$# title
panel
$#     pid     secid       mid     eosid      hgid      grav    adpopt      tmid
        20         9        14         0        10         0         0         0
*PART
$# title
support
$#     pid     secid       mid     eosid      hgid      grav    adpopt      tmid
        30        11        11         0        10         0         0         0
*PART
$# title
spotweld
$#     pid     secid       mid     eosid      hgid      grav    adpopt      tmid
       120       100       100         0         0         0         0         0
$$$$$$$$$$$$$$$$$$$$$$$$$$$$$$$$$$$$$$$$$$$$$$$$$$$$$$$$$$$$$$$$$$$$$$$$$$$$$$$
$ Sections
$$$$$$$$$$$$$$$$$$$$$$$$$$$$$$$$$$$$$$$$$$$$$$$$$$$$$$$$$$$$$$$$$$$$$$$$$$$$$$$
*SECTION_SOLID_TITLE
ALE
$#   secid    elform       aet
         1        11         0
*SECTION_SHELL_TITLE
Shell3-2mm
$#   secid    elform      shrf       nip     propt   qr/irid     icomp     setyp
         8         2  1.000000         2         1         0         0         1
$#      t1        t2        t3        t4      nloc     marea      idof    edgset
  2.000000  2.000000  2.000000  2.000000     0.000     0.000     0.000         0
*SECTION_SHELL_TITLE
Shell3-2mm
$#   secid    elform      shrf       nip     propt   qr/irid     icomp     setyp
         9         2  1.000000         2         1         0         0         1
$#      t1        t2        t3        t4      nloc     marea      idof    edgset
  3.200000  3.200000  3.200000  3.200000     0.000     0.000     0.000         0
*SECTION_SHELL_TITLE
Shell19mm
$#   secid    elform      shrf       nip     propt   qr/irid     icomp     setyp
        10         2  1.000000         2         1         0         0         1
$#      t1        t2        t3        t4      nloc     marea      idof    edgset
 19.000000 19.000000 19.000000 19.000000     0.000     0.000     0.000         0
*SECTION_SHELL_TITLE
Shell8mm
$#   secid    elform      shrf       nip     propt   qr/irid     icomp     setyp
        11         2  1.000000         2         1         0         0         1
$#      t1        t2        t3        t4      nloc     marea      idof    edgset
  8.000000  8.000000  8.000000  8.000000     0.000     0.000     0.000         0
*SECTION_SHELL_TITLE
Shell8mm
$#   secid    elform      shrf       nip     propt   qr/irid     icomp     setyp
        12         2  1.000000         2         1         0         0         1
$#      t1        t2        t3        t4      nloc     marea      idof    edgset
 14.000000  14.00000 14.000000  14.00000     0.000     0.000     0.000         0
*SECTION_BEAM
```

```
$#   secid    elform      shrf   qr/irid       cst     scoor       nsm
       100         9  1.000000         2         1     0.000     0.000
$#     ts1       ts2       tt1       tt2     print
 10.000000 10.000000     0.000     0.000     0.000
*END
```

A.2.2 Matlab function to generate secondary combustion load curve

```
filename = '/home/tom/Work/validation/A4/lcidA4.k';
lcid =10;
runtime=100;
endtime = 15;
timestep= 0.1;
b = 1.5; %energy release coefficient
o = 7.5; % energy release offset
t = [0:timestep:endtime];
ekg = 4E6; % afterburn energy per kg
mass= 0.08;% of charge
te = ekg*mass;
volume = 728*1456*2980;
specen = te/volume;
int = 1./(1+exp(-b*(t))); % find where this = 0, then shift assign that t (s)
%s = t(max(find(int<=1E-03)));
dy = (specen*b.*exp(-b.*(t-o)))./(1+exp(-b.*(t-o))).**2;
plot(t,dy)
curve = [t' dy'];
fout = fopen(filename,'wt');
fprintf(fout,'$#b=%0.2f,o=%0.2f\n',b,o)
fprintf(fout,'*DEFINE_CURVE\n')
fprintf(fout,'$#lcid,sidr,sfa,sfo,offa,offo,dattyp\n')
fprintf(fout,'%i,0,1.00,1.00,0.000,0.000,0\n',lcid)
fprintf(fout,'$#x axis,y axis\n')
fprintf(fout,'%0.2f,%0.5E\n',curve')
fprintf(fout,'*END')
fclose(fout)
```

A.3 Rail vehicle models

C1 model input

```
$*******************************************************************************
$ Tom Anthistle, UoS MERail Rail Research Group
$*******************************************************************************
$*******************************************************************************
$ Initial and Boundary Conditions
$*******************************************************************************
*KEYWORD
*INCLUDE
mesh_30.k
*INCLUDE
tracerD2.k
*CONTROL_TERMINATION
$#  endtim    endcyc     dtmin    endeng    endmas
     1.000         0     0.000     0.000     0.000
*CONTROL_OUTPUT
$#   npopt    neecho    nrefup    iaccop     opifs    ipnint    ikedit    iflush
         0         0         0         0     0.000         0       100      1000
$#   iprtf    ierode     tet10    msgmax    ipcurv
         0         0         2        50         0
*CONTROL_TIMESTEP
$#  dtinit    tssfac      isdo    tslimt     dt2ms      lctm     erode     ms1st
     0.000  0.600000         0     0.000     0.000         0         0         0
$#  dt2msf   dt2mslc     imscl
     0.000         0         0
*INITIAL_ALE_MAPPING
$#     pid       typ    ammsid
         2         1        50
$#      x0        y0        z0       vid
     0.000     0.000  1329.000         1
*BOUNDARY_SPC_SET
$#    nsid       cid      dofx      dofy      dofz     dofrx     dofry     dofrz
         1         0         1         0         0         0         1         1
*BOUNDARY_SPC_SET
$#    nsid       cid      dofx      dofy      dofz     dofrx     dofry     dofrz
        11         0         1         0         0         0         1         1
*BOUNDARY_SPC_SET
$#    nsid       cid      dofx      dofy      dofz     dofrx     dofry     dofrz
         2         0         0         1         0         1         0         1
*BOUNDARY_SPC_SET
$#    nsid       cid      dofx      dofy      dofz     dofrx     dofry     dofrz
        12         0         0         1         0         1         0         1
*BOUNDARY_SPC_SET
$#    nsid       cid      dofx      dofy      dofz     dofrx     dofry     dofrz
         3         0         0         0         1         1         1         0
*BOUNDARY_SPC_SET
```

```
$#     nsid       cid      dofx      dofy      dofz     dofrx     dofry     dofrz
         8         0         1         1         1         1         1         1
*BOUNDARY_SPC_SET
$#     nsid       cid      dofx      dofy      dofz     dofrx     dofry     dofrz
         9         0         1         1         1         1         1         1
*BOUNDARY_SPC_SET
$#     nsid       cid      dofx      dofy      dofz     dofrx     dofry     dofrz
        20         0         0         0         1         0         0         0
$*********************************************************************************
$ Output / database details
$*********************************************************************************
*DATABASE_BINARY_D3PLOT
$#      dt      lcdt      beam     npltc    psetid
     20.00         0         0         0         0
$#   ioopt
         0
*DATABASE_BINARY_D3PART
$#      dt      lcdt      beam     npltc    psetid
  2.000000         0         0         0         3
*DATABASE_GLSTAT
$#      dt    binary      lcur     ioopt
 1.5300E-3         1         0         1
*DATABASE_MATSUM
$#      dt    binary      lcur     ioopt
 1.5300E-3         1         0         1
*DATABASE_TRHIST
$#      dt    binary      lcur     ioopt
 1.5300E-2         1         0         1
$*********************************************************************************
$ Material Cards
$*********************************************************************************
*MAT_HIGH_EXPLOSIVE_BURN_TITLE
$# becomes mat null on 3d card
ChargeC4
$#     mid        ro         d       pcj      beta         k         g      sigy
         1 1.6050E-6 8040.0000 28.000001     0.000     0.000     0.000     0.000
*MAT_NULL_TITLE
Air
$#     mid        ro        pc        mu     terod     cerod        ym        pr
         2 1.3000E-9 -1.000E-6     0.000     0.000     0.000     0.000     0.000
*MAT_PLASTIC_KINEMATIC_TITLE
6005-T6 plastic kinematic
$#     mid        ro         e        pr      sigy      etan      beta
        10 2.684E-06  69.00000  0.300000  0.275000  0.660000     0.000
$#     src       srp        fs        vp
         0  0.000000  0.300000     0.000
*MAT_JOHNSON_COOK
$#     mid        ro         g         e        pr       dtf        vp    rateop
        11 2.684E-06    26.000    69.000     0.300     0.000     0.000     0.000
$#       a         b         n         c         m        tm        tr      epso
      0.27     0.134     0.514     0.008     0.703   893.000   293.000    1E-06
$#      cp        pc     spall        it        d1        d2        d3        d4
   910.000         0  2.000000     0.000     0.060     0.497    -1.551    0.0286
$#      d5      c2/p      erod     efmin
     6.800     0.000         0 1.0000E-6
$ This model is for 6005-T6 \cite{borvik2005experimental}
*MAT_LAMINATED_GLASS_TITLE
Pane
$#     mid        ro        eg       prg       syg       etg       efg        ep
        13 2.5000E-6 70.000000  0.230000  0.030000  0.060000  0.001500  0.950000
$#     prp       syp       etp
  0.490000  0.015000  0.010000
$#      f1        f2        f3        f4        f5        f6        f7        f8
     0.000     0.000  1.000000  1.000000     0.000     0.000     0.000     0.000
*MAT_SPOTWELD
$#     mid        ro         e        pr      sigy        et        dt     tfail
        100 7.5000E-6   210.000     0.300     0.800     0.200     0.000     0.000
$#   efail       nrr       nrs       nrt       mrr       mss       mtt        nf
     0.400     0.000     0.000     0.000     0.000     0.000     0.000     0.000
*MAT_RIGID
$#     mid        ro         e        pr         n    couple         m     alias
        200 7.5000E-6   207.000     0.300     0.000     0.000     0.000
$#     cmo      con1      con2
     0.000         0         0
$# lco or a1      a2        a3        v1        v2        v3
     0.000     0.000     0.000     0.000     0.000     0.000
$*********************************************************************************
$ Equations of State
$*********************************************************************************
*EOS_JWL_TITLE
Charge
$#   eosid         a         b        r1        r2      omeg        e0        vo
         1 598.20001  13.75000  4.500000 1.5000000  0.320000  8.700000  1.000000
*EOS_LINEAR_POLYNOMIAL_TITLE
Air
$#   eosid        c0        c1        c2        c3        c4        c5        c6
         2     0.000     0.000     0.000     0.000  0.400000  0.400000     0.000
```

```
$#      e0        v0
 2.6000E-4  1.000000
*EOS_LINEAR_POLYNOMIAL_TITLE
6005-T6A1
$#    eosid        c0        c1        c2        c3        c4        c5        c6
        20     0.000    76.000     0.000     0.000  0.000000  0.000000     0.000
$#      e0        v0
     0.710  1.000000
$*******************************************************************************
$ ALE Specific Cards
$*******************************************************************************
*ALE_MULTI-MATERIAL_GROUP
$#     sid    idtype    gpname
         1         1
         2         1
         5         1
*SET_MULTI_MATERIAL_GROUP_LIST
$ This is used in the mapping
        50
         1         2         0         0         0         0         0         0
*CONSTRAINED_LAGRANGE_IN_SOLID
$ Need one for each set
$#    slave    master     sstyp     mstyp     nquad     ctype     direc     mcoup
         3         1         0         0         0         4         1         0
$#    start       end      pfac      fric    frcmin      norm   normtyp      damp
     0.0001.0000E+10  0.100000     0.000  0.300000         0         1     0.000
$#       cq      hmin      hmax     ileak     pleak   lcidpor     nvent  blockage
     0.000     0.000     0.000         0  0.110000         0         0         0
$#  iboxid   ipenchk   intforc   ialesof    lagmul    pfacmm      thkf
$         0         0         0         0     0.000         0     0.000
$*******************************************************************************
$ initial volume fraction / alemmg setup
$*******************************************************************************
*INITIAL_VOLUME_FRACTION_GEOMETRY
$#    fmsid   fmidtyp     bammg    ntrace
         2         1         2         3
$# conttyp   fillopt     fammg        vx        xy        xz    radvel    unused
         2         1         3     0.000     0.000     0.000     0.000         0
$#    sgsid   normdir   xoffset    unused    unused    unused    unused    unused
       100         0     0.000         0         0         0         0         0
$*******************************************************************************
$ Control Cards
$*******************************************************************************
*CONTROL_ALE
$#     dct       nadv       meth       afac       bfac       cfac       dfac       efac
        -1          0         -2      0.000      0.000      0.000      0.000      0.000
$#    start        end     aafac      vfact       prit        ebc       pref   nsidebc
     0.0001.0000E+20  1.000000 1.0000E-6          0          0  1.04E-04          0
$#     ncpl       nbkt     imascl     checkr
         1         50          0     0.000
*CONTROL_ENERGY
2,2,1,1
$*******************************************************************************
$ Contact
$*******************************************************************************
*CONTACT_TIED_NODES_TO_SURFACE
$ slave = nodes, master = segments
$  4 = node set, 0 = segment set
$#     cid                                                                title
$#    ssid      msid     sstyp     mstyp    sboxid    mboxid       spr       mpr
         60        60         4         0         0         0         0         0
$#      fs        fd        dc        vc       vdc    penchk        bt        dt
     0.000     0.000     0.000     0.000     0.000         0     0.0001.0000E+20
$#     sfs       sfm       sst       mst      sfst      sfmt       fsf       vsf
  1.000000  1.000000     0.000     0.000  1.000000  1.000000  1.000000  1.000000
*CONTACT_AUTOMATIC_SURFACE_TO_SURFACE_TIEBREAK
$ sstyp & mstyp 0 = segment set
$#     cid                                                                title
$#    ssid      msid     sstyp     mstyp    sboxid    mboxid       spr       mpr
         21        20         0         0         0         0         0         0
$#      fs        fd        dc        vc       vdc    penchk        bt        dt
     0.000     0.000     0.000     0.000     0.000         0     0.0001.0000E+20
$#     sfs       sfm       sst       mst      sfst      sfmt       fsf       vsf
  1.000000  1.000000     0.000     0.000  1.000000  1.000000  1.000000  1.000000
$#  option      nfls      sfls     param    eraten    erates     ct2cn        cn
         2     0.016     0.100     0.000     0.000     0.000     0.000     0.000
*CONTACT_TIED_SURFACE_TO_SURFACE
$#     cid  typ 0 = seg set                                 title
$#    ssid      msid     sstyp     mstyp    sboxid    mboxid       spr       mpr
        201       202         0         0         0         0         0         0
$#      fs        fd        dc        vc       vdc    penchk        bt        dt
     0.000     0.000     0.000     0.000     0.000         0     0.0001.0000E+20
$#     sfs       sfm       sst       mst      sfst      sfmt       fsf       vsf
  1.000000  1.000000     0.000     0.000  1.000000  1.000000  1.000000  1.000000
*CONTROL_CONTACT
$#  slsfac     rwpnal     islchk     shlthk     penopt     thkchg      orien     enmass
  0.100000      0.000          2          0          0          0          1          0
```

```
$#  usrstr    usrfrc     nsbcs    interm     xpene     ssthk      ecdt   tiedprj
         0         0         0         0  4.000000         0         0         0
$#   sfric     dfric       edc       vfc        th     th_sf    pen_sf
     0.000     0.000     0.000     0.000     0.000     0.000     0.000
$#  ignore    frceng   skiprwg    outseg   spotstp   spotdel   spothin
         0         0         0         0         0         0     0.000
$#    isym    nserod    rwgaps    rwgdth     rwksf      icov    swradf    ithoff
         0         0         0     0.000  1.000000         0     0.000         0
$#  shledg    pstiff    ithcnt    tdcnof     ftall    unused    shltrw
         0         0         0         0         0         0     0.000
$*******************************************************************************
$ MISC (vectors, integration definitions, etc...)
$*******************************************************************************
*DEFINE_VECTOR
         1     0.000     0.000     0.000     1.000     1.000     0.000         0
*HOURGLASS_TITLE
ALE
$#    hgid       ihq        qm       ibq        q1        q2    qb/vdc        qw
         1         1 1.0000E-6         0  1.500000  0.060000  0.100000  0.100000
*HOURGLASS_TITLE
LAG
$#    hgid       ihq        qm       ibq        q1        q2    qb/vdc        qw
        10         1  0.100000         0  1.500000  0.060000  0.100000  0.100000
*INTEGRATION_SHELL
$#    irid       nip      esop   failopt
         1         6         0         0
$#       s        wf       pid
  0.670800  0.240000        35
  0.350800  0.240000        35
  0.015400  0.020000        35
 -0.015400  0.020000        35
 -0.350800  0.240000        35
 -0.670800  0.240000        35
$*******************************************************************************
$ Part sets
$*******************************************************************************
*SET_PART_LIST_TITLE
ALE
$#     sid       da1       da2       da3       da4    solver
         1     0.000     0.000     0.000     0.000MECH
$#    pid1      pid2      pid3      pid4      pid5      pid6      pid7      pid8
         1         2         0         0         0         0         0         0
*SET_PART_LIST_TITLE
Lagrangian
$#     sid       da1       da2       da3       da4    solver
         3     0.000     0.000     0.000     0.000MECH
$#    pid1      pid2      pid3      pid4      pid5      pid6      pid7      pid8
        18        19        20        21        22        24        26        27
        28        29        30        31        32        33        34        35
        36        40       100
$*******************************************************************************
$ Parts
$*******************************************************************************
*PART
Charge
$#     pid     secid       mid     eosid      hgid      grav    adpopt      tmid
         1         1         1         1         1         0         0         0
*PART
Air
$#     pid     secid       mid     eosid      hgid      grav    adpopt      tmid
         2         1         2         2         1         0         0         0
*PART
Air
$#     pid     secid       mid     eosid      hgid      grav    adpopt      tmid
         5         1         2         2         1         0         0         0
*PART
P18
$#     pid     secid       mid     eosid      hgid      grav    adpopt      tmid
        18        23        10         0        10         0         0         0
*PART
P19
$#     pid     secid       mid     eosid      hgid      grav    adpopt      tmid
        19        11        10         0        10         0         0         0
*PART
P20
$#     pid     secid       mid     eosid      hgid      grav    adpopt      tmid
        20        21        10         0        10         0         0         0
*PART
P21
$#     pid     secid       mid     eosid      hgid      grav    adpopt      tmid
        21        22        10         0        10         0         0         0
*PART
P22
$#     pid     secid       mid     eosid      hgid      grav    adpopt      tmid
        22        12        10         0        10         0         0         0
*PART
P24
```

```
$#     pid     secid       mid     eosid      hgid      grav    adpopt      tmid
        24        19        10         0        10         0         0         0
*PART
P26
$#     pid     secid       mid     eosid      hgid      grav    adpopt      tmid
        26        19        10         0        10         0         0         0
*PART
P27
$#     pid     secid       mid     eosid      hgid      grav    adpopt      tmid
        27        20        10         0        10         0         0         0
*PART
P28
$#     pid     secid       mid     eosid      hgid      grav    adpopt      tmid
        28        14        10         0        10         0         0         0
*PART
P29
$#     pid     secid       mid     eosid      hgid      grav    adpopt      tmid
        29        18        10         0        10         0         0         0
*PART
P30
$#     pid     secid       mid     eosid      hgid      grav    adpopt      tmid
        30        16        10         0        10         0         0         0
*PART
P31
$#     pid     secid       mid     eosid      hgid      grav    adpopt      tmid
        31        13        10         0        10         0         0         0
*PART
P32
$#     pid     secid       mid     eosid      hgid      grav    adpopt      tmid
        32        17        10         0        10         0         0         0
*PART
P33
$#     pid     secid       mid     eosid      hgid      grav    adpopt      tmid
        33        10        10         0        10         0         0         0
*PART
doors
$#     pid     secid       mid     eosid      hgid      grav    adpopt      tmid
        34        14        10         0        10         0         0         0
*PART
windows
$#     pid     secid       mid     eosid      hgid      grav    adpopt      tmid
        35         3        13         0        10         0         0         0
*PART
doorrib
$#     pid     secid       mid     eosid      hgid      grav    adpopt      tmid
        36        15        10         0        10         0         0         0
*PART
pass
$#     pid     secid       mid     eosid      hgid      grav    adpopt      tmid
        40         9       200         0        10         0         0         0
*PART
spotweld
$#     pid     secid       mid     eosid      hgid      grav    adpopt      tmid
       100       100       100         0         0         0         0         0
*PART
rigidshell
$#     pid     secid       mid     eosid      hgid      grav    adpopt      tmid
       200        10       200         0         0         0         0         0
$*******************************************************************************
$ Sections
$*******************************************************************************
*SECTION_SOLID_TITLE
ALE
$#   secid    elform       aet
         1        11         0
*SECTION_SHELL_TITLE
Shell-Window
$#   secid    elform      shrf       nip     propt   qr/irid     icomp     setyp
         3         2  1.000000         6         1        -1         0         1
$#      t1        t2        t3        t4      nloc     marea      idof    edgset
 10.000000 10.000000 10.000000 10.000000     0.000     0.000     0.000         0
$*SECTION_SHELL_TITLE
$Shell-Window
$#   secid    elform      shrf       nip     propt   qr/irid     icomp     setyp
$         3         2  1.000000         2         1         0         0         1
$#      t1        t2        t3        t4      nloc     marea      idof    edgset
$ 10.000000 10.000000 10.000000 10.000000     0.000     0.000     0.000         0
*SECTION_SHELL_TITLE
pass
$#   secid    elform      shrf       nip     propt   qr/irid     icomp     setyp
         9         2  1.000000         2         1         0         0         1
$#      t1        t2        t3        t4      nloc     marea      idof    edgset
  2.000000  2.000000  2.000000  2.000000     0.000     0.000     0.000         0
*SECTION_SHELL_TITLE
Shell2.5mm
$#   secid    elform      shrf       nip     propt   qr/irid     icomp     setyp
        10         2  1.000000         2         1         0         0         1
```

```
$#      t1        t2        t3        t4      nloc     marea      idof     edgset
  2.500000  2.500000  2.500000  2.500000     0.000     0.000     0.000         0
*SECTION_SHELL_TITLE
Shell3mm
$#    secid    elform      shrf       nip     propt   qr/irid     icomp     setyp
        11         2  1.000000         2         1         0         0         1
$#      t1        t2        t3        t4      nloc     marea      idof     edgset
  3.000000  3.000000  3.000000  3.000000     0.000     0.000     0.000         0
*SECTION_SHELL_TITLE
Shell3.4mm
$#    secid    elform      shrf       nip     propt   qr/irid     icomp     setyp
        12         2  1.000000         2         1         0         0         1
$#      t1        t2        t3        t4      nloc     marea      idof     edgset
  3.400000  3.400000  3.400000  3.400000     0.000     0.000     0.000         0
*SECTION_SHELL_TITLE
Shell4mm
$#    secid    elform      shrf       nip     propt   qr/irid     icomp     setyp
        13         2  1.000000         2         1         0         0         1
$#      t1        t2        t3        t4      nloc     marea      idof     edgset
  4.000000  4.000000  4.000000  4.000000     0.000     0.000     0.000         0
*SECTION_SHELL_TITLE
Shell4.5mm
$#    secid    elform      shrf       nip     propt   qr/irid     icomp     setyp
        14         2  1.000000         2         1         0         0         1
$#      t1        t2        t3        t4      nloc     marea      idof     edgset
  4.500000  4.500000  4.500000  4.500000     0.000     0.000     0.000         0
*SECTION_SHELL_TITLE
Shell5mm
$#    secid    elform      shrf       nip     propt   qr/irid     icomp     setyp
        15         2  1.000000         2         1         0         0         1
$#      t1        t2        t3        t4      nloc     marea      idof     edgset
  5.000000  5.000000  5.000000  5.000000     0.000     0.000     0.000         0
*SECTION_SHELL_TITLE
Shell6mm
$#    secid    elform      shrf       nip     propt   qr/irid     icomp     setyp
        16         2  1.000000         2         1         0         0         1
$#      t1        t2        t3        t4      nloc     marea      idof     edgset
  6.000000  6.000000  6.000000  6.000000     0.000     0.000     0.000         0
*SECTION_SHELL_TITLE
Shell6.4mm
$#    secid    elform      shrf       nip     propt   qr/irid     icomp     setyp
        17         2  1.000000         2         1         0         0         1
$#      t1        t2        t3        t4      nloc     marea      idof     edgset
  6.500000  6.500000  6.500000  6.500000     0.000     0.000     0.000         0
*SECTION_SHELL_TITLE
Shell6.8mm
$#    secid    elform      shrf       nip     propt   qr/irid     icomp     setyp
        18         2  1.000000         2         1         0         0         1
$#      t1        t2        t3        t4      nloc     marea      idof     edgset
  7.000000  7.000000  7.000000  7.000000     0.000     0.000     0.000         0
*SECTION_SHELL_TITLE
Shell8mm
$#    secid    elform      shrf       nip     propt   qr/irid     icomp     setyp
        19         2  1.000000         2         1         0         0         1
$#      t1        t2        t3        t4      nloc     marea      idof     edgset
  8.000000  8.000000  8.000000  8.000000     0.000     0.000     0.000         0
*SECTION_SHELL_TITLE
Shell10mm
$#    secid    elform      shrf       nip     propt   qr/irid     icomp     setyp
        20         2  1.000000         2         1         0         0         1
$#      t1        t2        t3        t4      nloc     marea      idof     edgset
 10.000000 10.000000 10.000000 10.000000     0.000     0.000     0.000         0
*SECTION_SHELL_TITLE
Shell12mm
$#    secid    elform      shrf       nip     propt   qr/irid     icomp     setyp
        21         2  1.000000         2         1         0         0         1
$#      t1        t2        t3        t4      nloc     marea      idof     edgset
 12.000000 12.000000 12.000000 12.000000     0.000     0.000     0.000         0
*SECTION_SHELL_TITLE
Shell15mm
$#    secid    elform      shrf       nip     propt   qr/irid     icomp     setyp
        22         2  1.000000         2         1         0         0         1
$#      t1        t2        t3        t4      nloc     marea      idof     edgset
 15.000000 15.000000 15.000000 15.000000     0.000     0.000     0.000         0
*SECTION_SHELL_TITLE
Shell16mm
$#    secid    elform      shrf       nip     propt   qr/irid     icomp     setyp
        23         2  1.000000         2         1         0         0         1
$#      t1        t2        t3        t4      nloc     marea      idof     edgset
 16.000000 16.000000 16.000000 16.000000     0.000     0.000     0.000         0
*SECTION_BEAM
$#    secid    elform      shrf   qr/irid       cst     scoor       nsm
       100         9  1.000000         2         1     0.000     0.000
$#     ts1       ts2       tt1       tt2     print
  7.000000  7.000000     0.000     0.000     0.000
*END
```

Appendix B

GNU Octave scripts to calculate injury

B.1 Initial conditions and visualising data

generate.m

```
% need to generate input data for risk models
% database_tracer file
% 'D' matrix for frag1.m (as a mat file?)
file_D = '/home/tom/Work/vehicles/C8passD1/D.mat';
file_T = '/home/tom/Work/vehicles/C8passD1/tracer.k';
  if exist(file_D) == 2
   error 'file(s) to generate already exist!'
  elseif exist(file_T) == 2
   error 'file(s) to generate already exist!'
  else
   continue
  end
mesh_d = 30;
rad = 152 ; % radius of BTD
r = mesh_d/2 +rad;
h = 1300 ; % z position of BTD sensors
A = [ 1250 1100 ; ...
      2050 650 ; ...
      2850 1100 ; ...
      5150 1100 ; ...
      5950 1100 ; ...
      6750 650 ; ...
      8350 1100 ];% define positions of person centers -
% rearrange D so that is ordered by position from device, closest to furthest.
B = [ A hypot(A(:,1),A(:,2)) ] ;
D = sortrows(B,3);
D(:,3) = [];
save(file_D,'D');
l = length(D);
pos = [];
  for i = 1:l
    p1 = [D(i,1) D(i,2)-r];
    p2 = [D(i,1)-r D(i,2)];
    p3 = [D(i,1) D(i,2)+r];
    p4 = [D(i,1)+r D(i,2)];
    pos = [pos ; p1 ; p2 ; p3 ; p4] ;
  end
lpos = length(pos);
u = ones(lpos,1);
time = 0*u;
dbt = [time u pos u*h] ; % generates 0 1 x y z matrix
fout = fopen(file_T,'wt');
 fprintf(fout,'$ x and y positions from generate.m \n')% write corresponsing x y
      positions out as a comment above? to aid preprocessing
fprintf(fout,'$ %-0.3f,%-0.3f\n',D')
fprintf(fout,'*DATABASE_TRACER\n')
fprintf(fout,'$#,time,track,x,y,z,,\n')
fprintf(fout,'%i,%i,%-0.3f,%-0.3f,%-0.3f,,\n',dbt')
fprintf(fout,'*END')
fclose(fout)
```

riskviz.m

```
% Produce visualisation of risks, using data from risk functions
% Tom Anthistle, MERail Research Group, University of Sheffield
```

```
clear
fileout = 'C1/C1_nisst1_2.eps';
fileout2 = 'C1/C1_nissf1_2.eps';
fileout3 = 'C1/C1_asii_2.eps';
fileout4 = 'C1/C1_cwv_2.eps';
file_chestvel = 'C1/C1D2.mat';
file_frag = 'C1/D2fragout_01.mat';
r = 305/2 ;
% ================================================================
% read frag data      INJ_F = [ INJ_F ; i D(i,1) D(i,2) F(1) F(2) F(3) ]
load(file_frag);
% INJ_F = [ person_id x y AIS(1) AIS(2) AIS(3) ]
% ================================================================
% read chest wall data
load(file_chestvel); % this is a 2-by-p matrix, called INJ_C
% INJ_C = [ person_id AIS ASII CWV ]
% ================================================================
% combine chest wall + frag injuries, delete lowest, create 'inj'
AIS = [ INJ_F(:,4:6) INJ_C(:,2) ];
AIS_s = sort(AIS,2); % sort horizontally, put smallest in col 1
AIS_s(:,1) = []; % remove smallest values
nissf = sum(INJ_F(:,4:6).^2,2);
nisst = sum(AIS_s(:,1:3).^2,2);
nisst(nisst>75) = 75; % ensure any nisst values greater than 75 are reset - see
    AIScw
inj = [ INJ_F(:,1:3) nisst nisst ]; % person id, positions, niss
% injury = id x y nisst nissf asii cwv
injury = [ inj(:,1) inj(:,2)-r inj(:,3)-r inj(:,4) inj(:,5) INJ_C(:,3) INJ_C(:,4) ]
    ;
%
c_iss = flipud(hot(76)) ;
g_iss = flipud(gray(76)) ;
c_asii = flipud(hot(21)) ; % sometimes this will need to be 24, sometimes 36 (
    dependes on out of range)
g_asii = flipud(gray(21)) ;
c_cwv = flipud(hot(33)) ;
g_cwv = flipud(gray(33)) ;
% ========NISSt (0-75)==========
clf
axes('Box','on')
axis equal
axis([0 9500 0 1300])
hold on
  for i = 1:length(injury)
  rectangle('position',[injury(i,2),injury(i,3),r,r],'curvature',[1,1],'FaceColor',
      c_iss(round(injury(i,4))+1,:))
  end
caxis([0,75])
pos=get(gca,'pos');
set(gca,'pos',[pos(1) pos(2) pos(3) pos(4)]);
colormap(c_iss);
hc = colorbar('location','southoutside','Position',[pos(1) pos(2)*3 pos(3) pos(4)
    *0.05 ],...
     'XTick',0:18.75:75,'XDir','reverse','XTickLabel',{'very␣low', 'low', 'medium',
         'high','very␣high'});
hold off
print('-depsc',fileout)
% ========NISSf (0-75)==========
clf
axes('Box','on')
axis equal
axis([0 9500 0 1300])
hold on
  for i = 1:length(injury)
  rectangle('position',[injury(i,2),injury(i,3),r,r],'curvature',[1,1],'FaceColor',
      c_iss(round(injury(i,5))+1,:))
  end
caxis([0,75])
pos=get(gca,'pos');
set(gca,'pos',[pos(1) pos(2) pos(3) pos(4)]);
colormap(c_iss);
hc = colorbar('location','southoutside','Position',[pos(1) pos(2)*3 pos(3) pos(4)
    *0.05 ],...
     'XTick',0:18.75:75,'XDir','reverse','XTickLabel',{'very␣low', 'low', 'medium',
         'high','very␣high'});
hold off
print('-depsc',fileout2)
% =========ASII (1-8) =========
clf
axes('Box','on')
axis equal
axis([0 9500 0 1300])
hold on
  for i = 2:length(injury)
  rectangle('position',[injury(i,2),injury(i,3),r,r],'curvature',[1,1],'FaceColor',
      c_asii(ceil(injury(i,6)*4),:))
  end
```

```
caxis([0,5]) % sometimes 0,12, when top line is 36
pos=get(gca,'pos');
set(gca,'pos',[pos(1) pos(2) pos(3) pos(4)]);
colormap(c_asii);
hc = colorbar('location','southoutside','Position',[pos(1) pos(2)*3 pos(3) pos(4)
    *0.05 ],...
     'XTick',0:1.25:5,'XDir','reverse','XTickLabel',{'0', '1.25', '2.5', '3.75','5'
         });
hold off
print('-depsc',fileout3)
% =========CWV (1-20) =========
clf
axes('Box','on')
axis equal
axis([0 9500 0 1300])
hold on
  for i = 2:length(injury)
  rectangle('position',[injury(i,2),injury(i,3),r,r],'curvature',[1,1],'FaceColor',
      c_cwv(ceil(injury(i,7)*3),:))
  end
caxis([0,11])
pos=get(gca,'pos');
set(gca,'pos',[pos(1) pos(2) pos(3) pos(4)]);
colormap(c_cwv);
hc = colorbar('location','southoutside','Position',[pos(1) pos(2)*3 pos(3) pos(4)
    *0.05 ],...
     'XTick',0:2.5:10,'XDir','reverse','XTickLabel',{'0', '2.5', '5', '7.5','10'});
hold off
print('-depsc',fileout4)
```

B.2 Chest Velocity

CV3.m

```
% Calculate chest wall velocties from a 4 pressure histories
% Tom Anthistle, MERail Research Group, University of Sheffield
% Variables and functions
% get pressure history files
rawPdata = dlmread("/home/tom/Work/vehicles/C9passD3/C9D3.csv",",");
% rawPdata = dlmread('~/Work/vehicles/case1/out.csv',',');
rawPdata(1,:)=[]; % make the first row empty
rawPdata(:,end)=[]; % make the last column empty because of extra comma
%---------------------------------------
l = rows(rawPdata); % find number of entries for each pressure sensor
nc = columns(rawPdata); % number of columns in the data file
t=rawPdata(:,1);
P=rawPdata(:,2:nc);
ncp = columns(P); % number of columns in pressure data
num_persons = ncp/4;
%if mod(ncp,4) ~= 0 % number of BTD if this number is not an integer, there is a
    problem!
% error "Ensure 4 pressure histories are defined for each BTD location"
%end
% --------- Boundary / initial coniditons
x = zeros(l,ncp); % initialise matrices for displacement and velocity
y = zeros(l,ncp); % x, y and P all same dimensions
% x(1) =
x(1,:) = 0;% displacement
y(1,:) = 0;% dx/dt (velocity)
% ---------------------------------------
% Use Runge-Kutta method to solve diff. eq.
for i = 1:ncp % columns
  for j = 1:l-1 % rows (l-1 because of j+1 at l44)
       h = t(j+1) - t(j); % time step. t only has 1 dimension.
       c11=h*y(j,i); %dx/dt
       c21=h*f2(P(j,i),x(j,i),y(j,i)); %dy/dt
       c12=h*(y(j,i)+0.5*c21);
       c22=h*f2(P(j,i)+(P(j+1,i)-P(j,i))/2,x(j,i)+0.5*c11,y(j,i)+0.5*c21);
       c13=h*(y(j,i)+0.5*c22);
       c23=h*f2(P(j,i)+(P(j+1,i)-P(j,i))/2,x(j,i)+0.5*c12,y(j,i)+0.5*c22);
       c14=h*(y(j,i)+c23);
       c24=h*f2(P(j+1,i),x(j,i)+c13,y(j,i)+c23);
       x(j+1,i)=x(j,i)+(1/6)*(c11+2*c12+2*c13+c14);
       y(j+1,i)=y(j,i)+(1/6)*(c21+2*c22+2*c23+c24);
  end
end

fBTD = [];
for k = 1:4:ncp
  fBTD = [fBTD 0.25*sum(y(:,k:k+3),2)] ;% sum 4 columns across, for each sensor in
       an individual BTD, generating a single column of average velocity for each
       BTD
end
% get the max value for each BTD (each col in BTD)
```

```
[CWVp] = max(fBTD); % Chest Wall Velocity peak
ASII = (0.124+0.117.*CWVp).**2.63;
inj = arrayfun(@AIScw,ASII);
file = "~/Work/vehicles/C9passD3/C9D3.mat";
persons = 1:num_persons ;
INJ_C = [persons ; inj ; ASII ; CWVp]' ; % put ASII and CWVp in here too
save(file,'INJ_C','-V7')
velhist = [t fBTD] ;
dlmwrite("~/Work/vehicles/C9passD3/vth.csv",velhist,',')
```

B.2.1 Functions used in `CV2.m`

f2.m

```
% differential equation function for chest velocity
% Tom Anthistle, MERail Research Group, University of Sheffield
function b = f2(p,x,y) % returns value of 2nd derivative for 3 inputs
M = 2.03; %kg
J = 0.696; % Ns/m (once converted into model units, as with all below)
K = 989E-06; % N/m
A = 82000; % m^2
P0 = 0.000104; % Pa
V0 = 1820000; % m^3
g = 1.2;
pn = sign(V0/(V0-A*x));
sub = sqrt((V0/(V0-A*x))**2)**g;
b = 1/M*(A*(p + P0 - P0*pn*sub) - J*y - K*x);
end
```

AIScw.m

```
% differential equation function for chest velocity
% get out AIS result
% Tom Anthistle, MERail Research Group, University of Sheffield
function [val] = AIScw(asii) % returns value of 2nd derivative for 3 inputs
if nargin ~= 1
  error('Please␣provide␣an␣input␣argument');
end
  if (asii) <= 0.2
   val = 0 ;
  elseif (asii) <= 0.7
   val = 1 ;
  elseif (asii) <= 1.6
   val = 2 ;
  elseif (asii) <= 2.5
   val = 3 ;
  elseif (asii) <= 3.6
   val = 4 ;
  elseif (asii) <= 7.1
   val = 5 ;
  else
   val = 8.66 ; % cheaty way of ensuring AIS values of 6 give a NISS of 75
  end
end % end function
```

B.3 Projectiles

Assuming a normal distribution for angular spread in 2 directions from a flat surface, and normally distributed velocities with the highest velocities at the lowest angular spreads, it is necessary to randomly sample from a trivariate normal distribution to generate the initial conditions for a sample of n projectiles. It is possible to use the `mvnrnd` function in Matlab or GNU Octave to generate an $n \times d$ matrix, where d is the number of dimensions in which random variables are required, which is 3 in this case. Statistically, the mean, μ of the variable in each direction is required, as well as a covariance matrix Σ which defines the relationship between the variables in all dimensions. The form of the covariance matrix for the 3 variables required, projection angles θ and ϕ, and velocity v (see Figure B.1) is shown in (B.1).

Statistically, the variance σ^2 is a measure of the spread in a set of data, and is always positive or zero, with a variance of zero corresponding to a set of identical numbers, and high variance indicating a large spread in the numbers within a set. The standard deviation is the more commonly referred to statistical measure, and shows the average variation of each variable in a population from the mean of the entire population. For a normal distribution, 99.7% of all values will lie within 3 standard deviations ($\pm 3\sigma$) of the mean.

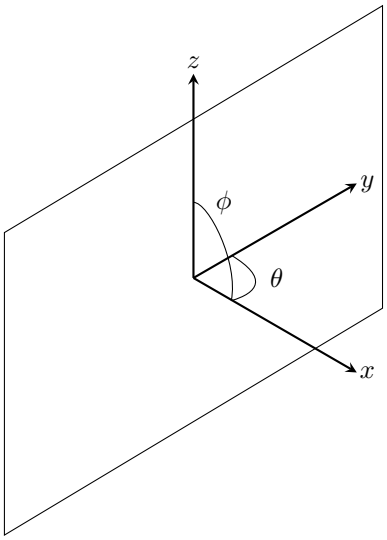

Figure B.1: Definition of angles θ and ϕ

The covariance is the spread of two related variables, and is a measure of how well one variable can be predicted with a linear function of the other [198]. The covariance is defined for two random variables x and y by Equation (B.2) [199]. As the covariance is a function of two variables that can either be negatively or positively correlated, the value can either be positive or negative, and the square root has neither a mathematical or physical meaning. The standard deviation σ_x, σ_y, covariance $\sigma_{x,y}$, and correlation $\rho_{x,y}$ are connected by Equation (B.3)[200, 171].

$$\Sigma_{\theta,\phi,v} = \begin{bmatrix} \sigma_{\theta,\theta} & \sigma_{\theta,\phi} & \sigma_{\theta,v} \\ \sigma_{\phi,\theta} & \sigma_{\phi,\phi} & \sigma_{\phi,v} \\ \sigma_{v,\theta} & \sigma_{v,\phi} & \sigma_{v,v} \end{bmatrix} \tag{B.1}$$

$$\sigma_{x,y} = \frac{1}{n-1}\sum_{i=1}^{n}(x_i - \mu_x)(y_i - \mu_y) \tag{B.2}$$

$$\rho_{x,y} = \frac{\sigma_{x,y}}{\sigma_x \sigma_y} \tag{B.3}$$
$$\text{where} \quad -1 \leq \rho_{x,y} \leq 1$$

The structure of the covariance matrix is such that the diagonal is simply the variance of an individual variable, and non-diagonal elements are the covariances. A diagonal matrix indicated no correlation between variables, and the distribution of each variable is purely a function of it's own mean and variance. The covariance is defined such that $(\sigma_{x,y}) = (\sigma_{y,x})$, so it follows that the covariance matrix must always be symmetric.

It is outside the scope of this test to undertake tests to identify the statistical parameters μ and σ^2, so the following assumptions are made about the projectile ejection pattern:

- all parameters will be normally distributed
- the mean angular projection for both direction will be 0^o
- 99.7% of all projectiles will fall within the following angular spreads from 0^o
  - $\theta_{3\sigma} = 70^o$
  - $\phi_{3\sigma} = 45^o$

- the mean velocity will be the Gurney velocity
- fragments travelling at a zero velocity are very unlikely, so $v_{6\sigma} = \mu_v$
- there is no correlation between the two angles of projection, so $(\sigma_{\theta,\phi}) = (\sigma_{\phi,\theta}) = 0$
- the correlation between angle and velocity is the same for both the θ and ϕ directions, so $\sigma_{v,\theta} = \sigma_{v,\phi}$
- angle and velocity are negatively correlated and will have negative covariances, calculated using (B.3) with a correlation value of -0.5

The projectile impact can be calculated with a vehicle occupant can be calculated, by assuming the occupant can be simplified as a collection of cylinders, with dimensions for the human body taken from BS EN ISO 7250 [201]. With this assumption, a range of angles each cylinder (body part) occupies in both the θ and ϕ directions can be calculated using simple relations. For simplicity, two orientations are chosen for the cylinders, as this can represent the positions of most limbs within a rail vehicle that are subject to a high risk of injury. Cylinders are assumed to be aligned with their axis in either the z or x direction, but if so desired this model could easily be extended to cylinders aligned with the y axis. The range of angles is defined, with reference to Figure B.1, as follows. The angles are calculated by assuming a rectangular area in space, defined by the outer edge of a cylinder, is the area exposed to a projectile.

For a cylinder with an axis aligned with the z axis, the angular ranges θ_r and ϕ_r are given by (B.4) and (B.5), where x, y and z are the positions of the centre of the cylinder, and r and h are the radius and height of the cylinder respectively.

$$\theta_r = \tan^{-1}\frac{y}{x} \pm \sin^{-1}\left(\frac{r}{\sqrt{x^2+y^2}}\right) \tag{B.4}$$

For the cylinder side

$$\begin{aligned}\alpha &= \tan^{-1}\frac{\sqrt{x^2+y^2}}{z} \\ \phi_r &= \left(\frac{\pi}{2} - \alpha\right) \pm \sin^{-1}\left(\frac{(h/2)\sin\alpha}{\sqrt{x^2+y^2+(z-h/2)^2}}\right)\end{aligned} \tag{B.5}$$

For the cylinder end

$$\begin{aligned}\beta &= \tan^{-1}\left(\frac{z-h/2}{\sqrt{x^2+y^2}}\right) \\ \phi_{r2} &= \beta \pm \sin^{-1}\left(\frac{r\sin\beta}{\sqrt{x^2+y^2+(z-h/2)^2}}\right)\end{aligned} \tag{B.6}$$

For a cylinder aligned with the x axis...

B.3.1 Example text output from multi-projectile model

```
number of passengers: 7
mass of charge: 5.00 kg
number of projectiles: 250
mass of projectiles: 1.03 kg
------------------ Occupant injury data -----------------
Person 1
Hit 12 times
legL     legR     torso    neck     head     armL     armR
1        0        5        0        3        0        3
NISS score for person 1 is: 75
-+-+-+-+-+-+-+-+-+-+-+-+-+-+-+-+-+-+-+-+-+-+-+-+-+-+-+-+-
Person 2
```

```
Hit 24 times
legL     legR    torso   neck    head    armL    armR
8        3       9       0       0       3       1
NISS score for person 2 is: 75
-+-+-+-+-+-+-+-+-+-+-+-+-+-+-+-+-+-+-+-+-+-+-+-+-+-+-+-+-+-+-+-+-+-+-+-
Person 3
Hit 17 times
legL     legR    torso   neck    head    armL    armR
3        2       7       1       4       0       0
NISS score for person 3 is: 75
-+-+-+-+-+-+-+-+-+-+-+-+-+-+-+-+-+-+-+-+-+-+-+-+-+-+-+-+-+-+-+-+-+-+-+-
Person 4
Hit 2 times
legL     legR    torso   neck    head    armL    armR
0        1       0       0       0       0       1
NISS score for person 4 is: 32
-+-+-+-+-+-+-+-+-+-+-+-+-+-+-+-+-+-+-+-+-+-+-+-+-+-+-+-+-+-+-+-+-+-+-+-
Person 5
Hit 3 times
legL     legR    torso   neck    head    armL    armR
1        1       1       0       0       0       0
NISS score for person 5 is: 57
-+-+-+-+-+-+-+-+-+-+-+-+-+-+-+-+-+-+-+-+-+-+-+-+-+-+-+-+-+-+-+-+-+-+-+-
Person 6
Hit 3 times
legL     legR    torso   neck    head    armL    armR
1        2       0       0       0       0       0
NISS score for person 6 is: 48
-+-+-+-+-+-+-+-+-+-+-+-+-+-+-+-+-+-+-+-+-+-+-+-+-+-+-+-+-+-+-+-+-+-+-+-
Person 7
Hit 2 times
legL     legR    torso   neck    head    armL    armR
0        1       0       0       1       0       0
NISS score for person 7 is: 41
-+-+-+-+-+-+-+-+-+-+-+-+-+-+-+-+-+-+-+-+-+-+-+-+-+-+-+-+-+-+-+-+-+-+-+-
**********************************************************
**                   end of output data                 **
**********************************************************
```

B.3.2 Top level code - `frag1.m`

```
% Projectile throwout and position calculations
% Tom Anthistle, MERail Rail Research Group, University of Sheffield
% ---------------------- user inputs ------------------------------
clear -all
GE = 2.35E03; %gurney energy sqrt(2E)  \cite{dobratz1985llnl} p8-28
C = 5;% total mass of explosive
Mp = 0.0041;% mass of an individual projectile (10mm radius ball bearing, 4.15gr)
n = 250; %number of projectiles, based on 1kg from D200.2
Mt = Mp*n;% total mass of projectiles
N = 10; %mass of backing material
corr = -0.5; %covariance correlation
%D = [150 300 ; 300 450 ]; % position of people centres in mm [x1 y1 ; x2 y2 etc]
load('/home/tom/Work/fragtest/D2.mat','D')
lD = length(D);
hc = 1330; % height of charge in mm
%-----------------------------------------------
% ----- Calculate variances ----------------
At = (1+2**(Mt/C))/(1+2**(N/C));
muve = GE*(( (1+At**3)/(3*(1+At)) + At**2*(N/C) + Mt/C)**-0.5); % calculate the
     gurney velocity for a flat plate
sdevth = 70/3; % standard deviation in the theta direction
sdevph = 45/3;
sdevve = muve/6;
varang_v = corr*sdevph*sdevth; % variance for angle and velocity
% --------- Assemble covariance matrix and mu array -------
COV = [ sdevth**2 0 varang_v ; 0 sdevph**2 varang_v ; varang_v varang_v sdevve**2];
mu = [0 0 muve];
% ------------------ Take draws from normal distibution -------
IC = mvnrnd(mu,COV,n);
% ------------------ visualise the generated projectile matrix --
%P = zeros(n,1);
%quiver3(P(:,1),P(:,1),P(:,1),IC(:,1),IC(:,2),IC(:,3))
% --------------------- generate a hit matrix --------------------
A = person(D(:,1),D(:,2),lD,hc); %angles of the 'people' person(x,y,%first item is
     ...
bphm = [490-hc 490-hc 1217-hc 1485-hc 1633-hc 1132-hc 1132-hc ; 75 75 155 30.5 90.7
      43 43]; % body position height matrix for z
HM = []; % hit matrix
for j=1:lD % person
 for i=1:n % frag
  for k=0:6 % body part
   h = iswithin2(IC(i,1),IC(i,2),A(j,1+4*k),A(j,2+4*k),A(j,3+4*k),A(j,4+4*k));
   if h == 1
   d = hypot(D(j,1),D(j,2),bphm(1,k+1)); % this is d in mm
   v = velocity(IC(i,3),d/1000); % input in m, output in m/s
```

```
    pend = (dop(v))*1000; % input in m/s gives depth of penetration in mm
    HM = [HM; j k i v pend AIS(k,pend,bphm(2,k+1))] ;% velocity = IC(i,3)
    IC(i,3) = vupdate(pend/bphm(2,k+1),v); % update the velocity
    continue
    elseif h == 0
    continue
    end
   endfor
  endfor
endfor
mr1 = sortrows(HM,1); % sort rows so all hits to a person are grouped together by
     person

file_frag = '/home/tom/Work/fragtest/fragtest2_03.mat';
file = '/home/tom/Work/fragtest/fragtest2_03.txt';
fout = fopen(file,'wt');
INJ_F = [];
%fprintf(fout,'-+-+-+-+-+-+-+-+-+-+-+-+-+-+-+-+-+-+-+-+-+-+-+-+-+-+-+-+-+-+-\n');
fprintf(fout,'number of passengers: %i \n',lD);
%%fprintf(f,'%i',lD);
fprintf(fout,'mass of charge: %0.2f kg \n',C);
fprintf(fout,'number of projectiles: %i \n',n);
fprintf(fout,'mass of projectiles: %0.2f kg \n',Mt);
fprintf(fout,'------------------ Occupant injury data -----------------\n');
for i=1:lD
    fprintf(fout,'Person %i \n',i);
    start = find(mr1(:,1)== i,1) ; % find the point at which this 'person' starts
         in mr1
    hits = sum(mr1(:,1) == i); % find the number of hits, from the of times they
         occur in the hit matrix
    fprintf(fout,'Hit %i times \n',hits);
    fprintf(fout,'legL \t legR \t torso \t neck \t head \t armL \t armR \n')
    legL = sum(mr1(start:start+hits-1,2) == 0);
    legR = sum(mr1(start:start+hits-1,2) == 1);
    torso = sum(mr1(start:start+hits-1,2) == 2);
    neck = sum(mr1(start:start+hits-1,2) == 3);
    head = sum(mr1(start:start+hits-1,2) == 4);
    armL = sum(mr1(start:start+hits-1,2) == 5);
    armR = sum(mr1(start:start+hits-1,2) == 6);
    fprintf(fout,'%i \t %i \t %i \t %i \t %i \t %i \t %i \n',legL,legR,torso,
         neck,head,armL,armR)
    F = sort(mr1(start:start+hits-1,6),'descend'); % sort column by AIS
    Q = 3-length(F);
    Q(Q<0)=0;
    B = zeros(Q,1);
    C = [F ; B];
    F2 = C(1:3); % top 3 AIS values - what if there isn't 3 values!?
    INJ_F = [ INJ_F ; i D(i,1) D(i,2) F2(1) F2(2) F2(3) ];
    niss = sum(F2.**2); % 3 highest AIS values for AIS column with person i
    fprintf(fout,'NISS score for person %i is: %i \n',i,niss);
    fprintf(fout,'-+-+-+-+-+-+-+-+-+-+-+-+-+-+-+-+-+-+-+-+-+-+-+-+-+-+-+-+-+-+-\n');
end
fprintf(fout,'************************************************************\n');
fprintf(fout,'**                  end of output data                    **\n');
fprintf(fout,'************************************************************\n');
fclose(fout);
save(file_frag,'INJ_F','-V7')
```

B.3.3 Functions developed for use in `frag1.m`

person.m

```
% Define representative cylinder for a 50th percentile human
% Tom Anthistle, MERail Rail Research Group, University of Sheffield
% Data taken from statistical samples for a 50th percentile male human
% Data taken for head, chest arm and leg
% From an (x,y) position of a person (assumed standing), define values required by
     other functions for each cylinder
function A = person(l,w,n,hc)  % \cite{ISO7250-2}
    if nargin ~=4
        error('wrong number of input arguments')
    end
 x = l; % might not always want random people!!
 y = w;
 W = ones(n,1);
%height = 1750
% ================ leg ========================
rl = 75*W; % ((570/(2*pi)) + (375/(2*pi)))/2 ; % average of calf and thigh
xl = x;
yl1 = y.+187.5-rl; % plus and minuses the other way round for other leg
yl2 = y.-187.5+rl;
hl = 980*W; % 830; % maybe add thigh clearance
zlt = (980).*W -hc ;% zl = (hl/2)*ones(n,1);
zlb = (0).*W -hc;
[thminl1,themaxl1] = thetar(xl,yl1,rl);
[pminl1,pmaxl1] = phi(xl,yl1,zlt,zlb);
[thminl2,themaxl2] = thetar(xl,yl2,rl);
```

```
[pminl2,pmaxl2] = phi(xl,yl2,zlt,zlb);
%[phminl,phmaxl] = phir(xl,yl,zl,hl)
%[ph2minl,ph2maxl] = phir2(xl,yl,zl,hl,rl)
% ================ torso ========================
rt = 155.1*W; % 975/(2*pi) ; % from chest circumference
ht = 475*W; % 625-150; % shoulder height minus thigh clerance
xt = x;
yt = y;
ztt = hl+ht-hc;
ztb = hl-hc;
[thmint,themaxt] = thetar(xt,yt,rt);
[pmint,pmaxt] = phi(xt,yt,ztt,ztb);
% ================ neck ========================
rn = 60.5*W; %380/(pi*2) from neck circumfrence
hn = 60*W; % makes up the total height from all the others (not including arms
    obviously)
xn = x;
yn = y;
znt = hl+ht+hn-hc;
znb = hl+ht-hc;
[thminn,themaxn] = thetar(xn,yn,rn);
[pminn,pmaxn] = phi(xn,yn,znt,znb);
% ================ head ========================
rh = 90.7*W; % 570/(2*pi); % from head circumfrence
hh = 235*W; % 115 + (1750 - 1630); % face length plus (height - eye height)
xh = x;
yh = y;
zht = hl+ht+hn+hh-hc;
zhb = hl+ht+hn-hc;
[thminh,themaxh] = thetar(xh,yh,rh);
[pminh,pmaxh] = phi(xh,yh,zht,zhb);
% ================ arm ========================
ra = 43*W; % 270/(2*pi); % from circumference of forearm on TJA
ha = 685*W; % 1450-765; % shoulder height - fist height
xa = x;
ya1 = y+rt+ra; % minus the numbers for the other arm
ya2 = y-rt-ra;
zat = 1450-hc; % top of cylinder at shoulder height
zab = 1450-ha-hc; % Shoulder height - half cylinder height
[thmina1,themaxa1] = thetar(xa,ya1,ra);
[pmina1,pmaxa1] = phi(xa,ya1,zat,zab);
[thmina2,themaxa2] = thetar(xa,ya2,ra);
[pmina2,pmaxa2] = phi(xa,ya1,zat,zab);
A = [thminl1 themaxl1 pminl1 pmaxl1 thminl2 themaxl2 pminl2 pmaxl2 thmint themaxt
    pmint pmaxt thminn themaxn pminn pmaxn thminh themaxh pminh pmaxh thmina1
    themaxa1 pmina1 pmaxa1 thmina2 themaxa2 pmina2 pmaxa2];
%A = [thminl1 themaxl1 pminl1 pmaxl1];
end
```

thetar.m

```
function [trmin,trmax] = thetar(x,y,r)
if nargin ~= 3
 error "3 variables must be defined!"
 print_usage;
end
a = atand(y./x);
b = asind(r./(sqrt(x.**2 + y.**2)));
tr1 = a - b;
tr2 = a + b;
trmin = min(tr1,tr2);
trmax = max(tr1,tr2);
end
```

phi.m

```
function [phimin,phimax] = phi(x,y,ht,hb)
if nargin ~= 4
 error "4 variables must be defined!"
end
ph1 = phical(x,y,ht);
ph2 = phical(x,y,hb);
phimin = min(ph1,ph2);
phimax = max(ph1,ph2);

function angle = phical(ax,by,cz)
angle = asind(cz./sqrt(ax.**2+by.**2+cz.**2));
end
end
```

iswithin.m

```
function y = iswithin(a,b,x1,x2,y1,y2)
 if nargin ~= 6
  error "Please supply 6 input arguments";
 end
```

```
xmin = min(x1,x2) ;
xmax = max(x1,x2);
ymin = min(y1,y2);
ymax = max(y1,y2);
y = (a > xmin) && (a < xmax) && (b > ymin) && (b < ymax);
end
```

velocity.m

```
function v = velocity(vm,x) % inputs and outputs in metric units
 if nargin ~=2
 error "Please supply 2 input arguments"
 end
vi = vm*3.2808; % convert from m/s to ft/s
xi = x* 3.2808; % convert from m to ft
ri = 5e-3*3.2808; % frag radius in ft
am = pi*ri**2; % mean projected area in ft2
qm = 1.333333*pi*ri**3;
a = am/qm**0.6666;
m = 0.146387; % fragment mass in oz (4.25g ball bearing)
ss = 1126;
 if vi >= ss
 vi2 = vi*exp((-0.00204*xi*a)/m**0.333333) ;
 else
 vi2 = vi*exp((-0.00137*xi*a)/m**0.333333) ;
 end
v = vi2*0.3048006 ;
end
```

dop.m

```
function d = dop(v) % intial velocity in m/s
 if nargin ~= 1
 error "Please provide 1 input argument"
 end
v1 = v*3.2808; % convert from m/s to ft/s
m = 4.15; % mass
mc = m*0.03527; % grams to ounces
den = 1060;% target density
denc = den*0.062427; % convert from kg/m3 to lb/ft3
A = 7.854e-5; % presented frag area
Ac = A*10.7639; % convert m2 to ft2
cd = 0.47; % drag coeff for sphere (1.05 for cube)
% ========
t2 = v1 - ((80*Ac)/mc**1.3) ;
t1 = 0.022*mc**0.95;
d1 = (t1/(denc*Ac*cd)) .* ((t2./400)**0.55); % this output in whatver converted
     units are
d = d1*0.3048;
```

AIS.m

```
function IN = AIS(bp,dp,th) % dp in mm, th in mm
 if nargin ~=3
 error('Please␣supply␣3␣input␣arguments')
 end
 if bp < 0 || bp > 6
 error('%i␣is␣not␣a␣known␣body␣part',bp)
 end

perf = dp/th;

 if (bp == 2) || (bp == 4)
  if perf > 0.75
  IN = 5 ;
  elseif perf > 0.4
  IN = 4 ;
  elseif dp > 10
  IN = 3 ;
  elseif dp < 10 && dp > 0
  IN = 2;
  else
  IN = 1;
  end
 else
  if perf > 0.75
  IN = 4 ;
  elseif perf > 0.4
  IN = 3 ;
  elseif dp > 10
  IN = 2 ;
  elseif dp < 10 && dp > 0
  IN = 1;
  else
  IN = 1;
  end
```

```
 end

end % end function
```

vupdate.m

```
function newv = vupdate(perf,v)
 if perf > 1
 newv = (1-1/perf)*v;
 elseif perf <= 1
 newv = 0;
 end
end
```

Appendix C

GNU Octave scripts used to process data

C.1 Read, process and butterworth filter data from all sensors

```
% process data from experimental data
% read in data files from experiments
% apply supply voltage correction
% filter data to remove noise
% multiply by calibration factors
% user supplied info ========================
% addpath('/home/tom/Downloads/signal/inst')
raw = dlmread('/home/tom/Work/experimental/raw/TBB001_1806.csv',';',3,0);
fout1 = fopen('/home/tom/Work/experimental/processed/A1S3_processed_P.csv','wt');
fout2 = fopen('/home/tom/Work/experimental/processed/A1S3_processed_I.csv','wt');
drive_voltage = 10.02 ;
voltage_offset = drive_voltage/10; %supplied voltage
PT = 8439;
sh=500;
time = raw(:,1);
timeMS = time*1000; % get time in ms
s312r = raw(:,2)./voltage_offset; % raw voltage from oscilloscope
s402r = raw(:,3)./voltage_offset;
s358r = raw(:,4)./voltage_offset;
s311r = raw(:,5)./voltage_offset;
s101r = raw(:,6)./voltage_offset;
ta312 = 1.4;
ta402 = 2.6;
ta358 = 5.3;
ta311 = 0.83;
ta101 = 1.6;
C = 6.894745; % conversion from psi to kPa
B = 100;% convert from bar to kPa
% ============================================
% Calibration factors---convert to bar-------
cf312 = (-1000/0.201)*C; % convert to mV, divide by CF and convert to bar.
cf402 = (-1000/0.383)*C;
cf358 = (-1000/14.396)*B;
cf311 = (-1000/0.200)*C;
cf101 = (-1000/0.903)*C; % =6.225959 mv / kPa
%=622 mv / bar
%--------------------------------------------
%---------------- Filter---------------------
fsam = 1.562e06; % sampling frequency
fnyq = fsam/2;
fc=1/4;
fco = (fc/fnyq);
[b,a] = butter(9,0.02);
% -------------------------------------------
 % \ all pressures by this value
%raw = dlmread('/home/tom/Work/experimental/raw/TBB_RD_TP16-17_001_18062013_temp.
    csv',',',3,0);
% -------------------------------------------
% - offset, filter, calibrate ---------------
% ta = 1.4ms
on312 = floor((ta312/1000)*fsam + (6.4/1000)*fsam); % calculate number of samples
     used to calculate zero shift
s312o = s312r.-sum(s312r((on312-sh):on312))/sh; % calculate zero shift and subtract
      from raw volatages
%s312o = s312r.-sum(s312r(1:on312)/on312); % calculate zero shift and subtract from
      raw volatages
s312_pressure=s312o.*cf312; % convert to pressure
```

```
s312fp = filter(b,a,s312_pressure); % filter
%s312fp = movavg(s312_pressure,5,5);
s312_i = cumtrapz(timeMS(on312:end),s312fp(on312:end)); % integrate from shock wave
     arrival time
s312_impulse = padarray(s312_i,(size(timeMS) - size(s312_i)),0,'pre'); % pad before
     shock wave arrival with 0's
%---------------------------------
% ta = 2.6
on402 = floor((ta402/1000)*fsam + (6.4/1000)*fsam);
s402o = s402r.-sum(s402r((on402-sh):on402))/sh;
% s402o = s402r.-sum(s402r(1:on402)/on402);
s402_pressure=s402o.*cf402;
s402fp = filter(b,a,s402_pressure);
%s402fp = movavg(s402_pressure,5,5);
s402_i = cumtrapz(timeMS(on402:end),s402fp(on402:end));
s402_impulse = padarray(s402_i,(size(timeMS) - size(s402_i)),0,'pre');
%---------------------------------
on358 = floor((ta358/1000)*fsam + (6.4/1000)*fsam);
s358o = s358r.-sum(s358r((on358-sh):on358))/sh;
% s358o = s358r.-sum(s358r(1:on358)/on358);
s358_pressure=s358o.*cf358;
s358fp = filter(b,a,s358_pressure);
%s358fp = movavg(s358_pressure,5,5);
s358_i = cumtrapz(timeMS(on358:end),s358fp(on358:end));
s358_impulse = padarray(s358_i,(size(timeMS) - size(s358_i)),0,'pre');
%---------------------------------
%ta = 0.83
on311 = floor((ta311/1000)*fsam + (6.4/1000)*fsam);
s311o = s311r.-sum(s311r((on311-sh):on311))/sh;
% s311o = s311r.-sum(s311r(1:on311)/on311);
s311_pressure=s311o.*cf311;
s311fp = filter(b,a,s311_pressure);
%s311fp = movavg(s311_pressure,5,5);
s311_i = cumtrapz(timeMS(on311:end),s311fp(on311:end));
s311_impulse = padarray(s311_i,(size(timeMS) - size(s311_i)),0,'pre');
%---------------------------------
% ta - 1.6
on101 = floor((ta101/1000)*fsam + (6.4/1000)*fsam);
s101o = s101r.-sum(s101r((on101-sh):on101))/sh;
% s101o = s101r.-sum(s101r(1:on101)/on101);;
s101_pressure=s101o.*cf101;
s101fp = filter(b,a,s101_pressure);
%s101fp = movavg(s101_pressure,5,5);
s101_i = cumtrapz(timeMS(on101:end),s101fp(on101:end));
s101_impulse = padarray(s101_i,(size(timeMS) - size(s101_i)),0,'pre');
%-----------------------------------------------
% ----------- get cumulative impulse ---------
p_data = [timeMS(PT:end) s312fp(PT:end) s402fp(PT:end) s358fp(PT:end) s311fp(PT:end
    ) s101fp(PT:end)]; % remove 5.4s of pretrigger
i_data = [timeMS(PT:end) s312_impulse(PT:end) s402_impulse(PT:end) s358_impulse(PT:
    end) s311_impulse(PT:end) s101_impulse(PT:end)];
fprintf(fout1,'time,S312,S402,S358,S311,S101\n');
fprintf(fout1,'%E,%E,%E,%E,%E,%E\n',p_data');
fprintf(fout2,'time,S312,S402,S358,S311,S101\n');
fprintf(fout2,'%E,%E,%E,%E,%E,%E\n',i_data');
fclose(fout1);
fclose(fout2);
% axis([-0.001,0.02,-0.2,0.6])
% print('/home/tom/Work/experimental/raw/figs/A001_Shot1_S312.pdf','-dpdf','-F
    :5','-landscape','-S640,400')
```

C.2 Read, process and apply different filtering methods to data from one sensor

```
% import data for sensors and filter data from one for comparison
% write filteterd pressure and impulse data out to separate files
raw = dlmread('/home/tom/Work/experimental/raw/TBB001_1806.csv',';',3,0);
fout1 = fopen('/home/tom/Work/experimental/processed/Filt-params/MA_P.csv','wt');
fout2 = fopen('/home/tom/Work/experimental/processed/Filt-params/MA_I.csv','wt');
fout3 = fopen('/home/tom/Work/experimental/processed/Filt-params/BUT_P.csv','wt');
fout4 = fopen('/home/tom/Work/experimental/processed/Filt-params/BUT_I.csv','wt');
fout5 = fopen('/home/tom/Work/experimental/processed/Filt-params/WAV_P.csv','wt');
fout6 = fopen('/home/tom/Work/experimental/processed/Filt-params/WAV_I.csv','wt');
fout7 = fopen('/home/tom/Work/experimental/processed/Filt-params/RAW_P.csv','wt');
fout8 = fopen('/home/tom/Work/experimental/processed/Filt-params/RAW_I.csv','wt');
drive_voltage = 10.02 ;
voltage_offset = drive_voltage/10; %supplied voltage
PT = 8439;
sh=500;
time = raw(:,1);
timeMS = time*1000; % get time in ms
s312r = raw(:,2)./voltage_offset; % raw voltage from oscilloscope
ta312 = 1.4;
C = 6.894745; % conversion from psi to kPa
B = 100;% convert from bar to kPa
```

```
cf312 = (-1000/0.201)*C; % convert to mV, divide by CF and convert to bar.
fsam = 1.562e06; % sampling frequency
fnyq = fsam/2;
fc=1/4;
fco = (fc/fnyq);
[b1,a1] = butter(9,0.05);
[b2,a2] = butter(9,0.02);
[b3,a3] = butter(9,0.011);
[b4,a4] = butter(9,0.01);
% let's measure how long things take!
%t = cputime; surf(peaks(40)); e = cputime-t
%tic ();
 %          # many computations later...
  %         elapsed_time = toc ();
%============ moving average
     ========================================================
% movavg (asset, lead, lag, alpha) alpha is a weighting, 0,5 is square root moving
     average blah
% =========== normal filtering and processing of data
     ================================
on312 = floor((ta312/1000)*fsam + (6.4/1000)*fsam); % number of samples to foot of
     shock
s312_p = s312r.*cf312; % convert to pressure =====================
s312_pressure = s312_p.-sum(s312_p((on312-sh):on312))/(sh+1); % / voltage offset
     gauges driven at 10.02 will read highe
s312BUT1P = filter(b1,a1,s312_pressure); % filter
s312BUT1Itemp = cumtrapz(timeMS(on312:end),s312BUT1P(on312:end)); % integrate from
     shock wave arrival time
s312BUT1I = padarray(s312BUT1Itemp,(length(timeMS) - length(s312BUT1Itemp)),0,'pre'
     );
s312BUT2P = filter(b2,a2,s312_pressure); % filter
s312BUT2Itemp = cumtrapz(timeMS(on312:end),s312BUT2P(on312:end)); % integrate from
     shock wave arrival time
s312BUT2I = padarray(s312BUT1Itemp,(length(timeMS) - length(s312BUT2Itemp)),0,'pre'
     );
s312BUT3P = filter(b3,a3,s312_pressure); % filter
s312BUT3Itemp = cumtrapz(timeMS(on312:end),s312BUT3P(on312:end)); % integrate from
     shock wave arrival time
s312BUT3I = padarray(s312BUT3Itemp,(length(timeMS) - length(s312BUT3Itemp)),0,'pre'
     );
s312BUT4P = filter(b4,a4,s312_pressure); % filter
s312BUT4Itemp = cumtrapz(timeMS(on312:end),s312BUT4P(on312:end)); % integrate from
     shock wave arrival time
s312BUT4I = padarray(s312BUT4Itemp,(length(timeMS) - length(s312BUT4Itemp)),0,'pre'
     );
%============ moving average
     ========================================================
% movavg (asset, lead, lag, alpha) alpha is a weighting, 0,5 is square root moving
     average blah
s312MA10_P = movavg(s312_pressure,5,5);
s312MA10_I_temp = cumtrapz(timeMS(on312:end),s312MA10_P(on312:end));
s312MA10_I = padarray(s312MA10_I_temp,(length(timeMS) - length(s312MA10_I_temp)),0,
     'pre');
s312MA50_P = movavg(s312_pressure,25,25);
s312MA50_I_temp = cumtrapz(timeMS(on312:end),s312MA50_P(on312:end));
s312MA50_I = padarray(s312MA50_I_temp,(length(timeMS) - length(s312MA50_I_temp)),0,
     'pre');
s312MA100_P = movavg(s312_pressure,50,50);
s312MA100_I_temp = cumtrapz(timeMS(on312:end),s312MA100_P(on312:end));
s312MA100_I = padarray(s312MA100_I_temp,(length(timeMS) - length(s312MA100_I_temp))
     ,0,'pre');
% ============== wavelet processing
     ================================================
s312_pressureR=resample2(s312_pressure,300,228,0); %131072
GRR = length(s312_pressureR)-131072;
s312_pressureW = s312_pressureR(GRR+1:end);
% ============= make some different QMF's
     ============================================
QMFS8 = MakeONFilter('Symmlet',8);
QMFH8 = MakeONFilter('Haar',8);
QMFC3 = MakeONFilter('Coiflet',3);
QMFD12 = MakeONFilter('Daubechies',12);
% ====================================
[yS,coefS] = NormNoise(s312_pressureW',QMFS8); % normalise signal to noise level 1
[yH,coefH] = NormNoise(s312_pressureW',QMFH8); % normalise signal to noise level 1
[yC,coefC] = NormNoise(s312_pressureW',QMFC3); % normalise signal to noise level 1
[yD,coefD] = NormNoise(s312_pressureW',QMFD12); % normalise signal to noise level 1
% ++++++++++++++++++++++++++ Different shrinkage types
     ++++++++++++++++++++++++++++++++
[s312WP_VISU_long,s312WP1] = WaveShrink(yS,'Visu');
s312WP_VISU_short = resample2(s312WP_VISU_long,228,300,0); % resample array to
     change length but preserve time over which data recorded
s312WP_VISU = (padarray(s312WP_VISU_short',(100000 - length(s312WP_VISU_short)),0,'
     pre'))./coefS; % pad pre shock arrival with zeros to get precise length for use
      with WaveShrink
s312WP_VISU_I_temp = cumtrapz(timeMS(on312:end),s312WP_VISU(on312:end));
s312WP_VISU_I = padarray(s312WP_VISU_I_temp,(length(timeMS) - length(
```

```
    s312WP_VISU_I_temp)),0,'pre'); % pad preshock arrival with zeros to ensure all
    impulse arrays are same length
% ----------------------
[s312WP_SURE_long,s312WP2] = WaveShrink(yS,'SURE');
s312WP_SURE_short = resample2(s312WP_SURE_long,228,300,0); %100000
s312WP_SURE = (padarray(s312WP_SURE_short',(100000 - length(s312WP_SURE_short)),0,'
    pre'))./coefS;
s312WP_SURE_I_temp = cumtrapz(timeMS(on312:end),s312WP_SURE(on312:end));
s312WP_SURE_I = padarray(s312WP_SURE_I_temp,(length(timeMS) - length(
    s312WP_SURE_I_temp)),0,'pre');
% -------
[s312WP_MinMax_long,s312WP3] = WaveShrink(yS,'Hybrid');
s312WP_MinMax_short = resample2(s312WP_MinMax_long,228,300,0); %100000
s312WP_MinMax = (padarray(s312WP_MinMax_short',(100000 - length(s312WP_MinMax_short
    )),0,'pre'))./coefS;
s312WP_MinMax_I_temp = cumtrapz(timeMS(on312:end),s312WP_MinMax(on312:end));
s312WP_MinMax_I = padarray(s312WP_MinMax_I_temp,(length(timeMS) - length(
    s312WP_MinMax_I_temp)),0,'pre');
% +++++++++++++++++++++++++++++++++ soft and hard thresholding
    ++++++++++++++++++++++
s312WP_ST = ThreshWave(yS,'S',1,std(yS(1:8500)));
s312WP_ST_short = resample2(s312WP_ST,228,300,0); %100000
s312WP_soft = (padarray(s312WP_ST_short',(100000 - length(s312WP_ST_short)),0,'pre'
    ))./coefS;
s312WP_soft_I_temp = cumtrapz(timeMS(on312:end),s312WP_soft(on312:end));
s312WP_soft_I = padarray(s312WP_soft_I_temp,(length(timeMS) - length(
    s312WP_soft_I_temp)),0,'pre');
% ----------
s312WP_HT = ThreshWave(yS,'H',1,std(yS(1:8500)));
s312WP_HT_short = resample2(s312WP_HT,228,300,0); %100000
s312WP_hard = (padarray(s312WP_HT_short',(100000 - length(s312WP_HT_short)),0,'pre'
    ))./coefS;
s312WP_hard_I_temp = cumtrapz(timeMS(on312:end),s312WP_hard(on312:end));
s312WP_hard_I = padarray(s312WP_hard_I_temp,(length(timeMS) - length(
    s312WP_hard_I_temp)),0,'pre');
% ###################################
[s312WP_haar_long,s312WP2] = WaveShrink(yH,'Hybrid');
s312WP_haar_short = resample2(s312WP_haar_long,228,300,0); %100000
s312WP_haar = (padarray(s312WP_haar_short',(100000 - length(s312WP_haar_short)),0,'
    pre'))./coefH;
s312WP_haar_I_temp = cumtrapz(timeMS(on312:end),s312WP_haar(on312:end));
s312WP_haar_I = padarray(s312WP_haar_I_temp,(length(timeMS) - length(
    s312WP_haar_I_temp)),0,'pre');

[s312WP_coif_long,s312WP2] = WaveShrink(yC,'Hybrid');
s312WP_coif_short = resample2(s312WP_coif_long,228,300,0); %100000
s312WP_coif = (padarray(s312WP_coif_short',(100000 - length(s312WP_coif_short)),0,'
    pre'))./coefC;
s312WP_coif_I_temp = cumtrapz(timeMS(on312:end),s312WP_coif(on312:end));
s312WP_coif_I = padarray(s312WP_coif_I_temp,(length(timeMS) - length(
    s312WP_coif_I_temp)),0,'pre');

[s312WP_daub_long,s312WP2] = WaveShrink(yD,'Hybrid');
s312WP_daub_short = resample2(s312WP_daub_long,228,300,0); %100000
s312WP_daub = (padarray(s312WP_daub_short',(100000 - length(s312WP_daub_short)),0,'
    pre'))./coefD;
s312WP_daub_I_temp = cumtrapz(timeMS(on312:end),s312WP_daub(on312:end));
s312WP_daub_I = padarray(s312WP_daub_I_temp,(length(timeMS) - length(
    s312WP_daub_I_temp)),0,'pre');
% ====================================

MA_P = [timeMS(PT:end) s312MA10_P(PT:end) s312MA50_P(PT:end) s312MA100_P(PT:end)];
    % remove 5.4s of pretrigger
MA_I = [timeMS(PT:end) s312MA10_I(PT:end) s312MA50_I(PT:end) s312MA100_I(PT:end)];
BUT_P = [timeMS(PT:end) s312BUT1P(PT:end) s312BUT2P(PT:end) s312BUT3P(PT:end)
    s312BUT4P(PT:end)];
BUT_I = [timeMS(PT:end) s312BUT1I(PT:end) s312BUT2I(PT:end) s312BUT3I(PT:end)
    s312BUT4I(PT:end)];
WAV_P = [timeMS(PT:end) s312WP_VISU(PT:end) s312WP_SURE(PT:end) s312WP_MinMax(PT:
    end) s312WP_soft(PT:end) s312WP_hard(PT:end) s312WP_haar(PT:end) s312WP_coif(PT
    :end) s312WP_daub(PT:end)];
WAV_I = [timeMS(PT:end) s312WP_VISU_I(PT:end) s312WP_SURE_I(PT:end) s312WP_MinMax_I
    (PT:end) s312WP_soft_I(PT:end) s312WP_hard_I(PT:end) s312WP_haar_I(PT:end)
    s312WP_coif_I(PT:end) s312WP_daub_I(PT:end)];
RAW_P = [timeMS(PT:end) s312_pressure(PT:end)];
RAW_imp = cumtrapz(timeMS(on312:end),s312_pressure(on312:end));
RAW_imp2 = padarray(RAW_imp,(length(timeMS) - length(RAW_imp)),0,'pre');
RAW_I = [timeMS(PT:end) RAW_imp2(PT:end)];

fprintf(fout1,'time,MA10,MA50,MA100\n');
fprintf(fout1,'%E,%E,%E,%E\n',MA_P');
fclose(fout1);
fprintf(fout2,'time,MA10,MA50,MA100\n');
fprintf(fout2,'%E,%E,%E,%E\n',MA_I');
fclose(fout2);
fprintf(fout3,'time,BUT_0.05,BUT_0.02,BUT_0.011,BUT_0.01\n');
fprintf(fout3,'%E,%E,%E,%E,%E\n',BUT_P');
```

```
fclose(fout3);
fprintf(fout4,'time,BUT_0.05,BUT_0.02,BUT_0.011,BUT_0.01\n');
fprintf(fout4,'%E,%E,%E,%E,%E\n',BUT_I');
fclose(fout4);
fprintf(fout5,'time,VISU,SURE,MinMax,soft,hard,haar,coif,daub\n');
fprintf(fout5,'%E,%E,%E,%E,%E,%E,%E,%E,%E\n',WAV_P');
fclose(fout5);
fprintf(fout6,'time,VISU,SURE,MinMax,soft,hard,haar,coif,daub\n');
fprintf(fout6,'%E,%E,%E,%E,%E,%E,%E,%E,%E\n',WAV_I');
fclose(fout6);
fprintf(fout7,'time,RAW_P\n');
fprintf(fout7,'%E,%E\n',RAW_P');
fclose(fout7);
fprintf(fout8,'time,RAW_I\n');
fprintf(fout8,'%E,%E\n',RAW_I');
fclose(fout8);
```

C.3 Plot data using pyxplot

```
clear
set terminal pdf
set nokey
set grid
set output "~/Work/experimental/figs/filtering/WAV_I_QMFcomp.pdf"
set multiplot
width=8
set yrange [0:550]
set xrange [0:10.999]
set origin 0*width, 0*width/goldenRatio
set texthalign left
set textvalign center
#####
unset xtics
unset xformat
unset yformat
set xlabel "Time (ms)"
set ylabel "Impulse (kPa)"
set label 1 "(b) Haar" at graph width*0.73 , graph width/goldenRatio*0.9
plot '/home/tom/Work/experimental/processed/Filt-params/WAV_I.csv' every ::2 using
    1:7 title '10␣point' with lines lt 2 linewidth 0.8
set axis x linked item 1 x
set axis y linked item 1 y
#####
set origin 0*width, 1*width/goldenRatio
set label 1 "(a) Raw data" at graph width*0.73 , graph width/goldenRatio*0.9
set xformat "" ; set xlabel ""
plot '/home/tom/Work/experimental/processed/Filt-params/RAW_I.csv' every ::2 using
    1:2 title 'RAW' with lines lt 3 linewidth 0.8
#####
unset xformat
set xlabel "Time (ms)"
set origin 1*width, 0*width/goldenRatio
set label 1 "(d) Daubechies" at graph width*0.65 , graph width/goldenRatio*0.9
set yformat "" ; set ylabel ""
plot '/home/tom/Work/experimental/processed/Filt-params/WAV_I.csv' every ::2 using
    1:9 title '100␣point' with lines lt 3 linewidth 0.8
#####
set origin 1*width, 1*width/goldenRatio
set label 1 "(c) Coiflet" at graph width*0.73 , graph width/goldenRatio*0.9
set xformat "" ; set xlabel ""
plot '/home/tom/Work/experimental/processed/Filt-params/WAV_I.csv' every ::2 using
    1:8 title '50␣point' with lines lt 4 linewidth 0.8 ;
#--------------------------- ($3*1000000) every ::2 using 1:($9*1000000) using ($1
    -0.02):($2+104)
#[-5:20][-100:250]
# ==================== IMPULSE
    ========================================================
# set xformat "" ; set xlabel ""
# set yformat "" ; set ylabel ""
```

Appendix D

Test arrangment drawings

DRAFT

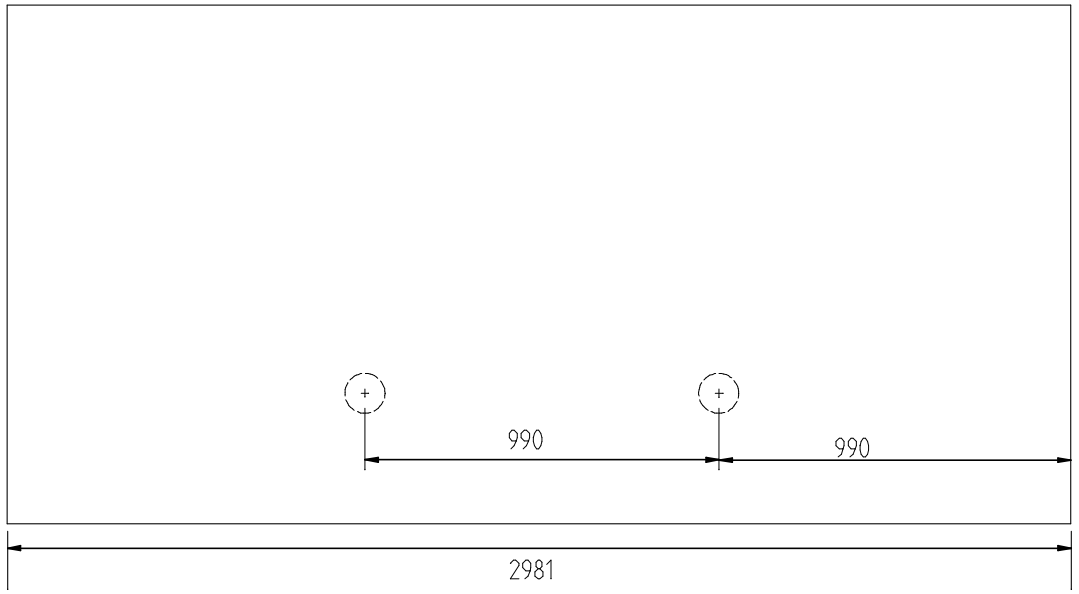

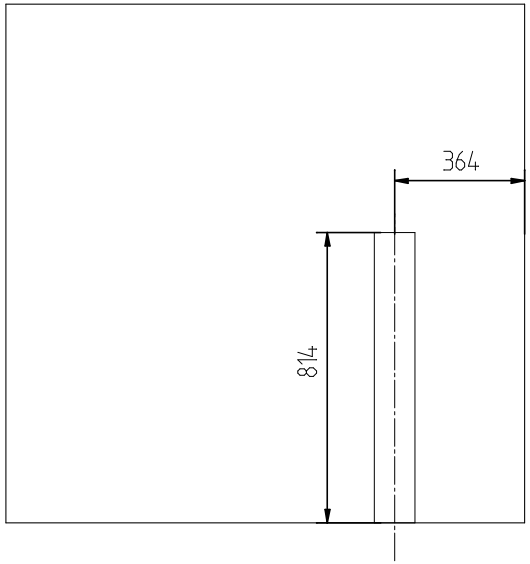

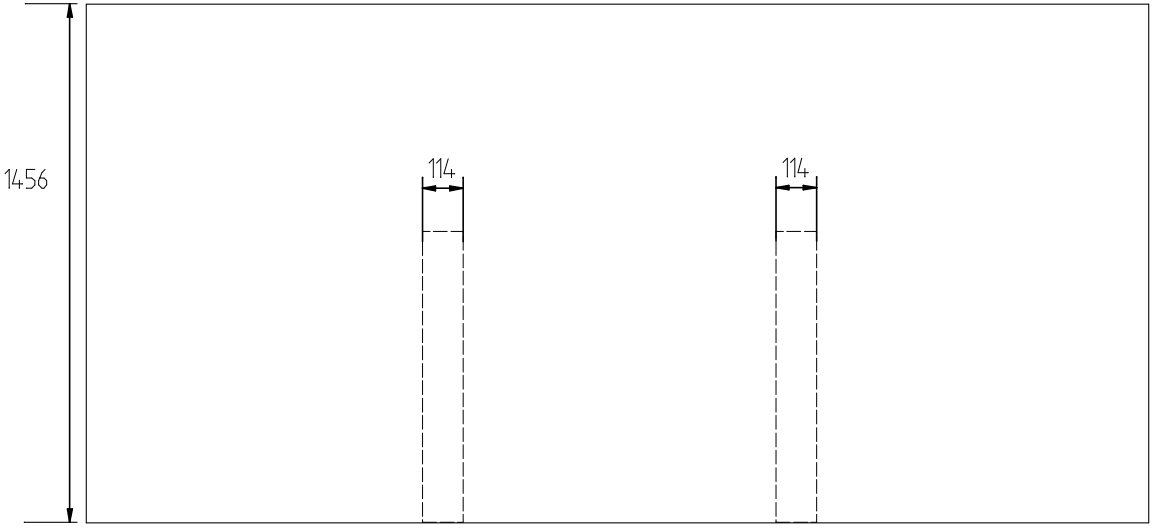

Title Control test setup	**Scale** 1:15 **Date**	
Drg. No. Test plan 001	**Drawn by** Tom Anthistle	**Material** Steel

DRAFT

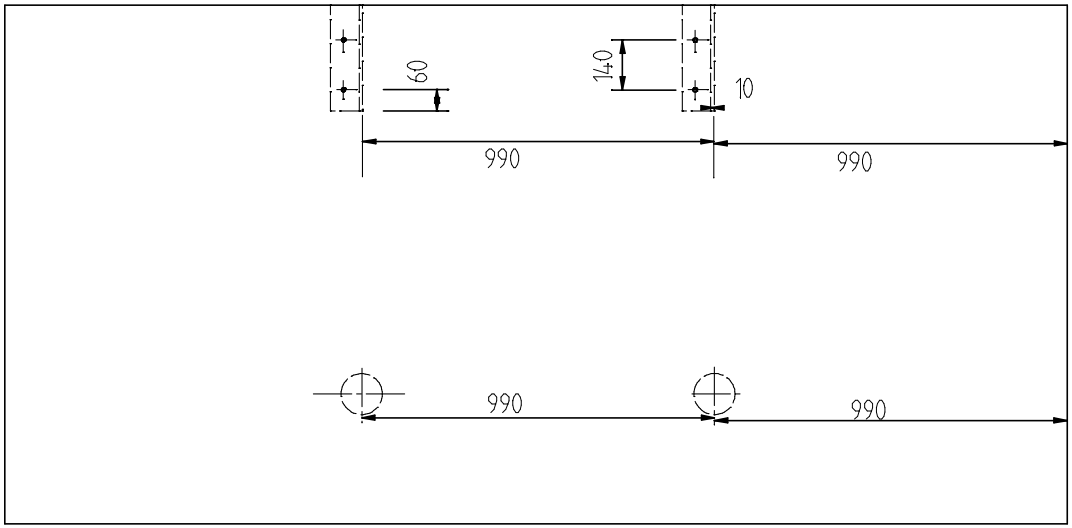

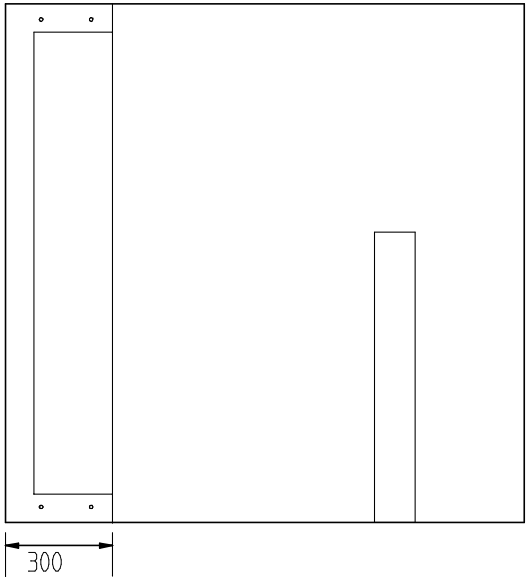

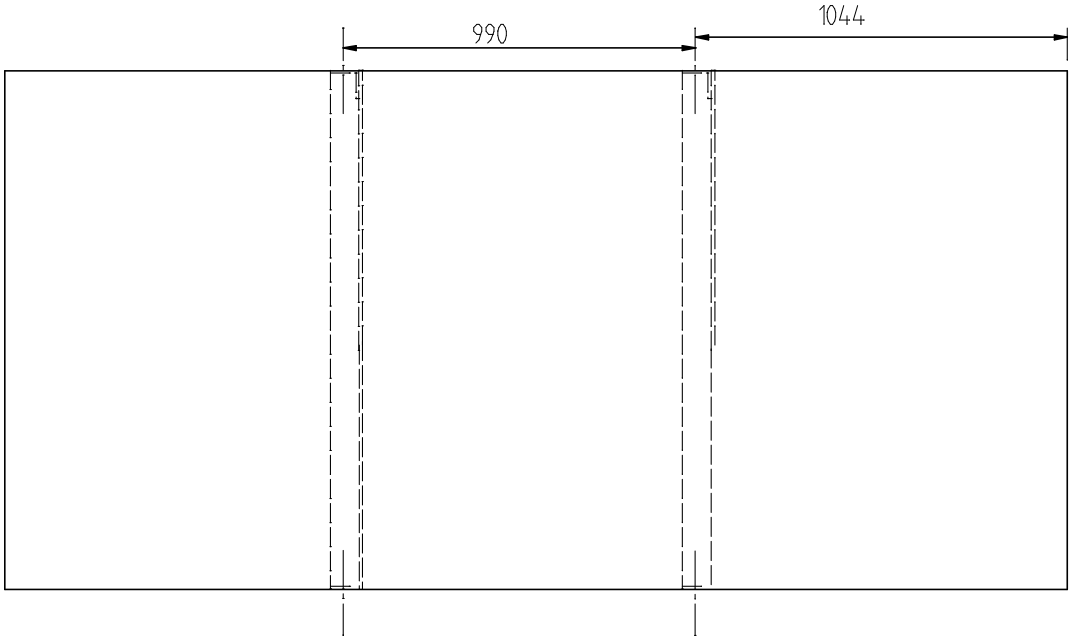

Title Baffle setup 1	**Scale** 1:15 **Date**	
Drg. No. FSI 002	**Drawn by** Tom Anthistle	**Material** Steel

DRAFT

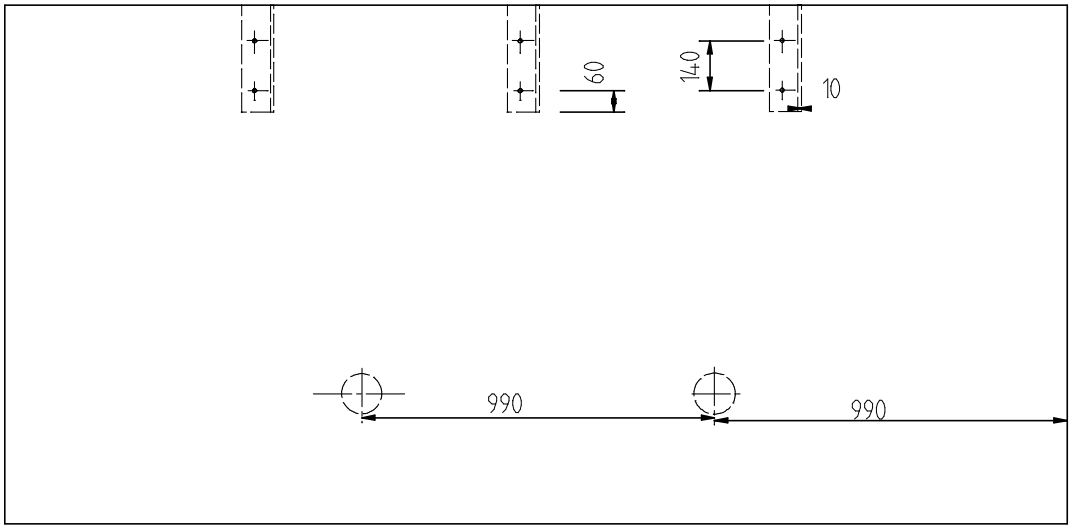

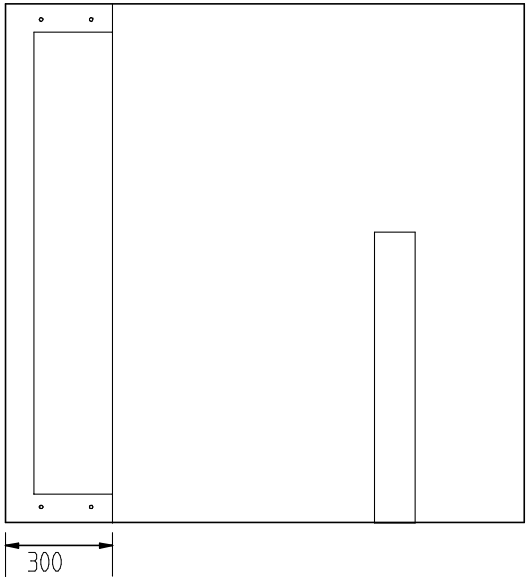

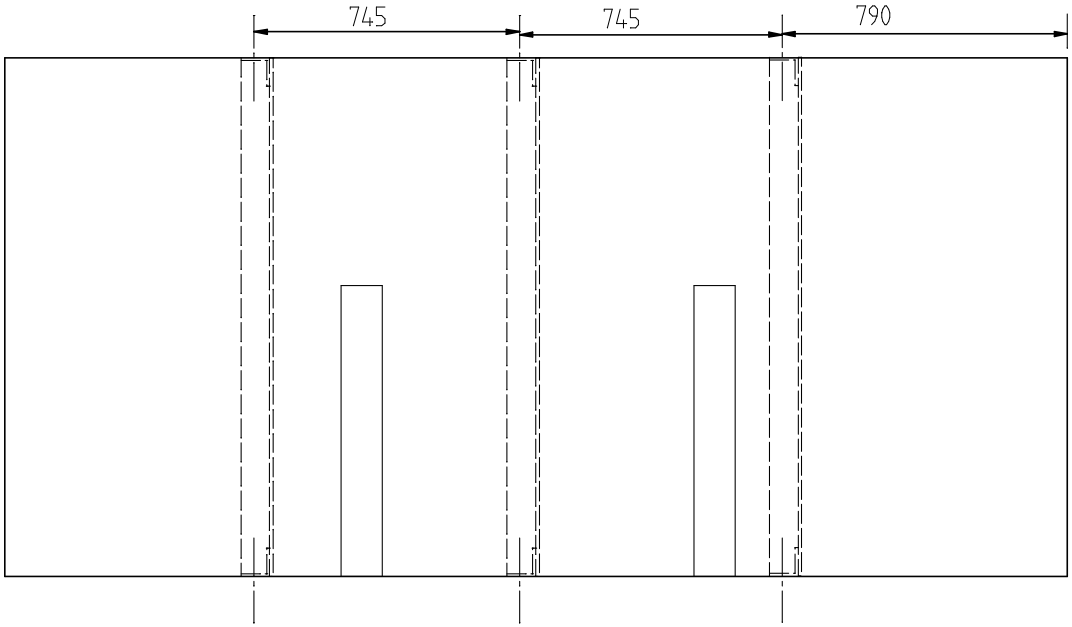

Title Baffle setup 2	**Scale** 1:15 **Date**	
Drg. No. FSI 002	**Drawn by** Tom Anthistle	**Material** Steel

DRAFT

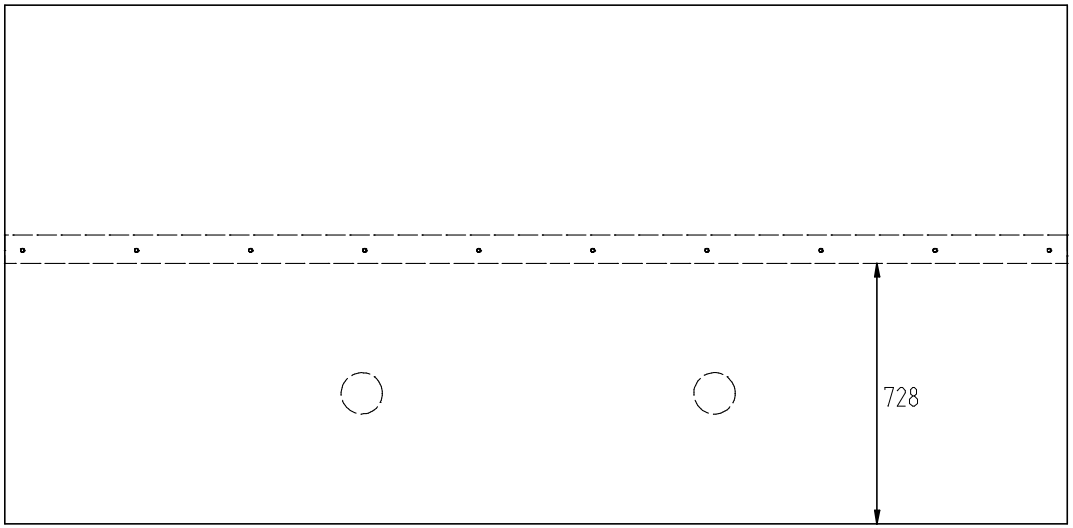

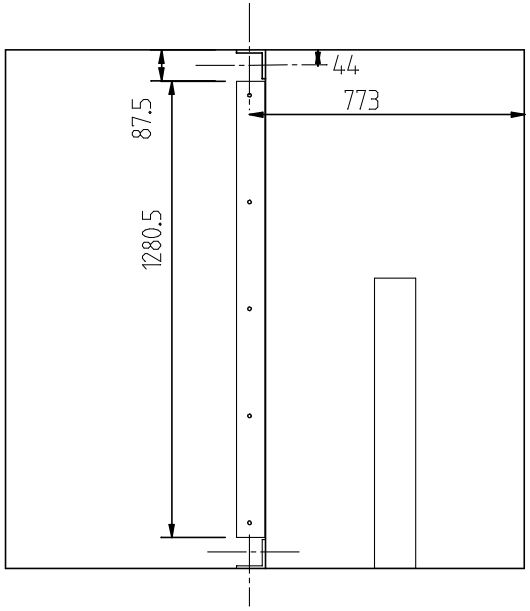

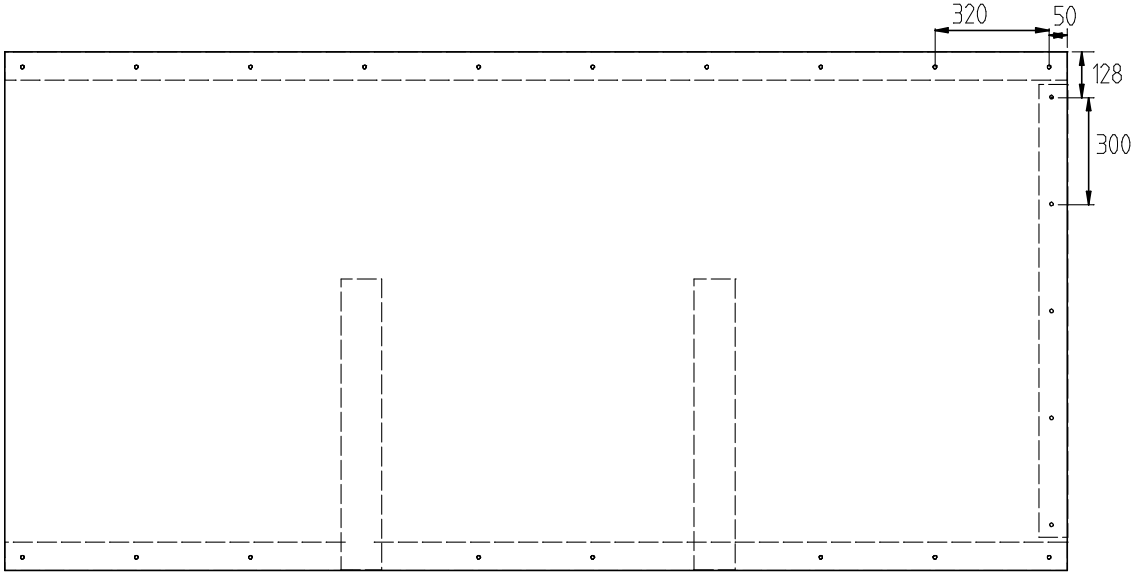

Title FSI 1 test setup	**Scale** 1:15 **Date**	
Drg. No. FSI 001	**Drawn by** Tom Anthistle	**Material** Steel / Aluminium

Appendix E

Fabricated parts

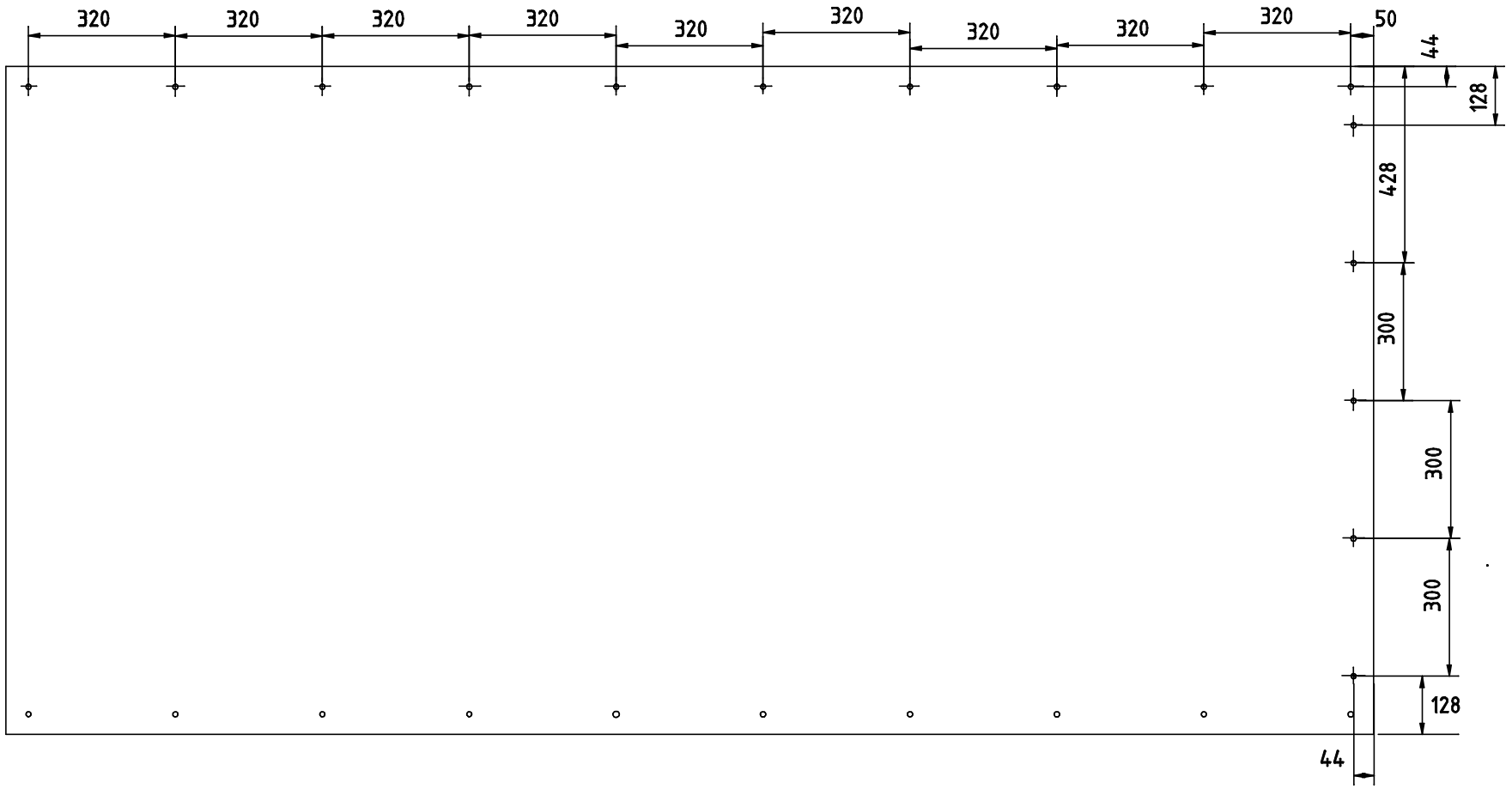

Title Alu panel hole locations	Scale 1:10 Date	
Drg. No.	Drawn by Tom Anthistle	Material Aluminium

1 off

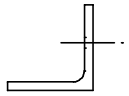

4 off

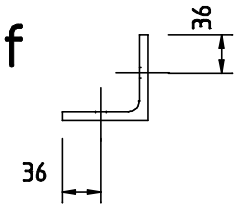

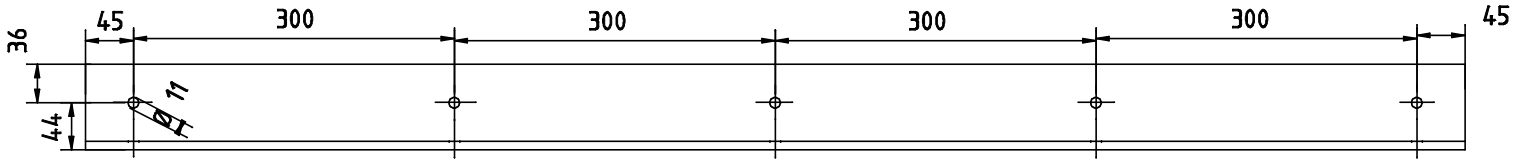

Title vertical support flange	Scale 1:5 Date	
Drg. No.	Drawn by Tom Anthistle	Material mild steel

2 off

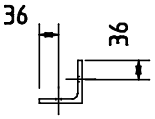

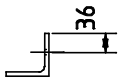

2 off

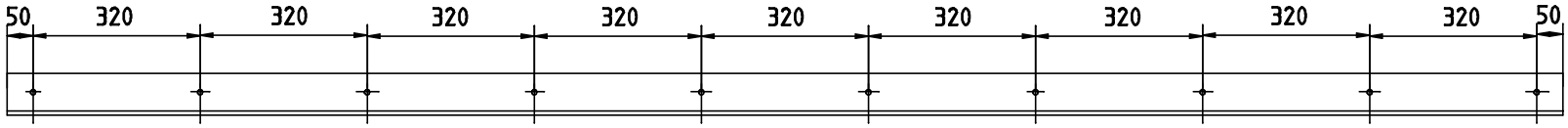

Title horizontal retaining flange (long)	Scale 1:20 Date	
Drg. No.	Drawn by Tom Anthistle	Material mild steel

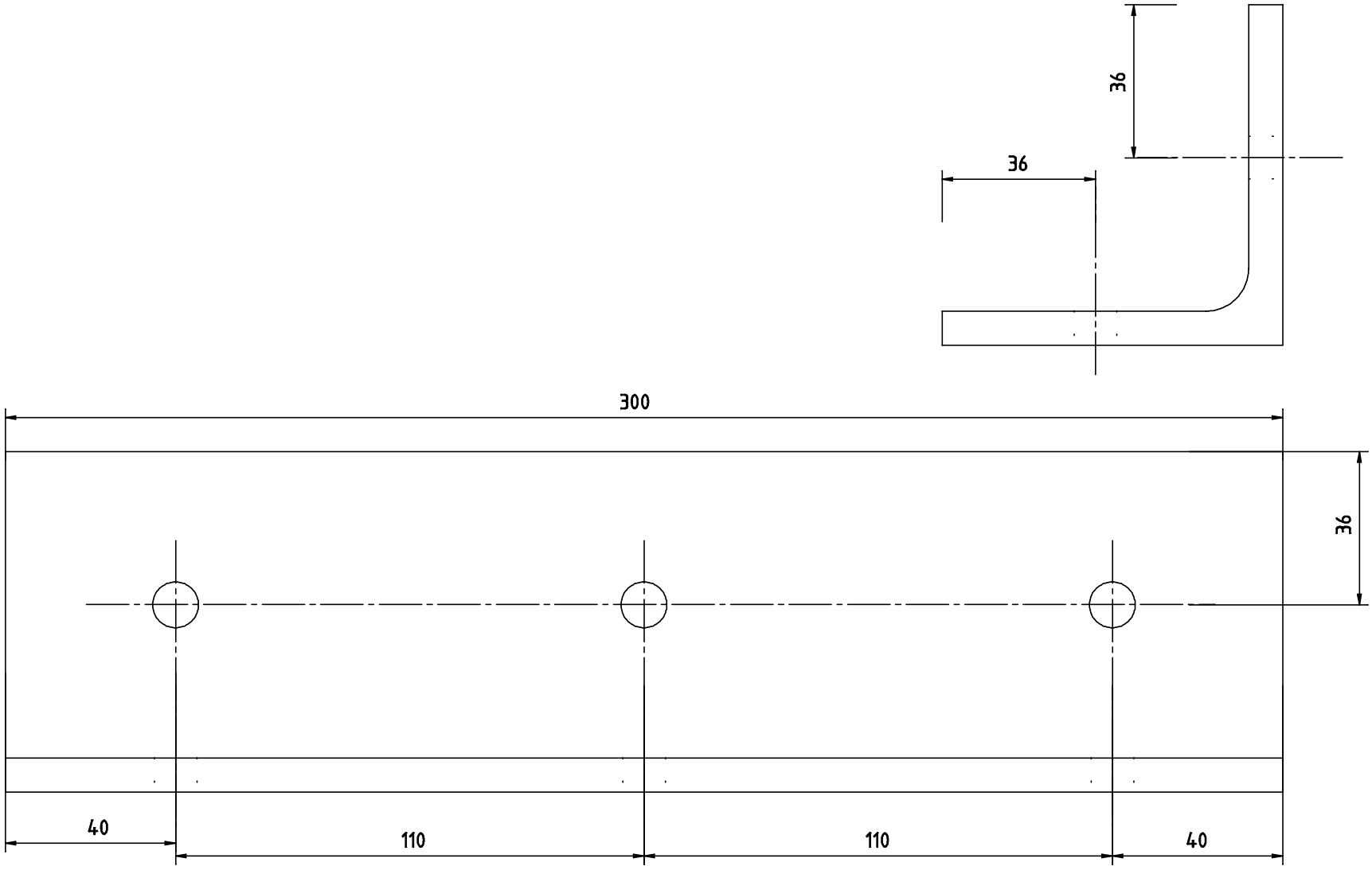

Title horizontal baffle retaining flange	Scale 1:2 Date	
Drg. No.	Drawn by Tom Anthistle	Material mild steel

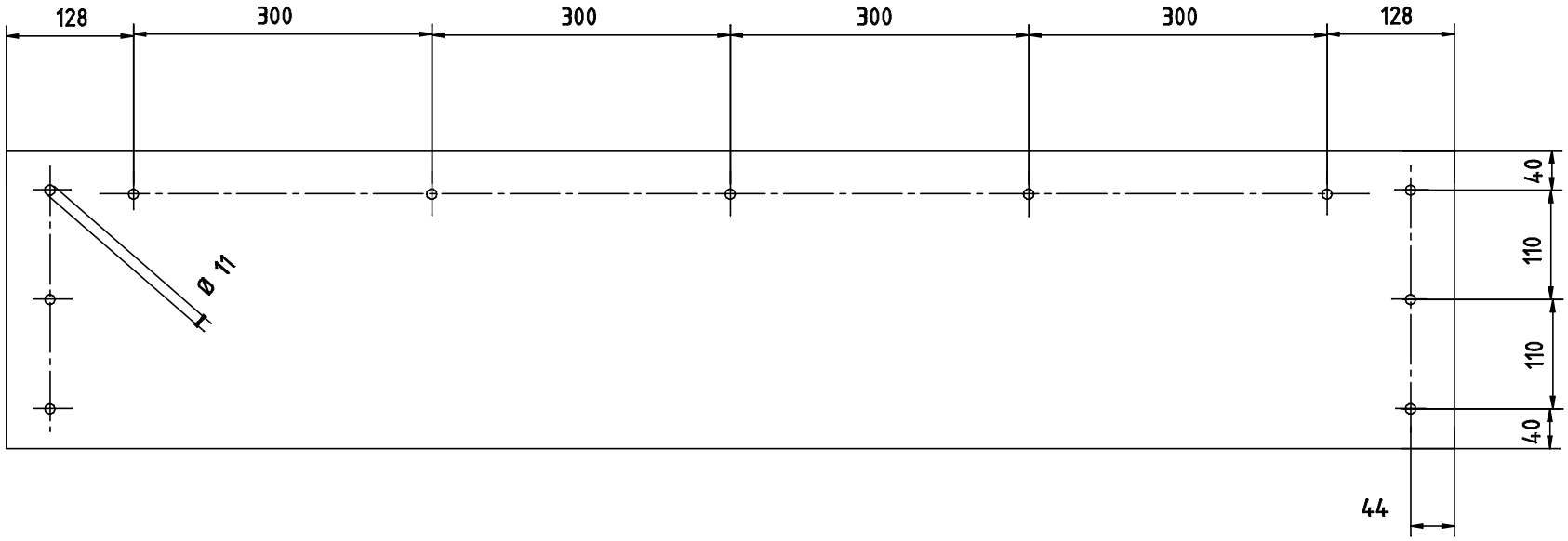

Title mild steel baffle	Scale 1:10 Date	
Drg. No.	Drawn by Tom Anthistle	Material

Appendix F

Filtering Data

Three methods were considered for filtering data:

- moving average
- butterworth filter
- wavelet transform

To identify how effective these methods are at removing noise and preserving underlying physical data, pressure and cumulative impulse curves from a pressure sensor are plotted for different methods and different parameters. Cumulative impulse is a particularly useful measure, as it is very sensitive to changes in the underlying data. It is also important to compare the time taken to filter or denoise data due to the size of the data sets. Comparison of the following methods and parameters is presented:

- number of moving average points
  - 10 point
  - 50 point
  - 100 point
- butterworth filter normalised cutoff frequency (ω_c, see Eq. (F.1))
  - $\omega_c = 0.050$
  - $\omega_c = 0.020$
  - $\omega_c = 0.011$
  - $\omega_c = 0.010$
- wavelet transform (WaveShrink and ThreshWave functions from WaveLab [202])
  - shrinkage type (WaveShrink)
  - soft and hard thresholding (ThreshWave)

$$\omega = \frac{2\pi f}{f_s} \tag{F.1}$$

Filtered data is produced from raw experimental data using GNU Octave. The full script can be found in Appendix C.2. Data from sensor 312, (shot 1 arrangement 1) is plotted using PYXPLOT up to 10ms for clarity.

Figure F.1 shows pressure time histories from raw data as well as 10, 50 and 100 point moving averages. For a 10 point moving average (F.1(b)), peak values are well resolved, but significant noise still exists. As would be expected, 50 and 100 point averages (F.1(c) and F.1(d)) offer better reduction in noise but tend to cut off peaks. Despite

this, Figures F.2(a–d), show that all 3 methods, as well as raw data have, identical cumulative impulses.

Butterworth filters are commonly used in signal processing, and are ideal for processing this kind of data. The effect of changing the normalised cut off frequency, ω_c can be seen in Figures F.3(a–d). All plots show that pressure peaks are cut off to a level similar to a 100 point moving average, but lower values of ω_c (0.01 and 0.011) show a better level of noise reduction. The amount that peaks are cut off by appears arbitrary, with $\omega_c = 0.02$ showing the least reduction in the highest peak at 2.75ms. Figure F.4 shows how the cumulative impulse is affected by changing ω_c, and Figures F.4(c) and (d) show significant deviation from the impulses shown in F.4(a) and (b), which are identical to Figures F.2(a–d). The altered impulse in F.4(c) and (d) also doesn't show a trend; (c) shows a lower impulse and (d) a much larger impulse. From this it is easy to conclude that ω_c values < 0.02 should be avoided to maintain the correct cumulative impulse.

Wavelet denoising is slightly more involved, as signals need to be transformed into the wavelet domain (similar in principle to a fourier transform), normalised, denoised and then transformed back into the time domain, all of which adds computational effort. The ThreshWave and WaveShrink denoising tools in WaveLab are used here to remove noise. WaveShrink offers soft thresholding shrinkage using various options. Hybrid offers similar performance to 10PMA, whereas SURE provides almost no noise removal. Visu offers very good denoising but cuts off peaks more than when a 100 point moving average is used, shown in Figure F.5. None of the WaveShrink methods offer advantages over moving averages or Butterworth filters in terms of noise reduction in pressure signals, but all methods maintain impulse, unlike Butterworth filter with low cutoff frequencies, as shown in Figure F.6.

The effect of soft and hard thresholding is compared using the ThreshWave tool, shown in Figure F.7. The soft threshold option, F.7(b) shows very good noise reduction, but has also lowered peak recorded values, as seen with other methods. Hard thresholding, F.7(c), shows equally good noise reduction but maintain peak values better than all other methods except the 10 point moving average. The hard threshold also preserves the impulses better than the soft threshold method, as shown in Figure F.8. The hard threshold method does introduce some spiky wavelet features to the data, which are in places almost discontinuities. As the technique is so efficient at removing noise, if these disconuities occur in the wrong place they could be misinterpreted as physical features of the data.

Results presented about show that although wavelet techniques offer the best removal of data, features introduced by wavelet transforms, or resolution of peaks or both mean that without further research, which is outside of the scope of this work, they do not offer as reliable results as Butterworth filtering. Butterworth filtering with $\omega_c = 0.02$ will be used to denoise data from pressure sensors, and similar investigation undertaken to determine parameters to be used for other sensors.

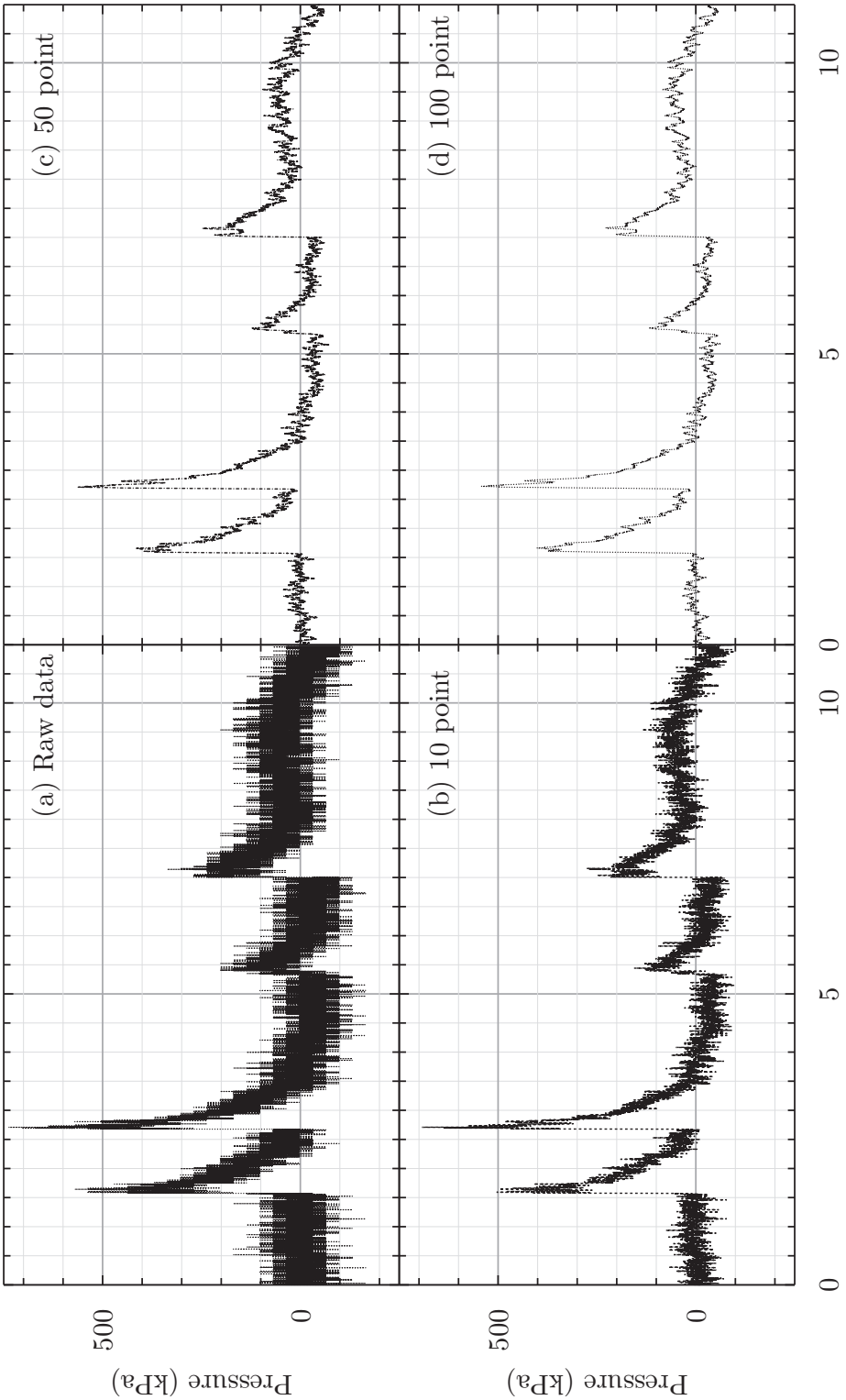

Figure F.1: Comparison of pressures curves from raw data using different moving averages

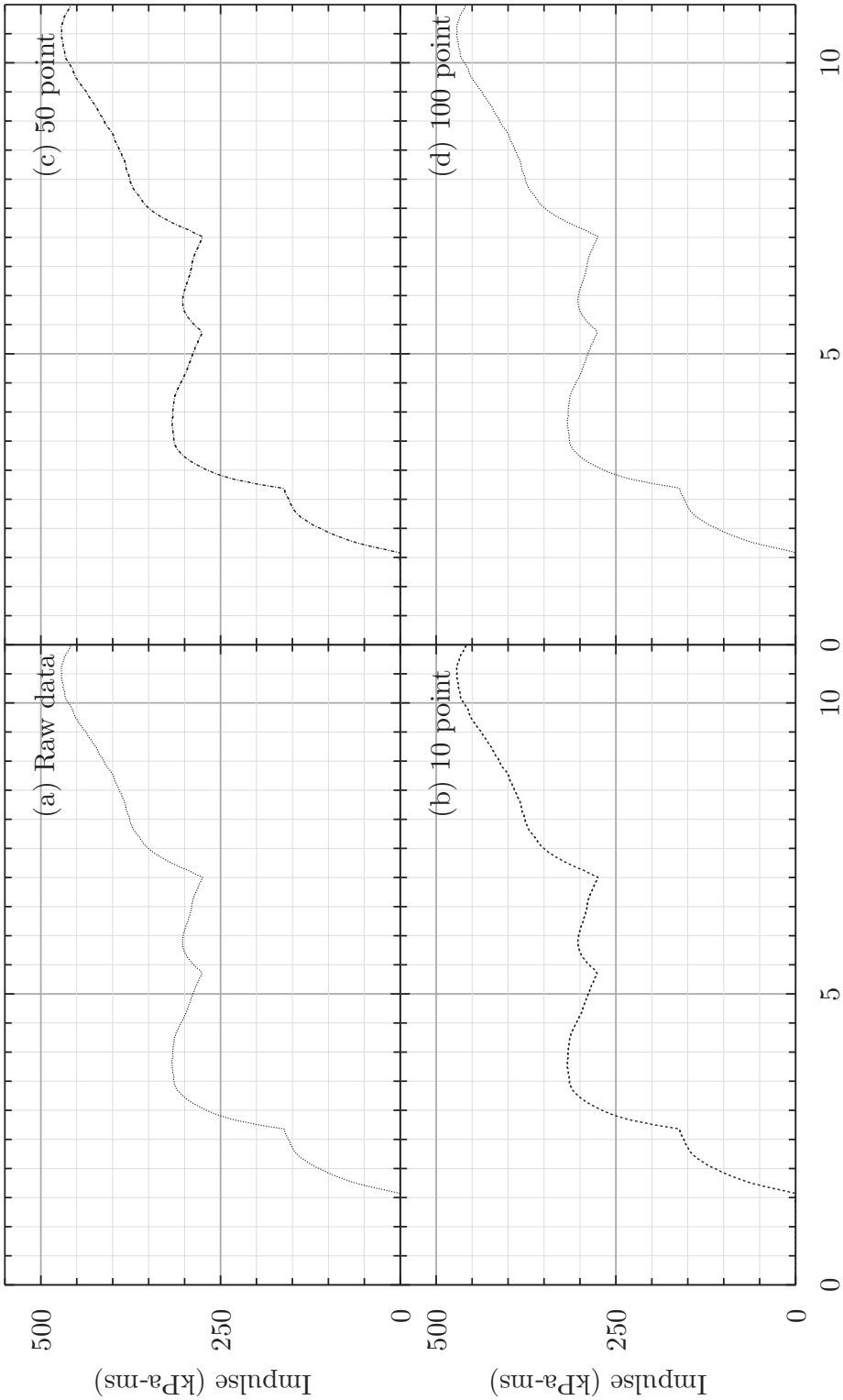

Figure F.2: Comparison of cumulative impulse from raw data using different moving averages

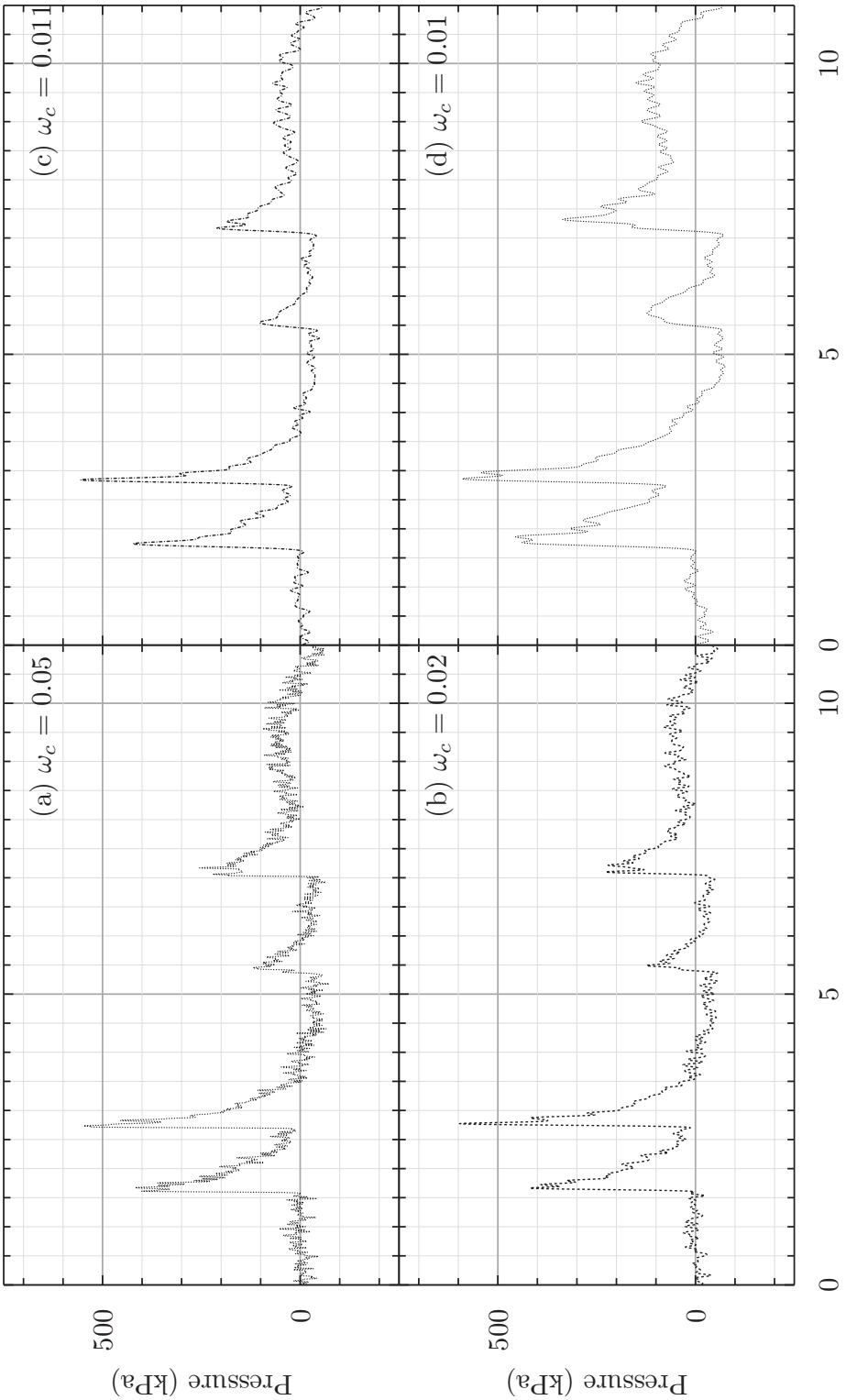

Figure F.3: Comparison of pressures curves using a Buterworth filter with various normalised cutoff frequencies ω_c

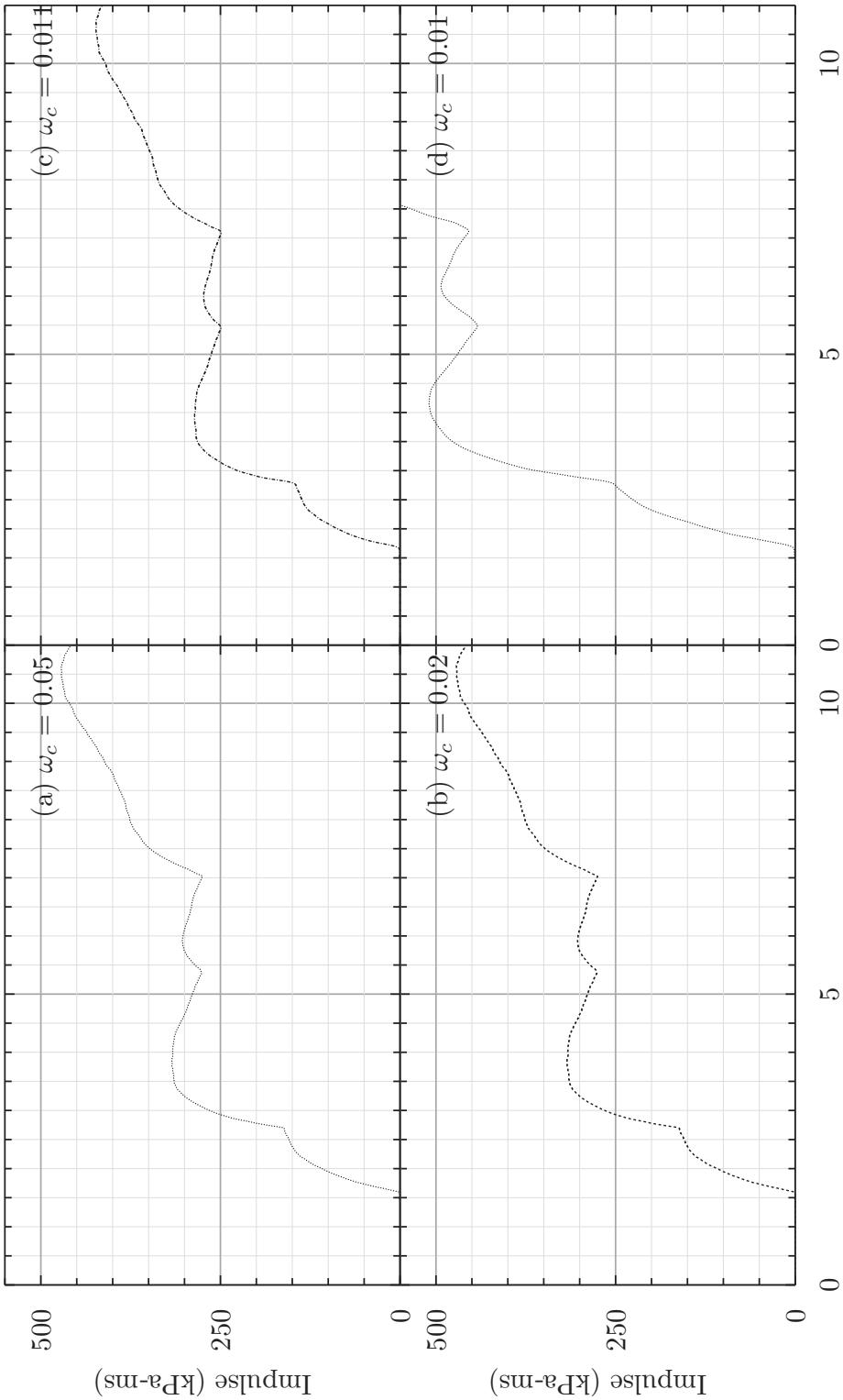

Figure F.4: Comparison of cumulative impulse using a Buterworth filter with various normalised cutoff frequencies ω_c

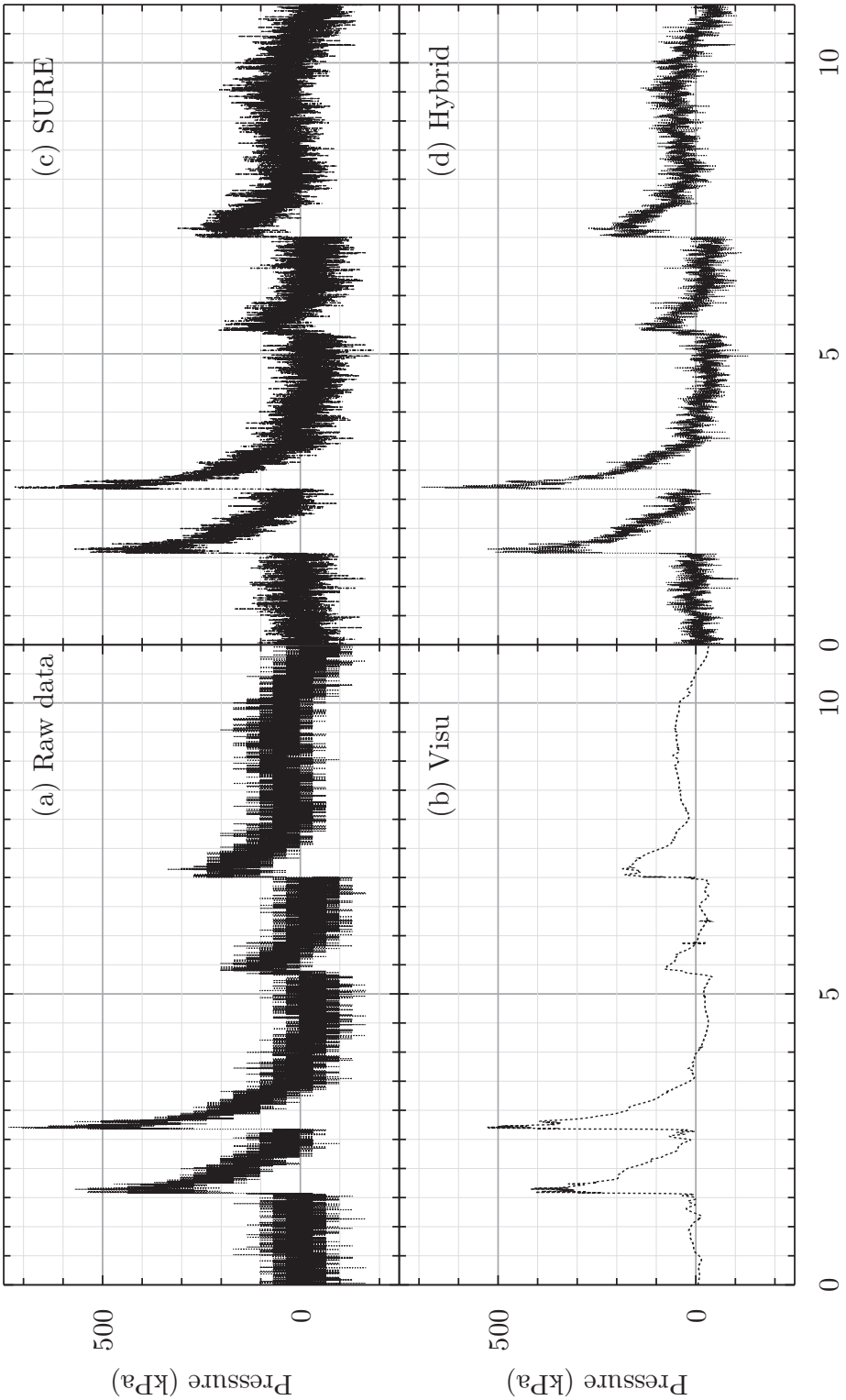

Figure F.5: Comparison of pressure curves from raw data and denoised using different WaveShrink types

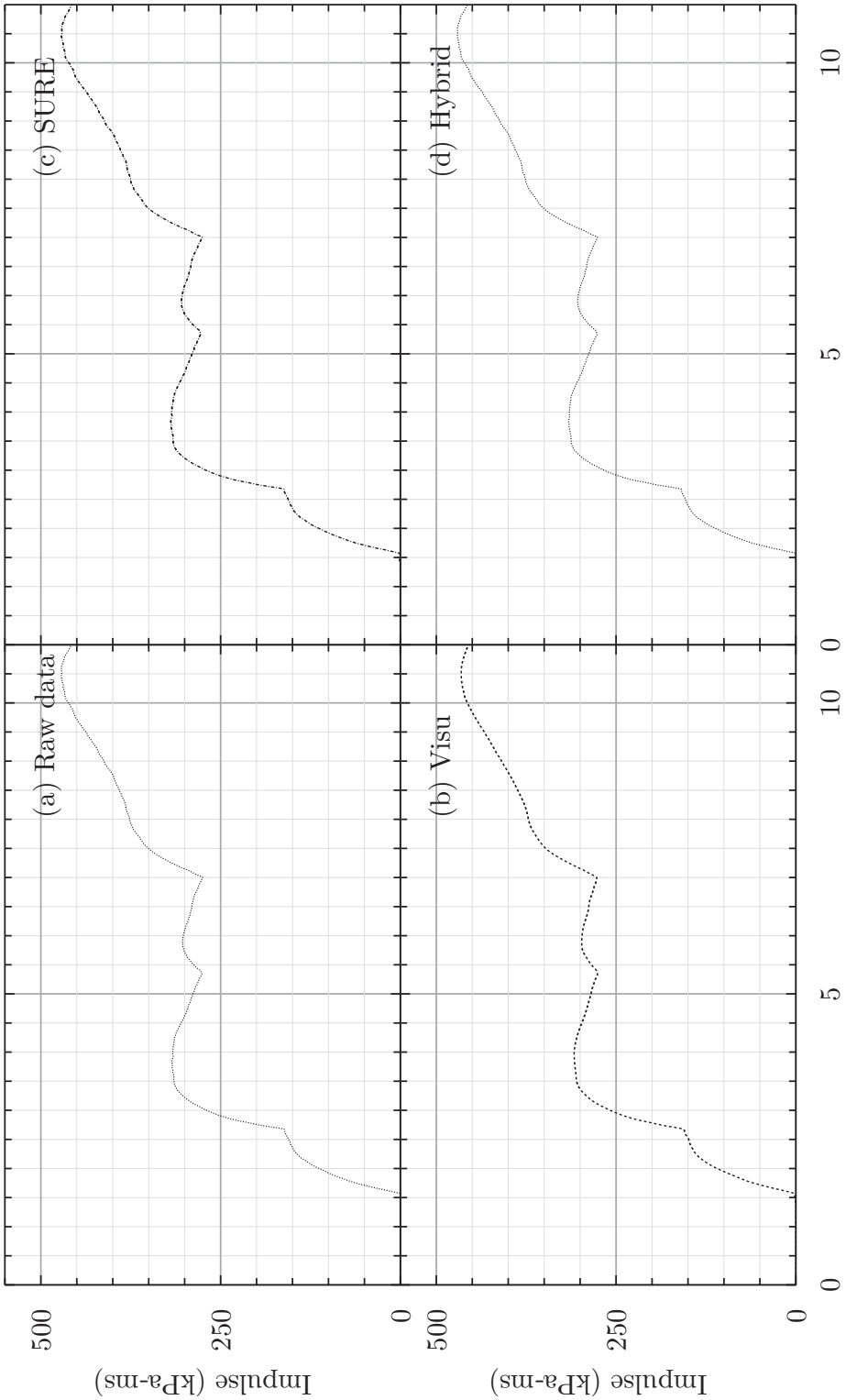

Figure F.6: Comparison of cumulative impulse ufrom raw data and denoised using different WaveShrink types

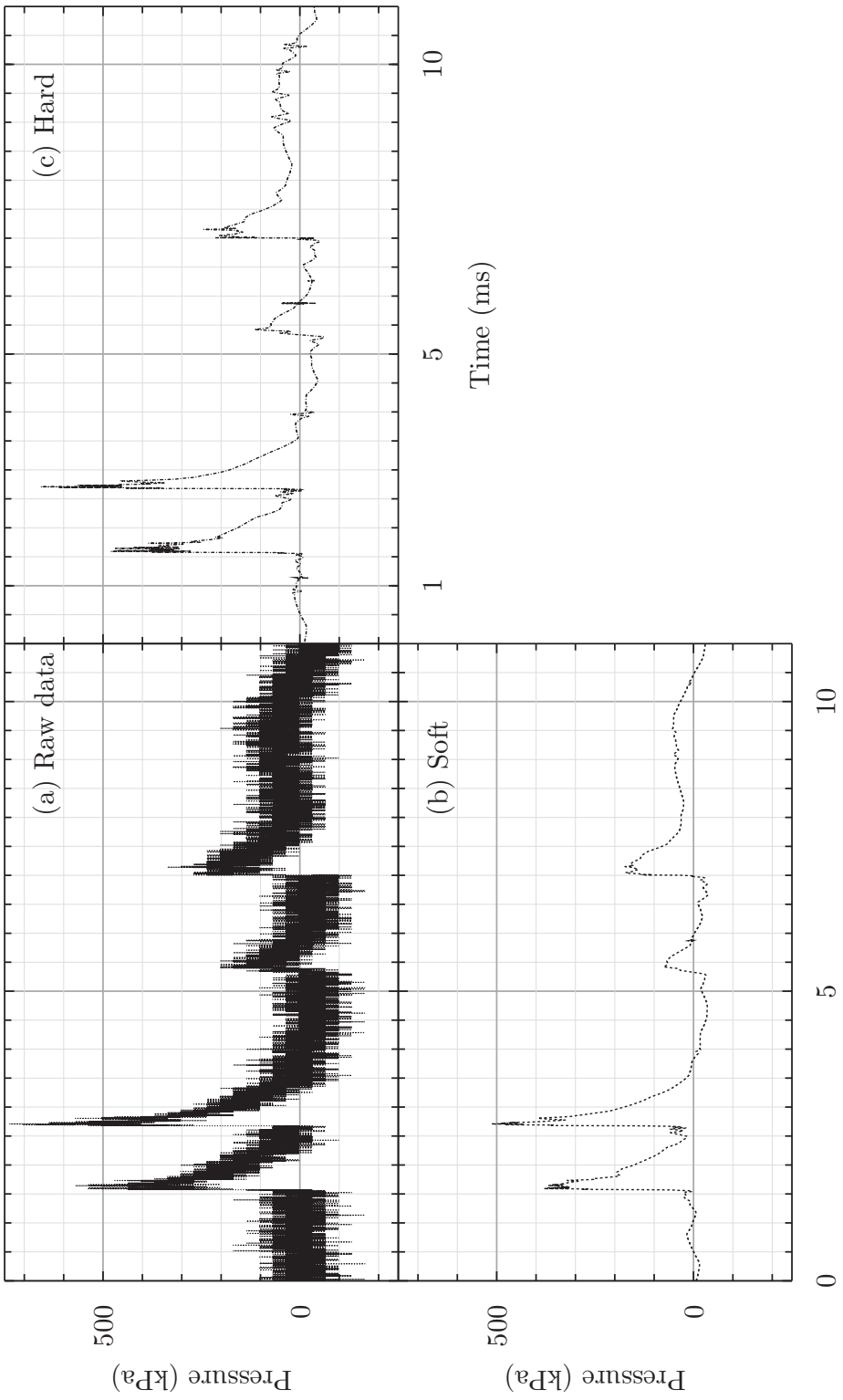

Figure F.7: Comparison of pressure curves from raw data and denoised using soft and hard thresholding in ThreshWave threshold types

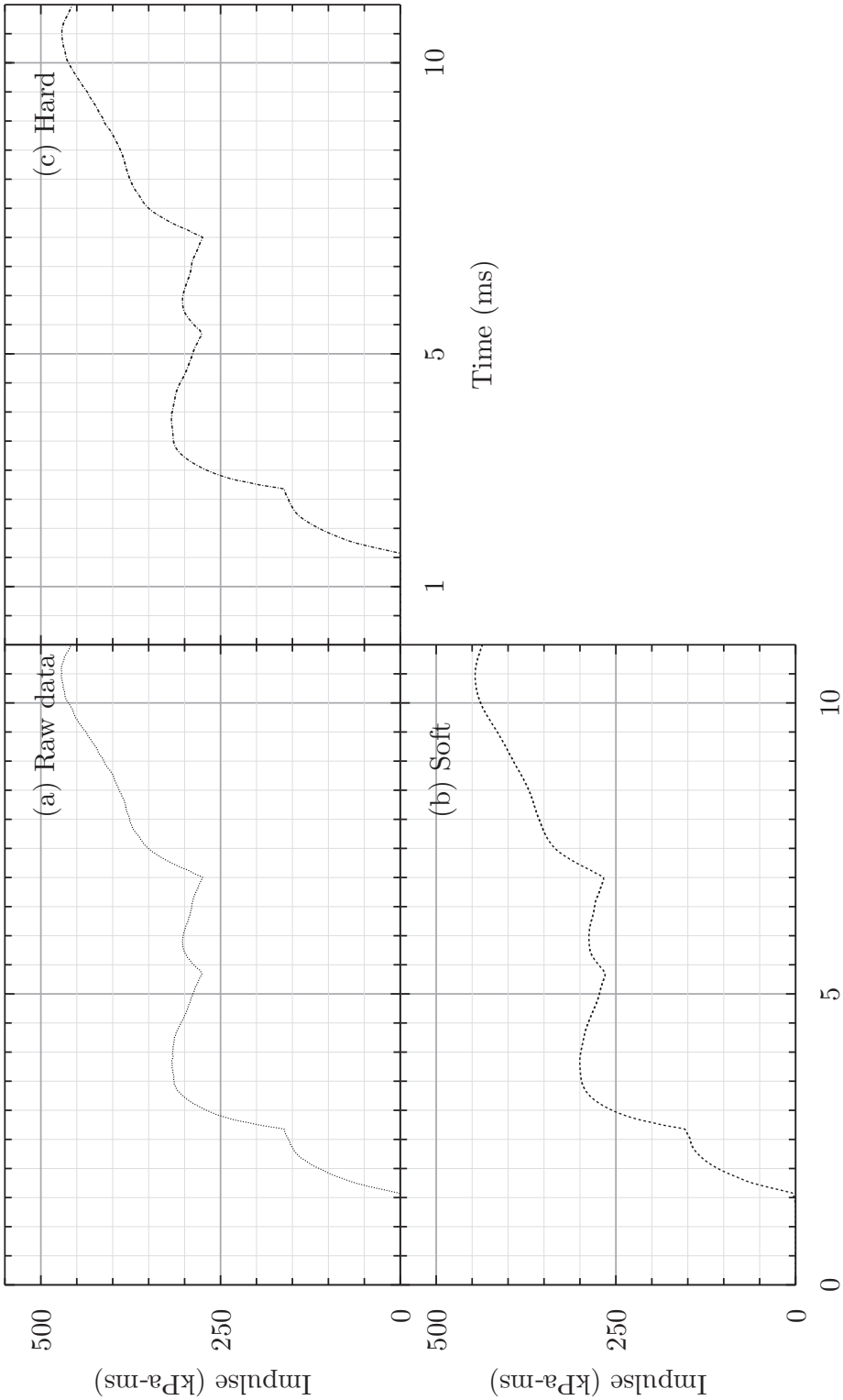

Figure F.8: Comparison of cumulative impulse ufrom raw data and denoised using soft and hard thresholding in ThreshWave

Appendix G

Additional experimental data sets

This Appendix contains the experimental data sets which were included in the analysis and discussion of results in Chapter 5.

G.1 Arrangement 1

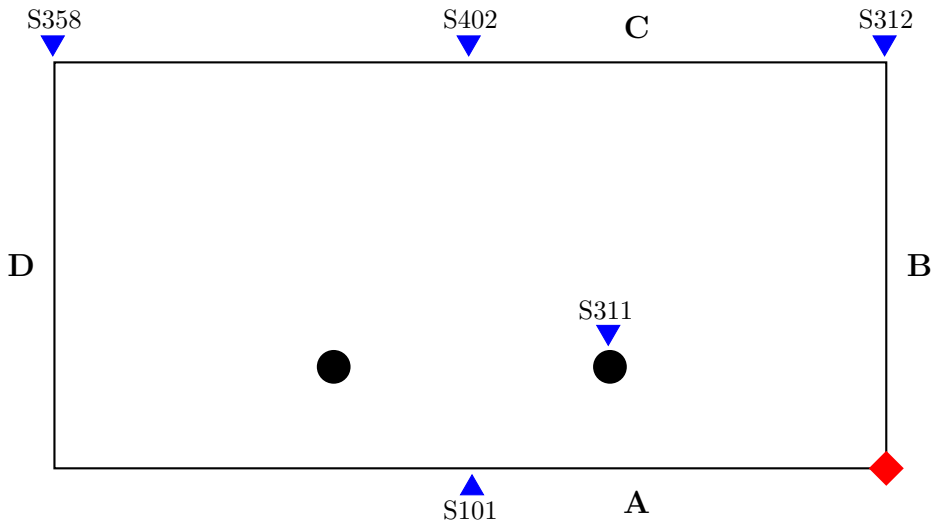

Figure G.1: Sensors and positions for test arrangement 1, shots 1 – 3

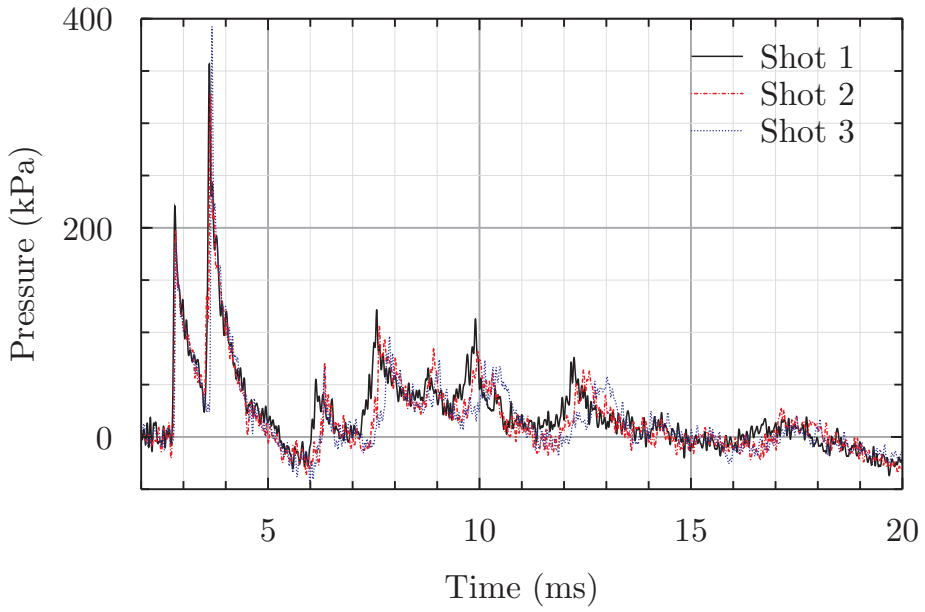

(a) Overpressure

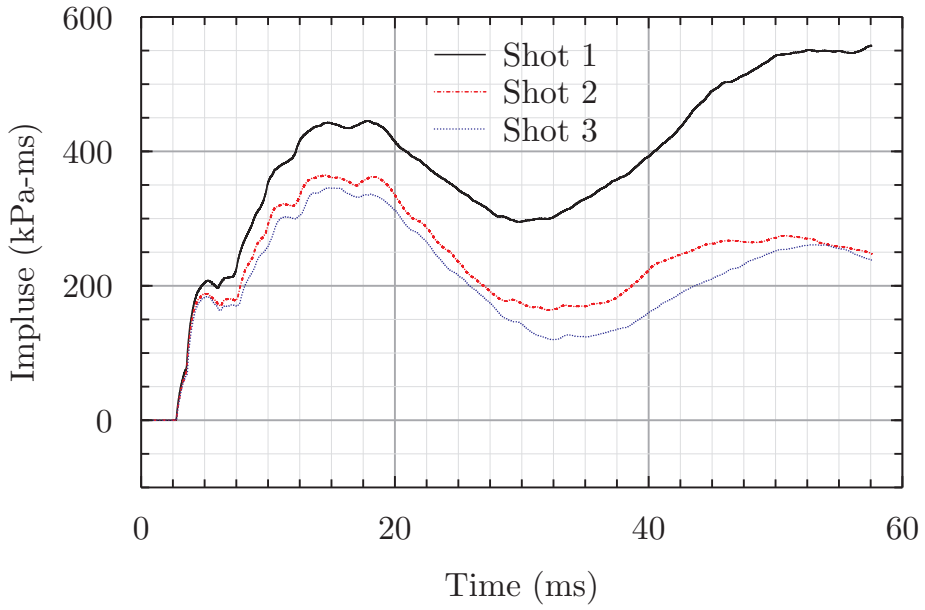

(b) Cumulative impulse

Figure G.2: Sensor 402, comparison between shots

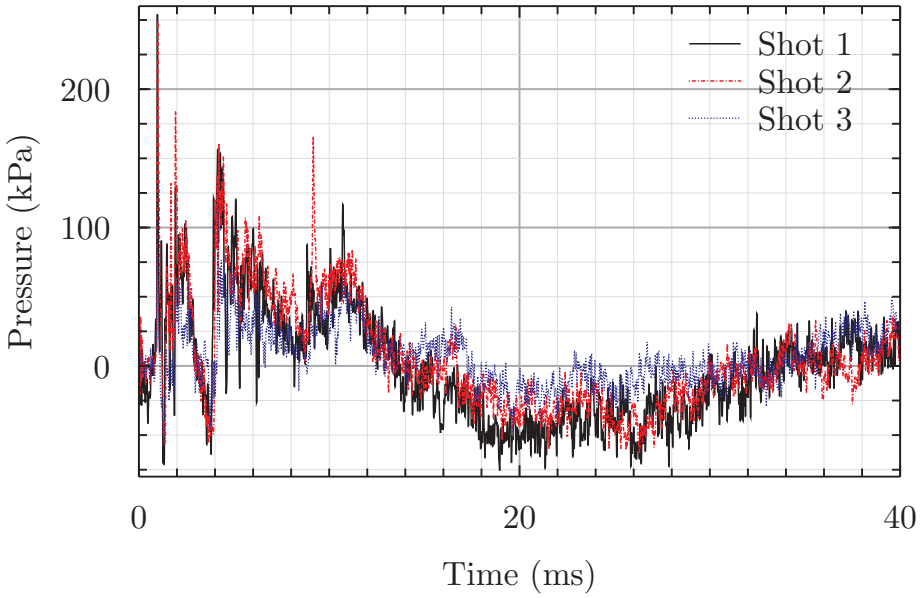

(a) Pressure

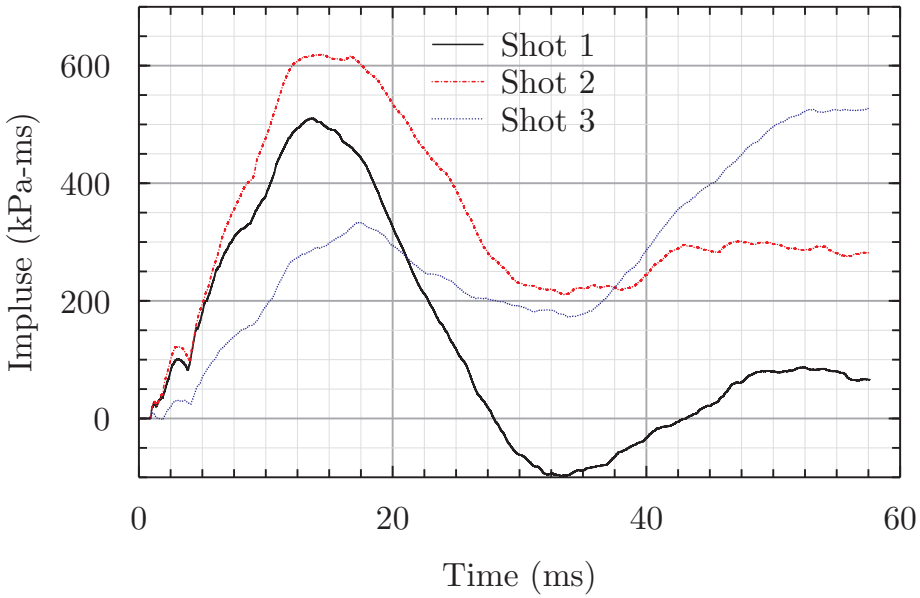

(b) Impulse

Figure G.3: Sensor 311, comparison between shots

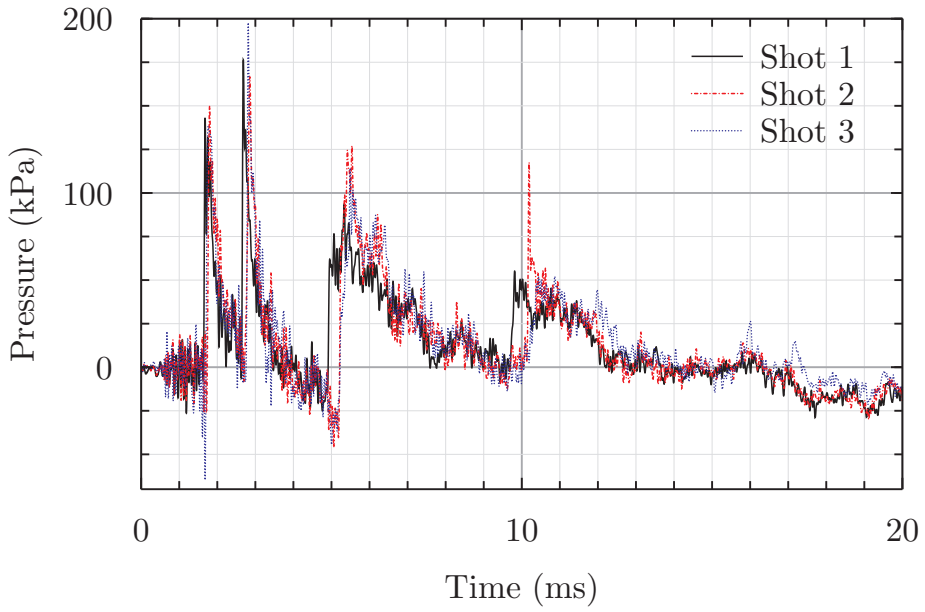

(a) Overpressure

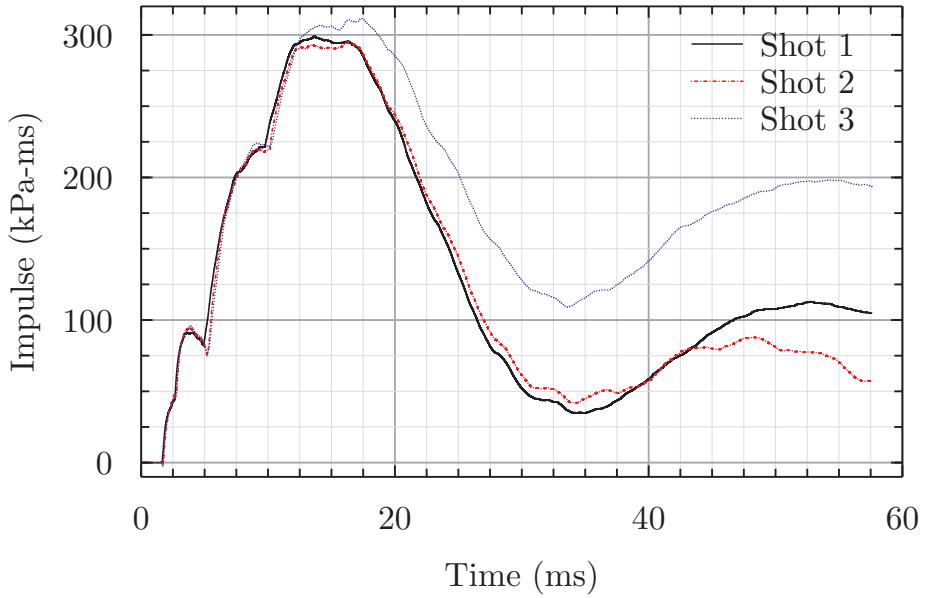

(b) Cumulative impulse

Figure G.4: Sensor 101, comparison between shots

G.2 Arrangement 2

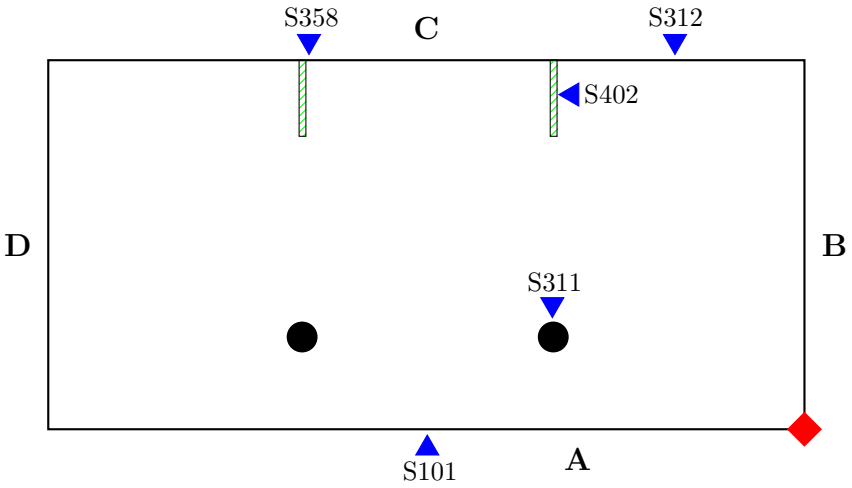

Figure G.5: Sensor locations for test arrangment 2

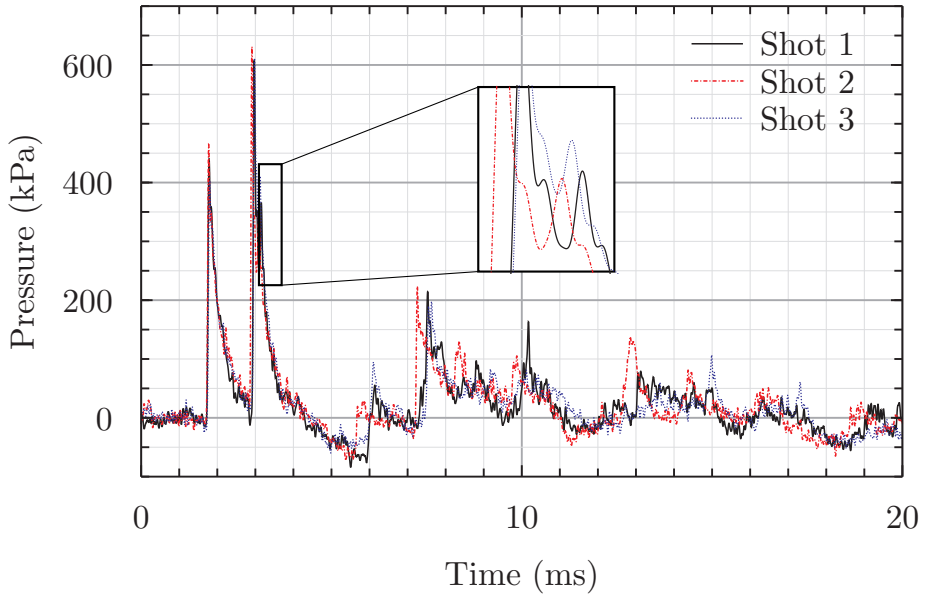

(a) Overpressure

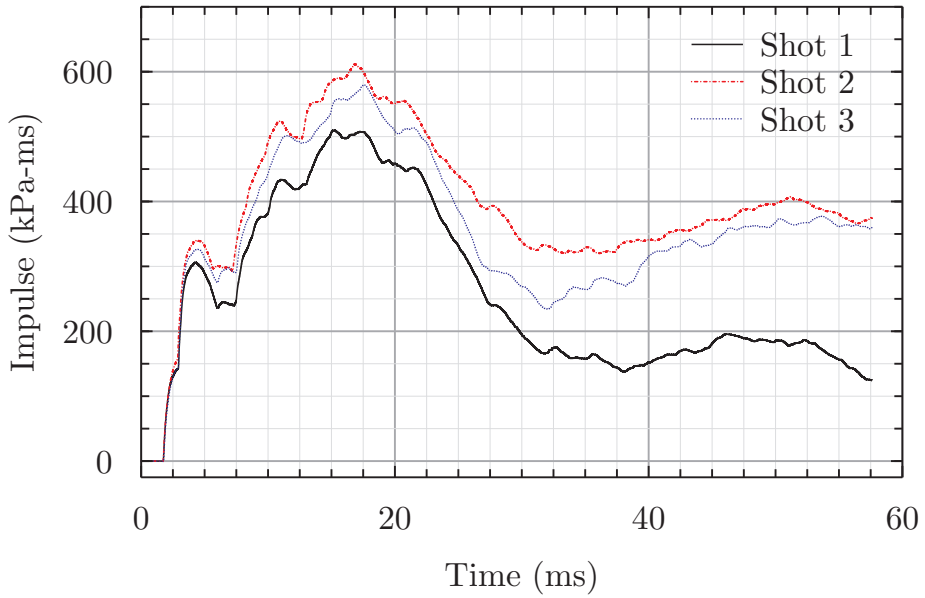

(b) cumulative impulse

Figure G.6: Sensor 312, arrangement 2, comparison between shots

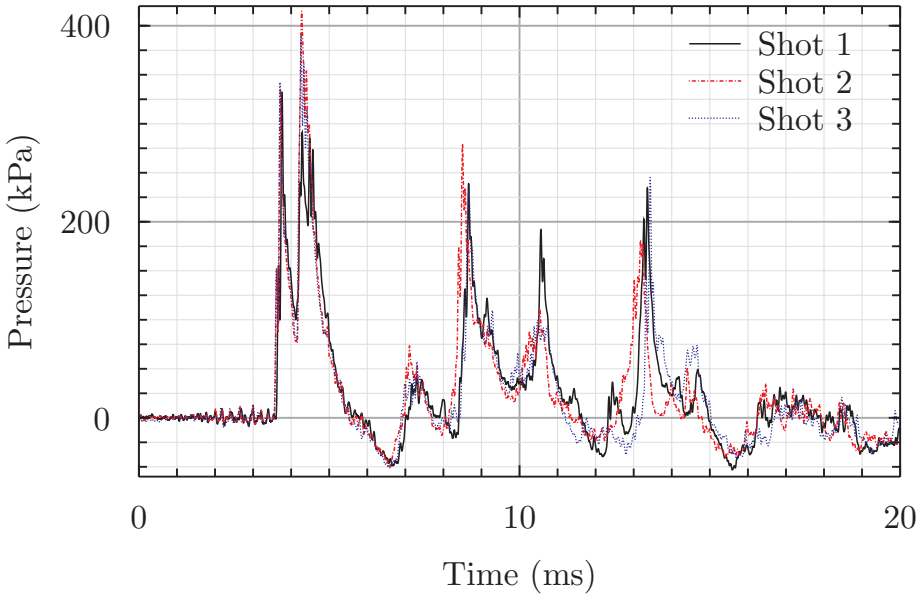

(a) Overpressure

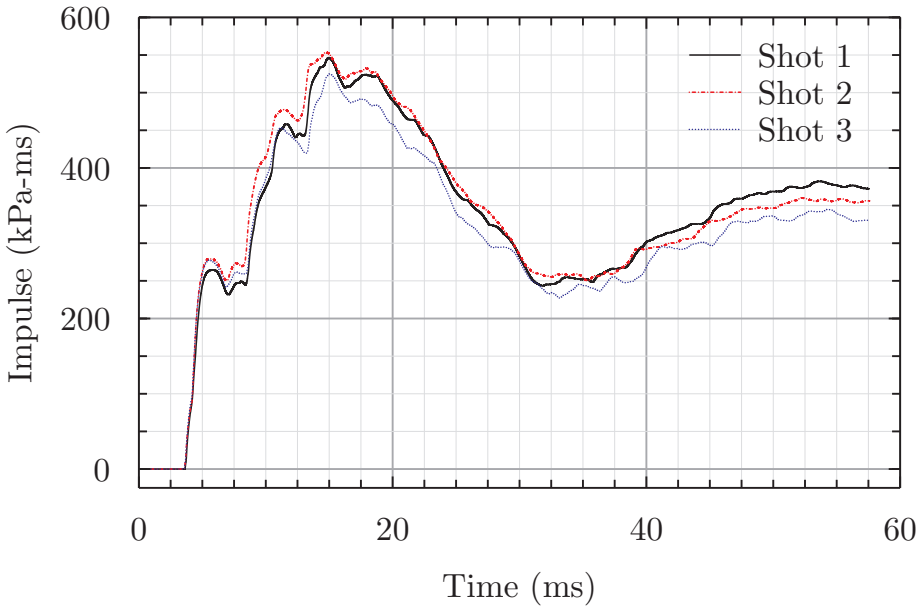

(b) Cumulative impulse

Figure G.7: Pressure and cumulative impulse data for sensor 358, arrangement 2

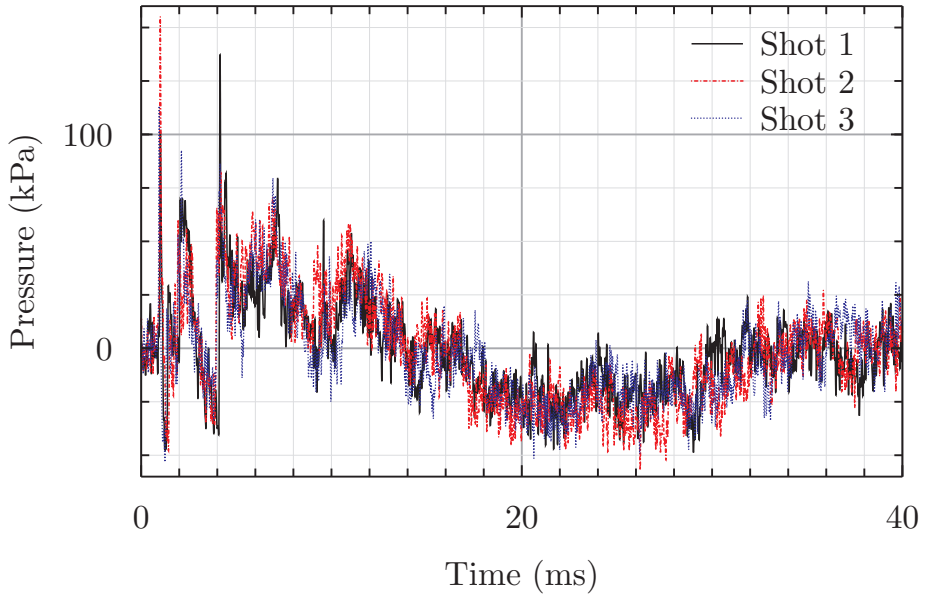

(a) Overpressure

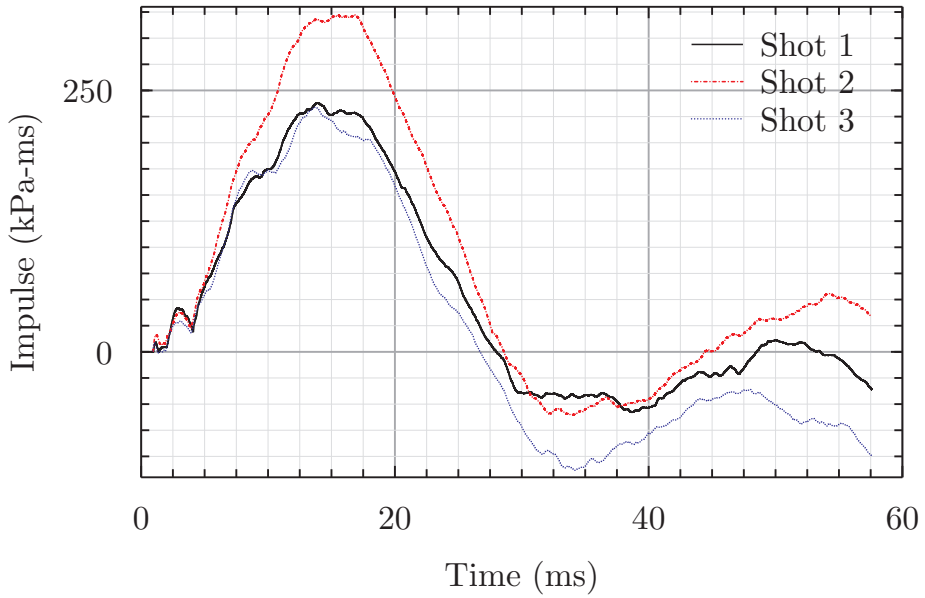

(b) Cumulative impulse

Figure G.8: Pressure and cumulative impulse data for sensor 311, arrangement 2

G.3 Arrangement 3

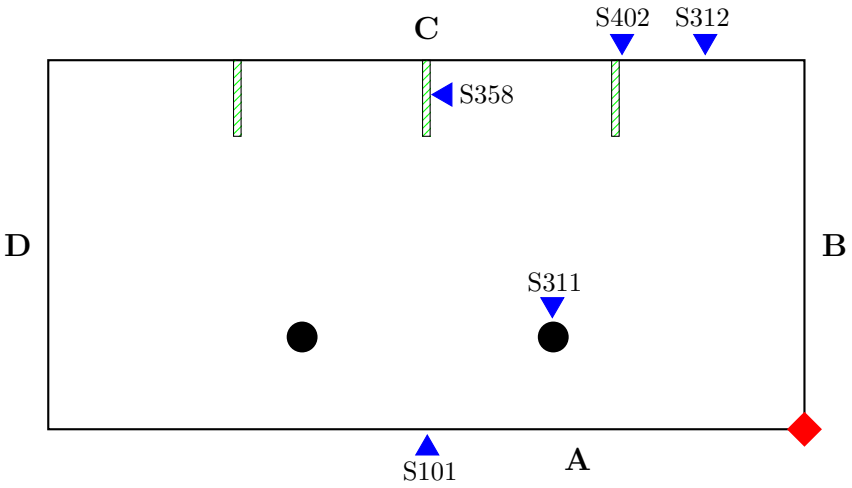

Figure G.9: Sensor locations for arrangement 3

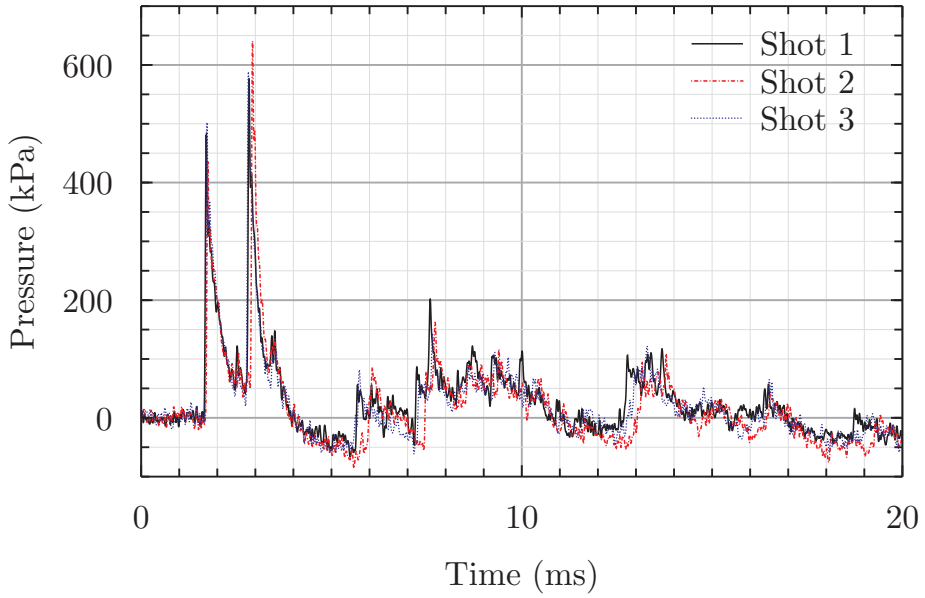

(a) Overpressure

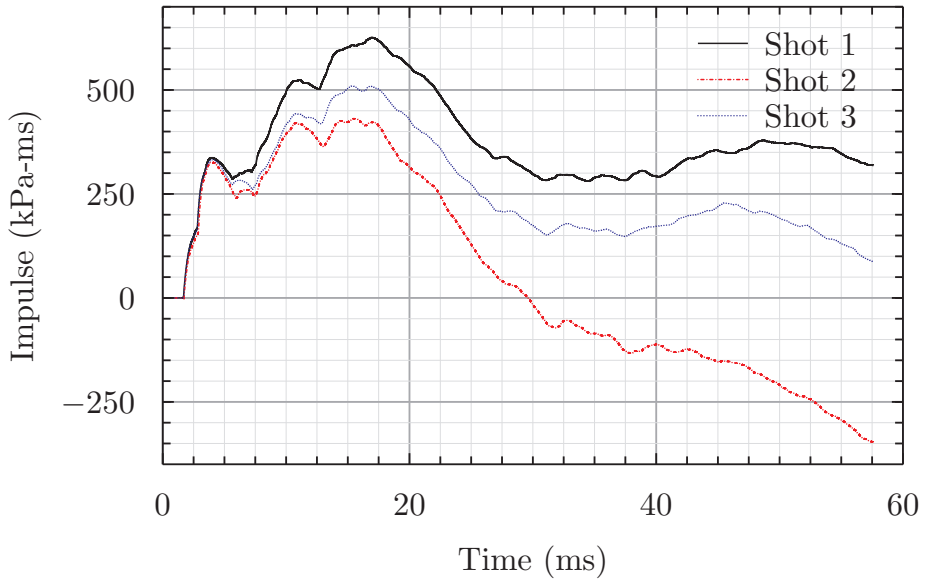

(b) Cumulative impulse

Figure G.10: Pressure and cumulative impulse data for sensor 312, arrangement 3

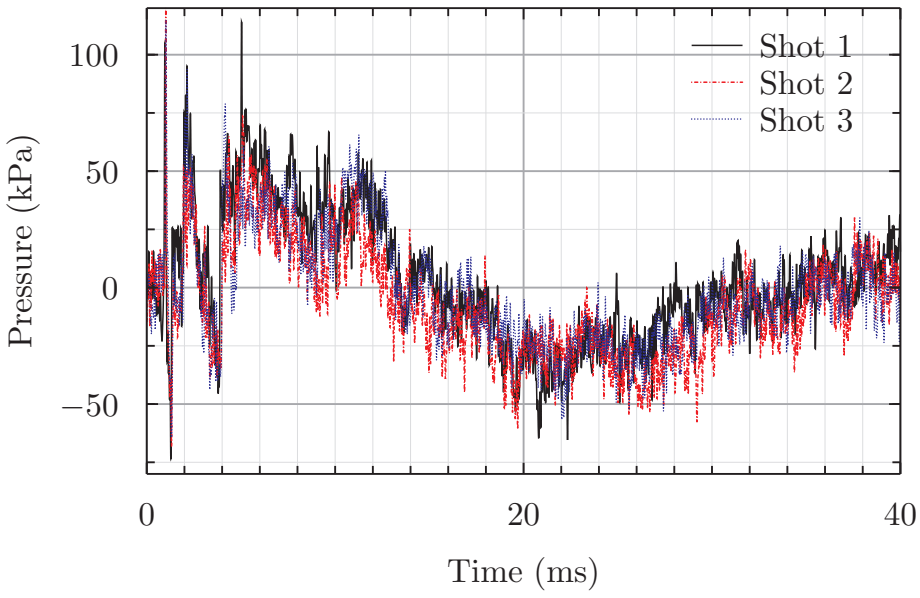

(a) Overpressure

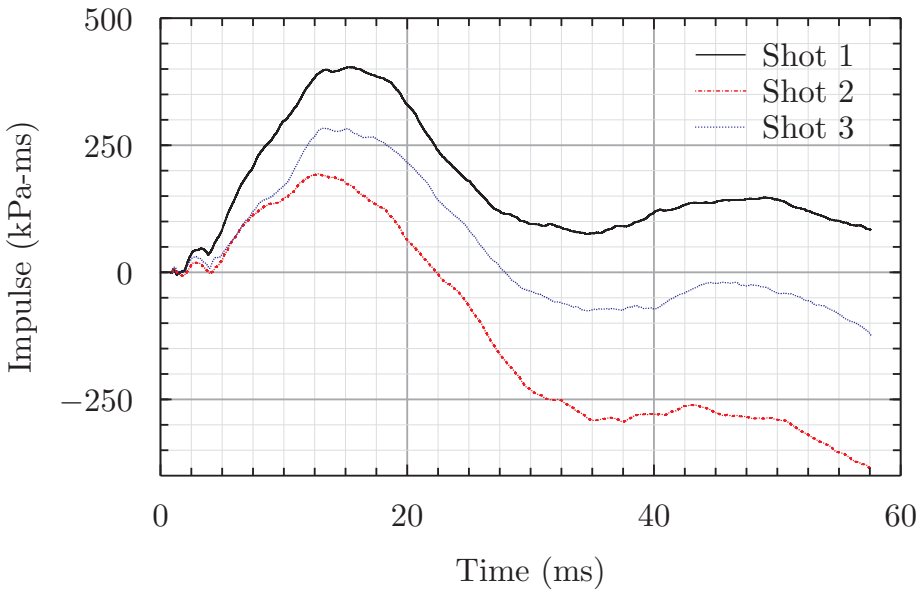

(b) Cumulative impulse

Figure G.11: Pressure and cumulative impulse data for sensor 311, arrangement 3

G.4 Arrangement 4

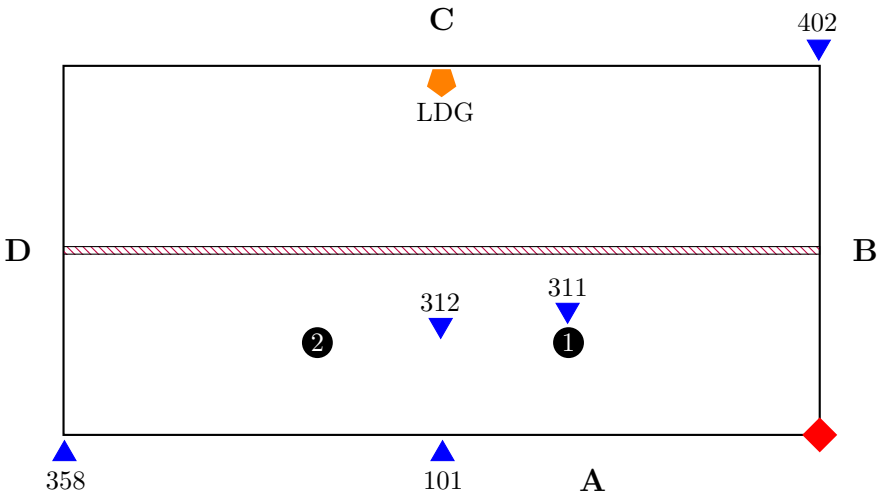

Figure G.12: Plan view of test A4

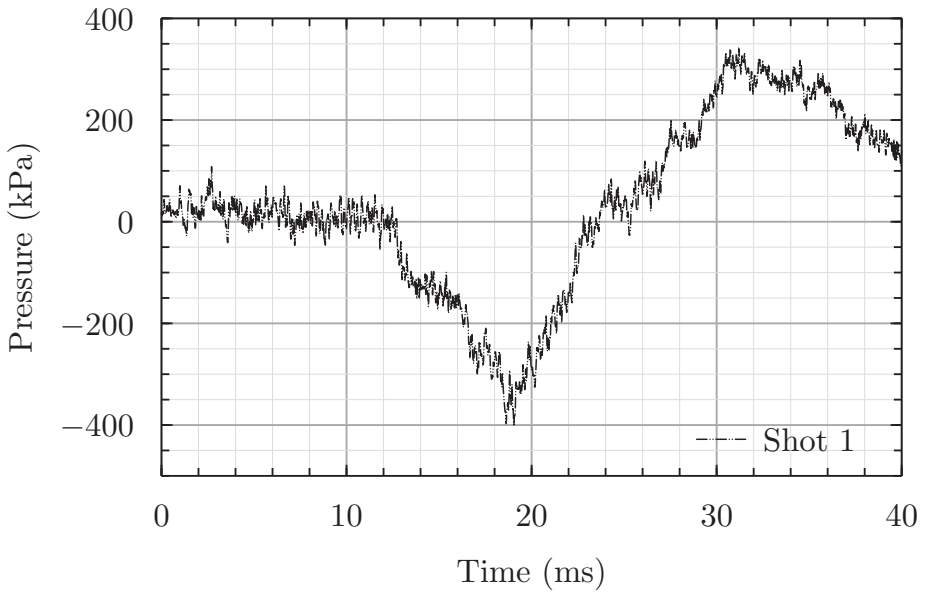

(a) Overpressure

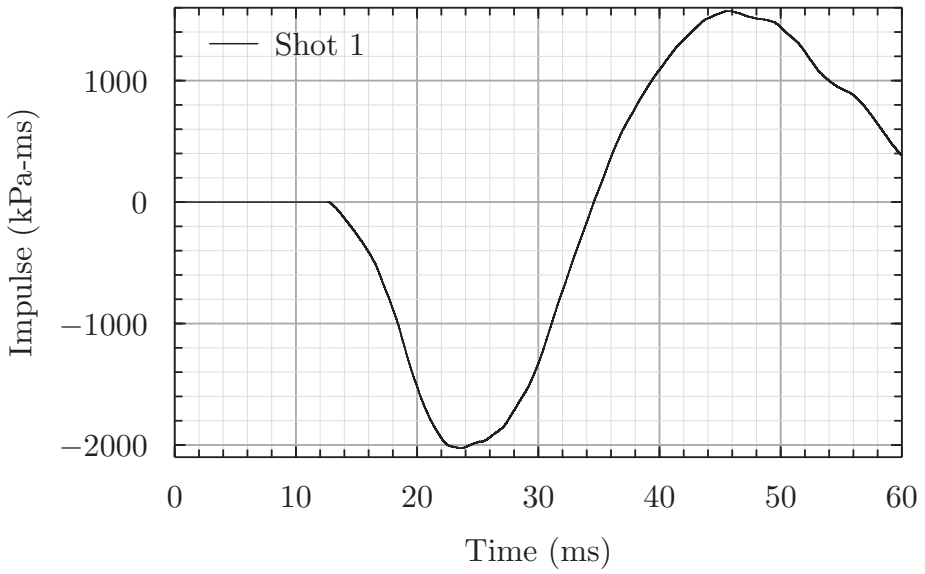

(b) Cumulative impulse

Figure G.13: Pressure and cumulative impulse data for sensor 311, arrangement 4

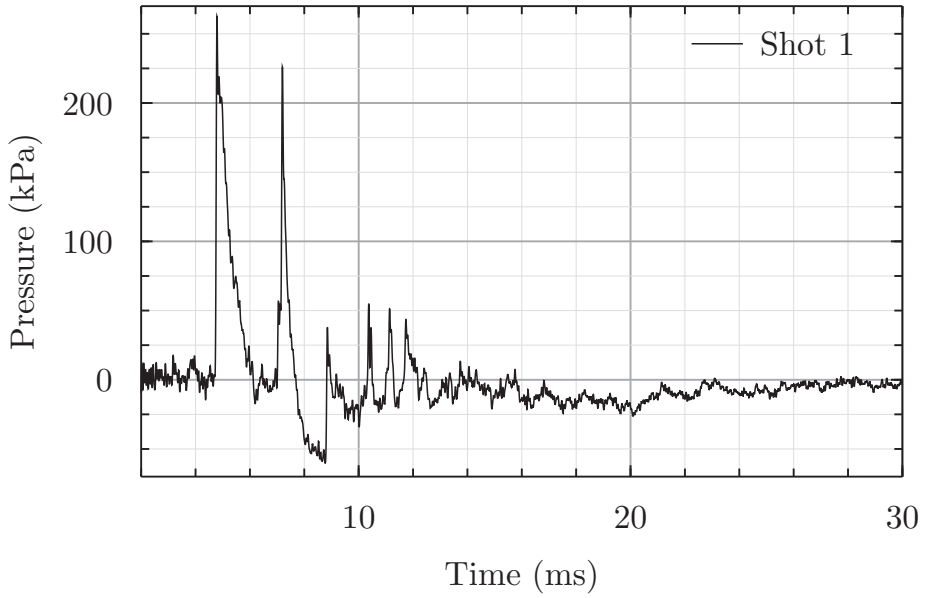

(a) Overpressure

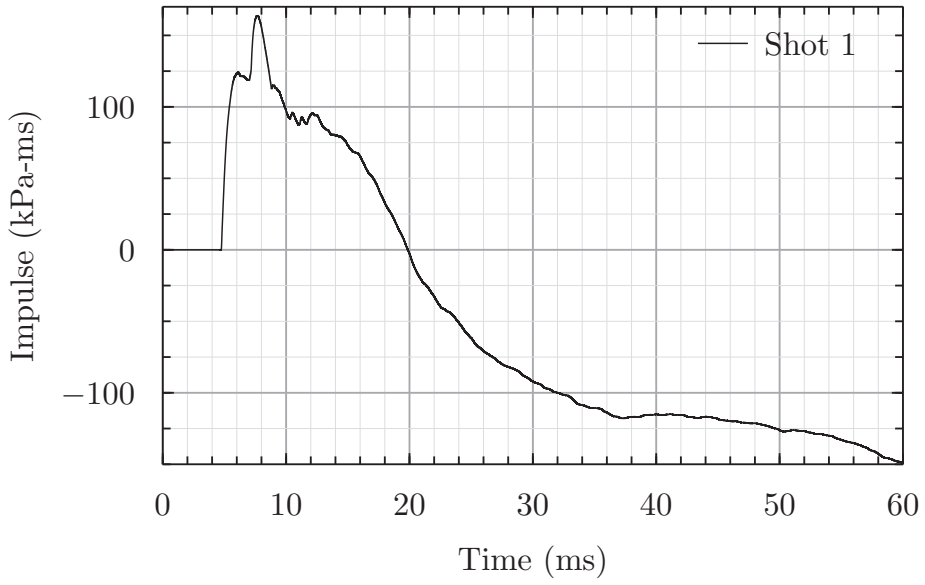

(b) Cumulative impulse

Figure G.14: Pressure and cumulative impulse data for sensor 358, arrangement 4

Appendix H

Modelling parameter study

This work was initially included within Chapter 6, but was considered an aside to the main story of this work, and has thus been moved here.

H.1 Variable study description

H.1.1 Structural boundary condition

The effects of different descriptions for the structural boundary are investigated by modifying the nodal constraints on the central boundary, and by altering the description for the outer walls of the test cell. Four separate models were generated, with different combinations of definition for the test cell walls (cell geometry) and boundaries in xy and yz planes (inner boundary). The identifier for each model and a comparison between them is shown in Table H.1. Where the CONSTRAINED_LAGRANGE_IN_SOLID (CLIS) is used and the geometry of the test cell is represented with shells elements, the air domain that surrounding the structure was chosen to be $5000 \times 2500 \times 2000$mm, shown in Figure H.1. This size is chosen because it is larger than any of the ALE domains chosen as part of the ALE domain size study, which are shown in Table H.2.

H.1.2 ALE domain size

As seen in Chapter 4, the size of the ALE domain can cause errors in pressure measurements if it is not chosen correctly. Extending the mesh boundaries in the x, y and z direction increases the number of elements present within the solution, which increases the time taken to run the model to completion time. Although it is clear an appropriate size boundary is required to ensure accuracy, it is also important to avoid unnecessary extra elements that will extend the run time without bringing significant improvements in accuracy. To achieve this, a series of models with different sizes of ALE domain were constructed, where all other parameters are kept the same as described in Section 6.2.2. The sizes of the ALE domain in x, y and z direction are shown in Table H.2, and directions are consistent with those shown in Figure 6.2.

Table H.1: Boundary condition summary

	inner boundary		cell geometry	
identifier	Fixed	Sym	NC	CLIS
A1a	0	1	1	0
A1b	1	0	1	0
A1c	0	1	0	1
A1d	1	0	0	1

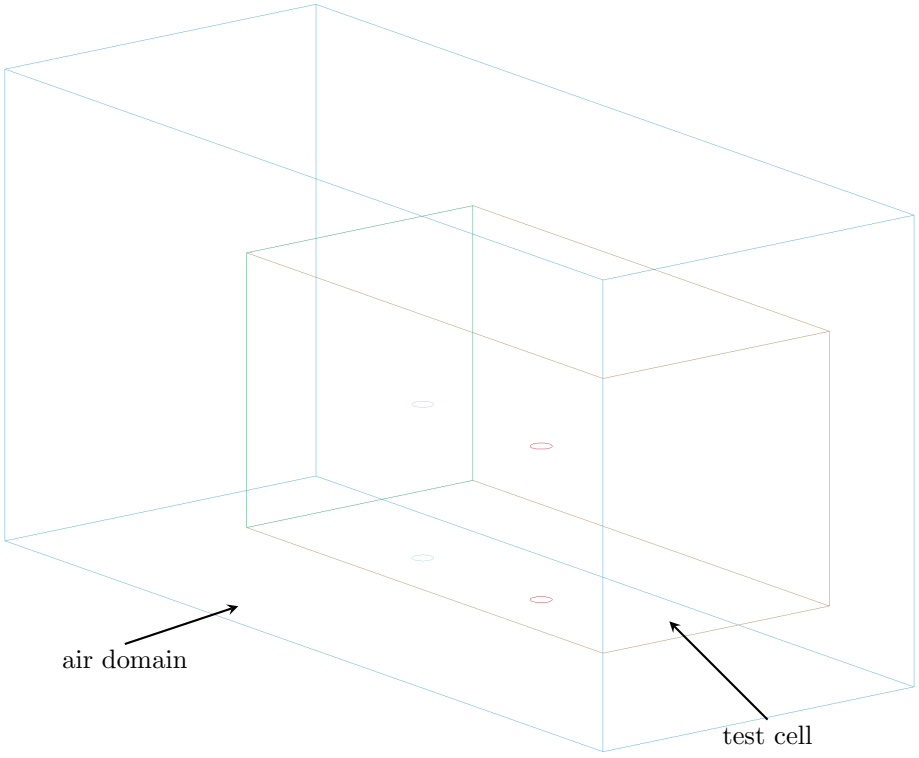

Figure H.1: Air domain and test cell configuration for A1c and A1d

Table H.2: Air domain sizes

	air domain size (mm)			ALE
identifier	x	y	z	elements
M1	3250	1700	1620	1,115,370
M2	3500	1860	1800	1,464,750
M3	4000	2200	1800	1,998,000
M4	4500	2200	1800	2,197,800
M5	5000	2500	1960	3,125,000

H.1.3 Mesh refinement

The size of the mesh elements was discussed in Chapter 4, and a similar mesh refinement study was conducted here. Three levels of refinement were chosen, as shown in Table H.3. The meshes were generated so that all elements that are enclosed by the test cell geometry are of the refined size, but outside of the test cell, where elements are included simply to extend the mesh boundaries, the value of the pressure is not so critical so larger elements can be used, helping to reduce the total number of elements. Section H.2.3 gives the results of the mesh refinement study

Table H.3: Mesh refinement levels and number of elements

identifier	primary element size	number of elements
R1	20mm	2,037,428
R2	15mm	3,482,434
R3	11mm	6,749,600

H.2 Results

H.2.1 Symmetry boundary

Figure H.2 shows a comparison between pressure histories from the 4 specified model configurations and experimental data from sensor 358 located at the end of the test cell. Comparisons are made between the model data and experimental data to confirm the most accurate of the boundary conditions. All models were run on a desktop Linux workstation using LS-Dyna R6, single precision shared memory parallel, and took approximately 14 hours using 3 CPU's.

It is obvious that there are qualitative and quantitative similarities between the results, but they also shows where specific model configurations do not provide accurate data. Both models A1a and A1b, where the geometry of the test cell is modelled by constraining nodal points on the edge of air domain, show a late and over predicted value for the first peak overpressure in Fig H.2(a) when compared to experimental data, but a very steep decay from the peak pressure which does not correspond with the decay shown in the experimental data. This is clearly seen between 6.2 and 7ms, where numerical model data from A1a and A1b show negative pressure occurring much earlier and a much higher underpressure at 7ms, compared to experimental data. Between 9ms and 10ms, and 13ms and 14ms, numerical data from A1a and A1b predicts a pressure approximately equal to atmospheric, whereas experimental data and results from A1c and A1d show pressures approximately 50kPa below atmospheric.

Impulse data in Fig H.2(b) gives a more clear idea of which models behave in the most physically realistic way. It is clear that although the peak pressure is higher for A1a and A1b, the rapid decay and early fall below zero lead to a significantly reduced impulse at 6.5ms, and a cumulative impulse that is much lower than the other models and experimental data between 6.5 and 10ms. Experimental data shows a sharp increase in impulse when a shock arrives at 10ms, but this is not shown by any numerical data at this time. Both A1c and A1d do show a rise in impulse, but delayed by 0.7ms compared to experimental data. As the pressure is negative during this time in the models, a prolonged drop in cumulative impulse occurs, which leads as well to a significant difference in the peaks seen in experimental and numerical impulse history at 11.7 and 12.4ms, but nevertheless shows good similarity between the general behaviour of the models at this point. Model data from A1a and A1b does not show this similarity in behaviour, and the shape of the curve does not show much qualitative or quantitative agreement with the experimental data.

Data from experimental sensor 101 and point 5 in numerical models is shown Figure H.3, which is located on the plane which is specified in the various models as either a fixed nodal or a symmetry boundary. A different pattern is noticed in the data at this location, with the type of boundary specified being of greater importance than the size of the air domain and definition of the test cell walls.

Pressure histories in Figure H.3(a) show models A1b and A1d over predict the peak value of the first three shock waves at 1.8, 3 and 5.5ms, as well as having a much shaper decay than the experimental results and A1a and A1c. Both models A1a and A1c predict the decay seen in the experimental results between 3 and 5ms, whereas a number of oscillations are seen in the data from A1b and A1d, which do not occur in the experimental data. All numerical models predict late arrival of the 3rd shock, and a quicker decay than that seen in the experimental data. Between 7 and 13ms, there is no significant difference between the different modelling methods, with all predicting later arrival of shocks at 7.5 and 10.2ms than is seen in the experimental results. The effect of this late arrival can be clearly seen in Figure H.3(a), and as negative phases continue for longer than happens in reality there is a significant drop in the cumulative impulse.

The results above point to a clear single method that is the most appropriate, A1c, which performs in the most realistic manner at both point 3 and point 5. Although the data after 10ms doesn't match the experimental data quantitatively, it shows the same trend in the cumulative impulse that is seen in the experimental data, which is not shown in any way in the other models. In the current model, A1c under predicts peak pressures and predicts later arrival than occurs in reality, both of which are expected given the coarseness of the mesh, demonstrated in Chapter 4. This combination of model

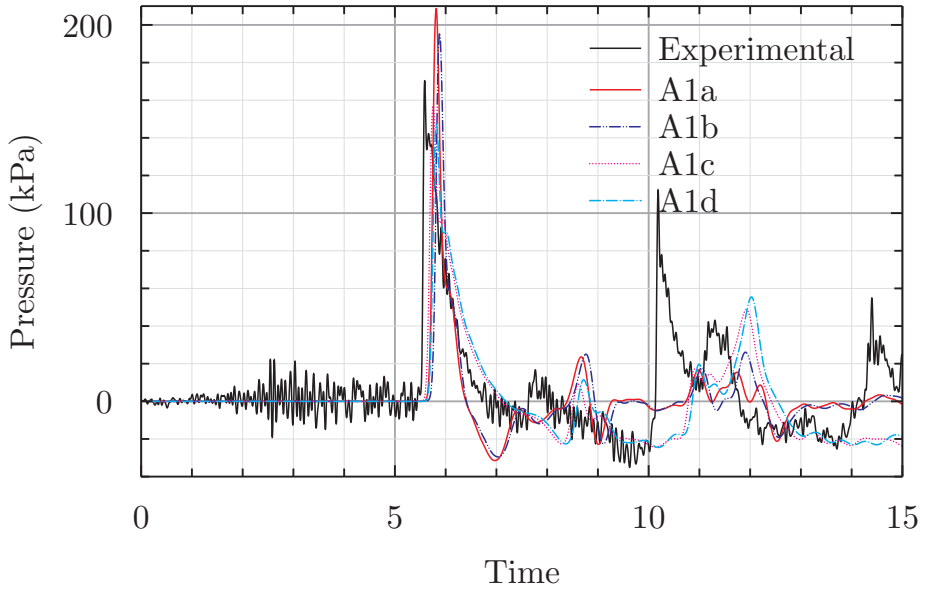

(a) Pressure history

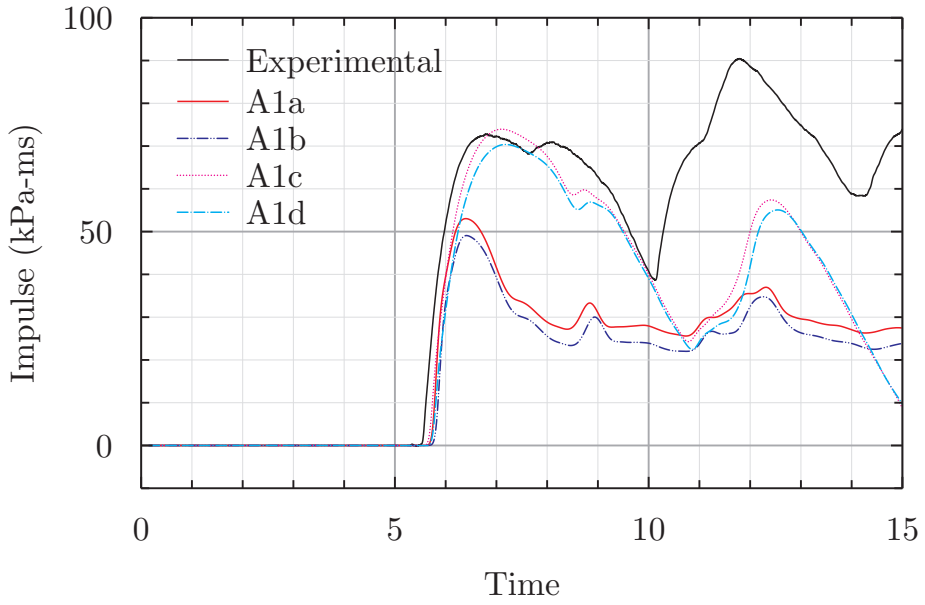

(b) Cumulative impulse

Figure H.2: Data for the 4 model configurations at sensor 3, compared with a single series of experimental data from sensor 358

parameters for the test cell geometry and inner boundaries provides a base from which further improvements can be made to the model.

H.2.2 Free air boundary and air domain size

Effects of ALE domain size were considered using a series of 5 models with different ALE domain sizes. As above, runs were completed on a Linux desktop using LS-Dyna R6, and took between 5 and 15 hours to run to completion at 15ms. The sizes of the model air domain and identifiers for each model are shown in Table H.2.

The effects of changing the size of the ALE boundary on pressure and impulse histories can be seen in Figures H.4, H.5 and H.6. It is clear from Figure H.4 that the size of the boundary makes negligible differences to either the pressure or cumulative impulse at sensor point 1, which was anticipated. The magnitude of the boundary effect is small compared to the pressure of the shocks created by the detonation, and any boundary

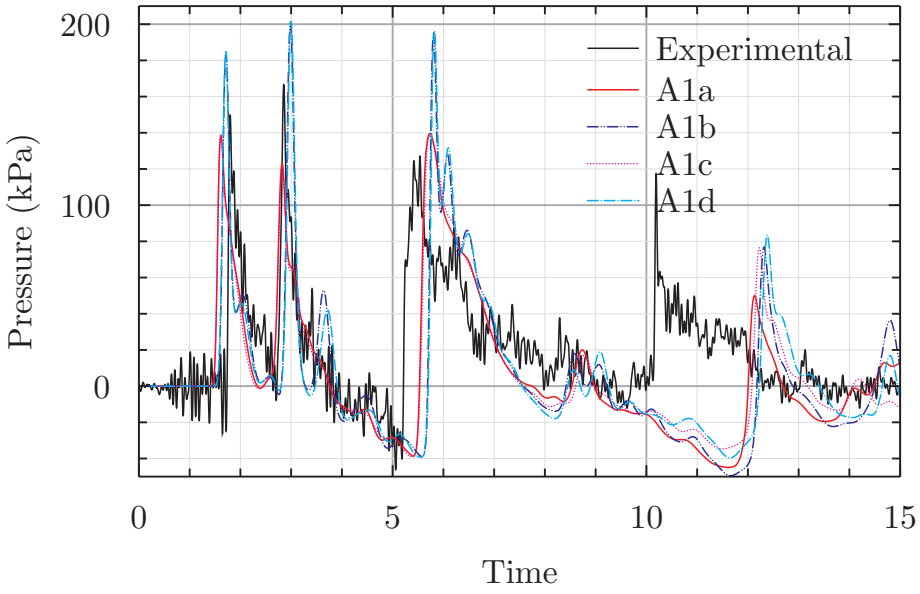

(a) Pressure history

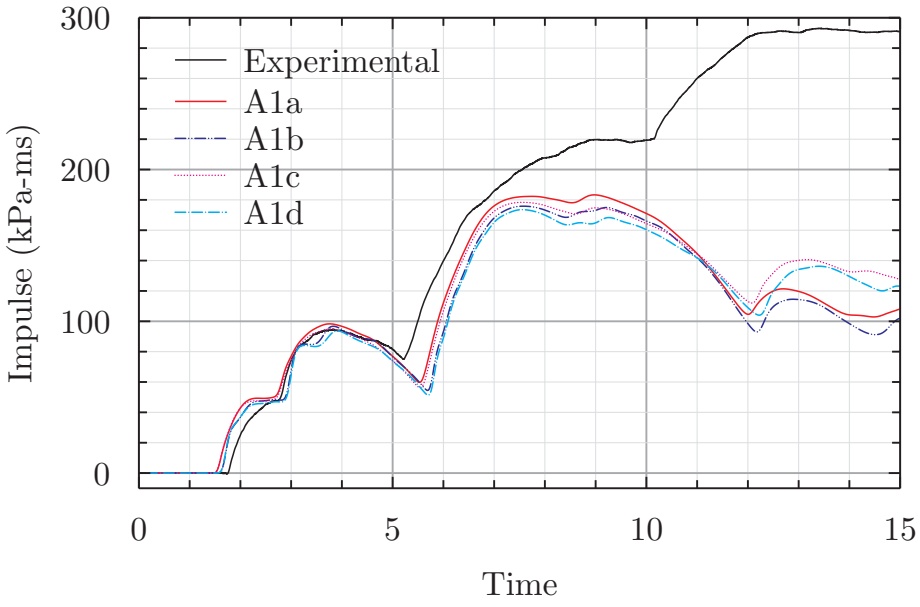

(b) Cumulative impulse

Figure H.3: Data for the 4 model configurations at sensor 5, compared with a single series of experimental data from sensor 101

effects have a larger distance travel to alter the pressure near the detonation end of the test compared with open end of the test cell, both of these effects ensuring that no boundary effects are seen at point 1.

Data at sensor point 2, shown in Figure H.5 shows generally the same behaviour from all ALE domain sizes, but towards the end of the solution boundary effects are visible in the pressure history in M1. At 13.6ms in Figure H.5(a), a pressure jump is visible in the data from M1, where other models do not display this jump. Figure H.5(b) shows that the impulse in M1 begins to deviate from other models at 12.6ms, and crosses the decreasing cumulative impulse curve for other meshes at 14ms.

As expected from previous models, boundary effects are much stronger when data is taken close to the boundary in question. Figure H.6(a) shows that pressures in M1 and M2 for location 3 begin to deviate from others significantly beginning at around 9ms. Between 9ms and 11ms and the pressure at point 3 in M1 rises while for others it falls,

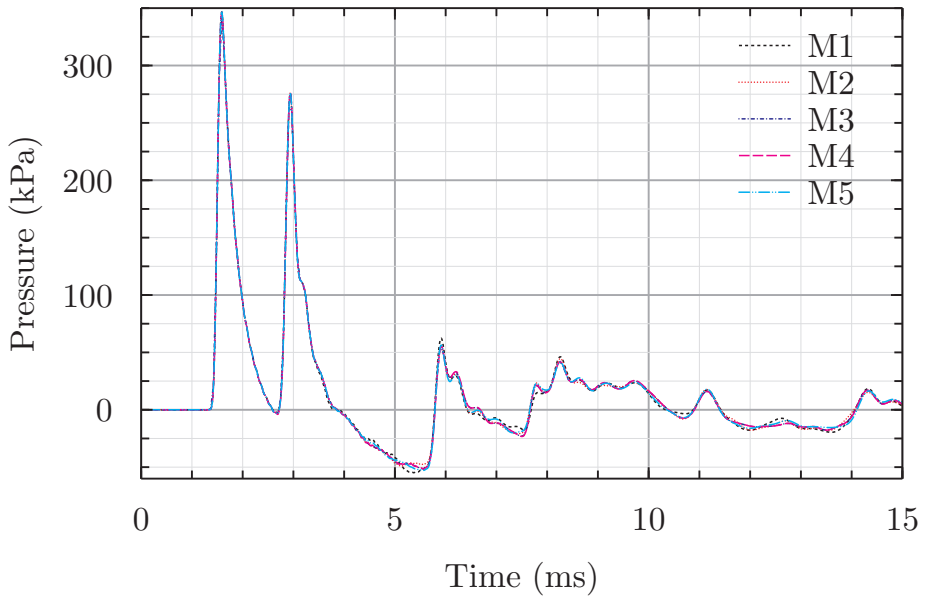

(a) Pressure history

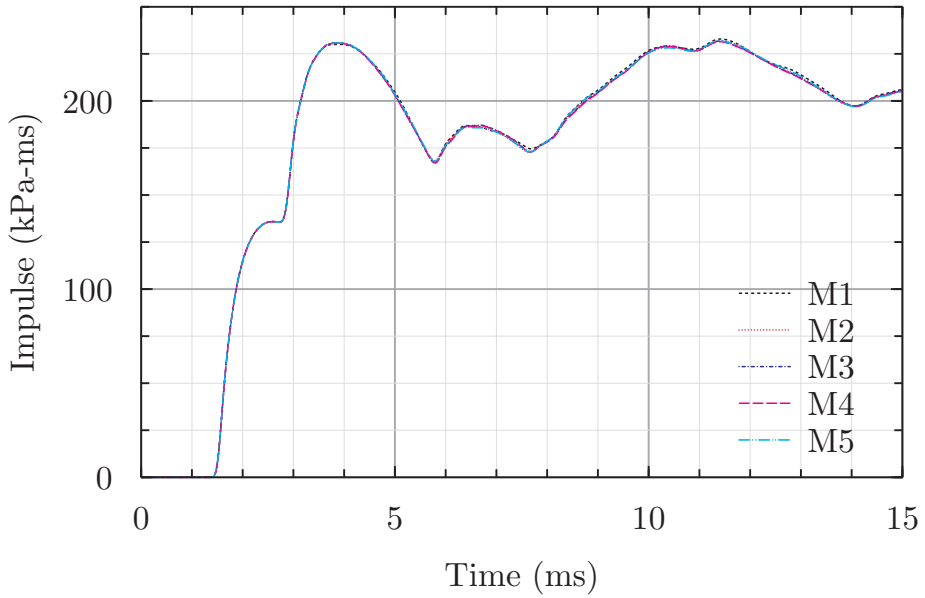

(b) Cumulative impulse

Figure H.4: Pressure and cumulative impulse history for five different ALE domain sizes at model measurement location 1

leading to a 50kPa difference in pressure between M1 and the model with the largest domain, M5. Beyond 12.5ms, significant rises and oscillations are seen in both M1 and M2, and corresponding impulses in Figure H.6(b) begin to deviate significantly from those seen in M3, M4 and M5.

It is clear from Figure H.6 that the ALE domains M1 and M2 are unsuitable, as both lead to boundary effects that add non-physical pressures to the results. It appears that the distance from the open end of the test cell is critical, and that the solution is more sensitive to the size of the ALE domain in the x direction than z direction. Although not identical, mesh extensions in M3, M4 and M5 make little significant difference to the pressures and impulses at sensor location 3 up to 15ms. It is therefore necessary that ALE domain dimensions are at least as large those for M3, as shown in Table H.2.

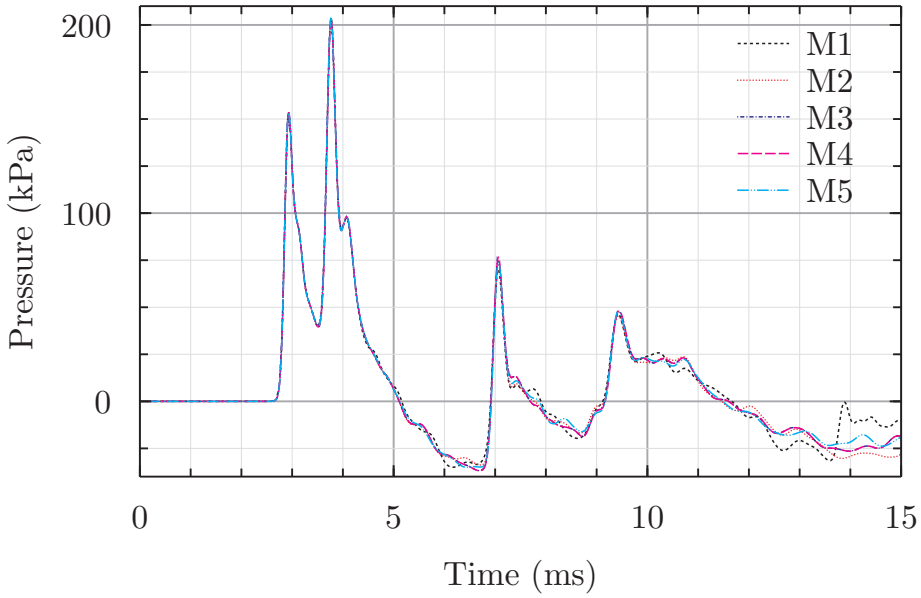

(a) Pressure history

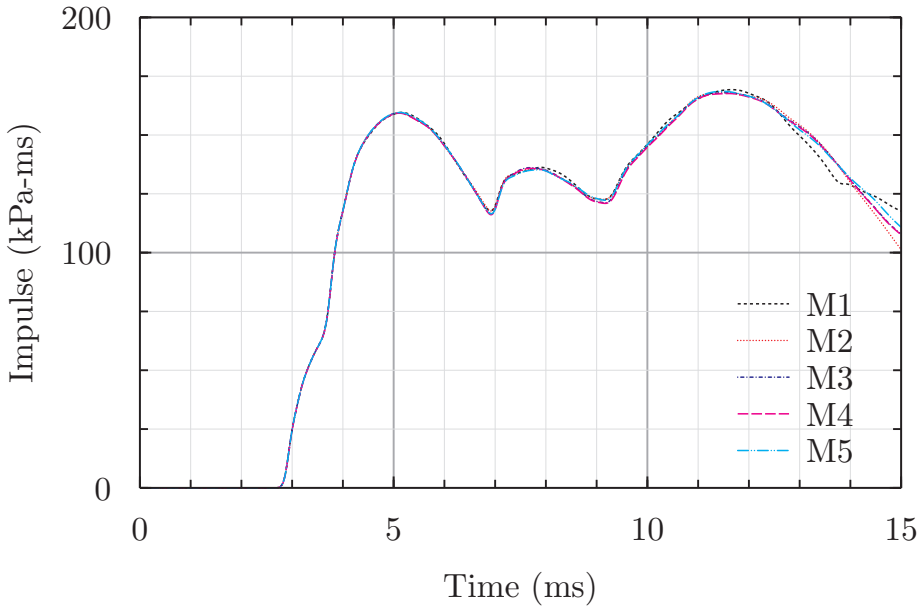

(b) Cumulative impulse

Figure H.5: Pressure and cumulative impulse history for five different ALE domain sizes at model measurement location 2

H.2.3 Mesh refinement

It was seen in Chapter 4 that the size of the ALE domain could make significant differences to the peak pressure and impulse predicted by numerical models. Figures H.7, H.8 and H.10 show the pressure history and cumulative impulse for three numerical models of the experimental arrangement A1 each with different levels of mesh refinement.

Pressure histories in Figure H.7(a) show only a limited difference between the results for the three different meshes. The first shock arrives at 1.4ms across all levels of mesh refinements, and the gradient of the rise to the first peak pressure is also very similar between all 3 meshes, shown more clearly in Figure H.9(a). The peak pressure at this first shock is similar between the 10mm and 15mm mesh at 390kPa, but the 20mm mesh predicts a peak value of 340kPa. All of these values are lower than the measured experimental value of 510kPa, and the peak pressure 0.2ms earlier in the

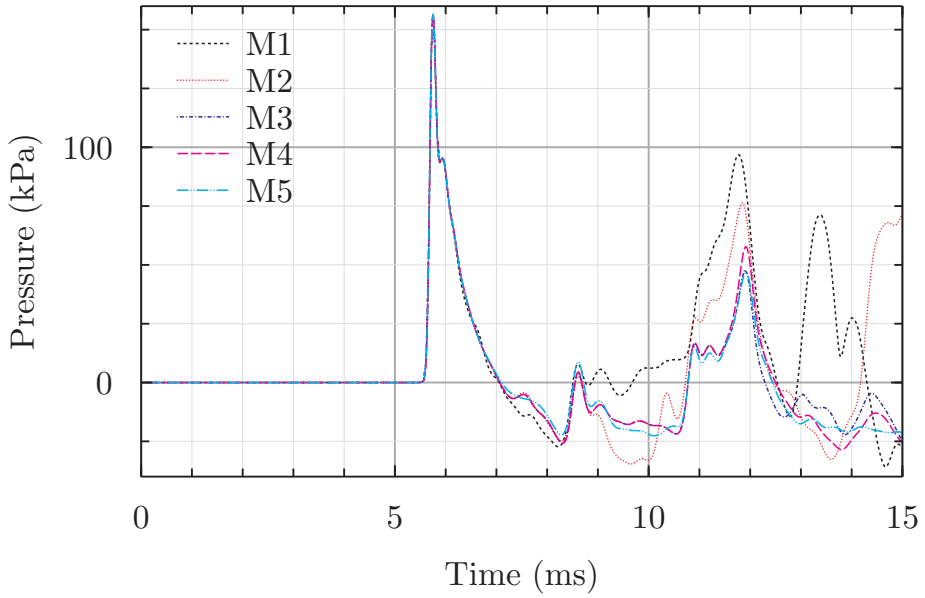

(a) Pressure history

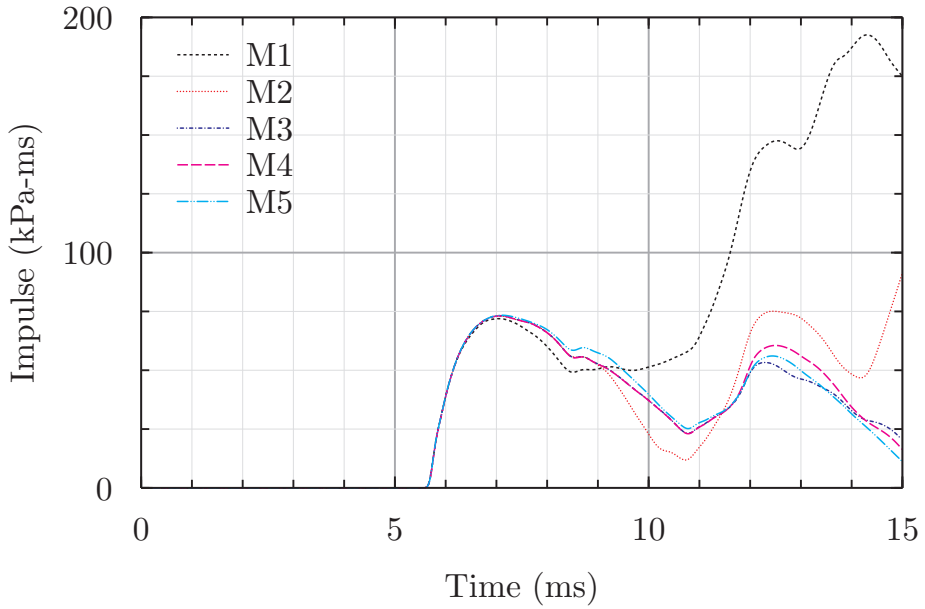

(b) Cumulative impulse

Figure H.6: Pressure and cumulative impulse history for five different ALE domain sizes at model measurement location 3

models compared with experiments. The arrival time of the second shock is predicted similarly by all three models, and compares well with the experimental time of 2.8ms. The peak pressure of the second shock is noticeably underpredicted by all the models compared to experimental results, but with each level of mesh refinement delivering a 40kPa increase in the predicted peak pressure, with the 20mm model predicting a peak of 270kPa, and the 10mm model predicting 350kPa, compared to the experimental value of 760kPa. The decay is predictions from all 3 models match well with each other and experimental results, and the arrival time of the third shock at 5.7ms is also well predicted. At this point the shape of the numerical and experimental data curves begin to diverge, with the rise much slower in numerical models than seen in experimental data, although the subsequent decay is somewhat predicted by numerical models, again with little noticeable difference between them. Numerical models miss the shocks 7.5ms and 12.8ms, but all three models predict reasonably the pressure behaviour seen in

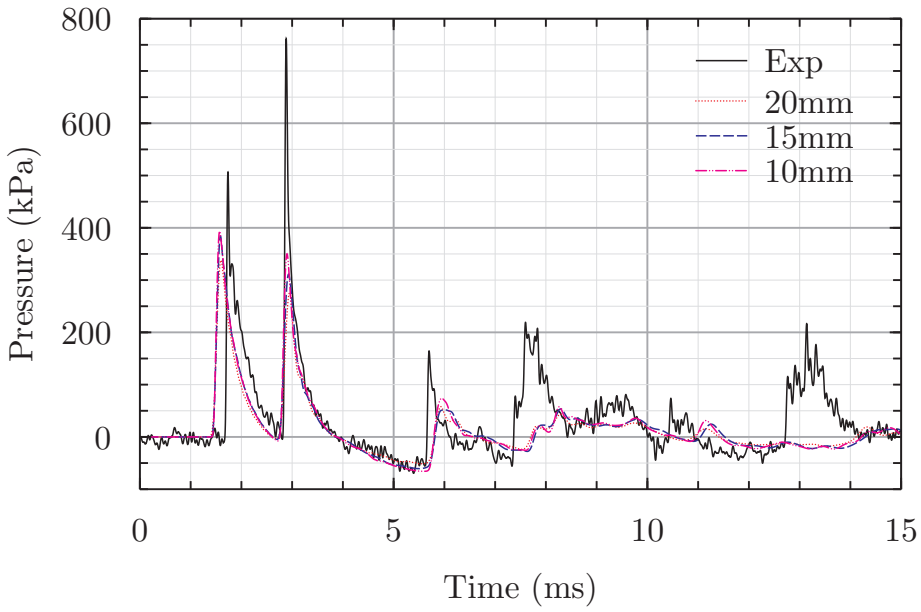

(a) Pressure history

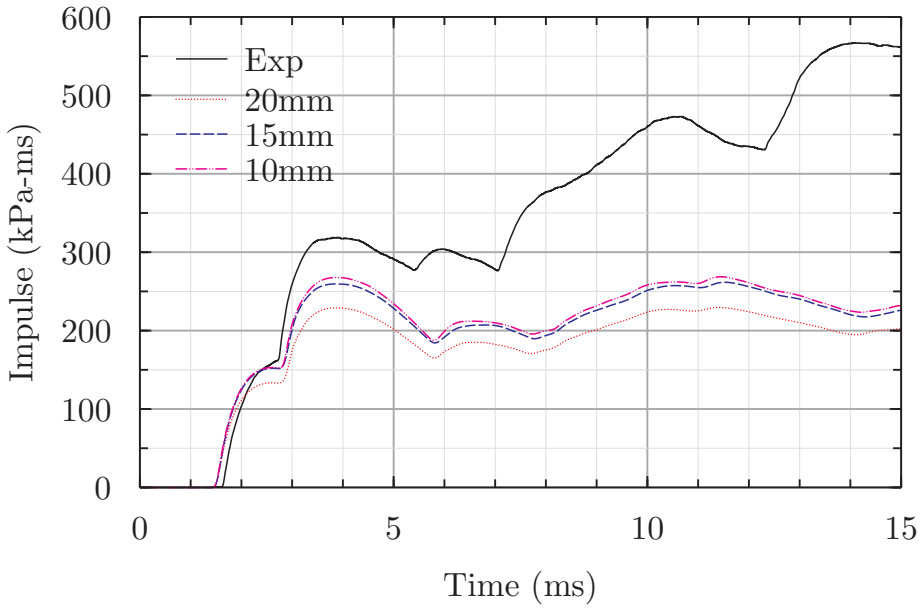

(b) Cumulative impulse

Figure H.7: measurement location 1 in 3 separate numerical models, showing the effect of increasing mesh refinement

experimental data between 8 and 12.5ms.

Differences between levels of refinement are clearer in the impulse curve shown in Figure H.7(b). The model with the coarsest mesh shows a consistently lower impulse than seen in other models, primarily due to differences in the pressure over the first 2 shocks, as the difference remains constant over the remaining time between 4ms and 15ms, indicating the pressures are very similar between all models. Although the magnitude of the impulse is under predicted by the models compared to experiments, the features and shape of the impulse curves up to 12ms compare reasonably, with a sharp divergence in shape only seen once the shock arrives in the experiment at 12.7ms, where a negative pressure is predicted by the models.

Data from Figure H.8 shows similar behaviour of the models at measurement location 2, compared to sensor location 1 discussed above, but showing better similarity between

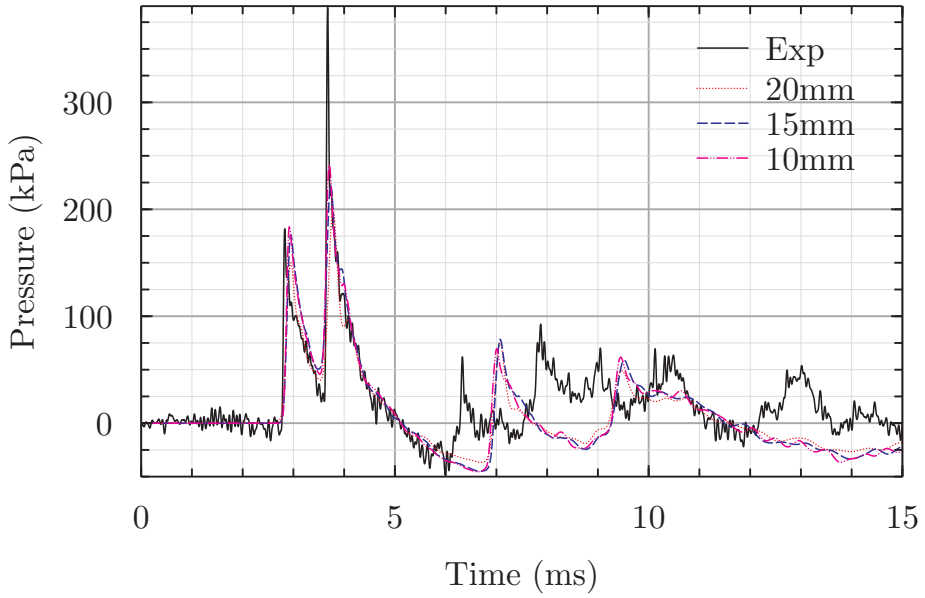

(a) Pressure history

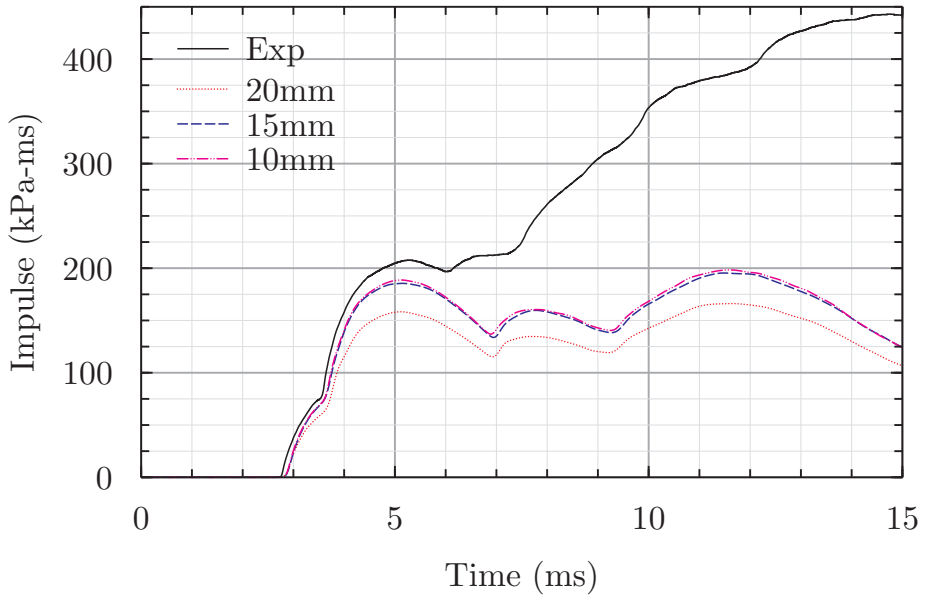

(b) Cumulative impulse

Figure H.8: measurement location 2 in 3 separate numerical models, showing the effect of increasing mesh refinement

model data and experimental data. The arrival time of the first shock is the same for all 3 models and the experimental data, and the peak experimental pressure for this first shock of 180kPa is predicted well by both the models with 10mm and 15mm mesh, but less well by the 20mm model, as shown in more detail by Figure H.9(b). The arrival time of the second shock is also predicted well between different models and experimental data, and as with previous models the second shock is under predicted by models compared to experimental data, with subsequent refinement showing increases in peak pressure. The third shock in Figure H.8(a) is well predicted in shape and magnitude by all models, but the arrival time is later by 0.8ms, with the peak values 0.7ms apart. The subsequent decay, negative phase and fourth shock seen in experimental data is predicted in magnitude by all models, but there is time difference of 2.4ms between peaks as opposed to 1.7ms in experimental data.

Impulses at sensor location 2 from Figure H.8(b) show a closer agreement between

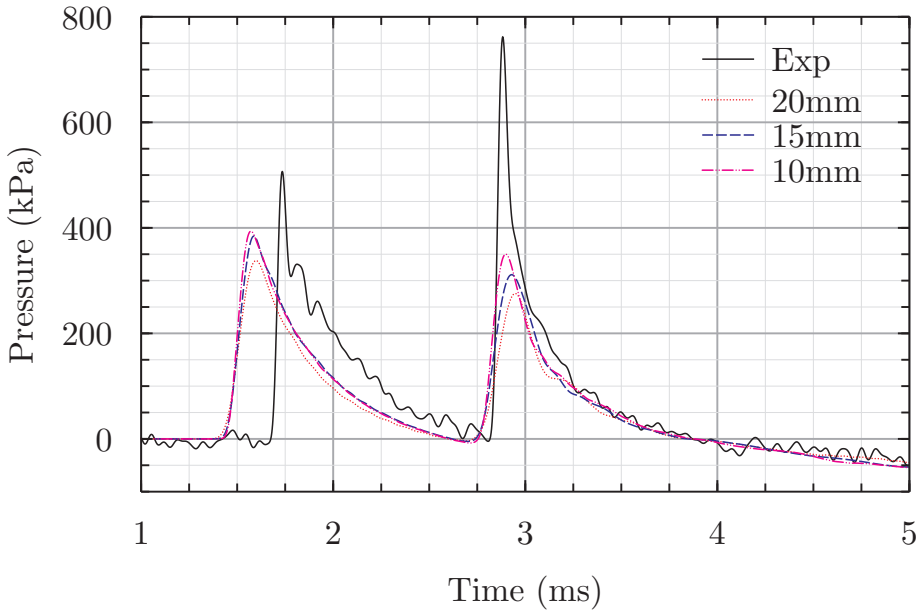

(a) Pressure history for sensor point 1 in numerical models

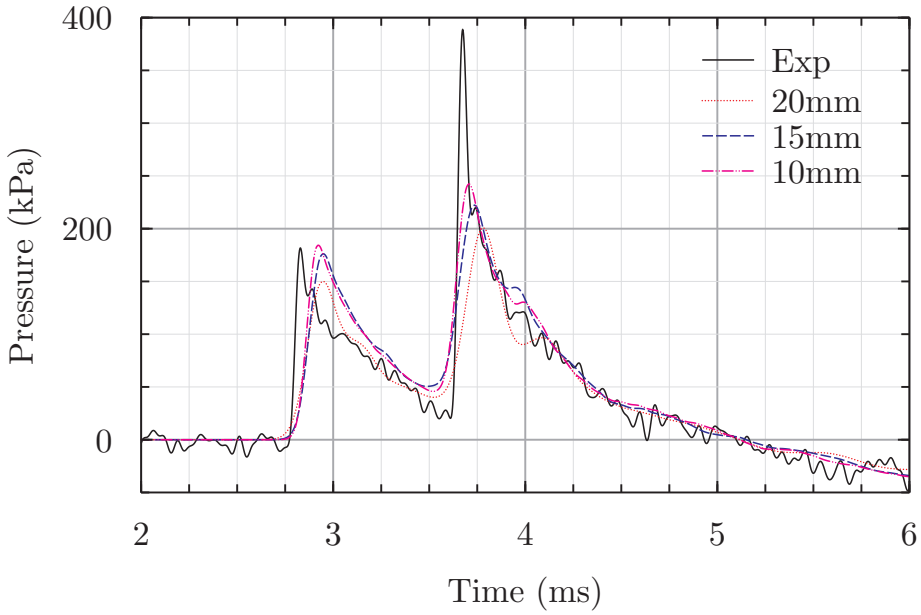

(b) Pressure history for sensor point 2 in numerical models

Figure H.9: Pressure histories plotted over 5ms for two different measurement locations with three levels of refinement, showing how refinement alters the peak pressure

the 15mm and 10mm mesh than seen at location 1, but similarly shows a greater under prediction by the coarser 20mm mesh. Impulses up to 5ms are well predicted by the finer 2 models, but the extended negative phase before the arrival of the of the third shock leads to a larger drop in the impulse in the models compared to the experimental data. The longer gap between peaks of third and fourth shocks in the model compared to experiment also reduces the impulse compared with experimental data. The pressure in the model becomes negative at 12ms, whereas there is a rising positive pressure in the experimental, so cumulative impulses between all three models and the experiment begin to diverge at this point.

Figure H.10 shows pressure and cumulative impulse histories for data sensor location 5, again showing good agreement between the three models and experimental data, but with a smaller difference between experimental data and the predicted pressures from

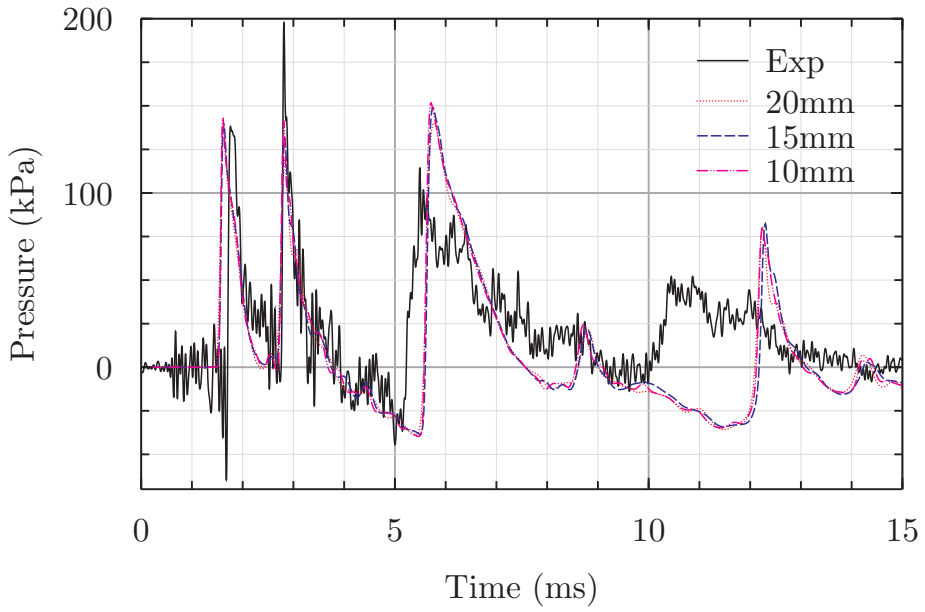

(a) Pressure history

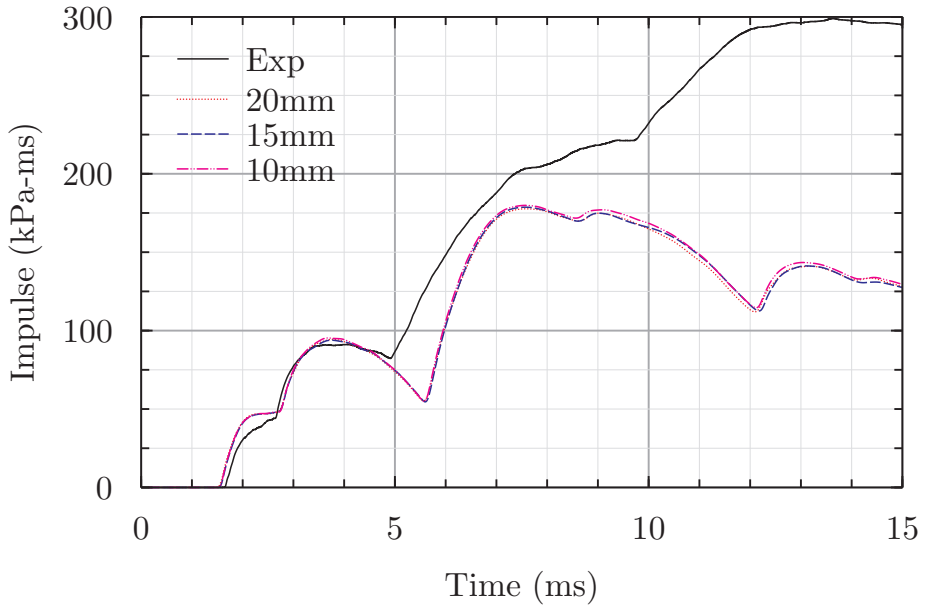

(b) Cumulative impulse

Figure H.10: measurement location 5 in 3 separate numerical models, showing the effect of increasing mesh refinement

the three different models. The first shock arrives slightly earlier in the three numerical models than seen in the experiment, shown in Figure H.10(a), but all three models predict the peak pressure of 140kPa. The arrival and decay of the second shock is also predicted well by all three models, although the peak pressure here is under predicted by 50kPa. The third shock in the numerical model over predicts that seen experimental value and decays slightly faster, with an extra shock in the numerical result at 8.5ms that is not seen in the experimental data, although some real features of the experimental data are obscured by some signal noise. A shock wave arrives at 10ms in experimental data, but the pressure remains negative until 12ms in the model data, leading to the increase in rate of deviation between model and experimental data at 12ms, shown in Figure H.10(b), and the discrepancy between the model and the experimental data is maintained over the measured time.

The models presented here show that the mesh size can affect the overall accuracy of the predictions made by the numerical models. In all three models, the second shock was significantly under predicted and subsequent mesh refinement operations show that the peak pressure increases as the element size decreases, but the level of refinement that would be required to accurately predict this second peak pressure would lead to a an exceptionally large model, most likely with elements as small as 1 or 2 millimeters. For elements of 1mm, to model the inside of the test cell alone (not including the required extension of the air domain to limit boundary effects) would require 6.35×10^9 elements. This would likely require thousands of gigabytes of RAM and hard disk storage space, which is not currently available. Other features of the model show little change with mesh refinement, and for the three model measurement locations shown here, little if any difference is seen between the cumulative impulse histories for the 10mm and 15mm meshed models. This indicates that the mesh resolution is unlikely to be responsible for differences between experimental data and model data.

Appendix I

Vehicle pressure time histories

Pressure time histories from passenger positions in rail vehicle models are presented here, which accompany the discussions presented in Chapter 7. Sensor naming convention of S1 to S4 for each passenger is the same as used in Chapter 7, with S1 facing towards the vehicle aisle, S2 towards the point of detonation, S3 towards the vehicle bodyside and S4 towards the vehicle end.

I.1 C1 to C4

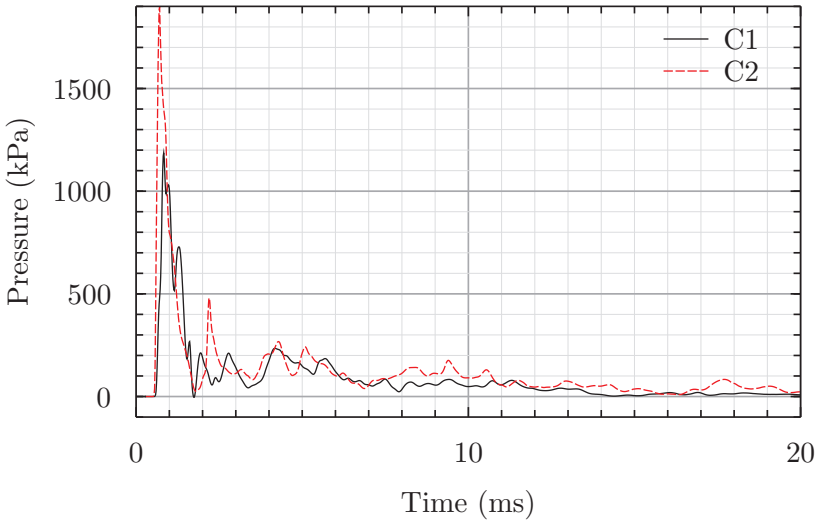

Figure I.1: Comparison of pressure time history data for passenger location 1, sensor 3, for cases C1 and C2

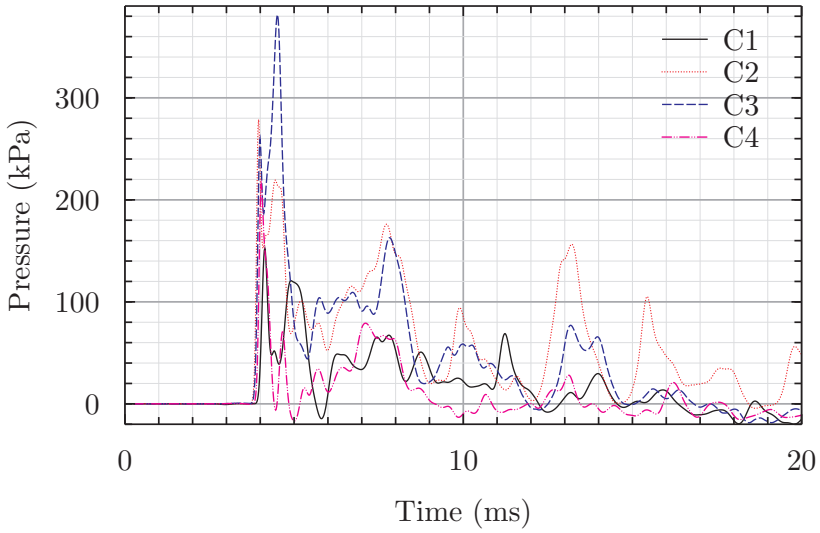

Figure I.2: Comparison of pressure time history data from the sensor facing the door (S3), for a passenger location by the door in C1 to C4

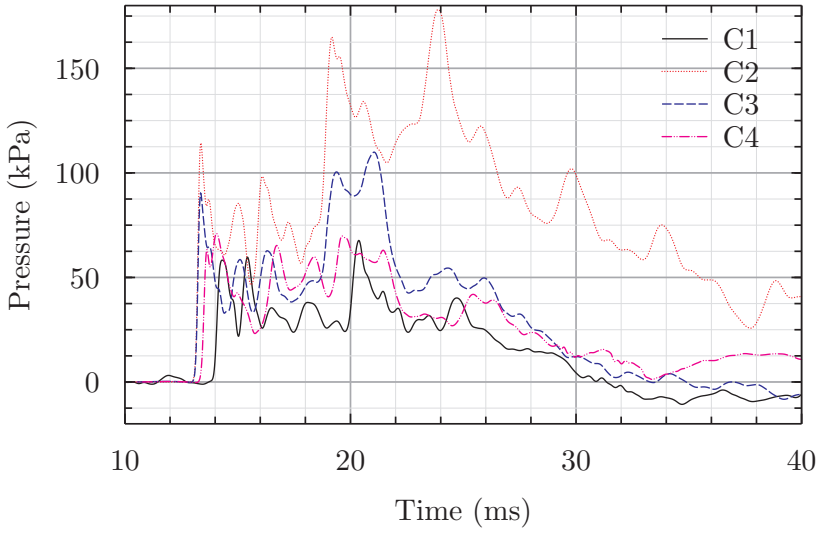

Figure I.3: Pressure history for S3 at location C in C1 to C4

I.2 C5 and C6

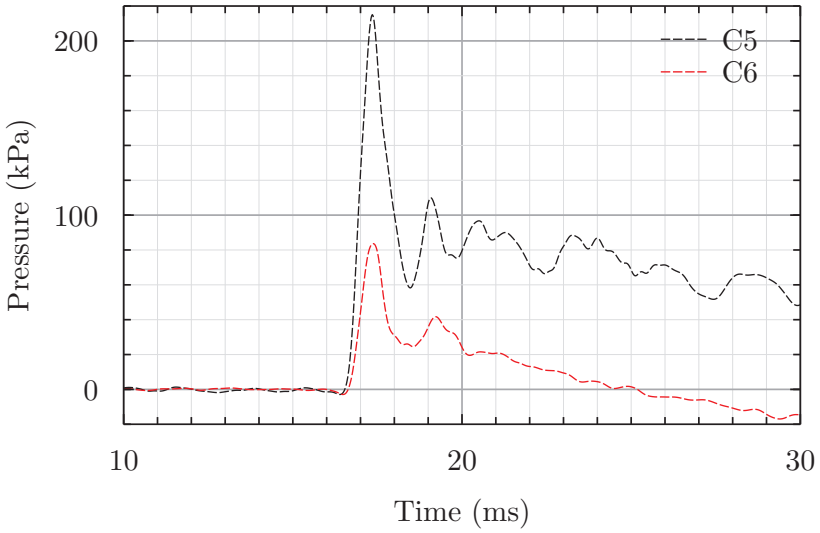

Figure I.4: Pressure history for S4 (facing vehicle end) at passenger 18 in C5 and C6

I.3 C1 and C7

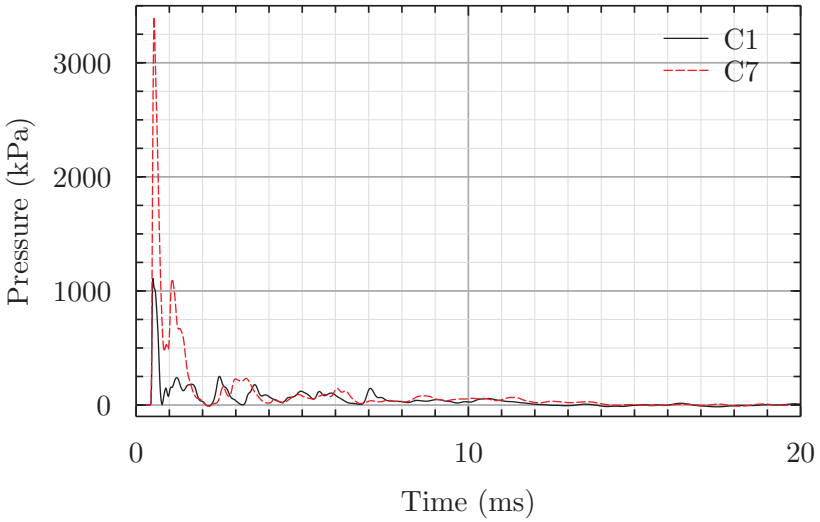

Figure I.5: Pressure history for passenger location 1 in C1 and C7, showing much higher pressures at S4 (facing seat) for C7 compared to C1

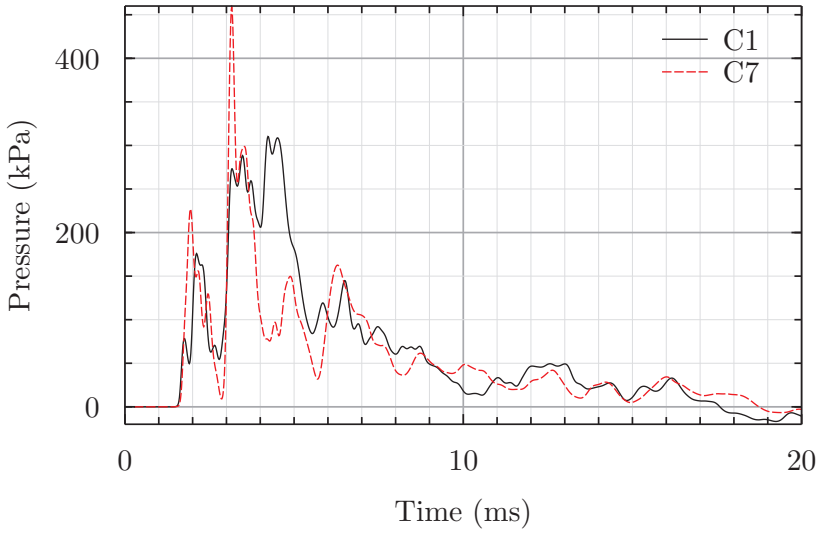

Figure I.6: Pressure history for passenger location 3 in C1 and C7, showing much higher pressures at S4 (facing seat) for C7 compared to C1

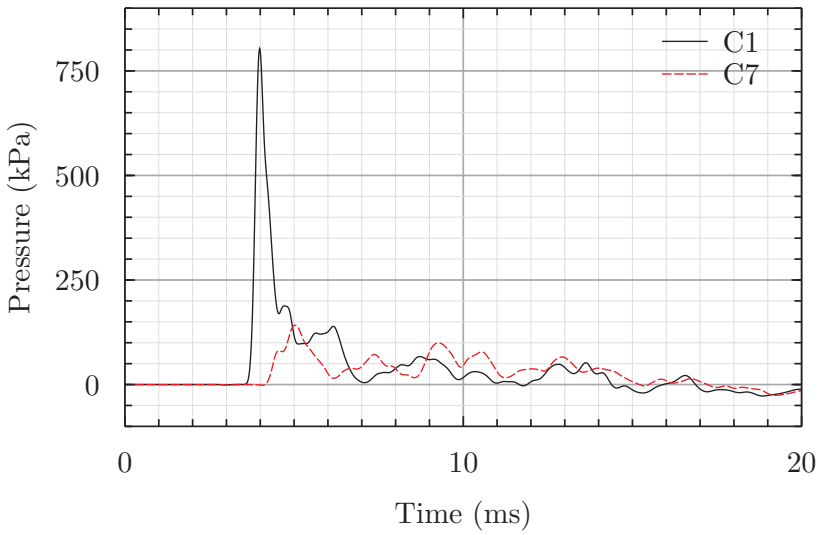

Figure I.7: Pressure history for S2 (facing draught screen) at passenger position 6, showing a significantly lower pressure in C7 compared to C1

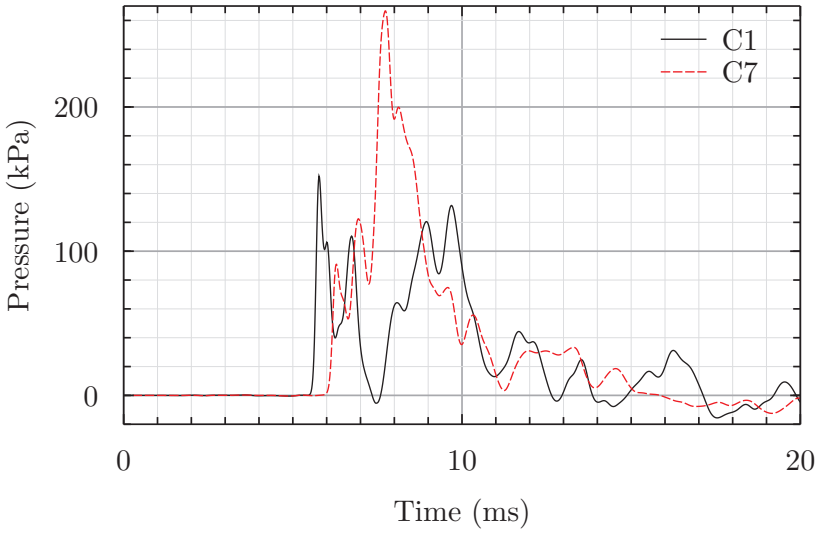

Figure I.8: Pressure history for S3 (facing vehicle bodyside) at passenger position 7, showing a significantly high reflected pressure in C7 compared to C1

I.4 Passenger density

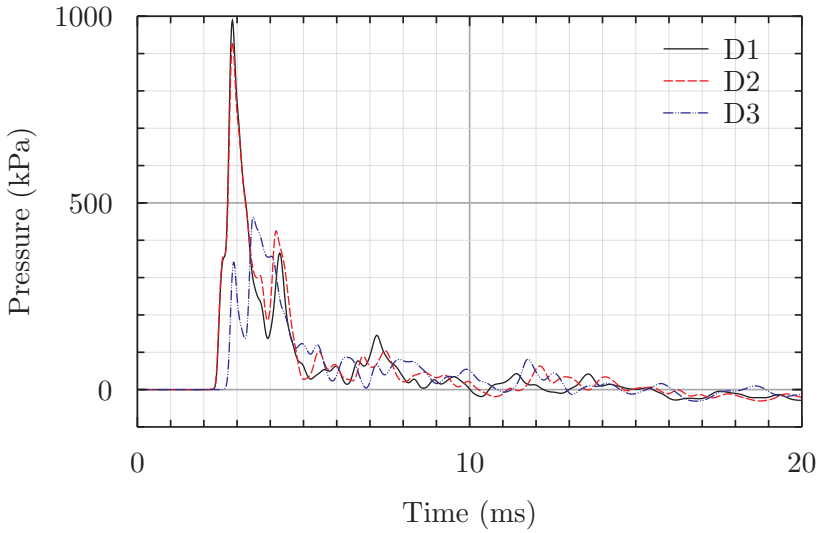

Figure I.9: Pressure time history for sensor location 2 (S2) at reference position A for 3 different passenger densities

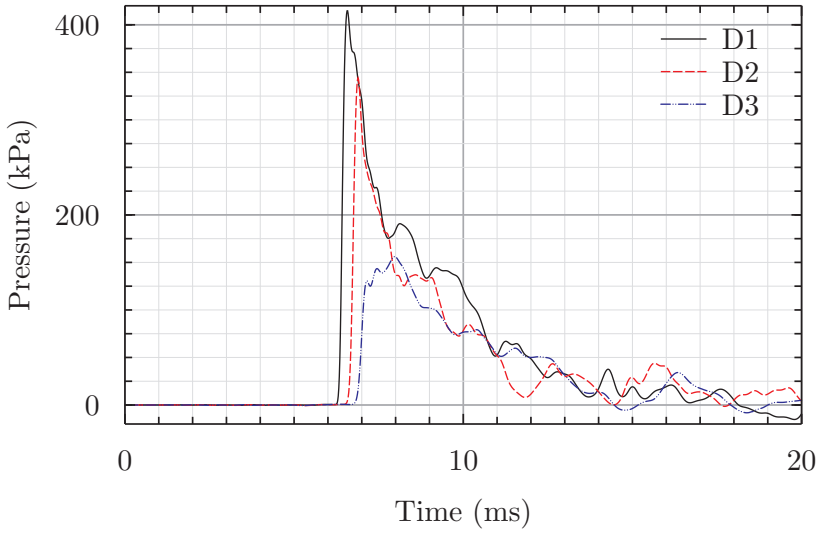

Figure I.10: Pressure time history for sensor location 2 (S2) at reference position B for 3 different passenger densities

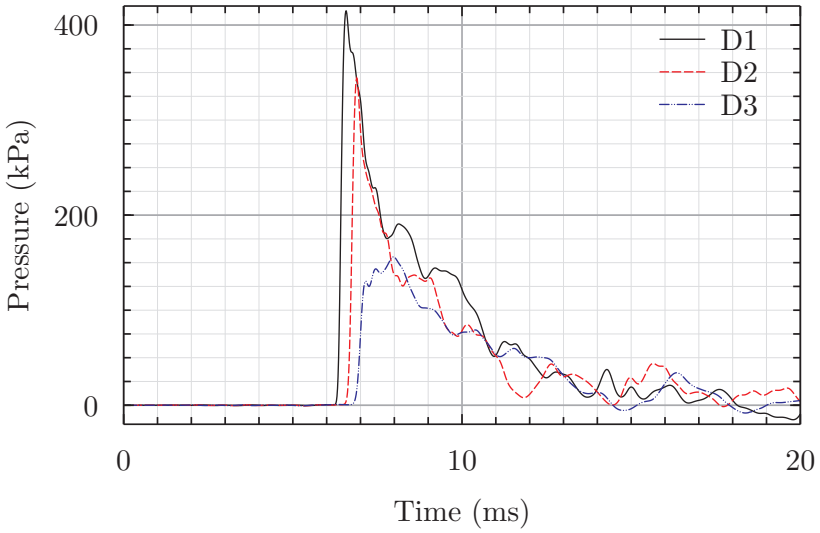

Figure I.11: Pressure time history for sensor location 2 (S2) at reference position C for 3 different passenger densities